The protracted magmatism and hydrothermal activity associated with the Gibraltar porphyry Cu-Mo deposit, south central British Columbia, Canada.

Christopher Kobylinski

A thesis submitted to the
University of Ottawa
In partial fulfillment of the requirements for the
M.Sc degree in Earth Sciences

Ottawa-Carlton Geoscience Centre
Faculty of Science
University of Ottawa

Abstract

The Gibraltar porphyry-Cu deposit is a large open pit porphyry Cu mine in Canada with the geological tonnage (production and reserves) of 3.2 Mt Cu. The Gibraltar deposit is hosted by the Granite Mountain Batholith (GMB), a tonalitic batholith with the surface exposure over 150 km^2. All rocks within the batholith are tonalites with minor quartz diorites. The batholith intrudes into mafic volcanoclastic rocks of the Nicola group in the Quesnel terrane of the Canadian Cordillera. The Cu mineralization at Gibraltar is confined to a small 4.5 km^2 area in the central part of the batholith and occurs primarily as disseminated chalcopyrite.

New U-Pb dating on zircon shows protracted late Triassic magmatism spanning ~25 m.y. for the formation of the GMB. Early magmatism is dated at 229.2±4.4 Ma in unmineralized tonalites. Later, at least three magmatism form the Cu mineralization during a period spanning from 218.9±3.1 Ma to 205.8±2.1 Ma. These fertile magmas form in a more mature arc setting, superseded early barren magmatic activity in a more juvenile arc setting for the bulk of the GMB. Epidote in the GMB shows compositional zoning with Fe-poor cores and Fe-rich rims. The zoning in the mineralized intrusions likely reflects changes in hydrothermal fluid, from S-rich to S-poor.

The data from the Gibraltar deposit shows that an economic porphyry Cu deposit may be found in igneous rocks with low Sr/Y in bulk rocks and low Eu/Eu* in zircon. In the Gibraltar deposit, Ce anomalies in zircon reflect oxidation conditions and are correlated with Cu resource associated with their respective intrusion.

Acknowledgments

Firstly, I would like to thank my thesis supervisor, Keiko Hattori. Without her continual patience, mentoring and support this project and thesis would not have been possible. My growth and a geoscientist at the University of Ottawa is due in no small part to her infinite patience and pushing me to undertake goals that only few years prior, I would have deemed impossible.

Secondly, I would also like to thank Alain Plouffe at the Geological Survey of Canada, for creating the Research Affiliate Program bursary. He is also thanked for mentoring throughout the project. This project was supported by the Targeted Geoscience Initiative Phase 5 project on Porphyry related mineral systems at Natural Resources of Canada, and Natural Science and Engineering Research Council of Canada Discovery Grant to KH. CHK acknowledges a Research Affiliate Program (RAP) bursary through the program.

I would like to thank Scott Smith who generously offered his time, knowledge and expertise to help with field work at the Gibraltar Mine. Additionally, I would like to thank Chris Gallagher at Gibraltar for his help with digital maps of the area.

I would also like to thank Jefferey H. Hedenquist for his continued advice, suggestions, encouragement and assistance with field work.

I would like to thank the LA-ICPMS team at the University of Ottawa. Samuel Morfin and Duane Petts were and continue to be a great help and resource for zircon analysis and age determinations. We also thank Glenn Poirier, of the University of Ottawa for his help with SEM and EPMA analysis of epidote.

I thank William Davis of the Geological Survey of Canada for his constructive thorough comments concerning the presentation of LA-ICPMS data. I would like to thank my friend Marc Morrison for his help with learning and implementing Python scripts to facilitate data reduction.

Finally, I would thank my girlfriend, Michelle Charron, for continuously believing and supporting me throughout this endeavor.

Table of Contents

CHAPTER 1.
Global Introduction

1.1 Preamble

Porphyry-type metal deposits are an important source of the world's Cu, Mo and Au. They contain over 60% of the Cu and over 90% of the world's Mo reserves (Sinclair, 2007). They occur in the root zones of stratovolcanoes, in subduction related continental or island arc settings. Porphyry deposits occur in orogen parallel belts hundreds or thousands of kilometers long during defined metalogenic epochs (exemplified by Andes and the Western Cordillera). Magmatic hydrothermal fluids released from cooling intrusions at shallow crustal levels interact with the intrusion and surrounding country rock to produce a variety of alteration. Typically, alteration includes an early proximal potassic alteration zone followed by an intermediate chlorite-sericite alteration zone, wrapped laterally by a propylitic alteration zone forming a typical telescoped pattern. Overprinting alteration is common. In some porphyry systems, much of the Cu can be contained in the sericitic zone. Mineralized intrusions have vertical extents from 2-4 km (Sillitoe, 2010).

Exploration for porphyry deposits includes examination of alteration haloes (e.g. large pyrite haloes), soil and stream sediment analysis, induced polarization and magnetic surveys (Sinclair, 2007). It is understood that porphyry-Cu deposits form in close association with highly oxidized intrusions (Ishihara, 1977; Sillitoe, 2010; Sun et al., 2013). This is attributed to the greater capacity of oxidized magma to dissolve sulfur as sulphate and transport it to shallower crustal levels (Hattori and Keith, 2001, Jugo et al., 2005). This suggests that oxidation conditions of intrusions can be used in exploration of yet undiscovered porphyry Cu deposit. One promising approach to determining oxidation conditions for porphyry intrusions uses zircon. Magmatic zircon is well known to be resistant to alteration and thus can provide information about the magmas from which it crystalizes. Many studies have used Ce anomalies in zircon as a proxy for magmatic oxidation conditions (Ballard et al., 2002; Shen et al., 2015; Hattori et al., 2017; Loader et al., 2017). Additionally, zircon can be recovered down streams and ice flow in sediments providing a vectoring tool.

Many porphyry deposits are also are associated with large intrusion or batholiths (Dilles, 1987; Villeneuve et al., 2001; Whalen et al., 2001; D'Angelo et al., 2017; Whalen et al., 2017) but the role of these batholiths is poorly understood. Another attribute to economic porphyry-Cu deposits is their high (>35) Sr/Y ratios, which is suggested to be related to elevated magmatic water contents (Loucks, 2014). Alteration minerals are also used in exploration for porphyry-Cu deposits. Epidote has been the subject of many studies regarding porphyry deposit exploration (Jago, 2008; Jago et al., 2014; Wilkinson et al., 2017; Cooke et al., 2014; Cooke et al., 2017) due to its robust nature (allowing it to survive fluvial transport and be recovered in outlying glacial till) and ability to incorporate many elements several of which show promise as pathfinders (light rare earth elements, Mn, Zn, Mo, Au, Sn, Tl, Pb, Th and U) (Jago et al., 2014). Additionally, epidote proximal to Cu-mineralization (1-2 km outside pyrite halos) has been shown to be produced by magmatic derived fluids as opposed to meteoric fluids (Cooke et al., 2014). Propylitic alteration generating epidote often has the largest footprint associated with a porphyry deposit (Sillitoe, 2010). The Gibraltar deposit provides a site to evaluate the relationship between the mineralization and the tonalitic Granite Mountain Batholith, test these fertility indicators and evaluate if zircons and epidote are potentially useful in exploration. Additionally, the Gibraltar deposit is located in a terrain variably covered in a layer of glacial till providing sample materials to identify porphyry Cu indicator minerals (Plouffe and Ferbey, 2015; Plouffe and Ferbey, 2017; Wolfe, 2017; Wolfe et al., 2017).

1.2 Research objectives

i. Establish a magmatic history for the formation of the Granite Mountain Batholith.
ii. Identify magmatism responsible for the Cu-mineralization of the Gibraltar deposit.
iii. Asses the usefulness of trace element analysis of magmatic zircon in evaluating fertility of magmas.
iv. Evaluate the applicability of fertility indicators for porphyry Cu deposits including bulk rock and zircon compositions.
v. Assess the origin of epidote spatially associated with the porphyry-Cu mineralization in the Gibraltar deposit.

1.3 Thesis outline

This thesis comprises 6 chapters, starting with a global introduction that includes a preamble, thesis objectives, statements of original contributions and a thesis outline. The last chapter gives a global summary of the thesis and conclusions.

Chapter 2 is the geological setting of the study area including the regional geology and the Granite Mountain batholith which hosts the Gibraltar porphyry Cu-Mo deposit.

Chapter 3 is a manuscript published as Geological Survey of Canada Open File Report 8025 in 2015. It presents the lithology of various phases of the GMB and characterizes various alteration assemblages. It describes the occurrence of epidote alteration and igneous and alteration mineralogy. This study documents chemical variations in epidote, titanite and rutile. Chapter 3 was moved to Appendix 8 since much of the interpretations and information within is in contradiction or has been proven obsolete by later chapters.

Chapter 4 is a manuscript published as Geological Survey of Canada Open File Report 8279 in 2016. It presents the compositional variation of epidote in the GMB and Nicola volcanic rock. All studied grains of epidote in the GMB was compositionally zoned, whereas those in the Nicola volcanic rocks are Fe rich with abundant mineral inclusions. This study shows REE-rich epidote and allanite in an area close <2km to open pits. An addendum was added after Chapter 4 addressing questions and concerns discussed during the defense of this thesis and discuss some of the interpretations made in the chapter.

Chapter 5 is a publication in preparation that uses trace element and U-Pb ages of zircon determined by LA-ICPMS. The chapter reports crystallization temperatures, Ce anomalies, Eu anomalies, fO_2 and the relationship between Ce^{4+}/Ce^{3+} and Cu mineralization. This manuscript was submitted to be considered for publication in Economic Geology in April 2019.

1.4 Previous Work relevant to the thesis project.

1.4.1 Previous study of zircon, oxidation conditions and porphyry-Cu deposits

Ballard et al. (2002) proposed the method to calculate Ce^{4+}/Ce^{3+} of zircon assuming the whole rock composition represented the parental melt. They reported REE concentrations in zircon from 14 barren and 7 ore bearing calk-alkaline intrusions from the Chuquicamata-El Abra

Cu belt in northern Chile. They found higher Ce^{4+}/Ce^{3} in zircon from ore bearing intrusions than those from 14 barren intrusions. They suggest that the ore bearing porphyries were more oxidized than the barren intrusions. These Ce^{4+}/Ce^{3+} ratios can then be used as a relative proxy for oxidation conditions of intrusions.

fO_2 values of magmas were calculated using Ce^{4+}/Ce^{3+} in zircon based on the calculation proposed by Smythe and Brennan (2016). Smythe and Brennan (2016) obtained the empirical equation based on the data of fO_2 and zircon compositions from three locations: The Bishop tuff (California, USA), Oba Tuff (Indonesia) and the Umiakovik pluton (Labrador, Canada).

Cerium anomalies in zircon are compared with the tonnage of porphyry copper deposits in the Central Asian Orogenic belt by Shen et al. (2015). They find that Ce^{4+}/Ce^{3+} from ore bearing intrusive rocks from porphyry-Cu are higher in intermediate (1.5- 4 Mt Cu) and large sized (>4 Mt Cu) porphyry compared to small sized (<1.5 Mt Cu) deposits and that Eu/Eu* in zircon generally follows this trend.

Cerium anomalies are examined for the Cerro Cerrona porphyr-Cu-Au deposit (0.9 Mt Cu) by Hattori et al. (2017). They find Ce^{4+}/Ce^{3+} ranging from 354 to 570 quartile values.

Lu et al. (2016) reported Ce/Nd, Eu/Eu* and CeNd/Y in zircon from various porphyry deposits in Iran and China and compared the values from barren rocks in USA and Australia. Unless otherwise noted, all resource and reserve figures for porphyry deposits in this thesis are from Singer et al. (2008).

1.4.2 Epidote associated with porphyry-Cu deposits

Epidote is a common alteration mineral around porphyry Cu deposits. Several studies show that epidote is associated with Cu mineralization. The Elatsite porphyry Cu deposit (1.37 MtCu), Bulgaria, shows local epidote-chlorite-quartz-carbonate alteration contemporaneous with the magnetite-bornite-chalcopyrite assemblage (Strashimiriov and Kanazirski, 2002 and references therein). The Qulong porphyry-Cu deposit (7.89 MtCu), Tibet, has reported Cu-mineralization in a Jurassic granite porphyry (182.3 Ma), characterized by abundant pyrite veins and quartz–sericite alteration locally with minor epidote alteration (Yang et al., 2009). Additionally, in the late Rongmucuola pluton (19.5 Ma) of the same deposit, epidote veins show many characteristics similar to the quartz - anhydrite-chalcopyrite ± molybdenite ± pyrite and quartz – molybdenite ± anhydrite ± chalcopyrite ± pyrite veins such as irregular to planar shape, occurring perpendicular to veins walls, and being superimposed by late feldspar-destructive alteration (phyllic alteration). They suggest that propylitic alteration may have formed simultaneously with biotite alteration (Yang et al., 2009). The Miduk porphyry Cu deposit (1.5 MtCu), Iran, shows strongly altered sections of syn-mineralization porphyry dykes that contain epidote (Boomeri et al., 2009).

Epidote has been suggested as a possible indicator mineral for porphyry-Cu deposits (Jago, 2008; Jago et al., 2014; Wilkinson et al., 2017; Cooke et al., 2014; Cooke et al., 2017). Cooke et al. (2014), found La in epidote is high in areas adjacent to the pyrite alteration halos for porphyry-Cu deposits in the Baguio district, Philippines. Jago et al. (2014), reported a decrease in REE fractionation and decreased LREEs in epidote moving away from the Mt Milligan porphyry-Cu deposit, Canada. Jago et al. (2014), studied pyrite associated with epidote and found that epidote and pyrite are enriched in similar elements such as Mn, Zn, Mo, La, Au, Sn, Tl, Pb, Th and U. Epidote associated with sulfides is able to incorporate elements from hydrothermal fluids.

References

Ballard, J R., Palin, M. J., and Campbell, I.H. 2002, Relative oxidation states of magmas inferred from Ce (IV)/Ce (III) in zircon: application to porphyry Cu deposits of northern Chile: Contributions to Mineralogy and Petrology, v. 144, p. 347-364.

Blundy, J., and Wood, B., 1994, Prediction of crystal–melt partition coefficients from elastic moduli: Nature, v. 372(6505), p. 452.

Boomeri, M., Nakashima, K., and Lentz, D. R., 2009, The Miduk porphyry Cu deposit, Kerman, Iran: A geochemical analysis of the potassic zone including halogen element systematics related to Cu mineralization processes: Journal of Geochemical Exploration, v. 103(1), p. 17-29.

Cooke, D. R., Baker, M., Hollings, P., Sweet, G., Chang, Z., Danyushevsky, L., and Inglis, S., 2014, New advances in detecting the distal geochemical footprints of porphyry systems—epidote mineral chemistry as a tool for vectoring and fertility assessments: SEG Special Publication Number 18, p. 127-152.

Cooke, D., Agnew, P., Hollings, P., Baker, M., Chang, Z., Wilkinson, J.,and Fox, N., 2017, Porphyry indicator minerals (PIMS) and porphyry vectoring and fertility tools (PVFTS)–

indicators of mineralization styles and recorders of hypogene geochemical dispersion halos: Confrence paper, Exploration 17: Sixth Decennial International Conference on Mineral Exploration, p. 67-77.

Dilles, J. H., 1987, Petrology of the Yerington Batholith, Nevada; evidence for evolution of porphyry Cu ore fluids: Economic Geology, v. 82(7), p. 1750-1789.

D'Angelo, M., Miguel, A., Hollings, P., Byrne, K., Piercey, S., and Creaser, R. A., 2017, Petrogenesis and Magmatic Evolution of the Guichon Creek Batholith: Highland Valley Porphyry Cu±(Mo) District, South-Central British Columbia: Economic Geology, v. 112(8), p. 1857-1888.

Ferry, J. M., & Watson, E. B., 2007, New thermodynamic models and revised calibrations for the Ti-in-zircon and Zr-in-rutile thermometers: Contributions to Mineralogy and Petrology, v. 154(4), p. 429-437.

Hattori, K. H., and Keith, J. D., 2001, Contribution of mafic melt to porphyry Cu mineralization: evidence from Mount Pinatubo, Philippines, and Bingham Canyon, Utah, USA: Mineralium Deposita, 36(8), p. 799-806.

Hattori, K. H., Wang, J., Baumgartner, R., Kobylinski, C. H., Morfin, S., and Shen, P., 2017. Zircon composition: indicator of fertile igneous rocks related to porphyry Cu deposits: Society for Geology Applied to Mineral Deposits (SGA) biennial meeting, Quebec City, Canada extended abstracts, vol. 1, p 295 -298

Ishihara, S., 1977, The magnetite-series and ilmenite-series granitic rocks: Mining Geology, v. 27(145), p. 293-305.

Jago, C. P., 2008, Metal-and alteration-zoning, and hydrothermal flowpaths at the moderately-tilted, silica-saturated Mt. Milligan Cu-gold alkalic porphyry deposit: Unpublished PhD thesis, University of British Columbia, 210p.

Jago, C. P., Tosdal, R. M., Cooke, D. R., and Harris, A. C., 2014, Vertical and lateral variation of mineralogy and chemistry in the Early Jurassic Mt. Milligan alkalic porphyry Au-Cu deposit, British Columbia, Canada: Economic Geology, v. 109(4), p. 1005-1033.

Jugo, P., Luth, R. and Richards, J., 2005, Experimental data on the speciation of sulfur as a function of oxygen fugacity in basaltic melt: Geochimica Cosmochimica Acta, v. 69, p. 497–503.

Loader, M. A., Wilkinson, J. J., and Armstrong, R. N., 2017, The effect of titanite crystallization on Eu and Ce anomalies in zircon and its implications for the assessment of porphyry Cu deposit fertility: Earth and Planetary Science Letters, v. 472, p. 107-119.

Loucks, R. R. 2014, Distinctive composition of Cu-ore-forming arc magmas: Australian Journal of Earth Sciences, v. 61(1), p. 5-16.

Plouffe, A., and Ferbey, T., 2015, Till composition near Cu-porphyry deposits in British Columbia: Highlights for mineral exploration: TGI 4 - Intrusion Related Mineralization Project: New Vectors to Buried Porphyry-Style Mineralization. Geological Survey of Canada, Open File 7843, p. 15-37.

Plouffe, A. and Ferbey, T., 2017, Porphyry Cu indicator minerals in till: A method to discover buried mineralization: Indicator Minerals in Till and Stream Sediments of the Canadian Cordillera, (eds.) T. Ferbey, A. Plouffe, and A. Hickin; Mineral Association of Canada, Topics in Mineral Sciences Volume 47, Geological Association of Canada, Special Paper 50, p. 129-159.

Shen, P., Hattori, K., Pan, H., Jackson, S., and Seitmuratova, E., 2015, Oxidation condition and metal fertility of granitic magmas: Zircon trace-element data from porphyry Cu deposits in the Central Asian Orogenic Belt: Economic Geology, v. 110(7), p. 1861-1878.

Sillitoe, R. H., 2010, Porphyry Cu systems: Economic geology, v. 105(1), p. 3-41.

Smythe, D. J., and Brenan, J. M., 2016, Magmatic oxygen fugacity estimated using zircon-melt partitioning of cerium: Earth and Planetary Science Letters, v. 453, p. 260-266.

Sinclair, W. D., 2007, Porphyry deposits. Mineral deposits of Canada: A synthesis of major deposit-types, district metallogeny, the evolution of geological provinces, and exploration methods: Geological Association of Canada, Mineral Deposits Division, Special Publication, v. 5, 223-243.

Strashimirov, S., Petrunov, R., and Kanazirski, M., 2002, Porphyry-Cu mineralisation in the central Srednogorie zone, Bulgaria: Mineralium deposita, v. 37(6-7), p. 587-598.

Sun, W. D., Liang, H. Y., Ling, M. X., Zhan, M. Z., Ding, X., Zhang, H., and Fan, W. M., 2013, The link between reduced porphyry Cu deposits and oxidized magmas: Geochimica et Cosmochimica Acta, v. 103, p. 263-275.

Whalen, J. B., Anderson, R. G., Struik, L. C., and Villeneuve, M. E., 2001, Geochemistry and Nd isotopes of the François Lake plutonic suite, Endako batholith: host and progenitor to the Endako Mo camp, central British Columbia: Canadian Journal of Earth Sciences, v. 38(4), p. 603-618.

Whalen, J.B., Davis, W.J. and Anderson, R.A., 2017, Temporal and geochemical evolution of the Guichon Creek Batholith and Highland Valley porphyry Cu district, British Columbia: Implications for generation and tectonic setting of porphyry systems: Geological Survey of Canada, Open File 8334, 46p.

Wilkinson, J. J., Baker, M. J., Cooke, D. R., Wilkinson, C. C., and Inglis, S., 2017, Exploration targeting in porphyry Cu systems using propylitic mineral chemistry: a case study of the El Teniente deposit, Chile. Proceedings of the 14th SGA Biennial Meeting: Mineral Resources to Discover, 20-23 August 2017, Quebec City, Canada, pp. 1112-1114.

Wolf, L., 2017, Chemistry of refractory indicator minerals in tills around the Gibraltar porphyry Cu deposit, southcentral British Columbia; unpublished B.Sc. thesis, University of Ottawa, Ottawa, 56 p.

Wolf, L., Hattori, K., and Plouffe, A., 2017, Glacial dispersal of refractory minerals from the Gibraltar porphyry Cu deposit, south central British Columbia, Canada: Geological Survey of Canada, Scientific Presentation 73, https://doi.org/10.4095/30582

Yang, Z., Hou, Z., White, N. C., Chang, Z., Li, Z., and Song, Y., 2009, Geology of the post-collisional porphyry Cu–Mo deposit at Qulong, Tibet: Ore Geology Reviews, v. 36(1-3), p. 133-159.

1.5 Statement of the Author's Contribution

This thesis combines original research conducted by Christopher H. Kobylinski under the supervision of Professor Keiko Hattori at the University of Ottawa. The following outlines the contribution of the author and collaborators to each chapter.

Chapter 3. Epidote associated with the porphyry Cu-Mo mineralization at the Gibraltar deposit, south-central British Columbia

C.H. Kobylinski, K. Hattori, A. Plouffe, and S.W. Smith

Contributions:

- C. H. Kobylinski wrote the chapter and produced all figures and tables
- Field work in the summer of 2015 and 2016 was assisted by J. Hedenquist and K. Hattori
- Thin and thick section preparation by George Masrek and Alain Mauviel at the University of Ottawa
- C. H. Kobylinski conducted petrographic studies on thin sections
- C. H. Kobylinski conducted scanning electron microscope (SEM) work with the assistance of Glenn Poirier at the University of Ottawa
- C. H. Kobylinski conducted electron probe micro-analyzer (EPMA) work with the assistance of Glenn Poirier at the University of Ottawa
- K. Hattori and A. Plouffe edited and reviewed the manuscript
- C. H. Kobylinski acted as the corresponding author during the submission and review process

Various aspects of the report were published in meeting abstracts and presented orally or by poster and are listed in Appendices 4 and 5.

Chapter 4. Protracted island arc magmatism at the Gibraltar porphyry Cu-Mo deposit, British Columbia: U-Pb ages and trace element geochemistry of zircon

C.H. Kobylinski, K. Hattori, A. Plouffe, and S.W. Smith

Contributions:

- C. H. Kobylinski wrote the chapter and produced all figures and tables
- Field work in the summer of 2015 and 2016 was assisted by J. Hedenquist and K. Hattori.
- Separating, mounting and polishing of zircon grains into epoxy resin by C. H. Kobylinski
- C. H. Kobylinski conducted laser ablation inductively coupled plasma mass spectrometry (LA-ICPMS) at the University of Ottawa with the assistance of Samuel Morfin and Duane Petts. C. H. Kobylinski conducted data reduction.
- K. Hattori, J. Hedenquist and A. Plouffe edited and reviewed the manuscript and provided valuable comments.
- C. H. Kobylinski acted as the corresponding author during the submission and review process

Various aspects of the report were published in meeting abstracts and presented orally or by poster and are listed in Appendix 4 and 5.

Appendix 8. Report on the composition and assemblage of minerals associated with the porphyry Cu-Mo mineralization at the Gibraltar deposit, south central British Columbia, Canada

C.H. Kobylinski, K. Hattori, S.W Smith and A. Plouffe

Contributions:

- Field work in the summer of 2015 was assisted by J. Hedenquist and K. Hattori
- Hand sample preparation conducted by C. H. Kobylinski
- Thin and thick section preparation conducted by George Masrek (Teaching and Rock Preparation Laboratory Technician) Alain Mauviel (Teaching and Rock Preparation Laboratory Technician) at the University of Ottawa
- C. H. Kobylinski wrote the chapter and produced all figures and tables
- C. H. Kobylinski conducted petrographic studies on thin sections at the University of Ottawa
- C. H. Kobylinski conducted Scanning electron microscope (SEM) work with the assistance of Glenn Poirier (lab manager) at the University of Ottawa
- K. Hattori and A. Plouffe edited and reviewed the manuscript
- C. H. Kobylinski acted as the corresponding author during the submission and review process

Various aspects of the report were published in meeting abstracts and presented orally or by poster and are listed in in Appendix 4 and 5.

CHAPTER 2.

Geological setting of the study area

2.1 Regional Geology

The Quesnel terrane in the Canadian Cordillera is the host of the Gibraltar porphyry-Cu-Mo deposit (Fig. 2.1). The Quesnel terrane, a volcanic arc terrane, extends along the length of the Canadian Cordillera from central Yukon to the southern limit of British Columbia (Colpron and Nelson, 2011; Fig. 2.1). The terrane is mainly characterized by Middle to Upper Triassic mafic volcanoclastic rocks of the Nicola Group, together with Late Triassic to Early Jurassic calcalkaline and alkaline intrusions (Schiarizza, 2015). The Quesnel terrane is bounded by the oceanic Slide Mountain terrane to the east and the oceanic Cache Creek terrane to the west (Schiarizza, 2015). In the southern Quesnel terrane, intrusive rocks form four linear belts of alternating calc-alkaline and alkaline plutons, younging to the east (Fig. 2.1).

The Quesnel terrane is an allochthon formed as an oceanic arc and accreted to the North American continent from 180 to 150 Ma (Ghosh, 1995, and references therein). The Cache Creek terrane is comprised of Paleozoic to early Mesozoic carbonate rocks which are also an allochthon, accreted to the North American continent during the Mesozoic (Johnston and Borel, 2007). The GMB intrudes the Nicola mafic volcaniclastics of the Quesnel terrane. The GMB is juxtaposed against the Cache Creek rocks leading to a debate over which terrane the GMB belongs (Ash et al., 1999a, b).

The Canadian Cordillera has undergone several glaciation events. The most recent in the study area is the Late Wisconsin Fraser Glaciation (Clague and Ward, 2011). The majority of the landscape surrounding the GMB is covered in a variably thick layer of glacial till (Plouffe and Ferbey, 2015). Only near the Gibraltar Mine have three major paleo ice movement directions been identified during Late Wisconsin Fraser Glaciation.

2.2 Porphyry Copper deposits in the Quesnel terrane

The Quesnel terrane is an important metallogenic province, containing over 19 past- and present-producing mines of porphyry Cu±Mo±Au deposits in Mesozoic granitic intrusions (Fig. 2.1). In the vicinity of the study area there are several significant porphyry Cu deposits; the Highland Valley Copper deposit (3.6 Mt Cu), Mount Polley deposit (0.6 Mt Cu) (Fig. 2.1), and the Woodjam porphyry-Cu prospect (0.71 Mt Cu).

The Highland Valley Copper (HVC) deposit is the largest open pit mine in Canada as of 2019 and is located 235 km south east of the Gibraltar deposit. It is hosted by five mineralized intrusions and shows two barren precursor intrusions. The HVC deposit consists of granodiorites and granites and some porphyritic rocks.

The Mount Polly deposit also intrudes the mafic volcaniclastic rocks of the Nicola Group as multiphase intrusions consisting of syenite, diorite, and monzodiorite with comparable timing to the Gibraltar deposit at ~ 205 Ma (Hodgson et al. 1976; Fraser et al. 1993, 1995; Rees, 2013).

The Woodjam porphyry-Cu prospect intrudes the Nicola volcanoclastic rocks as multiple Jurassic monzonite and syenite intrusions. These intrusions are components of the mostly barren composite calcalkalic Takomkane Batholith. Mineralization and alteration style indicate that these intrusions within the Woodjam porphyry-Cu prospect are likely related (Del Real et al., 2012).

2.3 Geology of the Granite Mountain Batholith

The Gibraltar deposit was first mapped by Tipper (1959, 1978) and the GMB was mapped by Panteleyev (1978) and Ash et al. (1999a and b). Detailed studies on the geology and mineralization of the Gibraltar deposits were conducted by Sutherland Brown (1958, 1967, 1973), Eastwood (1970), Simpson (1970), Drummond et al. (1973, 1976), Bysouth et al. (1995), Raffle (1999), Ash and Riveros (2001), Oliver et al. (2009), Harding (2012), van Straaten et al. (2013), and Mostaghimi et al. (2014). A more recent study on the geological setting of the GMB by Schiarizza (2014, 2015 and references therein) divided the GMB into 4 phases based on differences in primary mineralogy and textures. The phases use the terminology of Bysouth et al. (1995). They are from south west to north east: Border phase, Mine phase, Granite Mountain Phase and Burgess Creek stock (Fig. 2.2).

Border phase: The majority of the Border phase is quartz diorite that grades locally into tonalites and diorites. It consists of white mica altered plagioclase and 25-40% chloritized hornblende and 2-15% quartz. Textures are equigranular, typically weakly to strongly foliated, and rarely isotropic (Schiarizza, 2014).

Mine phase: North east of the Border phase is the Mine phase, which hosts the Gibraltar deposit. It comprises medium to coarse-grained, equigranular, isotropic to well-foliated tonalite, commonly with 15-25% chloritized mafic minerals and 25-30% quartz, together with sericitized plagioclase and epidote.

Granite Mountain phase: This phase comprises more than 50% of the volume of the GMB (Fig. 2.2). It is a coarse grained leucocratic tonalite with approximately equal parts plagioclase and quartz (Schiarizza, 2014). It commonly contains unaltered mafics (hornblende and biotite) and is the least altered phase of the GMB.

Burgess Creek stock: Comprised of a heterogeneous assemblage of tonalites, quartz diorites and diorites that intrude the Nicola group volcanoclastics (Schiarizza, 2014). There still is some debate as to the relationships of the Burgess Creek stock to the GMB. Previous U-Pb dating showed it to be 4-5 Ma older than the Granite Mountain phase of the GMB and interpreted to be separate from the batholith. Ages from this thesis put it in the range of the GMB.

We follow this classification in the reports comprising Chapters 3 and 4. Subsequently, it became obvious that the distribution of these phases was not well defined. Therefore, we use the simplified terms of mineralized tonalites and unmineralized tonalites for the subdivision of the GMB in the introduction (Chapter 1), summary (Chapter 6) and the manuscript comprising Chapter 5.

2.4 Cu-Mo mineralization, and hydrothermal alteration in the GMB

Cu mineralization at Gibraltar occurs primarily as disseminated chalcopyrite in foliated tonalites in the central part of the GMB. Cu content of rocks show several separate mineralized zones focused in the central part of the GMB. The largest ones are located around the Pollyanna, Gibraltar East and Granite Lake pits. There are several other isolated mineralized areas; 100m east and 200m north east of the Granite Lake pit, ~500m east and 500m north east of the Granite Lake pit, and 200m north west of the Gibraltar East pit. Cu-mineralization is vertically continuous forming chimney-like distribution of high Cu rocks. Such “chimneys” at the Granite Lake pit and Pollyanna are over 500 m to 1000 m in height. Molybdenite is not abundant and occurs as dissemination and in quartz veins.

Hydrothermal alteration is pervasive in proximity to the mineralization as revealed in the mine pits. Alteration minerals include quartz, secondary K-feldspar, secondary biotite after hornblende, rutile and titanite in chloritized biotite, epidote after plagioclase and hornblende, and chlorite replacing biotite and hornblende.

Quartz forms veins and veinlets with chalcopyrite ±chlorite ±magnetite ± epidote in mineralized intrusions. Mono-minerallic quartz veins are rare but occur in mineralized samples. Quartz veins are commonly surrounded by haloes of white mica.

Potassic alteration, forming secondary K-feldspar and secondary biotite, is only recognized in thin section from samples proximal (<1.1 km) to and within mine pits. K-feldspar grains are commonly replaced by a mixture of white mica and minor epidote and secondary biotite is recognized as aggregates of fine-grained biotite replacing hornblende crystals. Secondary biotite is extensively overprinted by chlorite. White mica is ubiquitous and prominent in hand specimens up to 2.5 km from the mine pits. White mica replaces plagioclase and forms mono-mineralic veinlets. Its abundance decreases with distance from the open pits. Potassic and white mica alteration show overlapping distribution, proximal (< 1.1 km for potassic, <2.5 km for white mica) to the mine pits.

Titanite and rutile also occur as alteration minerals of biotite, forming small aggregates with chlorite.

Epidote is common in the GMB. Its abundance increases with increasing distance from mine pit. It replaces plagioclase, and forms aggregates and veins/veinlets with or without quartz. The occurrence of epidote gives a lime-green color to the white tonalitic rocks and is observed even 10 km from the mine pits in the margins of the GMB.

Chlorite is common throughout the GMB. In mineralized intrusions, it replaces mafic minerals. It is also common rimming these mafic minerals in unmineralized intrusions.

2.5 Dating of the GMB by previous workers

The U-Pb zircon ages are summarized in Schiarizza (2014). Two samples from the Burgess Creek stock have been dated by Sensitive High-Resolution Ion Microprobe (SHRIMP) and produced ages of 222.71±0.22 and 221.25±0.2 Ma. The north east edge of the Granite Mountain Phase has been dated using SHRIMP at 217.15±0.2 Ma (Richard Friedman, cited by Schiarizza, 2014).

One U-Pb age date has been reported for the Mine phase tonalite 211.9±4.3 Ma using LA-ICPMS (Oliver et al., 2009).

Harding (2012) reported Re-Os ages of molybdenite from three quartz-molybdenite veins in the Granite Lake and East pits: 215±1 Ma, 212.7±0.9 Ma, 210.01±0.9 Ma. These are interpreted to be contemporaneous with timing of Cu mineralization at Gibraltar.

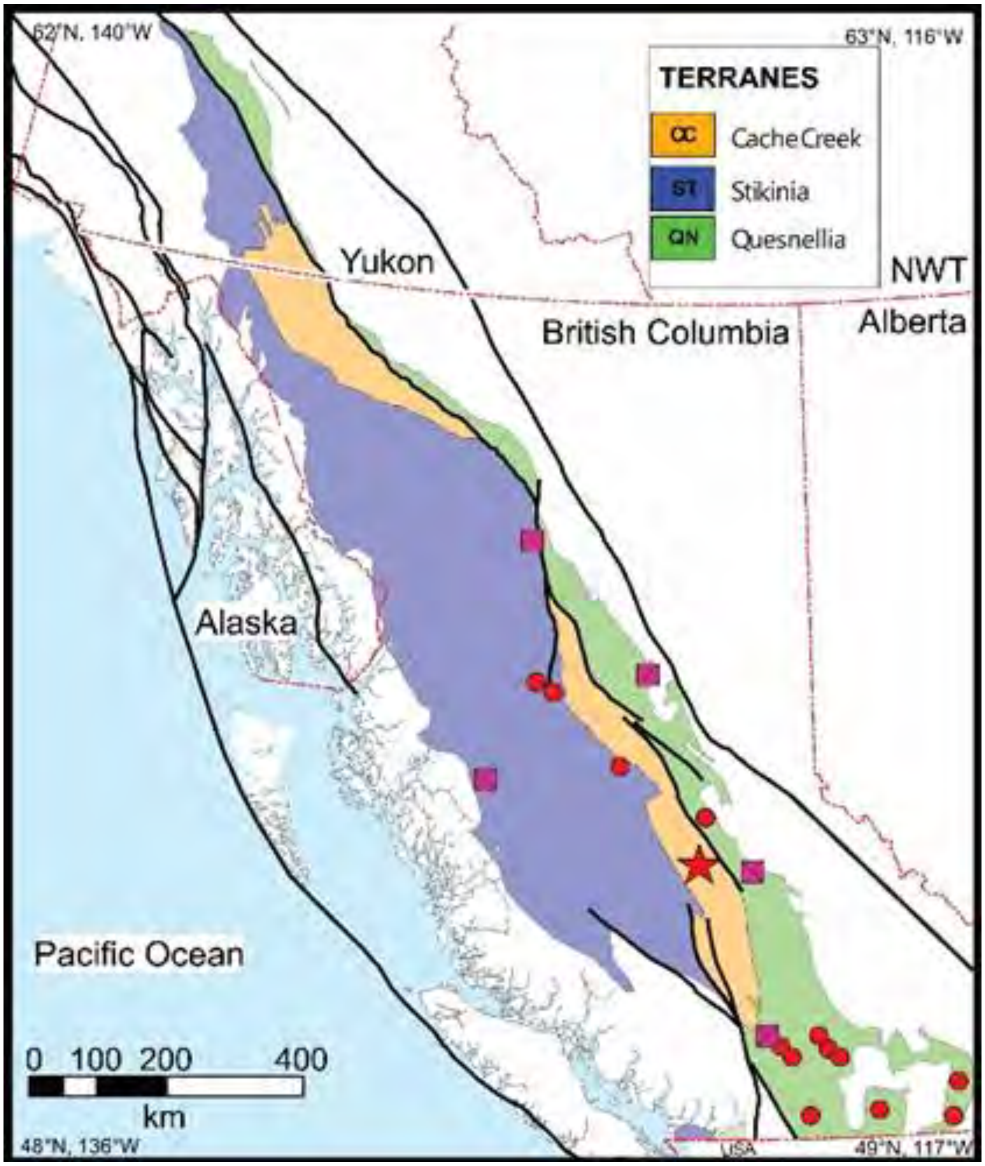

Figure 2.1: Simplified geological map of the northern Cordillera of British Columbia, Canada, modified after Nelson and Colpron (2011). The red star indicates the location of the Gibraltar porphyry Cu mine. Other porphyry Cu deposits are shown as pink squares with crosses (currently producing mine) and red circles (past producing mine).

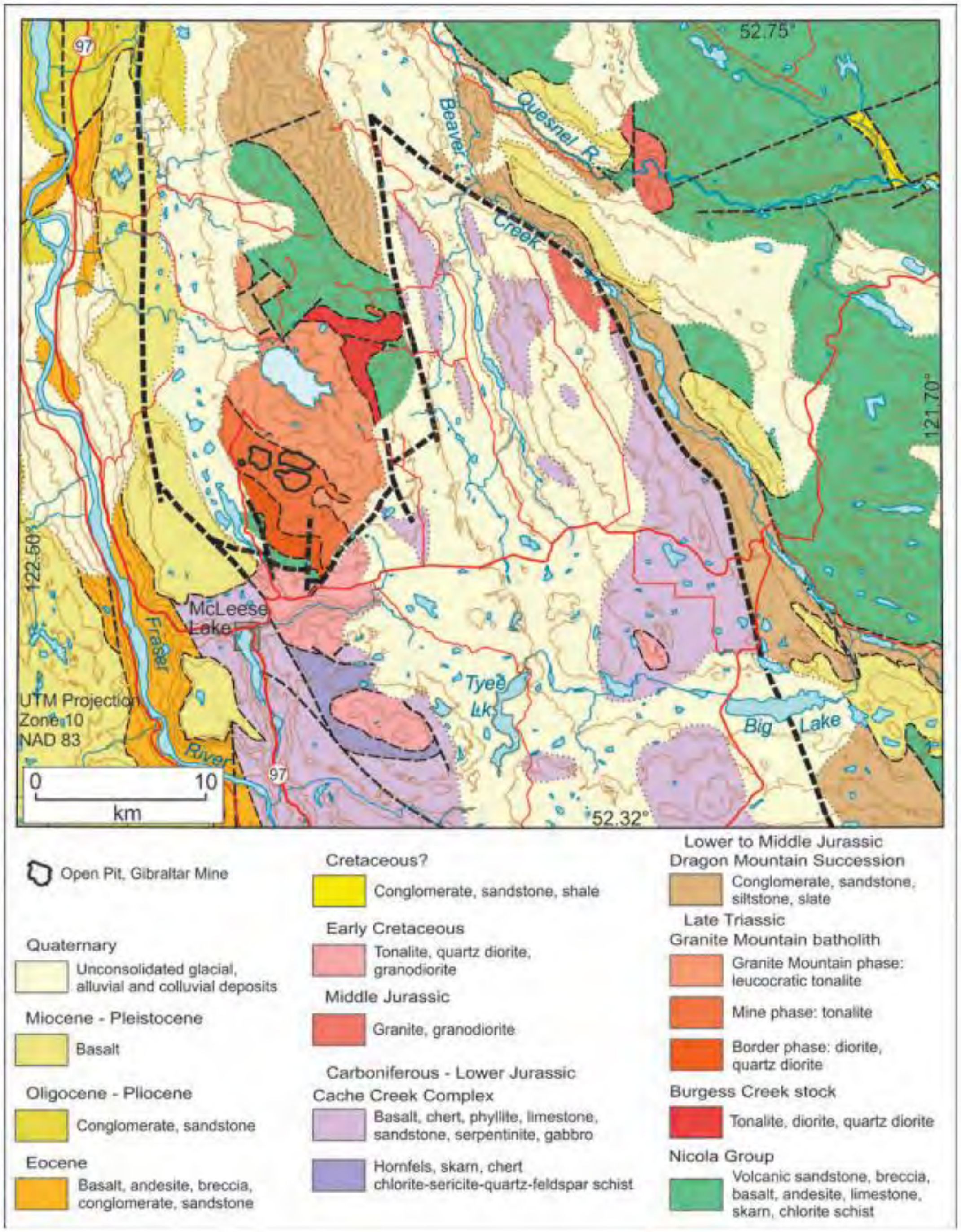

Figure 2.2: Geological map of the Gibraltar deposit, GMB and surrounding area. After Schiarizza (2014).

References

Ash, C.H.., Panteleyev, A., MacLellan, K.L., Payne, C.W., and Rydman, M.O., 1999a, Geology of the Gibraltar Mine area (93B/6&9): British Columbia Ministry of Energy and Mines, Open File 1999-7, scale 1:50,000.

Ash, C.H., Panteleyev, A., MacLennan, K.L., Payne, C.W., and Rydman, M.O., 1999b, Geology of the Gibraltar mine area (93B/8,9): British Columbia Ministry of Energy and Mines, British Columbia Geological Survey Open File 1999-7; scale 1:50 000.

Ash, C.H., and Riveros, C.P., 2001, Geology of the Gibraltar Cu-molybdenite deposit, east-central British Columbia (93B/9): Geological Fieldwork 2000. British Columbia Ministry of Energy and Mines, Victoria, Paper. 1, p. 119-134.

Bysouth, G.D., Campbell, K.V., Barker, G.E., and Gagnier, G.K., 1995, Tonalite-trondhjemite fractionation of peraluminous magma and the formation of syntectonic porphyry Cu mineralization, Gibraltar mine, central British Columbia: Schroeter, T.G. (Ed.), Porphyry deposits of the northwestern cordillera of North America, Canadian Institute of Mining, Metallurgy and Petroleum, Special Volume 46, p. 201-213.

Clague, J. J., and Ward, B., 2011, Pleistocene glaciation of British Columbia: Developments in Quaternary Sciences v. 15, p. 563-573.

Colpron, M. and Nelson, J.L., 2011, A Digital Atlas of Terranes for the Northern Cordillera: BC GeoFile 2011- 11.

Del Real, I., Hart, C. J. R., Bouzari, F., Blackwell, J. L., Rainbow, A., Sherlock, R., and Skinner, T., 2012, Paragenesis and alteration of the Southeast Zone and Deerhorn porphyry deposits, Woodjam property, central British Columbia (parts of 093A). Geoscience BC Summary of Activities, 2013-1.

Drummond, A.D., Tennant, S.J., and Young, R.J., 1973, The interrelationship of regional metamorphism, hydrothermal alteration and mineralization at the Gibraltar Mines Cu deposit in B.C: Canadian Institute of Mining and Metallurgy Bulletin, v. 66, p. 48-55.

Drummond, A.D., Sutherland Brown, A., Young, R.J., and Tennant, S.J., 1976, Gibraltar – regional metamorphism, mineralization, hydrothermal alteration and structural development: Sutherland Brown, A. (Ed.), Porphyry deposits of the Canadian Cordillera, Canadian Institute of Mining and Metallurgy, Special Volume 15, p. 195-205.

Eastwood, G.E.P., 1970, McLeese Lake: Geology of the Granite Mountain stock: Geology, Exploration and Mining in British Columbia 1969, British Columbia Department of Mines and Petroleum Resources, p. 162-172.

Fraser, T.M., Godwin, C.I., Thompson, J.F.H. and Stanley, C.R., 1993, Geology and alteration of the Mount Polley alkalic porphyry copper-gold deposit, British Columbia (93A/12): Grant, M. & Newell, J. M. (eds) Geological Fieldwork 1992, British Columbia Ministry of Energy and Mines, Victoria, Paper 1993-1, p. 295–300.

Fraser, T.M., Stanley, C.R., Nikic, Z.T., Pesalj, R. and Gorc, D. 1995, The Mount Polley alkalic porphyry copper-gold deposit, south-central British Columbia: Schroeter, T.G (ed.) Porphyry Deposits of the Northwestern Cordillera of North America. CIM Special v. 46, p. 609–622.

Ghosh, D.K., 1995, Nd–Sr isotopic constraints on the interactions of the Intermontane Superterrane with the western edge of North America in the southern Canadian Cordillera: Canadian Journal of Earth Sciences, v. 32, p. 1740–1758.

Harding, B., 2012, The characterization of Mo mineralization at the Gibraltar mines Cu-Mo porphyry, central British Columbia: B. Sc. thesis, Kingston, Canada, Queen's University, 52p.

Hodgson, C.J., Bailes, R.J. and Verzosa, R.S., 1976, Cariboo-Bell: Sutherland Brown, A. (ed.) Porphyry Deposits of the Canadian Cordillera. Canadian Institute of Mining and Metallurgy, Special v. 15, p. 388–396.

Johnston, S. T., and Borel, G. D., 2007, The odyssey of the Cache Creek terrane, Canadian Cordillera: Implications for accretionary orogens, tectonic setting of Panthalassa, the Pacific superwell, and break-up of Pangea: Earth and Planetary Science Letters, v. 253(3-4), p. 415-428.

Logan, J.M., Schiarizza, P., Struik, L.C., Barnett, C., Nelson, J.L., Kowalczyk, P., Ferri, F., Mihalynuk, M.G., Thomas, M.D., Gammon, P., Lett, R., Jackaman, W., and Ferbey, T., 2010, Bedrock geology of the QUEST map area, central British Columbia: British Columbia Ministry of Energy, Mines and Petroleum Resources, British Columbia Geological Survey Geoscience Map 2010-1; scale 1:500 000 (also Geoscience BC, Report 2010-5; Geological Survey of Canada, Open File 6476).

Mostaghimi, N., Kennedy, L.A., and Gabites, J., 2014, Geological setting, structural geology and timing of deformation at the Gibraltar Cu-Mo porphyry deposit, Cariboo region, British Columbia: Geological Society of America, Abstracts with Programs, v. 46-6, p. 588

Oliver, J., Crozier, J., Kamionko, M., and Fleming, J., 2009, The Gibraltar Mine, British Columbia. A billion tonne deep Cu-Mo porphyry system: structural style, patterns of mineralization and rock alteration: Association for Mineral Exploration British Columbia, 2009 Mineral Exploration Roundup, Vancouver, Canada, Abstracts, p. 35-36.

Panteleyev, A., 1978, Granite Mountain project (93B/8): Geological Fieldwork 1977, British Columbia Ministry of Energy, Mines and Petroleum Resources, British Columbia Geological Survey Paper, 1977-1, p. 39-42.

Plouffe, A., and Ferbey, T,. 2015, Till composition near Cu-porphyry deposits in British Columbia: Highlights for mineral exploration: TGI 4 - Intrusion Related Mineralization Project: New Vectors to Buried Porphyry-Style Mineralization. Geological Survey of Canada, Open File 7843, p. 15-37.

Plouffe, A. and Ferbey, T., 2017, Porphyry Cu indicator minerals in till: A method to discover buried mineralization: Indicator Minerals in Till and Stream Sediments of the Canadian Cordillera, (eds.) T. Ferbey, A. Plouffe, and A. Hickin; Mineral Association of Canada, Topics in Mineral Sciences Volume 47, Geological Association of Canada, Special Paper 50, p. 129-159.

Raffle, K.J., 1999, Structure, deformation and element mobility of the Gibraltar Cu-Mo Mine, south-central British Columbia: B.Sc. thesis, The University of British Columbia, 58p.

Rees, C., 2013, The Mount Polley Cu-Au porphyry deposit, south-central British Columbia, Canada: Logan, J.S. (ed.) 2013 Society of Economic Geologists. Whistler, British Columbia, p. 67–98.

Schiarizza, P., 2014, Geological setting of the Granite Mountain batholith, host to the Gibraltar porphyry Cu-Mo deposit, south-central British Columbia: Geological Fieldwork 2013, British Columbia Ministry of Energy and Mines, British Columbia Geological Survey, Paper, 2014-1, p. 95-110.

Schiarizza, P., 2015, Geological setting of the Granite Mountain batholith, south-central British Columbia: Geological Fieldwork 2014, British Columbia Ministry of Energy and Mines, British Columbia Geological Survey Paper, p. 19-39.

Simpson, R.Y., 1970. Geology of the Gibraltar – Pollyanna Cu deposit: B.Sc. thesis, The University of British Columbia, 43 p.

Sutherland Brown, A., 1958, Williams Lake: McLeese – Cuisson lakes area: Annual Report of the Minister of Mines for 1957, British Columbia Department of Mines, p. 14-18.

Sutherland Brown, A., 1967, Geology of the Granite Mountain – Cuisson Lake area: Annual Report of the Minister of Mines and Petroleum Resources for 1966, British Columbia Ministry of Mines and Petroleum Resources, p. 121-124.

Sutherland Brown, A., 1973, Gibraltar Mine (93B-12, 13): Geology, Exploration and Mining in British Columbia 1973, British Columbia Ministry of Energy, Mines and Petroleum Resources, p. 299-318.

Tipper, H.W., 1959. Quesnel, British Columbia: Geological Survey of Canada, Map 12-1959; scale 1:253 440.

Tipper, H.W., 1978, Northeastern part of Quesnel (93B) map-area, British Columbia: Current Research, Part A, Geological Survey of Canada, Paper 78-1A, pp. 67-68

Van Straaten, B.I., Oliver, J., Crozier, J., and Goodhue, L., 2013, A summary of the Gibraltar porphyry Cu-Mo deposit, south-central British Columbia, Canada: Porphyry systems of central and southern British Columbia: Tour of central British Columbia porphyry deposits from Prince George to Princeton: Society of Economic Geologists, Field Trip Guidebook, Series, v. 43, p. 55-66.

Villeneuve, M., Whalen, J. B., Anderson, R. G., and Struik, L. C., 2001, The Endako batholith: episodic plutonism culminating in formation of the Endako porphyry molybdenite deposit, north-central British Columbia: Economic Geology, v. 96(1), p. 171-196.

Wolfe, L., 2017a, Chemistry of refractory indicator minerals in tills around the Gibraltar porphyry Cu deposit, southcentral British Columbia; unpublished B.Sc. thesis, University of Ottawa, Ottawa, 56 p.

Wolfe, L., Hattori, K., and Plouffe, A., 2017b, Glacial dispersal of refractory minerals from the Gibraltar porphyry Cu deposit, south central British Columbia, Canada: Geological Survey of Canada, Scientific Presentation 73, https://doi.org/10.4095/30582

CHAPTER 3

Epidote associated with the porphyry Cu-Mo mineralization at the Gibraltar deposit, south-central British Columbia

C.H. Kobylinski, K. Hattori, S. Smith and A. Plouffe

Published as a GEOLOGICAL SURVEY OF CANADA OPEN FILE 8279 in 2017

Abstract

The Gibraltar porphyry-copper molybdenum deposit in the Canadian Cordillera is hosted by the late Triassic Granite Mountain Batholith (GMB). The batholith is tonalitic and composed of quartz, plagioclase and minor hornblende and biotite in varying proportions. The rocks in the batholith show phyllic and propylitic alteration. Propylitic alteration (green rock alteration) is characterized by epidote and chlorite and is extensive throughout the batholith. The name epidote is used in this paper for epidote group minerals which include clinozoisite, epidote (sensu stricto), allanite, ferriepidote and ferriallanite. Epidote occurs as dissemination, isolated grains, aggregates, mono-minerallic veins and epidote-bearing veins in the batholith. These veins (>2 cm in width) in the batholith generally strike towards the mineralized centre. Epidote enclosed by chalcopyrite or pyrite is compositionally homogeneous and Fe- poor, suggesting that Fe is preferentially incorporated into sulphides when epidote crystallized together with sulphide minerals. Individual grains of epidote in epidote-bearing veins show compositional zoning with Fe-poor cores and Fe-rich rims. Epidote grains disseminated in the batholith show similar compositional zoning with Fe-poor cores and Fe-rich rims. Allanite and REE-rich epidote are identified in the GMB less than 2 km from mineralization and within the Burgess Creek Stock (10 km from mineralization). Epidote containing 0.01 -1 wt.% REEs is common in aggregates throughout GMB. Epidote with high REEs (> 1 wt.% REEs) occurs only in rocks with a bulk composition >70 ppm REEs. Compositional zoning of epidote suggests that the hydrothermal history of the GMB consisted of early S-rich hydrothermal activity, followed by S-poor barren hydrothermal activity. Epidote in the Nicola volcanics and Cuisson Lake Unit near the GMB is homogeneous and Fe-rich and commonly contains inclusions of apatite and titanite. The contents of REEs in epidote in the Nicola volcanics are all below the detection limits of SEM (1000 – 5000 ppm) and EPMA (La, 470 ppm; Ce, 380 ppm; Pr, 640 ppm; Nd, 330 ppm).

3.1 Introduction

Porphyry Cu mineralization is accompanied by extensive alteration within the host rocks and surrounding country rocks (e.g. Sillitoe, 2010). Propylitic alteration associated with Cu-mineralization produces chlorite and epidote and is called green rock alteration. It can extend a few kilometers from mineralization centres. These alteration minerals can be disseminated in the host and country rocks. Epidote can also form veins and veinlets far from the deposits. Furthermore, epidote is also a common alteration mineral of feldspars, micas, pyroxenes amphiboles and garnets and thus occur variety of rocks that are not related to porphyry Cu-Mo mineralization. Epidote is also an important constituent of greenschist facies metamorphic rocks. Although rare, epidote can occur as a primary igneous mineral in tonalites. Our objective is to identify the textural and chemical characteristics of epidote associated with porphyry Cu mineralization so that it can be used as an indicator mineral in detrital sediments (e.g. till) to detect propylitic alteration associated with Cu porphyry mineralization. This study on epidote is centered on the Gibraltar porphyry Cu-Mo deposit, the second largest open pit Cu mine in Canada. The deposit is hosted in the late Triassic Granite Mountain Batholith (GMB), which intruded the Nicola Group mafic volcanic rocks of the Quesnel terrane. Epidote is common within the batholith and abundant in the Nicola volcanic rocks. Furthermore, the Cretaceous Sheridan Creek Stock, which is barren and in contact with the GMB, contains abundant epidote. This paper presents the occurrence and composition of epidote group minerals in the ore zone of the Gibraltar deposit, the GMB, the Nicola volcanic rocks, the Cuisson Lake Unit, and the Sheridan Creek Stock.

3.1 Regional geology

3.1.1 Cache Creek terrane

The GMB was recently interpreted as intrusions in the Quesnel terrane close to the border with the Cache Creek terrane to the west (Schiarizza, 2014). Rocks of the Cache Creek terrane underlie the eastern and southern part of the study area (Fig. 3.1). At a regional scale, it comprises chert, limestone and basalt. Only limestone and chert are present within the study area and these rocks do not contain epidote.

3.1.2 Quesnel terrane

The Quesnel terrane, a volcanic arc terrane, extends along the length of the Canadian Cordillera from central Yukon to the southern limit of British Columbia (Colpron and Nelson, 2011). The Quesnel Terrane is in large part represented by Middle and Upper Triassic submarine volcanic and volcaniclastic rocks, which are assigned to the Takla Group in northern and central British Columbia and to the Nicola Group in the south. The terrane is characterized by pyroxene-phyric basalt, and alkaline to calc-alkaline intrusions (Schiarizza, 2015). The Quesnel terrane is bounded by the oceanic Slide Mountain terrane to the east and the oceanic Cache Creek terrane to the west (Schiarizza, 2015). In the southern Quesnel terrane, intrusive rocks form four linear belts of alternating calc-alkaline and alkaline plutons, younging to the east, and many are accompanied by base metal mineralization (Schiarizza, 2015).

3.1.3 Nicola Group

The volcanic rocks of the Nicola Group are mostly pale green, fine to medium grained tuffs and matrix- supported lapilli tuff breccias of basaltic to andesitic compositions (Schiarizza, 2015). The Nicola Group also contains intercalated siliclastic sedimentary rocks that are dominated by laminated mudstone-siltstone and lesser medium-grained volcanic sandstone (Schiarizza, 2015).

3.2 Geology of the study area

The bedrock geology in the region of the Gibraltar deposit was mapped by Ash et al. (1999b) and more recently by Schiarizza (2014; 2015). The classification of the bedrock units presented below is based on their mapping.

3.2.1 Cuisson Lake Unit (formerly Ash Metamorphic Unit)

The Cuisson Lake Unit, consisting mainly of chlorite schist, limestone and skarn, forms a narrow belt in the southwestern part of the study area, between the GMB and the Sheridan Creek Stock (Figs. 3.1 and 3.2). Most rocks in the unit are well foliated and recrystallized, such that primary mineralogy and texture are not preserved (Schiarizza, 2015). Ash et al., (1999a) interpreted the unit as an intensely deformed and recrystallized mafic phase of the GMB. This interpretation led to the old name Ash Metamorphic Unit. Schiarizza (2015) describes the Cuisson Lake Unit as feldspathic volcanoclastic rocks intercalated with limestone which he correlates to the Nicola Group. Volcanic rocks of the Cuisson Lake Unit exposed along the east side of Gibraltar Mine Road, 4 km south of the mine are dark green, fine grained, chloritized and contain abundant epidote (>40 vol.%). They are similar in appearance to the Nicola volcanic rocks in the northern part of the study area, but their bulk composition is slightly different. Mafic rocks of the Cuisson Lake Unit contain less SiO_2 (40.19 wt.% compared to 50.37-51.81 wt%), similar Fe2O3(t)(11.35 wt.% compared to 9.18-13.32 wt.%), and higher CaO (27.01 wt.% compared to 8.2-8.6 wt.%) than the Nicola volcanic rocks. High CaO is explained by abundant calcite veinlets (Fig. 3.2). In the northern part of the study area (Figs. 3.1 and 3.2), Nicola volcanics are mingled with limestone. It is possible that the limestone belongs to the adjacent Cache Creek Group and that the Cuission Lake Unit in the southern section of the study area is a metamorphic product of these mingled rocks.

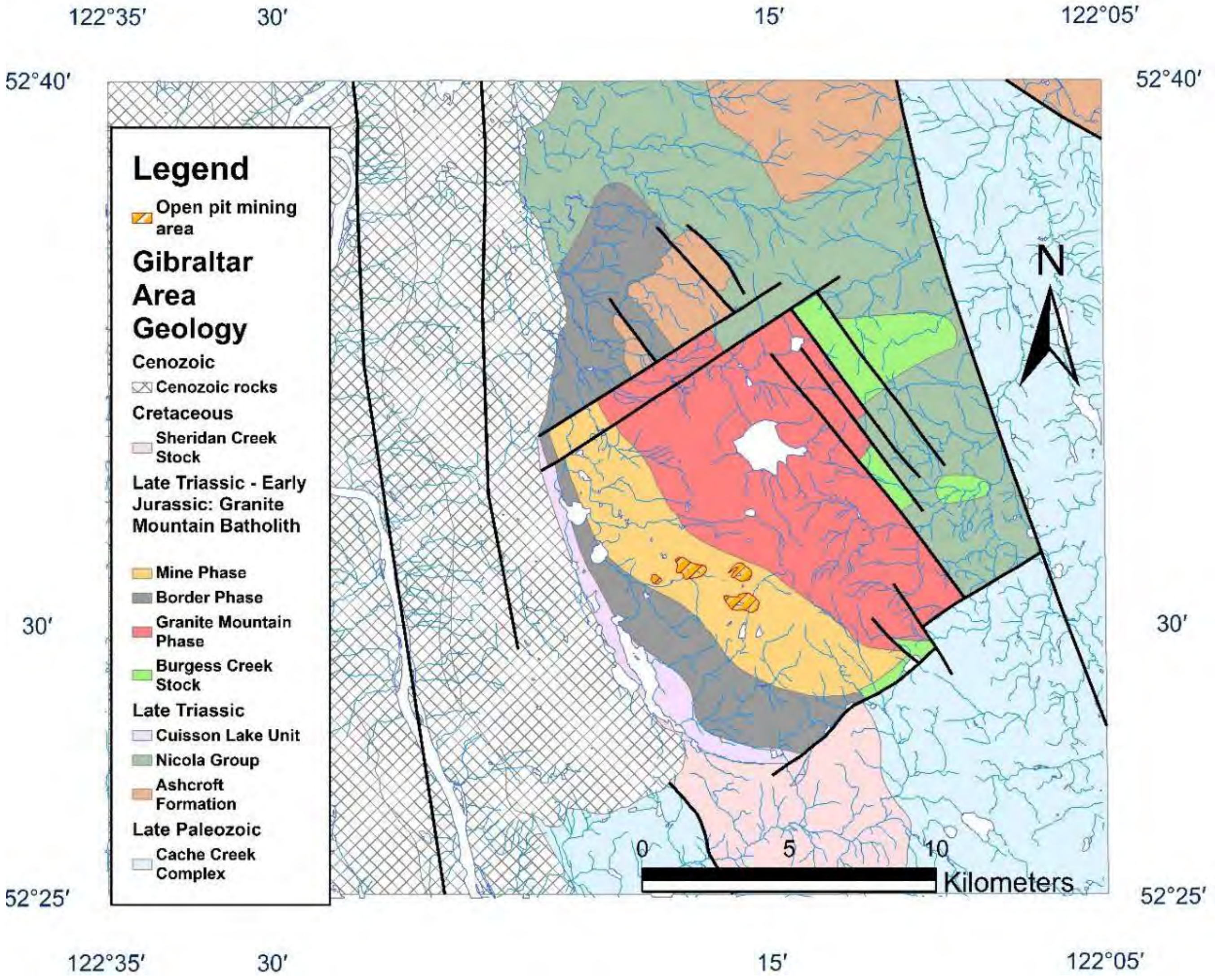

Figure 3.1. Geological map of the study area modified from Plouffe and Ferbey (2015). Names of the phases and units within the study area taken from Schiarizza (2015).

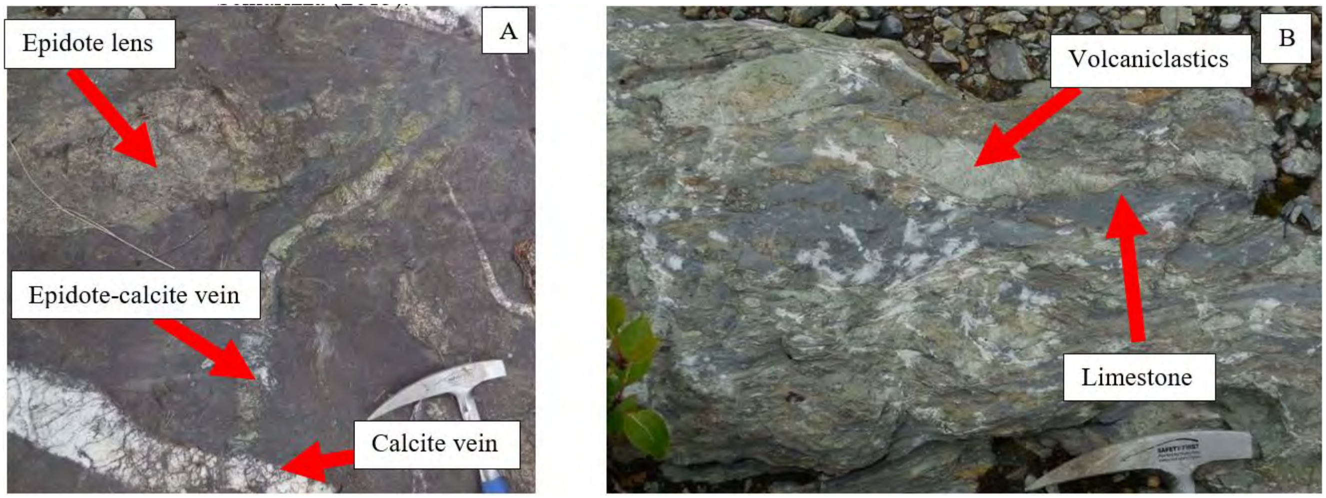

Figure 3.2. Outcrop photographs with rock hammer for scale. (A) The Cuisson Lake Unit along Gibraltar Mine road (Easting 0547384 Northing 5814942 (NAD 83, Zone 10 N)) with deformed veins of epidote, epidote-calcite and calcite and a dark green fine-grained matrix. (B) Outcrop of Nicola volcanic rocks (Easting 0549808 Northing 5829201 (NAD 83, Zone 10 N)) north of the GMB, showing green volcaniclastic rock and blue-grey limestone.

3.2.2 Granite Mountain Batholith

The GMB is divided into four phases based on mineralogy and texture (Drummond et al., 1976; Ash et al., 1999b; van Straaten et al., 2013; Schiarizza, 2014, 2015). They are the Burgess Creek Stock, Granite Mountain Phase, Mine Phase, and the Border Phase (Fig. 3.1). Propylitic alteration, characterized by epidote and chlorite, is common in all four phases of the batholith with variable intensity. Phyllic alteration, identified by the occurrence of white mica and pyrite is limited to the Mine Phase, Border Phase and the south west section of the Granite Mountain Phase, proximal to mine pits. Quartz is abundant in rocks of the GMB as a primary mineral and a major component of various veins. The Granite Mountain Phase is the least altered and the Mine Phase and Border Phase are generally more altered based on abundances of pyrite, white mica, epidote and chlorite.

Burgess Creek Stock. The Burgess Creek Stock occurs at the northeast margin of the GMB (Fig. 3.1). It consists of tonalites, quartz diorites, and diorites that intrude the Nicola Group

(Schiarizza, 2014). The tonalitic rocks of this phase are leucocratic with less than 10 vol.% mafic minerals. The dioritic rocks contain plagioclase (60-70 vol.%) and up to 30 vol.% mafic minerals. The Burgess Creek Stock was previously interpreted to be younger than the GMB (Panteleyev, 1978; Bysouth et al., 1995). This interpretation may be in part due to its intrusive contact with the Nicola volcanic rocks, which were previously considered younger than the GMB (Ash et al., 1999a, b). The stock yielded U-Pb zircon ages of 222.7±0.3 Ma and 221.25±0.2 Ma (Schiarizza 2015), which are older than the ages of the GMB. Ash et al (2001) reported 215 ± 0.8 Ma and Schiarizza (2015) obtained 217.15±0.2 Ma from the adjacent Granite Mountain Phase of the batholith. These data suggest that the stock is an old unit of the GMB.

Granite Mountain Phase of the GMB. The Granite Mountain Phase is the most voluminous and most leucocratic phase of the GMB. This phase is equigranular and isotropic. It comprises tonalitic rocks with various modalities of quartz, plagioclase and minor chloritized mafic minerals (5-10 vol.%). The epidote content is low (<15 vol.%) and it replaces plagioclase. U-Pb zircon ages date the Granite Mountain Phase of the GMB at 217±0.2 Ma (Schiarrizza, 2015).

Mine Phase of the GMB. The Mine Phase hosts the Cu-Mo mineralization at Gibraltar. It consists of tonalitic rocks with variable modalities of quartz, plagioclase and completely chloritized mafic minerals (15-25 vol.%). It is more leucocratic than the Border Phase. Rocks in this phase are highly foliated and equigranular. The epidote content ranges from 10-30 vol.%.

Border Phase of the GMB. The Border Phase comprises various modalities of quartz (up to 30 vol.%), plagioclase (up to 40 vol.%) and mafic minerals (up to 40 vol.%). Mafic minerals are hornblende ± biotite and are partially to completely chloritized. It is equigranular and isotropic to slightly foliated. The epidote content is moderate (10-20 vol.%).

3.2.3 Sheridan Creek Stock

The Sheridan Stock is composed of equigranular isotropic quartz diorite and tonalite (15-25 vol.% quartz, < 70 vol.% plagioclase, 10-20 vol.% mafic minerals). Pristine unaltered plagioclase, biotite and dark brown hornblende are common minerals of the stock. U-Pb zircon date, 108.1 ±0.6 Ma (Ash et al., 2001), confirms the late Cretaceous age of the intrusion.

Mafic minerals are dark brown hornblende and biotite with low (<10 vol.%) epidote content. Epidote-quartz veins generally strike east-west (Fig. 3.3 A).

3.3 Analytical methods

SEM-EDS

Chemical compositions of epidote group minerals were determined from 12 carbon-coated polished thin sections using a JEOL 6610LV scanning electron microscope equipped with energy dispersive detector (SEM-EDS) at the University of Ottawa. The compositions were determined using energy- dispersive spectroscopy with the acquisition time of 40 s and an accelerating voltage of 20 kV. Analyses were conducted without references for individual elements. All detected element oxide values are normalized to 100%. Detection limits are 0.1-0.5 wt% for all elements. SEM back scattered electron (BSE) images were acquired as 16 bit greyscale. Up to 256 shades of grey were used to represent different mean atomic masses of different minerals and mineral compositions. These shades were converted to up to 30 colors using imageJ photo software by assigning each shade(s) of gray to a color. Brighter areas in gray scale BSE image within epidote grain represent higher Fe content. Blue, green and magenta were used to identify titanite, chlorite and chalcopyrite respectively, and separate these minerals from similar shades of grey in epidote. The gray color of apatite was left as the original color.

EPMA

Quantitative analysis for the major and minor elemental compositions of the epidote group minerals was carried out using a JEOL 8230 electron probe micro-analyzer (EPMA) at the University of Ottawa. Epidote minerals were analyzed at an accelerating voltage of 15 kV, a beam current of 20nA using a focused beam of 1µm. Counting times were 20 s on- peak and 10 s off-peak for all elements except for F (150 s on and 75 s off), Cl (50 s on and 25 s off), Y (40 s on and 20 s off) Sc (40 s on 20 s off), Si (10 s on and 5 s off). F, Cl Y, Sc, Th, Pb, Cr, Nb and K were all below detection levels for epidote analysis by EPMA and are not reported. References and limit of detections are indicated in Table 3.1.

Field observations

The orientation of 1 to 10 epidote-bearing veins were measured at 10 outcrops for a total of 50 measurements. Six out of 10 outcrops and 36 out of 50 measurements of epidote-bearing veins were in the GMB (Fig. 3.3 A). The rest of the orientation measurements were taken on epidote-bearing veins in the Nicola volcanic rocks, the Sheridan Creek Stock or the Cuisson Lake Unit. The dominant orientation was determined after compiling all measurements from one outcrop. Typically, 80% of the veins at a site have a similar orientation with ± 5° of variability which we consider the dominant orientation at the outcrop. The rest of the veins (about 20%) showed variable strikes with more than 50° difference from the dominant vein orientation.

3.5Epidote occurrences and composition

3.5.1 Nomenclature

Epidote group minerals with the general formula $A_2M_3(T_2O_7)(TO_4)(O,F)(OH,O)$ are divided into 3 subgroups: clinozoisite, allanite and dollaseite subgroups. The clinozoisite subgroup is defined by homovalent substitution of Al by Fe^{3+} in M sites. The allanite subgroup is defined by REE rich phases where trivalent REEs reside in the A site. The third subgroup is the dollaseite subgroup with high Mg and is not found in our study area. Ferriepidote, epidote and clinozoisite form a continuous solid solution in the clinozoisite subgroup with varying Fe^{3+} and Al in the M sites (Fig. 3.4). Clinozoisite has Al in three M sites. Epidote (sensu stritco) has Al in two M sites (M1 and M2) and Fe^{3+} in the M3 site. Ferriepidote has Fe^{3+} in two M sites (M1 and M3) and Al in the M2 site (Armbruster et al., 2006) (Fig. 3.4). Epidote (sensu stritco) is defined to contain greater than 0.5 Fe^{3+} in the M3 site, whereas clinozoisite contains greater than 0.5 Al in the M3 site (Armbruster et al., 2006) (Fig. 3.4). Ferriepidote has a greater than 0.5 Fe^{3+} in the M1 and the M3 site is filled with Fe^{3+} (Armbruster et al., 2006). The Fe(t)/[Fe(t) + Al] apfu ratios in the clinozoisite subgroup are > 0.5 for ferriepidote, 0.165-0.5 for epidote and <0.165 for clinozoisite (Armbruster et al., 2006).

The allanite subgroup is defined to contain $[M^{3+}+M^{4+}]A2 > 0.5$ and $[M^{2+}]M3 > 0.5$, where M^{3+} and M^{4+} are REE, Y, U and Th substituting Ca^{2+} in the A2 site and M^{2+} a divalent cation in the M3 site to retain charge balance (Armbruster et al., 2006) (Fig. 3.4).

Epidote in the study area shows a large compositional variation mostly due to varying Fe, Al and REE contents. The atomic ratios of Fe(t)/[Fe(t) + Al] are between 0.05 and 0.5 in studied samples and some grains also contain up to 21 wt.% $La_2O_3 + Ce_2O_3 + Pr_2O_3 + Nd_2O_3$.

Epidote in the GMB shows compositional zoning with Fe-poor cores and Fe-rich rims. The boundaries between cores and rims are sharp in individual grains and there is no epidote with intermediate compositions. Based on our observation of Fe-Al zoning in epidote and clinozoisite of the GMB, we define "Fe-poor epidote" as having Fe(t)/[Fe(t) + Al] ratios <0.29 and "Fe-rich epidote" with ratios>0.29. In this study, REE+Y vary from 0.01 wt.% oxides to 21.7 wt.% oxides. We classify epidote as allanite (>15 wt.% REE oxides), REE-rich (1 to 15 wt.% REE oxides) and REE-bearing (0.01-1 wt.% REE oxides).

Table 3.1. List of elements and calibration standards used for electron probe micro-analyzer.

Elements	**Calibration standards**	**Detection limits**
Si, Al, K	Sanidine	Si (180 ppm), Al (100 ppm), K (130 ppm)
Fe	Hematite	Fe (150 ppm)
F	Mg-mica	F (390 ppm)
Na	Albite	Na (110 ppm)
Cl	Tugtupite	Cl (60 ppm)
Sr	Celestine	Sr (490 ppm)
Nd	Synthetic $NdPO_4$	Nd (330 ppm)
Pr	PrPO4	Pr (640 ppm)
Ce	CePO4	Ce (380 ppm)
La	LaPO4	La (470 ppm)
Th	ThO2	Th (360 ppm)
Ca, Mg	Diopside	Ca (160 ppm), Mg (110 ppm)
Pb, V	Vanadinite	Pb (310 ppm), V(180 ppm)
Mn	Tephroite	Mn (440 ppm)

Y	Yttrium aluminum garnet	Y (2100 ppm)
Ti	Rutile	Ti (180 ppm)
Cr	Chromite	Cr (150 ppm)
Sc	REE-glass (synthetic glass with 1 wt.% of Sc)	Sc (200 ppm)
Nb	Synthetic manganocolumbite	Nb (540 ppm)

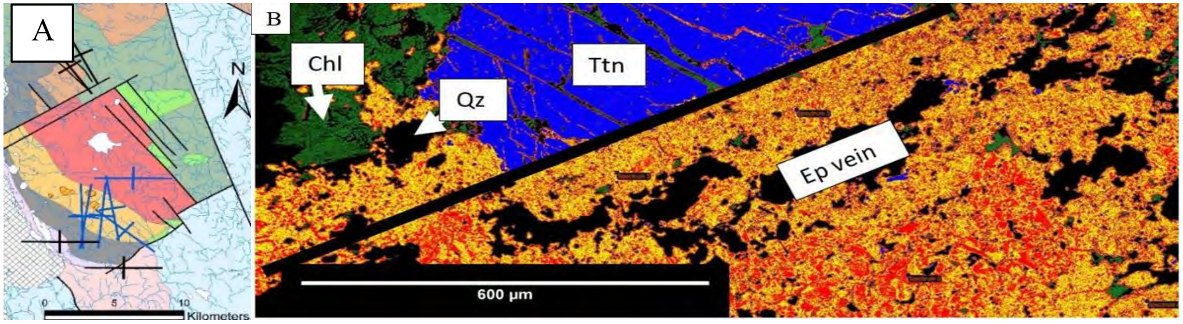

Figure 3.3. (A) Dominant orientations of epidote-bearing veins (greater than 2 cm in width) in the study area. Note dominant vein orientations in blue are in the GMB and veins strike east-west in the Granite Mountain Phase. Dominant vein orientations in black are not in the GMB. (B) Colorized SEM- BSE perpendicular to strike section of an Ep-Qz vein (1 cm in width) the Mine Phase of the batholith (sample GBR-2-7) comprising zoned epidote grains with Fe-poor centres (10.57 wt.% Fe_2O_3(t), Fe(t)/[Fe(t) + Al] = 0.21) rimmed by Fe-rich borders (16.52 wt.% Fe_2O_3(t), Fe(t)/[Fe(t) + Al] = 0.33). Epidote grains in the centre of the veins have large Fe-poor cores. Epidote grains on the border of veins have less prominent Fe-poor cores. Abbreviations: Chl – chlorite; Ep – epidote; Qz – quartz; Ttn – titanite. Sample locations and SEM data are found in Appendix 1, Tables A1-1, A1-2, A1-3 and A1-4.

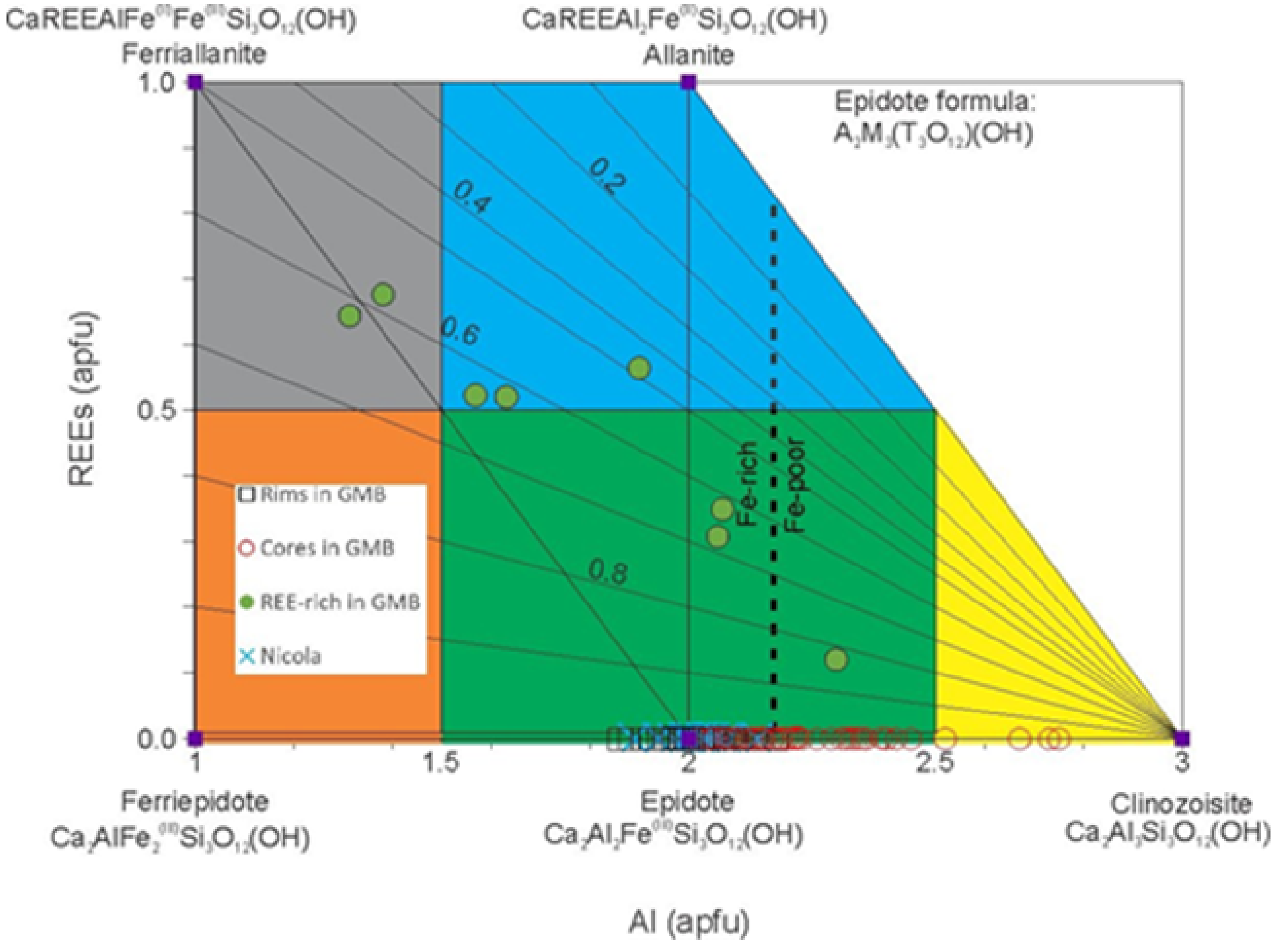

Figure 3.4. Total Al atoms per formula unit (apfu) vs. REEs (apfu) diagram showing solid solutions in the clinozoisite subgroup and the allanite subgroup after Petrik et al. (1995). Lines radiating from the clinozoisite end-member are $Fe^{3+}/(Fe^{3+}+Fe^{2+})$. End member compositions are shown as purple squares. Division of Fe- poor and Fe-rich epidotes in this study is shown with a dashed black line. The compositional ranges for epidote sensu stricto clinozoisite ferriepidote, allanite, and ferriallanite are shown as green, yellow, orange, blue and grey fields, respectively, following the classification of Armbruster et al. (2006).

3.5.2 Epidote occurrences in the GMB

Disseminated epidote. Disseminated epidote in the GMB replaces 5 to 100 vol.% of plagioclase grains (Fig. 3.5). Individual grains of epidote in plagioclase have a prismatic shape (Fig. 3.5) with up to 30 μm in length and show zoning with Fe-rich rims and Al-rich cores. Replacement of plagioclase by epidote occurs in all phases of the GMB. Total pseudomorphic replacement of plagioclase by aggregates of epidote grains (Fig. 3.6) is common only in the Mine Phase of the GMB.

Aggregates. Epidote forms aggregates (0.5 – 1 mm) consisting of small anhedral epidote grains (50-100 µm). Grains do not contain inclusions. The individual grains within the aggregates are zoned with Fe-rich rims and Al-rich cores. Aggregates are commonly surrounded by chlorite. Epidote aggregates occur in all phases of the GMB. Grains in some aggregates are REE-bearing.

Isolated grains. Epidote forms large (up to 400µm) isolated grains associated with quartz phenocrysts. These grains are not associated with plagioclase or chlorite. The grains are euhedral to subhedral. Their composition ranges from Fe-poor epidote in the cores to Fe-rich epidote in the rims (Fig. 3.6). Some contain significant concentrations (>5 wt.%) of REE oxides (Fig. 3.7) and these REE-rich grains are not compositionally zoned. Isolated grains of epidote occur in all phases of the GMB.

Veins and veinlets. Epidote-bearing veins and veinlets occur in all phases of the GMB. Three types of veins (1-15 cm wide) and veinlets (0.1-3 mm wide) are observed: mono-minerallic epidote, epidote- quartz and epidote-quartz-chlorite. They contain minor hydrothermal magnetite. Individual grains of epidote show compositional zoning with Fe-poor cores (Fig. 3.3). Thirty-six measurements of vein orientation within the GMB show that they generally strike towards the mineralized areas (Fig. 3.3). Epidote- bearing veins are found up to 10 km from mineralization. This is farther than the disseminated epidote which extends up to 5 km.

Epidote in ore zone in the Mine Phase of the GMB. Epidote grains in contact with, or in the proximity of pyrite or chalcopyrite (Figs. 3.8 and 3.9) are mostly subhedral and occur as aggregates (up to 600 µm) or isolated grains ranging from 50 to 400 µm. Grains enclosed by sulphides are unzoned, with low Fe ($Fe_2O_{3(t)}$<12.7 wt.%, equivalent to Fe(t)/[Fe(t)+Al] < 0.22) whereas those in contact, but not totally enclosed by sulphide minerals are zoned (Fig. 3.8).

REE-bearing epidote. REE-bearing (up to 0.2 wt% REE oxides) epidote occurs in all phases of GMB as aggregates and show zoning with Fe-rich rims and Fe-poor cores in individual grains. Due to high detection limits of REEs, REE-bearing epidote was not detected with SEM-

EDS. There is a higher proportion (54 %) of epidote that is REE-bearing in samples collected proximal to mine pits (<2 km). In contrast, samples collected far (>2 km) from mine pits have a lower proportion (25 %) of REE-bearing epidote grains.

Allanite and REE-rich epidote. Allanite and REE- rich epidote are only found in REE-rich (>70 ppm) rocks of the Mine Phase, Border Phase, and the Burgess Creek Stock of the GMB (Fig. 3.10). Grains of REE-rich epidote and allanite show patchy compositional variations with Ce_2O_3 contents ranging from 5 to 15 wt.%, La_2O_3 from 6 to -10 wt.%, Pr_2O_3 from 0.3 to -1 wt.% and Nd_2O_3 from 0.4 to 1.3 wt.%. No Fe-Al zoning is observed in REE-rich epidote or allanite (Fig. 3.7).

3.5.3 Epidote in the Nicola volcanic rocks

Epidote occurs as large isolated subhedral grains (up to 400 μm, Fig. 3.5), and as aggregates (up to 500 μm) of small (<50 μm) grains. Epidote grains and aggregates are commonly associated with chlorite. Grains are homogeneous in composition and classify as Fe-rich with $Fe_2O_{3(t)} > 15.3$ wt.%. The larger isolated grains commonly contain apatite and titanite inclusions (Fig. 3.5). Nicola volcanic rocks near (< 500 m) the contact with the GMB contain more epidote (>40 vol.%) than volcanic rocks far (>500 m) from the GMB, which contain less than 30 vol.% epidote. Epidote in Nicola volcanic rocks does not contain REEs above the detection limits of SEM and EPMA. Tables 3.2 and 3.3 present a summary of epidote composition in the GMB and the Nicola volcanic rocks.

3.5.4 Epidote in the Sheridan Creek Stock

Disseminated epidote replacing plagioclase is present in the Sheridan Creek Stock. Epidote abundances are lower in the Sheridan Creek Stock (~5-10 vol.%) compared to the GMB (>10 vol.%).

3.5.5 Epidote in the Cuisson Lake Unit

In the Cuisson Lake Unit, epidote occurs in wide (>5 cm) deformed veins of epidote, epidote-quartz and epidote-calcite. Coarse grained epidote also occurs in lenses along with calcite

(Fig. 3.2). Epidote and chlorite are major components of the fine-grained matrix of the Cuisson Lake unit. In total, epidote constitutes up to 40 vol.% of this unit.

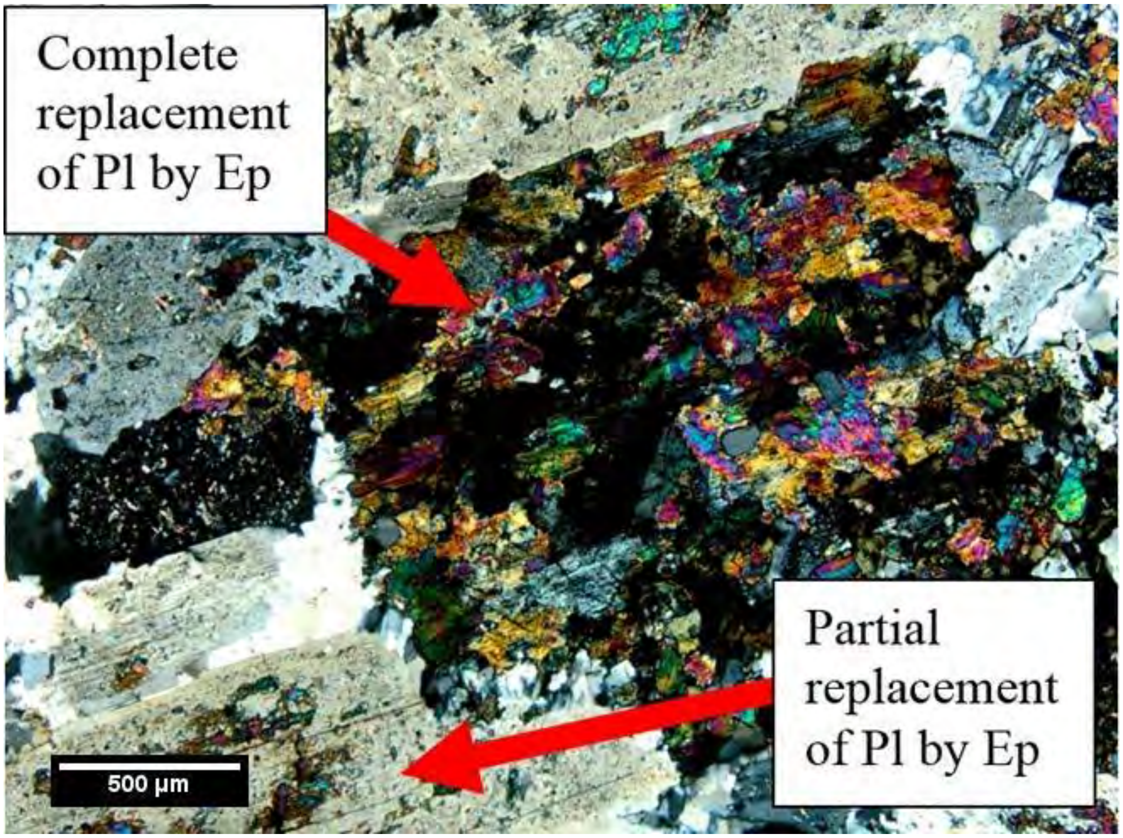

Figure 3.5. Photomicrograph showing variable degrees of replacement of plagioclase (Pl) by epidote (Ep) in the GMB. Sample number GBR-16 from the Mine Phase of the GMB, sample locations are listed in Appendix 1, Table A1-1.

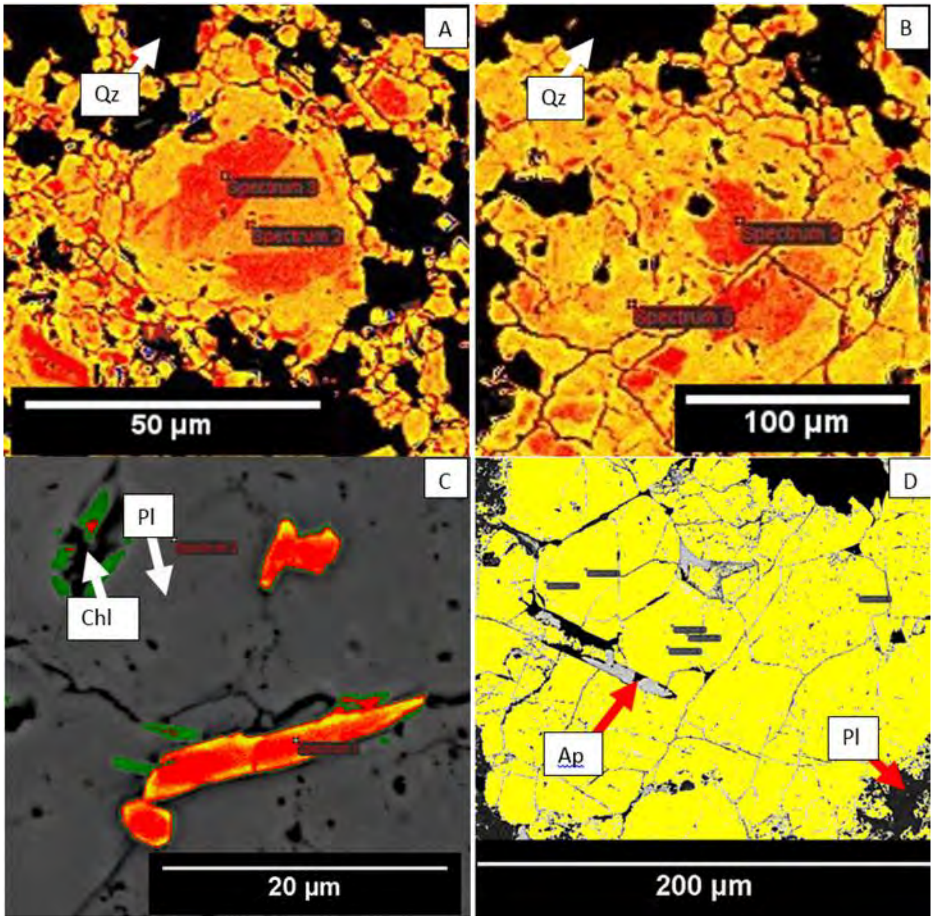

Figure 3.6. Colorized scanning electron microscopy-back scattered electron image (BSE) of epidote (Ep) surrounded by quartz (Qz) and plagioclase (Pl) in tonalitic rocks of the batholith (A, B, C) and epidote in Nicola volcanic rocks surrounded by plagioclase (D). (A) Ep aggregate in Mine Phase of the batholith showing Fe-poor cores (red, 10.07 wt.% Fe2O3(t), Fe(t)/[Fe(t) + Al] = 0.2) and Fe-rich rims (yellow, 16.03 Fe2O3(t) wt.%, Fe(t)/[Fe(t) + Al] = 0.31); sample GBR2-10; (B) Isolated Ep grain in the Border Phase of the batholith showing Fe-poor cores (red, 11.97 Fe2O3(t) wt.%, Fe(t)/[Fe(t) + Al] = 0.24) and Fe-rich rims (yellow, 18.72 Fe2O3(t) wt.%, Fe(t)/[Fe(t) + Al] = 0.36); sample GBR2-8; (C) Disseminated Ep in Granite Mountain Phase of the batholith showing Fe-poor cores (red, 8.74 Fe2O3(t) wt.%, Fe(t)/[Fe(t) + Al] = 0.17) and Fe-rich rims (yellow, 18.53 Fe2O3(t) wt.%, Fe(t)/[Fe(t) + Al] = 0.36); sample GBR2-34; (D) Isolated Fe-rich (17.56 Fe2O3(t) wt.%, Fe(t)/[Fe(t) + Al] = 0.34) epidote grain in the Nicola volcanics showing no zoning and inclusions of apatite (Ap). Sample GBR2-4. Abbreviations; Chl – chlorite, sample locations and SEM data are found in Appendix 1, Tables A1-1, A1-2, A1-3, and A1-4.

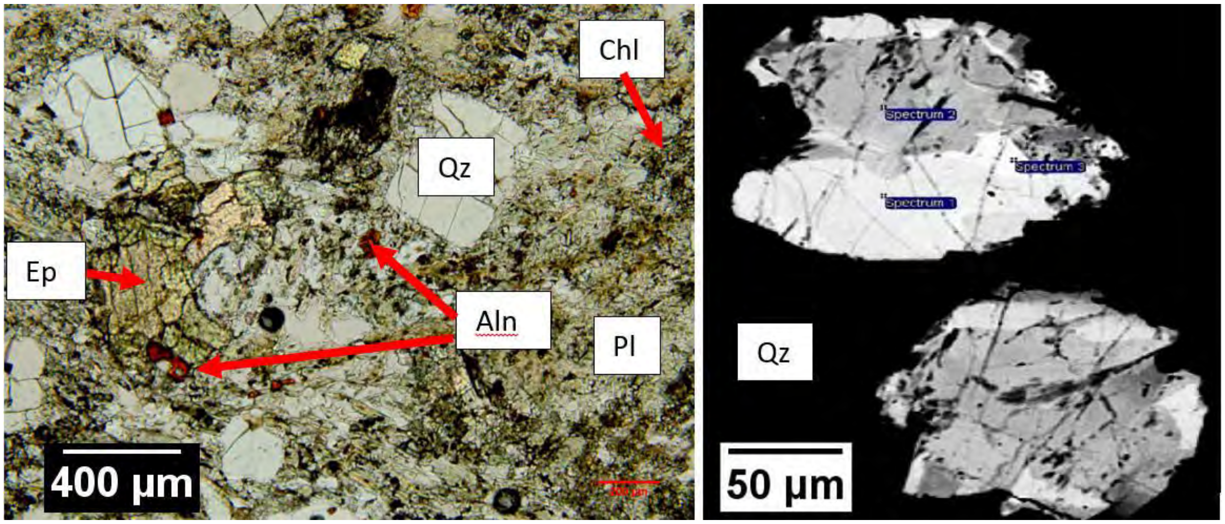

Figure 3.7. (A) Photomicrograph in PPL and (B) SEM –BSE image of allanite in the Mine Phase of the GMB; sample GBR-11. (A) Allanite (Aln, red-orange grains) surrounded by Ep, Qz and Chl.(B) Patchy zoning in allanite with brighter areas with $Ce_2O_3 > 10$ wt.% and darker areas with $Ce_2O_3 <5$ wt.%. Sample location and SEM data found in Appendix 1, Tables A1-1, A1-5 and A1-8.

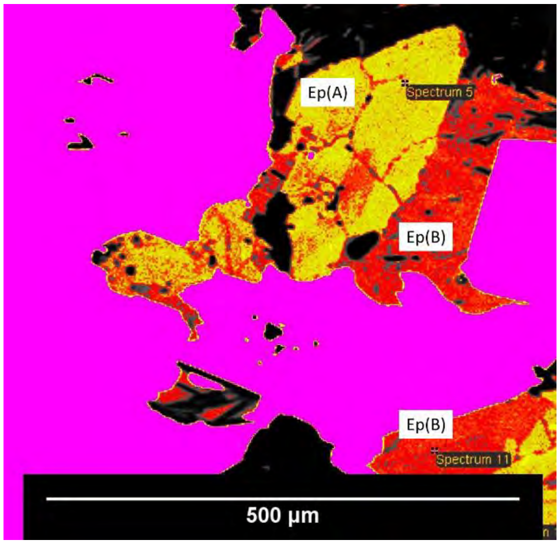

Figure 3.8. Colorized SEM-BSE of epidote (Ep) in contact with chalcopyrite (Ccp, pink) in sample SVA 7-14.13, collected in the Mine Phase of the GMB. Zoning with relatively Fe-rich rims (yellow, 13.15 wt.% FeO(t), Fe(t)/[Fe(t) + Al] = 0.25) and Fe-poor-cores (11.02 wt.% Fe2O3(t), Fe(t)/[Fe(t) + Al] = 0.21) in Ep(A) in contact but not surrounded by Ccp. Ep (B) enclosed by Ccp shows no zoning and is Fe-poor (11.53 wt.% Fe2O3(t), Fe(t)/[Fe(t) + Al] = 0.23). Sample location and SEM data found in Appendix 1, Tables A1-1 and A1-9.

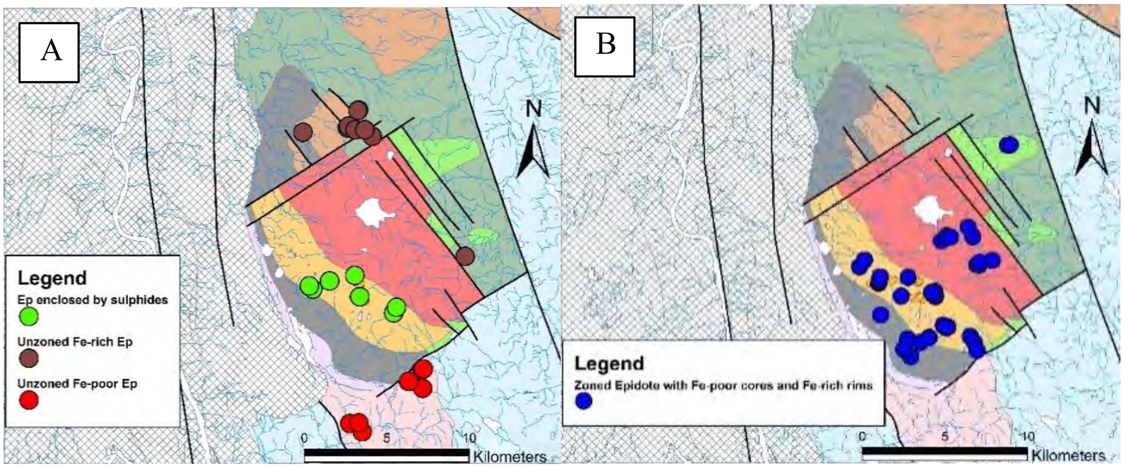

Figure 3.9. (A) Location of zoned epidote (Fe-poor cores and Fe-rich rims) in the Border Phase, Mine Phase, Granite Mountain Phase, and Burgess Creek Stock of the GMB. (B) Location of unzoned epidote in the study area. Fe-rich unzoned epidote is found in the Nicola volcanic rocks (brown), Fe-poor unzoned epidote is found replacing plagioclase in the Sheridan Creek Stock. Unzoned Fe-poor epidote is found in the Mine Phase enclosed in sulphides.

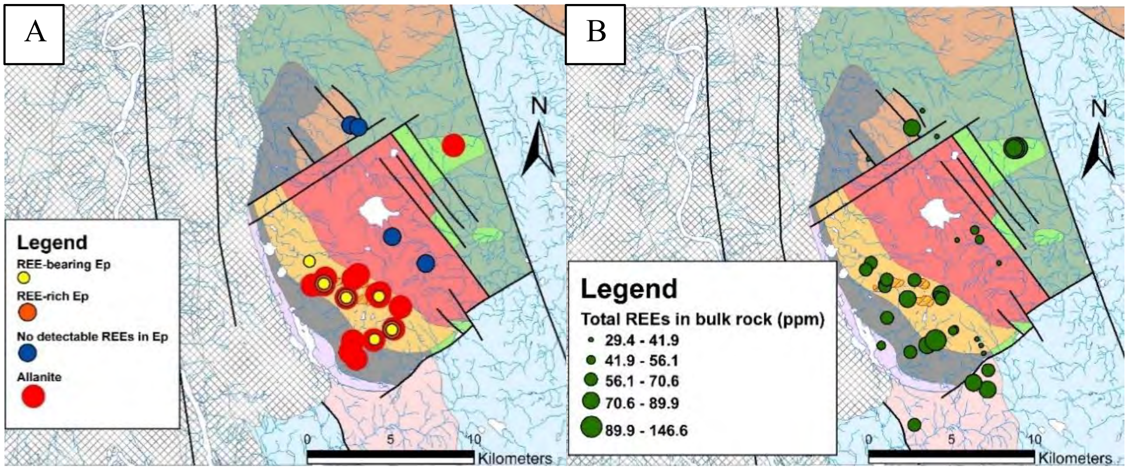

Figure 3.10. (A) Location of REE-bearing epidote, REE-rich epidote, Allanite and epidote with no detectable REEs in the GMB. (B) Whole rock REE concentrations and sample locations. Areas with REEs in epidote correlate with higher REEs in whole rock (Mine phase, Border phase and Burgess Creek Stock).

3.6 Discussion

3.6.1 Epidote in the batholith

Epidote occurs in all phases of the GMB (Fig. 3.10). A Fe(t)/[Fe(t) + Al] value of 0.29 separates compositions of cores from rims in zoned epidote grains (Fig. 3.11). Epidote enclosed by chalcopyrite and pyrite is homogeneous and Fe-poor suggesting the preferential incorporation of Fe in sulfides. All other epidote in the GMB shows compositional zoning; Fe-poor, Al-rich cores and Fe- rich, Al- poor rims (Fig. 3.9). We interpret this zoning as reflecting early S-rich hydrothermal activity that produced pyrite and chalcopyrite, leaving the associated epidote relatively low in Fe. Later hydrothermal activity with relatively less S did not form sulphides leaving Fe enriched fluids for the formation of Fe-rich rims in epidote.

3.6.2 REE-bearing epidote, REE-rich epidote and allanite in the batholith

REE-bearing epidote occurs in all phases of the GMB, except in the Granite Mountain Phase (Fig. 3.9 A). Minute grains forming epidote aggregates commonly contain REEs, but the contents are lower than 1 wt.% REE oxides. On the other hand, all grains of REE-rich epidote and allanite form isolated grains. REE-rich epidote and allanite are restricted within the GMB (Fig. 3.9). They are a hydrothermal product. The presence of allanite and REE-rich epidote only in rocks that contain >70 ppm REEs suggest that the rocks and epidote were enriched in light REE during hydrothermal activity or that the original rocks contain high REEs. The allanite subgroup has the potential to substitute Y, U and Th. Allanite and REE- rich epidote in this study do not have detectable Y, U or Th.

3.6.3 Epidote veins in the batholith

Veins of epidote are common throughout the batholith and extend up to 10 km from mineralization. Some are monomineralic, some are epidote-quartz or epidote-quartz-chlorite. Epidote grains in veins carry the same zoning pattern as observed in hydrothermal epidote of the GMB indicating that the veins were produced by the hydrothermal activity for crystallization of disseminated epidote. Although the number of measurements on vein orientations is limited (n=36), the dominant orientation at each site generally strike towards the centre of the mineralization (Fig. 3.3 A). If this is proven to be the case, epidote vein orientation in an intrusion could serve to vector towards mineralization.

3.6.4 Epidote in Nicola volcanic rocks

We suggest that epidote in the Nicola volcanic rocks near the GMB is a contact metamorphic product related to the intrusion of GMB, based on high abundance of epidote close to the contact with the GMB and that epidote in the Nicola volcanic rocks does not share the zoning pattern or composition of epidote in the GMB. Alternatively, increases in epidote modality near the contact may be due to enhanced fluid flow along the contact between the Nicola volcanic rocks and the GMB. Nicola epidote may be hydrothermal in origin, created by hydrothermal fluid input via intrusion of the GMB. Nicola epidote plots as Fe-rich (Fig. 3.11). Fe-rich composition of epidote may be explained by fluids interacting with mafic volcanic rocks because Fe/Al ratios are higher in mafic volcanic rocks compared to tonalitic rocks of the GMB.

Table 3.2. Summary, compositional zoning of epidote grains in the GMB based on SEM-EDS and EPMA determinations.

Occurrence	**Zoning in individual grains**	**Fe2O3 (t) (wt.%) rims** [number of grains analyzed]	**Fe2O3(t) (wt.%) cores** [number of grains analyzed]
Enclosed by Ccp or Py	No zoning Al-rich	9.96 -13.9 [3]	
In contact with Ccp or Py	Fe-rich rims, Al- rich cores	13.8 - 15.5 [5]**	9.8 – 12.3 [6]**
In veins*	Fe-rich rims, Al-rich cores	14.6 - 16.6 [13]**	10.7- 12.5 [17]**
Isolated grains/ Grains within aggregates	Fe-rich rims, Al- rich cores	13.8 - 15.3 - [24]**	8.4 - 10.9[27]**
Disseminated	Fe-rich rims, Al- rich cores	12.8 - 14.3 [7] **	2.1 – 9.4 [12] **

*Epidote grains in veins are zoned

**Presence of compositional zoning was apparent in all grains of epidotes in thin section under crossed polarizing light and also in SEM-BSE images. Only a small number of representative grains were selected for the composition analysis.

Table 3.3. Summary, epidote composition in Nicola volcanics based on SEM-EDSand EPMA determinations.

Occurrence	**Zoning of grains**	**Fe2O3 (t) (wt.%) average** [number of grains	**Inclusions**
Isolated grains	None	15.3[10]**	Apatite and titanite
Aggregates	None	15.5[7]**	Not present

**Presence of compositional zoning was absent in all grains of epidotes in thin section under crossed polarizing light and also in SEM-BSE images. Only a small number of representative grains were selected for the composition analysis.

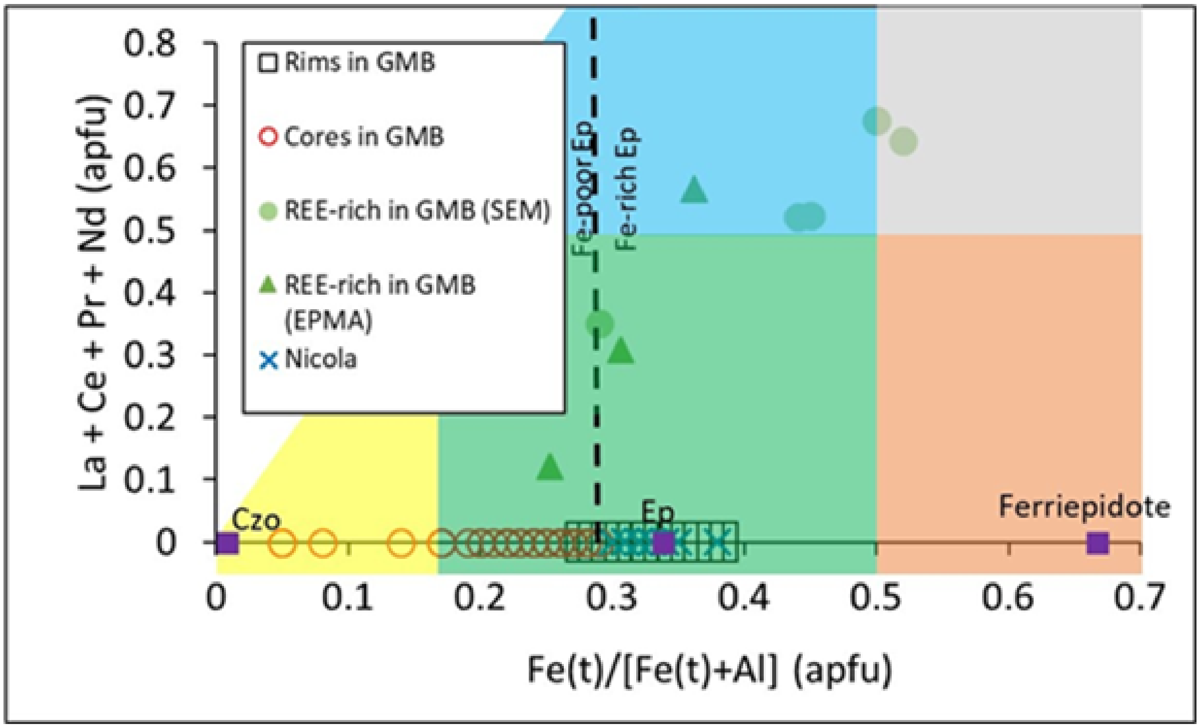

Figure 3.11. Composition of epidote in the GMB and the Nicola volcanic rocks based on SEM and EPMA data. Atom per formula unit calculated based on 12.5 O. End member compositions of clinozoisite (Czo, $Ca_2Al_3(SiO_4)(Si_2O_7)(O)(OH)$), epidote (Ep, $Ca_2Al_2Fe^{(III)}(SiO_4)(Si_2O_7)(O)(OH)$) and ferriepidote ($Ca_2AlFe_2^{(III)}(SiO_4)(Si_2O_7)(O)(OH)$) are shown as purple squares. Ranges for clinozoisite (yellow field), epidote (green field), ferriepidote (orange field), allanite (blue field) and ferriallanite (grey field) following the nomenclature and classification of Armbruster et al. (2006). This paper classifies epidote as Fe-rich or Fe-poor with a boundary at 0.29 Fe(t)/[Fe(t)+Al] shown by the dashed black line. Fe-poor epidote

includes clinozoisite. Epidote in Nicola volcanic rocks are all Fe-rich, >0.29 Fe(t)/[Fe(t) + Al] ratios. REE-rich epidote and allanite contain Fe^{2+} and have ratios of Fe(t)/[Fe(t) + Al] > 0.24.

3.7 Summary

Epidote in the GMB shows a variety of textures, occurrences, compositions and forms: pseudomorphic replacement of plagioclase, dissemination in plagioclase, aggregates, isolated grains, veins and veinlets. Epidote grains in the GMB contain no mineral inclusions. Almost all grains show compositional zoning with Fe-rich rims and Al-rich cores except for grains enclosed by sulphides, REE-rich epidote and allanite. Grains enclosed by sulphides are all Fe-poor and REE-rich epidote and allanite are mostly Fe-rich.

REE-bearing epidote (0.01-1 wt.% REE oxides) occur as pseudomorphic replacement of plagioclase, dissemination replacing plagioclase, aggregates, isolated grains, veins and veinlets and is found in all phases of the batholith. It shows the same compositional zoning as epidote in the GMB and contains no mineral inclusions.

REE-rich epidote (1-15 wt.% REE oxides) and allanite are found in REE-rich (>70 ppm) rocks in the GMB, dominantly in less than 2 km from the mineralization and in the Burgess Creek Stock. REE-rich epidote also occurs in the Burgess Creek Stock, the oldest unit of the batholith. REE-rich epidote occurs only in REE-rich rocks suggesting that host rocks were originally rich in REE or hydrothermal enrichment in REEs.

Strike and dip measurements on a limited number (n=36)of epidote veins in the GMB indicate a general pattern of veins striking towards mineralization (Fig. 3.3 A). Epidote vein orientation could be a vectoring tool in mineral exploration.

The Al-Fe zoning found in most epidote grains from the GMB is not observed in epidote from the unmineralized Nicola volcanic rocks. Epidote grains in the Nicola volcanic rocks are Fe-rich and have similar compositions independent of the locations. They commonly contain inclusions of apatite and titanite. Their REE content is below detection limits of 470 ppm for La, 380 ppm for Ce, 640 ppm for Pr and 330 ppm for Nd.

Epidote could be a useful indicator mineral for porphyry Cu mineralization. Compositional zoning or REE enrichment may be used to trace towards the mineralization. Another use of epidote in exploration is mapping of vein orientations and frequency in outcrops. If epidote veins show similar signatures (consisting of zoned grains as described above), they could be used to vector towards mineralization if the strike and dip pattern discussed in this report is proven to be correct.

Acknowledgements

This project was funded by Natural Resources of Canada through the Targeted Geoscience Initiative 5 program including a Research Affiliate Program Bursary to C.K. We also thank Glenn Poirier of the University of Ottawa for his help with SEM and EMPA analyses. The manuscript was improved following the internal GSC review completed by S.E. Jackson.

References

Armbruster, T., Bonazzi, P., Akasaka, M., Bermanec, V., Chopin, C., Gieré, R., Heuss-Assbichler, S., Liebscher, A., Menchetti, S., Pan, Y. and Pasero, M., 2006, Recommended nomenclature of epidote-group minerals; European Journal of Mineralogy, v. 18, p. 551-567.

Ash, C.H., Rydman, M.O., Payne, C.W., and Panteleyev, A., 1999a, Geological setting of the Gibraltar mine, south-central British Columbia (93B/8, 9); in: Exploration and Mining in British Columbia 1998, British Columbia Ministry of Energy and Mines, p. A1-A15.

Ash, C.H., Panteleyev, A., MacLennan, K.L., Payne, C.W., and Rydman, M.O., 1999b, Geology of the Gibraltar mine area, NTS 93B/8, 9; British Columbia Ministry of Energy and Mines, British Columbia Geological Survey Open File 1999-7; scale 1:50 000.

Ash, C.H. and Riveros, C.P., 2001, Geology of the Gibraltar copper-molybdenite deposit, east-central British Columbia (93B/9); in: Geological Fieldwork 2000, British Columbia Ministry of Energy and Mines, Paper 2001-1, p. 119-134.

Bysouth, G.D., Campbell, K.V., Barker, G.E., and Gagnier, G.K., 1995, Tonalite-trondhjemite fractionation of peraluminous magma and the formation of syntectonic porphyry copper mineralization, Gibraltar mine, central British Columbia; *in:* Porphyry Deposits of the Nortwestern Cordillera of North America, (ed.) T.G. Schroeter; Canadian Institute of Mining, Metallurgy and Petroleum, Special Volume 46, Montréal, p. 201-213.

Colpron, M. and Nelson, J.L., 2011, A digital atlas of terranes for the Northern Cordillera; British Columbia Ministry of Energy and Mines, British Columbia Geological Survey, GeoFile 2011-11.

Drummond, A.D., Sutherland Brown, A., Young, R.J., and Tennant, S.J., 1976, Gibraltar - Regional metamorphism, mineralization, hydrothermal alteration and structural development; *in:* Porphyry Deposits of the Canadian Cordillera, (ed.) A. Sutherland Brown; Canadian Institute of Mining and Metallurgy, Special Volume 15, p. 195-205.

Panteleyev, A., 1978, Granite Mountain project (93B/8); *in:* Geological Fieldwork 1977, British Columbia Ministry of Energy and Mines, British Columbia Geological Survey, Paper 1978-1, p. 39-42.

Petrík, I., Broska, I., Lipka, J., and Siman, P., 1995, Granitoid allanite-(Ce): substitution relations redox conditions and REE distributions (an example of I-type granitoids, Western Carpathians, Slovakia); Geologica Carpathica, v. 46, p. 79–94.

Plouffe, A., and Ferbey, T., 2015, Till composition near Cu-porphyry deposits in British Columbia: Highlights for mineral exploration; *in: TGI* 4 - Intrusion Related Mineralisation Project: New Vectors to Buried Porphyry-Style Mineralisation, (ed.) N. Rogers; Geological Survey of Canada, Open File 7843, p. 15-37.

Schiarizza, P., 2014, Geological setting of the Granite Mountain batholith, host to the Gibraltar porphyry Cu-Mo deposit, south-central British Columbia; *in*: Geological Fieldwork 2013, British Columbia Ministry of Energy and Mines, British Columbia Geological Survey, Paper 2014-1, p. 95-110.

Schiarizza, P., 2015, Geological setting of the Granite Mountain batholith, south-central British Columbia; *in:* Geological Fieldwork 2014, British Columbia Ministry of Energy and Mines, BritishColumbia Geological Survey Paper 2015-1, p. 19-39.

Sillitoe, R.H., 2010, Porphyry Copper Systems; Economic Geology, v. 105, p. 3-41.

van Straaten, B.I., Oliver, J., Crozier, J., and Goodhue, L., 2013, A summary of the Gibraltar porphyry copper-molybdenum deposit, south- central British Columbia, Canada; *in:* Porphyry Systems of Central and Southern British Columbia: Tour of Central British Columbia Porphyry Deposits from Prince George to Princeton, (eds.) J.M. Logan and T.G. Schroeter; Society of Economic Geologists, Field Trip Guidebook, Series 43, p. 55-66.

3.8 Addendum: Geological Map of the GMB, and the Origin and Composition of Epidote in the GMB

This addendum describes the composition of Fe-rich and Fe-poor epidote, and discusses the origins of epidote in the GMB and Nicola volcanoclastic rocks.

Table 3.4: Number of analysis on epidote for this report.

	Number of analysis with SEM-EDS*	Number of analysis with EPMA *
Epidote Cores from GMB	50	8
Epidote rims from the GMB	50	17
Epidote from Nicola rocks	17	0
REE-bearing epidote	5	3
Epidote in contact with sulphides	11	0

*Details for each analysis in Appendix 1, Table A1-2 to A1-9

3.8.1 Geological map of the GMB.

Following the previous workers, this chapter uses names of phases in the GMB; Border phase, Mine phase, Granite Mountain phase and Burgess Creek stock (Fig. 3.1). However, since different phases and their boundaries are not well defined subsequent chapters use a simplified classification: mineralized and unmineralized tonalites in Chapters 4 and 5.

3.8.2. Definition of Fe-poor and Fe-rich epidote.

This report uses the terms Fe-rich and Fe-poor epidote. The boundary between Fe-rich and Fe-poor epidote is within the composition of epidote (sensu-stricto). Fe-poor epidote contains Al, greater than 2.2 Al apfu (Fig. 3.4). The clinozoisite is defined as those with more than 2.5 Al apfu, the boundary for Fe-poor and Fe-rich was selected to separate the Fe-rich rims and Fe-poor cores of epidote found in the GMB. This threshold is equivalent to 0.29 Fe(t)/[Fe(t) + Al] ratios (apfu), or 14.8 wt.% Fe_2O_3(t).

3.8.3 Origin of epidote

Epidote is commonly associated with hydrothermal activity as an important component of propylitic alteration associated with cooling intrusions at shallow crustal levels (Zaluski et al., 1994; Sheets et al., 1996; Dilles et al., 2000; Proffett, 2003). Though the occurrences are rare, magmatic epidote has been documented in tonalitic rocks (Schmidt and Poli, 2004 and references therin) and thus the possible occurrence of magmatic epidote is considered.

Bysouth et al. (1995) and Ash et al. (1999) interpret the entire GMB to have undergone greenschist facies metamorphism. Thus, the possibility of metamorphic epidote is also considered.

Possible origin as magmatic epidote. Epidote can be a minor accessory mineral in tonalitic rocks (Schmidt and Poli, 2004). Texturally, magmatic epidote tend to be euhedral to subhedral in shape with sharp and clear grain boundaries with hexagonal or prismatic shapes. Magmatic epidote usually shows and ophitic texture and is associated with primary igneous minerals such as hornblende and biotite. Magmatic epidote tends to have high TiO_2 content (>0.2 wt. %). Magmatic epidote typically shows oscillatory zoning with REE-rich cores. Magmatic epidote composition is typically 0.3 to 0.7 $Fe^{3+}/(Fe^{3+}+Al)$ (Schmidt and Poli, 2004). Magmatic epidote crystalizes above certain pressure (0.3 to 0.7 GPa) (Schmidt and Poli, 2004). These criteria exclude the possibility of GMB epidote being magmatic. Only 2 of 158 analysis by SEM-EDS and EPMA show $TiO_2 > 0.2$ wt.% (GBR-4 and GBR-11 respectively, Appendix 1, Tables A1-8 and A1-7). Epidote in the GMB is associated only with alteration minerals such as chlorite and white mica and is not observed to be associated with primary hornblende and biotite. Furthermore, approximately half the epidote shows $Fe^{3+}/(Fe^{3+}+Al)$ below 0.3, these epidotes (78 of 158) are mostly the Fe-poor cores of the zoned epidote of the GMB. Additionally, although we do see zoning, the Fe-poor cores of these epidotes do not contain detectable REEs. We have pressure and depth estimates using amphibole compositions (see Chapter 5, section 5.5.8) of 0.0045 GPa, equivalent to 1.5 km depth. This suggests that unless epidote crystalized much earlier than amphibole, it is unlikely that epidote in GMB is magmatic. Combining all the evidence listed above, epidote observed in GMB is unlikely of a magmatic origin.

Possible origin as metamorphic epidote. The criteria for metamorphic epidote are vague. Fe-Al compositional zoning is common and metamorphic epidote shows a compositional array ranging from 0 to 1 $Fe^{3+}/(Fe^{3+}+Al)$. Thus it cannot serve to rule out any of the epidote from the GMB. However, allanite-rich cores and REE-bearing epidotes are not metamorphic (Dawes and Evans, 1991). This rules out metamorphic origins for REE-epidote from this study. Many low-grade metamorphic rocks show Fe content in epidote decreasing with increasing metamorphic grade. For example, for the temperature range of 325 to 405°C metamorphic epidote compositions become more aluminous with increasing temperature (Apted and Liou, 1983). This suggests that if the zoned epidote in the GMB is metamorphic, it would have to have grown during retrograde metamorphism. We cannot rule out a metamorphic origin for epidote of the GMB.

Hydrothermal epidote. If epidote in the GMB is indeed of hydrothermal origin there are several factors that affected epidote composition. The composition of epidote depends directly on the ratio of the activities of Fe^{3+} and Al^{3+} in hydrothermal fluids (Arnason et al., 1993). Small shifts in fluid composition during isothermal growth of epidote can produce compositional zoning patterns defined by Fe^{3+} and Al^{3+} substitution in the M sites of the epidote crystal structure (Arnason et al., 1993). However, host rock composition, temperature, oxygen fugacity and pH can also contribute to epidote composition. Epidote formed from a host rock with higher Fe_2O_3/Al_2O_3 ratios are significantly higher in Fe_2O_3 (Arnason et al., 1993). As discussed in Chapter 4, activities of Al^{3+} and Fe^{3+} can affect hydrothermal epidote composition. Aqueous complexation of Al^{3+} and Fe^{3+} with OH^-, Cl^-, HS^-, SO_4^{2-} and CO_3^{2-} and the concentrations of these ligands depend on pH, sulfur fugacity, oxygen fugacity and carbon dioxide fugacity (Arnason et al., 1993). Changes in fluid composition leading to changes in epidote composition can be independent of temperature and pressure variables (Arnason et al., 1993). Higher fO_2 results in higher Fe^{3+}/total Fe and thus form more Fe rich epidote (Holdaway, 1972; Liou, 1973). Since Al^{3+} and Fe^{3+} occur predominantly as hydroxide complexes, small changes in pH can cause large variations in the Fe^{3+}-Al^{3+} substitutions in epidote, with increasing pH leading to lower activity of Fe^{3+} in fluids, leading to more Fe-poor epidote. If all epidote in the GMB is hydrothermal the zoning pattern (Fe-poor cores with Fe-rich rims) can be explained by depletion of Fe via the precipitation of sulfides in a S-rich hydrothermal fluid. An increase in fO_2, or a decrease of pH in fluids can also form this zoning. The effect of host rock composition is likely not a large factor as most rocks of the GMB are tonalites with only minor variations in the abundances of Al and total Fe.

Since the GMB has been shown to be a composite batholith (see chapter 5, section 5.5.1), hydrothermal origins for epidote even in distal rocks from mineralization is plausible. The zoning pattern can be produced by sulfide deposition in the mineralized intrusions, but there is little sulphides far from the mineralization. Therefore the distal (>5km from mineralized intrusions) zoned epidote is not likely related to sulphides and can perhaps be explained by the factors discussed above.

Origin of Allanite. Allanite has been reported as an igneous, metamorphic and hydrothermal product. In calc-alkaline granites igneous allanite commonly occurs as the REE-rich cores of magmatic epidote and typically displays zoning with REE-rich cores and REE-poor rims (Gieré, and Sorensen, 2004). We do not observe magmatic epidote in the GMB, thus magmatic allanite is unlikely.

Metamorphic allanite has been reported in pelitic and mafic rocks as well as in granitic gneisses and in carbonate rocks in metamorphic settings (Gieré, and Sorensen, 2004 and references therin). None of these settings applies the GMB, thus we rule out metamorphic origins for allanite.

Hydrothermal allanite crystilizes from either REE-rich hydrothermal fluids or the mobilization of REEs from other minerals. Jagged, irregualar grain boundaries and patchy zoning are reported in hydrothermal allanite (Gieré, and Sorensen, 2004). Allanite in the GMB in BSE imagery shows these characteristics (Fig. 3.7). Allanite is only associated with other alteration minerals such as secondary quartz, epidote and chlorite. Additionally, allanite is only located proximal to mineralized intrusions. This combined evidence supports the hydrothermal origins of allanite in the GMB.

Origin of epidote in the Nicola volcaniclastics. The Nicola group rocks in our study area are described as sandstone and gritty pebbly sandstone with local intercalated conglomerate, mafic and felsic volcanic breccia, siltstone, limestone and basalt (Schiarizza, 2015). We only examined Nicola group rocks near the GMB and they are green mafic volcaniclastics rocks, rich in chlorite and epidote. We discount the possibility of magmatic epidote since magmatic epidote has not been observed in the types of rocks mentioned above. This leaves the possibility of epidote with metamorphic or hydrothermal origin, and since the Nicola rocks have been documented to be intruded by the GMB, and having undergone greenschist metamorphism. We have documented a marked increase in epidote modality (>40 vol.%) proximal (<500m) to the contact with the GMB compared to rocks distal (>500m) from the GMB where epidote is less than 30 vol%. This observation has three possible interpretations. The heat from the intrusion of the GMB increased contact metamorphism locally generating more epidote. The fluids released from a cooling intrusive of the GMB interacted with the host rock to generate epidote, or a combination of the two processes. The lack of zoning in the Nicola volcanics is explained by high Fe (11-13 wt.% FeO total) and low Al (7-10 wt.%) compared to tonalitic rocks of the GMB (< 6 wt.%. FeO and >13 wt.% Al_2O_3). The other possibility is that the heat from the intrusion of the GMB generated epidote through contact metamorphism. Since we only have 12 samples of the Nicola volcanics and 3 thin sections, further discussion to the origin of epidote in the Nicola rocks is impossible. We can only say that the intrusion of the GMB influenced epidote in the Nicola rocks by metamorphism, hydrothermalism or both.

References in Addendum

Apted, M. J., and Liou, J. G. 1983, Phase relations among greenschist, epidote-amphibolite, and amphibolite in a basaltic system. American Journal of Science, v. 283(A), p. 328-354.

Arnason, J. G., Bird, D. K., and Liou, J. G. 1993, Variables controlling epidote composition in hydrothermal and low-pressure regional metamorphic rocks.

Dawes, R. L., and Evans, B. W. 1991, Mineralogy and geothermobarometry of magmatic epidote-bearing dikes, Front Range, Colorado. Geological Society of America Bulletin, v. 103(8), p. 1017-1031.

Dilles, J. H., Einaudi, M. T., Proffett, J., and Barton, M. D. 2000, Overview of the Yerington porphyry copper district: Magmatic to nonmagmatic sources of hydrothermal fluids: Their flow paths and alteration effects on rocks and Cu-Mo-Fe-Au ores. Society of Economic Geologists Guidebook Series, 32(Part 1), p. 55-66.

Gieré, R., and Sorensen, S. S. 2004, Allanite and other REE-rich epidote-group minerals. Reviews in Mineralogy and Geochemistry, v. 56(1), p. 431-493.

Holdaway, M. J. 1972, Thermal stability of Al-Fe epidote as a function of $ƒO2$ and Fe content. Contributions to Mineralogy and Petrology, v. 37(4), p. 307-340.

Liou, J. G. 1973, Synthesis and stability relations of epidote, $Ca_2Al_2FeSi_3O_{12}(OH)$. Journal of Petrology, v. 14(3), p. 381-413.

Proffett, J. M. 2003, Geology of the Bajo de la Alumbrera porphyry copper-gold deposit, Argentina. Economic Geology, v.98(8), p.1535-1574.

Sheets, R. W., Nesbitt, B. E., and Muehlenbachs, K. 1996, Meteoric water component in magmatic fluids from porphyry copper mineralization, Babine Lake area, British Columbia. Geology, v. 24(12), p. 1091-1094.

Schmidt, M. W., and Poli, S. 2004, Magmatic epidote. Reviews in Mineralogy and Geochemistry, v. 56(1), p. 399-430.

Zaluski, G., Nesbitt, B., and Muehlenbachs, K. 1994, Hydrothermal alteration and stable isotope systematics of the Babine porphyry Cu deposits, British Columbia; implications for fluid evolution of porphyry systems. Economic Geology, v. 89(7), p. 1518-1541.

CHAPTER 4.

Protracted magmatism and mineralized hydrothermal activity in the Quesnelia island arc for the Gibraltar porphyry Copper-molybdenum deposit, British Columbia.

C.H. Kobylinski, K. Hattori, S. Smith and A. Plouffe

To be submitted to Economic Geology

Abstract

The Gibraltar porphyry Cu-Mo deposit with the total tonnage of 3.2 Mt Cu in the Canadian Cordillera is hosted by the Late Triassic Granite Mountain Batholith (GMB). The batholith formed through multiple tonalitic intrusions in a period of ~ 25 m.y beginning at 229.2 ±4.4 Ma in the Quesnel island arc. After the batholith was essentially established, fertile intrusions intruded in the centre of the batholith during at least three events over a period from 218.9±3.1 Ma to 205.8±2.1 Ma. These intrusions produced potassic alteration and white mica alteration and resulted in chalcopyrite-quartz veinlets and disseminated chalcopyrite. Zircon in the oldest mineralized intrusion (218.9±3.1 Ma) shows high Ce^{4+}/Ce^{3+} (680± 414, [2σ], n=15) compared to those (123± 56, [2σ], n=118) from older unmineralized intrusions. Oxidation conditions for parental magmas of intrusions were calculated based on the compositions of zircon and amphibole. The two methods yielded similar results. Mineralized intrusions are oxidized (average ΔFMQ = +1.7±1.8, [2 σ], n = 73), whereas those for older unmineralized intrusions, have a slightly lower fO_2 (average ΔFMQ = +1.3±1.4, [2σ], n =108), although the values are overlapping for the two. The bulk rocks of mineralized intrusions show low Sr/Y ratios (< 22) compared to those associated with many other porphyry Cu deposits in the world. The data suggest that igneous rocks elsewhere with low Sr/Y may have potentials to host economic Cu deposits.

Ratios of Ce/Nd and Ce/Ce* (=Ce/[Nd*Sm]$^{1/2}$) in zircon are positively correlated with the Ce^{4+}/Ce^{3+} in zircon from the GMB. Since the former two ratios can be obtained solely from zircon composition, the values for detrital zircon are useful in evaluating the occurrences of oxidized intrusions in regional mineral exploration.

4.1. Introduction

Porphyry-type metal deposits commonly occur in close spatial association with large batholith-size intrusions. Examples include the Yerington porphyry-Cu deposit in the Yerington batholith, Nevada, USA (Dilles, 1987), the Highland Valley Cu deposit within the Guichon Creek batholith, British Columbia, Canada (D'Angelo et al., 2017; Whalen et al., 2017), and the Endako porphyry Mo deposit in the Endako batholith, British Columbia, Canada (Villeneuve et al., 2001; Whalen et al., 2001). In other deposits, the occurrences of large batholiths are predicted below porphyry deposits based on plugs and stocks with similar compositions. Examples include the Bajo de la Alumbrera deposit, Argentina (Proffett, 2003), and the Endeavour deposits (Endeavour 22, 26, 27 and 48 deposits) in Australia (combined, 0.7 Mt Cu; Heithersay and Walshe, 1995; Lickfold et al., 2003). The northwestern section of the Bingham Canyon deposit, USA, may also overlie a large magma chamber that fed porphyritic dykes (Redmond and Einaudi, 2010). On the other hand, some batholiths spatially associated with porphyry Cu deposits appear to have no genetic relationship with the mineralization. For example, large intrusive bodies in the Escondida porphyry districts (144 MtCu) in Chile are barren and predate the mineralization (Hervé et al., 2012).

The Gibraltar porphyry Cu-Mo deposit, located in south central British Columbia, Canada, provides a site to evaluate the relationship between the mineralization and the tonalitic Granite Mountain Batholith (GMB). Following our petrographic and mineralogical study of the GMB (Kobylinski et al., 2016, 2017), this paper presents U-Pb ages and trace-element abundances of zircon grains from the representative rocks of the GMB and evaluate the relationship between the batholith and the mineralization. The paper also discusses the applicability of fertility indicator of igneous rocks, proposed by previous workers.

4.2 Geology of the study area

4.2.1 Regional geology

The Gibraltar porphyry Cu-Mo deposit is hosted by the GMB, which intruded the Nicola Group mafic volcaniclastic rocks of the Quesnel terrane, close to the boundary with the Cache Creek terrane (Fig. 4.1; Schiarizza, 2015). The Quesnel terrane is an allochthon formed as an oceanic arc and accreted to the North American continent during the middle Jurassic (180 - 150 Ma) (Ghosh, 1995, and references therein). The Cache Creek terrane is comprised of Paleozoic to early Mesozoic carbonate rocks which are also an allochthon, accreted to the North American continent during the Mesozoic (Johnston and Borel, 2007). The Quesnel terrane of over 1,250 km in length is an important metallogenic province, containing over 19 past- and present-producing porphyry Cu±Mo±Au deposits in Mesozoic granitic intrusions (Fig. 4.1), including the Gibraltar and Highland Valley mines.

4.2.2. Geology of the Granite Mountain Batholith

The GMB has a surface exposure of ~150 km^2, ~10 km east-west and ~15 km north south. It consists of mostly tonalite with minor quartz diorite (Fig. 4.2). The rocks in the batholith are all holocrystalline with no porphyritic plugs and dikes. The GMB is in fault contact with carbonate rocks of the Cache Creek terrane in the southeast, and in intrusive contact with the Nicola group volcanoclastic rocks to the east and northeast. The western part of the batholith is covered by Cenozoic flood basalts of the Chilcotin group (Fig. 4.2).

Primary igneous minerals of GMB are plagioclase, quartz, biotite, hornblende, titanite, magnetite, zircon and apatite in order of abundance (Appendix 2, Table A2-1). The modality of these minerals varies within the batholith. Among these minerals, primary hornblende and biotite proximal (<4 km) to mine pits are recognized only by relict textures in thin sections as they are altered to secondary biotite ± chlorite and chlorite ± titanite and rutile respectively. Unaltered hornblende and biotite are observed only in unmineralized tonalites distal (> 5 km) from the mine pits. Primary titanite and magnetite are common in all rocks of the GMB. Titanite forms large euhedral crystals (up to 1 mm long and 0.3 mm wide). Primary magnetite occurs as small euhedral cubes (up to 200μm wide) in trace quantities in all samples.

Previous studies divided the GMB into four phases based on texture, lithology and degrees of alteration. They include the Border phase (quartz diorite), Mine phase (tonalite), Granite Mountain phase (leucocratic tonalite), and the Burgess Creek stock (leucocratic tonalite) in the northeastern part of the GMB (Bysouth et al., 1995; Schiarizza, 2015). As noted by previous researchers, the distribution of phases is poorly defined because intrusive contacts are not exposed. Furthermore, no distinctive features characterize each phase due to large variations in the grain size and modality of minerals and textures within one phase. Therefore, this study simply divides the rocks of the GMB into mineralized and unmineralized intrusions (Fig. 4.2). The mineralized intrusions are those containing visible chalcopyrite. Unmineralized intrusions contain less than 110 ppm Cu.

The regional geology, lithology of GMB and the mineralization are described in Sutherland Brown (1976), Drummond et al. (1976), Panteleyev (1978), Bysouth et al. (1995), Ash et al. (1999a, b), Ash and Riveros (2001), van Straaten et al. (2013), and Schiarizza (2014, 2015).

4.2.3. Gibraltar porphyry Cu-Mo deposit

The Cu mineralization at Gibraltar occurs primarily as disseminated chalcopyrite and as chalcopyrite in quartz veins and veinlets in foliated tonalite in the central part of the GMB (Fig. 4.2). The contents of Cu show several mineralized areas in the central part of the GMB (Fig. 4.2). The largest ones are around the Pollyanna, Gibraltar East and Granite Lake pits (Fig. 4.2). Among these three pits, the mineralization in the Granite Lake pit is the largest at 0.72 Mt Cu of geological reserves (past production since 2004 and reserves), which is followed by 0.51 Mt Cu from the Polyanna pit and 0.26 Mt Cu from the Gibraltar East pit (compiled from annual data at www.sedar.com). There are several other isolated mineralized areas; 100m east and 200m north east of the Granite Lake pit, ~500m east and 500m north east of the Granite Lake pit, and 200m north west of the Gibraltar East pit (Fig. 4.2). The mineralization is vertically continuous forming chimney-like distribution of high Cu rocks (Fig. 4.3). Such “chimneys” at the Granite Lake pit and Pollyanna are over 500 m to 1000 m in height from the current surface. (Fig. 4.3).

The Gibraltar porphyry Cu-Mo mine is operated by Taseko Mines Ltd. Its mining began in 1972 and it was temporarily closed between 1999 and 2004 and reopened in 2004. From 1972 to 2018, 1.5 Mt Cu were extracted from the Gibraltar deposit. The estimated reserves in 2019 of the mine are 1.7 Mt Cu which makes the total tonnage (past production plus reserves) 3.2 Mt Cu (data compiled from MINEFILE No-093B-012, Ministry of Energy, Mines and Petroleum Resource of British Columbia).

Molybdenite is not abundant and occurs as dissemination and in quartz veins. Molybdenite samples from quartz veins in the Granite Lake pit gave Re-Os ages of 212.7 ±-0.9 Ma and 215±1 Ma and one disseminated sample from the Gibraltar East pit yielded 210.0±0.9 Ma (Harding, 2012).

4.2.4. Hydrothermal alteration in Granite Mountain Batholith

Hydrothermal alteration is pervasive close to the mine pits, although the original igneous textures are well preserved. Alteration minerals include quartz, secondary K-feldspar, secondary biotite after hornblende, rutile and titanite in chloritized biotite, epidote after plagioclase and hornblende, and chlorite replacing biotite and hornblende. The potassic alteration, forming secondary K-feldspar and secondary biotite, is only recognized proximal (<1.1 km) to and within mine pits. Secondary K-feldspar forms veinlets (several mm in width) close to the mine pits and replaces plagioclase. These K-feldspar grains are commonly replaced by a mixture of white mica and minor epidote. The secondary biotite is recognized as aggregates of fine-grained biotite replacing hornblende crystals (Fig. 4.4 A). The secondary biotite is extensively overprinted by chlorite and the potassic alteration is identified only in thin sections (Fig. 4.4 A).

White mica is ubiquitous and prominent in hand specimens up to 2.5 km from the mine pits. Its abundance decreases with increasing distance from the open pits (Fig. 4.5 A). Aggregates of white mica replace plagioclase crystals (Figs. 4.4 C, D) and form mono-mineralic veinlets, up to 1 cm in width (Fig. 4.4 C). Abundant white mica with quartz is one of the characteristic features associated with the Cu mineralization.

Pyrite in unmineralized rocks is absent or rare whereas pyrite in mineralized samples is common but minor in volume. Pyrite occurs as disseminated small (up to several mm) cubes and small (20 μm) inclusions in epidote. Rare pyrite cubes are found in quartz veins.

Secondary magnetite is present in mineralized tonalite and occurs within quartz veins along with epidote, chalcopyrite, white mica and chlorite. It is distinct from primary magnetite by its anhedral form, and occurrence with alteration minerals.

Epidote is common in the GMB, but its abundance generally increases with increasing distance from mine pit (Fig. 4.5 B). It replaces plagioclase (Fig. 4.4 B), and forms aggregates and veins/veinlets with or without quartz. The occurrence of epidote gives a lime-green color to the white tonalitic rocks and is observed even 10 km from the mine pits in the margins of the batholith (Kobylinski et al., 2016).

Chlorite is common throughout the GMB. In mineralized intrusions, it commonly replaces mafic minerals, such as primary and secondary biotite and hornblende. It is also common rimming these mafic minerals in unmineralized intrusions. Titanite and rutile also occur in the alteration of biotite, forming small aggregates with chlorite. Since primary biotite contains significant Ti, chloritization of primary biotite releases Ti to form titanite (~50 μm in length, ~25μm in width) and rutile needles (~25 μm in length, ~10μm in width) (Kobylinski et al., 2016).

Hydrothermal quartz forms veins and veinlets with chalcopyrite ±chlorite ±magnetite and ± epidote in mineralized intrusions. Mono-minerallic quartz veins are rare but occur in mineralized samples. Quartz veins are commonly surrounded by haloes of white mica.

Potassic and white mica alteration show overlapping distribution, proximal, < 1.1 km for potassic, <2.5 km for white mica, to the pits (Fig. 4.5). Furthermore, these rocks commonly contain chalcopyrite, suggesting the two alteration types are associated with mineralizing hydrothermal activity.

4.3. Samples and analytical methods

4.3.1. Sampling

A total of 101 samples were collected for the study of the GMB. After careful petrographic examinations of samples (Kobylinski et al., 2016, 2017), 16 tonalite samples were selected for trace-element study of zircon, and 10 of these samples were dated by the U-Pb zircon method, to represent different lithologies, locations, degrees of alteration and presence of Cu mineralization (Table 4.1). The sample locations are shown in Fig. 4 2. Their mineralogy, textures and location coordinates are presented in Appendix 2, Tables A2-1.

4.3.2. Analytical methods for bulk-rock compositions

Rock samples were washed with de-ionized water, and weathered sections were removed. Veins of quartz, sulfide minerals and epidote are removed before pulverization. Selected samples were stained using sodium cobaltinitrite to examine the distribution of K-feldspar. For bulk-rock analysis, pulverized samples were fused with lithium metaborate and lithium tetraborate. The fused glass was dissolved in 5% nitric acid to determine the abundance of major, minor and trace elements using a Perkin Elmer Sciex 9000 ICP/MS at Actlabs (analytical code 4LITHOS) in Ancaster, Ontario, Canada. Precision of the analysis was determined by comparing unmarked duplicate samples. Accuracy was calculated by comparing measured values to certified values of international standards NIST 694, DNC-1, GBW 07113, LKSD-3, TDB-1, W-2a, SY-4, CTA-AC-1, BIR-1a, NCS DC86312, NCS DC70009, OREAS 100a, OREAS 101a, OREAS 101b, and JR-1. Most elements show accuracy better than 95%. Loss on ignition (LOI) was measured at the University of Ottawa using 1-5 grams of pulverized samples after heating the samples at 1050°C for 2 hours. The bulk rock compositions of samples, and the accuracy and precision of the analysis are listed in Appendix 2, Table A2-2.

4.3.3. Analytical methods for zircon

Zircon grains ranging in size from 80 to 350 μm were concentrated by magnetic and density separation, the latter with di-iodomethane (3.3 g/cm^3). Clear grains were handpicked under a binocular microscope, mounted in an epoxy resin and polished to expose the centers of grains. Zircons in epoxy resin were examined using a transmitted light microscope to identify mineral inclusions and fractures. Back scattered electron (BSE) and cathodoluminescence (CL) images were collected for individual grains using a JEOL 6610LV scanning electron microscope equipped with CL detector at the University of Ottawa. Since sector-zoned zircon is known to show highly heterogeneous distribution of elements (Griffin et al., 2002; Corfu et al., 2003), only grains without sector zoning were selected for trace-element analysis (Fig. 4.6; Tables 4.3 and 4.4).

4.3.3.1. Laser ablation ICP-MS analysis. Trace element analysis and U-Pb dating used a Photon Machines Analyte Excite 193 nm excimer laser attached to an Agilent 7700x ICP-MS (LA-ICP-MS) at the University of Ottawa. Detailed operating conditions are described in Appendix 2, Table A2-5. Counts of ^{140}Ce, ^{31}P, ^{42}Ca, ^{56}Fe, and ^{88}Sr were monitored during the analysis and high counts of any of P, Ca, Fe and Sr were discarded as they represent inclusions of calcite, phosphate minerals or Fe-oxides. Raw counts of elements were reduced using the GLITTER! software (Griffin et al., 2008).

4.3.3.2. Trace element analysis. The composition of 191 zircon grains was determined. The concentration of trace elements are obtained using the count ratios of the elements to Si in NIST 612G (Jochum et al., 2011) and sample zircon assuming the stoichiometric concentration of 152852 ppm Si in zircon. Accuracy and precision of the analytical data was verified using the following internal standards: 91500 zircon (Wiedenbeck et al., 1995), BCR-2G glass (Jochum et al., 2011), GSEG1 synthetic basalt glass (Jochum et al., 2011). Plešovice zircon (Sláma et al., 2008) was used as an external standard. These reference materials were ablated for every five unknown zircon grains. For the concentration of Ti, a factor of 1.16 was applied to the values to account for the matrix effect, as suggested by Page et al. (2007) and Fu et al. (2008). Analytical results with a larger than 10% error between obtained values and preferred 91500 values of any elements were discarded.

4.3.3.3. U-Pb geochronology. During analysis, raw counts for U-Pb dating were reduced using the UPb.age script in the R software environment (Solari and Tanner, 2011). The script removes outliers (±2σ), data containing mineral inclusions, corrects for instrumental drift and downhole isotope fractionation using the accepted values of 91500 zircon (Wiedenbeck et al., 1995). Ages were calculated using $^{207}Pb/^{235}U$ and $^{206}Pb/^{238}U$ ratios for zircons using Isoplot v.4.14 (Ludwig, 2012) and 137.818 as the present-day ratio of $^{238}U/^{235}U$ (Hiess et al., 2012). Data are plotted on a Concordia diagram with 2σ propagated systematic errors (Appendix 2, Concordia diagrams). Plešovice zircon was used as an external standard for validation of calculated ages and to calculate excess variance. Systematic uncertainty due to the ratio uncertainty of reference material [S_y, 2σ], excess variance of validation material(s) [ε', 2σ] and an error of decay constant [λ] was propagated to uncertainty (S_x) of the age population. A systematic error of 6.8% for $^{207}Pb/^{235}U$ and 3.4% for $^{206}Pb/^{238}U$ was identified for this study. Analytical results were discarded when there were outliers using a weight average test. Since the counts of ^{204}Pb were low, possible contribution of common Pb was not corrected.

Error propagation and validation of the data based on reference material are described in detail in Appendix 2, Table A2-4. Acquisition parameters for U-Pb and trace element data are listed in Appendix 2, Table A2-5.

4.3.4 Analytical methods for amphibole

Igneous amphibole grains were examined with a SEM to select compositionally homogeneous, unaltered grains for the quantitative analysis for the major and minor elemental abundances using a JEOL 8230 electron probe micro-analyzer (EPMA) at the University of Ottawa. The operating conditions are an accelerating voltage of 15 kV, a beam current of 20 nA using a focused beam of 5µm. Counting times were 20 s on-peak and 20 s off-peak for all elements except for F (40 s on and 40 s off), Cl (40 s on and 40 s off). Amphibole composition, reference material for quantification, accuracy, detections limits and precision of the analysis are listed in Appendix 2, Table A2-6. Amphibole analysis was conducted on the unmineralized tonalite sample GBR2-34, the nearest sample analyzed using zircon is GBR2-30 a unmineralized tonalite 200m west of GBR2-34 (Fig. 4.2).

4.4. Results

4.4.1. Bulk rock compositions

The samples used for this study are tonalitic with SiO_2 ranging from 63 to 72 wt.%. Low MgO wt.% values of unmineralized intrusions are reflected by leucocratic nature of rocks with high SiO_2, >65.5 wt.%, and low Sc, <11 ppm, whereas high MgO wt.% of mineralized intrusions are consistent with low SiO_2, <67.7 wt.% and high Sc, > 9 ppm (Fig. 4.7, Appendix 2, Table A2-2). All samples show a gently negative slope of the normalized rare earth element (REE) pattern; light REEs (La to Gd) ranging from 55 to 196 times chondrite values and heavy REEs (Tb to Lu) from 46 to 150 times chondrite values (Fig. 4.8; Appendix 2, Table A2-2). The ratios of normalized values of La/Lu, La_N/Lu_N, for all samples vary from 1.8 to 14. Unmineralized intrusions show a steeper slope (average $La_N/Lu_N = 8.4$) than those of mineralized intrusions (average $La_N/Lu_N = 2.8$; Fig. 4.8; Appendix 2, Table A2-2). This is consistent with a more evolved nature of unmineralized intrusions with lower Mg#, higher SiO_2 than mineralized intrusions. Bulk-rock Eu anomalies, Eu/Eu* ($=Eu_N/(Sm_N*Gd_N)^{1/2}$), range from 0.57 to 1.2. The higher values of Eu/Eu* (>0.95) are associated with unmineralized intrusions, whereas lower Eu/Eu* values (0.57-0.73) characterize the mineralized intrusions (Table 4.2).

Bulk rock Sr/Y ratios of unmineralized intrusions show a wide range from 6 to 46, whereas the values of mineralized intrusions range from 9 to 22 (Figs. 4.9, 5.11; Table 4.2). Strontium is a fluid mobile element, but the ratios of Sr/Y likely reflect the primary values, Sr contents are not correlated with the enrichment of K (correlation coefficient of 0.39). Neither Sr/Y nor 1/Sr values correlate with the degrees of alteration, as represented by LOI (1.1-3.34 wt. %) with correlation coefficients of 0.29 and 0.06, respectively.

4.4.2. Zircon composition

Zircon grains have prismatic faces with length to width ratios ranging from 1 to 3 (Fig. 4.6). Zircon grains commonly contain apatite inclusions (5–30 μm in length; Fig. 4.6 B) and these areas are avoided during LA-ICP-MS analysis. Zircon grains (n=191) show sharp oscillatory zoning in CL images (Fig. 4.6), with Th/U ratios ranging from 0.18 to 1.44 and Th concentrations of 4.9 to 90.5 ppm (Appendix 2, Table A2-3). The majority of zircon grains (182 grains out of 191) show Th/U ratios greater than 0.2 (Appendix 2, Table A2-3). These high ratios, > 0.2, confirm igneous origin of zircon (Hoskin and Ireland, 2000; Hoskin and Schaltegger, 2003). Combining the sharp zoning, morphology and Th/U ratios, the majority of the Gibraltar grains are considered to be magmatic zircon. Ten grains (out of 191) have low Th/U ratios, < 0.2, and the origins of these grains were examined whether they have undergone modification by subsolidus processes. Zircon grains that undergo subsolidus alteration are enriched in light rare earth elements (LREE) because LREEs are mobile compared to heavy rare earth elements (HREE) in aqueous fluids (Hoskin et al., 2000; Hoskin and Schaltegger, 2003). The Nd/Yb ratios of all studied zircons range from 0.0009 to 0.002 (Appendix 2, Table A2-3), independent of Th/U ratios. The Nd/Yb values in our samples are lower than the range of values, 0.003-0.01, for hydrothermal zircon reported by Hoskin et al. (2000). These observations suggest that zircon grains with low Th/U in our samples are magmatic and that the values reflect those of the parental magmas. Only one zircon grain in sample GBR-7 appears to be an exception, with resorbed core surrounded by a patchy oscillatory zoned rim. The rim has a low Th/U values (0.10) and relatively high Nd/Yb ratio (0.027), suggesting that its overgrowth may have occurred under subsolidus conditions. The compositional data of this grain was discarded. Cl images of each zircon are found in Appendix 6.

4.4.3. U-Pb zircon ages

U-Pb zircon ages indicate at least four distinct intrusive events in the GMB. The oldest group, 229.2 ±4.4 Ma (n=11), is obtained from unmineralized intrusions (n= 4) (Table 4.4). These rocks (GBR2-16, GBR2-25, GBR2-30, GBR2-38) are distal (>5 km) from mine pits (Fig. 4.2) and contain unaltered primary biotite and hornblende. They show epidote, chlorite and very minor white mica and pyrite, but no evidence of potassic alteration.

Mineralized intrusions show an age range of at least 7 m.y. and three distinct age groups; 218.9±3.1 Ma (n=1), 213.2±2.4 Ma (n=1), 205.8±2.1Ma (n=4; Table 4.4). These chalcopyrite-bearing intrusions are all medium to coarse-grained equigranular foliated to isotropic tonalite. They show similar primary and alteration minerals, and texture. There are no discernible differences among intrusions of different ages in the outcrops, hand specimens and in thin sections. They all show white mica and quartz veinlets with minor epidote, chlorite, a mixture of titanite and rutile in altered biotite. Relict primary biotite is also noted in samples.

The oldest among mineralized intrusions is represented by sample GBR 7 (218.9±3.1 Ma), which was collected in the Granite Lake pit and ~1 km south of the other two mine pits (Fig. 4.2). This sample shows pervasive white mica alteration with minor epidote. The bulk rock composition shows relatively low Cu content of 350 ppm (Appendix 2, Table A2-2), but the hand specimen contains chalcopyrite-quartz veinlets and these veins were removed before the pulverization for bulk rock analysis. The youngest age of the entire GBR was obtained from mineralized sample GBR-16 (201.9 ±5.0 Ma), which was collected 500 m northwest of the Gibraltar East pit (Fig. 4.2) (Table 4.4). This sample is a coarse grained equigranular isotopic tonalite that shows abundant white mica with minor epidote. Again, the bulk rock contains low Cu content of 240 ppm because chalcopyrite-bearing quartz veinlets and veins were mostly removed before pulverization of bulk rock analysis.

4.5. Discussion

4.5.1. Timing of intrusion of the Granite Mountain Batholith

U-Pb zircon dating from this study suggests that the GMB formed over ~25 m.y. through multiple intrusive events. The oldest group of intrusions in the GMB is represented by unmineralized rocks (average 229.2 ±4.4 [2σ] Ma; Fig. 4.10; Table 4.4) collected distal, > 5 km, from open pits (Fig. 4.2). These barren rocks are voluminous with large exposure (Fig. 4.2), and older than the mineralized intrusions (Table 4.4).

Previous researchers reported varying U-Pb zircon ages for the GMB. Our U-Pb zircon ages from different sites explain the reason for the wide variation in ages. Shiarizza (2015) reports U-Pb zircon ages from three locations (X_1, X_2, X_3 in Fig. 4.2) in the northeastern portion of the GMB, previously called the Burgess Creek Stock, which is barren with very weak white mica alteration (Fig. 4.5). The ages of 222.71±0.21 Ma at the site X1 and 221.25±0.20 at X_2 are comparable to those of unmineralized intrusions in this study (Table 4.4; Fig. 4.10). The sample at the site X_3 in the central part of the GMB yielded the age 217.15±0.20 Ma, which is contemporaneous with the oldest group of mineralized intrusions (Group A). A U-Pb zircon age of 215±0.8 Ma is also reported by Ash et al. (1999b) for tonalite approximately 1.5 km north east of the Gibraltar mill, which is located adjacent to the Gibraltar East pit (Fig. 4.2). Oliver et al. (2009) reports an even younger U-Pb zircon age of 211.9 ±4.3 Ma for tonalite less than 200 m from the Polyanna pit (Fig. 4.2). Although the descriptions of these dated rocks by previous researchers are not available, they are most likely intrusions related to the mineralization judging from the sample locations. These ages, 215 and 212 Ma, correspond to the periods for the intrusions of Cu fertile magmas determined in this study (Table 4.4; Fig. 4.10).

4.5.2. Tectonic setting of the Granite Mountain Batholith and mineralization

The Quesnel island arc is considered to be accreted to the North American continent at ~ 180 – 150 Ma (Ghosh, 1995). The ages of intrusions of the GMB obtained in this study suggest that batholith formation and the mineralization took place in the Quesnel island arc, before its accretion to the North American continent. The proposed interpretation is consistent with zircon geochemistry. The Th/U ratios of zircon in early unmineralized intrusions are low (0.15 – 0.44, average 0.28; n=118), and increase to higher values (0.16- 1.44, average 0.4; n=73) for mineralized intrusions (Table 4.3). The ratios of Th/U in zircon generally increase during fractional crystallization of magmas because Th with a larger ionic radius than U is less compatible than U within rock-forming minerals (Kirkland et al., 2015).This means that zircon in unmineralized intrusions should have higher Th/U ratios than those in later mineralized intrusions because the earlier intrusions contain higher SiO_2 and Sc and lower MgO than the later intrusions (Fig. 4.7). Our data shows the opposite where earlier zircon grains have low Th/U.

The change in Th/U in zircon grains is likely related to the evolution of the Quesnel island arc in which GMB formed. Primitive island arc magmas contain low Th, whereas continental arc magmas show generally high Th/U ratios because crustal rocks contain high Th (Barth et al., 2017 and references therein). Zircon from continental granitic rocks shows generally high ratios of Th/U, greater than 0.4 (e.g., Belousova et al., 2005; Yang et al., 2011). By contrast, zircon from the primitive intra-oceanic island arcs shows low Th/U ratios < 0.5 (Barth et al., 2017). In the Izu-Bonin island arc, Barth et al. (2017) documented an increase in the ratios of Th/U in zircon from 0.5 to 1.4 in the period of 8 m.y. during the increasing maturity of the arc. We suggest that the overall low Th/U ratios of zircon observed in unmineralized intrusions and their increase with time in the GMB are related to the evolution of Quesnel island arc. We suggest that the bulk of the GMB formed in a primitive island arc and the younger Cu fertile magmas formed after the island arc had evolved (Fig. 4.11).

U has multiple oxidation states, 4+ and 6+ in crustal conditions. Conversely Th is almost always 4+. This may lead to a potential fractionation of Th and U since highly oxidized magmas may have more U as U^{6+}. Zircon incorporates U^{4+} in the Zr^{4+} site then U^{6+} due similar charge. Thus, relatively oxidized magmas of the mineralized intrusions from this study may have a high Th/U in zircon. Based on Ce^{4+}/Ce^{3+}, the first mineralized magma (GBR-7, 218.9±3.1) is the most oxidized (Ce^{4+}/Ce^{3+} average of 681±414 [2σ], n=15) and subsequent magmas (213.2±2.4 and 205.8±2.1) are less oxidized (Ce^{4+}/Ce^{3+} average of 259±107 [2σ], n=14 and 189±96 [2σ], n=43, respectively), while Th/U still increases. This suggests that the effect of oxidation on the state of U in the melt may be a contributing factor when comparing relatively reduced unmineralized intrusions with oxidized mineralized intrusions, but the continual rise of Th/U through time in mineralized intrusions (Fig. 4.11) with diminishing oxidation suggests that arc evolutions plays a more important role in Th/U ratios.

4.5.3. Bulk rock Sr/Y ratios as a magma fertility indicator

High Sr/Y (>35) values of bulk-rock compositions have been suggested to be a fertility indicator of intrusions for porphyry Cu mineralization (Müller and Groves, 2000; Richards, 2011; Loucks, 2014; Fig. 4.12). A recent study by Agnew (2018) of the Bougainville island, host of the Panguna porphyry Cu-Au deposit (6.6 Mt Cu; Singer et al., 2008), appears to support this notion that Cu-fertile intrusions have high Sr/Y ratios, >35 (Fig. 4.12).

High Sr/Y ratios of magmas result from a variety of processes, including partial melting of young or delaminated slabs, and high-water content of magmas (Kay and Kay, 1993; Richards, 2011). Although such adakitic geochemical signatures are observed in many igneous rocks, few occur above young subducting slabs or delaminated slabs (e.g., Kay and Kay, 2002; Chung et al., 2003; Rodriquez et al., 2007; Chiaradia et al., 2012). Therefore, high Sr/Y ratios of igneous rocks associated with porphyry Cu deposits are attributed to a water-rich nature of the magmas (e.g., Richards, 2011; Loucks, 2014). High water contents suppress plagioclase crystallization (Sisson and Grove, 1993) and promotes crystallization of amphibole that incorporates Y, resulting in high Sr/Y values in the residual melt. Water-rich magmas for porphyry Cu mineralization are consistent with the general model for the mineralization involving immiscible separation of aqueous magmatic fluids.

Hornblende is common in intrusions in the GMB, which is consistent with water-rich nature of the parental magmas. However, mineralized rocks of the GMB show low bulk-rock Sr/Y values ranging between 8 and 22 (Fig. 4.9). Although unmineralized intrusions show higher Sr/Y than mineralized intrusions, the values are still low compared to the majority of igneous rocks associated with porphyry-type deposits in Figure 4.9. There are possible explanations for such low Sr/Y ratios in a water-rich magma. The fractional crystallization of plagioclase may have lowered Sr since Sr^{2+} can easily replace Ca^{2+} in plagioclase. This is consistent with low Eu/Eu*in bulk rocks and zircon grains discussed below. Titanite fractionation would also deplete Sr in a residual melt. Another factor that may affect Sr/Y values of bulk rock composition is alteration. Alteration may lead to Sr loss since Sr is a fluid mobile element and plagioclase is one of the most reactive mineral, however Sr values do not corelate with the Ishikawa alteration index (= $100*(K_2O + MgO)/(K_2O + MgO + Na_2O + CaO)$), chlorite carbonate pyrite index (=

100* (MgO + FeO)/(MgO + FeO + Na_2O + K_2O), Na_2O wt.%, K_2O wt.% or loss on ignition %. The Ishikawa alteration index defined by the replacement of albite by sericite the replacement of sericite by chlorite. However mineralized rocks (highly altered) do show lower Sr/Y ratios (8 - 22) when compared to relatively unaltered unmineralized rocks of this study (20 – 46) which puts back into question the effect of alteration. Sr/Y ratios in zircon show the same relationship, zircons from mineralized rocks show lower Sr/Y then zircons from unmineralized rocks, suggesting that the low Sr/Y ratios are inherited from magmas and not affected by subsequent alteration (Fig. 4.13).

Thus, our results from GMB samples associated with the Gibraltar porphyry Cu-Mo deposit suggest that high Sr/Y ratios are not a universally applicable indicator of fertility of igneous rocks (Figs. 4.9, 4.12), and that intrusions with low Sr/Y can also be associated with an economic porphyry Cu deposit.

4.5.4. Magma crystallization temperatures

The crystallization temperatures of zircons are calculated using Ti-in-zircon geothermometry of Ferry and Watson (2007). The calculation requires the activities of TiO_2 (αTiO_2) and SiO_2 in the melt. The activity of SiO_2 is 1 because of the abundance of quartz in the rocks. The value of αTiO_2 should be below 1 because there is no magmatic rutile in the samples. However, primary titanite is common throughout the GMB and therefore, we use a value of 0.7 for αTiO_2, as suggested by Watson et al. (2006) and Fu et al. (2008) for titanite-bearing igneous rocks. Furthermore, experimental work by Hayden and Watson (2007) shows that αTiO_2 in a felsic to intermediate melt is generally > 0.6 at temperatures between 650 and 1200°C. To verify our assumed value of αTiO_2, the zircon crystallization temperatures are compared to zircon saturation temperatures (described below). Similar temperatures of the two suggest that the value of 0.7 for αTiO_2 is reasonable. The use of 0.8 or 0.6 for αTiO_2 would decrease or increase the calculated temperatures by ~17°C and ~14°C, respectively.

The zircon crystallization temperatures are high (average 828°C, n=73) for the mineralized intrusions, and lower (average = 800°C, n=118) for unmineralized intrusions (Table 4.3). This is consistent with higher MgO wt.% of the mineralized intrusions and more leucocratic nature of unmineralized intrusions (Fig. 4.7).

Zircon saturation temperatures are calculated from bulk-rock compositions based on the equation of Watson and Harrison (1983). Since inherited zircons were not observed in our samples, the content of Zr is considered to represent that of the parental magma and the zircon crystallization temperatures should be similar to the zircon saturation temperatures. Among 191 crystallization temperatures of zircon grains, 143 grains have temperatures within uncertainties of their respective saturation temperatures, whereas 47 grains indicate significant differences, up to 50°C, between the two. The saturation temperatures in these cases are cooler than crystallization temperatures. Among the 47 grains, 40 grains are from mineralized intrusions. The discrepancy is likely due to the alteration of these mineralized rocks, since the calculation of saturation temperatures requires concentrations of K, Na and Ca, all of which are mobile in aqueous fluids. The mineralized intrusions contain abundant white mica due to the enrichment of K during hydrothermal alteration. The mineralized intrusions contain higher K_2O (average 1.38 wt %., n=6), and lower Na_2O (average 3.29 wt.%, n=6) than unmineralized intrusions (average 1.28 wt% K_2O and 4.40 wt.% Na_2O, n=10). An increase in K_2O by 0.1 wt.% and decrease in Na_2O by 1 wt.% would result in an overall decrease of 6.7°C in the calculated saturation temperature. Average CaO contents are similar for mineralized and unmineralized intrusions at 3.04 and 3.18 wt.%, respectively, but the compositions of intrusions before hydrothermal alteration are not known. For example, the mineralized intrusions likely had higher Ca before the extensive alteration considering higher Mg# and lower SiO_2 than unmineralized intrusions. Therefore, the Ti-in-zircon geothermomery likely provides the accurate temperature of crystallization.

4.5.5. Oxidation conditions of parental magmas

Oxidation conditions of magmas can be evaluated with a variety of methods, including Fe^{3+}/total Fe of bulk rocks, Fe-Ti oxide composition, and the presence of minerals that reflect high fO_2, such as anhydrite, titanite and Fe-Ti-oxides (e.g. Hattori, 1993). Evaluating magmatic oxidation conditions using bulk rock compositions is not useful for intrusions associated with porphyry-type mineralization because hydrothermal alteration changes the compositions. The use of Fe-Ti oxides is also not suitable for plutonic rocks due to rapid re-equilibration during cooling (DeHoog et al., 2004).

The intrusions in the GMB contain primary magnetite and titanite plus relict primary hornblende, which indicates that the parental magmas had an fO_2 above FMQ (fayalite-magnetite-quartz buffer) at ~650°C and above FMQ+0.5 (+0.5 logarithmic unit above the FMQ buffer) at ~700°C (Wones, 1989). Coarse-grained titanite is clearly of igneous origin, based on its euhedral crystal habit and low Al (1-2 wt.% Al_2O_3) compared to hydrothermal titanite (2 -6 wt.% Al_2O_3; Kobylinski et al., 2016). Zircon is a robust mineral that retains its chemical composition at the time of crystallization, generally unaffected by subsolidus processes such as alteration (Cherniak et al., 1997). Therefore, its composition is used to evaluate the oxidation conditions of parental magmas.

4.5.6 Cerium anomalies in zircon.

Cerium is present as Ce^{4+} and Ce^{3+} in a magma. Zircon Ce^{4+}/Ce^{3+} is a proxy to the oxidation conditions of parental magmas. From the total abundance of Ce, the Ce^{4+}/Ce^{3+} ratio of zircon is calculated using the bulk-rock and zircon compositions following the method of Ballard et al. (2002).

Zircon grains from the GMB show a large range in Ce^{4+}/Ce^{3+} (Fig. 4.14). Zircon grains in unmineralized intrusions show low values for Ce^{4+}/Ce^{3+}. High values of $Ce^{4+}/Ce^{3+} > 1000$, are found in the oldest mineralized intrusion (Group A). This intrusion (sample GBR-7) is from the Granite Lake pit which has produced consistently high Cu grade (average 0.3 %) and the largest tonnage since 2004 among three open pits (annual production data at www.sedar.com). Zircons from Groups B and C mineralized intrusions show Ce^{4+}/Ce^{3+} values ranging from 94 to 457 (n=14) and from 83 to 288 (n=44), respectively, where the ranges are lower and upper quartile values. Zircons from Group B are samples from the Pollyanna pit, where the second highest Cu grade (average 0.266 % Cu) and second largest tonnage was mined since 2004. Two of the 4 samples from Group C are from the Gibraltar East Pit and one is less then 500 m from the Gibraltar East pit. The Gibraltar East pit produced Cu ore with an average grade of 0.26% and the lowest tonnage among three pits since 2004 (annual production data at www.sedar.com).

Values of Ce^{4+}/Ce^{3+} (86 to 415, n=73) for mineralized intrusions are markedly higher than those (38-170, n=118) for unmineralized intrusions and high values in mineralized intrusions are spatially associated with high Cu resource. Moreover, average Ce^{4+}/Ce^{3+} is significantly higher in the mineralized intrusion Groups B and C (260±130, [2σ], n=14 and 193±140, [2σ], n=44, respectively), than those of the unmineralized intrusion (123±56, [2σ], n=118) (Fig. 4.10).

4.5.7. Europium anomalies in zircon

Europium anomalies have the potential to reflect the oxidation state of magmas, given that Eu is present as 2+ in reduced magmas and 3+ in oxidized magmas (e.g., Drake, 1975). The GMB zircon grains show Eu anomalies, expressed as Eu/Eu* ($=Eu_N/(Sm_N*Gd_N)^{1/2}$), varying from 0.27 to 0.31 in quartile values (Fig. 4.14; Fig. 4.15; Table 4.3). These values do not correlate with Ce/Ce* in zircon (Fig. 4.15; Table 4.3). Thus, our data suggest that Eu anomalies are largely controlled by factors unrelated to the redox conditions of magmas. Our data support the findings of Loader et al. (2017), who suggested that Eu anomalies are primarily controlled by crystallization of plagioclase and other phases, such as titanite and hornblende. For our GMB samples, large negative Eu anomalies are likely related to fractional crystallization of plagioclase prior to zircon saturation which depletes Eu in the melt generating a negative Eu anomaly. Zircon Eu anomalies can also be affected by the prior or concurrent crystallization of titanite, which increase Eu/Eu* because titanite has a strong affinity for middle and heavy rare earth elements (Glazner et al., 2008; Loader et al., 2017). Low Eu/Eu* in mineralized tonalite is also reflected in bulk rock, where mineralized rocks show Eu/Eu* ranging from (0.57-0.73) and unmineralized rocks showing Eu/Eu* closer to unity (>0.95) (Fig. 4.15). All rock of the GMB contain both abundant plagioclase and trace igneous titanite suggesting both effects are plausible, however low Eu/Eu* in both bulk rock and zircon suggest that overall the melt was depleted in Eu and that plagioclase fractionation is the dominant effect, especially in mineralized tonalite. The proposed interpretation of plagioclase fractionation is consistent with low Sr/Y values (exceptionally low in mineralized tonalites) (Figs. 4.9 and 4.12) because Sr is easily incorporated into plagioclase. Since, Eu/Eu* does not corelate with Ce/Ce* we suggest that Eu/Eu* is a poor proxy for magmatic oxidation conditions due to confounding factors.

4.5.8. *f*O_2 values of magmas for the GMB

Several methods have been proposed to quantify *f*O_2 values of melt from zircon compositions, such as Ce anomalies alone (Trail et al., 2012; Burnham and Berry, 2012). In our study we used the model proposed by Smythe and Brennan (2016a, b), which is based on an empirical relationship observed between *f*O_2 and four parameters (bulk-rock composition, water content of magma, zircon crystallization temperature and Ce^{4+}/Ce^{3+} in zircon). The bulk rock composition and water content affect the ratios of non-bridging oxygens to tetrahedrally coordinated oxygen in a magma. Our calculation uses the ratios in hydrated magmas. Temperatures of magmas use the crystallization temperatures of zircon based on Ti-in-zircon geothermometry. Our calculation uses 0.7 as αTiO_2, but the value has a minor effect on the results. For example, sample GBR2-15 yielded a calculated FMQ+2±1.3 with $\alpha TiO_2=0.7$, and $\alpha TiO_2=0.4$ yields FMQ+1.9±1.2.

The solubility water in melt is controlled by the melt composition, temperatures and pressures. An experimental study by Caroll and Wyllie (1990) shows that tonalitic magmas crystallizing biotite, hornblende and plagioclase can contain up to ~ 4.5 wt% H_2O at ~825°C and ~10 wt.% H_2O at 700°C and 15 kbar (~5 km depth). The result is comparable with the experiment by Holtz et al. (2001) where the water content in a granitic melt was 9.97 wt.% at 800°C at 5 kbar (~1.5 km depth). These data suggest that the parental magmas of the unmineralized intrusions of the GMB may have had a higher water content considering their cooler crystallization temperatures, below ~ 800°C, than the mineralized intrusions. The maximum water content for the parental magmas in the GMB is estimated here to be 10 wt.% at 700°C and 4.5 wt% at 800°C. The *f*O_2 values were calculated using 4.5 wt% H_2O. Increasing the water content from 4.5 to 10 wt.% would increases *f*O_2 by 1.9 to 2.6 logarithmic units.

The calculated *f*O_2 for GMB intrusions ranges from FMQ+0.5 to FMQ+2.5, consistent with the occurrence of titanite, magnetite and hornblende as this assemblage indicates magmatic *f*O_2 above FMQ (Wones 1989). Among the samples, higher *f*O_2 values, > FMQ+1.3, are obtained mostly from mineralized intrusions, and low *f*O_2 values are primarily obtained from unmineralized intrusions (Fig.4.16; Table 4.3). To verify the *f*O_2 values obtained from zircon composition, the values are also calculated using amphibole composition using the method proposed by Ridolfi et al. (2010). Unaltered amphibole composition in unmineralized tonalite (GBR2-34, 200m east of unmineralized tonalite sample GBR2-30) yields fO_2 values of ΔFMQ+2.6±0.4 [2σ] (n=25). While the sample analyzed using amphibole to calculate $fO2$ is not the same as the samples used to calculate fO_2 using zircon, they are all unmineralized tonalites and the amphibole sample is within 200m of the closest zircon sample (Fig. 4.2). The values are within the maximum uncertainty of fO_2 values obtained from zircon composition. Similar fO_2 values for the parental magmas using two different methods and minerals endorse the validity of the results.

High Ce anomalies and high fO_2 values suggest that the parental magmas for the mineralized intrusions were more oxidized than those for the unmineralized (Figs. 4.10, 4.15; Table 4.3). Mineralized intrusions show Ce^{4+}/Ce^{3+} ranging from 130-954 with an average of 680±210 [2σ], n=15 for intrusive group A, 95-448 with an average of 260±130 [2σ], n=14 for intrusive group B and 88-295 with an average 193±140 [2σ], n=44 for intrusive group C, whereas unmineralized intrusions show Ce^{4+}/Ce^{3+} from 38 to 170 with an average of 123±56 [2σ], n=118 (Fig. 4.10; Table 4.3). Ranges are given as upper and lower quartile values.

The difference in Ce^{4+}/Ce^{3+} in zircon reflect that of oxidation conditions of parental magmas, mineralized intrusions generally showing higher fO_2 values (FMQ+1.6–FMQ+1.9, average FMQ+1.7±1.8, [2σ], n=73) than unmineralized intrusions (FMQ+1.1–FMQ+1.7, average FMQ+1.3±1.5, [2σ], n=118) (Fig. 4.16).

4.5.9. Magmas responsible for Gibraltar porphyry Cu mineralization

The igneous rocks of the GMB are mostly tonalites with minor quartz diorite. Their primary mineralogy is similar in the GMB. All samples contain plagioclase, quartz, hornblende and biotite as major igneous minerals. Minor igneous minerals (less than 5% modality) are titanite, apatite, zircon and magnetite. Rocks are all similar independent of ages except for hydrothermal alteration. Mineralized rocks show the evidence for potassic alteration, intense white mica alteration and lesser epidote alteration. Mineralized rocks of Groups A, B and C show some minor lithological differences. Rocks of group A are medium grained, isotropic and equigranular whereas rocks form group B and C are medium grained, not equigranular with mafic minerals being larger than the quartz and plagioclase grains. Group A is foliated and

Groups B and C are intensely foliated. All three groups are similarly altered with intense white mica alteration replacing plagioclase and forming veins with lesser epidote alteration replacing plagioclase and forming isolated aggregates with chlorite. Mafics minerals are always completely chloritized in all three groups.

Our zircon age data from mineralized intrusions show at least three distinct age groups (A, B and C above); 218.1±3.1 Ma, 213.2±2.4 Ma and 205.8±2.1 (Fig. 4.10 and Table 4.4). The time gaps between different age groups of mineralized intrusions are greater than 0.2 m.y. even considering the analytical uncertainties (Fig. 4.10 and Table 4.4). Furthermore, the age gaps are greater than the length of time generally required for the solidification of a large magma chamber (Cathles et al., 1997). Therefore, each age group is considered to represent separate magmatism.

It may be argued that the youngest group of intrusions (Group C of mineralized intrusions) brought Cu for the deposit and produced mineralization in older intrusions. We discount this possibility because all three Groups A, B and C mineralized intrusions show the evidence for the crystallization of secondary biotite and abundant white mica suggesting their parental magmas likely contributed to hydrothermal activity. Separate mineralized magmatic hydrothermal activity is supported by the occurrence of three distinct chimney-like distributions of high Cu rocks at the Gibraltar deposit (Fig. 4.3). The evidence suggests that parental magmas for Groups A, B, C intrusions likely contributed to mineralizing hydrothermal activity.

This is further supported by Re-Os ages of molybdenite, 215.0±1.0 Ma and 212.7±0.9 Ma, reported from the Granite Lake and Gibraltar East pits by Harding (2012). The U-Pb zircon ages of Groups A and B intrusions, 218.9±3.1 and 213.2±2.4 Ma, overlap with these ages, suggesting the mineralization ocurred during the intrusions of Groups A and B. Thus, we suggest that the Gibraltar porphyry Cu deposit formed during at least three distinct mineralization events, separated by quiescent periods. Such repeated magmatic-hydrothermal activity likely contributed to the increased tonnage of the Gibraltar deposit.

4.5.10. Comparison with other porphyry Cu deposits

Within the Quesnel Terrane

Several porphyry Cu deposits are present in the Quesnel terrane. In the vicinity of the study area there are several significant porphyry Cu deposits; the Highland Valley Copper deposit (3.6 Mt Cu), Mount Polley deposit (0.6 Mt Cu) (Fig. 4.1), and the Woodjam porphyry-Cu prospect (0.71 Mt Cu; www.woodjamcopper.com/). Unless otherwise noted, all resource and reserve figures for porphyry deposits in this paper are from Singer et al. (2008).

The Highland Valley Copper deposit is hosted by the Guichon Creek batholith, 235 km southeast of the Gibraltar deposit (Fig. 4.1). The mineralization is hosted by Bethlehem facies (210.3±0.04 Ma, Whalen et al., 2017) and Bethsaida phase (209.1±0.3 Ma, 206.96±0.22; Whalen et al., 2017, D'Angelo et al., 2017) and these intrusive ages are similar to the Re-Os ages of molybdenite; 208.4±0.9 Ma (D'Angelo et al., 2017) and 206.3±1.2 Ma (Ash et al., 2007 cited in Whalen et al., 2017). The timing of the mineralization of the Highland Valley Copper deposit is synchronous with the emplacement of Group C of mineralized intrusions in the GMB at 205.8±2.1 Ma and corresponds to the prolific 6 Ma epoch of porphyry mineralization centered on 205 Ma within the Cordillera (Logan and Mihalynuk, 2014). Zircon trace element data from the Highland Valley Copper and Gibraltar deposits are also similar. Ward (2008) obtained high Ce^{4+}/Ce^{3+} ranging from 63 to 215 with an average of 189 (n=22) for zircon from mineralized intrusions in the Guichon Creek batholith. The values are comparable to the range of Ce^{4+}/Ce^{3+} of 93-443 with an average of 305±134 [2σ] (n=73) from all mineralized intrusions of the Gibraltar deposit (this study). Similar zircon ages and compositions from the two major deposits in the Quesnel terrane suggest that the tectonic setting of the Quesnel island arc, in the late Triassic, appears favorable for the production of Cu-fertile magmas.

Comparison with other porphyry Cu deposits worldwide

Zircon values of Eu/Eu* and Ce^{4+}/Ce^{3+} from the mineralized intrusions of the Gibraltar deposit are similar to those for other porphyry Cu deposits with similar tonnage reported by previous workers. They include zircon data reported by Ballard et al. (2002) for diorite porphyry hosting the Los Picos-Fortuna deposit, Chile (5.1 Mt Cu), and those reported by Shen et al. (2015) for andesite porphyry in the Erdenet deposit (9 Mt Cu) and granodiorite porphyry associated with the Tuwu-Yandong deposit (2.1 Mt Cu) in the Central Asian Orogenic belt (Fig. 4.15).

Multiple intrusions at a focused area are features associated with large porphyry Cu deposits (Sillitoe, 2010). Recurrent magmatism in one area is also recognized as a factor contributing to large tonnage deposits. One example is at the Chuquicamata porphyry Cu-Mo deposit (126 Mt Cu), Chile, where at least two distinctly separate mineralizing events resulted in the giant deposit (Ballard et al., 2001). In the Escondida district, at least four major deposits formed in an area of ~5x10 km over an interval of ~4 to 5 m.y. (Hervé et al., 2012).

Relatively oxidized magmas are known to be preferentially associated with porphyry Cu deposits (Ishihara, 1977; Sillitoe, 2010; Sun et al., 2013). Many igneous rocks associated with porphyry Cu deposits report fO_2 values greater than FMQ+2 for their parental magmas based on mineral assemblages, mineral chemistry and melt-inclusion studies (reviewed by Hattori, 2018). Oxidized magmas are capable to transport high concentrations of S to the mineralization site at upper crustal levels of a few km depth (Hattori and Keith, 2001).

Although oxidized conditions of magmas are important for the formation of large porphyry Cu deposits, small porphyry deposits may be formed by magmas with low $fO_{2,}$ lower than ~FMQ+1. Examples include 17 Mile Hill deposit in Australia (0.03 Mt Cu), Catface deposit in Canada (1 Mt Cu) and the Baogutu deposit in China (0.63 Mt Cu) (Rowins, 2000; Smith et al., 2012; Cao et al., 2016).

4.5.11. Use of zircon for exploration

Cerium anomalies in zircon are evaluated in three ways in this study: Ce^{4+}/Ce^{3+}, Ce/Ce* and Ce/Nd. This study shows that the values of $Ce^{4+}/Ce^{3+}$are positively correlated with Ce/Ce* and Ce/Nd with correlation coefficients of 0.84 to 0.94, respectively (Fig. 4.17). Ce/Ce* and Ce/Nd correlations are reliable, however, correlations with Ce^{4+}/Ce^{3+} become less reliable at higher Ce^{4+}/Ce^{3+} (>500) (Fig. 4.17). High Ce^{4+}/Ce^{3+} of zircon grains are from intrusions associated with large tonnage Cu in the open pits. The correlation suggests that Ce/Nd or Ce/Ce* may be used to evaluate Ce^{4+}/Ce^{3+} values of zircon and evaluate the potential of intrusions for Cu resource. The calculation of Ce^{4+}/Ce^{3+} requires the compositions of both zircon and bulk rock because the concentrations of Ce^{3+} are obtained using partition coefficients of other REEs between zircon and bulk rock by assuming bulk rock REE abundance representing those of parental magmas. On the other hand, the ratios of Ce/Nd or Ce/Ce* can be obtained directly from zircon compositions. Therefore, these ratios are very useful for evaluating the Ce anomalies of zircon grains in highly altered rocks with no reliable REE abundances for bulk rocks. Furthermore, the bulk rock compositions of parental rocks are not available for detrital zircon grains in stream and glacial sediments. The values of Ce/Nd and Ce/Ce* from detrital zircon grains may be used to estimate the oxidation conditions of an intrusion and its fertility potential.

4.6. Conclusions

The GMB in Canadian Cordillera formed from multiple intrusions over a period of ~25 m.y. in the Quesnel island arc, prior to its accretion to the North American continent. The bulk of the GMB was emplaced before fertile tonalite magmas intruded in the central part of the batholith. The fertile magmas intruded during at least three distinct time periods (Groups A, 218.9±3.1 Ma, n=16; Group B, 213.2 ± 2.4 Ma, n=27; Group C, 205.8±2.1 Ma, n=39) with the oldest Group having the highest Ce anomalies. These magmas are spatially associated with large geological reserves totalling 3.2 Mt Cu during multiple mineralization events over ca. 10 m.y. These mineralizing intrusions show higher Ce anomalies in zircon, 305±134 [2σ] (n=73), than early unmineralized intrusions, 123±56, [2σ] n=118. Zircon compositions yield fO_2, FMQ+1.6 to 1.9, for the mineralized intrusions.

The mineralized intrusions have low Sr/Y bulk-rock compositions (< 22) and low Eu/Eu* (0.2-0.4) in zircon. The data from the Gibraltar deposit show that an economic porphyry Cu deposit may be found in igneous rocks with low Sr/Y and low Eu/Eu* in zircon.

Ce^{4+}/Ce^{3+} ratios of zircon correlate positively with Ce/Nd (ranging from ~1-25) and Ce/Ce* (ranging from ~3-200), with correlation coefficients, 0.94 and 0.84, respectively, suggesting that all three ratios reflect the oxidation conditions of parental magmas. Since Ce/Nd and Ce/Ce* values are determined from measured compositions of zircon, they are useful in evaluating the oxidation conditions of parental magmas for intensely altered rocks and detrital zircon in stream and glacial sediments.

Acknowledgements

This project was supported by the Natural Resources of Canada Targeted Geoscience Initiative (TGI) Phase 5 project on "Porphyry-related mineral systems", and a Natural Sciences and Engineering Research Council of Canada Discovery Grant to KH. CHK acknowledges a Research Affiliate Program bursary through the TGI program. We thank William Davis (Geological Survey of Canada) for his helpful comments concerning presentation of LA-ICPMS data, Glenn Poirier (University of Ottawa) for his assistance with SEM analysis, Samuel Morfin and Duane Petts (University of Ottawa) for their help during LA-ICPMS analysis, and Chris Gallagher for making a pseudosection of Cu contents in the mine.

References

Agnew, M., 2018, Return to Bougainville—Reassessing the mineral potential of a long-forgotten island: SEG Newsletter April 2018, number 113, p. 1, 18-24.

Ash, C.H., Panteleyev, A., MacLellan, K.L., Payne, C.W., and Rydman, M.O., 1999a, Geology of the Gibraltar Mine area (93B/6 and 9): British Columbia Ministry of Energy and Mines, Open File 1999-7, scale 1:50,000.

Ash, C.H., Rydman, M.O., Payne, C.W., and Panteleyev, A., 1999b, Geological setting of the Gibraltar Mine, South Central British Columbia (93B/93A): Exploration and mining in British Columbia 1998. British Columbia Ministry of Energy and Mines, p. A1–A15.

Ash, C.H., and Riveros, C.P., 2001, Geology of the Gibraltar copper-molybdenite deposit, east-central British Columbia (93B/9): Geological Fieldwork 2000, British Columbia Ministry of Energy and Mines, Victoria, Paper. 1, p. 119-134.

Ballard, J. R., Palin, J. M., Williams, I. S., Campbell, I. H., and Faunes, A., 2001, Two ages of porphyry intrusion resolved for the super-giant Chuquicamata copper deposit of northern Chile by LA-ICP-MS and SHRIMP: Geology, v. 29(5), p. 383-386.

Ballard, J.R., Palin, M.J., and Campbell, I.H., 2002, Relative oxidation states of magmas inferred from Ce (IV)/Ce (III) in zircon: application to porphyry copper deposits of northern Chile: Contributions to Mineralogy and Petrology, v. 144, p. 347-364.

Barth, A.P., Tani, K., Meffre, S., Wooden, J. L., Coble, M.A., Arculus, R.J., and Shukle, J.T., 2017, Generation of silicic melts in the early Izu- Bonin arc recorded by detrital zircons in proximal arc volcaniclastic rocks from the Philippine Sea: Geochemistry, Geophysics, Geosystems, v. 18(10), p. 3576-3591.

Belousova, E.A., Griffin, W.L. and O'Reilly, S.Y., 2005, Zircon crystal morphology, trace element signatures and Hf isotope composition as a tool for petrogenetic modelling: examples from Eastern Australian granitoids: Journal of Petrology, v. 47(2), p. 329-353.

Burnham, A.D. and Berry, A.J., 2012, An experimental study of trace element partitioning between zircon and melt as a function of oxygen fugacity: Geochimica et Cosmochimica Acta, v.95, p. 196-212.

Bysouth, G.D., Campbell, K.V., Barker, G.E., and Gagnier, G.K., 1995, Tonalite-trondhjemite fractionation of peraluminous magma and the formation of syntectonic porphyry copper mineralization, Gibraltar mine, central British Columbia: Schroeter, T.G. (Ed.), Porphyry deposits of the northwestern cordillera of North America, Canadian Institute of Mining, Metallurgy and Petroleum, Special Volume 46, p. 201-213.

Cathles, L.M., Erendi, A.H.J., and Barrie, T., 1997, How long can a hydrothermal system be sustained by a single intrusive event?: Economic Geology, v. 92, p. 766–771.

Cao, M., Qin, K., Li, G., Evans, N. J., Hollings, P., and Jin, L., 2016, Genesis of ilmenite-series I-type granitoids at the Baogutu reduced porphyry Cu deposit, western Junggar, NW-China: Lithos, v. 246, p. 13-30.

Caroll, M. R., and Wyllie, J., 1990, The system tonalite-H_20 at 15 kbar and the genesis of calc-alkaline magmas: American Mineralogist, v. 75, p. 345-357.

Cherniak, D.J., Watson, E.B., and Hanchar, J.M., 1997, Rare-earth diffusion in zircon: Chemical Geology, v. 134, p. 289–301.

Chiaradia, M., Ulianov, A., Kouzmanov, K. and Beate, B., 2012, Why large porphyry Cu deposits like high Sr/Y magmas?: Scientific Reports, v. 2, no. 685.

Chung, S-L., Liu, D., Ji, J., C, M-F., Lee, H-Y, W, D-J, L, C-H, Lee, T-Y, Qian, Q., Zhang, Q., 2003, Adakites from continental collision zones: melting of thickened lower crust beneath southern Tibet: Geology, v.31 (11), p.1021-1024.

Corfu, F., Hanchar, J. M., Hoskin, P. W., and Kinny, P., 2003, Atlas of zircon textures: Reviews in mineralogy and geochemistry, v. 53(1), p. 469-500.

D'Angelo, M., Miguel, A., Hollings, P., Byrne, K., Piercey, S., and Creaser, R. A., 2017, Petrogenesis and magmatic evolution of the Guichon Creek Batholith: Highland Valley porphyry Cu±(Mo) district, South-Central British Columbia: Economic Geology, v. 112(8), p. 1857-1888.

DeHoog, J.C.M., Hattori, K.H., and Hoblitt., R.P., 2004, Oxidized sulfur-rich mafic magma at Mount Pinatubo, Philippines: Contributions to Mineralogy and Petrology, v. 146, p. 750–761.

Dilles, J. H., 1987, Petrology of the Yerington Batholith, Nevada; evidence for evolution of porphyry copper ore fluids: Economic Geology, v. 82(7), p. 1750-1789.

Drake, M., 1975, The oxidation state of europium as an indicator of oxygen fugacity: Geochimica et Cosmochimica Acta, v. 39, p. 55-64.

Drummond, A.D., Sutherland Brown, A., Young, R.J., and Tennant, S.J., 1976, Gibraltar – regional metamorphism, mineralization, hydrothermal alteration and structural development: Sutherland Brown, A. (Ed.), Porphyry deposits of the Canadian Cordillera, Canadian Institute of Mining and Metallurgy, Special Volume 15, p. 195-205.

Ferry, J. M., and Watson, E. B. 2007, New thermodynamic models and revised calibrations for the Ti-in-zircon and Zr-in-rutile thermometers: Contributions to Mineralogy and Petrology, v. 154(4), p. 429-437.

Fu, B., Page, F. Z., Cavosie, A. J., Fournelle, J., Kita, N. T., Lackey, J. S., and Valley, J. W., 2008, Ti-in-zircon thermometry: applications and limitations: Contributions to Mineralogy and Petrology, v. 156(2), p. 197-215.

Ge, W., Wu, F., Zhou, C., and Zhang, J., 2007, Porphyry Cu-Mo deposits in the eastern Xing'an-Mongolian Orogenic Belt: Mineralization ages and their geodynamic implications: Chinese Science Bulletin, v. 52(24), p. 3416-3427.

Ghosh, D.K., 1995, Nd–Sr isotopic constraints on the interactions of the Intermontane Superterrane with the western edge of North America in the southern Canadian Cordillera: Canadian Journal of Earth Sciences, v. 32, p. 1740–1758.

Glazner, A.F., Coleman, D.S., Bartley, J.M., 2008, The tenuous connection between high-silica rhyolites and granodiorite plutons: Geology, v. 36, p.183–186.

Griffin, W. L., Wang, X., Jackson, S. E., Pearson, N. J., O'Reilly, S. Y., Xu, X., and Zhou, X., 2002, Zircon chemistry and magma mixing, SE China: in-situ analysis of Hf isotopes, Tonglu and Pingtan igneous complexes: Lithos, v. 61(3-4), p. 237-269.

Griffin, W. L., Powell, W. J., Pearson, N. J., and O'Reilly, S. Y., 2008, GLITTER: data reduction software for laser ablation ICP-MS. Laser Ablation-ICP-MS in the earth sciences: Mineralogical Association of Canada Short Course Series, v. 40, p. 204-207.

Harding, B., 2012, The characterization of molybdenum mineralization at the Gibraltar mines Cu-Mo porphyry, central British Columbia: B. Sc. thesis, Kingston, Canada, Queen's University, 52 p.

Hattori, K. 1993, High-sulfur magma, a product of fluid discharge from underlying mafic magma: Evidence from Mount Pinatubo, Philippines: Geology, v. 21, p.1083-1086.

Hattori, K. H., and Keith, J. D., 2001, Contribution of mafic melt to porphyry copper mineralization: evidence from Mount Pinatubo, Philippines, and Bingham Canyon, Utah, USA: Mineralium Deposita, v.36(8), p. 799-806.

Hattori, K., Wang, J., Baumgartner, R., Kobylinski, C. H., Morfin, S., and Shen, P., 2017, Zircon composition: indicator of fertile igneous rocks related to porphyry copper deposits [ext. abs]: Society for Geology Applied to Mineral Deposits (SGA) biennial meeting, Quebec City, Canada extended abstracts, v. 1, p 295 -298.

Hattori, K., 2018, Porphyry copper potential in Japan based on magmatic oxidation state: Resource Geology, v. 68(2), p. 126-137.

Hayden, L. A., and Watson, E. B., 2007, Rutile saturation in hydrous siliceous melts and its bearing on Ti-thermometry of quartz and zircon: Earth and Planetary Science Letters, v. 258(3-4), p. 561-568.

Heithersay, P. S., and Walshe, J. L., 1995, Endeavour 26 North; A porphyry copper-gold deposit in the Late Ordovician, shoshonitic Goonumbla volcanic complex, New South Wales, Australia: Economic Geology, v. 90(6), p. 1506-1532.

Hervé, M., Sillitoe, R. H., Wong, C., Fernández, P., Crignola, F., Ipinza, M., and Camus, F., 2012, Geologic overview of the Escondida porphyry copper district, Northern Chile: Economic Geology Special Publication, v. 16, p. 55-78.

Hiess, J., Condon, D. J., McLean, N., and Noble, S. R., 2012, $^{238}U/^{235}U$ systematics in terrestrial uranium-bearing minerals: Science, v. 335(6076), p. 1610-1614.
Holtz, F., Johannes, W., Tamic, N., and Behrens, H., 2001, Maximum and minimum water contents of granitic melts generated in the crust: a re-evaluation and implications: Lithos, v. 56(1), p. 1-14.

Hoskin, P. W., and Ireland, T. R., 2000, Rare earth element chemistry of zircon and its use as a provenance indicator: Geology, v. 28(7), p. 627-630.

Hoskin, P. W., and Schaltegger, U., 2003, The composition of zircon and igneous and metamorphic petrogenesis: Reviews in Mineralogy and Geochemistry, v. 53(1), p. 27-62.

Ishihara, S., 1977, The magnetite-series and ilmenite-series granitic rocks: Mining Geology, v. 27(145), p. 293-305.

Jochum, K. P., Weis, U., Stoll, B., Kuzmin, D., Yang, Q., Raczek, I., and Günther, D., 2011, Determination of reference values for NIST SRM 610–617 glasses following ISO guidelines: Geostandards and Geoanalytical Research, v. 35(4), p. 397-429.

Johnston, S. T., and Borel, G. D., 2007, The odyssey of the Cache Creek terrane, Canadian Cordillera: Implications for accretionary orogens, tectonic setting of Panthalassa, the Pacific superwell, and break-up of Pangea: Earth and Planetary Science Letters, v. 253(3-4), p. 415-428.

Kay, R. W., and Kay, S. M. 1993, Delamination and delamination magmatism: Tectonophysics, v. 219(1-3), p. 177-189.

Kay, R.W. and Kay, S.M., 2002, Andean adakites: three ways to make them: Acta Petrologica Sinica, v. 18 (3), p.303-311.

Kirkland, C. L., Smithies, R. H., Taylor, R. J. M., Evans, N., and McDonald, B., 2015, Zircon Th/U ratios in magmatic environs: Lithos, v. 212, p. 397-414.

Kobylinski, C. H., Hatori, K. H., Smith, S., and Plouffe, A., 2016, Report on the composition and assemblage of minerals associated with the porphyry Cu-Mo mineralization at the Gibraltar deposit, south central British Columbia, Canada: Geological Survey of Canada, Open File 8025, 30 p.
Kobylinski, C. H., Hattori, K. H., Plouffe, A., and Smith, S W., 2017, Epidote associated with the porphyry Cu-Mo mineralization at the Gibraltar deposit, south-central British Columbia: Geological Survey of Canada, Open File 8279, 31 p.

Lickfold, V., Cooke, D. R., Smith, S. G., and Ullrich, T. D., 2003, Endeavour copper-gold porphyry deposits, Northparks, New South Wales: Intrusive history and fluid evolution: Economic Geology, v. 98(8), p. 1607-1636.

Loader, M. A., Wilkinson, J. J., and Armstrong, R. N., 2017, The effect of titanite crystallisation on Eu and Ce anomalies in zircon and its implications for the assessment of porphyry Cu deposit fertility: Earth and Planetary Science Letters, v. 472, p. 107-119.

Logan, J.M. and Mihalynuk, M.G., 2014, Tectonic controls on Early Mesozoic paired alkaline porphyry deposit belts (Cu-Au ± Ag-Pt-Pd-Mo) within the Canadian Cordillera: Economic Geology, v. 109, p. 827-858.

Loucks, R. R. 2014, Distinctive composition of copper-ore-forming arc magmas: Australian Journal of Earth Sciences, v. 61(1), p. 5-16.

Lu, Y.-J., Loucks, R.R., Fiorentini, M., McCuaig, T.C., Evans, N.J., Yang, Z.-M., Hou, Z.-Q., Kirkland, C.L., Parra-Avila, L.A., and Kobussen, A., 2016, Zircon composition as a pathfinder for porphyry Cu ± Mo ± Au deposits in tectonics and metallogeny of the Tethyan orogenic Belt: Society of Economic Geologists, Special Publication No. 19, Littleton, Colorado, p. 329-347.

Ludwig, R. K., 2012, Isoplot 4.15 A geological toolkit for Microsoft Excel: Berkeley Geochronology Center Special Publication No. 5, 75 p.
McDonough, W. F., and Sun S., 1995, The composition of the Earth: Chemical Geology, v. 120, p. 223-253.

Colpron, M. and Nelson, J.L., 2011, A Digital Atlas of Terranes for the Northern Cordillera: BC GeoFile 2011- 11.

Oliver, J., Crozier, J., Kamionko, M., and Fleming, J., 2009, The Gibraltar Mine, British Columbia. A billion tonne deep copper-molybdenum porphyry system: structural style, patterns of mineralization and rock alteration [ext. abs]: Association for Mineral Exploration British Columbia, 2009 Mineral Exploration Roundup, Vancouver, Canada, Abstracts, p. 35-36.

Page, F. Z., Fu, B., Kita, N. T., Fournelle, J., Spicuzza. M, J., Schulze, D. J., Viljoen. F, Basei. M, A. S, and Valley, J, W., 2007, Zircons from kimberlite: new insights from oxygen isotopes, trace element, and Ti in zircon thermometry: Geochimica et Cosmochimica Acta, v. 71, p. 3887–3903
Panteleyev, A., 1978, Granite Mountain project (93B/8): Geological Fieldwork 1977, British Columbia Ministry of Energy, Mines and Petroleum Resources, British Columbia Geological Survey Paper, 1977-1, p. 39-42.

Plouffe, A., and Ferbey, T., 2015, Till composition near Cu-porphyry deposits in British Columbia: Highlights for mineral exploration: TGI 4 - Intrusion Related Mineralisation Project: New Vectors to Buried Porphyry-Style Mineralisation: N. Rogers (Ed.), Geological Survey of Canada, Open File 7843, p. 15-37.

Proffett, J. M., 2003, Geology of the Bajo de la Alumbrera porphyry copper-gold deposit, Argentina: Economic Geology, v. 98(8), p. 1535-1574.

Redmond, P. B., and Einaudi, M. T., 2010, The Bingham Canyon porphyry Cu-Mo-Au deposit. I. Sequence of intrusions, vein formation, and sulfide deposition: Economic Geology, v. 105(1), p. 43-68.

Richards, J. P., 2011, High Sr/Y arc magmas and porphyry Cu±Mo±Au deposits: just add water: Economic Geology, v. 106, p. 1075–1081.

Richards, J. P., Spell, T., Rameh, E., Razique, A., and Fletcher, T., 2012, High Sr/Y magmas reflect arc maturity, high magmatic water content, and porphyry Cu±Mo±Au potential: Examples from the Tethyan arcs of central and eastern Iran and western Pakistan: Economic Geology, v. 107, p. 295-332.

Ridolfi, F., Renzulli, A., and Puerini, M., 2010, Stability and chemical equilibrium of amphibole in calc-alkaline magmas: an overview, new thermobarometric formulations and application to subduction-related volcanoes: Contributions to Mineralogy and Petrology, v. 160(1), p. 45-66.

Rodriquez, C., Selles, D., Dungan, M., Langmuir, C., Leeman, W., 2007, Adakitic dacites formed by intracrustal crystal fractionation of water-rich parent magmas at Negado de LongviVolcano (36.2S; Andean Southern Volcanic Zone, Central Chile): Journal of Petrology, v. 48 (11), p. 2033-2061.

Rowins, S. M., 2000, Reduced porphyry copper-gold deposits: A new variation on an old theme: Geology, v. 28(6), p. 491-494.

Schiarizza, P., 2014, Geological setting of the Granite Mountain batholith, host to the Gibraltar porphyry Cu-Mo deposit, south-central British Columbia: Geological Fieldwork 2013, British Columbia Ministry of Energy and Mines, British Columbia Geological Survey Paper, 2014-1, p. 95-110.

Schiarizza, P., 2015, Geological setting of the Granite Mountain batholith, south-central British Columbia: Geological Fieldwork 2014, British Columbia Ministry of Energy and Mines, British Columbia Geological Survey Paper, 2015-1, p. 19-39.

Shen, P., Hattori, K., Pan, H., Jackson, S., and Seitmuratova, E., 2015, Oxidation condition and metal fertility of granitic magmas: Zircon trace-element data from porphyry Cu deposits in the Central Asian Orogenic Belt: Economic Geology, v. 110(7), p. 1861-1878.

Sillitoe, R. H., 2010, Porphyry copper systems: Economic geology, v. 105(1), p. 3-41.
Singer, D. A., Berger, V. I., and Moring B. C., 2008, Porphyry copper deposits of the world: database and grade and tonnage models: U.S. Geological Survey Open-File Report 2008-1155.

Sisson, T. W., and Grove, T. L. 1993, Experimental investigations of the role of H_2O in calc-alkaline differentiation and subduction zone magmatism: Contributions to Mineralogy and Petrology, v. 113(2), p. 143-166.

Sláma, J., Košler, J., Condon, D. J., Crowley, J. L., Gerdes, A., Hanchar, J. M., and Schaltegger, U., 2008, Plešovice zircon—a new natural reference material for U–Pb and Hf isotopic microanalysis: Chemical Geology, v. 249(1-2), p. 1-35.

Smith, C. M., Canil, D., Rowins, S. M., and Friedman, R., 2012, Reduced granitic magmas in an arc setting: the Catface porphyry Cu–Mo deposit of the Paleogene Cascade Arc: Lithos, v. 154, p. 361-373.

Smythe, D. J., and Brenan, J. M., 2016a, Cerium oxidation state in silicate melts: Combined fO2, temperature and compositional effects: Geochimica et Cosmoochimica Acta, v.170, p. 173-187.

Smythe, D. J., and Brenan, J. M., 2016b, Magmatic oxygen fugacity estimated using zircon-melt partitioning of cerium: Earth and Planetary Science Letters, v. 453, p. 260-266.

Solari, L. A., and Tanner, M., 2011, UPb.age, a fast data reduction script for LA-ICP-MS U-Pb geochronology: Revista Mexicana de Ciencias Geológicas, 28p.

Sun, W. D., Liang, H. Y., Ling, M. X., Zhan, M. Z., Ding, X., Zhang, H., and Fan, W. M., 2013, The link between reduced porphyry copper deposits and oxidized magmas: Geochimica et Cosmochimica Acta, v. 103, p. 263-275.

Sutherland Brown, A., 1976, Morphology and classification. Porphyry deposits of the Canadian Cordilleran: Canadian Institute of Mining and Metallurgy Special, v. 15, p. 44-51.

Trail, D., Watson, E.B. and Tailby, N.D., 2012, Ce and Eu anomalies in zircon as proxies for the oxidation state of magmas: Geochimica et Cosmochimica Acta, v.97, p. 70-87.

Villeneuve, M., Whalen, J. B., Anderson, R. G. and Struik, L. C., 2001, The Endako batholith: Episodic plutonism culminating in formation of the Endako porphyry molybdenite deposit, north-central British Columbia: Economic Geology, v. 96(1), p. 171-196.

Van Straaten, B.I., Oliver, J., Crozier, J., and Goodhue, L., 2013, A summary of the Gibraltar porphyry copper-molybdenum deposit, south-central British Columbia, Canada: Porphyry systems of central and southern British Columbia: Tour of central British Columbia porphyry deposits from Prince George to Princeton: Society of Economic Geologists, Field Trip Guidebook Series, v. 43, p. 55-66.

Ward, R. S., 2008, Isotope geochemistry of zircon from the Guichon batholith, Highland Valley copper deposit: southern British Columbia: Relationship between Ce^{4+}/Ce^{3+} in zircon, oxidation state in magmas and ore genesis: Unpublished B.Sc thesis, Ottawa, Canada, Carlton University, 72p.

Watson, E. B., and Harrison, T. M., 1983, Zircon saturation revisited: temperature and composition effects in a variety of crustal magma types: Earth and Planetary Science Letters, v. 64(2), p. 295-304.

Watson, E. B., Wark, D. A., and Thomas, J. B., 2006, Crystallization thermometers for zircon and rutile: Contributions to Mineralogy and Petrology, v. 151(4), 413, 31p.

Whalen, J. B., Anderson, R. G., Struik, L. C., and Villeneuve, M. E., 2001, Geochemistry and Nd isotopes of the François Lake plutonic suite, Endako batholith: host and progenitor to the Endako molybdenum camp, central British Columbia: Canadian Journal of Earth Sciences, v. 38(4), p. 603-618.

Whalen, J.B., Davis, W.J. and Anderson, R.A., 2017, Temporal and geochemical evolution of the Guichon Creek Batholith and Highland Valley porphyry copper district, British Columbia: Implications for generation and tectonic setting of porphyry systems: Geological Survey of Canada, Open File 8334, 46p.

Wiedenbeck M., Allé P., Corfu F., Griffin W. L, Meier M., Oberli F., von Quadt A., Roddick J.C., and Spiegel W., 1995, Three natural zircon standards for U-Th-Pb, Lu-Hf, trace element and REE analyses: Geostandards Newsletter, v. 19 (1) p. 1-23.

Wones, D. R., 1989, Significance of the assemblage titanite+ magnetite+ quartz in granitic rocks: American Mineralogist, v. 74(7-8), p. 744-749.

Yang, T. N., Zhang, H. R., Liu, Y. X., Wang, Z. L., Song, Y. C., Yang, Z. S., and Hou, K. J., 2011, Permo-Triassic arc magmatism in central Tibet: evidence from zircon U–Pb geochronology, Hf isotopes, rare earth elements, and bulk geochemistry: Chemical Geology, v. 284(3), p. 270-282.

Zhang, H., Ling, M. X., Liu, Y. L., Tu, X. L., Wang, F. Y., Li, C. Y., and Sun, W. D., 2013, High oxygen fugacity and slab melting linked to Cu mineralization: evidence from Dexing porphyry copper deposits, southeastern China: The Journal of Geology, v. 121(3), p. 289-305.

Tables

Table 4.1. List of samples used for zircon trace element analysis and U-Pb dating

	Sample number
Mineralized intrusions[1]	***GBR-2***, ***GBR-7***, ***GBR-12***, ***GBR-15***, ***GBR-16***, ***GBR-21***
Unmineralized intrusions[2]	***GBR2-30***, ***GBR2-38***, ***GBR2-25***, ***GBR2-16***, GBR-11, GBR-28, GBR-32, GBR2-26, GBR2-15, GBR2-17

1: "Mineralized" is defined as samples containing visible chalcopyrite

2: "Unmineralized" samples do not contain visible grains of chalcopyrite

Samples in bold, underlined and italics used for both trace-element analysis and U-Pb dating. Other samples used only for trace elements analysis

Table 4.2: Bulk rock composition of samples used for this study.

	Number of samples	Y (ppm)	Sr/Y	Dy_N/Yb_N	La_N/Lu_N	Eu/Eu*[1]
Mineralized intrusions	6	16-20	9-22	1.5-1.6	2.2-2.6	0.57-0.73
Unmineralized intrusions	10	7-26	6-46	0.9-1.7	1.8-13.5	0.57-1.16

1: Eu/Eu* = $Eu_{N}/((Sm_{N}*Gd_{N})^{1/2}$

Table 4.3: Zircon trace element data

Phase		**Th/U**	**Nd/Yb**	**Ti (ppm)**	**Zircon crystallization temperatures (°C)**^{1}	**Eu/Eu***^{2}	**Ce^{4+}/Ce^{3+}**^{3}	**Ce/Ce***^{4}	**Ce/Nd**	**Δ FMQ**^{5}
Mineralized intrusions n=73	range	0.16-1.44	0.0009-0.0077	2.8-19.3	691-886	0.19-0.4	21-1780	9.6-459	2.1-35.2	1.3-2.1
	Mean	0.4	0.0029	12	828	0.29	305	87	10.1	1.7±1.8
	Median	0.32	0.0022	12.6	836	0.29	172	70	8.9	1.8±1.8
Unmineralized intrusions n=118	range	0.15-0.44	0.00005-0.017	2.9-14.8	683-869	0.18-0.59	9-555	2.6-274	1.3-25	0.5-2.5
	Mean	0.28	0.002	9.8	800	0.35	123	61	9	1.3±1.4
	Median	0.27	0.002	9.7	810	0.3	100	54	8.3	1.2±1.3

n=number of zircon grains analyzed

1: Calculated based on the equation of Ferry and Watson (2007) using activity of $TiO_2 = 0.7$

2: $Eu/Eu^* = Eu_N/((Sm_N * Gd_N)^{1/2}$

3: Calculated using the method proposed by Ballard et al. (2002)

4: $Ce^* = \left(\frac{(Nd_N)^2}{Sm_N}\right)$, proposed by Loader et al. (2017)

5: Calculated based on the equation of Smythe and Brennan (2016a, b) using the values of (non-bridging oxygen)/(tetrahedrally coordinated oxygen) on hydrous melt. fO_2 expressed as logarithmic units above or below the fayalite-magnetite-quartz buffer (FMQ)

Table 4.4: Zircon U-Pb ages

Unit		Age (Ma)	MSWD	Age (Ma)	MSWD
Unmineralized intrusions		229.2±4.4 (n=11)	1.8	231.7±7.4 (n=4)	0.33
				232 ±11(n=2)	0.022
				227 ±10(n=2)	0.99
				226.8 ±8.3(n=3)	0.86
Mineralized intrusions	Group A	218.9±3.1	0.68	218.9±3.1(n=16)	0.68
	Group B	213.2±2.4	0.62	213.2 ± 2.4(n=27)	0.62
	Group C	205.8±2.1 (n=39)	2.3	206.8 ±4.0(n=11)	1.7
				205.9 ±3.7(n=12)	0.84
				205.6 ±4.4(n=9)	0.88
				201.9 ±5.0(n=7)	0.037

n=number of zircon grains analyzed

Figures

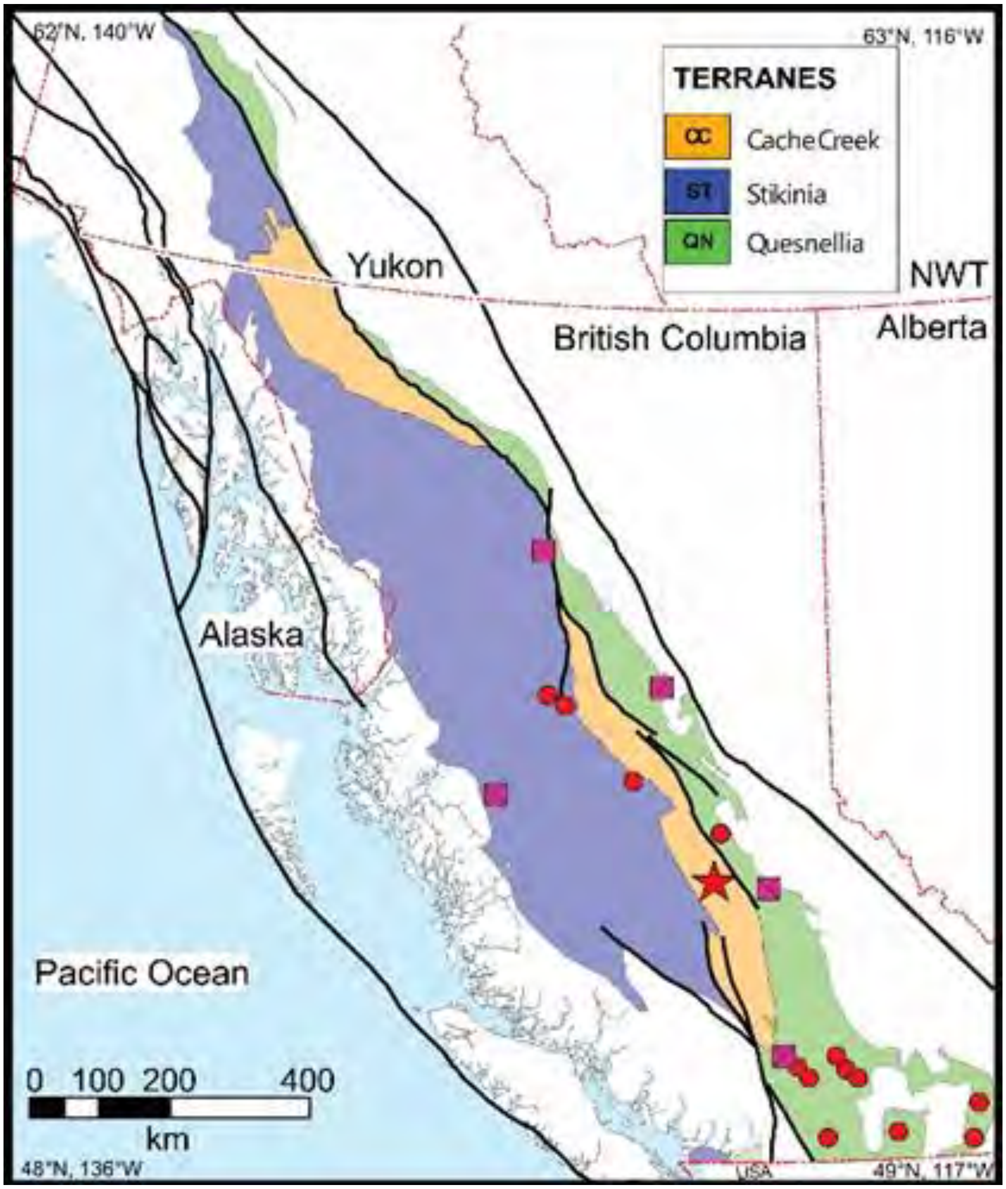

Figure 4.1. Simplified geological map of the northern Cordillera of British Columbia, Canada, modified after Nelson and Colpron (2011). The red star indicates the location of the Gibraltar porphyry Cu mine. Other porphyry Cu deposits are shown as pink squares (currently producing mine) and red circles (past producing mine).

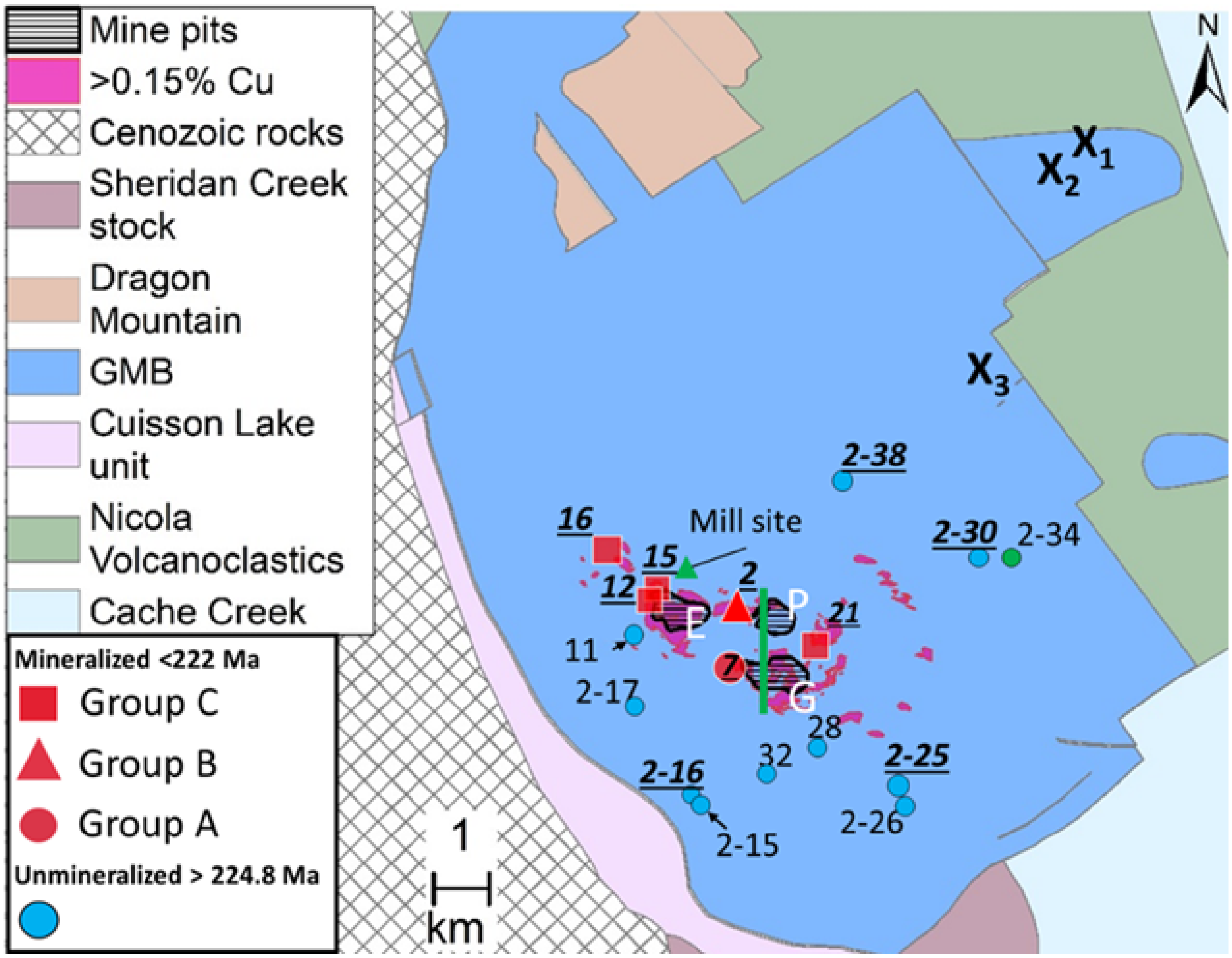

Figure 4.2. Simplified geological map of the study area, modified from Plouffe and Ferbey (2015). Sample numbers omit the prefix of "GBR-". Sample names underlined, italic and bold correspond to age dated samples. Ages of samples are listed in Table 4.4. Open pits are labelled, E = East pit, P=Pollyanna pit and G = Granite Lake pit. Pink areas correspond to areas with >0.15% Cu shown in Fig. 4.3. X's denote the locations of samples for U-Pb zircon dating by Schiarizza (2015). X1 = 222.71±0.22 Ma, X2= 221.25±0.20 Ma and X3= 217.15±0.20 Ma. The green circle is the location of sample used in amphibole analysis. The thick green line is the cross section shown in Fig. 4.3.

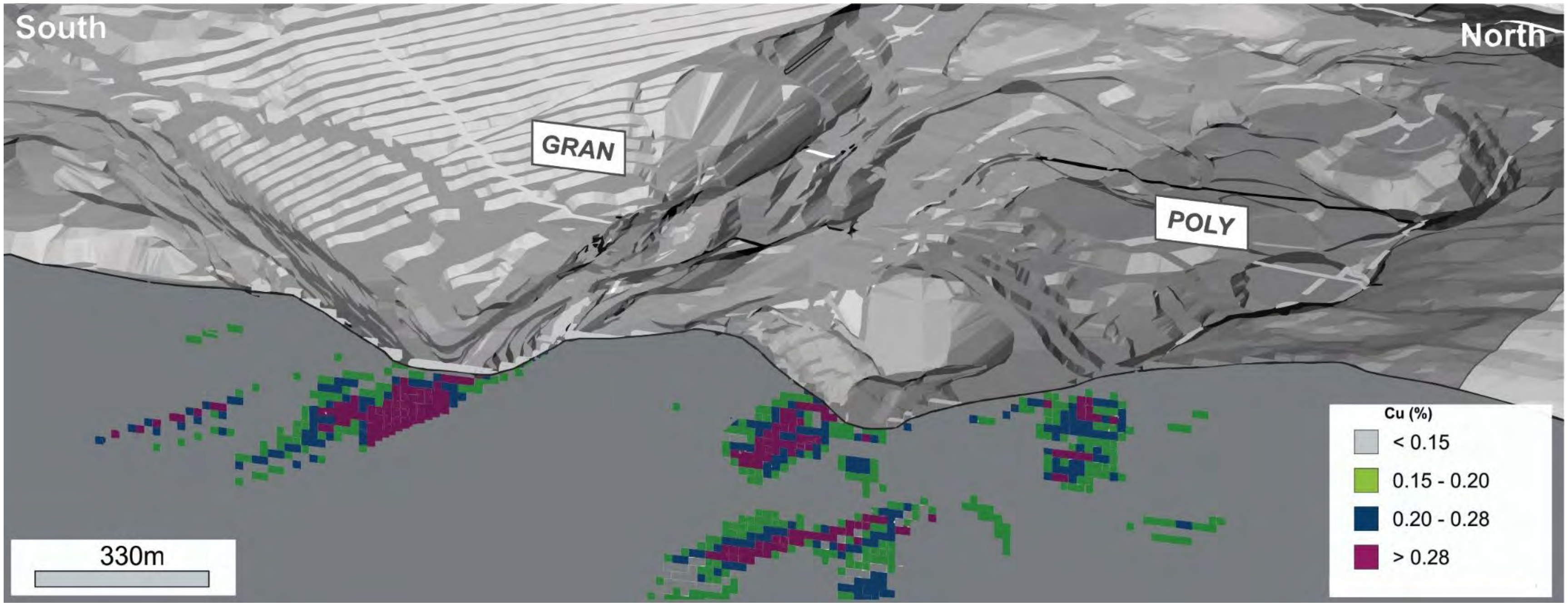

Figure 4.3. The contents of Cu along the north south cross section (shown in Fig. 4.2) through the Pollyanna (POLY) and Granite Lake (GRAN) pits. The map was based on Cu contents of drill cores in April, 2018 by Taseko Gibraltar Mines Limited. The top of the bench and the bottom of the Granite Lake pit are 1200m above sea level and 900m above sea level, respectively.

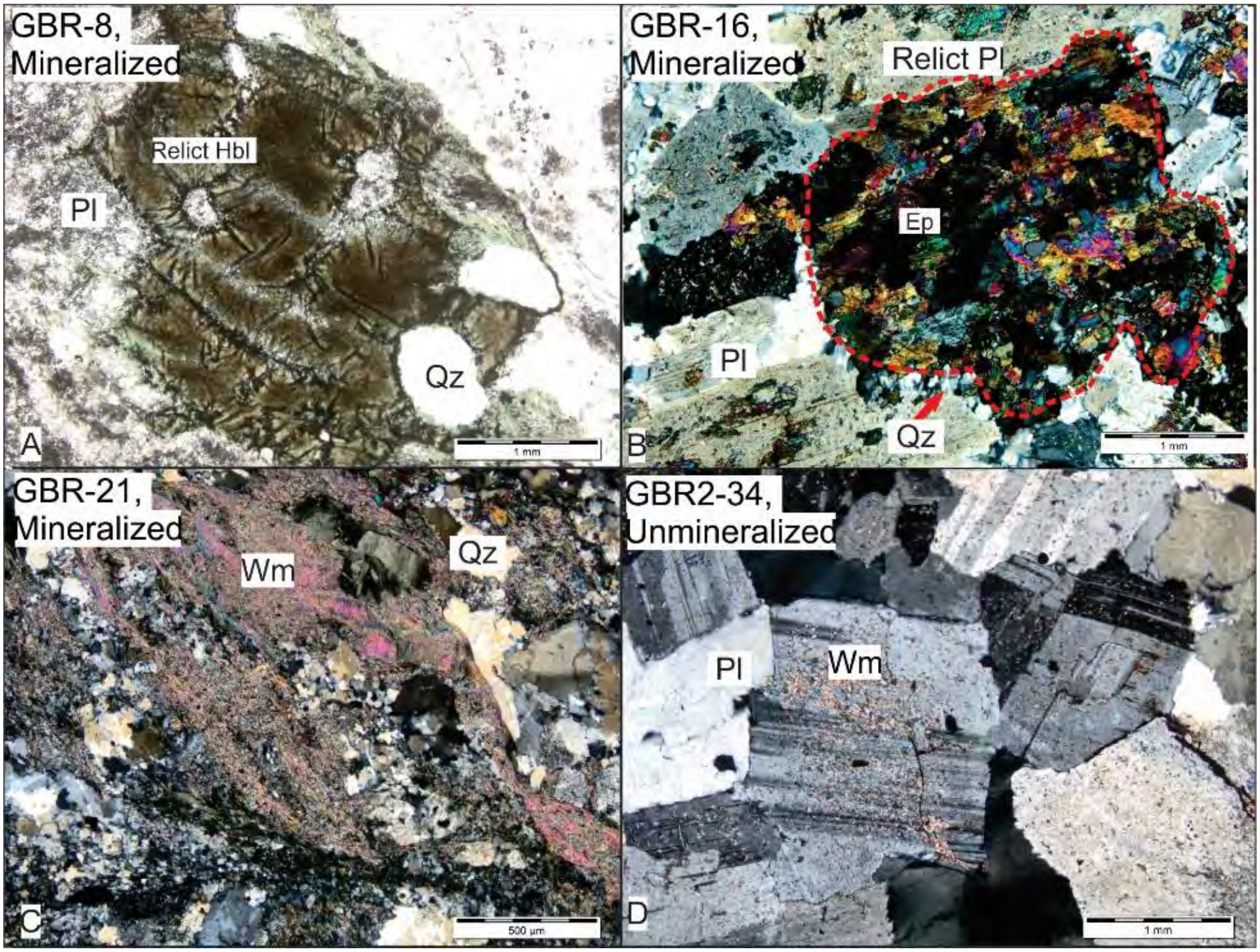

Figure 4.4. (A) Plain polarized light image of relict hornblende (Hbl) replaced by secondary biotite (Bt). Rims are replaced by chlorite (Chl). (B) Photomicrograph of epidote (Ep) replacing plagioclase (Pl) under crossed polarizers (XPL). (C) XPL photomicrograph of white mica (Wm) replacing Pl and forming a veinlet. (D) XPL photomicrograph of minor Wm in Pl. Sample locations are in the Appendix 1, Table A1-1.

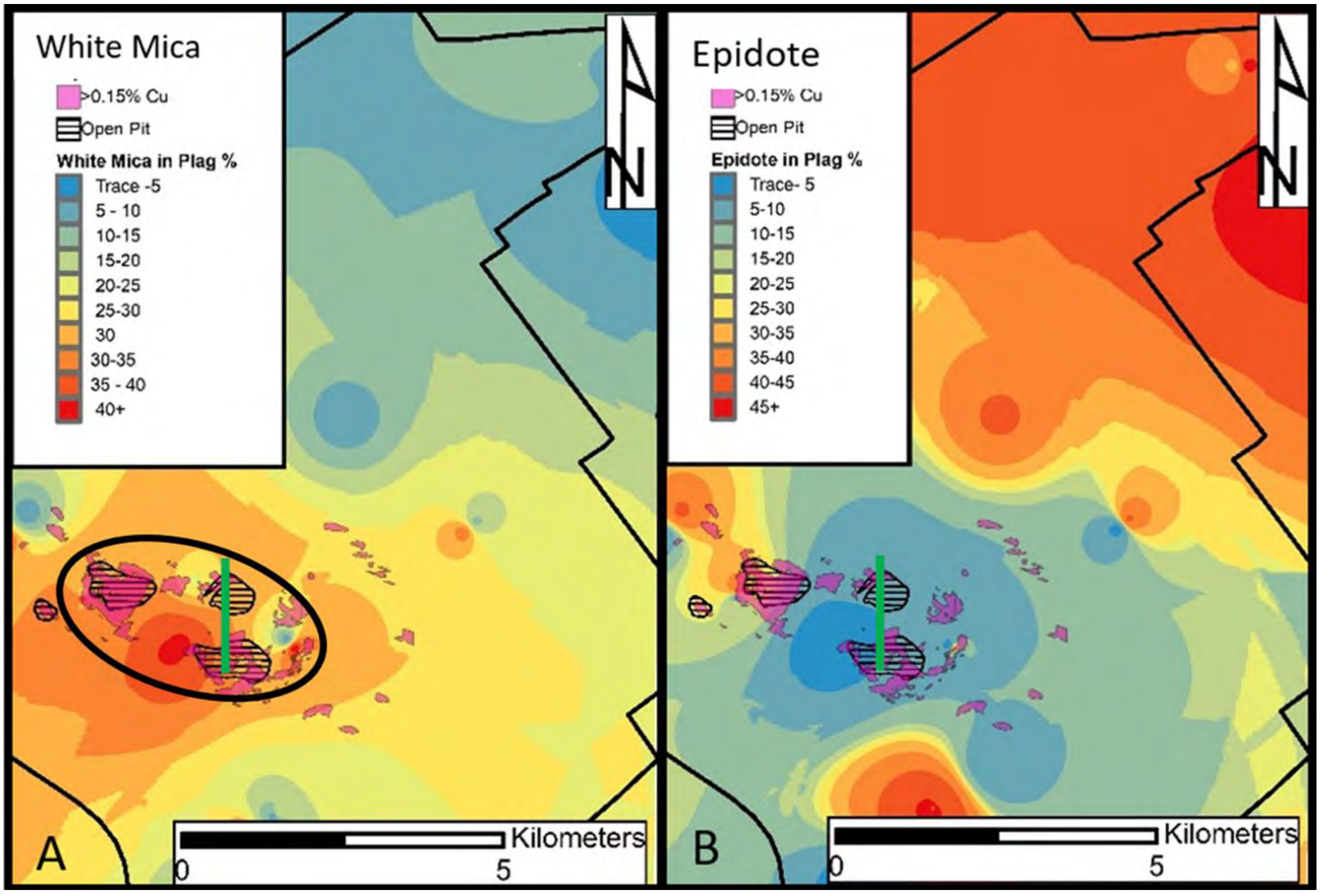

Figure 4.5. Maps showing the fraction of white mica (A) and epidote (B) replacing plagioclase. The black lines outline the GMB. Pink areas correspond to those with >0.15% Cu (Fig. 4.2).

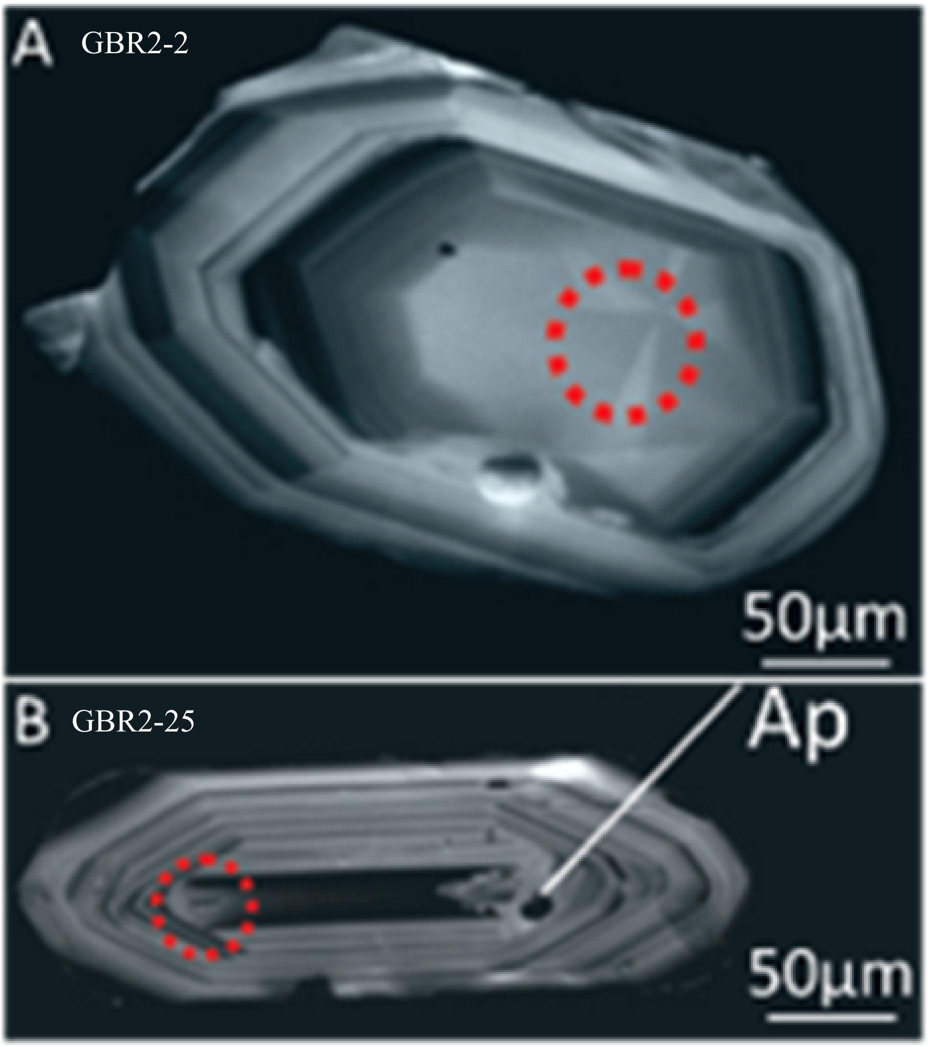

Figure 4.6. CL-SEM images of zircon from the mineralized (A) and unmineralized (B) tonalite showing oscillatory zoning and apatite (Ap) inclusion. The locations for laser ablation are shown in red dashed circles.

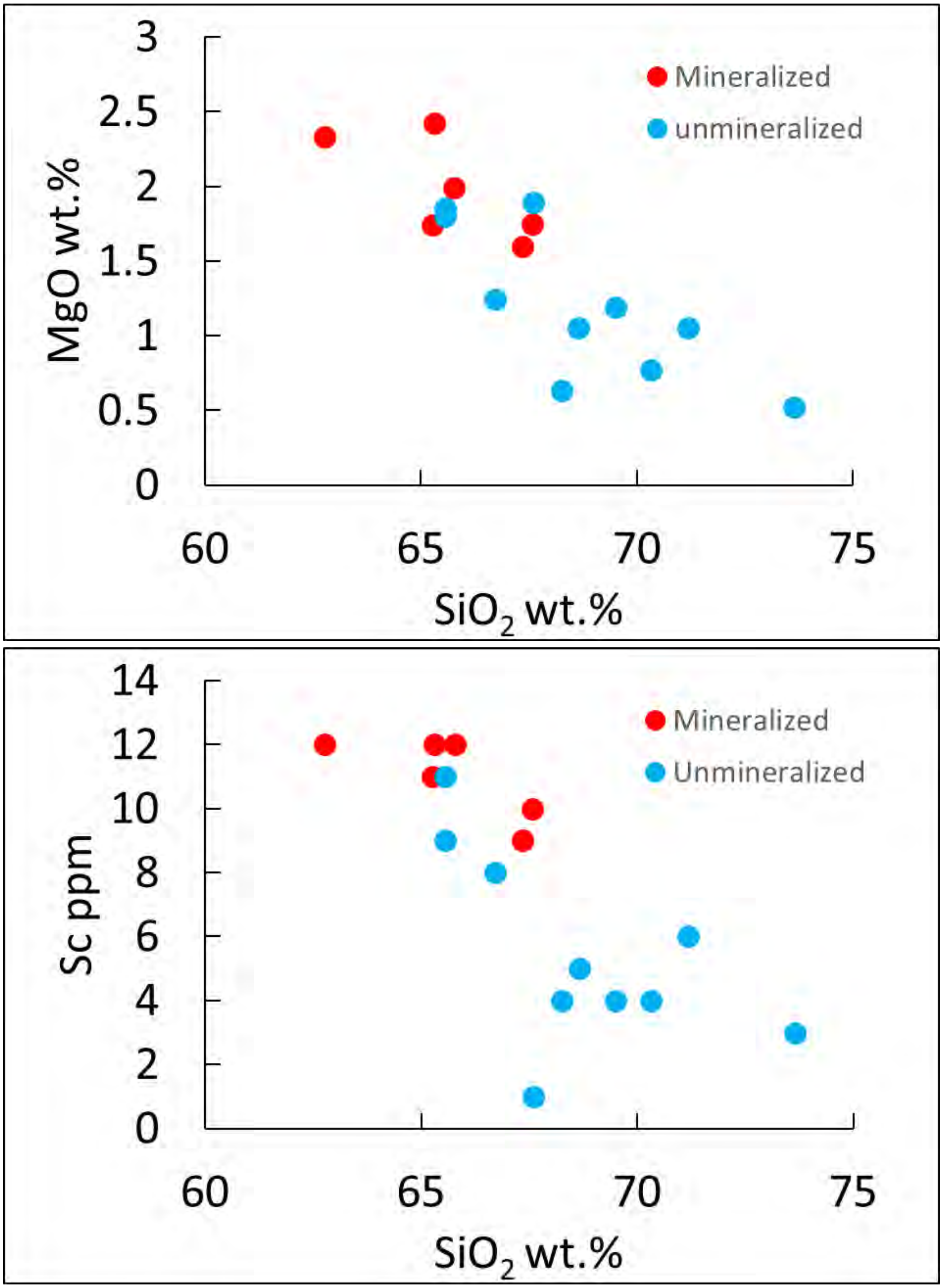

Figure 4.7. SiO_2-MgO (upper) and SiO_2-Sc (lower) plots of intrusions of GMB.

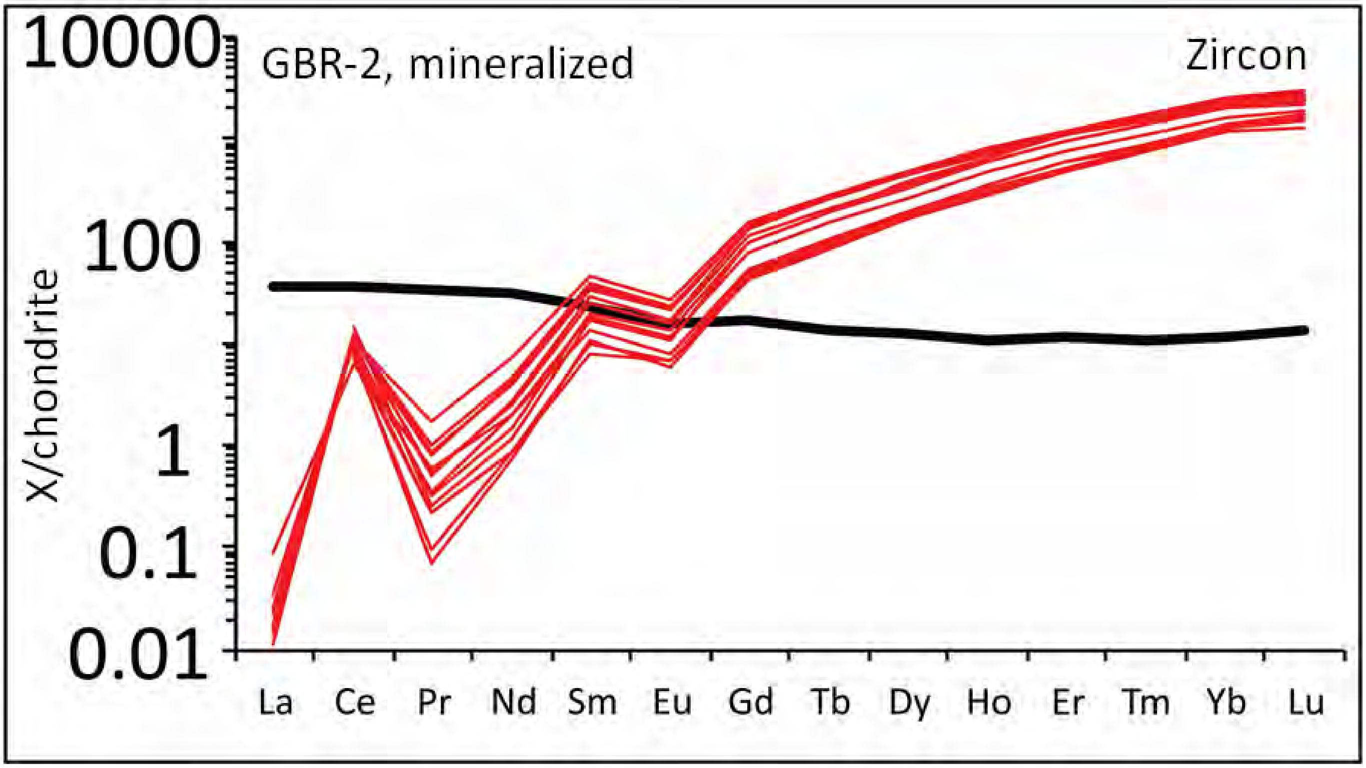

GBR-2, mineralized
Zircon
X/chondrite
10000
100
1
0.1
0.01
La
Ce
Pr
Nd
Sm
Eu
Gd
Tb
Dy
Ho
Er
Tm
Yb
Lu

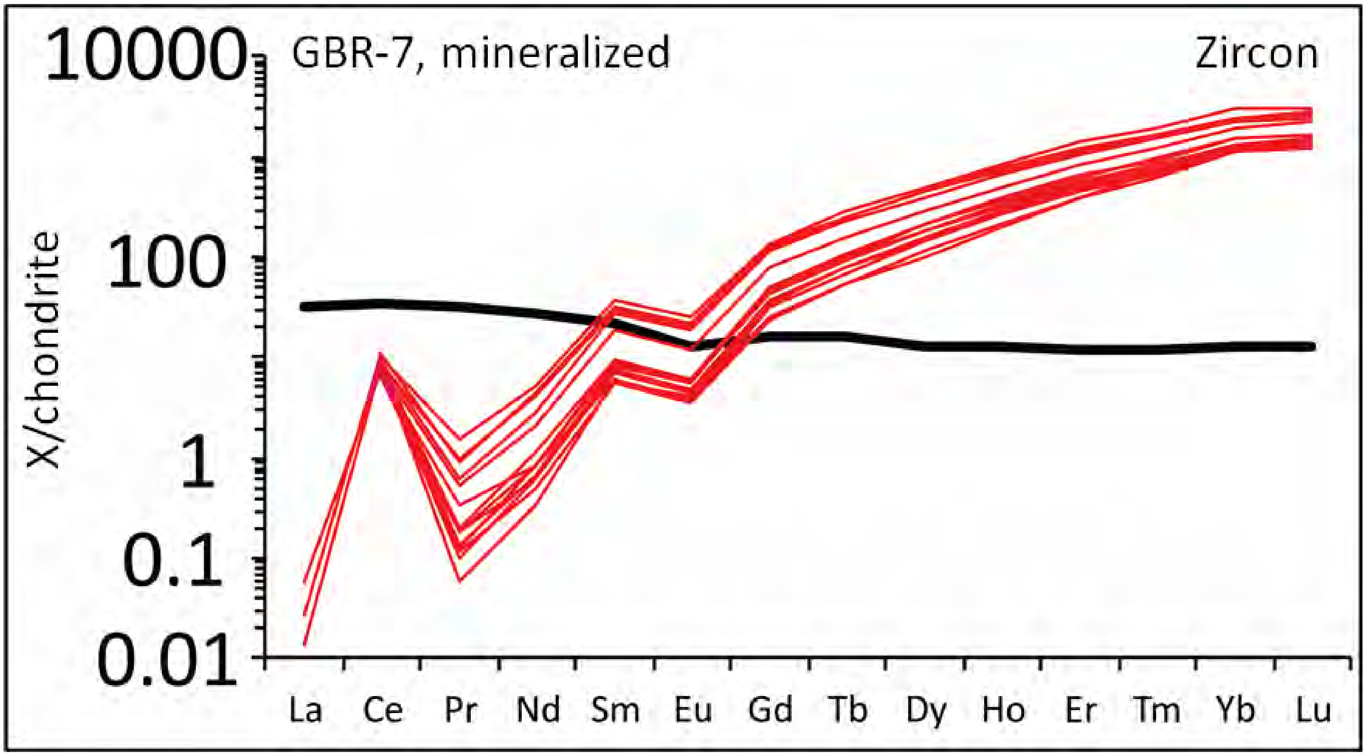

GBR-7, mineralized
Zircon
X/chondrite
10000
100
1
0.1
0.01
La
Ce
Pr
Nd
Sm
Eu
Gd
Tb
Dy
Ho
Er
Tm
Yb
Lu

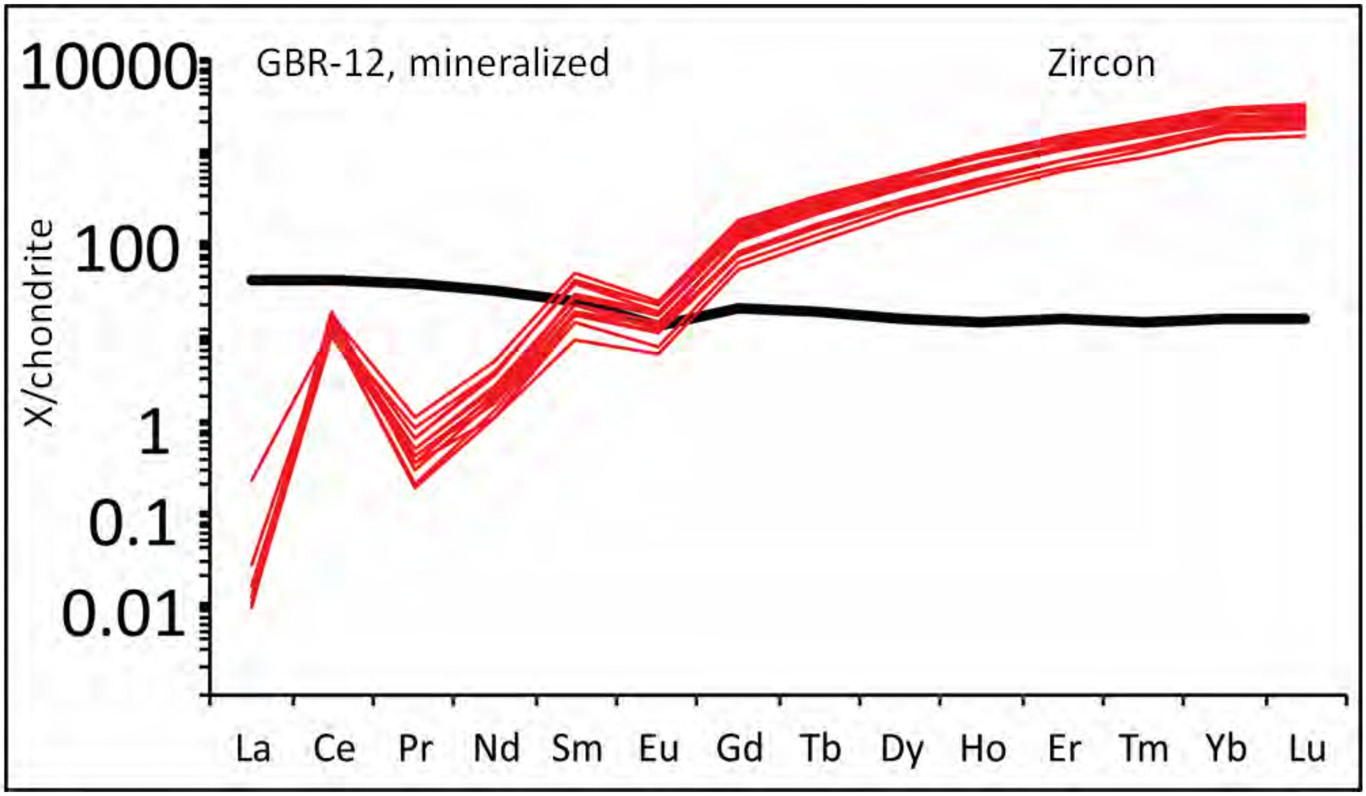
10000
100
1
0.1
0.01
X/chondrite
GBR-12, mineralized
Zircon
La
Ce
Pr
Nd
Sm
Eu
Gd
Tb
Dy
Ho
Er
Tm
Yb
Lu

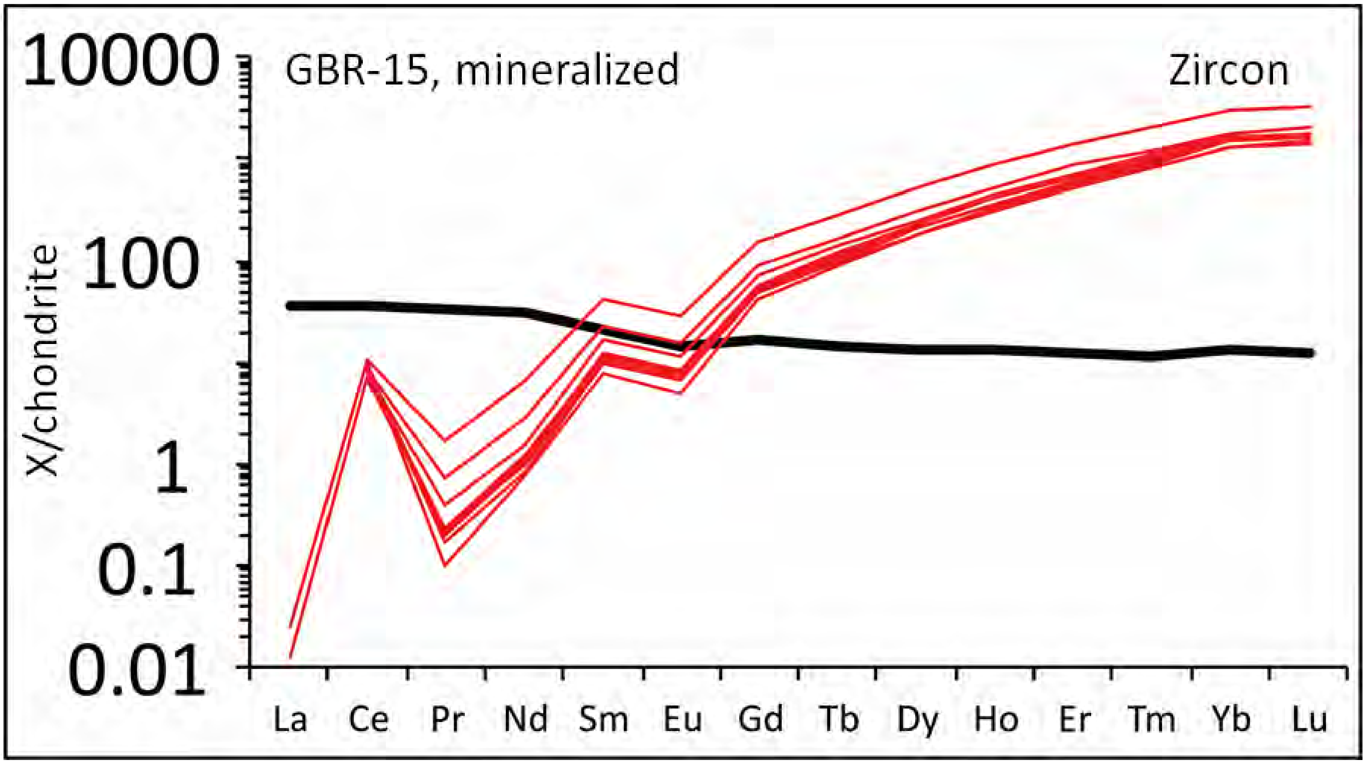
10000
100
1
0.1
0.01
X/chondrite
GBR-15, mineralized
Zircon
La
Ce
Pr
Nd
Sm
Eu
Gd
Tb
Dy
Ho
Er
Tm
Yb
Lu

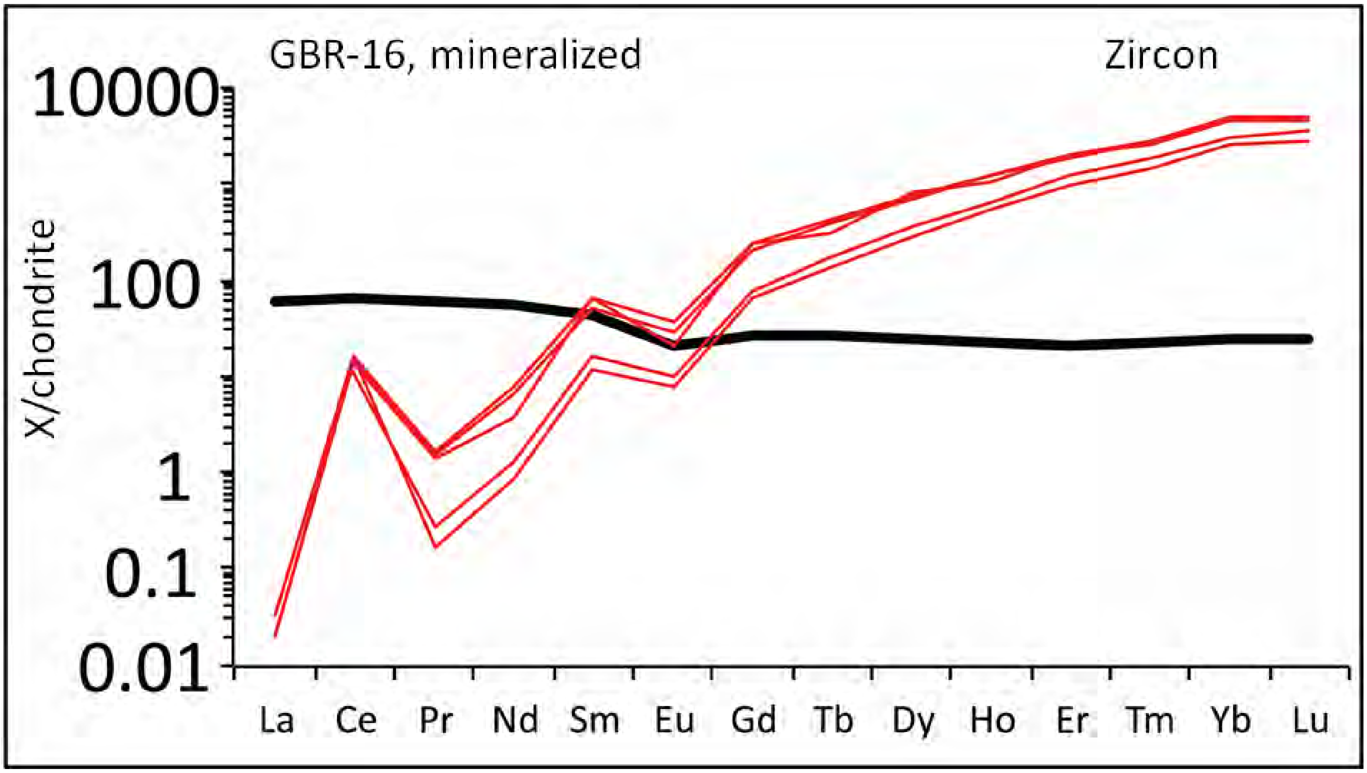
GBR-16, mineralized
Zircon
10000
100
1
0.1
0.01
X/chondrite
La
Ce
Pr
Nd
Sm
Eu
Gd
Tb
Dy
Ho
Er
Tm
Yb
Lu

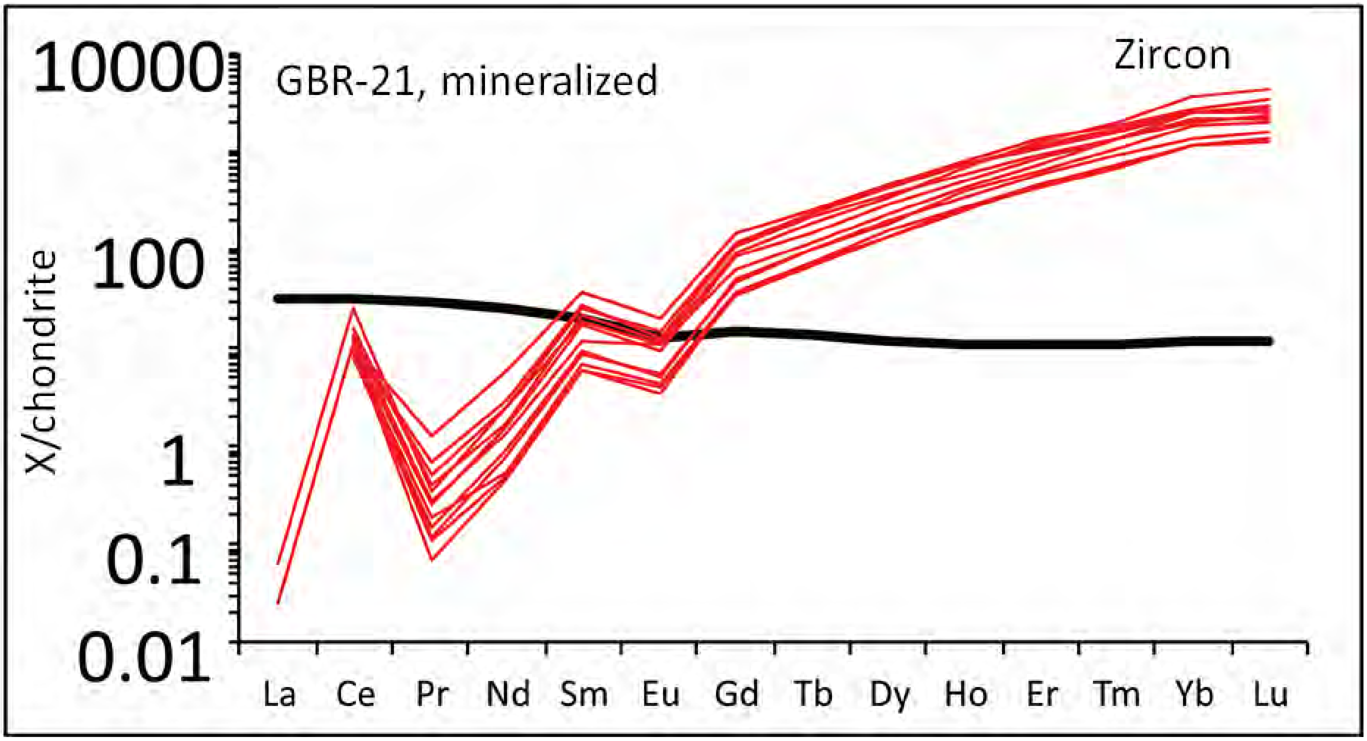
GBR-21, mineralized
Zircon
10000
100
1
0.1
0.01
X/chondrite
La
Ce
Pr
Nd
Sm
Eu
Gd
Tb
Dy
Ho
Er
Tm
Yb
Lu

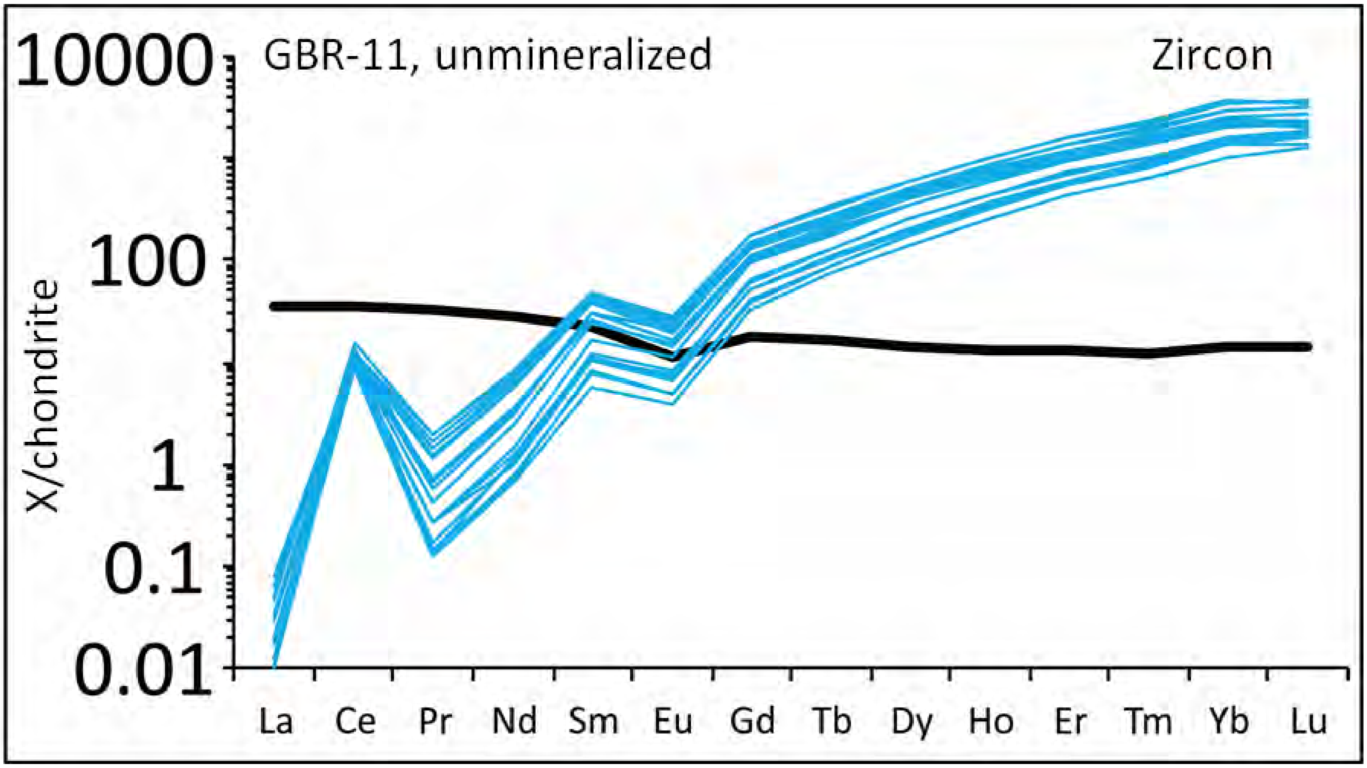
GBR-11, unmineralized
Zircon
X/chondrite
10000
100
1
0.1
0.01
La
Ce
Pr
Nd
Sm
Eu
Gd
Tb
Dy
Ho
Er
Tm
Yb
Lu

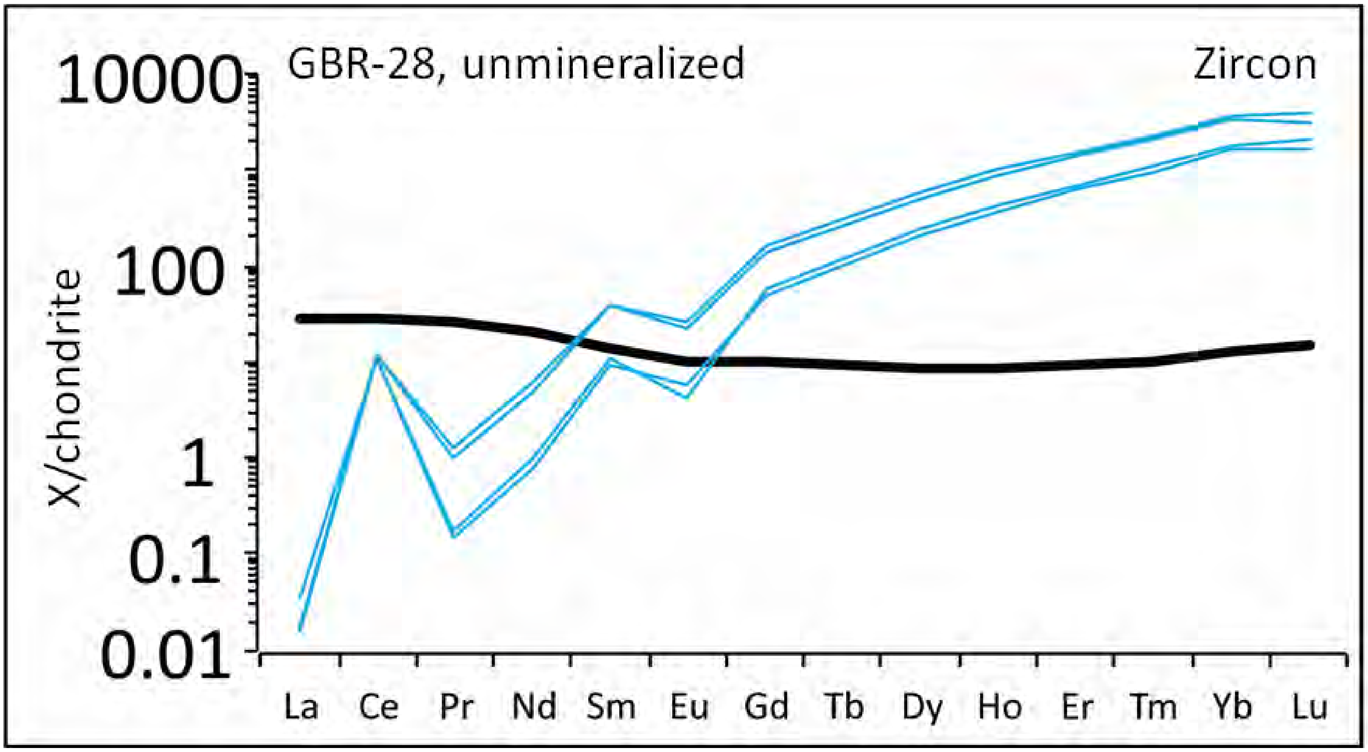
GBR-28, unmineralized
Zircon
X/chondrite
10000
100
1
0.1
0.01
La
Ce
Pr
Nd
Sm
Eu
Gd
Tb
Dy
Ho
Er
Tm
Yb
Lu

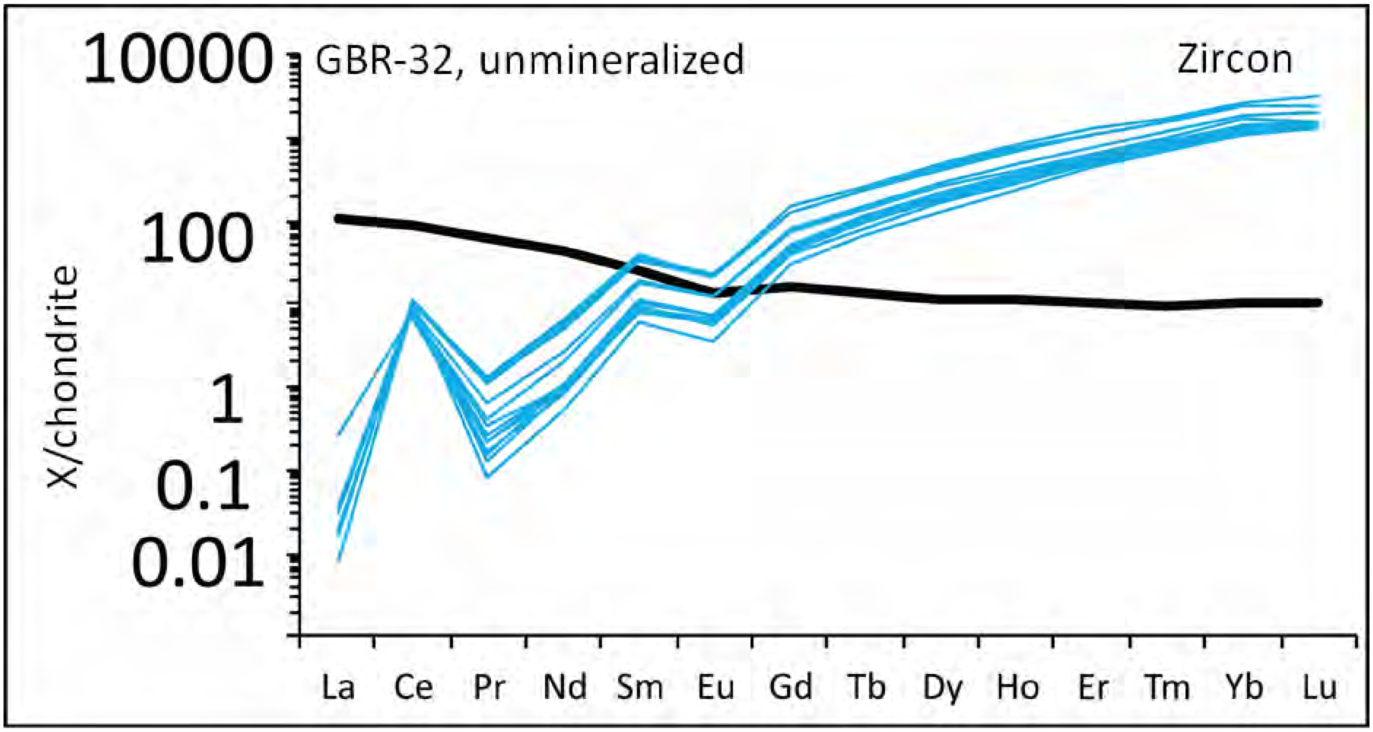
GBR-32, unmineralized
Zircon
10000
100
1
0.1
0.01
X/chondrite
La
Ce
Pr
Nd
Sm
Eu
Gd
Tb
Dy
Ho
Er
Tm
Yb
Lu

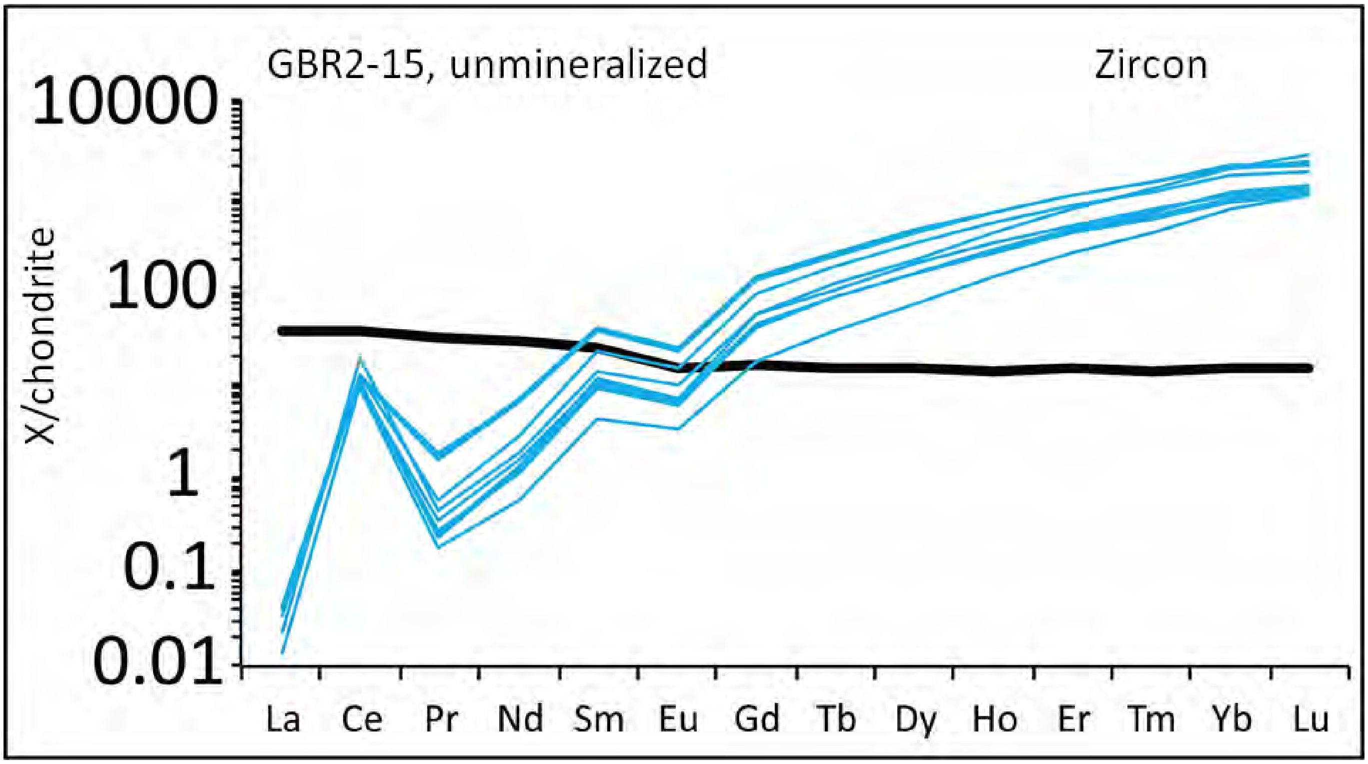
GBR2-15, unmineralized
Zircon
10000
100
1
0.1
0.01
X/chondrite
La
Ce
Pr
Nd
Sm
Eu
Gd
Tb
Dy
Ho
Er
Tm
Yb
Lu

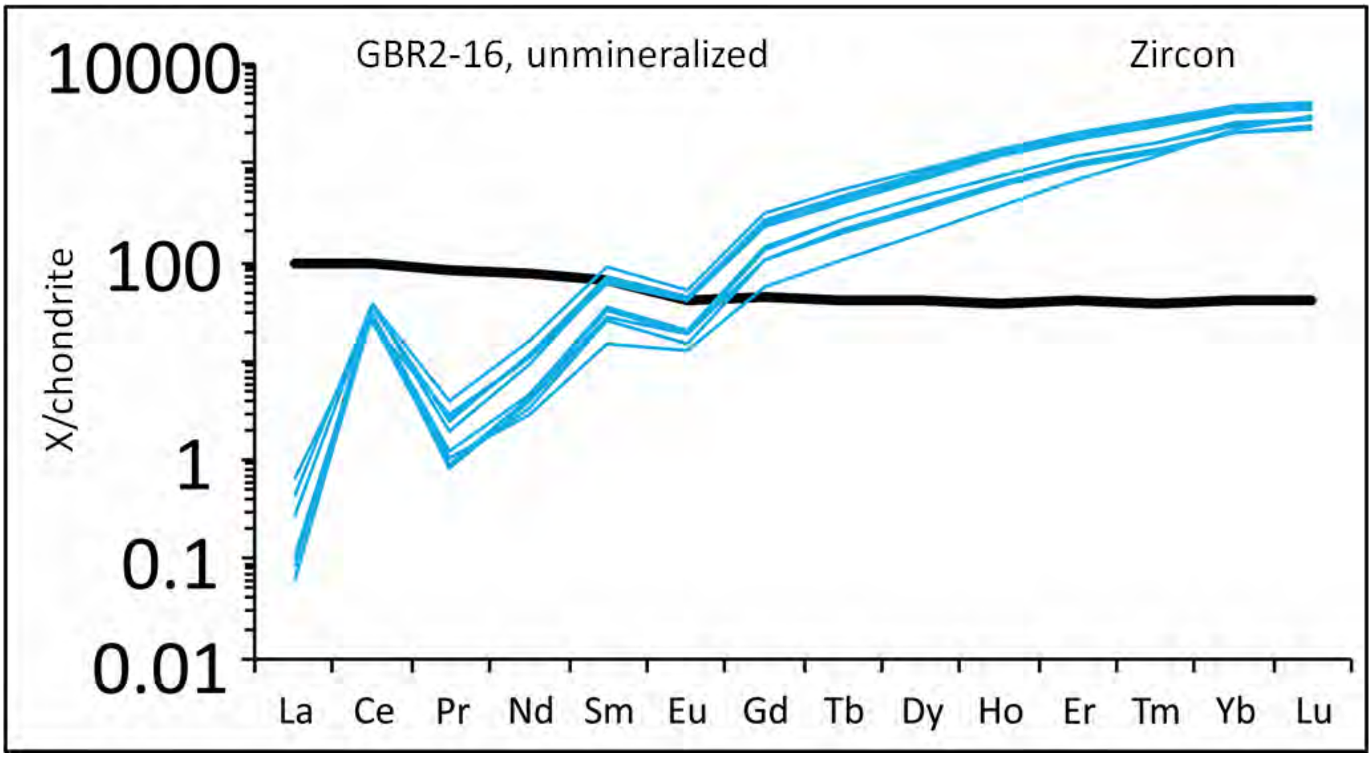
10000
100
1
0.1
0.01
X/chondrite
GBR2-16, unmineralized
Zircon
La
Ce
Pr
Nd
Sm
Eu
Gd
Tb
Dy
Ho
Er
Tm
Yb
Lu

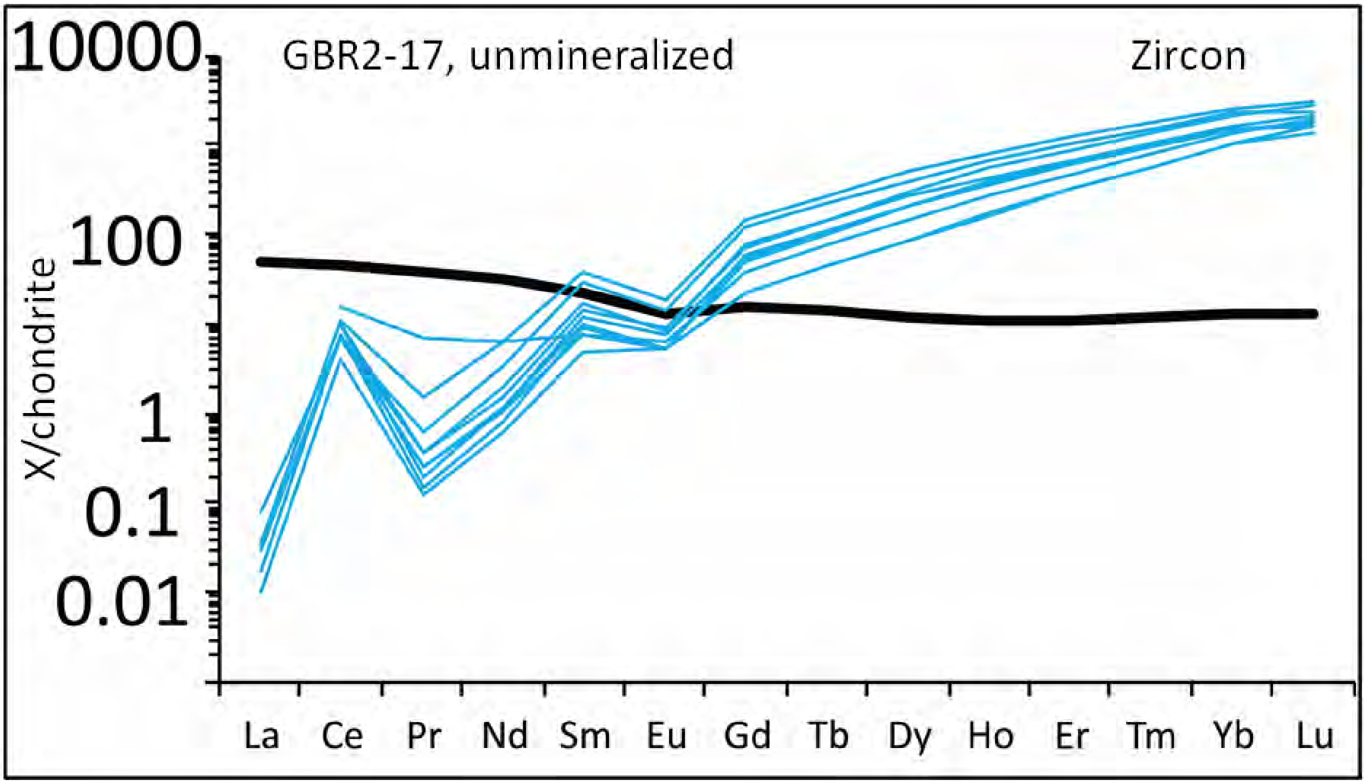
10000
100
1
0.1
0.01
X/chondrite
GBR2-17, unmineralized
Zircon
La
Ce
Pr
Nd
Sm
Eu
Gd
Tb
Dy
Ho
Er
Tm
Yb
Lu

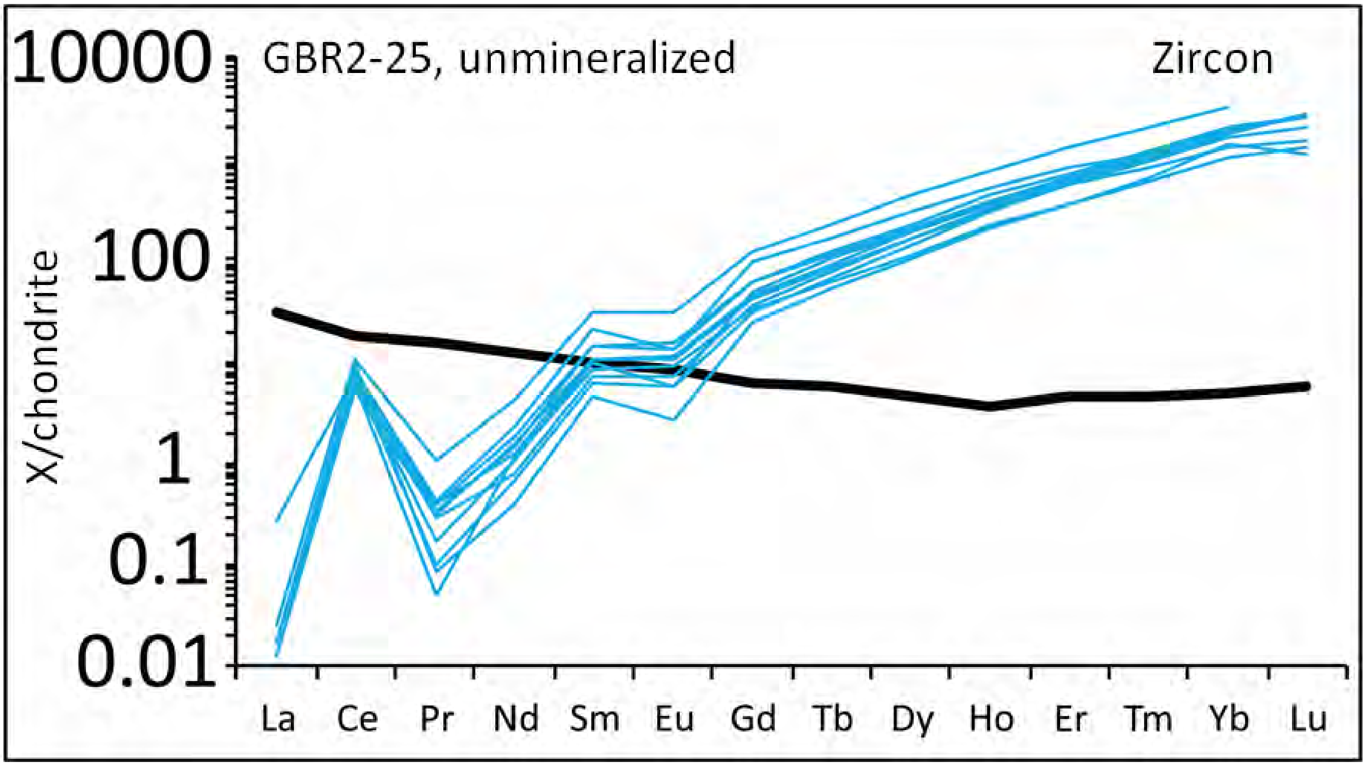

GBR2-25, unmineralized
Zircon
10000
100
1
0.1
0.01
X/chondrite
La
Ce
Pr
Nd
Sm
Eu
Gd
Tb
Dy
Ho
Er
Tm
Yb
Lu

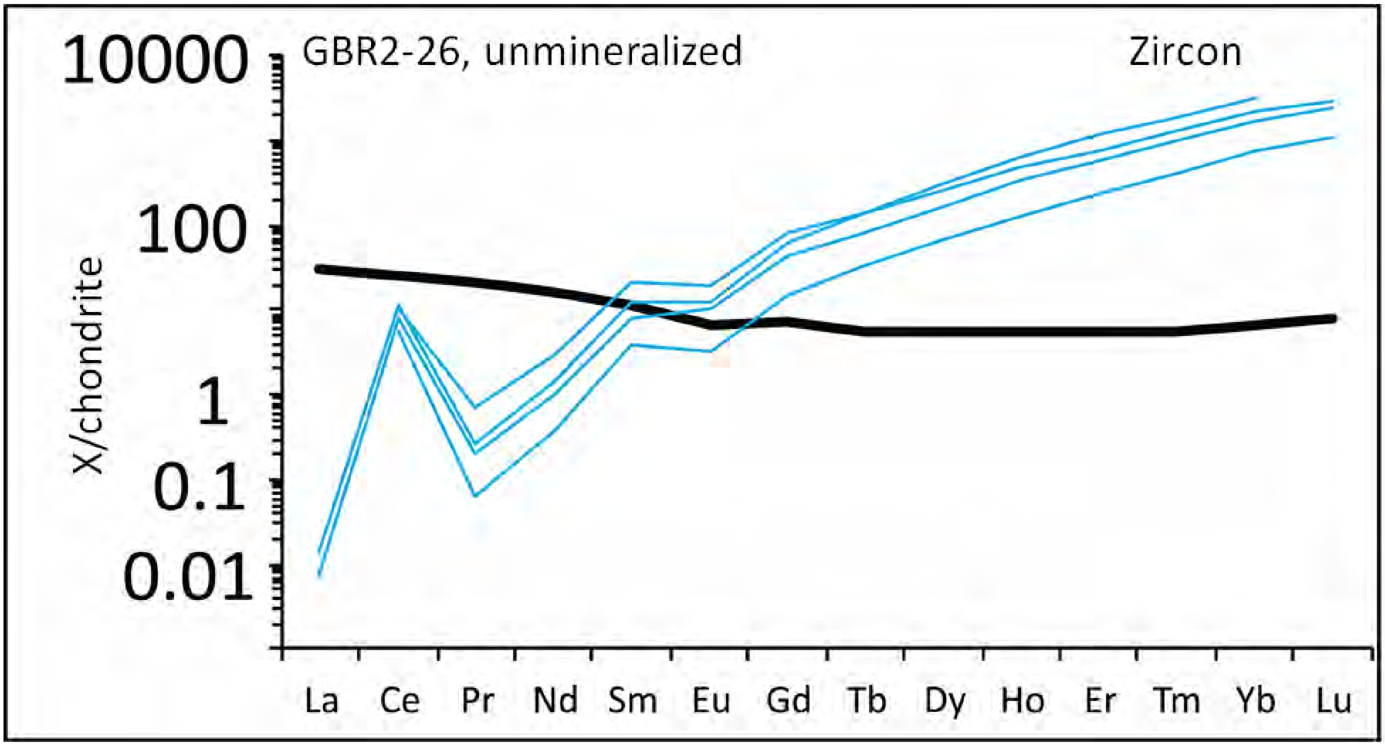

GBR2-26, unmineralized
Zircon
10000
100
1
0.1
0.01
X/chondrite
La
Ce
Pr
Nd
Sm
Eu
Gd
Tb
Dy
Ho
Er
Tm
Yb
Lu

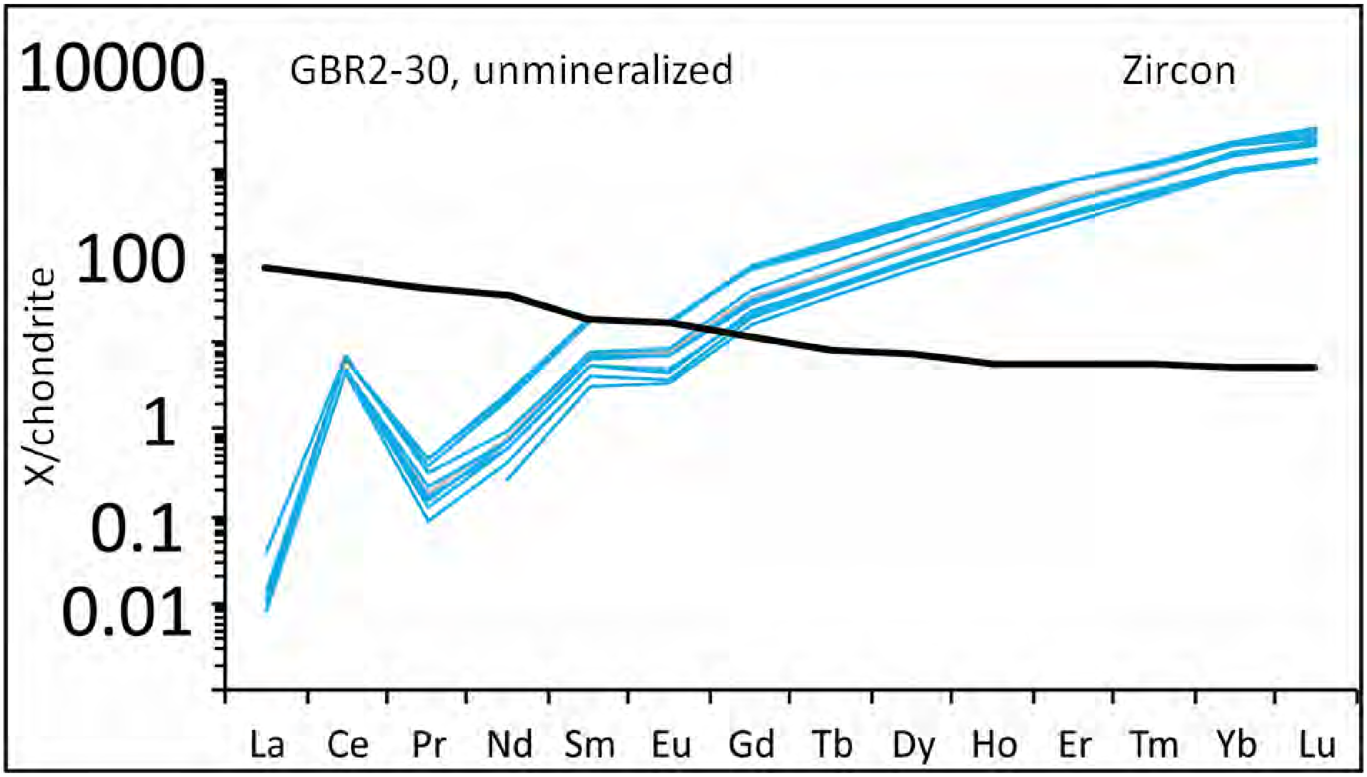
GBR2-30, unmineralized
Zircon
10000
100
1
0.1
0.01
X/chondrite
La
Ce
Pr
Nd
Sm
Eu
Gd
Tb
Dy
Ho
Er
Tm
Yb
Lu

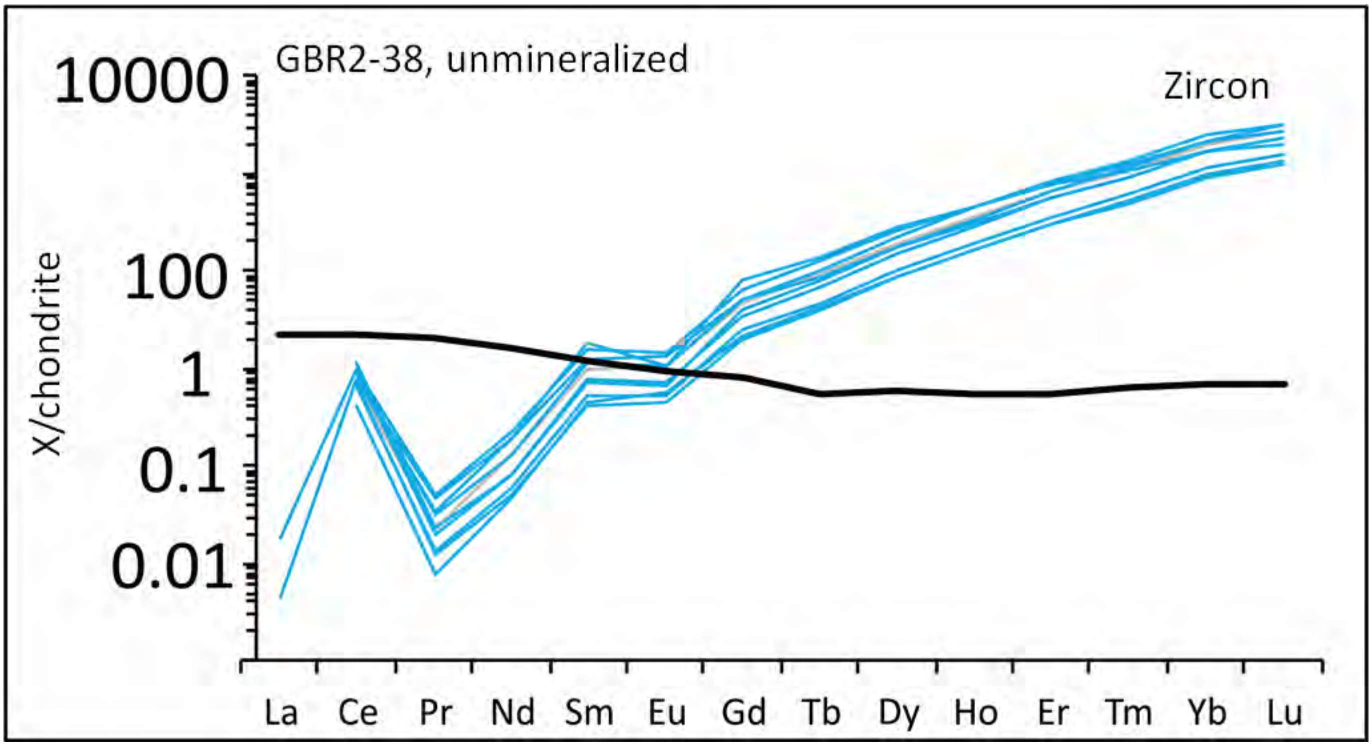
GBR2-38, unmineralized
Zircon
10000
100
1
0.1
0.01
X/chondrite
La
Ce
Pr
Nd
Sm
Eu
Gd
Tb
Dy
Ho
Er
Tm
Yb
Lu

Figure 4.8. Chondrite-normalized REE patterns for zircon (red and blue lines) and its bulk rock (black thick line). Red lines are mineralized intrusions and blue are unmineralized intrusions. Chondrite values based on McDonough and Sun (1995).

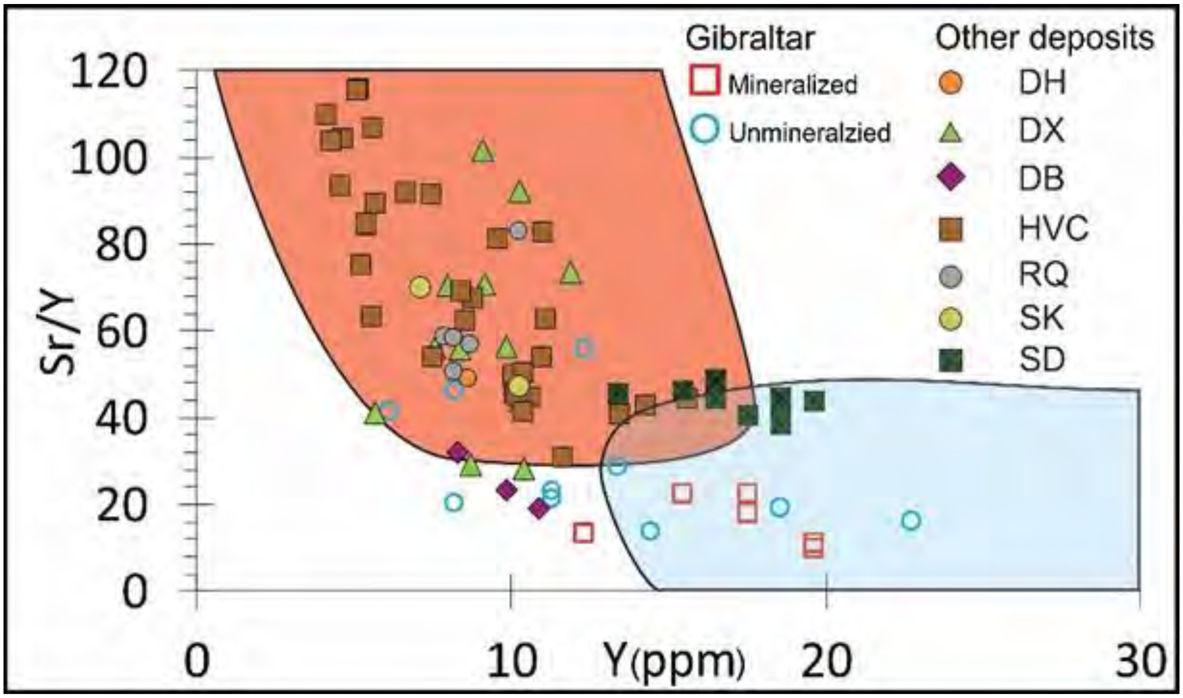

Figure 4.9. Sr/Y vs. Y diagram showing fields for adakite-like rocks (orange) and normal arc rocks (blue) from Defant and Drummond (1993). Data sources: Dexing Cu-Mo-Au deposit (DX; Zhang et al., 2013); Shadan Cu-Au (SD), Saindak Cu (SK) and Reko Diq Cu-Au (RD) (Richards et al., 2012); Duobaoshan Cu (DB) and Deheishan Cu-Mo (DH) (Ge et al., 2007); and Highland Valley Copper Cu-Mo (HVC)(Whalen et al., 2017).

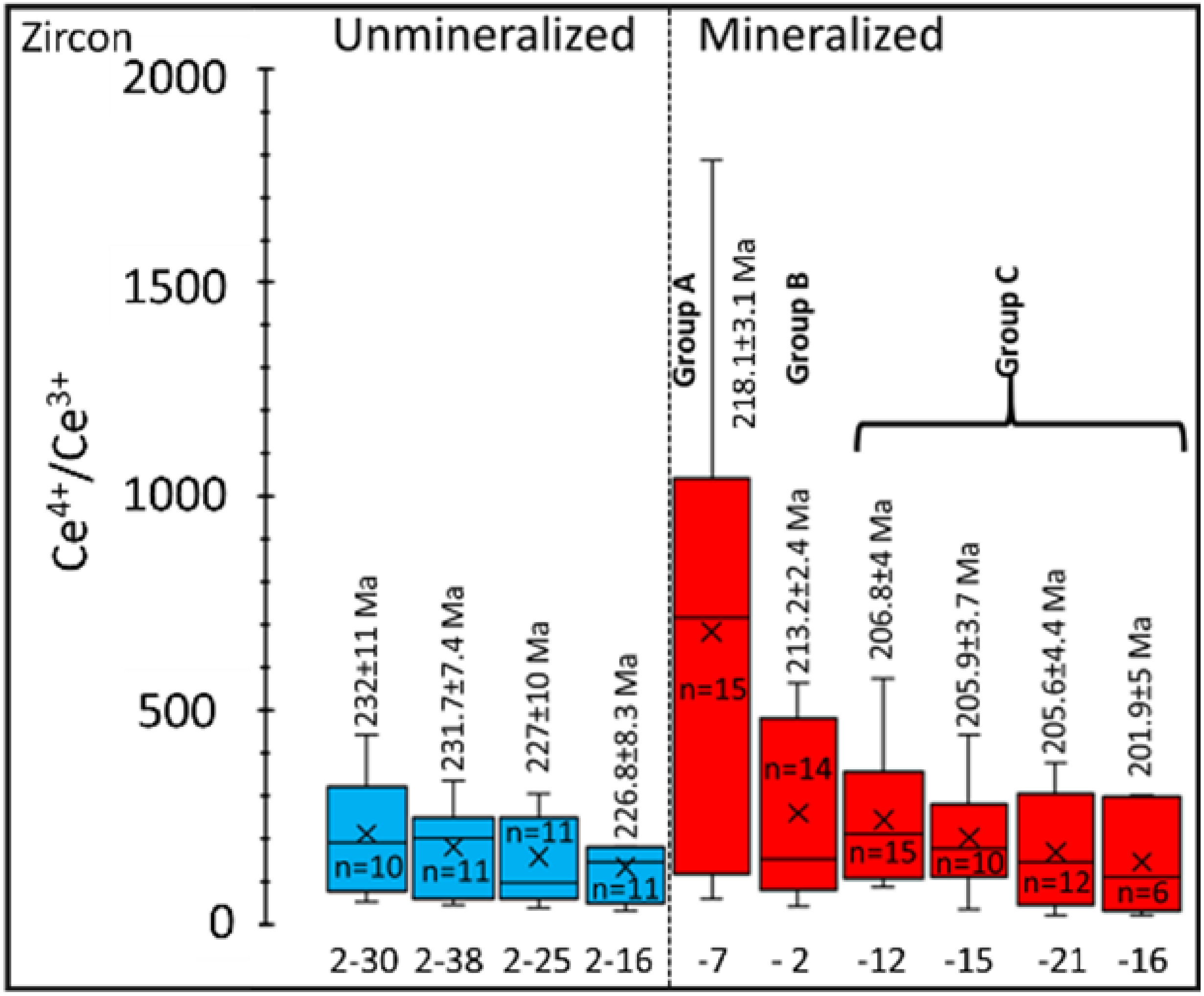

Figure 4.10. Box-and whisker plots of Ce^{4+}/Ce^{3+} values in zircon from the GMB. Ce^{4+}/Ce^{3+} is calculated using the method proposed by Ballard et al. (2002). A box is defined by upper and lower quartile values. X represents the mean value for each group. Uncertainties of ages are 2sigma. Sample numbers are indicated below each box-and whisker plot omitting the prefix "GBR".

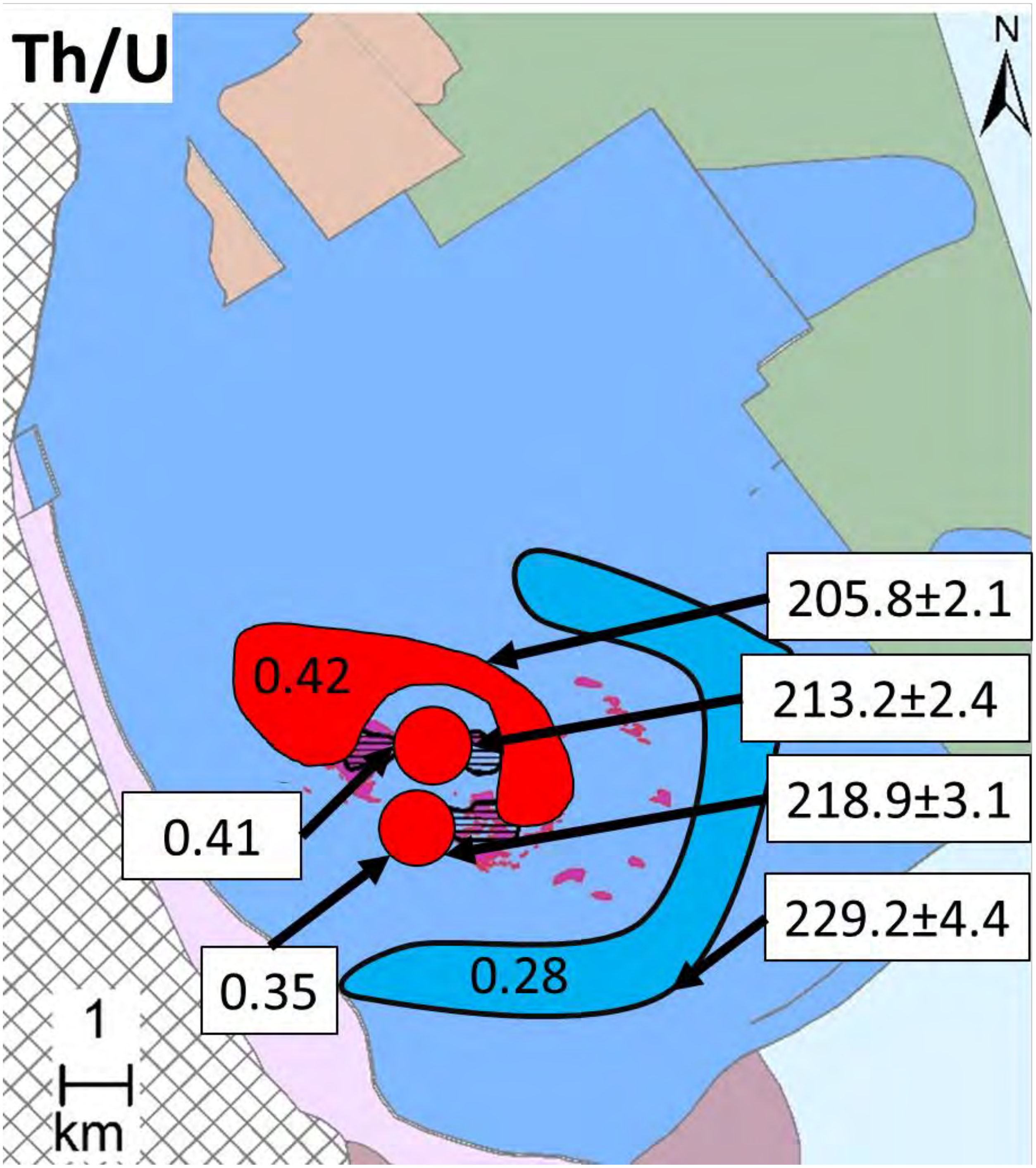

Figure 4.11: Simplified map of the GMB and the 4 identified magmas from this study. Each magma has corresponding U-Pb age data attached to it and Th/U ratios in zircon.

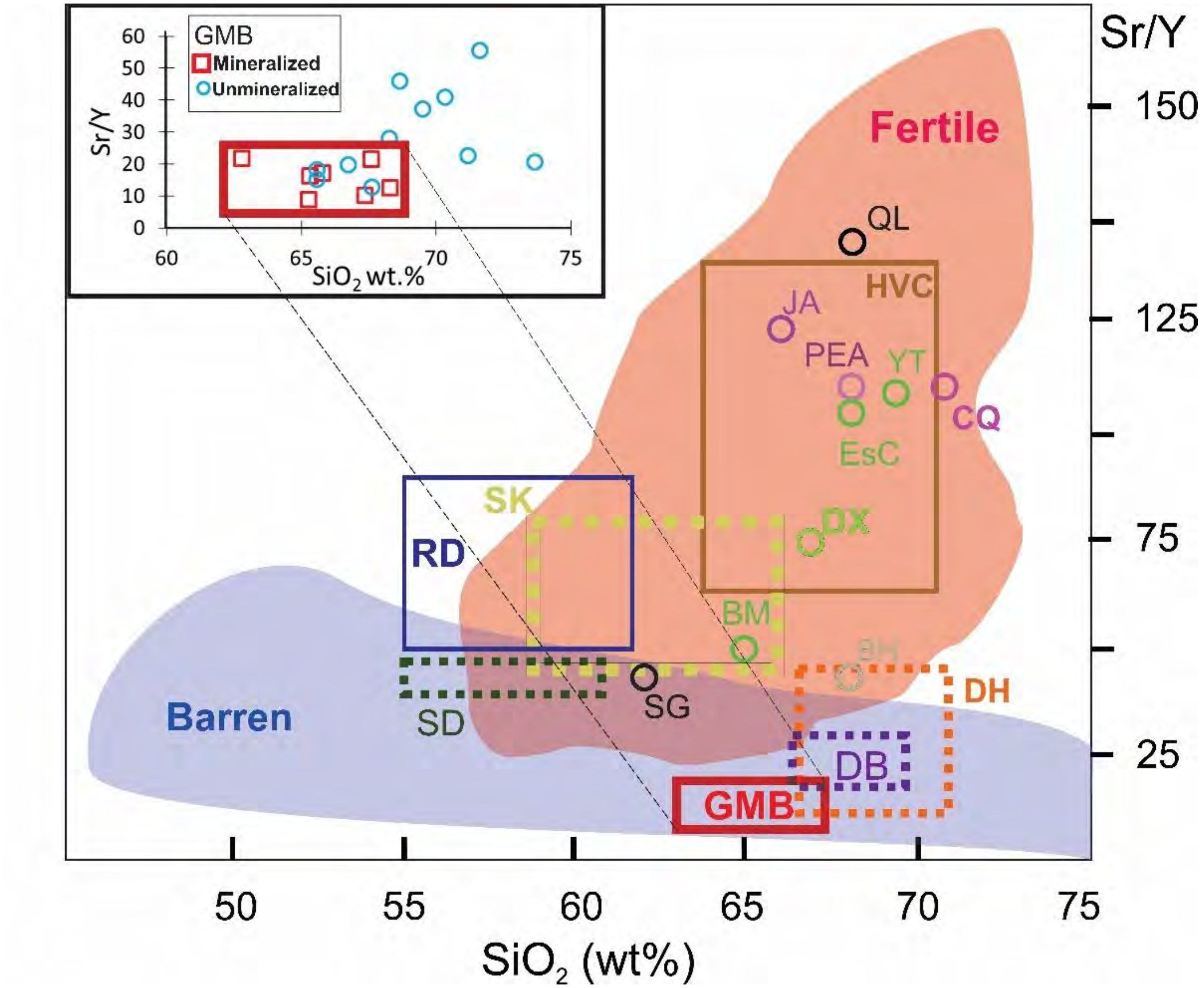

Figure 4.12. Bulk rock Sr/Y vs. SiO_2 discrimination diagram showing the compositions of fertile (dark orange) and barren (blue) intrusions, after Loucks (2014). All rectangles are full range of bulk rock data. The red square shows the range of values for the mineralized intrusions from the GMB (this study). The brown square with HVC represents rocks from the mineralized Bethsaida and Bethlehem phases of the Highland Valley porphyry Cu deposit (Whalen et al., 2017). The open circles are values for deposits discussed in this paper with data from Loucks (2014). Data sources and abbreviations are the same as those for Fig. 4.9. Additional deposits are Batu Hijau Cu-Au (BH), Bingham Cu (BM), Chuquicamata Cu-Mo (CQ), Escondida Cu-Mo (EsC), Jiama Cu-Mo (JA), Pajonal El-Abra Cu (PEA), and Qulong Cu-Mo (QL) and the sources are Loucks (2014).

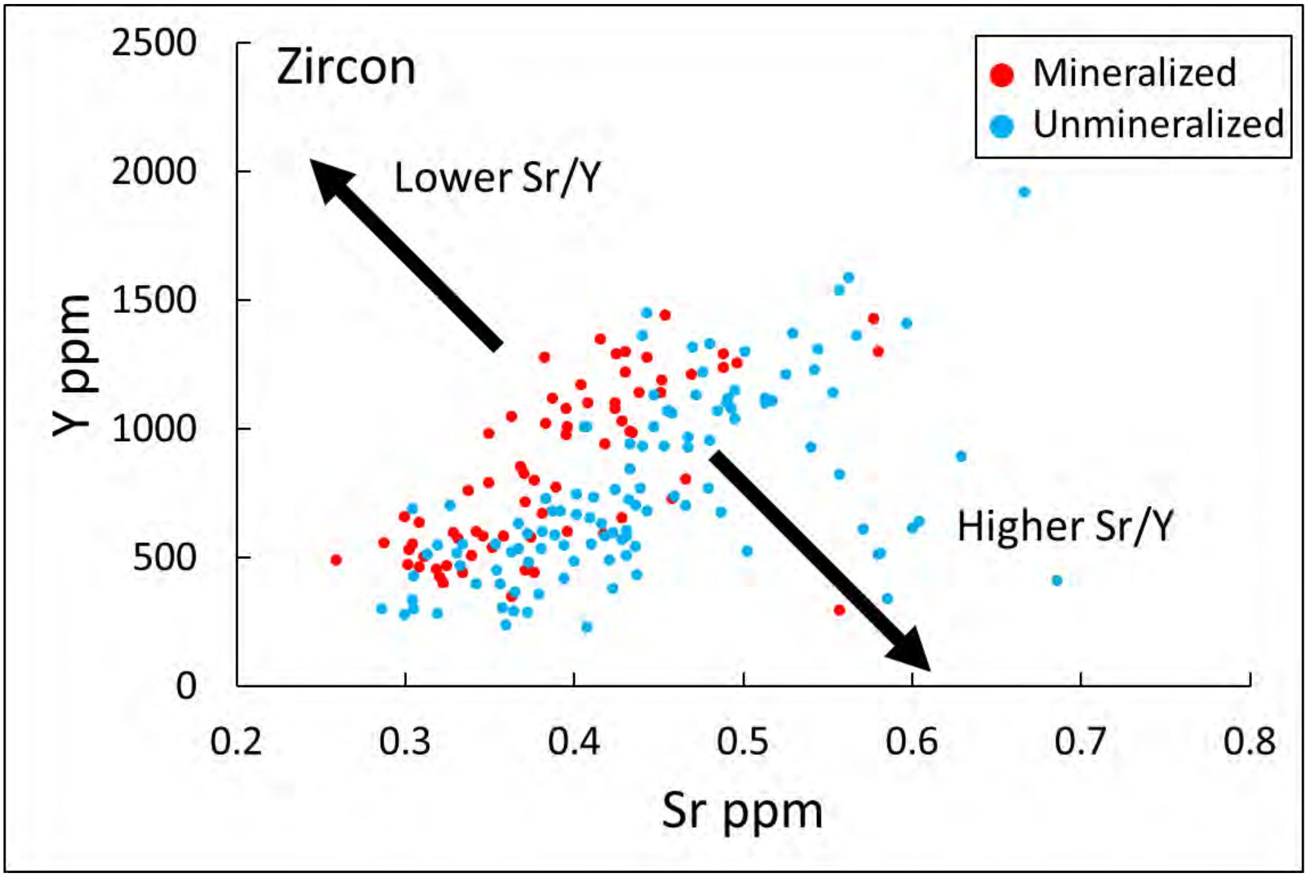

Figure 4.13. Sr-Y plot comparing mineralized and unmineralized samples of the GMB. The arrows indicate the general direction of samples that would plot with lower or higher Sr/Y ratios.

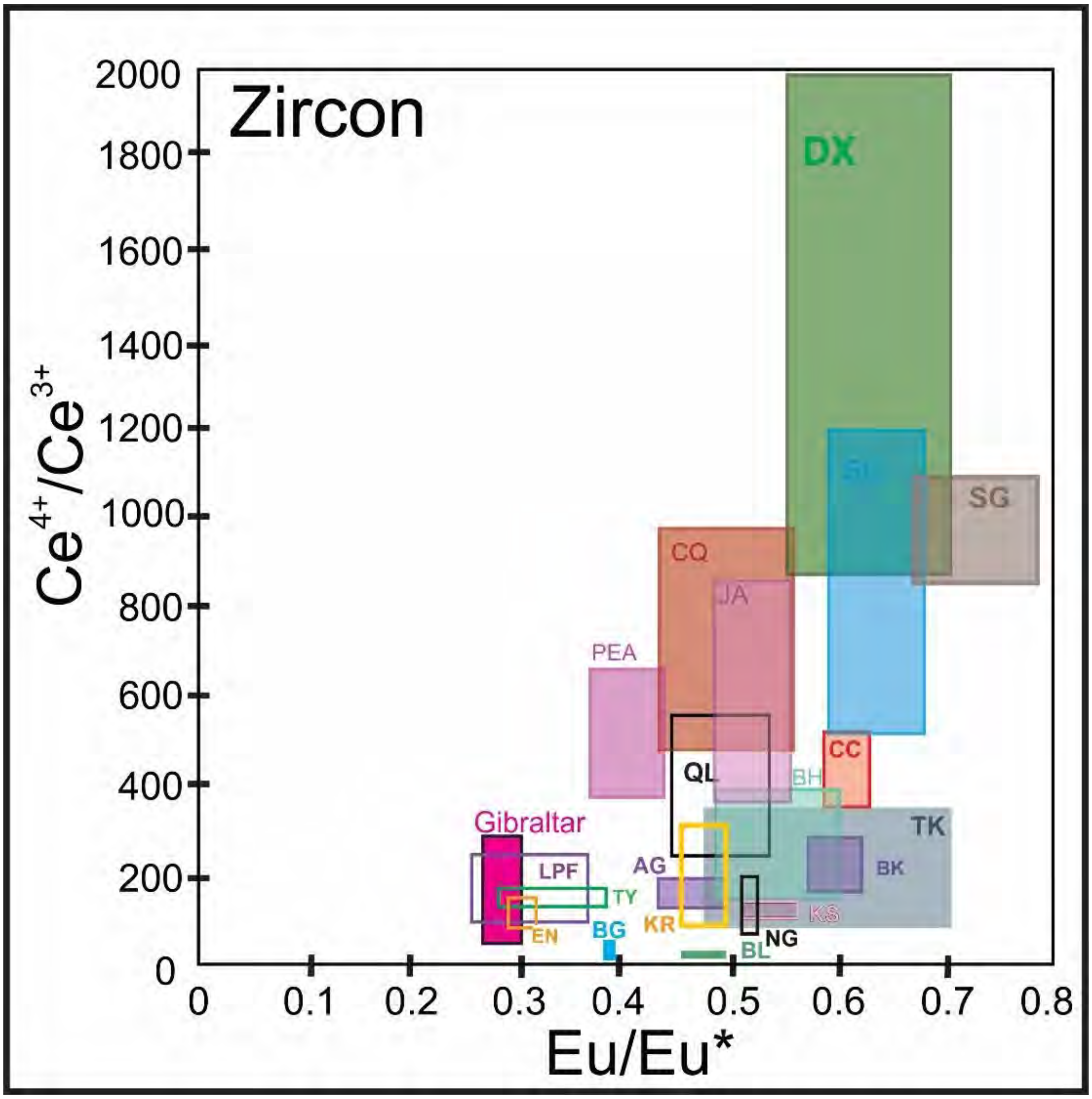

Figure 4.14. Box plots of Ce^{4+}/Ce^{3+} vs. Eu/Eu* for zircons from porphyry Cu deposits. A box shows lower and upper quartile values. Data sources: Pajonal-El Abra, Los Picos-Fortuna Cu (LPF) and Chuquicamata (Ballard et al., 2002); Cerro Corona Cu-Au (CC), (Hattori et al., 2017); Baogutu Cu (BG), Borly Cu-Mo (BL), Tuwu-Yandong Cu-Au (TY), Koksai Cu-Mo (KS), Erdnet Cu-Mo (EN), Aktogai Cu-Mo (AG), Kounrad Cu (KR), Nurkazghan Cu (NG) and Bozshakol Cu-Mo (BK) (Shen et al., 2015). The values of Ce4+/Ce3+ for the Batu Hijau Cu-Au (BH), Tampakan Cu-Au (TK), Dexing Cu-Mo-Au (DX), Qulong Cu-Mo (QL), Jiama Cu-Mo (JA), Sar Cheshmeh Cu-Mo-Au (SC) and Sungun Cu-Mo (SG) deposits were calculated from Ce/Nd values reported by Lu et al. (2016) using the correlation (Ce^{4+}/Ce^{3+} = 7.28 (Ce/Nd(1.35) determined (this study). Abbreviations are the same as those for Fig. 4.9 and Fig. 4.11.

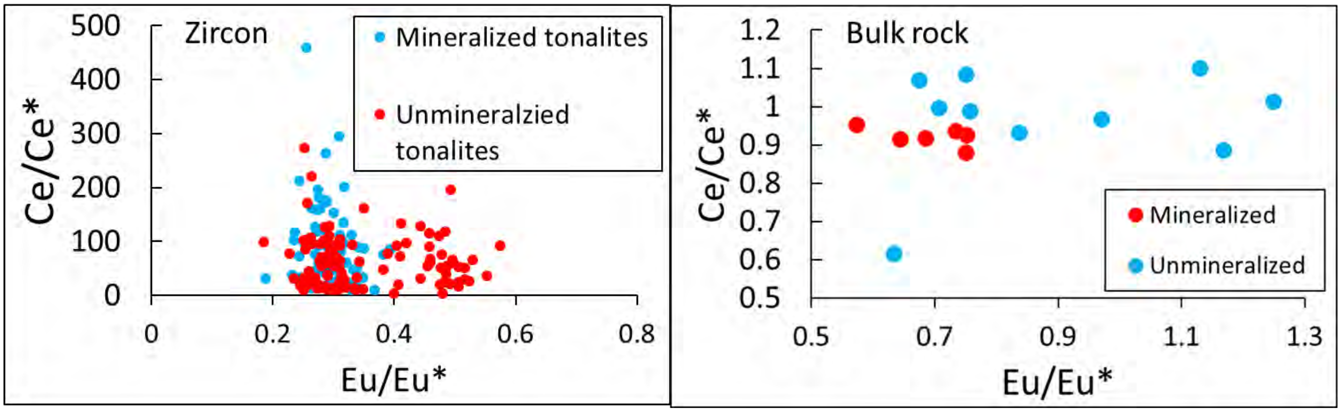

Figure 4.15. Comparison between Eu anomalies and Ce anomalies in both zircon(left) and bulk rock (right). Eu/Eu* = $Eu_N/((Sm_N*Gd_N)^{1/2}$ and Ce/Ce* =$Ce_N/[Nd_N*Sm_N]^{1/2})$

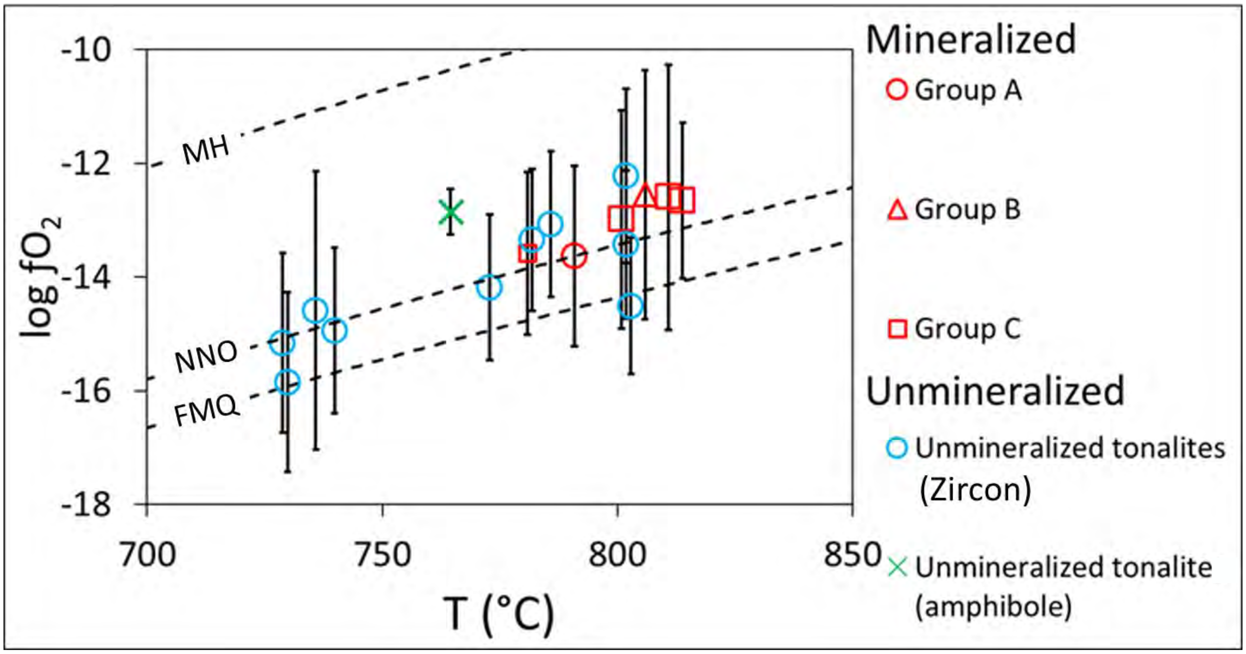

Figure 4.16. log *f*O2 vs. Temperature for tonalites of the GMB. Unless otherwise indicated by a parentheses in the legend, log fO_2 values are calculated using zircon, based on the model of Smythe and Brenan (2016a, b) using hydrous based ratios of (non-bridging oxygen)/(tetrahedral oxygen). The calculation uses average Ce^{4+}/Ce^{3+} for each sample, 4.5 wt.% water content and temperatures obtained with Ti-in-zircon thermometry of Ferry and Watson (2007). fO_2 and

crystallization temperature using amphibole composition is based on the model of Ridolfi et al. (2010). Mineral redox buffers of fayalite-magnetite-quartz (FMQ), nickel-nickel oxide (NNO) and magnetite-hematite (MH) are shown as dashed black lines. Error bars are 2σ. Detailed explanations for the calculation are in the text. Uncertainties are based on propagated uncertainties of compositions of bulk rock and zircon.

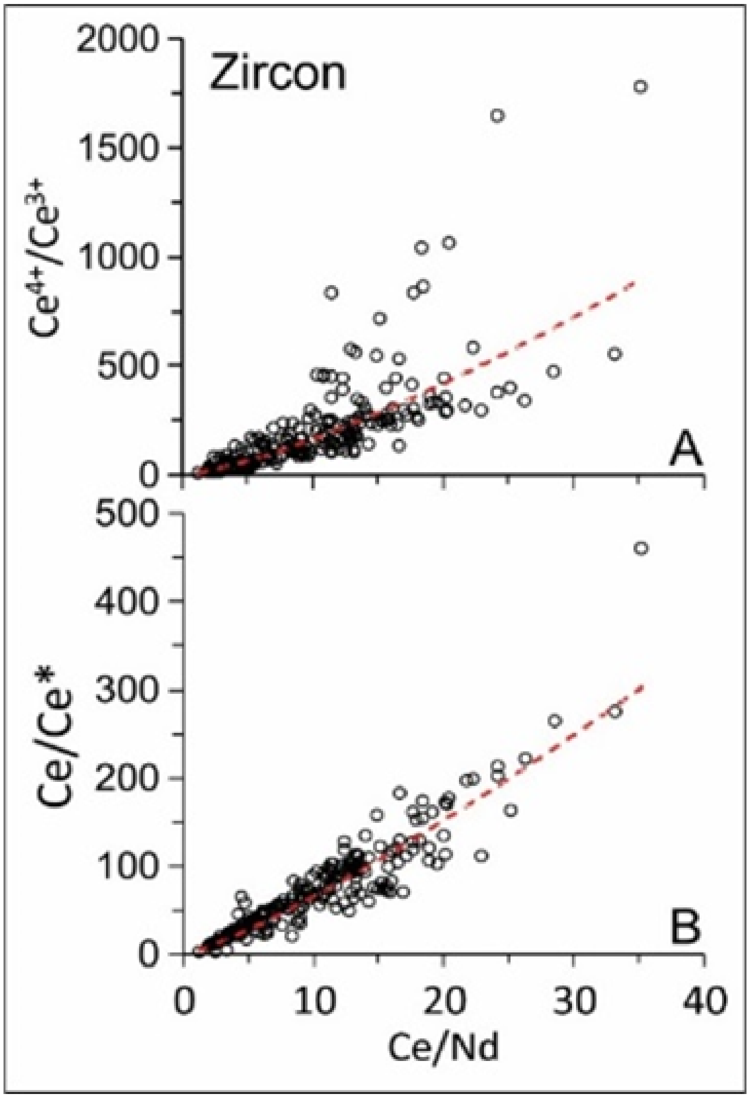

Figure 4.17. (A) Ce^{4+}/Ce^{3+} vs. Ce/Nd in zircon with the correlation coefficient of 0.90. The red dashed line shows the relationship of the two, Ce^{4+}/Ce^{3+} = 7.28(Ce/Nd)(1.35). (B) Ce/Ce* vs. Ce/Nd in zircon with a correlation coefficient of 0.94. The relationship of Ce/Ce* = 3.94(Ce/Nd)(1.21) is shown with red dashed line. Ce^{4+}/Ce^{3+} values are correlated with Ce/Ce* with a correlation coefficient of 0.84 and the relationship of Ce^{4+}/Ce^{3+} = 2.71 (Ce/Ce*)0.92.

CHAPTER 5.

Global Summary & Conclusions

5.1 Summary

Primary mineralogy

Primary mineralogy is similar throughout the GMB with all rocks being tonalite and minor quartz diorite and diorite. All rocks contain quartz, plagioclase, biotite, hornblende, titanite, apatite, zircon and magnetite. Mineralized intrusions near (< 4 km) the mine pits are highly altered and only show relict hornblende and biotite as they are replaced by secondary biotite and/or chlorite. Unmineralized intrusions show unaltered and contain partially altered hornblende and biotite.

Primary titanite forms euhedral tabular crystals with low Al_2O_3 (1.2-1.21 wt.%) and is common in all samples in this study. The occurrence of primary titanite, magnetite and hornblende suggests ƒO2 > FMQ+0.5 at 700°C.

Primary hornblende, biotite and plagioclase suggest that the parental magmas for all rocks of the GMB likely contained more than 4.5 wt% H_2O assuming a placement depth of 5km and a crystallization temperature of 825°C.

Alteration

Alteration mineralogy varies with distance from Cu-mineralization. Alteration minerals are: Epidote, chlorite, white mica, titanite rutile, magnetite, calcite, hematite and pyrite.

Titanite occurs as an alteration mineral of biotite, forming small aggregates with chlorite. Since primary biotite contains significant Ti, chloritization of primary biotite releases Ti to form titanite (~50 µm in length, ~25µm in width) and rutile needles (~25 µm in length, ~10µm in width).

Epidote

Epidote is ubiquitous throughout the batholith and shows three types of occurrences within the GMB with modalities up to 40%; Small isolated grains replacing plagioclase, disseminated aggregates of epidote grains and poly- or mono-mineralic veins and veinlets. Epidote composition varies primarily due to Fe and Al contents within grains and between grains within one thin section (Chapters 3 and 4). Allanite and light rare earth element (LREE)-bearing epidote is restricted to near mineralization (< 2 km), suggesting a mechanism for the incorporation of LREE proximal to Cu-mineralization.

Epidote from the GMB is distinct compared to epidote from the Nicola volcanic rocks. Epidote from the GMB is compositionally zoned and lacking mineral inclusions. Epidote in the Nicola mafic volcanoclastic rocks is relatively Fe-rich without significant compositional zoning and shows inclusions of apatite and titanite.

Epidote grains in the GMB show oscillatory zoning of Fe-poor and Fe-rich (Chapter 4). Some grains multiple oscillations (Appendix 3, Fig. A3-1). Epidote grains surrounded by sulphides are relatively Fe poor (9.96 - 13.9 wt.% Fe2O3(t)). We suggest that the composition of epidote in mineralized intrusions reflects hydrothermal fluid composition controlled by sulphide precipitation. Early fluids initially rich in S and Fe would initially precipitate sulphides. Epidote would preferentially incorporate Fe into its structure leaving the fluids relatively Fe-poor, forming Fe-poor core of epidote. Subsequently fluids low in S are introduced, and thus Fe in the hydrothermal fluids form the Fe-rich rims in epidote. The fluids generated in the mineralized intrusions would have spread to the entire GMB, producing epidote with Fe-poor ore and Fe-rich rims throughout the batholith. This process may repeat many times. This is consistent with epidote showing multiple oscillating Fe-Al rich rims around Fe-poor cores (Appendix 3, Fig. A3-1) and the identification of multiple separate magmas (Chapter 5). Epidote in unmineralized intrusions is also compositionally zoned with Fe-poor cores. The composition is likely influenced by the changes in pH, temperature of hydrothermal fluids moving away from mineralization.

U-Pb ages of Zircon

Zircon analysis from the GMB (Chapter 5) identified at least 4 distinct magmatic events forming the GMB over ~25 Ma with time gaps (>0.2Ma) between different events.

- The first magma crystallized in a juvenile oceanic arc at 229.2±4.4 Ma. It is relatively cool, reduced in oxidation state, evolved and barren for the mineralization.
- Later, at 218.9±3.1Ma, another magma crystallized in the central section of the GMB. This magma is formed in a more mature island arc setting with a thicker crust. It shows the highest average and highest third quartile value for Ce^{4+}/Ce^{3+} among magmas for the GMB.

It is more Mg-rich, hotter and fertile then previous barren magmatism. It contributed to the Cu mineralization. This magma is associated with the Cu ore in the Granite Lake pit that produces the highest grade ore in the Gibraltar deposit.

- Another magma crystallized in the central section of the GMB at 213.2±2.4 Ma. This magma is formed in a mature oceanic arc setting, shows a lower Ce^{4+}/Ce^{3+} than the previous magma. This magma is similarly Mg-rich and hot compared to the earlier barren magmas. It too contributed to the Cu-mineralization. This magma is associated with Cu ore in the Pollyanna pit that shows the second highest grade ore in the Gibraltar deposit.
- The youngest magma in the studied samples crystallized at 205.8±2.1 Ma. It is formed in a mature island arc setting, shows the lowest average and lowest quartile range for Ce4+/Ce3+ of the fertile magmas. It is similarly Mg-rich and hot compared to the last two fertile magmas in the GMB. It contributes to the Cu-mineralization. This magma is associated with Cu ore in the Gibraltar East pit, which produces the lowest grade ore among all mining pits.

5.2 Conclusions and implications

- White mica alteration is associated with the Cu-mineralization at Gibraltar.
- Unmineralized intrusions lack significant white mica alteration.
- Multiple magmas in the same area led to an overprinting alteration where early potassic alteration is only identified by relict textures.
- Epidote in the GMB shows characteristics different from epidote in the surrounding Nicola mafic volcanoclastic rocks.
- Epidote composition in the mineralized intrusions of the GMB is interpreted to reflect hydrothermal fluid composition mitigated by sulphide precipitation and S and Fe content of fluids. Multiple Fe-rich and Fe-poor rims around Fe-poor epidote cores may be related to the multiple magmas identified for formation of the GMB.

- LREE-rich epidote and allanite are found in the area near the Cu-mineralization. This suggests the incorporation of LREEs into epidote proximal to Cu-mineralization at Gibraltar.
- The first magma is a barren forming the majority of the volume of the GMB at 229.2±4.4.
- The first mineralizing fertile magma forms at 218.9±3.1. The data suggests that this magma brought a majority of Cu-mineralization.
- Two subsequent magmas brought additional Cu-mineralization, adding to the tonnage of Cu at the Gibraltar deposit at 213.2±2.4 and 205.8±2.1 Ma respectively.
- When compared to other porphyry Cu deposits worldwide, the mineralized magmas of the Gibraltar deposit show moderate Ce anomalies and very low Eu anomalies in zircon. Mineralized rocks of the Gibraltar deposit show very low Sr/Y ratios. This suggests that highly oxidized magmas with high Sr/Y ratios are not necessary for the formation of economic porphyry deposits. These can be formed by the emplacement of multiple moderately oxidized magmas within close proximity.
- Sr/Y ratios in bulk rock and Eu/Eu* in zircon are affected by fractional crystallization of plagioclase at Gibraltar, thus are inadequate fertility indicators.
- Ce/Nd and Ce/Ce* in detrital zircon has the potential to be used as a vectoring tool towards undiscovered buried porphyry deposits.

APPENDICES.

Appendix 1 Supplementary material for Chapter 3

Table A1-1, GPS locations, geological unit and lithology of all samples in this study

Samples	Easting*	Northing*	Classification/Unit	Lithology
Polyana pit center	549109	5818410	Mineralized Tonalite	Shear zone medium grained folaited tonalite
GBR-12 (most mineralized)	547595	5818686	Mineralized Tonalite	Shear zone medium grained folaited tonalite
GBR-01-02	549353	5818912	Mineralized Tonalite	Medium grained tonalite with Ep-Chl-Qz Veinlets, mineralized with Ccp and Bn
GBR-03-04	548947	5817768	Mineralized Tonalite	Medium grained tonalite with Ep-Chl-Qz Veinlets , mineralized with Ccp and Bn
GBR-5	549117	5817924	Mineralized Tonalite	Medium grained tonalite with Ep-Chl-Qz Veinlets , mineralized with Ccp and Bn
GBR-6-7-8	548947	5817768	Mineralized Tonalite	Shear zone medium grained folaited tonalite, mineralized with Ccp and Bn
GBR-9	547580	5818531	Mineralized Tonalite	Medium grained tonalite, very oxidized, intense WM alteration
GBR-10	547585	5818572	Mineralized Tonalite	Medium grained tonalite, very oxidized, intense WM alteration
GBR-11	547590	5818600	Unmineralized Tonalite	Medium grained tonalite with Ep-Chl-Qz veins
GBR-12	547595	5818686	Mineralized Tonalite	Medium grained foliated tonalite with moderate Wm alteration
GBR-13	547604	5818717	Mineralized Tonalite	Medium grained foliated tonalite with large mineralized Qz veins
GBR-14	547715	5818877	Mineralized Tonalite	Intensly foliated medium grained tonalite, mineralized with Ccp
GBR-15	547683	5818931	Mineralized Tonalite	Foliated medium grained tonalite with Mal, oxidized
GBR-16	546716	5819933	Mineralized Tonalite	Foliated and fractured medium grained tonalite, mineralized with Ccp
GBR-17	546435	5819858	Unmineralized Tonalite	Foliated medium grained tonalite
GBR-18	546416	5819525	Unmineralized Tonalite	Foliated medium grained tonalite
GBR-19	550967	5818070	Mineralized Tonalite	Intensly foliated medium grained tonalite, mineralized with Ccp
GBR-20	551227	5818323	Mineralized Tonalite	Foliated medium grained tonalite, mineralized with Ccp
GBR-21	550908	5817854	Mineralized Tonalite	Leucocratic mediumgrained tonalite with large scale (1cm+) Ep veins, mineralized with Ccp
GBR-22	551026	5817754	Mineralized Tonalite	Medium grained tonalite with large scale (1cm+) Ep veins, mineralized with Ccp
GBR-23	550979	5817808	Mineralized Tonalite (float)	Medium grained tonalite, moderate Ep alteration, mineralized with Ccp
GBR-24	550773	5818002	Mineralized Tonalite	Melanocratic medium grained tonalite with pink alteration
GBR-25	551820	5816476	Unmineralized Tonalite	Melanocratic medium grained tonalite
GBR-26	551923	5816797	Unmineralized Tonalite	Medium grained tonalite with moderate Wm and Ep alteration
GBR-27	551791	5815919	Unmineralized Tonalite	Leucocratic medium grained tonalite with Ep veinlets
GBR-28-29	551694	5815871	Unmineralized Tonalite	Medium grained tonalite rich in Ep veins, contains leucocratic dykes
GBR-30	551505	5816016	Unmineralized Tonalite	Leucocratic tonalite with large scale (1cm+) Ep veins
GBR-31	550921	5815386	Unknown unit	Fine grained grabbro
GBR-32	550656	5815284	Unmineralized Tonalite	Medium grained tonalite with Ep-Chl-Qz veins, Bt intact
GBR-33	550145	5814979	Unmineralized Tonalite	Medium grained tonalite with Ep-Chl-Qz veins
GBR-34	554832	5827378	Dragon Mountain Succession	Slaty mud and sandstones
GBR-35	555290	5826955	Unmineralized Tonalite	Medium grained tonalite with Ep-Chl-Qz veins
GBR-36	555304	5826943	Unmineralized Tonalite	Leucocratic coarse grained tonalite, 10% fully chloritized mafics, Ep veins and apeltic dyke cross cuts
GBR-37	555304	5826943	Unmineralized Tonalite	Sample of the apelitic dyke, fine grained Qz
GBR-38	555183	5826595	Nicola volcanics (subcrop)	Medium grained mafic volcanoclastic
GBR-39	555489	5826958	Unmineralized Tonalite	Medium grained isotropic tonalite with Ep veins and apelitic dyke
GBR-40	555489	5826958	Unmineralized Tonalite	Sample of the apelitic dyke, fine grained Qz
GBR-41	555136	5827698	Nicola volcanics	Coarse grained mafic volcanoclastics
GBR-42	555217	5827704	Nicola volcanics	Coarse grained mafic volcanoclastics with finer grained intercalated layers volcanoclatic material
GBR-43-44	554581	5827882	Nicola volcanics (Float)	Coarse grained mafic volcanoclastics, intense Ep
GBR-45	556542	5828171	Unknown unit	Serpentinite
GBR-46	556466	5828592	Unknown unit	Qz rich volcaniclastic sandstone, very orange oxidization
GBR-47	556834	5825064	Nicola volcanics	Coarse grained mafic volcanoclastics
GBR-48-49	556597	5825452	Unknown unit	Fine grained basalt
GBR-50-51-52	556482	5825357	Nicola volcanics	Coarse grained mafic volcanoclastics
GBR2-1	543080	5808865	Endako mafic volcanics	Fine grained basalt
GBR2-2	546527	5826228	Unmineralized Tonalite	Melanocratic Qz-diorite
GBR2-3	550649	5827608	Nicola volcanics	Fine grained mafic volcanoclastic
GBR2-4	549132	5828117	Nicola volcanics	Medium grained mafic volcanoclastic
GBR2-5	549808	5829201	Nicola volcanics mingled with Cache Creek	Limestone and mafic volcanoclatics mixed
GBR2-6	549769	5829170	Nicola volcanics	Fine grained mafic volcanoclastic hosting larger clasts
GBR2-7	550608	5815245	Unmineralized Tonalite	Medium grained tonalite with Ep-Chl veinlets
GBR2-8	550608	5815245	Unmineralized Tonalite	Centimetre scale Ep vein sample from GBR2-7
GBR2-9	551501	5816009	Unmineralized Tonalite	Coarse grained isotropic tonalite with Chl-Ep veinlets
GBR2-10	551741	5815902	Unmineralized Tonalite	Centimetre scale Ep vein sample from GBR2-11
GBR2-11	551741	5815902	Unmineralized Tonalite	Medium granined tonalite with Ep veinlets
GBR2-12	549349	5815170	Unmineralized Tonalite	Melanocratic Qz-diorite
GBR2-13	549349	5815170	Unmineralized Tonalite	Medium granined tonalite with Ep veinlets
GBR2-14	549555	5814109	Unmineralized Tonalite	Medium grained melanocratic tonalite
GBR2-15	549195	5814506	Unmineralized Tonalite	Corase graiend leucocratic tonalite with Ep veins
GBR2-16	549133	5814555	Unmineralized Tonalite	Coarse grained isotropic tonaltie with Bt intact
GBR2-17	547717	5816619	Unmineralized Tonalite	Medium grained tonalite with Ep-Chl veinlets
GBR2-18	547384	5814942	Cuisson Lake Unit	Fine grained metamorphosed mafic volcanic, large Ep and Cal veins
GBR2-19	549407	5810156	Sheridan Creek Stock	Medium quartz diorite, mafics intact
GBR2-20	550163	5809660	Sheridan Creek Stock	Medium quartz diorite, mafics intact
GBR2-21	549954	5810203	Sheridan Creek Stock	Medium quartz diorite, mafics intact
GBR2-22	553732	5813426	Sheridan Creek Stock	Fine grained quartz diorite, mafics intact
GBR2-23	553845	5813494	Sheridan Creek Stock	Medium grained foliated tonalite, mafics altered
GBR2-24	553144	5815364	Unmineralized Tonalite	Medium grained foliated tonalite with Ep veins
GBR2-25	553403	5814985	Unmineralized Tonalite	Coarse grained leucocratic tonalite
GBR2-26	553564	5814516	Unmineralized Tonalite	Medium grained foliated tonalite with Chl-Ep veinlets
GBR2-27	553564	5814516	Unmineralized Tonalite	Ep-Qz vein
GBR2-28	553813	5812316	Sheridan Creek Stock	Medium grained quartz diorite, mafics intact
GBR2-29	552957	5812733	Sheridan Creek Stock	Medium grained quartz diorite, mafics intact
GBR2-30	554452	5819974	Unmineralized Tonalite	Medium grained leucocratic tonalite with weak Ep alteration
GBR2-31	554452	5819974	Unmineralized Tonalite	Ep-Qz vein
GBR2-32	553518	5819695	Unmineralized Tonalite	Medium grained tonalite with Chl veinlets, 15 % fully chloritized mafics
GBR2-33	553649	5819685	Unmineralized Tonalite	Leucocratic coarse grained tonalite, 10% fully chloritized mafics
GBR2-34	553697	5819850	Unmineralized Tonalite	Medium grained tonalite with 10-15 % fully chloritized mafics
GBR2-35	551357	5821122	Unmineralized Tonalite	Coarse grained isotropic tonalite, some mafics intact (Hbl)
GBR2-36	551672	5821442	Unmineralized Tonalite	Coarse grained tonalite, isotropic, 10-15% chloritized mafics
GBR2-37	551704	5821431	Unmineralized Tonalite	Medium grained tonalite with 15% fully chloritized mafics
GBR2-38	551911	5821353	Unmineralized Tonalite	Coarse grained tonalite, mafics intact (Hbl)
GBR2-39	553258	5821390	Unmineralized Tonalite	Coarse grained tonalite, mafics intact (Hbl)
GBR2-40	552974	5821963	Unmineralized Tonalite	Coarse grained tonalite, mafics intact (Hbl)
GBR2-41	556337	5820355	Unmineralized Tonalite	Float of Nicloa rocks intruted by unmineralized tonalite
GBR2-42	546443	5827826	Unmineralized Tonalite	Medium grained tonalite with 20-30% completely chloritized mafics
GBR2-43	549194	5828217	Nicola volcanics	Coarser grained mafic volcanoclastic, Ep content is moderate compared to other Nichola vocanics
GBR2-44	549605	5827998	Nicola volcanics	Medium grained mafic volcanoclastics, Ep content is highest with Ep in large cm scale veins and matrix
GBR2-45	550195	5828007	Nicola volcanics	Medium grained mafic volcanoclastic, Ep content is low compared to other Nichola vocanics
GBR2-46	547922	5830102	Dragon Mountain Succession	Mudstone intercalated with sandstone
GBR2-47	546716	5819933	Mineralized Tonalite	Same as GBR-1, duplicate, with Ep-Qz vein
GBR2-48	544126	5818205	Chiclotin group volcanics	Fine grained basalt with small vesiculs and Opx phenocryts
GBR2-49	547315	5815097	Cuisson Lake Unit	Chl schist with fine grained Ep rich horizons
*All samples were collected in Zone 10 N using NAD 83				
Abbreviations: Tr = trace, Ep= epidote, Wm= white mica, Mal = malachite, Py = pyrite, Ccp= chalcopyrite, Bn = bornite, Pl = plagioclase, Qz = Quartz, Ttn = titanite				
Rt= rutile, Chl = chlorite, Mag = magnetite, Cal = calcite, Hbl = hornblende, Mal = malachite, Zr = Zircon, Cov = Covellite, Ol = olivine, Srp = serpentine, Px = pyroxene				
Fine grained= major grains (Pl, Qt) are between <1mm				
Medium grained= major grains (Pl, Qt) are between 1-2 mm				
Coarse grained= major grains (Pl, Qt) are >2mm				

Appendix Table A1-2. Compositions of epidote rims in the GMB, determined with SEM-EDS

Sample	GBR-2-4			GBR-2-10					
Location*	North west of BP			South-east of MP					
Analysis area	Rim 1	Rim 2	Rim 3	Rim 1	Rim 2	Rim 3	Rim 4	Rim 5	Rim 6
Al_2O_3	23.04	21.3	22.24	22.72	23.23	22.15	22.99	22.36	22.08
SiO_2	38.02	38.41	38.95	38.73	38.78	38.71	38.27	38	38.39
CaO	22.15	23.07	22.78	21.2	22.33	22.54	22.45	23.16	22.74
MnO	1.26	<0.01	0.64	1.52	<0.01	0.65	1.03	0.46	<0.01
$Fe_2O_3(t)$	15.53	17.23	15.39	15.83	15.66	15.95	15.25	16.03	16.79
Sum**	100	100	100	100	100	100	100	100	100
	apfu based on 12.5 O								
Ca^{2+}	1.86	1.95	1.91	1.78	1.87	1.89	1.89	1.95	1.91
Mn^{2+}	0.09	<0.01	0.04	0.1	<0.01	0.04	0.07	0.03	<0.01
A site	1.95	1.95	1.96	1.88	1.87	1.94	1.96	1.98	1.91
Fe^{3+***}	0.92	1.02	0.91	0.93	0.92	0.94	0.9	0.95	0.99
Al^{3+}	2.13	1.98	2.05	2.1	2.14	2.05	2.13	2.07	2.04
M site	3.05	3	2.96	3.03	3.06	2.99	3.03	3.02	3.04
Si^{4+}	2.99	3.03	3.05	3.03	3.02	3.04	3	2.99	3.02
T site	2.99	3.03	3.05	3.03	3.02	3.04	3	2.99	3.02
Fe(t)/[Fe(t)+Al]	0.3	0.34	0.31	0.31	0.3	0.31	0.3	0.31	0.33

Sample	GBR-2-7						GBR-2-36			
Location*	South-east of MP						Near tailing pond GMP			
Analysis area	Rim 1	Rim 2	Rim 3	Rim 3	Rim 4	Rim 5	Rim1	Rim 2	Rim 3	Rim 4
Al_2O_3	21.74	22.19	21.43	21.56	21.71	22.09	22.24	22.64	23.7	21.55
SiO_2	38.07	37.8	38.1	38.45	38.22	37.01	38.49	38.12	38.23	37.87
CaO	22.45	22.81	23.34	22.73	22.76	23.46	22.83	23.3	22.61	22.98
MnO	<0.01	<0.01	<0.01	<0.01	<0.01	<0.01	<0.01	<0.01	<0.01	<0.01
$Fe_2O_3(t)$	17.12	16.58	16.52	16.65	16.7	16.83	15.83	15.32	14.85	16.99
Sum**	100	100	100	100	100	100	100	100	100	100
	apfu based on 12.5 O									
Ca^{2+}	1.9	1.93	1.97	1.92	1.92	1.99	1.92	1.96	1.89	1.95
Mn^{2+}	<0.01	<0.01	<0.01	<0.01	<0.01	<0.01	<0.01	<0.01	<0.01	<0.01
A site	1.9	1.93	1.97	1.92	1.92	1.99	1.92	1.96	1.89	1.95
Fe^{3+***}	1.02	0.98	0.98	0.99	0.99	1	0.94	0.91	0.87	1.01
Al^{3+}	2.02	2.06	2	2	2.02	2.06	2.06	2.1	2.18	2.01
M site	3.04	3.05	2.98	2.99	3.01	3.07	2.99	3	3.06	3.02
Si^{4+}	3	2.98	3.01	3.03	3.01	2.93	3.02	3	2.99	2.99
T site	3	2.98	3.01	3.03	3.01	2.93	3.02	3	2.99	2.99
Fe(t)/[Fe(t)+Al]	0.33	0.32	0.33	0.33	0.33	0.33	0.31	0.3	0.29	0.33

Sample	GBR-2-36										
Location*	Near tailing pond GMP										
Analysis area	Rim 5	Rim 6	Rim 7	Rim 8	Rim 9	Rim 10	Rim 11	Rim 12	Rim 13	Rim 14	Rim 15
Al_2O_3	20.09	22.86	23.34	20.98	22.99	22.39	21.53	22.37	19.94	22	21.53
SiO_2	37.5	39.01	39.34	38.19	38.8	38.72	38.53	37.75	38.53	38.77	38.6
CaO	22.81	22.57	22.53	22.36	22.43	22.43	22.97	22.02	22.52	22.49	22.22
MnO	<0.01	<0.01	<0.01	<0.01	0.79	0.88	<0.01	<0.01	<0.01	<0.01	<0.01
$Fe_2O_3(t)$	19.6	15.55	14.8	18.47	14.99	15.59	16.97	17.85	19	16.75	17.65
Sum**	100	100	100	100	100	100	100	100	100	100	100
	apfu based on 12.5 O										
Ca^{2+}	1.94	1.89	1.88	1.89	1.88	1.88	1.94	1.86	1.91	1.89	1.87
Mn^{2+}	<0.01	<0.01	<0.01	<0.01	0.05	0.06	<0.01	<0.01	<0.01	<0.01	<0.01
A site	1.94	1.89	1.88	1.89	1.93	1.94	1.94	1.86	1.91	1.89	1.87
Fe^{3+***}	1.17	0.91	0.87	1.1	0.88	0.92	1.01	1.06	1.13	0.99	1.05
Al^{3+}	1.88	2.1	2.14	1.95	2.12	2.07	2	2.08	1.86	2.03	2
M site	3.06	3.02	3	3.05	3	2.99	3	3.13	2.99	3.02	3.04
Si^{4+}	2.98	3.04	3.06	3.02	3.03	3.04	3.03	2.97	3.05	3.04	3.03
T site	2.98	3.04	3.06	3.02	3.03	3.04	3.03	2.97	3.05	3.04	3.03
Fe(t)/[Fe(t)+Al]	0.38	0.3	0.29	0.36	0.29	0.31	0.33	0.34	0.38	0.33	0.34

Sample	GBR-2-34						GBR2-50				
Location*	Centre of GMP						South end of BP				
Analysis area	Rim 1	Rim 2	Rim 3	Rim 4	Rim 5	Rim 6	Rim 1	Rim 2	Rim 3	Rim 4	Rim 5
Al_2O_3	22.57	20.92	20.62	21.4	21.14	21.54	21.48	20.63	22.57	22.46	22.32
SiO_2	38.97	37.67	38.54	37.57	38.07	35.34	37.75	38.17	38.38	38.26	38.91
CaO	22.65	22.85	22.29	22.51	23.32	22.22	22.73	22.37	23.31	23.67	22.63
MnO	<0.01	<0.01	<0.01	<0.01	<0.01	<0.01	<0.01	<0.01	<0.01	<0.01	0.79
$Fe_2O_3(t)$	15.81	18.56	18.55	18.53	17.47	20.91	18.04	18.83	15.61	15.61	15.35
Sum**	100	100	100	100	100	100	100	100	100	100	100
	apfu based on 12.5 O										
Ca^{2+}	1.9	1.94	1.89	1.91	1.97	1.91	1.92	1.9	1.96	1.99	1.9
Mn^{2+}	<0.01	<0.01	<0.01	<0.01	<0.01	<0.01	<0.01	<0.01	<0.01	<0.01	0.05
A site	1.9	1.94	1.89	1.91	1.97	1.91	1.92	1.9	1.96	1.99	1.95
Fe^{3+***}	0.93	1.11	1.1	1.1	1.04	1.26	1.07	1.12	0.92	0.92	0.91
Al^{3+}	2.08	1.95	1.92	2	1.97	2.03		1.92	2.09	2.08	2.06
M site	3.01	3.06	3.02	3.1	3.01	3.29	3.07	3.04	3.01	3	2.97
Si^{4+}	3.05	2.98	3.04	2.97	3.01	2.83	2.98	3.02	3.01	3	3.05
T site	3.05	2.98	3.04	2.97	3.01	2.83	2.98	3.02	3.01	3	3.05
Fe(t)/[Fe(t)+Al]	0.31	0.36	0.36	0.36	0.35	0.38	0.35	0.37	0.31	0.31	0.31

Sample	GBR-2-8					GBR-2-14				
Location*	South end of MP					Centre of BP				
Analysis area	Rim 1	Rim 2	Rim 3	Rim 4	Rim 5	Rim 1	Rim 2	Rim 4	Rim 5	Rim 6
Al_2O_3	23.32	21.49	21.65	22.36	20.79	21.54	22.57	22.91	22.21	20.52
SiO_2	38.47	38.15	38.16	38.06	37.96	38.05	38.79	38.84	39.09	38.26
CaO	22.9	22.56	23.1	23.27	22.53	22.72	22.81	22.65	23.35	23.15
MnO	0.83	<0.01	<0.01	<0.01	<0.01	<0.01	<0.01	<0.01	<0.01	<0.01
$Fe_2O_3(t)$	14.49	17.8	17.09	16.31	18.72	17.68	15.83	15.6	15.35	18.07
Sum**	100	100	99.99	99.99	100	99.99	100	99.99	100	100
	apfu based on 12.5 O									
Ca^{2+}	1.92	1.91	1.95	1.96	1.91	1.92	1.91	1.9	1.96	1.96
Mn^{2+}	0.06	<0.01	<0.01	<0.01	<0.01	<0.01	<0.01	<0.01	<0.01	<0.01
A site	1.98	1.91	1.95	1.96	1.91	1.92	1.91	1.9	1.96	1.96
Fe^{3+***}	0.85	1.06	1.01	0.97	1.12	1.05	0.93	0.92	0.9	1.08
Al^{3+}	2.15		2.01	2.07	1.94	2	2.08	2.11	2.05	1.91
M site	3	3.05	3.02	3.04	3.05	3.05	3.01	3.03	2.95	2.99
Si^{4+}	3.01	3.01	3.01	2.99	3	3	3.03	3.03	3.06	3.03
T site	3.01	3.01	3.01	2.99	3	3	3.03	3.03	3.06	3.03
Fe(t)/[Fe(t)+Al]	0.28	0.35	0.34	0.32	0.36	0.34	0.31	0.3	0.31	0.36

* GPS coordinates are reported in Appendix Table 1

** Anhydrous component is normalized to 100%

*** All Fe is assumed to be Fe^{3+}

MP=Mine

GMP=Granite Mountain Phase

BP=Border Phase

Appendix Table A1-3. Compositions of epidote cores in the GMB, determined with SEM-EDS

Sample	GBR-2-4			GBR-2-10							
Location*	North west of BP			South-east of MP							
Analysis area	Core 1	Core 2	Core 3	Core 1	Core 2	Core 3	Core 4	Core 5	Core 6	Core 7	Core 8
Al_2O_3	23.23	24.3	24.29	24.03	26.77	28.11	25.72	25.89	25.83	25.28	23.47
SiO_2	39.48	38.49	39.03	38.28	39.45	40.25	39.56	39.75	39	39.22	39.58
CaO	23.88	24.07	23.57	23.45	24.08	24.36	23.51	22.67	22.87	23.04	23.15
MnO	<0.1	<0.1	<0.1	0.59	<0.1	<0.1	<0.1	0.93	0.53	1.09	<0.1
Fe_2O_3(t)	13.41	13.13	13.11	13.64	9.7	7.28	11.22	10.07	11.77	11.37	13.79
Sum**	100	100	100	100	100	100	100	100	100	100	100
apfu based on 12.5 O											
Ca^{2+}	1.99	2.01	1.96	1.96	1.98	1.98	1.94	1.88	1.89	1.91	1.93
Mn^{2+}	<0.1	<0.1	<0.1	0.04	<0.1	<0.1	<0.1	0.06	0.04	0.07	<0.1
A site	1.99	2.01	1.96	2	1.98	1.98	1.94	1.94	1.93	1.98	1.93
Fe^{3+}***	0.78	0.77	0.77	0.8	0.56	0.42	0.65	0.59	0.68	0.66	0.81
Al^{3+}	2.13	2.23	2.22	2.21	2.42	2.52	2.33	2.36	2.35	2.31	2.15
M site	2.91	3	2.99	3.01	2.98	2.93	2.98	2.94	3.03	2.97	2.95
Si^{4+}	3.07	3	3.03	2.99	3.03	3.06	3.04	3.07	3.01	3.03	3.07
T site	3.07	3	3.03	2.99	3.03	3.06	3.04	3.07	3.01	3.03	3.07
Fe(t)/[Fe(t)+Al]	0.27	0.26	0.26	0.27	0.19	0.14	0.22	0.2	0.23	0.22	0.27

Sample	GBR-2-7									
Location*	South-east of MP									
Analysis area	Core 1	Core 2	Core 3	Core 4	Core 5	Core 6	Core 7	Core 8	Core 9	Core 10
Al_2O_3	25.43	23.61	25.79	23.68	23.9	24.23	26.51	24.82	24.1	23.32
SiO_2	39.03	38.59	39.45	38.63	39.09	39.02	39.17	39.2	38.02	39.05
CaO	23.75	22.98	23.48	22.23	22.99	22.87	23.74	23.24	23.86	24.18
MnO	<0.1	0.69	0.7	1.68	0.83	0.61	<0.1	<0.1	<0.1	<0.1
Fe_2O_3(t)	11.79	14.13	10.57	13.78	13.19	13.26	10.59	12.73	14.02	13.45
Sum**	100	100.01	100	100	100	100	100	100	100	100
apfu based on 12.5 O										
Ca^{2+}	1.97	1.92	1.94	1.86	1.92	1.9	1.96	1.93	2	2.02
Mn^{2+}	<0.1	0.05	0.05	0.11	0.06	0.04	<0.1	<0.1	<0.1	<0.1
A site	1.97	1.97	1.98	1.97	1.97	1.94	1.96	1.93	2	2.02
Fe^{3+}***	0.69	0.83	0.61	0.81	0.77	0.78	0.61	0.74	0.82	0.79
Al^{3+}	2.32	2.17	2.34	2.18	2.19	2.22	2.4	2.26	2.22	2.14
M site	3	3	2.96	2.99	2.96	3	3.02	3.01	3.04	2.93
Si^{4+}	3.02	3.01	3.04	3.02	3.04	3.03	3.01	3.03	2.97	3.04
T site	3.02	3.01	3.04	3.02	3.04	3.03	3.01	3.03	2.97	3.04
Fe(t)/[Fe(t)+Al]	0.23	0.28	0.21	0.27	0.26	0.26	0.2	0.25	0.27	0.27

Sample	GBR-2-36							GBR-2-34						GBR-2-50
Location*	Near tailing pond GMP							Centre of GMP						South end
Analysis area	Core 1	Core 2	Core 3	Core 4	Core 5	Core 6	Core 7	Core 1	Core 2	Core 3	Core 4	Core 5	Core 6	Core 1
Al_2O_3	25.64	23.78	24.21	24.39	24.29	24.22	24.58	25.1	23.78	27.3	30.18	31.09	31.05	22.78
SiO_2	39.38	39.09	38.62	38.75	39.53	39.42	40.33	38.93	39.88	40.15	41.28	41.94	41.73	39.8
CaO	23.56	23.28	23.65	23.38	23.52	23.41	22.92	21.76	22.5	23.81	24.43	24.72	24.55	23.44
MnO	<0.1	<0.1	<0.1	<0.1	<0.1	<0.1	<0.1	1.47	<0.1	<0.1	<0.1	<0.1	<0.1	<0.1
Fe_2O_3(t)	11.42	13.85	13.52	13.48	12.66	12.94	12.17	12.75	13.84	8.74	4.12	2.29	2.34	13.99
Sum**	100	100	100	100	100	100	100	100	100	100	100	100	100	100
apfu based on 12.5 O														
Ca^{2+}	1.95	1.94	1.97	1.95	1.95	1.94	1.89	1.81	1.87	1.95	1.96	1.97	1.96	1.95
Mn^{2+}	<0.1	<0.1	<0.1	<0.1	<0.1	<0.1	<0.1	0.1	<0.1	<0.1	<0.1	<0.1	<0.1	<0.1
A site	1.95	1.94	1.97	1.95	1.95	1.94	1.89	1.91	1.87	1.95	1.96	1.97	1.96	1.95
Fe^{3+}***	0.66	0.81	0.79	0.79	0.74	0.75	0.7	0.74	0.81	0.5	0.23	0.13	0.13	0.82
Al^{3+}	2.33	2.18	2.22	2.23	2.22	2.21	2.23	2.29	2.17	2.45	2.67	2.73	2.75	2.09
M site	2.99	2.99	3.01	3.02	2.95	2.97	2.93	3.04	2.97	2.96	2.9	2.85	2.88	2.91
Si^{4+}	3.03	3.04	3	3.01	3.06	3.05	3.1	3.02	3.09	3.06	3.09	3.12	3.11	3.09
T site	3.03	3.04	3	3.01	3.06	3.05	3.1	3.02	3.09	3.06	3.09	3.12	3.11	3.09
Fe(t)/[Fe(t)+Al]	0.22	0.27	0.26	0.26	0.25	0.25	0.24	0.24	0.27	0.17	0.08	0.05	0.05	0.28

Sample	GBR-2-8							GBR-2-14							
Location*	South end of MP							Centre of BP							
Analysis area	Core 1	Core 2	Core 3	Core 4	Core 5	Core 6	Core 7	Core 1	Core 2	Core 3	Core 4	Core 5	Core 6	Core 7	Core 8
Al_2O_3	23.56	22.94	23.34	23.37	24.4	24.68	23.37	23.95	25.13	23.2	27.24	25.13	22.15	23.17	23.26
SiO_2	38.7	38.99	38.99	39.09	39.24	39.16	38.9	38.79	39.51	39.04	39.96	39.51	41.14	39.02	38.94
CaO	22.68	22.61	22.78	22.96	23.22	22.55	22.47	22.52	23.51	22.17	24.32	23.51	21.22	23.52	23.24
MnO	1.2	1.68	0.78	0.96	1.18	1.27	1.19	<0.1	0.88	0.89	<0.1	0.88	1.74	1.16	0.62
Fe_2O_3(t)	13.86	13.78	14.11	13.62	11.97	12.33	14.08	14.73	10.97	14.7	8.48	10.97	13.77	13.13	13.93
Sum**	100	100	100	100	100	100	100	100	100	100	100	100	100	100	100
	apfu based on 12.5 O							apfu based on 12.5							
Ca^{2+}	1.9	1.9	1.9	1.92	1.93	1.87	1.88	1.88	1.95	1.85	1.99	1.95	1.76	1.97	1.94
Mn^{2+}	0.08	0.11	0.05	0.06	0.08	0.08	0.08	<0.1	0.06	0.06	<0.1	0.06	0.12	0.08	0.04
A site	1.98	2.01	1.96	1.98	2.01	1.96	1.96	1.88	2	1.91	1.99	2	1.88	2.05	1.99
Fe^{3+}***	0.81	0.81	0.83	0.8	0.7	0.72	0.83	0.86	0.64	0.86	0.49	0.64	0.8	0.77	0.82
Al^{3+}	2.17	2.12	2.15	2.15	2.23	2.26	2.15	2.2	2.29	2.13	2.45	2.29	2.02	2.13	2.14
M site	2.98	2.93	2.97	2.95	2.93	2.98	2.98	3.06	2.93	3	2.94	2.93	2.83	2.91	2.96
Si^{4+}	3.02	3.05	3.04	3.05	3.05	3.04	3.04	3.02	3.05	3.05	3.05	3.05	3.19	3.05	3.04
T site	3.02	3.05	3.04	3.05	3.05	3.04	3.04	3.02	3.05	3.05	3.05	3.05	3.19	3.05	3.04
Fe(t)/[Fe(t)+Al]	0.27	0.28	0.28	0.27	0.24	0.24	0.28	0.28	0.22	0.29	0.17	0.22	0.28	0.27	0.28

* GPS coordinates are reported in Appendix Table 1

** Anhydrous component is normalized to 100%

***All Fe is assumed to be Fe^{3+}

MP= Mine Phase

GMP=Granite Mountain Phase

BP= Border Phase

Appendix Table A1-4. Compositions of epidote in Nicola volcanic rocks, determined with SEM-EDS

Sample	GBR-2-4			GBR-2-44								GBR-2-44					
Location*	North of GMB			North of GMB								North of GMB					
Analysis area	Rim	Core	Core	Rim	Core	Core	Rim	Core	Core	Rim	Core	Rim	Rim	Core	Core	Core	Core
Al_2O_3	21.36	20.77	20.19	23.1	21.17	22.24	22.29	22.16	22.04	21.96	22.31	21.55	21.5	22.31	22.43	21.85	21.66
SiO_2	37.59	37.74	37.96	37.84	38.17	38.96	38.03	38.92	37.9	38.13	37.81	38.38	37.72	38.38	38.16	38	38.39
CaO	22.87	23.04	22.16	23.12	22.92	22.79	23.16	23.57	23.06	23.6	22.96	22.59	23.19	22.62	22.26	22.81	22.84
Fe_2O_3(t)	17.56	17.83	19.07	15.33	17.12	15.39	15.91	15.35	16.38	15.69	16.31	16.87	16.97	16.08	16.53	16.73	16.49
Sum**	100	100	100	100	100	100	100	100	100	100	100	100	100	100	100	100	100
	apfu based on 12.5 O											apfu based on 12.5 O					
Ca^{2+}	1.94	1.96	1.89	1.95	1.94	1.91	1.95	1.97	1.95	1.99	1.94	1.91	1.97	1.9	1.87	1.93	1.93
A site	1.94	1.96	1.89	1.95	1.94	1.91	1.95	1.97	1.95	1.99	1.94	1.91	1.97	1.9	1.87	1.93	1.93
Fe^{3+}***	1.05	1.06	1.14	0.91	1.02	0.91	0.94	0.9	0.97	0.93	0.97	1	1.01	0.95	0.98	0.99	0.98
Al^{3+}	1.99	1.94	1.89	2.14	1.97	2.05	2.07	2.04	2.05	2.04	2.07	2	2.01	2.07	2.08	2.03	2.01
M site	3.04	3.01	3.03	3.05	2.99	2.96	3.01	2.94	3.02	2.97	3.04	3	3.02	3.02	3.06	3.02	2.99
Si^{4+}	2.98	2.99	3.01	2.97	3.02	3.05	2.99	3.04	2.99	3	2.98	3.02	2.98	3.01	3	3	3.02
T site	2.98	2.99	3.01	2.97	3.02	3.05	2.99	3.04	2.99	3	2.98	3.02	2.98	3.01	3	3	3.02
Fe(t)/[Fe(t)+Al]	0.34	0.35	0.38	0.3	0.34	0.31	0.31	0.31	0.32	0.31	0.32	0.33	0.34	0.32	0.32	0.33	0.33

* GPS coordinates are reported in Appendix Table 1

** Anhydrous component is normalized to 100%

*** All Fe is assumed to be Fe^{3+}

Appendix Table A1-5. Compositions of REE-rich epidote and allanite in the GMB, determined with SEM-EDS

Sample	GBR-28				
Location*	South east part of MP				
Analysis area	Core	Core	Core	Core	Core
MgO	<0.1	<0.1	0.99	1.59	1.29
Al_2O_3	22	15.72	15.27	12.43	13
SiO_2	38.14	34.01	34.41	34.11	33.45
CaO	17.03	14.04	13.78	11.44	11.71
MnO	1	0.89	0.89	0.99	0.99
Fe_2O_3(t)	15.86	21.36	21.43	23.82	22.67
Ce_2O_3	5.58	9.99	11.01	14.62	11.02
La_2O_3	1.99	6.13	5.35	4.97	9.43
Sum*	100	100	100	100	100
apfu based on 12.5 O					
Ca^{2+}	1.46	1.32	1.29	1.10	1.13
Ce^{3+}	0.16	0.32	0.35	0.48	0.36
La^{3+}	0.06	0.20	0.17	0.16	0.31
Mn^{2+}	0.07	0.07	0.07	0.08	0.08
Total REEs	0.35	0.52	0.52	0.64	0.68
A site	1.77	1.91	1.88	1.82	1.88
Fe^{2+}**	0.87	1.29	1.28	1.46	1.40
Al	2.07	1.63	1.57	1.31	1.38
Mg	<0.1	<0.1	0.13	0.21	0.17
M site	3.04	2.99	3.00	3.06	3.01
Si	3.04	2.99	3.00	3.06	3.01
T site	3.04	2.99	3.00	3.06	3.01
Fe(t)/[Fe(t)+Al]	0.29	0.44	0.45	0.53	0.5

*GPS locations are listed in Appendix Table 1

* Anhydrous component is normalized to 100%

** All Fe is assumed to be Fe^{2+} for apfu calculations of REE-rich epidote and allanite

MP=Mine Phase

Appendix Table A1-6. Compositions of epidote rims in the GMB, determined by EPMA

Sample	GBR-16		GBR-32		GBR-28			GBR-11
Location*	East pit		South of MP		South east of MP			East pit
Analysis area	Rim	Rim	Rim	Rim	Rim	Rim	Rim	Rim
CaO	22.79	23.1	22.05	22.62	22.82	22.19	23.4	22.93
SrO	0.29	0.14	0.11	0.19	0.09	0.35	0.4	0.36
Al_2O_3	21.39	20.63	20.78	20.35	19.29	21.59	21.18	21.5
TiO_2	0.04	0.04	0.17	0.1	<0.01	0.04	0.11	0.06
MnO	0.24	0.2	0.15	0.29	0.17	0.7	0.8	0.23
Fe_2O_3	15.88	16.9	17.7	18.8	18.26	14.73	14.64	14.7
FeO	0.03	<0.01	0.02	0.03	<0.01	<0.01	<0.01	<0.01
V_2O_3	0.06	0.09	0.06	0.05	0.06	0.04	0.06	0.07
La_2O_3	0.01	<0.01	<0.01	0.03	<0.01	<0.01	0.02	<0.01
Ce_2O_3	0.05	<0.01	0.05	<0.01	<0.01	0.03	<0.01	<0.01
Pr_2O_3	0.04	<0.01	<0.01	0.07	<0.01	<0.01	<0.01	<0.01
Nd_2O_3	0.01	<0.01	0.02	0.02	0.01	<0.01	<0.01	0.03
SiO_2	36.16	35.97	35.61	35.3	35.85	36.71	36.64	36.74
Sum	96.89	97.06	96.67	97.72	96.54	96.38	97.24	96.58
apfu based on 12.5 O								
Ca^{2+}	2	2.03	1.94	1.99	2.02	1.94	2.04	2
Sr^{2+}	0.01	0.01	0.01	0.01	0	0.02	0.02	0.02
Mn^{2+}	0.02	0.01	0.01	0.02	0.01	0.05	0.06	0.02
Ce^{3+}	0.0001	<0.0001	<0.001	0.0004	<0.001	0	0.0003	<0.0001
La^{3+}	0.001	<0.001	0.001	<0.001	<0.001	0	<0.001	<0.001
Pr^{3+}	0.001	<0.001	<0.001	0.001	<0.001	0	<0.001	<0.001
Nd^{3+}	<0.001	<0.001	<0.001	0	<0.001	0	<0.001	<0.001
Total REEs	0.0021	0	0.001	0.0014	0	0	0.0003	0
A site	2.03	2.05	1.96	2.01	2.04	2.01	2.12	2.04
Al^{3+}	2.06	1.99	2.01	1.97	1.88	2.08	2.03	2.07
Fe^{3+}**	0.97	1.04	1.09	1.16	1.14	0.91	0.9	0.9
V^{3+}	0.002	0.003	0.002	0.002	0.002	0.001	0.002	0.002
M site	3.04	3.04	3.11	3.13	3.02	2.99	2.93	2.97
Si^{4+}	2.95	2.95	2.93	2.89	2.97	3	2.98	3
Ti^{4+}	0.002	0.002	0.011	0.006	0	0.002	0.007	0.004
T site	2.96	2.95	2.94	2.9	2.97	3	2.99	3
Fe(t)/[Fe(t)+Al]	0.32	0.34	0.35	0.37	0.38	0.3	0.31	0.3

Cl, F, Y, Th, Pb, Cr, Nb and Sc were all below dection limits

* GPS coordinates are reported in Appendix Table 1

** All Fe is assumed to be Fe^{3+}

MP=Mine Phase

Appendix Table A1-7. Compositions of epidote cores in the GMB, determined by EPMA

Sample	GBR-16						GBR-21					GBR-28		GBR-4	GBR-11		
Location*	East pit						East of mine pits					South east of MP		East pit	East pit		
Analysis area	Core	Core	Core	Core	Core	Core	Core	Core	Core	Core	Core	Core	Core	Core	Core	Core	Core
CaO	23.65	22.94	23.06	24.11	22.88	23.65	22.97	22.55	23.26	23.3	23.14	23.3	22.58	23.79	23.73	23.73	23.63
SrO	0.33	0.3	0.25	0.18	0.43	0.25	0.33	0.18	0.25	0.06	0.17	0.33	0.12	0.23	0.29	0.15	0.26
Al_2O_3	25.39	22.14	22.51	21.71	21.75	22.21	24.7	24.74	23.83	22.68	22.99	22.7	22.3	21.99	22.9	21.82	22
TiO_2	0.14	0.1	0.11	0.05	0.05	0.08	0.05	0.05	0.03	0.16	0.05	0.04	0.13	0.81	0.04	0.03	0.04
MnO	0.32	0.64	0.49	0.19	0.47	0.22	0.22	0.37	0.38	0.27	0.31	0.35	0.53	0.17	0.4	0.24	0.35
Fe_2O_3	9.6	13.4	13.67	14.13	14.3	13.24	9.98	10.3	11.2	12.91	13.1	12.77	13.72	13.65	12.67	13.92	14.06
V_2O_3	0.03	0.07	0.09	0.08	0.07	0.1	0.01	0.02	0.04	0.09	0.14	0.05	0.12	0.1	0.04	0.02	0.08
La_2O_3	<0.01	0.02	<0.01	0.05	0.01	<0.01	<0.01	0.01	0.08	0.02	0.03	<0.01	0.01	0.03	<0.01	<0.01	0.04
Ce_2O_3	<0.01	<0.01	0.02	0.02	<0.01	<0.01	<0.01	0.03	<0.01	<0.01	<0.01	<0.01	0.02	0.02	0.01	<0.01	<0.01
Pr_2O_3	0.06	<0.01	0.01	0.03	0.01	<0.01	<0.01	<0.01	<0.01	<0.01	<0.01	<0.01	<0.01	0.04	<0.01	<0.01	0.02
Nd_2O_3	0.02	<0.01	0.04	0.01	<0.01	<0.01	<0.01	0.02	<0.01	<0.01	<0.01	<0.01	<0.01	<0.01	0.01	0.03	<0.01
SiO_2	37.46	36.7	36.74	36.86	36.94	36.98	37.77	37.54	37.15	36.83	36.83	36.92	36.91	36.62	37.26	37.13	36.83
Sum	96.84	96.3	96.94	97.37	96.9	96.73	96.02	95.81	96.22	96.31	96.76	96.47	96.43	97.4	97.33	97.04	97.29
apfu based on 12.5 O																	
Ca^{2+}	2.02	2.01	2	2.09	1.99	2.06	1.98	1.95	1.97	1.98	1.96	1.98	1.92	2.06	2	2.01	2
Sr^{2+}	0.02	0.01	0.01	0.01	0.02	0.01	0.02	0.01	0.02	0	0.01	0.03	0.01	0.01	0.02	0.01	0.02
Mn^{2+}	0.02	0.04	0.03	0.01	0.03	0.02	0.01	0.03	0.04	0.03	0.04	0.04	0.06	0.01	0.05	0.03	0.04
Ce^{3+}	<0.001	0.0003	<0.001	0.0007	0.0001	<0.001	<0.001	0.0001	0.002	<0.001	<0.001	<0.001	0.0002	0.0004	<0.001	<0.001	0.001
La^{3+}	<0.001	<0.001	<0.001	<0.001	<0.001	<0.001	<0.001	<0.001	<0.001	<0.001	<0.001	<0.001	<0.001	<0.001	<0.001	<0.001	<0.001
Pr^{3+}	0.001	<0.001	<0.001	<0.001	<0.001	<0.001	<0.001	<0.001	<0.001	<0.001	<0.001	<0.001	<0.001	0.001	<0.001	<0.001	<0.001
Nd^{3+}	<0.001	<0.001	0.001	<0.001	<0.001	<0.001	<0.001	<0.001	<0.001	<0.001	<0.001	<0.001	<0.001	<0.001	<0.001	<0.001	<0.001
Total REEs	0.001	0.0003	0.001	0.0007	0.0001	0	0	0.0001	0.002	0	0	0	0.0002	0.0014	0	0	0.001
A site	2.06	2.06	2.05	2.12	2.05	2.08	2.01	1.98	2.03	2.02	2.01	2.05	1.99	2.08	2.07	2.05	2.07
Al^{3+}	2.39	2.13	2.15	2.07	2.08	2.12	2.34	2.35	2.22	2.12	2.14	2.12	2.08	2.1	2.12	2.04	2.05
Fe^{3+}**	0.57	0.82	0.83	0.86	0.87	0.81	0.6	0.62	0.66	0.77	0.78	0.76	0.82	0.83	0.75	0.83	0.84
V^{3+}	0.001	0.002	0.003	0.003	0.002	0.003	0	0.001	0.002	0.005	0.008	0.003	0.006	0.003	0.002	0.001	0.004
M site	2.96	2.96	2.99	2.94	2.96	2.94	2.94	2.98	2.89	2.9	2.93	2.89	2.91	2.93	2.87	2.87	2.89
Si^{4+}	2.99	2.99	2.98	2.99	3	3	3.04	3.02	2.93	2.92	2.91	2.93	2.93	2.96	2.93	2.94	2.91
Ti^{4+}	0.008	0.006	0.007	0.003	0.003	0.005	0.003	0.003	0.003	0.016	0.005	0.004	0.01	0.049	0.004	0.003	0.004
T site	3	3	2.98	2.99	3.01	3.01	3.04	3.03	2.94	2.94	2.92	2.93	2.94	3.01	2.93	2.94	2.92
Fe(t)/[Fe(t)+Al]	0.19	0.28	0.28	0.29	0.3	0.28	0.21	0.21	0.23	0.27	0.27	0.26	0.28	0.28	0.26	0.29	0.29

Cl, F, Y, Th, Pb, Cr, Nb and Sc were all below dection limits

* GPS coordinates are reported in Appendix Table 1

** All Fe is assumed to be Fe3+

MP=Mine Phase

Appendix Table A1-8. Compositions of REE-rich epidote in the GMB, determined by EPMA

Sample	GBR-11	GBR-4	
Location*	East pit	East pit	
Analysis area	Ce rich zone	Ce rich zone	Ce rich zone
CaO	12.63	19.61	13.67
SrO	0.01	0.34	<0.01
Al_2O_3	16.53	22.83	18.12
TiO_2	0.41	<0.01	<0.01
MnO	0.74	0.29	1.14
FeO	11.9	10.75	11.16
V_2O_3	0.1	0.14	0.04
La_2O_3	3.9	0.93	1.49
Ce_2O_3	10.38	2.37	5.15
Pr_2O_3	0.99	0.21	0.9
Nd_2O_3	0.69	0.35	1.24
SiO_2	30.06	33.65	31.29
Sum	89.66	92.67	85.44
apfu based on 12.5 O**			
Ca^{2+}	1.31	1.79	1.41
Sr^{2+}	<0.01	0.02	<0.01
Mn^{2+}	0.06	0.02	0.09
Ce^{3+}	0.37	0.07	0.18
La^{3+}	0.14	0.03	0.05
Pr^{3+}	0.03	0.01	0.03
Nd^{3+}	0.02	0.01	0.04
Total REEs	0.57	0.12	0.31
A site	1.91	1.92	1.77
Al^{3+}	1.90	2.30	2.06
Fe^{2+}**	0.98	0.78	0.91
V^{3+}	0.01	0.01	<0.01
M site	2.89	3.08	2.97
Si^{4+}	2.91	2.87	3.00
Ti^{4+}	0.03	<0.01	<0.01
T site	2.94	2.87	3.00
Fe(t)/[Fe(t)+Al]	0.36	0.25	0.31

Cl, F, Y, Th, Pb, Cr, Nb and Sc were all below dection limits

* GPS coordinates are reported in Appendix Table 1

**apfu calculated assuming all Fe is Fe^{2+} for REE-rich epidote and

Appendix Table A1-9. Compositions of epidote in contact with Py or Ccp in the GMB, determined with SEM-EDS

Sample	SVA 7-14.13.3				SVA 7-14.13.4		SVA 7-14.13				
Location*	Granite Lake zone				Granite Lake zone		Granite Lake zone				
Analysis area	Rim 1	Rim 2	Rim 3	Rim 4	Rim 1	Enclosed 1	Core 1	Core 2	Rim 1	Rim 2	Enclosed 1
Al_2O_3	21.52	22.36	22.59	22.52	23.17	25.09	24.36	25.74	23.74	24.6	25.29
SiO_2	38.8	37.97	38.09	39.26	38.77	39.34	39.43	39.62	38.77	39.21	39.57
CaO	22.76	22.78	23.07	22.41	22.94	22.91	23.11	23.62	24.01	23.04	23.6
Fe_2O_3(t)	16.92	16.9	16.25	15.81	15.12	12.67	13.1	11.02	13.48	13.15	11.53
Sum*	100	100	100	100	100	100	100	100	100	100	100
apfu based on 12.5 O											
Ca^{2+}	1.92	1.92	1.94	1.87	1.92	1.91	1.92	1.92	2	1.91	1.95
A site	1.92	1.92	1.94	1.87	1.92	1.91	1.92	1.92	2	1.91	1.95
Fe^{3+}**	1	1	0.96	0.93	0.89	0.67	0.76	0.63	0.79	0.77	0.67
Al^{3+}	1.99	2.07	2.09	2.07	2.13	2.3	2.22	2.31	2.18	2.25	2.3
M site	2.99	3.07	3.05	3	3.02	2.97	2.99	2.94	2.97	3.01	2.97
Si^{4+}	3.05	2.99	2.99	3.06	3.03	3.06	3.05	3.01	3.02	3.04	3.05
T site	3.05	2.99	2.99	3.06	3.03	3.06	3.05	3.01	3.02	3.04	3.05
Fe(t)/[Fe(t)+Al]	0.33	0.33	0.31	0.31	0.29	0.22	0.26	0.21	0.27	0.25	0.23

* GPS coordinates are reported in Appendix Table 1

** Anhydrous component is normalized to 100%

*** All Fe is assumed to be Fe^{3+}

Appendix A2-1.Hand sample descriptions

Identifier		Rock name	Texture	Primary mineralogy (in order of abundance)	Alteration mineralogy (in order of abundance)	Sulfide minerals
GBR-2	Mineralized toanlite	Tonalite	Equigranular, isotropic, M-gr	Pl, Qz, Ttn, Ap, Zr, Mag	Wm, Chl, Ep, Ttn, Rt, Py, Mag	Cpy, Py
GBR-7	Mineralized toanlite	Tonalite	Slightly foliated, equigranular, M-gr	Pl, Qz, Ttn, Ap, Zr, Mag	Ep. Wm, Chl, Ttn, Rt, Mag	Cpy, Py
GBR-12	Mineralized toanlite	Tonalite	Foliated, equigranular, M-gr	Pl, Qz, Ttn, Ap, Zr, Mag	Chl, Wm, Ep, Ttn, Rt, Mag	Cpy, Py
GBR-11	Unmineralzied tonalite	Tonalite	Foliated, equigranular, M-gr	Pl, Qz, Ttn, Ap, Zr, Mag	Wm, Chl, Ep, Ttn, Rt, Py, Mag	Trace Py
GBR-15	Mineralized toanlite	Tonalite	C-gr, equigranular isotropic	Qz, Pl, Ttn, Ap, Zr, Mag	Wm, Cal, Ep, Py, Mag	Cpy, Py
GBR-16	Mineralized toanlite	Tonalite	C-gr, equigranular isotropic	Pl, Qt, Ttn, Ap, Zr, Mag	Wm, Ep, Chl, Mag, Py, Ttn, Rt	Cpy, Py
GBR-21	Mineralized toanlite	Leucocratic Tonalite	C-gr, equigranular isotropic	Qt, Pl. Ttn, Ap, Zr, Mag	Wm, Chl, Ep, Ttn, Rt, Mag	Cpy, Py
GBR-28	Unmineralzied tonalite	Tonalite	M-gr, slightly foliated, equigranular	Pl, Qt, Ttn, Ap, Zr, Mag	Ep, Chl, Wm, Ttn, Rt, Py, Mag	Trace Py
GBR-32	Unmineralzied tonalite	Tonalite	Equigranular, isotropic, M-gr	Pl, Qt, Ttn, Ap, Zr, Mag	Ep, Chl, Wm, Ttn, Rt, Mag	None
GBR2-15	Unmineralzied tonalite	Tonalite	C-gr, equigranular isotropic	Pl, Qt, Ttn, Ap, Zr, Mag	Ep, Chl, Wm, Ttn, Rt, Py, Mag	None
GBR2-16	Unmineralzied tonalite	Tonalite	C-gr, equigranular isotropic	Pl, Qt, Bt, Hrb Ttn, Ap, Zr, Mag	Ep, Wm	None
GBR2-17	Unmineralzied tonalite	Tonalite	C-gr, equigranular isotropic	Pl, Qt, Bt, Hrb,Ttn, Ap, Zr, Mag	Ep, Wm	None
GBR2-25	Unmineralzied tonalite	Leucocratic Tonalite	C-gr, equigranular isotropic	Pl, Qt, Ttn, Ap, Zr, Mag	Ep, Chl, Wm, Ttn, Rt	None
GBR2-26	Unmineralzied tonalite	Leucocratic Tonalite	M-gr, equigranular isotropic	Pl, Qt, Ttn, Ap, Zr, Mag	Ep, Chl, Wm, Ttn, Rt	Trace Py
GBR2-30	Unmineralzied tonalite	Leucocratic Tonalite	C-gr, equigranular isotropic	Pl, Qt, Ttn, Ap, Zr, Mag	Ep, Chl, Wm, Ttn, Rt	Trace Py
GBR2-38	Unmineralzied tonalite	Leucocratic Tonalite	C-gr, equigranular isotropic	Pl, Qt, Ttn, Ap, Zr, Mag	Ep, Chl, Wm, Ttn, Rt	None

M-gr = medium grain ~1cm grains

C-gr = Coarse grained >1cm grains

Abreveations: Ap = Apatite, Bt = Biotite, Cal = Calcite, Cpy = Chalcopyrite, Chl = Chlorite, Ep = Epidote, Hrb = Hornblende, Mag = Magnetite, Pl = Plagioclase, Qz = Quartz, Rt = Rutile, Ttn = Titanite, Zr = Zircon

Minor = 5-15% modality

Moderate =15-30% modality

Intense = >30% modality

Primary and secondary mineralogy determined by hand sample and thin section observations

Appendix A2-2. Bulk rock compositions of samples and accuracies and precisions of analysis

Mineralized tonalites

Analyte Symbol	SiO2	Al2O3	Fe2O3(T)a	MnO	MgO	CaO	Na2O	K2O	TiO2	P2O5	LOI	Total	Sc	V	Ba	Sr	Y	Zr	Co	Cu	Zn	Rb	Nb	Mo	Cs	La	Ce	Pr	Nd	Sm	Eu	Gd	Tb	Dy	Ho	Er	Tm	Yb	Lu	Hf	Th	U
Detection Limit	0.01	0.01	0.01	0.001	0.01	0.01	0.01	0.01	0.001	0.01			1	5	2	2	1	2	1	10	30	2	1	2	0.5	0.1	0.1	0.05	0.1	0.1	0.05	0.1	0.1	0.1	0.1	0.1	0.05	0.1	0.01	0.2	0.1	0.1
	%	%	%	%	%	%	%	%	%	%	%	%	ppm	ppm	ppm	ppm	ppm	ppm	ppm	ppm	ppm	ppm	ppm	ppm	ppm	ppm	ppm	ppm	ppm	ppm	ppm	ppm	ppm	ppm	ppm	ppm	ppm	ppm	ppm	ppm	ppm	ppm
GBR-02	65.3	17.2	3.7	0.09	2.4	3.1	3.3	1.5	0.54	0.1	2.93	100.1	12	87	585	295	18	194	7	200	100	24	2	2	< 0.5	8.8	21.9	3.09	13.8	3.5	0.9	3.4	0.5	3.1	0.6	1.8	0.3	1.9	0.3	4.9	1.5	1.5
GBR-07	65.8	15.7	5.2	0.07	2	3.7	2.9	1.5	0.53	0.1	2.64	99.9	12	118	768	311	18	122	8	350	< 30	25	2	< 2	0.6	7.4	20.4	2.98	13	3.3	0.7	3.2	0.6	3.2	0.7	1.9	0.3	2.1	0.3	3.5	1.1	0.8
GBR-12	65.3	15.8	5.5	0.07	1.7	1.8	3.1	1.9	0.51	0.1	2.96	98.8	11	94	949	179	20	123	13	9410	80	33	2	9	0.7	8.6	22.2	3.09	13.1	3.2	0.6	3.4	0.6	3.5	0.7	2.1	0.3	2.2	0.4	3.4	1.4	1.3
GBR-15	62.8	16.8	4.7	0.09	2.3	3.5	3.6	1.3	0.52	0.1	3.34	99	12	108	631	394	18	142	7	1710	80	21	2	< 2	< 0.5	8.4	21.8	3.05	13.5	3.2	0.8	3.3	0.5	3.3	0.7	1.9	0.3	2.1	0.3	3.8	1.5	1.2
GBR-16	67.3	15.8	3.1	0.13	1.6	2.3	6.3	0.6	0.53	0.1	1.6	99.5	9	68	320	207	20	229	6	240	90	9	2	< 2	< 0.5	8.5	23.9	3.5	15.3	3.9	0.8	3.5	0.6	3.8	0.8	2.2	0.4	2.5	0.4	5.6	1.6	0.8
GBR-21	67.6	14.9	4.4	0.06	1.8	4.1	3.4	1	0.46	0.1	2	99.7	10	97	635	347	16	127	8	1120	< 30	16	2	< 2	< 0.5	7.7	19.2	2.68	11.7	2.9	0.7	3	0.5	3	0.6	1.7	0.3	1.9	0.3	3.3	1.7	0.9

Unmineralized tonalites

GBR-11	67.6	15.8	5.1	0.1	1.9	3.9	ndb	1.1	0.45	0.1	ndb	>96	ndb	102	463	342	26	ndb	7	50	120	21	3	9	0.5	6.6	20.5	3.4	17.5	4	0.9	4.7	0.7	4.3	0.9	2.8	0.5	3.3	ndb	10	2.2	1.6
GBR-28	71.2	15	2.9	0.09	1.1	2.3	3.9	1.5	0.3	0.1	1.53	99.8	6	51	802	272	12	151	6	50	40	22	2	< 2	0.6	5.5	14.5	2	7.8	1.7	0.5	1.8	0.3	1.8	0.4	1.3	0.2	1.8	0.3	4.5	1.9	1.4
GBR-32	66.7	15.2	3.8	0.12	1.2	4.3	4.3	1.3	0.39	0.1	1.66	99.1	8	80	685	297	15	129	8	50	40	23	2	< 2	0.5	24.7	52.4	5.94	20.7	3.8	0.8	3.1	0.5	2.8	0.6	1.6	0.2	1.7	0.3	3.6	2.6	0.7
GBR2-25	69.5	15.4	3.1	0.16	1.2	3.2	4.3	1	0.3	0.1	1.66	99.9	4	46	867	337	9	85	6	80	60	13	2	< 2	< 0.5	7	11.1	1.48	5.7	1.4	0.5	1.2	0.2	1.1	0.2	0.7	0.1	0.8	0.1	2.5	0.6	0.4
GBR2-26	73.6	13.95	2.1	0.32	0.5	1.3	4.2	1.6	0.2	0.1	1.1	98.98	3	19	938	269	13	71	2	10	70	20	2	< 2	< 0.5	7	15.6	1.94	7.5	1.7	0.38	1.4	0.2	1.4	0.3	0.9	0.1	1.1	0.2	2.4	1.1	0.8
GBR2-15	68.3	16.1	2.6	0.1	0.63	4.1	4.3	1.6	0.21	0.07	1.3	99.2	4	53	765	394	14	221	4	30	< 30	26	1	< 2	< 0.5	8.2	18.5	2.4	9.3	1.8	0.7	1.6	0.3	1.6	0.3	1.1	0.2	1.4	0.2	5.9	2	1.1
GBR2-16	65.6	16.2	5.2	0.1	1.8	4.6	3.8	1.7	0.46	0.11	1.5	101	11	100	9	681	19	19	20	10	40	2	35	< 2	1	0.7	9.2	22.7	3	13.6	3.5	0.8	3.2	0.5	3.4	0.7	2.2	0.3	2.2	0.4	2.2	0.9
GBR2-17	65.6	15.1	4.7	0.24	1.9	4.4	3.4	1.8	0.46	0.09	1.6	99.2	9	88	797	354	23	141	10	20	40	31	2	< 2	0.6	11.2	26.5	3.4	14	3.2	0.7	3.1	0.5	3	0.6	1.8	0.3	2	0.3	4.2	1.8	0.7
GBR2-30	70.3	15.4	3	0.18	0.77	2.2	5.7	1.1	0.27	0.09	1.6	101	4	48	439	287	7	60	4	110	40	14	1	< 2	< 0.5	5.4	11	1.4	5.7	1.3	0.49	1.1	0.2	1	0.2	0.7	0.11	0.7	0.13	1.8	0.9	0.9
GBR2-38	68.7	16	3.1	0.2	1.1	4	4.6	1.2	0.29	0.09	1.4	101	5	45	679	414	9	73	5	0	40	18	2	< 2	< 0.5	5.4	13.5	1.85	7.6	1.8	0.54	1.6	0.2	1.4	0.3	0.9	0.16	1.1	0.17	1.8	0.5	0.4

a, Total Fe expressed as Fe2O3 b, nd=not determined

W, Tl, Cr, As, Ni, In, Sn, Sb, Pb, Ag and Bi are below detections limits of 1, 0.1, 20, 20, 5, 0.2, 0.5, 0.5, 5, 0.5 and 0.4 ppm respectively

Analytical conditions

Elements	**Accuracy**	**Precision**	**Detection limits**
SiO_2	99.02%	99.97%	0.01 Wt.%
Al_2O_3	97.22%	97.64%	0.01 Wt.%
Fe_2O_3	97.97%	99.76%	0.01 Wt.%
MnO	96.70%	99.49%	0.001 Wt.%
MgO	95.50%	97.9%	0.01 Wt.%
CaO	99.68%	99.72%	0.01 Wt.%
Na_2O	98.44%	99.75%	0.01 Wt.%
K_2O	93.82%	98.76%	0.01 Wt.%
TiO_2	96.22%	98.9%	0.001 Wt.%
P_2O_5	94.76%	88.88%	0.01 Wt.%
Sc	98.02%	100%	1 ppm
V	95.49%	98.94%	5 ppm
Ba	93.38%	99.79%	2 ppm
Sr	97.99%	99.75%	2 ppm
Y	88.85%	100%	1 ppm
Zr	96.20%	100%	2 ppm
Co	94.44%	90.9%	1 ppm
Cu	91.28%	66.66%	10 ppm
Zn	98.96%	100%	30 ppm
Rb	95.96%	100%	2 ppm
Nb	99.34%	100%	2 ppm
Ag	87.96%	83.30%	0.5 ppm
Cs	94.41%	100%	0.5 ppm
La	96.83%	95.45%	0.1 ppm
Ce	95.71%	96.15%	0.1 ppm
Pr	95.50%	96.5%	0.05 ppm
Nd	94.78%	96.9%	0.1 ppm
Sm	96.43%	95.65%	0.1 ppm
Eu	95.12%	92.06%	0.05 ppm
Gd	95.16%	91.66%	0.1 ppm
Tb	96.38%	100%	0.1 ppm
Dy	96.56%	95.83%	0.1 ppm
Ho	96.62%	100%	0.1 ppm
Er	96.64%	92.85%	0.1 ppm
Tm	94.30%	100%	0.05 ppm
Yb	97.54%	94.11%	0.1 ppm
Lu	94.91%	88.88%	0.1 ppm
Hf	96.46%	96.61%	0.2 ppm
Th	95.61%	88.88%	0.1 ppm
U	95.53%	100%	0.1 ppm

Appendix A2-3. Trace element concentrations in zircon in ppm

Mineralized tonalites

GBR-2

grain	Ca	Ti	Fe	Sr	Y	La	Ce	Pr	Nd	Sm	Eu	Gd	Tb	Dy	Ho	Er	Tm	Yb	Lu	Hf	Ce^{4+}/Ce^{3+}	Ce/Ce*	Ce/Nd
GBR2-1	<96.4	14.5	<1.75	0.3	468	<0.0027	4.3	0.01	0.4	1.19	0.39	8.02	2.89	39.1	15.7	75.8	18	185	32.5	9690	461	75	11
GBR2-2	<98.4	14.2	<1.76	0.3	762	<0.0031	5	0.03	0.9	2.67	0.66	15.38	5.52	65.6	25.5	119	26.4	267	45.5	9750	157	38	6
GBR2-3	<81.6	10.3	<1.46	0.4	979	0.003	7	0.05	1.14	3.72	0.89	22.39	7.63	88.4	33.2	149	33.4	333	53.7	9330	140	46	6
GBR2-4	<92.1	8.6	<1.55	0.3	507	<0.0028	5.2	0.02	0.39	1.42	0.38	8.59	3.21	39.4	16.2	80.2	19.5	228	42.1	10600	563	112	13
GBR2-5	<93.9	16.2	<1.56	0.4	1290	0.01	6.7	0.16	3.22	6.47	1.5	29.8	9.83	116	43.6	197	43.7	416	72.1	9220	41	10	2
GBR2-6	122	17.6	1300	1.6	587	0.02	3.9	0.05	0.95	2	0.45	10.5	3.68	47.7	19.3	93.1	20.5	202	38.4	8090	135	20	4
GBR2-7	<103	14.3	<1.68	0.5	1210	0.004	7	0.08	1.78	5.07	1.22	29.4	9.62	114	41.8	185	39.8	379	63.7	10400	81	26	4
GBR2-8	<88.1	13	<1.4	0.4	539	<0.002	5	0.01	0.33	1.52	0.34	9.24	3.41	44.8	18.4	83.9	18.7	199	36.2	11100	550	157	15
GBR2-9	<113	13.8	<1.75	0.4	592	<0.0032	4.4	0.02	0.39	1.5	0.39	9.51	3.61	48.8	19.8	97	21.9	215	41	10600	448	102	11
GBR2-10	<105	11.1	<1.67	0.5	1240	0.01	7.8	0.05	1.27	4.26	0.94	26	9.13	111	42.4	193	40.9	386	71.1	11200	147	47	6
GBR2-11	<71.3	15	<1.18	0.4	1010	0.01	6	0.03	0.69	2.86	0.75	18.8	6.73	82.6	32.4	153	33.6	315	54	10600	234	81	9
GBR2-12	<64.6	8.5	<1.04	0.4	1080	<0.0028	8.7	0.02	0.52	2.47	0.61	18.6	7.08	92.8	35.8	181	39.8	386	68.8	11100	536	181	17
GBR2-13	<65	13.6	<1.06	0.4	1170	0.004	6.8	0.08	1.89	5.25	1.19	29.1	9.43	107	39.7	175	38.6	377	60.6	9320	70	23	4
GBR2-14	<63.9	12.1	2.08	0.4	1120	0.003	7.1	0.09	2.07	5.66	1.25	28.4	9.37	111	38.6	173	37.3	360	58.2	9390	64	21	3

GBR-7

grain	Ca	Ti	Fe	Sr	Y	La	Ce	Pr	Nd	Sm	Eu	Gd	Tb	Dy	Ho	Er	Tm	Yb	Lu	Hf	Ce^{4+}/Ce^{3+}	Ce/Ce*	Ce/Nd
GBR7-1	<60.7	8.8	<0.97	0.4	442	<0.0023	4.2	0.01	0.23	0.82	0.23	6.36	2.5	35.6	14.2	70.5	17.5	180	30.7	10200	1040	153	18
GBR7-2	<59.1	8.9	<0.96	0.3	423	<0.0023	5.6	0.01	0.16	0.89	0.2	6.59	2.52	35.6	14.6	71.3	16.9	178	30.5	10200	1780	459	35
GBR7-3	<59.3	6.3	<0.96	0.3	402	0.01	4.5	0.03	0.39	0.88	0.22	5.05	1.94	28.5	11.9	63.3	17.5	206	38.9	11200	834	61	12
GBR7-4	<65.4	15.1	<1.07	0.4	1350	<0.0031	7	0.09	2.02	4.71	1.23	27.7	10.2	118	46.9	220	46.1	485	77.1	10300	93	19	3
GBR7-5	<61.6	12	<1.01	0.4	1140	0.01	6.1	0.14	2.32	5.56	1.39	27.8	8.99	111	39.3	187	40.9	398	66.1	9140	59	15	3
GBR7-6	<64.9	7.5	<1.05	0.4	347	<0.0048	5.5	0.01	0.23	0.81	0.21	4.75	1.95	25.5	11	60.5	15.5	180	35	11800	1646	201	24
GBR7-7	<62.8	13.3	<1.01	0.4	852	<0.0038	4.9	0.05	0.92	2.89	0.69	15.9	5.66	71	27.8	135	30.3	312	53.6	9990	170	38	5
GBR7-8	<64	12.9	<1.03	0.4	1080	<0.003	5.8	0.06	1.28	3.99	1.1	23.1	8.1	96.9	37.2	170	37.2	357	58.5	9970	116	33	5
GBR7-9	<65.5	11.6	<1.06	0.3	464	0.003	5.2	0.01	0.29	1.14	0.27	7.6	2.96	39.8	16	76.9	19	185	31.6	10800	836	161	18
GBR7-10	<71.9	15.9	1.76	0.4	1220	<0.0031	5.6	0.09	1.89	4.32	1.16	24.9	8.74	110	41.9	197	41.9	402	68	11100	82	16	3
GBR7-11	<62.6	10.6	<1.01	0.3	573	<0.00243	5.4	0.01	0.29	1.19	0.31	9.01	3.54	45.7	18.2	91.6	21.2	217	38	11000	868	173	19
GBR7-12	<54.5	9.8	<0.88	0.3	490	<0.0028	4.1	0.02	0.38	1.39	0.34	8.44	3.43	45.5	17	88	20.2	200	36.1	9050	454	91	11
GBR7-13	<60.7	9.2	<1.01	0.4	453	<0.00172	5.7	0.02	0.28	1.03	0.25	7.03	2.91	36.9	15.6	77.5	18.1	190	33.6	11000	1062	176	21
GBR7-14	<59.9	8.8	<0.94	0.3	600	<0.0023	5.2	0.02	0.5	1.46	0.35	9.92	3.9	51.1	20.7	104	22.9	239	41.7	9650	459	70	10
GBR7-15	<64.7	10	<1.03	0.3	636	<0.0021	5.7	0.01	0.37	1.29	0.33	9.77	3.7	51.1	20.6	95.5	24	252	40.2	10500	714	121	15

GBR-12

grain	Ca	Ti	Fe	Sr	Y	La	Ce	Pr	Nd	Sm	Eu	Gd	Tb	Dy	Ho	Er	Tm	Yb	Lu	Hf	Ce^{4+}/Ce^{3+}	Ce/Ce*	Ce/Nd
GBR12-1	<63.5	14.5	3.22	0.4	989	<0.0027	7.1	0.03	1	2.82	0.68	19.1	6.9	92.1	33.8	154	35.4	364	55.2	11000	211	46	7
GBR12-2	<71	11.6	<1.15	0.5	1440	<0.0024	9.5	0.10	2.18	6.24	1.15	33.3	11.5	136	49.2	225	49.7	486	76.2	11300	89	29	4
GBR12-3	<68.4	13.4	<1.10	0.4	776	<0.004	6.3	0.03	0.51	2.25	0.52	15.2	5.33	68.5	26.7	125	29	295	48	11400	389	127	12
GBR12-4	<68.7	14.2	<1.12	0.3	660	<0.0019	6.4	0.02	0.52	1.8	0.38	11.7	4.24	56.2	21.8	105	23.9	257	42.2	10800	443	99	12
GBR12-5	<60.9	12.2	<1.02	0.4	1300	<0.0041	7.9	0.06	1.68	5.1	1.08	31.5	9.9	118	45.3	200	43.6	432	66.1	10400	98	33	5
GBR12-6	<58	11.4	<0.94	0.4	1050	0.004	6.7	0.05	1.09	3.46	0.83	23.5	8.1	103	36.1	167	38.1	354	59.4	9770	150	44	6
GBR12-7	<64	15	<1.04	0.4	1100	0.01	6.6	0.08	1.66	4.86	0.95	25.4	8.86	104	38	182	38.9	367	62.8	10100	85	27	4
GBR12-8	<62.3	14.4	<1.02	0.3	792	0.002	5.5	0.04	0.91	2.77	0.6	15	5.7	69.2	27.3	125	28.1	292	47.9	10100	173	42	6
GBR12-9	<63.9	13.4	<1.03	0.3	980	<0.0025	6.4	0.02	0.64	2.42	0.65	18.9	7.05	89.7	34.1	157	35.7	339	55.7	10400	296	86	10
GBR12-10	<51.4	14.1	1.06	0.4	1100	<0.0027	7.3	0.05	1.14	3.48	0.83	23.4	8.34	108	36.8	163	42.6	392	56.1	9500	159	45	6
GBR12-11	<56.7	15.8	<0.93	0.4	715	<0.003	5.6	0.04	0.72	2.41	0.52	13.9	5.17	62.6	24.8	119	28	281	47	9130	236	61	8
GBR12-12	<62.9	12.2	1.06	0.3	558	0.05	6.5	0.03	0.5	1.17	0.32	9.47	3.46	47.6	18.6	89.6	21.2	209	35.5	10400	574	70	13
GBR12-13	<71.8	9.8	<1.15	0.5	1140	0.002	8.9	0.03	0.77	2.95	0.61	21.4	7.78	97.8	39.1	180	40.9	422	68.4	12300	354	102	12
GBR12-14	78.30	12.8	<1.22	0.5	1290	0.003	9.7	0.03	0.94	3.66	0.89	26.2	9.62	120	44.9	207	46.6	460	72.1	11800	271	92	10
GBR12-15	<71.8	14.9	<1.16	0.4	1280	<0.0035	8.0	0.06	1.55	5.39	1.12	28.9	9.99	117	43.5	197	43.1	421	67.1	10800	106	41	5

GBR-15

grain	Ca	Ti	Fe	Sr	Y	La	Ce	Pr	Nd	Sm	Eu	Gd	Tb	Dy	Ho	Er	Tm	Yb	Lu	Hf	Ce^{4+}/Ce^{3+}	Ce/Ce*	Ce/Nd
GBR15-1	<61	10.9	1.22	0.3	595	<0.0029	4.9	0.02	0.45	1.55	0.45	9.84	3.78	50	19.5	95.7	22.8	238	40.8	9330	177	87	11
GBR15-2	<63	9	<0.99	0.4	600	<0.0023	5.4	0.02	0.4	1.43	0.37	9.4	3.54	50	19.5	97.5	23.6	264	44	10400	350	112	13
GBR15-3	<62.9	13.4	<0.99	0.4	583	<0.0052	5.7	0.02	0.49	1.65	0.46	10.2	3.94	51.2	19.7	94.8	22.3	240	39.4	9350	251	89	12
GBR15-4	<61.7	12.7	<0.96	0.3	554	<0.0026	4	0.02	0.57	1.74	0.48	10.6	3.88	50.8	18.9	87.4	20.5	217	37.2	8500	139	49	7
GBR15-5	<59.1	15.5	13.56	0.6	1430	0.01	6.4	0.15	3.02	6.05	1.63	30.2	10.5	130	49.7	228	51.2	500	81.5	8720	34	10	2
GBR15-6	<66.2	10.4	<1.03	0.4	670	<0.0031	5.3	0.02	0.47	1.76	0.46	11.1	4.27	57	22.1	107	25.2	261	44.6	10200	255	96	11
GBR15-7	<66.5	13.6	2.28	0.5	728	<0.0037	4.7	0.04	0.73	2.39	0.63	13.9	4.94	60.3	24.1	116	27.4	291	49.8	9210	125	48	6
GBR15-8	<55	11.6	<0.88	0.4	801	<0.00238	5	0.07	1.31	3.41	0.85	18.4	6.02	76.2	28.6	138	30.4	292	51	8820	62	23	4
GBR15-9	<55	10.8	<0.89	0.3	532	0.003	4.2	0.02	0.53	1.61	0.4	10.1	3.54	44.5	18.3	87.5	20.7	209	34.7	9240	172	56	8
GBR15-10	<56.7	9.3	13.2	0.3	502	<0.003	5.9	0.01	0.36	1.14	0.28	8.51	3.3	42.6	16.7	83.1	19.8	205	33.9	9930	443	119	16

GBR-16

grain	Ca	Ti	Fe	Sr	Y	La	Ce	Pr	Nd	Sm	Eu	Gd	Tb	Dy	Ho	Er	Tm	Yb	Lu	Hf	Ce^{4+}/Ce^{3+}	Ce/Ce*	Ce/Nd
GBR-16-1-1	<70.6	10.1	<221	0.4	1030	0.005	5.5	0.1	1.26	5.63	0.74	25.8	6.15	102	29.6	160	30.9	351	52.5	7960	32	44	4
GBR-16-1-2	<63.2	14.2	<192	0.4	988	0.005	6	0.11	2.05	4.71	1.03	23.1	7.72	90.4	33.1	150	32.6	331	50.2	7670	24	15	3
GBR-16-2	<66.3	19.3	<197	0.6	298	0.002	9.1	0.01	3.65	0.78	1.6	4.64	12.1	24.3	54.4	49.7	57.3	132	81.9	8790	83	1	2
																				0			
GBR16-1	<58.2	12.9	<0.93	0.3	454	<0.0033	6.4	0.01	0.32	1.13	0.3	7.86	2.91	38.4	15.5	77.9	17.6	199	31.8	9510	294	169	20
GBR16-2	<59.3	13	3.4	0.4	1020	0.01	6.8	0.12	2.5	5.9	1.34	27.4	8.28	98.7	34.9	158	34.2	358	54.6	8980	21	15	3
GBR16-3	<64.4	13.2	<1.02	0.3	583	<0.0042	4.4	0.02	0.46	1.54	0.39	9.3	3.6	47.8	18.9	96.1	22.2	235	40.5	9910	135	74	10

GBR-21

grain	Ca	Ti	Fe	Sr	Y	La	Ce	Pr	Nd	Sm	Eu	Gd	Tb	Dy	Ho	Er	Tm	Yb	Lu	Hf	Ce^{4+}/Ce^{3+}	Ce/Ce*	Ce/Nd
GBR21-1	<60.5	11.9	<0.96	0.5	1190	<0.0029	7.5	0.05	1.21	3.73	0.81	24.2	8.34	105	39.6	176	39.1	400	62.4	10500	64	45	6
GBR21-2	<56.7	11.1	<0.90	0.4	580	<0.003	5.1	0.01	0.42	1.42	0.29	9.89	3.75	49.3	19.1	95.5	22.8	226	38.9	9810	168	94	12
GBR21-4	<62.7	7.7	<1	0.4	655	<0.0036	7.1	0.01	0.37	1.33	0.31	9.65	3.64	47	21	104	26.6	297	50.5	11800	330	161	24
GBR21-5	<65.7	12.7	<1.02	0.3	441	<0.0028	5.6	0.01	0.23	0.89	0.2	7.13	2.66	34.5	14.9	70.9	17.2	185	30.6	11100	376	212	13
GBR21-6	<62.6	2.8	295	1.1	1170	0.02	15.4	0.03	1.15	2.83	0.63	17.9	6.56	82.1	35.9	200	48.5	605	126.3	17000	255	76	22
GBR21-7	<62.6	13.7	120.89	0.3	473	<0.0037	5.7	0.02	0.26	1.03	0.25	7.67	2.76	40.1	15.3	75.2	18.7	191	31.2	10400	320	196	13
GBR21-8	<56.2	5.7	<0.9	0.5	804	<0.0034	8.4	0.03	0.63	1.78	0.6	12.3	4.1	57	23.3	121	34.7	417	70.5	12300	244	86	12
GBR21-9	<70.2	8.6	3.07	0.6	1300	<0.0056	9.6	0.04	0.77	3.17	0.7	23.1	8.42	110	42	211	46.7	434	82.7	12300	155	117	5
GBR21-10	<61.3	12.7	<0.98	0.5	13110	<0.0036	8.7	0.06	1.66	5.12	0.95	30.5	10.7	121	44.1	212	44.1	441	71.8	10600	47	37	3
GBR21-11	<56.4	12.5	<0.9	0.4	1280	0.01	6.9	0.12	2.63	5.71	1.14	30.2	9.38	116	41.5	191	43.3	404	64.8	9430	22	13	5
GBR21-12	<52.9	12.9	<0.85	0.4	942	<0.0028	6.3	0.07	1.32	4.01	0.74	21.3	7.54	90.2	32.2	153	33.8	325	55.9	9040	43	33	29
GBR21-13	<55	8.9	<0.98	0.4	450	<0.003	6.3	0.01	0.22	0.88	0.23	6.89	2.44	33.9	14.3	71.6	18.1	194	33.6	11000	477	263	9
GBR21-14	<49	9	1.11	0.4	826	<0.0031	6.5	0.02	0.73	2.6	0.53	16.9	5.52	73.1	27.5	133	32.9	353	51.4	9440	104	73	13

For Ce^{4+}/Ce^{3+} calculation see Symthe and Brenan 2016

Unmineralized tonalites

GBR-11

grain	Ca	Ti	Fe	Sr	Y	La	Ce	Pr	Nd	Sm	Eu	Gd	Tb	Dy	Ho	Er	Tm	Yb	Lu	Hf	Ce^{4+}/Ce^{3}	Ce/Ce*	Ce/Nd
GBR-11-1	<69.4	19.3	<2490	0.6	1540	0.01	9.1	0.18	3.65	7.23	1.6	34.6	12.1	148	54.4	245	57.3	598	81.9	7610	21	11	2
GBR-11-1	<82.2	11.8	<2110	0.5	1150	0.02	7.1	0.12	2.64	5.53	1.1	27.6	8.89	108	40.8	187	40.7	417	67.8	9110	23	13	3
GBR-11-2	<77.9	17	<1560	0.5	1370	0.01	7.1	0.15	3.26	6.08	1.32	29.1	10.1	126	48.3	220	47.5	473	77.7	8500	19	9	2
GBR-11-3	<73.9	12.9	<1240	0.5	1230	0.005	7	0.11	2.63	5.46	1.13	28.5	9.42	114	42	194	41.6	407	68.4	9630	22	13	3
GBR-11-4	<73.1	11.8	<1020	0.5	966	<0.0034	6	0.07	1.62	3.71	0.78	20.1	7.02	87.3	32.9	155	34.2	340	58.8	9390	36	19	4
GBR-11-5	<75.2	14.2	<930	0.5	1210	0.004	6.7	0.13	3.02	6.37	1.35	29.2	9.59	113	42.4	189	40.1	397	66.7	8780	17	11	2
GBR-11-6	<90.5	16.5	<981	0.6	1590	0.02	7.6	0.18	3.54	6.57	1.48	33.7	11.5	143	54	256	54.5	533	91.1	8640	20	9	2
GBR-11-7	<80.9	14.9	<788	0.6	1360	0.01	7.3	0.13	2.7	5.49	1.24	29	10.2	127	47.5	221	47.2	464	78.1	8550	25	13	3
GBR-11-8-	<72.9	11.8	<569	0.4	732	<0.00215	4.9	0.01	0.51	1.59	0.43	12.6	4.73	62.3	24.1	115	25.2	248	44.2	9490	122	70	10
GBR-11-8-	<70	8.64	<513	0.4	546	<0.0032	6.9	0.01	0.34	1.26	0.27	8.36	3.25	44	17.9	89.6	21.4	222	39.8	11100	289	171	20
GBR-11-9	<73	7.49	<498	0.4	544	<0.00250	6.3	0.01	0.36	1.1	0.27	7.65	3.06	42.1	17.2	89.3	22.2	251	43	10400	301	126	18
GBR-11-1	<73.3	13.1	<469	0.5	1100	0.01	6.9	0.06	1.57	4.5	1.12	25.6	8.69	104	38	171	36.4	355	58.8	9170	36	29	4
GBR-11-1	<83	11.8	<511	0.4	733	0.38	6.1	0.48	4.8	4.29	1.36	17.5	5.61	64.1	23.1	108	22.4	214	40.8	9860	9	3	1
GBR-11-12	<73.5	11.5	<425	0.5	704	0.003	5.6	0.02	0.5	1.73	0.45	12.2	4.70	62	23.9	113	25.6	263	42.2	9270	135	89	11
GBR-11-12	<78.5	9.04	<429	0.4	432	<0.0040	5.2	0.01	0.3	0.84	0.22	6.36	2.67	34.2	14.3	71.5	16.2	167	31.1	10400	271	111	17
GBR-11-1	<71.4	15.8	<343	0.3	552	<0.00217	5	0.02	0.58	1.61	0.4	10.4	3.75	47.7	18.7	87.7	20.2	222	34.7	8330	101	55	9
GBR-11-1	<71.2	11.6	<328	0.4	599	<0.0031	5.8	0.02	0.45	1.56	0.37	10.2	3.88	50.7	20	97.1	22.4	232	39.7	9110	162	103	13
GBR-11-1	<74	13.3	<325	0.4	679	<0.0023	5.3	0.04	0.97	2.77	0.61	14.6	5.12	63.5	23.4	107	24.6	260	39.2	8020	51	36	5
GBR-11-1	<69.5	10.6	<285	0.4	1010	<0.0032	7.9	0.06	1.57	4.54	0.9	22.7	8.17	99.9	35.6	157	36	409	53.2	8710	43	34	5
GBR-11-1	<69.7	13.2	<277	0.5	932	0.003	6.1	0.02	0.67	2.51	0.65	18.2	6.52	83.7	31.6	148	32.4	331	52.2	9110	97	78	9
GBR-11-1	<70.2	13	<266	0.4	940	0.002	6.5	0.04	1.13	3.47	0.87	20.9	7.29	87.4	32.5	146	32.6	334	49.8	8370	51	41	6
GBR-11-2	<64.3	15.2	<237	0.5	1080	<0.0033	6.8	0.05	1.45	4.48	1.14	25.2	8.46	104	36.6	162	36.1	364	56.2	8620	38	33	5
GBR-11s-1	<67.6	15.8	<129	0.5	1330	0.01	6.8	0.15	3.35	6.52	1.38	31.4	10.2	122	45.4	210	43.7	419	73	9100	16	9	2
GBR-11s-2	<72.2	10.7	<140	0.4	493	<0.0019	4.9	0.01	0.27	0.99	0.19	7.21	2.84	39	15.8	79.8	18	177	35.1	10400	263	152	18
GBR-11s-3	<67.2	12.4	<125	0.4	933	0.005	5.7	0.07	1.45	3.38	0.75	18.6	6.47	82.3	31.3	146	32.1	313	55	9960	39	21	4
GBR-11s-4	74.6	10.3	<132	0.4	1130	0.01	6.6	0.06	1.55	4.24	0.79	24.7	8.44	102	38.3	177	37.4	353	64.6	10400	38	27	4
GBR-11s-5	<64.3	9.99	<116	0.4	605	0.004	5.5	0.01	0.43	1.31	0.3	9.49	3.68	49.5	20	98.1	22.4	231	41	9880	183	91	13
GBR-11s-6	<64.5	4.5	<115	0.4	380	0.004	4.5	0.01	0.26	0.73	0.21	4.5	1.72	25.4	11.2	64.3	18.3	217	46	11600	414	117	18
GBR-11s-7	<69.3	9.81	<121	0.5	1060	<0.0030	7.2	0.03	0.98	3.19	0.69	20.6	7.47	94.1	35.8	167	36.4	361	61.8	11000	76	55	7
GBR-11s-8	<69.4	9.34	<117	0.4	570	<0.0032	5.1	0.01	0.39	1.28	0.24	8.74	3.47	46.5	18.7	92.8	22.2	224	40.2	10100	187	98	13
GBR-11s-9	<64.6	19.5	<108	0.7	1920	0.02	9	0.24	4.12	7.71	1.66	37.9	12.9	166	64.7	301	66	652	110.2	9440	21	9	2
GBR-11s-1	<66.2	7.67	<109	0.5	1110	<0.0028	7.9	0.03	1.09	3.43	0.75	21.6	7.77	96.6	36.3	173	38	381	68.2	10800	76	53	7
GBR-11s-1	<63	11.4	<103	0.5	956	<0.0031	6.2	0.04	0.91	2.92	0.62	18.1	6.53	83	31.4	144	32.2	325	52.9	9540	69	50	7

GBR-28

grain	Ca	Ti	Fe	Sr	Y	La	Ce	Pr	Nd	Sm	Eu	Gd	Tb	Dy	Ho	Er	Tm	Yb	Lu	Hf	Ce^{4+}/Ce^{3}	Ce/Ce*	Ce/Nd
GBR-28-1	<61.5	13.9	<98.6	0.5	1130	0.004	6.3	0.11	2.44	4.75	1.24	24.8	8.43	105	40.3	182	40.1	401	68.4	7780	15	12	3
GBR-28-2	<55.8	14.1	<88.1	0.5	929	0.004	6.3	0.09	2.08	4.7	1.08	22.4	7.5	90.7	34.4	159	35.8	391	53.2	7510	16	16	3
GBR-28-3	<59.1	10.4	<92.5	0.4	451	0.004	5.8	0.01	0.35	1.17	0.29	7.92	2.98	39.2	15.4	73.8	17.6	191	30	7950	137	129	17
GBR-28-4	<65	11.1	<102	0.3	519	0.01	5.8	0.02	0.43	1.4	0.22	9.08	3.38	45.1	18.2	84.3	19.6	201	36.3	9230	107	99	13

GBR-32

grain	Ca	Ti	Fe	Sr	Y	La	Ce	Pr	Nd	Sm	Eu	Gd	Tb	Dy	Ho	Er	Tm	Yb	Lu	Hf	Ce^{4+}/Ce^{3}	Ce/Ce*	Ce/Nd
GBR-32-1	<65.6	12.3	<189	0.4	598	<0.00201	5.7	0.02	0.49	1.71	0.42	10.8	4.11	52.5	20.4	96.5	21.8	227	38.4	9400	107	92	12
GBR-32-2	<66.1	12.6	<185	0.4	551	<0.00238	4.3	0.02	0.37	1.32	0.39	9.75	3.65	46	18.2	87.9	20.5	200	34.5	9030	115	94	12
GBR32-3	<58.5	13.7	<159	0.3	430	0.06	5	0.03	0.46	1.17	0.34	7.94	2.95	41.4	16.1	75.4	17.4	200	30.9	8620	118	63	11
GBR32-4	<63.1	13.4	<168	0.5	1120	0.01	6.5	0.11	2.45	5.27	1.15	26	8.84	103	38.1	176	38.4	374	60.6	8210	17	13	3
GBR32-5	<63.2	11	<164	0.3	469	<0.0030	3.9	0.02	0.42	1.37	0.31	8.17	3.05	40.3	15.8	77.1	17.4	179	32.2	9480	91	71	9
GBR32-6	<63.7	13.9	<153	0.5	1070	0.004	6.8	0.11	2.4	4.95	1.22	24.9	8.25	101	37.1	171	37.3	390	61.5	8270	19	13	3
GBR32-7	<64.7	15.4	<160	0.4	763	0.005	5.3	0.06	1.25	2.89	0.7	16.8	5.59	70.6	27.1	127	29.1	307	48.9	8360	35	23	4
GBR32-8	<78	15	<180	0.5	1320	0.004	6.4	0.13	2.93	5.69	1.25	29	9.69	122	46.2	210	43.2	410	76.5	9290	15	10	2
GBR32-9	<61.4	10.5	<139	0.3	511	<0.00227	6.2	0.01	0.43	1.40	0.31	8.95	3.45	43.9	17.4	81.4	19	198	32.8	8640	140	108	14
GBR32-10	<60.6	15.2	<136	0.5	1100	0.01	6.3	0.11	2.68	5.3	1.28	25.1	8.66	108	39.9	177	39.4	397	60.2	7690	16	11	2
GBR32-11	<64.4	12.2	<138	0.4	581	0.002	5.9	0.01	0.49	1.65	0.4	10.5	3.85	51.1	19.6	96.1	22.3	235	37.8	8880	118	94	12
GBR32-12	<60.1	7.85	<129	0.7	413	<0.00268	6.5	0.01	0.25	0.9	0.2	6.08	2.35	32.4	13.4	68.2	17	194	32.2	9750	340	221	26
GBR32-13	<53.3	12.4	<108	0.3	689	<0.00138	5	0.04	0.95	2.59	0.69	15.2	4.95	63.2	23.2	103	23.9	265	37.1	7040	40	33	5
GBR32-14	<60.4	11	<118	0.3	546	<0.0045	4.9	0.02	0.51	1.6	0.4	10.1	3.6	46.9	18.3	88.3	20.4	212	34.5	7950	92	71	10

GBR2-25

grain	Ca	Ti	Fe	Sr	Y	La	Ce	Pr	Nd	Sm	Eu	Gd	Tb	Dy	Ho	Er	Tm	Yb	Lu	Hf	Ce^{4+}/Ce^{3}	Ce/Ce*	Ce/Nd
2-25-1	<44.1	5.35	<22.4	0.4	584	0.06	4.6	0.03	0.36	1.09	0.41	6.89	2.7	39.3	17.7	94.8	25.2	299	62.3	8680	247	91	13
2-25-10	<42.1	5.84	<21.5	0.5	1310	0.01	6.2	0.1	1.93	4.4	1.68	23.3	8.2	106	41.6	206	49.3	532	109.5	8060	37	17	3
2-25-11	<44.6	3.07	<22.4	0.5	527	<0.0026	4.4	0.01	0.31	0.9	0.31	6.16	2.44	35.6	16	89.1	23.5	277	66.8	10700	304	93	14
2-25-2	<33.2	5.27	<17	0.4	367	0.004	3.7	0.005	0.54	1.22	0.51	6.47	2.13	27	11.9	55	15.7	225	27.7	6320	88	36	7
2-25-3	<36.8	3.60	<18.6	0.5	737	<0.0022	5.3	0.03	0.68	2.13	0.77	12.4	4.36	55.7	23.2	110	29.8	321	64	8930	96	55	8
2-25-4	<44.7	6.1	<22.4	0.4	655	<0.00192	4	0.04	0.83	2.14	0.85	11.8	4.06	52.4	20.8	103	25.2	293	57.8	8510	58	29	5
2-25-5	<42.2	11.1	<21.9	0.4	843	0.004	5.3	0.04	1.05	3.06	0.77	18.5	6.04	74.7	27.8	126	27.2	266	48.6	8310	41	34	5
2-25-6	<41.7	6.65	<21.6	0.4	357	<0.0024	6.1	0.01	0.18	0.66	0.15	4.75	1.81	25.9	11	58.1	14.5	163	32.7	10700	555	274	33
2-25-7	84.2	11.2	<21.9	3.5	566	<0.0031	4.5	0.02	0.48	1.41	0.33	9.4	3.61	46.6	18.5	87	20	202	37.9	8700	107	64	9
2-25-8	<41.3	7.97	<21.1	0.4	554	0.003	3.4	0.03	0.73	1.53	0.58	8.43	3.07	40.8	17	91.3	22.5	254	54.9	7640	67	22	5
2-25-9	<36.6	6.03	1070	0.6	609	<0.0014	4.6	0.04	0.57	1.56	0.64	9.01	3.19	46.8	19.3	104	28.1	339	60.8	7360	129	51	8

GBR2-26

grain	Ca	Ti	Fe	Sr	Y	La	Ce	Pr	Nd	Sm	Eu	Gd	Tb	Dy	Ho	Er	Tm	Yb	Lu	Hf	Ce^{4+}/Ce^{3}	Ce/Ce*	Ce/Nd
2-26-1	<42.8	3.71	<21.2	0.6	822	<0.0025	6.5	0.06	1.39	3.17	1.11	15.5	5.15	64.1	25.4	126	32.2	364	74.4	9130	42	25	5
2-26-2	<46.3	7.18	<23.1	0.4	231	<0.0029	3.3	0.01	0.18	0.55	0.19	3.05	1.17	16.6	7.1	37.9	10	117	26.6	9650	249	128	18
2-26-4	<43	2.91	<20.7	0.4	586	0.002	5	0.02	0.46	1.22	0.56	8.51	3.04	42.3	17.9	93.8	23.8	283	62.4	9340	147	66	11
2-26-5	<41.2	9.48	<20.8	0.6	1140	0.003	7.3	0.03	0.68	1.84	0.72	12.3	4.83	74.7	33.8	184	46.3	510	113.5	7880	175	67	11

GBR2-15

grain	Ca	Ti	Fe	Sr	Y	La	Ce	Pr	Nd	Sm	Eu	Gd	Tb	Dy	Ho	Er	Tm	Yb	Lu	Hf	Ce^{4+}/Ce^{3}	Ce/Ce*	Ce/Nd
2-15-1	<38.3	8.85	<38.8	0.4	537	0.002	5.4	0.02	0.59	1.46	0.37	8.99	3.29	42.6	17.6	88.1	21.4	236	42.9	10100	94	52	9
2-15-10	<36.7	14.8	<43.1	0.4	1360	0.005	6.5	0.12	2.68	5.75	1.34	31.6	10.5	129	47.8	213	46.4	445	75.6	9630	14	12	2
2-15-11	<39.3	6.12	146	0.6	892	0.003	11.8	0.03	0.71	1.93	0.5	12.2	4.6	62.2	26.6	149	38.3	444	96.2	13800	228	103	17
2-15-2	<39.1	14.3	42.3	0.6	1410	0.01	6.6	0.14	2.75	5.54	1.2	29.2	10	124	45.5	223	48.2	485	77.3	8770	16	11	2
2-15-3	<39.9	6.44	<41.1	0.4	288	<0.0026	5	0.01	0.2	0.55	0.16	3.49	1.4	19.2	8.6	48.5	12.9	157	32.7	11300	398	162	25
2-15-4	<38.6	9.92	<40.2	0.5	1040	<0.0029	7.6	0.04	1.04	3.34	0.76	20.7	7.41	91.6	34.6	163	36.7	368	62.8	10800	53	54	7
2-15-5	<37.1	11.1	<39.7	0.4	520	<0.0030	5.3	0.02	0.4	1.26	0.31	8.88	3.33	42	16.8	83	18.2	182	33.6	9240	118	96	13
2-15-7	<37.4	8.68	<41.9	1.1	675	0.002	5.5	0.02	0.55	1.6	0.39	10.9	4.01	53.6	22.4	110	25	270	49.6	10900	101	66	10
2-15-8	<41.2	12.3	<46.6	0.4	1450	0.01	7.3	0.13	2.94	6.26	1.37	32.4	10.7	131	48.4	222	48.1	449	83	9980	15	12	2
2-15-9	<40.7	13.3	<46.8	0.4	632	<0.0029	6.1	0.02	0.48	1.59	0.37	11.4	4.03	53.6	21.3	98.7	22.6	226	40.3	10200	110	96	13

GBR2-16

grain	Ca	Ti	Fe	Sr	Y	La	Ce	Pr	Nd	Sm	Eu	Gd	Tb	Dy	Ho	Er	Tm	Yb	Lu	Hf	Ce^{4+}/Ce^{3}	Ce/Ce*	Ce/Nd
2-16-1	<38.2	13.7	<46.3	0.4	1010	<0.0026	4.7	0.06	1.48	3.32	0.77	19.8	7.03	88.6	34.6	159	35.2	345	58.5	8720	33	16	3
2-16-10	<36	4.9	65.2	0.6	341	0.03	4.9	0.02	0.31	0.67	0.21	3.86	1.54	21.6	9.8	57.1	16.6	215	45.5	11600	399	77	16
2-16-11	<35.3	9.18	<51.6	0.4	1010	0.01	7.4	0.06	1.39	3.78	0.76	22.5	7.73	93.7	36.2	166	36	361	59.9	9600	50	33	5
2-16-2	<36.7	8.31	<46.1	0.4	680	0.002	6.3	0.02	0.54	1.68	0.37	11.7	4.25	54.3	21.3	105	24.2	257	42	10700	146	85	12
2-16-3	52.6	9.84	<50.6	0.5	1070	<0.00110	7.7	0.04	1.21	3.69	0.78	22.9	7.98	98.5	36.8	168	36.5	386	62.2	10300	60	44	6
2-16-4	<37	12.5	135	0.6	641	0.004	6.1	0.02	0.47	1.57	0.34	10.9	4.19	54.3	21.6	107	24.4	246	42.9	10200	169	102	13
2-16-5	<33.6	10.4	<44	0.5	1220	0.02	7.8	0.09	2.25	5.36	1	28.8	9.76	114	42.4	194	42.9	421	70.1	9750	29	19	3
2-16-6	<38.2	8.88	<48.9	0.5	1120	0.003	7.8	0.05	1.61	3.97	0.84	24	8.27	102	38.8	182	38.2	390	65.6	10500	47	27	5
2-16-7	<38.9	12	<52.7	0.6	512	<0.0035	5.9	0.01	0.43	1.33	0.33	8.23	3.36	42.7	16.9	84.5	19.4	203	35.3	10000	177	95	14
2-16-8	<39.1	12	<52.5	0.6	515	<0.0035	5.9	0.01	0.44	1.32	0.34	8.26	3.36	42.9	17	84.9	19.4	203	35.4	10100	176	92	13
2-16-9	<35.3	9.18	<49.3	0.4	482	<0.0029	4.9	0.02	0.36	1.18	0.26	8.09	3.09	40.6	16.3	80	18.2	191	32.6	9460	178	102	14

GBR2-17

grain	Ca	Ti	Fe	Sr	Y	La	Ce	Pr	Nd	Sm	Eu	Gd	Tb	Dy	Ho	Er	Tm	Yb	Lu	Hf	Ce^{4+}/Ce^{3}	Ce/Ce*	Ce/Nd
2-17-1	<31.6	5.99	<47	0.3	298	0.002	2.6	0.01	0.28	0.71	0.29	4.43	1.56	21.6	9.2	51	13.8	171	33.4	9100	162	53	9
2-17-2	<36	11.5	<55.6	0.5	1070	<0.0033	4.4	0.06	1.48	4.17	0.83	23.1	8.05	97.2	37.1	172	36.4	361	59.2	9000	24	19	3
2-17-3	<35.9	9.42	<56.1	0.4	592	<0.00215	4.7	0.01	0.37	1.29	0.3	9.43	3.76	48.9	19.9	98.7	22.7	238	42.4	9600	166	103	13
2-17-4	<36.6	14.3	<58	0.5	1300	0.01	6.6	0.15	2.89	5.8	1.07	29.2	9.93	119	44.4	201.9	43.1	422	72.9	9100	17	11	2
2-17-5	722.5	5.79	<53.7	1	293	<0.0033	9.8	0.63	2.9	1.12	0.29	4.37	1.56	20.6	8.8	49.9	13.5	168	38	9590	65	3	3
2-17-6	<33.7	12.1	<55.9	0.3	705	0.004	4.4	0.03	0.89	2.48	0.47	15.2	5.2	64.6	23.8	108	23.3	228	40.1	9290	42	32	5
2-17-10	<46.2	9.91	<25.2	0.4	668	<0.0029	6.2	0.02	0.52	1.49	0.31	11.2	4.16	52.7	21.5	99.9	22.9	228	44.4	9720	140	77	12
2-17-7	<46	8.46	<24.5	0.5	930	<0.0023	5.9	0.03	0.7	2.14	0.52	14.1	5.31	71.9	29.6	143	34.5	353	69.8	10200	111	60	8
2-17-8	<44.8	8.55	<24.7	0.4	680	0.02	4.3	0.02	0.51	1.69	0.41	10.7	4.07	52.9	21.7	105	24.5	256	49.9	9460	104	66	9
2-17-9	<43.9	6.7	<23.7	0.4	488	0.01	4.4	0.02	0.49	1.14	0.36	7.37	2.74	35.5	15.1	76.6	19.7	217	45.5	9690	137	48	9

GBR2-30

grain	Ca	Ti	Fe	Sr	Y	La	Ce	Pr	Nd	Sm	Eu	Gd	Tb	Dy	Ho	Er	Tm	Yb	Lu	Hf	Ce^{4+}/Ce^{3}	Ce/Ce*	Ce/Nd
2-30-1	<47.1	6.96	<22.2	0.4	422	<0.0025	2.8	0.02	0.38	1.1	0.41	6.37	2.3	31	13.2	72.9	19.2	228	48.9	8340	165	51	8
2-30-2	<44.5	6.26	<21.8	0.4	303.0	<0.0025	3	0.01	0.27	0.77	0.29	4.3	1.62	22.9	9.3	51.8	13.2	158	31.6	8740	244	75	11
2-30-3	<42.3	7.64	25.5	0.3	399	<0.00234	2.8	0.01	0.34	0.97	0.39	6.07	2.14	29.7	12.3	69.4	18.1	214	46.5	7670	187	54	8
2-30-4	<41.8	6.63	<19.6	0.3	301	<0.00229	3.1	0.02	0.28	0.76	0.25	4.65	1.63	22.6	9.4	52.1	13.2	153	30.6	7690	237	72	11
2-30-5	<43.4	7.34	<20.1	0.4	770	0.003	4	0.04	1.16	2.88	0.89	15.5	4.96	64.2	24.6	121	26.8	285	54.3	8130	44	20	3
2-30-6	<40	4.56	<19.3	0.3	283	0.002	2.7	0.01	0.2	0.6	0.21	3.78	1.45	20.1	8.7	48.1	12.4	149	32.5	8680	336	97	14
2-30-7	<42.7	5.43	<19.5	0.4	726	0.003	3.9	0.04	1.12	2.74	0.98	14.4	4.72	59.1	22.6	118	28.1	314	64.6	9020	51	20	3
2-30-8	<44.8	8.29	<20.6	0.5	678	0.01	4.3	0.03	0.44	1.19	0.49	7.67	2.85	43.6	19.7	112	27.6	306	73	8190	261	60	10
2-30-9	<40.4	6.38	<19	0.4	398	<0.00185	2.9	0.02	0.32	1	0.39	5.71	2.07	28.8	12.1	69.4	18.8	234	48.6	8010	212	66	9
2-30-10	<46.1	5.24	<21.1	0.4	702	0.003	3.9	0.03	0.96	2.53	0.97	13.5	4.46	56.4	21.9	112	26.9	300	61.2	9280	60	25	4
2-30-11	<40.5	4.57	<18.4	0.4	240	<0.00220	2.7	<0.0028	0.12	0.47	0.19	3.09	1.17	16.8	7.2	41	11.2	137	29.2	10400	585	197	22

GBR2-38

grain	Ca	Ti	Fe	Sr	Y	La	Ce	Pr	Nd	Sm	Eu	Gd	Tb	Dy	Ho	Er	Tm	Yb	Lu	Hf	Ce^{4+}/Ce^{3}	Ce/Ce*	Ce/Nd
2-38-1	45.8	5.12	<18.4	0.4	631	<0.0023	4.3	0.02	0.61	1.49	0.59	9.36	3.39	47.8	19.8	109	26.8	311	65.6	8760	119	40	7
2-38-2	<41.2	3.61	<18.2	0.4	292	<0.00162	4.3	0.01	0.23	0.62	0.25	3.99	1.46	21.3	8.9	50.7	13.3	161	34.1	8900	366	119	19
2-38-3	<41.2	7.81	<18.2	0.4	747	0.01	4.9	0.03	0.89	2.63	0.62	15.9	5.22	67.9	25	120	26.6	268	49.1	8980	51	37	5
2-38-4	<41.9	4.37	<18.5	0.3	334	<0.0023	4.2	0.01	0.26	0.8	0.31	4.86	1.74	25	10.1	57.2	14.9	188	38.4	8980	278	110	16
2-38-5	<44.1	5.93	<19.4	0.4	510	<0.00249	5.9	0.02	0.37	1.13	0.41	6.56	2.42	35.9	15.4	88.6	22.9	280	58.8	9270	307	115	16
2-38-6	<42	10.22	<18.6	0.5	771	<0.00194	5.4	0.03	0.58	1.64	0.62	10.3	3.69	56.5	23.6	134	33.7	412	79.8	7480	172	61	9
2-38-7	<40.9	4.92	<17.8	0.3	280	<0.00269	2.6	0.01	0.21	0.66	0.32	4.24	1.58	22	9	49.7	12.4	147	29.5	7590	208	92	13
2-38-9	<41.7	2.94	<18.1	0.6	614	<0.00230	7.3	0.02	0.36	1.04	0.38	7.73	2.95	43.6	18.6	107	28.2	337	75	10500	441	134	20
2-38-10	<43	5.62	<18.8	0.4	536	<0.0026	4.8	0.05	0.87	1.82	0.74	10.2	3.19	43.9	16.8	91.1	22.8	276	55.1	7850	76	27	6
2-38-11	55.1	8.49	<16.7	1.2	748	0.04	6	0.05	1.01	2.32	0.8	13.1	4.55	62.4	23.7	125	30	341	64.2	8790	77	31	6

For Ce^{4+}/Ce^{3+} calculation see Symthe and Brenan 2016

Appendix A2-4. U-Pb age dating and the data of reference zircon

Mineralized tonalites

GBR-2 (mineralized tonalite group B)

Identifier	207Pb/235U	2s % (Sx)	207Pb/235U Ssys %	Stotal	206Pb/238U	2s % (Sx)	206Pb/238U Ssys %	Stotal	Error correlation
GBR-2-1	0.221	24	6.8	25	0.032	4.6	3.4	5.7	0.2
GBR-2-2	0.229	24	6.8	25	0.033	5	3.4	6	0.2
GBR-2-3	0.242	24	6.8	25	0.033	5.4	3.4	6.4	0.3
GBR-2-4	0.298	22	6.8	23	0.033	4.8	3.4	5.9	0.3
GBR-2-5	0.274	28	6.8	29	0.033	5.4	3.4	6.4	0.2
GBR-2-6	0.225	30	6.8	30.8	0.033	5.0	3.4	6	0.2
GBR-2-7	0.241	22	6.8	23	0.033	4.4	3.4	5.6	0.2
GBR-2-8	0.223	11	6.8	13.3	0.033	3.4	3.4	4.8	0.4
GBR-2-9	0.219	17	6.8	18.3	0.033	4	3.4	5	0.3
GBR-2-10	0.235	22	6.8	23	0.033	4.8	3.4	5.9	0.3
GBR-2-11	0.261	19	6.8	20.2	0.033	4.4	3.4	5.6	0.3
GBR-2-12	0.267	22	6.8	23	0.033	4.6	3.4	5.7	0.2
GBR-2-13	0.190	32	6.8	33	0.033	5.4	3.4	6.4	0.2
GBR-2-14	0.238	18	6.8	18.9	0.033	4.2	3.4	5.4	0.3
GBR-2-15	0.240	30	6.8	31	0.033	5.4	3.4	6.4	0.2
GBR-2-16	0.303	20	6.8	21	0.034	4.8	3.4	5.9	0.3
GBR-2-17	0.215	26	6.8	27	0.034	5	3.4	6	0.2
GBR-2-18	0.277	17	6.8	18.1	0.034	4.4	3.4	5.6	0.3
GBR-2-19	0.232	10	6.8	11.9	0.034	3.4	3.4	4.8	0.4
GBR-2-20	0.203	28	6.8	29	0.034	4.8	3.4	5.9	0.2
GBR-2-21	0.295	28	6.8	29	0.034	6	3.4	7	0.2
GBR-2-22	0.219	26	6.8	27	0.035	5	3.4	6	0.2
GBR-2-23	0.266	24	6.8	25	0.035	4.8	3.4	5.9	0.2
GBR-2-24	0.217	24	6.8	25	0.035	4.6	3.4	5.7	0.2
GBR-2-25	0.326	26	6.8	27	0.035	5.4	3.4	6.4	0.2
GBR-2-26	0.220	32	6.8	33	0.035	5.2	3.4	6.2	0.2
GBR-2-27	0.223	24	6.8	25	0.035	4.6	3.4	5.7	0.2

Concordia Age = 213.2 ±2.4 Ma
(2σ, decay-const. errs included)
MSWD (of concordance) = 0.62,
Probability (of concordance) = 0.43

X-Y Weighted Mean:
X = 0.2374±0.010 2σ
Y = 0.03362±0.00038
X-Y error correlation = +0.26
MSWD = 0.98, Probability =0.52

GBR-7(mineralized tonalite group A)

Identifier	207Pb/235U	2s % (Sx)	207Pb/235U Ssys %	Stotal	206Pb/238U	2s % (Sx)	206Pb/238U Ssys %	Stotal	Error correlation
GBR-7-1	0.2	28	6.8	28.8	0.034	4.8	3.4	5.9	0.2
GBR-7-2	0.2	24	6.8	24.9	0.035	4.8	3.4	5.9	0.2
GBR-7-3	0.2	30	6.8	30.8	0.034	5.0	3.4	6	0.2
GBR-7-4	0.2	20	6.8	21.1	0.034	5	3.4	6	0.3
GBR-7-5	0.2	20	6.8	20.9	0.035	4.4	3.4	5.6	0.2
GBR-7-6	0.2	22	6.8	23	0.034	5	3.4	6	0.2
GBR-7-7	0.3	18	6.8	19.4	0.035	4.2	3.4	5.4	0.2
GBR-7-8	0.3	22	6.8	23	0.034	5.4	3.4	6.4	0.2
GBR-7-9	0.3	24	6.8	24.9	0.035	5.2	3.4	6.2	0.2
GBR-7-10	0.3	18	6.8	19	0.034	4.8	3.4	5.9	0.3
GBR-7-11	0.3	22	6.8	23	0.036	5	3.4	6	0.2
GBR-7-12	0.3	15	6.8	16.8	0.034	4.2	3.4	5.4	0.3
GBR-7-13	0.3	16	6.8	17	0.035	4.4	3.4	5.6	0.3
GBR-7-14	0.3	20	6.8	21.1	0.034	5.2	3.4	6.2	0.3
GBR-7-15	0.3	10	6.8	12.4	0.034	3.8	3.4	5.1	0.4
GBR-7-16	0.3	17	6.8	18.1	0.034	4.6	3.4	5.7	0.3

Concordia Age = 218.9 ±3.1 Ma
(2σ, decay-const. errs included)
MSWD (of concordance) = 0.68,
Probability (of concordance) = 0.41

X-Y Weighted Mean:
X = 0.2454±0.012 2σ
Y = 0.03452±0.00050
X-Y error correlation = +0.25
MSWD = 0.67, Probability =0.91

GBR-12 (mineralized tonalite group C)

Identifier	207Pb/235U	2s % (Sx)	207Pb/235U Ssys %	Stotal	206Pb/238U	2s %	206Pb/238U Ssys %	Stotal	Error correlation
GBR-12-1	0.215	26	6.8	26.9	0.0326	5.6	3.4	6.6	0.2
GBR-12-2	0.216	34	6.8	34.7	0.0338	6.4	3.4	7.2	0.2
GBR-12-3	0.226	17	6.8	17.9	0.0325	6	3.4	6.9	0.4
GBR-12-4	0.228	60	6.8	60.4	0.0328	5	3.4	6	0.1
GBR-12-5	0.231	14	6.8	15.9	0.0321	4.6	3.4	5.7	0.4
GBR-12-6	0.238	16	6.8	17.6	0.0324	5.6	3.4	6.6	0.4
GBR-12-7	0.238	20	6.8	21.1	0.0318	5	3.4	6	0.3
GBR-12-8	0.238	24	6.8	24.9	0.0334	5.8	3.4	6.7	0.3
GBR-12-9	0.25	22	6.8	23	0.0355	6.6	3.4	7.4	0.3
GBR-12-10	0.260	30	6.8	30.8	0.0309	6	3.4	6.9	0.2
GBR-12-11	0.3	14	6.8	15.5	0.0321	6	3.4	6.9	0.4

Concordia Age = 206.8 ±4.0 Ma
(2σ, decay-const. errs included)
MSWD (of concordance) = 1.7,
Probability (of concordance) = 0.19

X-Y Weighted Mean:
X = 0.2359±0.016 2σ
Y = 0.03256±0.00064
X-Y error correlation = +0.23
MSWD = 0.72, Probability =0.81

GBR-15(mineralized tonalite group C)

Identifier	207Pb/235U	2s % (Sx)	207Pb/235U Ssys %	Stotal	206Pb/238U	2s %	206Pb/238U Ssys %	Stotal	Error correlation
GBR-15-1	0.2	38	6.8	38.6	0.03	6.4	3.4	7.2	0.2
GBR-15-2	0.2	32	6.8	32.7	0.03	6	3.4	6.9	0.2
GBR-15-3	0.2	28	6.8	28.8	0.03	5.8	3.4	6.7	0.2
GBR-15-4	0.2	28	6.8	28.8	0.03	5.8	3.4	6.7	0.2
GBR-15-5	0.2	17.6	6.8	18.9	0.03	4.8	3.4	5.9	0.3
GBR-15-6	0.2	28	6.8	28.8	0.03	5.6	3.4	6.6	0.2
GBR-15-7	0.2	11.8	6.8	13.6	0.03	4	3.4	5.3	0.3
GBR-15-8	0.2	26	6.8	26.9	0.03	5.4	3.4	6.4	0.2
GBR-15-9	0.2	16.4	6.8	17.7	0.03	4.6	3.4	5.7	0.3
GBR-15-10	0.3	28	6.8	28.8	0.03	6	3.4	6.9	0.2
GBR-15-11	0.3	16	6.8	17.4	0.03	4.4	3.4	5.6	0.3
GBR-15-12	0.3	22	6.8	23.0	0.03	6.2	3.4	7.1	0.3

Concordia Age = 205.9 ±3.7 Ma
(2σ, decay-const. errs included)
MSWD (of concordance) = 0.84,
Probability (of concordance) = 0.36

X-Y Weighted Mean:
X = 0.2313±0.015 2σ
Y = 0.03244±0.00059
X-Y error correlation = +0.25
MSWD = 0.65, Probability =0.89

GBR-16(mineralized tonalite group C)

Identifier	207Pb/235U	2s % (Sx)	207Pb/235U Ssys %	Stotal	206Pb/238U	2s % (Sx)	206Pb/238U Ssys %	Stotal	Error correlation
GBR-16-1	0.2	30	6.8	30.8	0.03	5.4	3.4	6.4	0.2
GBR-16-2	0.2	30	6.8	30.8	0.031	6.6	3.4	7.4	0.2
GBR-16-3	0.2	28	6.8	28.8	0.032	5.2	3.4	6.2	0.2
GBR-16-4	0.3	24	6.8	24.9	0.032	5.4	3.4	6.4	0.3
GBR-16-5	0.2	36	6.8	36.6	0.031	6.6	3.4	7.4	0.2
GBR-16-6	0.2	24	6.8	24.9	0.033	5.2	3.4	6.2	0.2
GBR-16-7	0.3	30	6.8	30.8	0.033	6	3.4	6.9	0.2

Concordia Age = 201.9 ±5.0 Ma
(2σ, decay-const. errs included)
MSWD (of concordance) = 0.037,
Probability (of concordance) = 0.85

X-Y Weighted Mean:
X = 0.222±0.024 2σ
Y = 0.03181±0.00080
X-Y error correlation = +0.20
MSWD = 0.64, Probability =0.81

GBR-21(mineralized tonalite group C)

Identifier	207Pb/235U	2s % (Sx)	207Pb/235U Ssys %	Stotal	206Pb/238U	2s % (Sx)	206Pb/238U Ssys %	Stotal	Error correlation
GBR-21-1	0.2	26	6.8	26.9	0.033	5.6	3.4	6.6	0.2
GBR-21-2	0.2	34	6.8	34.7	0.034	6.4	3.4	7.2	0.2
GBR-21-3	0.2	16.6	6.8	17.9	0.033	6	3.4	6.9	0.4
GBR-21-4	0.2	60	6.8	60.4	0.033	5	3.4	6	0.1
GBR-21-5	0.2	14.4	6.8	15.9	0.032	4.6	3.4	5.7	0.4
GBR-21-6	0.2	16.2	6.8	17.6	0.032	5.6	3.4	6.6	0.4
GBR-21-7	0.2	20	6.8	21.1	0.032	5	3.4	6	0.3
GBR-21-8	0.2	24	6.8	24.9	0.033	5.8	3.4	6.7	0.3
GBR-21-9	0.3	30	6.8	30.8	0.031	6	3.4	6.9	0.2

Concordia Age = 205.6 ±4.4 Ma
(2σ, decay-const. errs included)
MSWD (of concordance) = 0.88,
Probability (of concordance) = 0.35

X-Y Weighted Mean:
X = 0.2321±0.017 2σ
Y = 0.03240±0.00070
X-Y error correlation = +0.29

Mineralized tonalite group C

Identifier	207Pb/235U	2s % (Sx)	207Pb/235U Ssys %	Stotal	206Pb/238U	2s % (Sx)	206Pb/238U Ssys %	Stotal	Error correlation
GBR-12-1	0.2	26	6.8	26.9	0.033	5.6	3.4	6.6	0.2
GBR-12-2	0.2	34	6.8	34.7	0.034	6.4	3.4	7.2	0.2
GBR-12-3	0.2	16.6	6.8	17.9	0.033	6	3.4	6.9	0.4
GBR-12-4	0.2	60	6.8	60.4	0.033	5	3.4	6	0.1
GBR-12-5	0.2	14.4	6.8	15.9	0.032	4.6	3.4	5.7	0.3
GBR-12-6	0.2	16.2	6.8	17.6	0.032	5.6	3.4	6.6	0.3
GBR-12-7	0.2	20	6.8	21.1	0.032	5	3.4	6	0.3
GBR-12-8	0.2	24	6.8	24.9	0.033	5.8	3.4	6.7	0.2
GBR-12-9	0.3	22	6.8	23	0.036	6.6	3.4	7.4	0.3
GBR-12-10	0.3	30	6.8	30.8	0.031	6	3.4	6.9	0.2
GBR-15-1	0.2	38	6.8	38.6	0.031	6.4	3.4	7.2	0.2
GBR-15-2	0.2	32	6.8	32.7	0.032	6	3.4	6.9	0.2
GBR-15-3	0.2	28	6.8	28.8	0.031	5.8	3.4	6.7	0.2
GBR-15-4	0.2	28	6.8	28.8	0.032	5.8	3.4	6.7	0.2
GBR-15-5	0.2	17.6	6.8	18.9	0.032	4.8	3.4	5.9	0.3
GBR-15-6	0.2	28	6.8	28.8	0.033	5.6	3.4	6.6	0.2
GBR-15-7	0.2	11.8	6.8	13.6	0.033	4	3.4	5.3	0.3
GBR-15-8	0.2	26	6.8	26.9	0.034	5.4	3.4	6.4	0.2
GBR-15-9	0.2	16.4	6.8	17.7	0.032	4.6	3.4	5.7	0.3
GBR-15-10	0.3	28	6.8	28.8	0.033	6	3.4	6.9	0.2
GBR-15-11	0.3	16	6.8	17.4	0.033	4.4	3.4	5.6	0.3
GBR-15-12	0.3	22	6.8	23	0.033	6.2	3.4	7.1	0.3
GBR-16-1	0.2	30	6.8	30.8	0.030	5.4	3.4	6.4	0.2
GBR-16-2	0.2	30	6.8	30.8	0.031	6.6	3.4	7.4	0.2
GBR-16-3	0.2	28	6.8	28.8	0.032	5.2	3.4	6.2	0.2
GBR-16-4	0.3	24	6.8	24.9	0.031	6.6	3.4	7.4	0.2
GBR-16-5	0.2	36	6.8	36.6	0.033	5.2	3.4	6.2	0.2
GBR-16-6	0.2	24	6.8	24.9	0.033	6	3.4	6.9	0.2
GBR-16-7	0.3	30	6.8	30.8	0.033	6	3.4	6.9	0.2
GBR-21-1	0.2	26	6.8	26.9	0.033	5.6	3.4	6.6	0.2
GBR-21-2	0.2	34	6.8	34.7	0.034	6.4	3.4	7.2	0.2
GBR-21-3	0.2	16.6	6.8	17.9	0.033	6	3.4	6.9	0.4
GBR-21-4	0.2	60	6.8	60.4	0.033	5	3.4	6.0	0.1
GBR-21-6	0.2	16.2	6.8	17.6	0.032	5.6	3.4	6.6	0.3

Concordia Age = 205.8 ±2.1 Ma
(2σ, decay-const. errs included)
MSWD (of concordance) = 2.3,
Probability (of concordance) = 0.13

X-Y Weighted Mean:
X = 0.2310±0.0086 2σ
Y = 0.03243±0.00034
X-Y error correlation = +0.25

Uncertainties quoted without components related to systematic error unless Stotal: Total systematic uncertainties (Ssys): ^{207}Pb/^{235}U = 6.8 % (2s), ^{206}Pb/^{238}U = 3.4 % (2s). Stotal is used for age calculation. Stotal = $(Sx^2 + Sy^2 + \varepsilon'^2 + \lambda^2)^{1/2}$

No excess variance was detected in using weighted average calculations on reference zircon, 91500 or Plesovice zircon

Decay constant	Decay constant error	%	
137.8	0.045	0.033	Hiess et al., 2012

Ɛ' %	Excess variance of the validation materials (Plesovice)
Sx	Ratio uncertainty for samples
Sy	Ratio uncertainty for reference materail (91500)
λ	Decay constant error
b.d.l	below detection limits

Unmineralzied Tonalites

GBR2-16

Identifier	207Pb/235U	2s % (Sx)	207Pb/23	Stotal	206Pb/238U	2s % (Sx)	206Pb/23	Stotal	Error correlation
GBR2-16-1	0.3	19.6	6.8	20.7	0.036	6.2	3.4	7.1	0.3
GBR2-16-2	0.3	26	6.8	26.9	0.036	5.6	3.4	6.6	0.2
GBR2-16-3	0.3	20	6.8	21.1	0.036	4.8	3.4	5.9	0.3

Concordia Age = 226.8 ±8.3 Ma
(2σ, decay-const. errs included)
MSWD (of concordance) = 0.86,
Probability (of concordance) = 0.36

X-Y Weighted Mean:
X = 0.265±0.034 2σ
Y = 0.03581±0.0013
X-Y error correlation = +0.29
MSWD = 0.062, Probability =0.993

GBR2-25

Identifier	207Pb/235U	2s % (Sx)	207Pb/23	Stotal	206Pb/238U	2s % (Sx)	206Pb/23	Stotal	Error correlation
GBR2-25-1	0.27453	26	6.8	26.9	0.036071	5.8	3.4	6.7	0.3
GBR2-25-2	0.27506	24	6.8	24.9	0.035675	5	3.4	6	0.2

Concordia Age = 227 ±10 Ma
(2σ, decay-const. errs included)
MSWD (of concordance) = 0.99,
Probability (of concordance) = 0.32

X-Y Weighted Mean:
X = 0.275±0.050 2σ
Y = 0.03585±0.0016
X-Y error correlation = +0.25
MSWD = 0.032, Probability =0.97

GBR2-30

Identifier	207Pb/235U	2s % (Sx)	207Pb/23	Stotal	206Pb/238U	2s % (Sx)	206Pb/23	Stotal	Error correlation
GBR2-30-1	0.2	26	6.8	26.9	0.037	6.2	3.4	7.1	0.3
GBR2-30-2	0.3	24	6.8	24.9	0.037	5.8	3.4	6.7	0.3

Concordia Age = 232 ±11 Ma
(2σ, decay-const. errs included)
MSWD (of concordance) = 0.022,
Probability (of concordance) = 0.88

X-Y Weighted Mean:
X = 0.261±0.048 2σ
Y = 0.03671±0.0018
X-Y error correlation = +0.27
MSWD = 0.18, Probability =0.84

GBR2-38

Identifier	207Pb/235U	2s % (Sx)	207Pb/23	Stotal	206Pb/238U	2s % (Sx)	206Pb/23	Stotal	Error correlation
GBR2-38-1	0.2	24	6.8	24.9	0.036	6.2	3.4	7.1	0.3
GBR2-38-2	0.3	19.2	6.8	20.4	0.037	5.2	3.4	6.2	0.3
GBR2-38-3	0.3	16.6	6.8	17.9	0.037	4.6	3.4	5.7	0.3
GBR2-38-4	0.3	22	6.8	23	0.037	6.6	3.4	7.4	0.3

Concordia Age = 231.7 ±7.4 Ma
(2σ, decay-const. errs included)
MSWD (of concordance) = 0.33,
Probability (of concordance) = 0.56

X-Y Weighted Mean:
X = 0.264±0.028 2σ
Y = 0.03659±0.0012
X-Y error correlation = +0.31
MSWD = 0.20, Probability =0.98

Unmineralzied tonalites

Identifier	207Pb/235U	2s % (Sx)	207Pb/23	Stotal	206Pb/238U	2s % (Sx)	206Pb/23	Stotal	Error correlation
GBR2-16-1	0.3	19.6	6.8	20.7	0.036	6.2	3.4	7.1	0.3
GBR2-16-2	0.3	26	6.8	26.9	0.036	5.6	3.4	6.6	0.2
GBR2-17-1	0.3	20	6.8	21.1	0.036	4.8	3.4	5.9	0.3
GBR2-25-1	0.3	24	6.8	24.9	0.036	5	3.4	6	0.2
GBR2-25-2	0.3	24	6.8	24.9	0.036	5	3.4	6	0.2
GBR2-30-1	0.2	26	6.8	26.9	0.037	6.2	3.4	7.1	0.3
GBR2-30-2	0.3	24	6.8	24.9	0.037	5.8	3.4	6.7	0.3
GBR2-38-1	0.2	24	6.8	24.9	0.036	6.2	3.4	7.1	0.3
GBR2-38-2	0.3	19.2	6.8	20.4	0.037	5.2	3.4	6.2	0.3
GBR2-38-3	0.3	16.6	6.8	17.9	0.037	4.6	3.4	5.7	0.3
GBR2-38-4	0.3	22	6.8	23	0.037	6.6	3.4	7.4	0.3

Concordia Age = 229.2 ±4.4 Ma
(2σ, decay-const. errs included)
MSWD (of concordance) = 1.8,
Probability (of concordance) = 0.18

X-Y Weighted Mean:
X = 0.2650±0.018 2σ
Y = 0.03619±0.00071
X-Y error correlation = +0.28
MSWD = 0.20, Probability =1.000

91500 zircon (refrence material)

Identifier	207Pb/235U	2s %	Sy %	206Pb/238U	2s %	Sy %	Error correla	Pb206 cps	Pb207 cps	Pb208 cps	Th232 cps	U238 cps
out stanc	1.8	7	7	0.2	3.4	3.4	0.5	33038	1760	1027	53977	666738
out stanc	1.8	7	7	0.2	3.6	3.6	0.5	16340	1261	1912	33718	99063
out stanc	1.8	7.6	7.6	0.2	3.8	3.8	0.5	16390	1290	1928	33840	99346
out stanc	1.8	6.8	6.8	0.2	3.4	3.4	0.5	16572	1295	1967	34373	101151
out stanc	1.9	7	7	0.2	3.6	3.6	0.5	16429	1272	1910	33966	100148
out stanc	1.9	7.8	7.8	0.2	4	4	0.5	16571	1259	1899	33965	101222
out stanc	1.9	6.2	6.2	0.2	3	3	0.5	16372	1249	1950	34546	99776
out stanc	1.9	6.2	6.2	0.2	3	3	0.5	14760	1177	1698	30094	88396
out stanc	2.0	6.4	6.4	0.2	3	3	0.5	15044	1150	1768	31102	89980
out stanc	1.9	6.2	6.2	0.2	3	3	0.5	13446	1004	1527	26528	77517
out stanc	1.8	6.6	6.6	0.2	3.2	3.2	0.5	16477	1232	1912	34396	100254
out stanc	1.9	6.4	6.4	0.2	3.2	3.2	0.5	15853	1194	1827	33769	97179
out stanc	1.8	7	7	0.2	3.6	3.6	0.5	16425	1263	1944	34455	101619
out stanc	1.9	6.4	6.4	0.2	3.2	3.2	0.5	14665	1108	1707	30898	87433
out stanc	1.8	6.8	6.8	0.2	3.2	3.2	0.5	15631	1181	1839	32533	91059
out stanc	1.8	7	7	0.2	3.4	3.4	0.5	13326	988	1554	27074	79439
out stanc	1.9	6.4	6.4	0.2	3.2	3.2	0.5	13493	992	1527	27155	80200
out stanc	1.8	6.6	6.6	0.2	3.4	3.4	0.5	13769	1029	1546	28183	81639
out stanc	1.8	6.8	6.8	0.2	3.4	3.4	0.5	13302	1015	1542	27373	79798
out stanc	1.8	6.8	6.8	0.2	3.6	3.6	0.5	15360	1173	1774	30578	95069
out stanc	1.8	6.4	6.4	0.2	3.2	3.2	0.5	14780	1116	1651	29958	91432
		Average	6.7			3.4						

91500 ag 1065.4 ± 0.6 Ma

Concordia Age = 1062.0 ±6.9 Ma
(2σ, decay-const. errs included)
MSWD (of concordance) = 0.24,
Probability (of concordance) = 0.62

X-Y Weighted Mean:
X = 1.851±0.027 2σ
Y = 0.17899±0.0013
X-Y error correlation = +0.50
MSWD = 0.60, Probability =0.98

Plesovice zircon (validation material)

Identifier	207Pb/235U	2s %	Sy %	206Pb/238U	2s %	Sy %	Error correla	Reference variance a	Reference va	Determined varian	Determined	Ɛ' %		Pb206 cps	Pb207 cps	Pb208 cps	Th232 cps	U238 cps
out stanc	0.4	6.2	6.2	0.1	3.2	3.2	0.5	0.4	0.1	2.3	0.7	0.6		33038	1760	1027	53977	666738
out stanc	0.4	6.4	6.4	0.1	3.4	3.4	0.5	0.4	0.1	2.3	0.7	0.6		24679	1338	720	37614	505650
out stanc	0.4	6.2	6.2	0.1	3.4	3.4	0.5	0.4	0.1	2.3	0.7	0.6		35947	1959	1098	58626	727093
out stanc	0.4	5.6	5.6	0.1	3	3	0.5	0.4	0.1	2.3	0.7	0.6		27220	1429	805	43293	550794
out stanc	0.4	5.4	5.4	0.1	3	3	0.6	0.4	0.1	2.3	0.7	0.6		32093	1693	929	50925	621681
out stanc	0.4	5.8	5.8	0.1	3	3	0.5	0.4	0.1	2.3	0.7	0.6		25539	1401	816	38189	492747
out stanc	0.4	5.8	5.8	0.1	3.2	3.2	0.6	0.4	0.1	2.3	0.7	0.6		37032	2010	1131	59436	752641
out stanc	0.4	5.6	5.6	0.1	3	3	0.5	0.4	0.1	2.3	0.7	0.6		30692	1667	910	49224	609658
out stanc	0.4	5.8	5.8	0.1	3.2	3.2	0.6	0.4	0.1	2.3	0.7	0.6		24773	1329	680	36648	499611
out stanc	0.4	5.6	5.6	0.1	3.2	3.2	0.6	0.4	0.1	2.3	0.7	0.6		30655	1638	944	49393	602295
out stanc	0.4	6.4	6.4	0.1	3.2	3.2	0.5	0.4	0.1	2.3	0.7	0.6		34053	1888	1046	55449	659806
out stanc	0.4	6.4	6.4	0.1	3.4	3.4	0.5	0.4	0.1	2.3	0.7	0.6		26625	1423	781	41861	520589
out stanc	0.4	5.6	5.6	0.1	3.2	3.2	0.6	0.4	0.1	2.3	0.7	0.6		33724	1829	1055	55050	656612
out stanc	0.4	6.6	6.6	0.1	3.2	3.2	0.5	0.4	0.1	2.3	0.7	0.6		50382	2677	2501	137882	968703
out stanc	0.4	6.2	6.2	0.1	3.2	3.2	0.5	0.4	0.1	2.3	0.7	0.6		34558	1838	1039	55796	681967
out stanc	0.4	6.4	6.4	0.1	3.2	3.2	0.5	0.4	0.1	2.3	0.7	0.6		50804	2735	2545	142131	1000598
out stanc	0.4	6.4	6.4	0.1	3.4	3.4	0.5	0.4	0.1	2.3	0.7	0.6		13493	992	1527	27155	80200
out stanc	0.4	6.4	6.4	0.1	3.2	3.2	0.5	0.4	0.1	2.3	0.7	0.6		52259	2782	2549	140306	998213
out stanc	0.4	6.8	6.8	0.1	3.6	3.6	0.5	0.4	0.1	2.3	0.7	0.6		42237	2253	1735	94963	827035
out stanc	0.4	6.6	6.6	0.1	3.4	3.4	0.5	0.4	0.1	2.3	0.7	0.6		51730	2754	2575	139556	984681
out stanc	0.4	6.2	6.2	0.1	3.4	3.4	0.5	0.4	0.1	2.3	0.7	0.6		53255	3034	3062	144515	1050460

Plesovice 337.13 ± 0.37 Ma

Concordia Age = 337.4 ±2.3 Ma
(2σ, decay-const. errs included)
MSWD (of concordance) = 0.057,
Probability (of concordance) = 0.81

X-Y Weighted Mean:
X = 0.3946±0.0052 2σ
Y = 0.05372±0.00038
X-Y error correlation = +0.5
MSWD = 0.53, Probability :

NIST612 (calibration and validation material. Jochum et al.. 2011)

Identifier	Al27	Si29	P31	Ca42	Ti49	Fe54	Sr88	Y89	Zr91	Nb93	Mo95	Ba137	La139	Ce140	Pr141	Nd146	Sm147	Eu151	Gd157	Tb159	Dv163	Ho165	Er167	Tm169	Yb173	Lu175	Hf177	Pb206	Pb207	Pb208	Th232	U235	U238
NIST612-1	10233.2	337028.5	41.2	80407.7	42.5	b.d.l	73.3	36.6	35.5	36.9	35.3	35.7	33.9	35.8	35.3	35.5	34.9	32.4	34.8	35.1	33	36.2	35.6	34.3	36.3	34.5	33.8	35.4	35	35.4	34.9	34.7	34.2
NIST612-2	10490.3	337028.5	49	82171.7	43.2	b.d.l	74.7	36.8	37	38.2	36.4	38	34.4	36.6	35.8	36.8	36.0	33.9	36.3	36.3	34.3	36.9	36.3	35.3	37.3	35.5	35.4	35.6	35.9	35.9	36.2	34.2	34.5
NIST612-3	10402.4	337028.5	38.5	81566	41.7	b.d.l	76.6	37.1	37.5	37.1	36.8	37.5	34.7	36.8	36.6	37.2	36.5	34.0	35.8	36.4	33.6	37.1	36.9	35.4	38.4	35.5	35.4	36.4	36.3	36.6	37	33.4	36.5
NIST612-4	10744.6	337028.5	59.1	84738.5	44.2	b.d.l	79.1	39.1	38.8	39.1	37.7	38.7	36.5	38.5	38.1	39.8	38.1	35.8	37.9	38	35.9	38.6	38.6	37.4	39.9	37.5	37	38.4	39	38.3	38.9	35.3	37.6
NIST612-5	10884.1	337028.5	42.6	85146.8	43.9	b.d.l	79.2	38.9	39	39.1	37.4	39.7	36.5	39.3	38.1	39.2	38.3	36.1	37.7	37.4	36.1	39	38.2	37.4	40.1	37.5	37.2	39.4	39	38.9	38.1	37.6	38.5
NIST612-6	10460.7	337028.5	38.9	82001.7	44.3	b.d.l	77.5	37.8	36.4	37.8	36.6	38.3	34.9	38	37	37.9	36.8	34.8	36.8	37.3	34.9	37.4	37	36	37.9	36	35.9	38.4	38.1	37.8	37.3	41.4	37.5
NIST612-7	10889.2	337028.5	48.6	87298.5	45	b.d.l	79	38.8	38.2	39.5	37.6	39.8	36.2	38.3	38.3	38.9	38.1	35.8	37.7	37.9	36.2	38.8	38.8	37.2	40.3	37.7	37.2	39	39.2	39	38.2	38.1	37.2
NIST612-8	11212.1	337028.5	36.9	89989.2	46.7	b.d.l	83.4	40.2	38.3	40.9	39.3	42.8	37.9	40.1	40	40.7	40.2	38.1	39.8	39.5	37.5	40.1	40.2	38.6	40.5	39	38.5	40.7	41.7	41.1	39.6	39.6	39.4
NIST612-9	10736.4	337028.5	55.4	89093.9	42.9	b.d.l	79	38	38.4	39.5	37.7	39.8	36.3	38.8	38.7	40.5	38.1	36	36.9	37.9	35.9	38.3	38.3	36.8	39.3	37.2	37.2	39.4	40.2	40.2	37.8	40.5	38.5
NIST612-10	11042.1	337028.5	37.7	84998.1	45.3	b.d.l	79.8	38.8	38.9	39.3	37.5	39.6	36.6	39.1	38.6	39.4	38.4	36.8	38	38.2	35.8	39.2	38.4	37.5	39.5	37.2	37.2	39.9	39.4	39.5	38.6	36.7	38.6
NIST612-11	10931.9	337028.5	59.9	86839.7	44.9	b.d.l	80.4	39.3	39	40.8	38.4	41.5	37.4	40.2	40	41.3	39.5	37.6	38.2	39.3	37.1	39.8	39.2	38.3	40.7	39.1	38.5	40.9	40.2	40.8	39.4	37.7	38.4
NIST612-12	10901.1	337028.5	51.5	86334.6	43.6	b.d.l	78.8	38.3	37.7	38.7	38.1	40.2	36.7	39.3	38.4	39.6	37.4	35.9	37.8	38.1	35.8	38.3	38.6	37.4	40.1	37.5	37.2	39.5	38.9	39.5	37.5	39.4	37.8
Average	10744	337028.5	46.6	85048.9	44	b.d.l	78.4	38.3	37.9	38.9	37.4	39.3	36	38.4	37.9	38.9	37.7	35.6	37.3	37.6	35.5	38.3	38	36.8	39.2	37	36.7	38.6	38.6	38.6	37.8	37.4	37.4
NIST612 Pref	10746.5	337558.4	46.6	85062.5	44	b.d.l	78.4	38.3	37.4	38.9	37.4	39.3	36	38.4	37.9	35.5	37.7	35.6	37.3	37.6	35.5	38.3	38	36.8	39.2	37	36.7	38.6	38.6	38.6	37.8	37.4	37.4
1s	278.5	0.0	8.1	2915.9	1.3	b.d.l	2.5	1	1.1	1.2	1	1.8	1.2	1.3	1.4	1.7	1.4	1.5	1.2	1.2	1.3	1.2	1.2	1.2	1.3	1.3	1.3	1.8	1.9	1.8	1.3	2.5	1.5
2s	557.1	0.0	16.2	5831.9	2.6	b.d.l	5.1	2.1	2.1	2.4	2	3.6	2.4	2.7	2.8	3.3	2.8	3.1	2.5	2.4	2.5	2.3	2.5	2.5	2.7	2.7	2.6	3.5	3.8	3.5	2.6	5	3.1
Error % (2s)	5.2	0.0	34.8	6.9	6	b.d.l	6.5	5.5	5.6	6.2	5.3	9.1	6.5	7	7.5	8.5	7.5	8.7	6.6	6.3	7.1	6	6.6	6.7	6.9	7.2	7.1	9.1	9.7	9.2	6.8	13.3	8.3
Average Detection limit on NIST612	0.44	135.41	11.44	87.01	0.47	b.d.l	0.01	0.01	0.09	0.01	0.07	0.08	0.003	0.003	0.002	0.01	0.01	0.004	0.02	0.002	0.01	0.002	0.01	0.002	0.01	0.00	0.01	0.04	0.03	0.02	0.003	0.76	0.003

GSE1G (calibration and validation material, Jochum et al., 2011)

Identifier	Al27	Si29	P31	Ca42	Ti49	Fe54	Sr88	Y89	Zr91	Nb93	Mo95	Ba137	La139	Ce140	Pr141	Nd146	Sm147	Eu151	Gd157	Tb159	Dy163	Ho165	Er167	Tm169	Yb173	Lu175	Hf177	Pb206	Pb207	Pb208	Th232	U235	U238
GSE1G-1	67198.1	251014.9	38.6	47293.1	451.4	1522917.9	390.7	359.6	362.1	408	356	383.6	346.6	366.5	408	432.5	427.5	357.6	434.4	429.6	453.5	439.5	514.1	434.9	449	448.5	343.8	348.3	302.6	320.1	340.5	570.8	362.3
GSE1G-2	65869.2	251014.9	35	45856.8	430.3	1512131.4	395.2	358	348.4	392.4	345.9	374.5	343.4	365.1	401.8	429.5	429.2	367.3	439.4	425.5	456.2	448.6	499.4	437.9	460.8	457	349.0	352.5	308	326.9	333.7	579.2	372.9
GSE1G-3	68858.1	251014.9	31.4	50634.4	463.9	1606753.6	421.4	385.5	382.2	422.8	376.3	418.5	375.6	402	438.9	461.7	458.6	384.7	469.1	466.4	491	479.1	495.3	478.6	489.9	489.3	374.4	382.6	333.8	352.9	353.9	603.2	402.1
GSE1G-4	70200.9	251014.9	36.6	50752.9	474.4	1676444.6	440.3	397.8	374	434.8	395.5	423.1	378.3	405.8	448.1	476.5	470.7	395	479	473.5	502.7	495.9	508.4	491.5	507.1	503.8	382.4	399.8	348	361.7	362.3	645.7	414.5
GSE1G-5	71287.2	251014.9	38.6	49089.5	465	1614046.1	432.5	393.6	387.1	427.8	373.2	418.6	380.1	393.3	448.8	473.9	467.2	396.7	475.7	482.7	503	499.5	497	500.8	511.4	499.8	388.5	399.6	353.1	361.2	352.3	629.1	405.3
GSE1G-6	70321.1	251015	39.2	48961.5	451.2	1613130.3	428.2	388.2	370.6	431.9	396.1	413.9	372.2	389.1	445.5	468.5	464.9	390.2	467.8	481.1	498.4	488	497.4	492.6	512	505.7	382.9	405.4	356.4	378.6	344.8	605.9	406.9
Average	68955.8	251014.9	36.6	48764.7	456	1590904	418	380.5	370.7	419.6	373.8	405.4	366	387	431.8	457.1	453	381.9	460.9	459.8	484.1	475.1	501.9	472.7	488.4	484	370.2	381.4	333.6	350.2	347.9	605.7	394
GSE Pref valu	68804	250994.0	70	52858	450	987306.3	447	410	410	420	390	427	392	414	460	453	488	410	514	480	524	501	595.0	500	520	518	395	378	378	378	380	420	420
2s	#REF!	#REF!	#REF!	#REF!	#REF!	#REF!	#REF!	#REF!	#REF!	#REF!	#REF!	#REF!	#REF!	#REF!	#REF!	#REF!	#REF!	#REF!	#REF!	#REF!	#REF!	#REF!	#REF!	#REF!	#REF!	#REF!	#REF!	#REF!	#REF!	#REF!	#REF!	#REF!	#REF!
BCR-1	69312.6	254287	1159.6	47095.8	13660.6	1491304.1	300.9	29.8	163.8	10.9	242	596.8	22.4	46.6	5.9	27.4	5.9	1.7	6.2	0.9	6	1.2	3.3	0.5	3.2	0.4	4.2	9.6	9	9.4	5.2	5.1	1.5
BCR-2	72852.2	254287	1171.8	48629.9	14319.8	1555075	323.5	33.5	183	11.5	250	640.5	24.2	48.7	6.3	29.6	6.4	1.9	6.3	1	6	1.3	3.5	0.5	3.4	0.5	4.8	10.6	9.8	9.9	5.6	7.6	1.6
BCR-3	76690.7	254287	1184.4	51763.9	15229.2	1664656.1	346.6	34.9	185.5	12.2	267.1	684.3	25.2	51.9	6.6	31.4	6.7	2	6.7	1.1	6.7	1.4	3.8	0.5	3.6	0.5	5.2	11.3	10.3	11	6.3	4.8	1.8
BCR-4	73823.6	252417.3	1201	49458.7	14606.4	1603801.5	328.1	33.6	180.8	11.6	256.7	668	24.7	50.5	6.4	30.3	6.6	2	6.6	1	6.2	1.3	3.6	0.5	3.3	0.5	5	11	10	10.4	5.9	4.9	1.7
BCR-5	75889.7	254287	1175.9	50848.9	15130.6	1658770.1	338.2	34.8	182.2	12.4	265.4	695.2	25.7	52.8	6.6	31.1	6.5	2	6.8	1.1	6.3	1.4	3.8	0.5	3.5	0.5	5.3	11.3	10.5	10.9	6.2	6.2	1.8
BCR-6	77700.9	254287	1183.7	52337.3	15470.7	1687666.1	345.1	35.3	188.1	12.4	270.9	701.5	25.8	53.2	6.7	32.1	6.7	2.1	7	1.1	6.7	1.4	3.8	0.5	3.6	0.6	5.1	11.5	10.6	11.2	6.5	6	1.8
Average	74378.3	253975.4	1179.4	50022.4	14736.2	1610212.2	330.4	33.6	180.6	11.8	258.7	664.4	24.7	50.6	6.4	30.3	6.5	1.9	6.6	1	6.3	1.3	3.6	0.5	3.4	0.5	4.9	10.9	10	10.5	5.9	5.8	1.7
BCR2G Pref v	71446	252959	1973	50856	13548	96398.4	346	37	184	12.5	270	683	25	53	6.7	28	6.6	2	6.8	1	6.4	1.3	3.7	0.5	3.5	0.5	4.8	11	11	11	5.9	1.7	1.7
1s	2797.9	696.8	12.7	1821	617.2	68970.4	15.6	1.9	7.9	0.5	10.2	36.2	1.2	2.3	0.3	1.5	0.3	0.1	0.3	0.1	0.3	0.1	0.2	0.03	0.2	0.04	0.4	0.6	0.5	0.6	0.5	1	0.1
2s	5595.8	1393.6	25.5	3642.0	1234.3	137940.7	31.2	3.7	15.7	1.1	20.4	72.4	2.3	4.7	0.6	3	0.5	0.3	0.6	0.1	0.6	0.2	0.4	0.1	0.3	0.1	0.7	1.2	1.1	1.3	0.9	1.9	0.2
Error % (2s)	7.8	0.6	1.3	7.2	9.1	143.1	9	10.1	8.5	8.7	7.5	10.6	9.3	8.8	8.2	10.8	7.8	12.8	8.1	12.9	9.4	11.9	10.9	10.4	8.8	17.1	15	11.4	9.6	11.7	15.4	113.7	12.8

Concordia diagrams

Mineralized tonalites

GBR-2, Mineralized tonalite group B.

The blue circles amidst red circles represent the best-fit age area calculated from a combination of all the red circles. The diameter of each circle in the X and Y-axis represents 2σ error

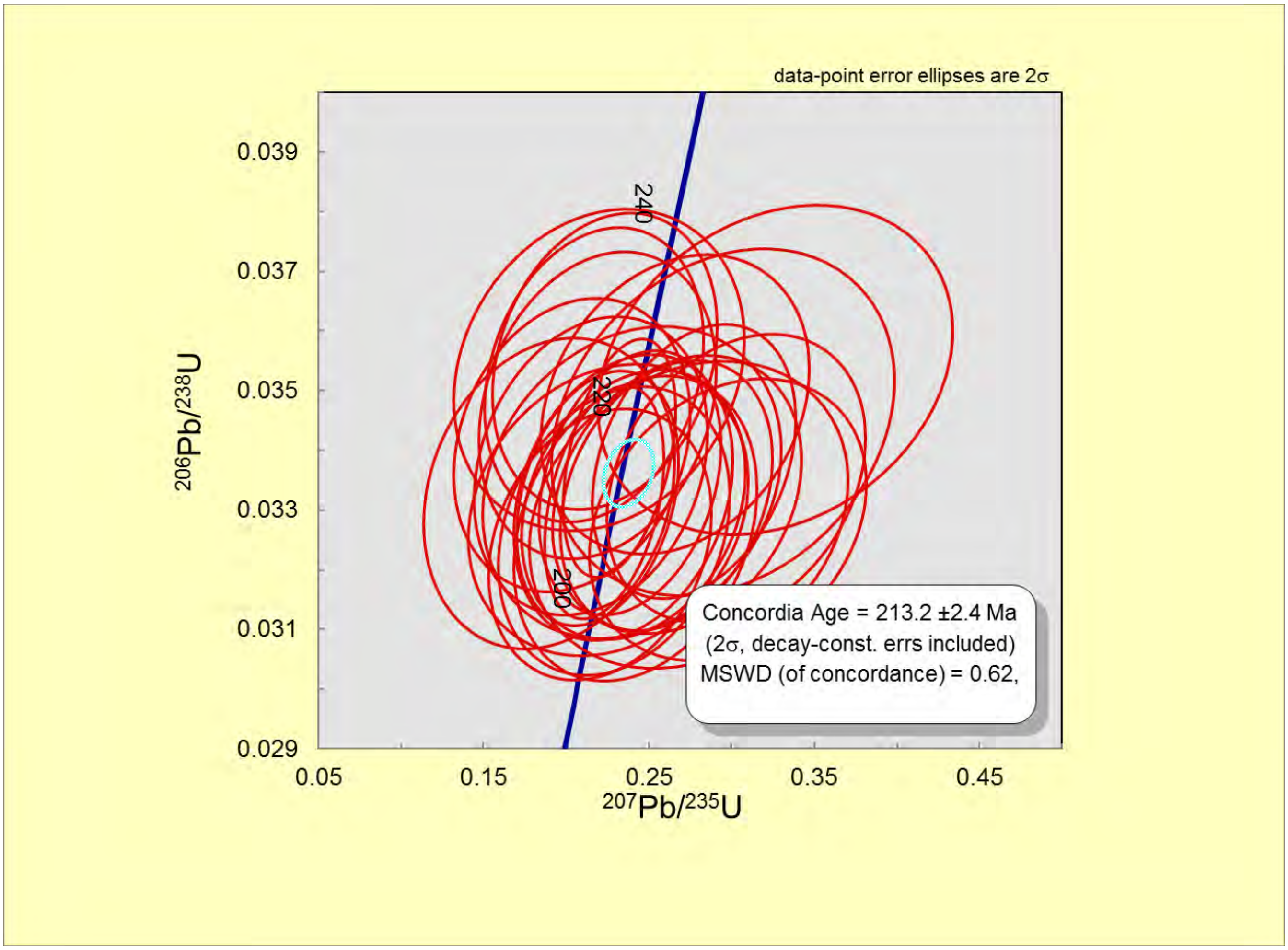

GBR-7, Mineralized tonalite group A

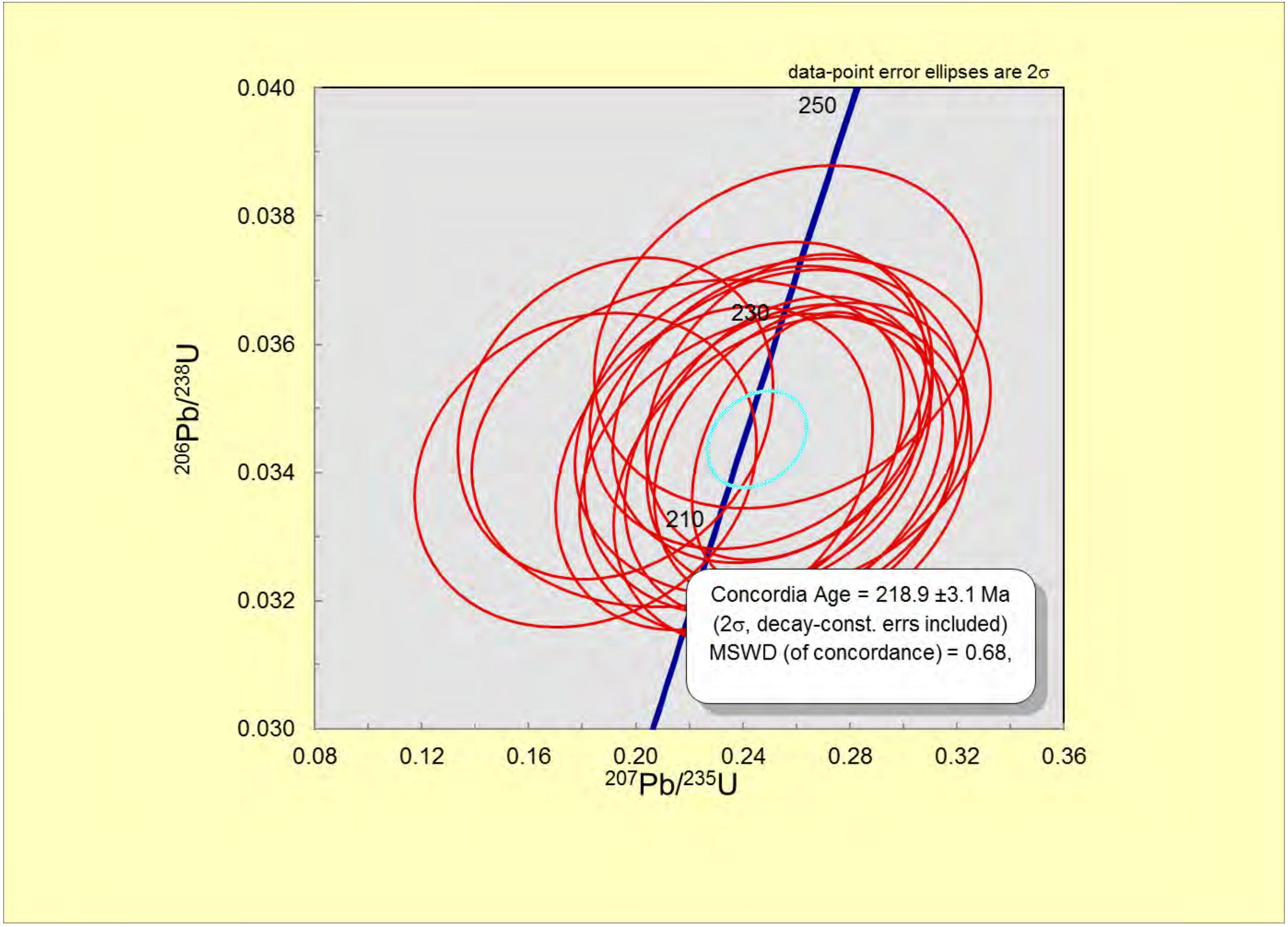

Concordia Age = 218.9 ±3.1 Ma
(2σ, decay-const. errs included)
MSWD (of concordance) = 0.68,

GBR-16, Mineralized tonalite group C

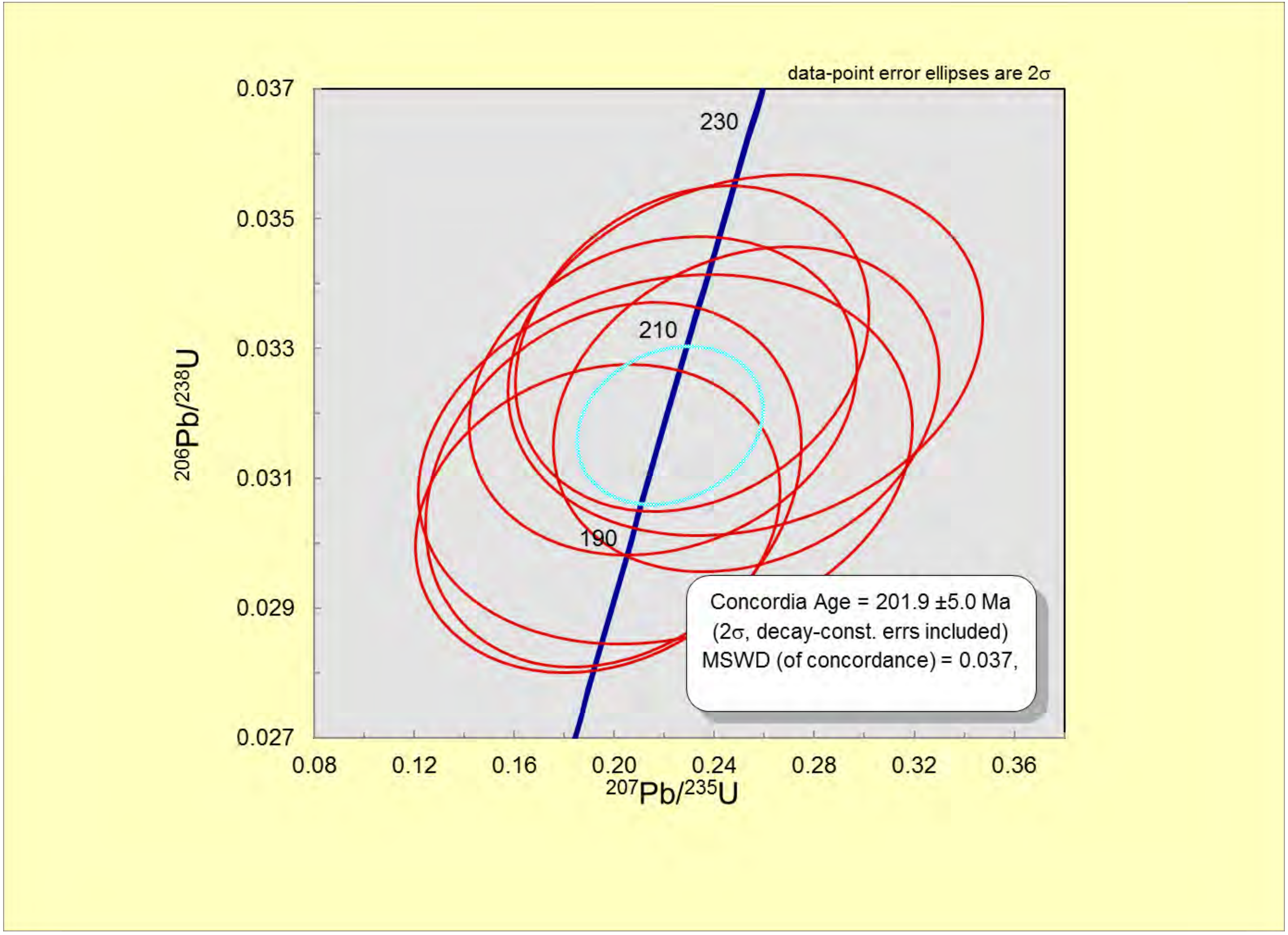

GBR-12, Mineralized tonalite group C

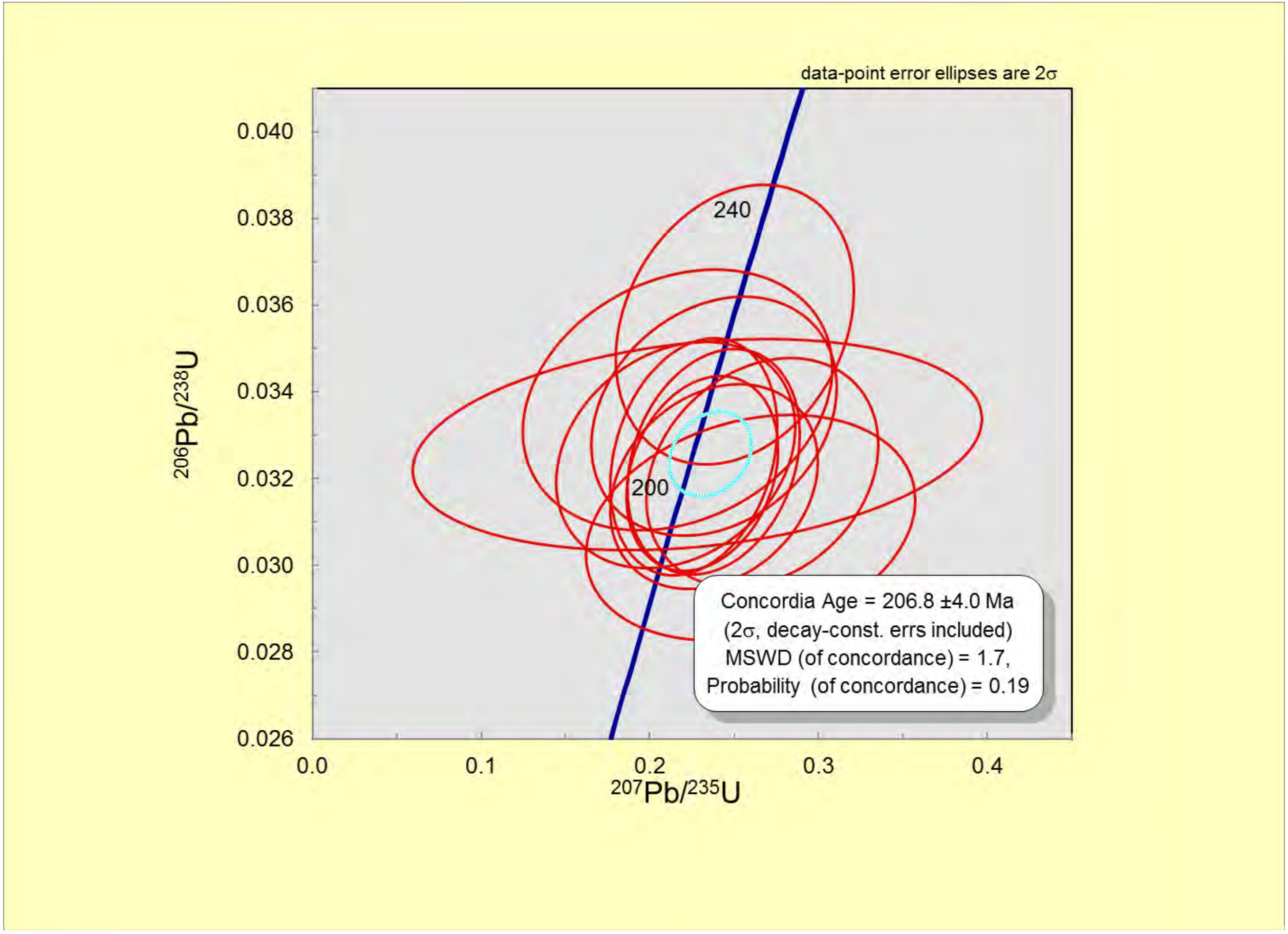

GBR-15, Mineralized tonalite group C

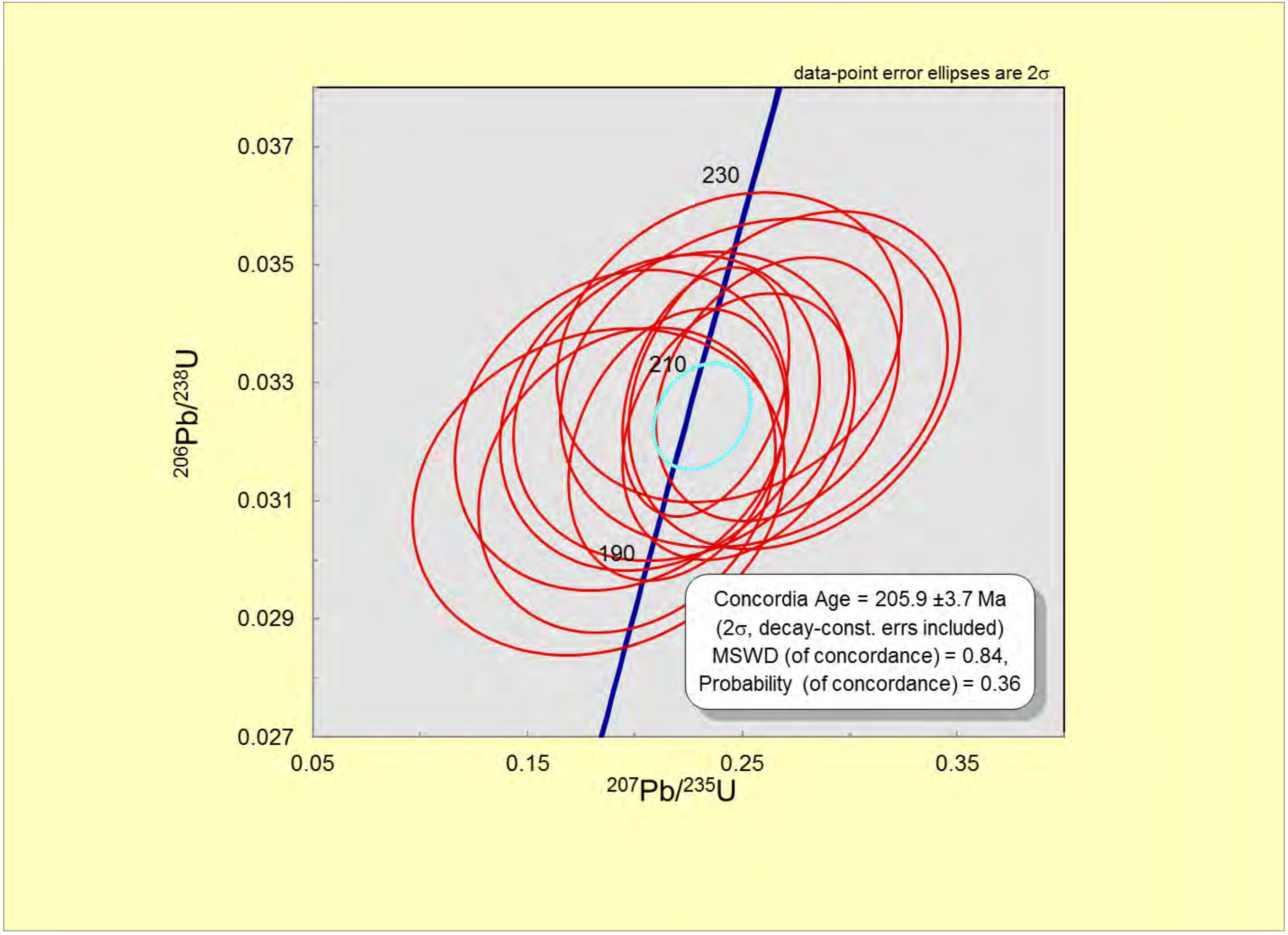

GBR-21, Mineralized tonalite group C

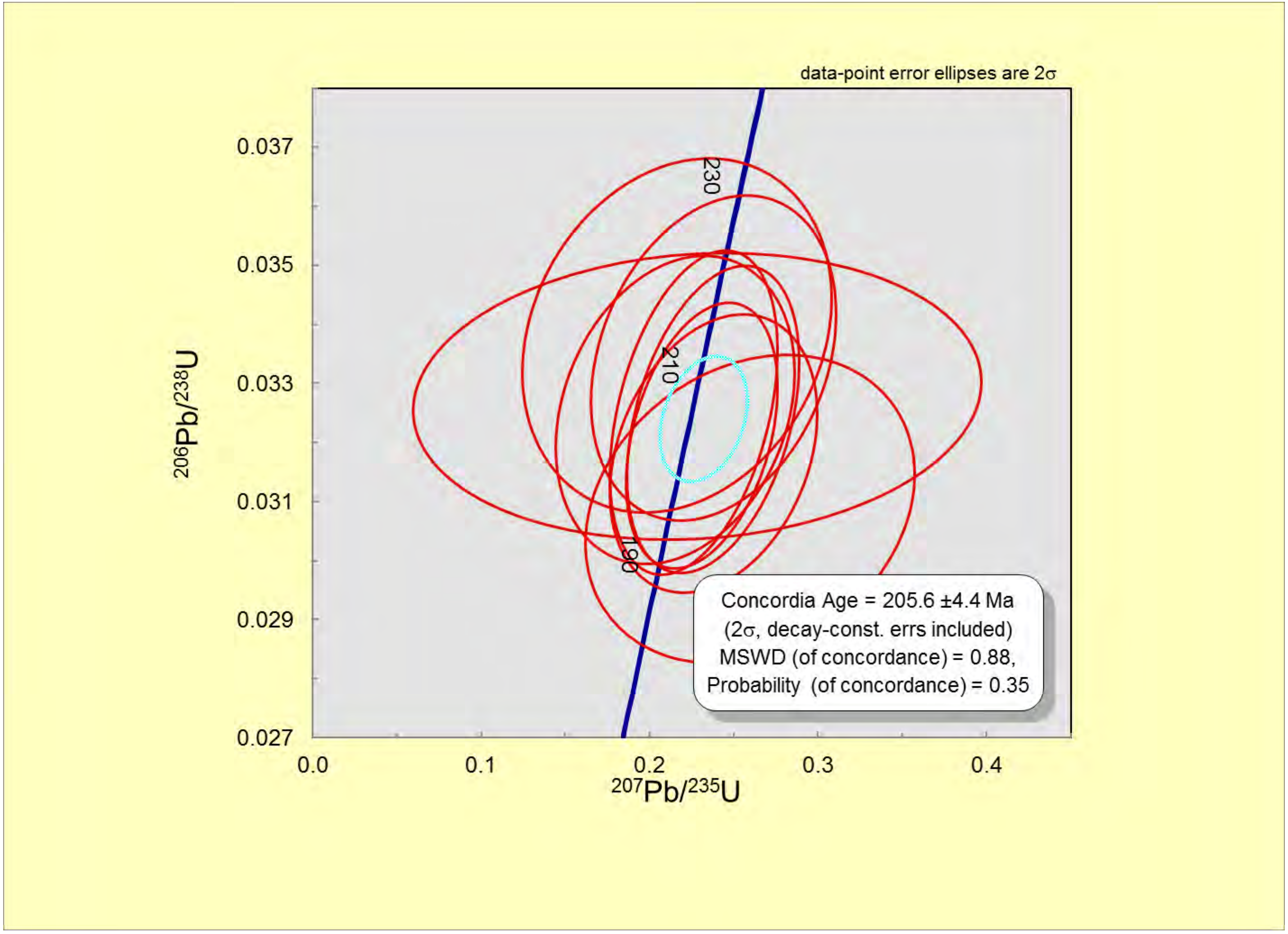

Combination of samples GBR-12-15-16-21, Mineralized tonalite group C

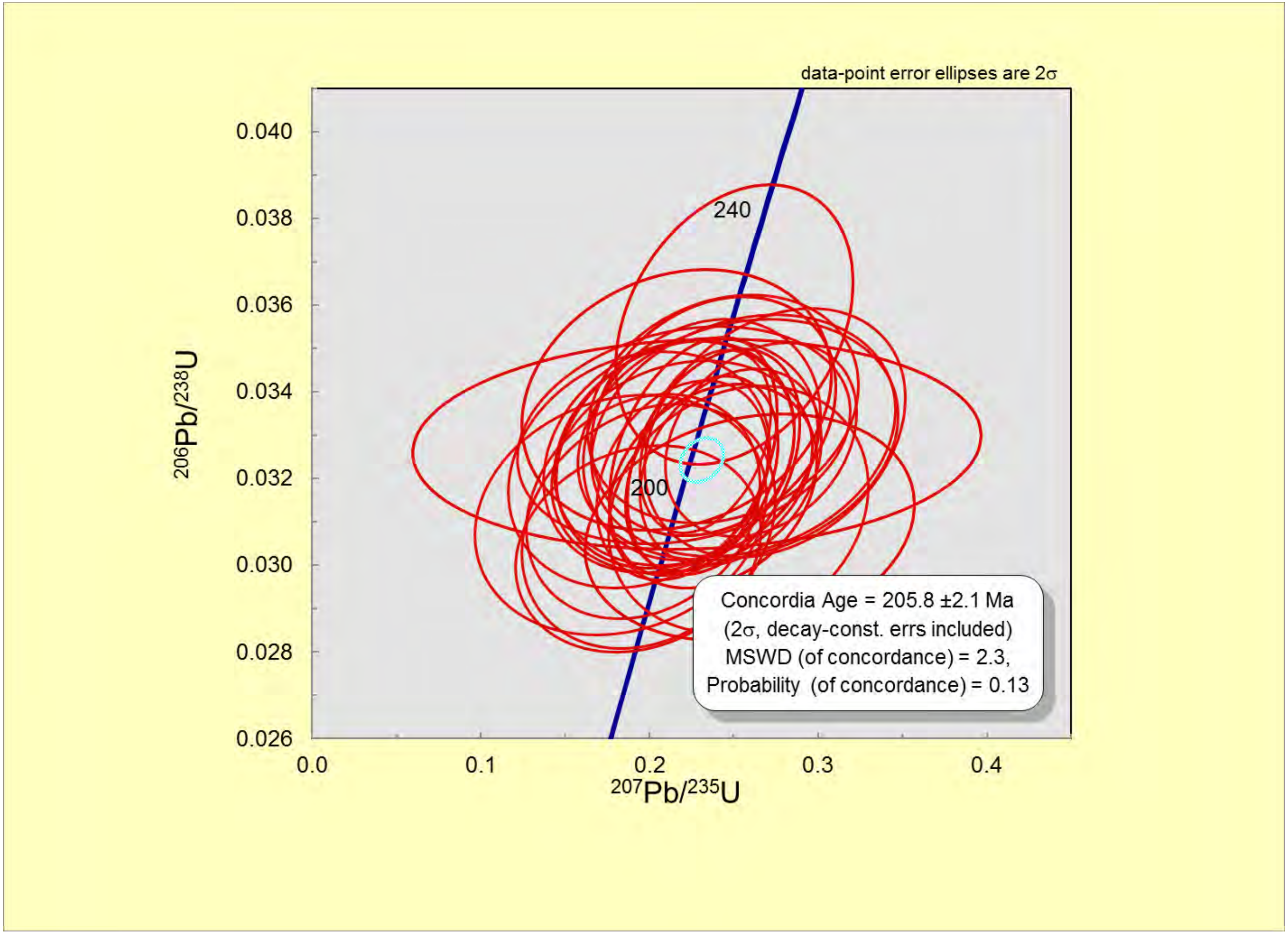

Standards, Plešovice

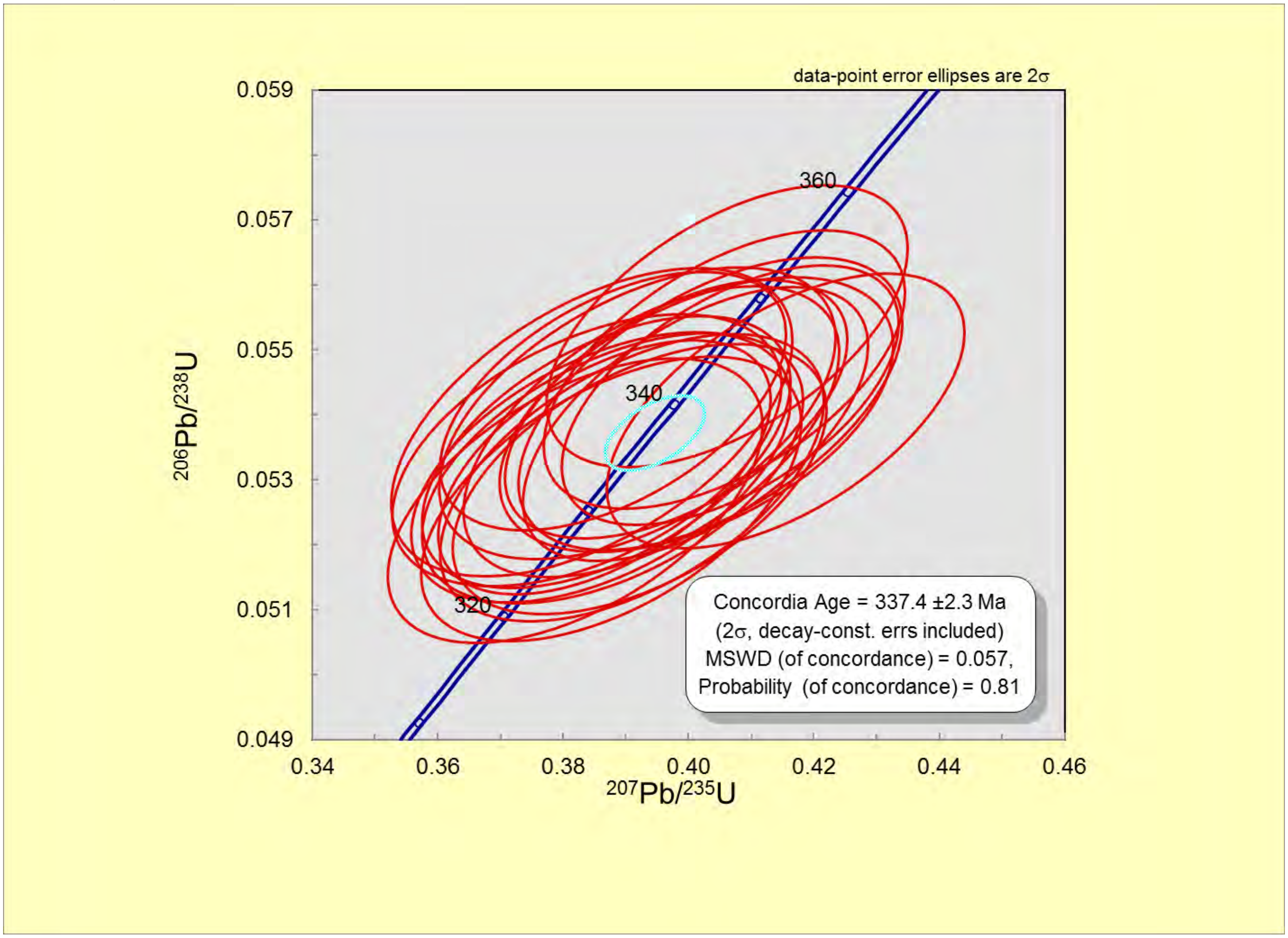

Standards, 91500

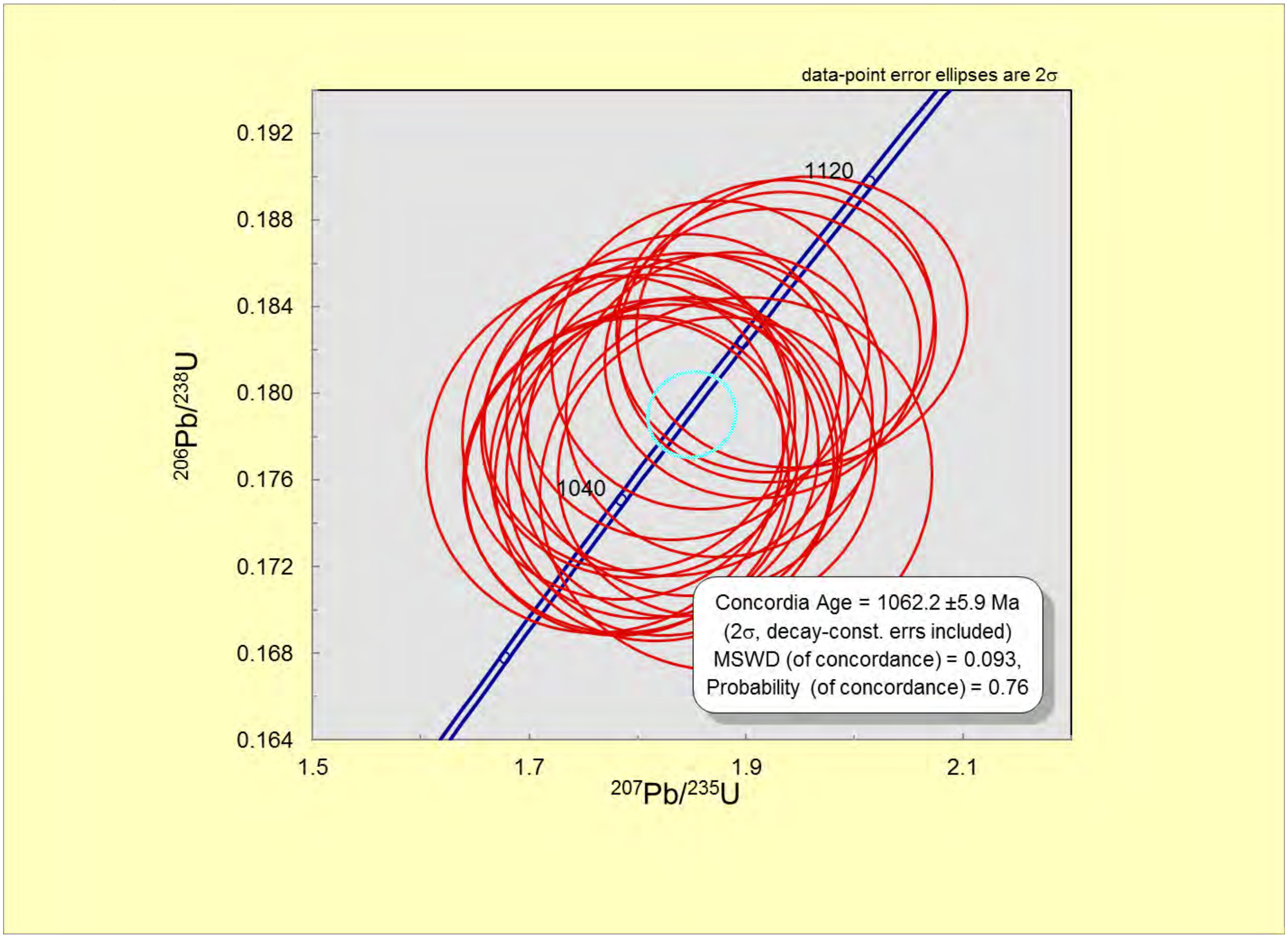

Concordia Age = 1062.2 ±5.9 Ma
(2σ, decay-const. errs included)
MSWD (of concordance) = 0.093,
Probability (of concordance) = 0.76

Unmineralized tonalites, GBR2-16

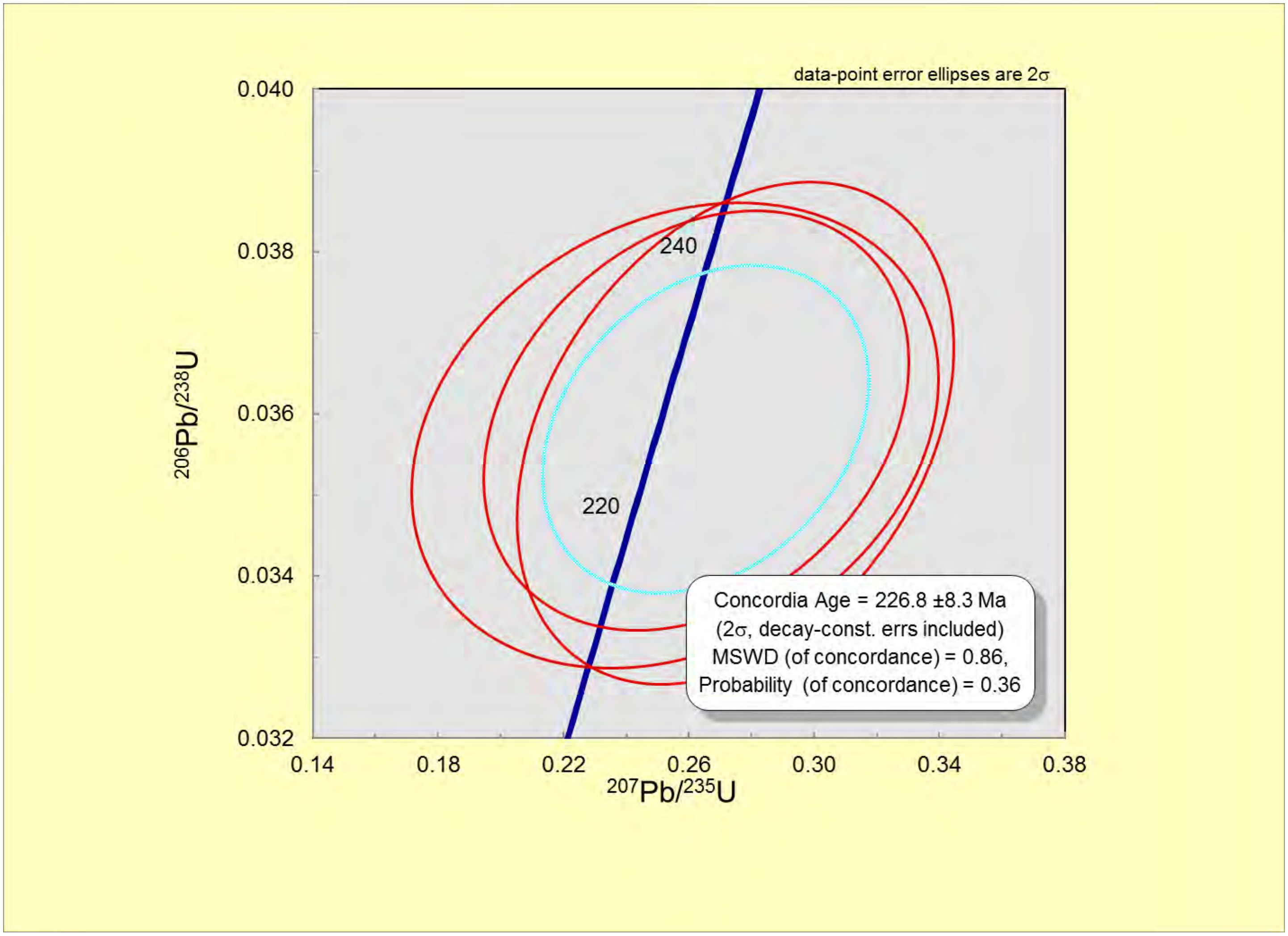

Unmineralized tonalites, GBR2-25

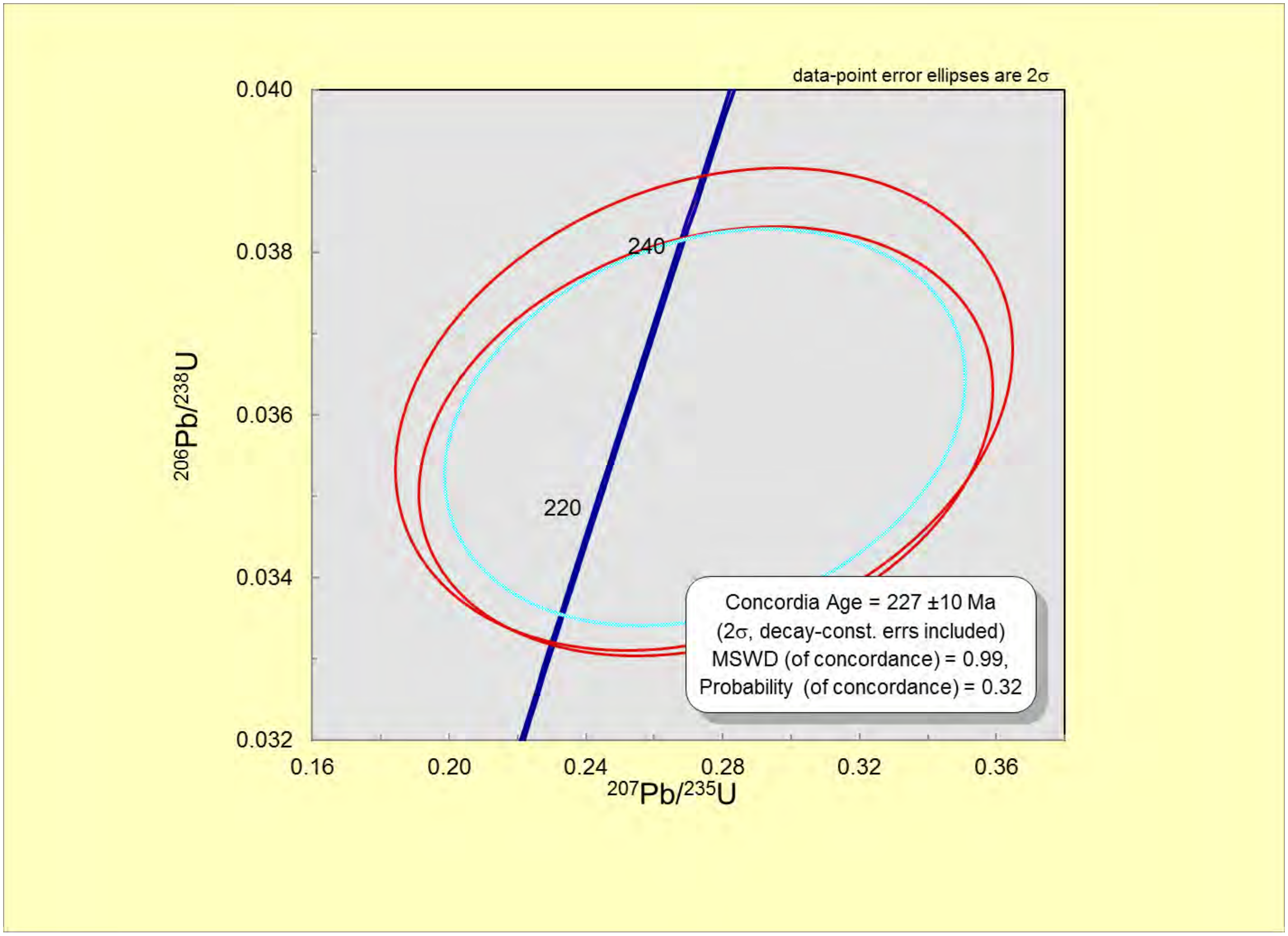

Concordia Age = 227 ±10 Ma
(2σ, decay-const. errs included)
MSWD (of concordance) = 0.99,
Probability (of concordance) = 0.32

Unmineralized tonalites, GBR2-30

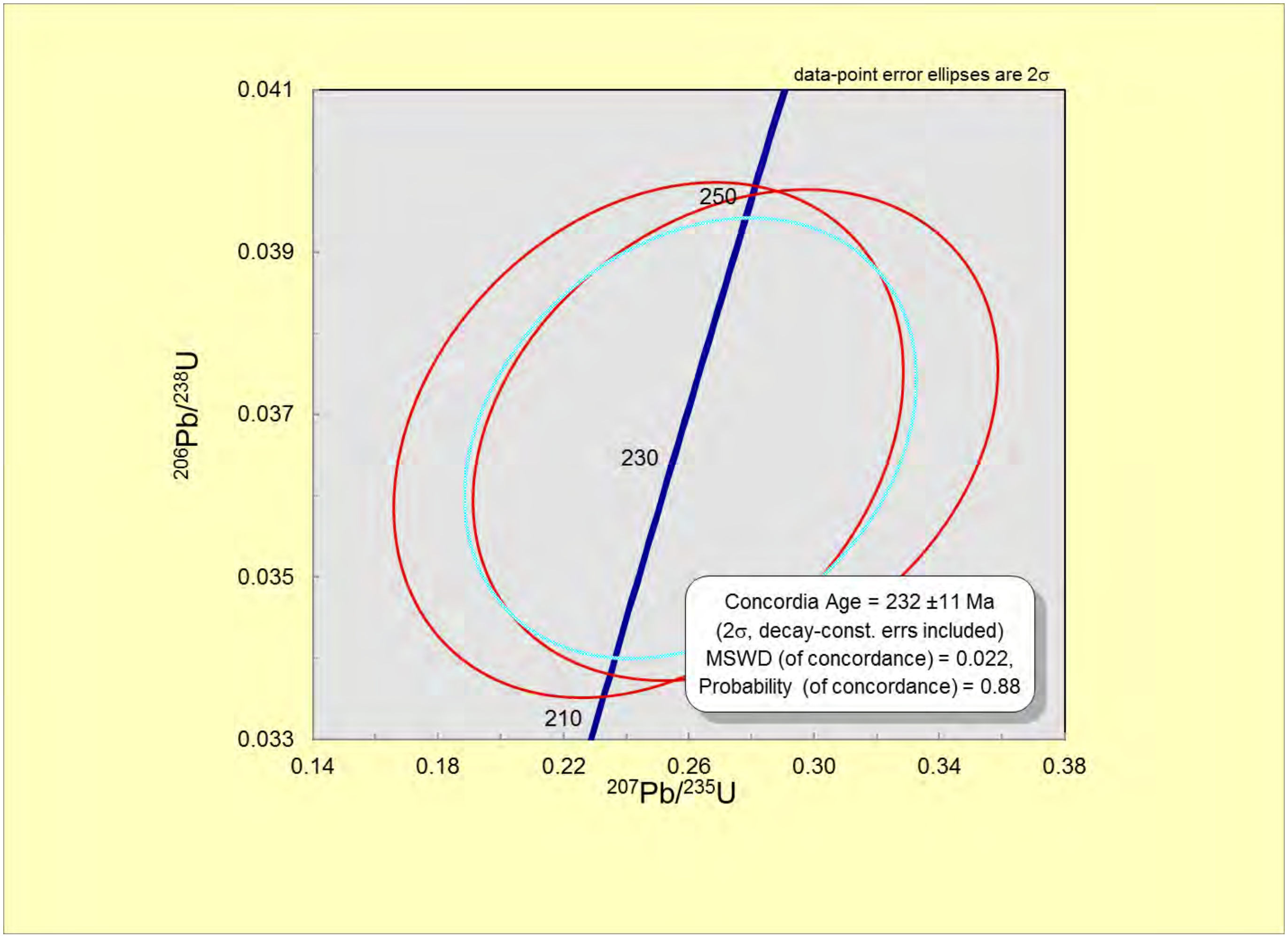

Unmineralized tonalites, GBR2-38

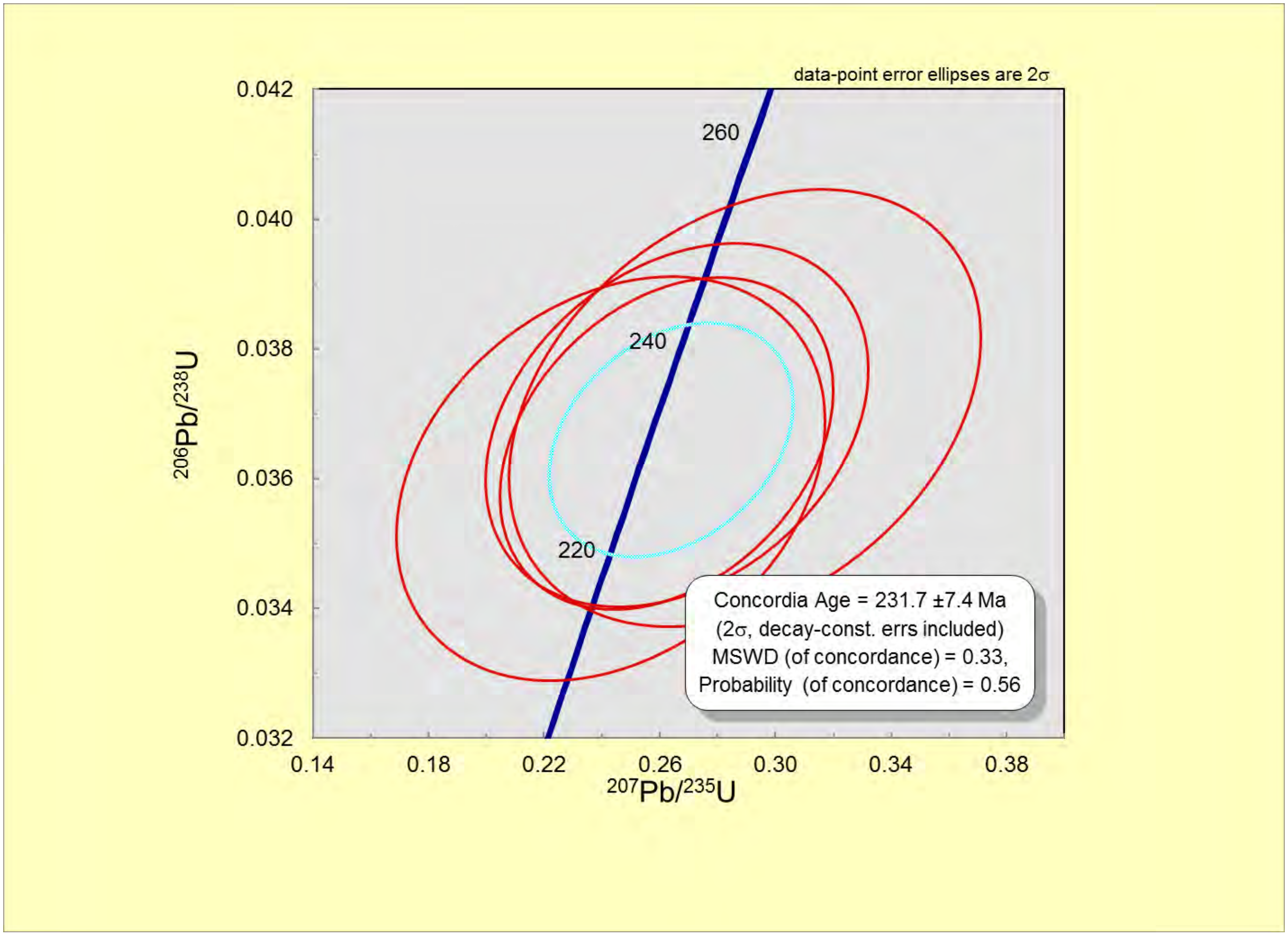

Unmineralized tonalites (combined)

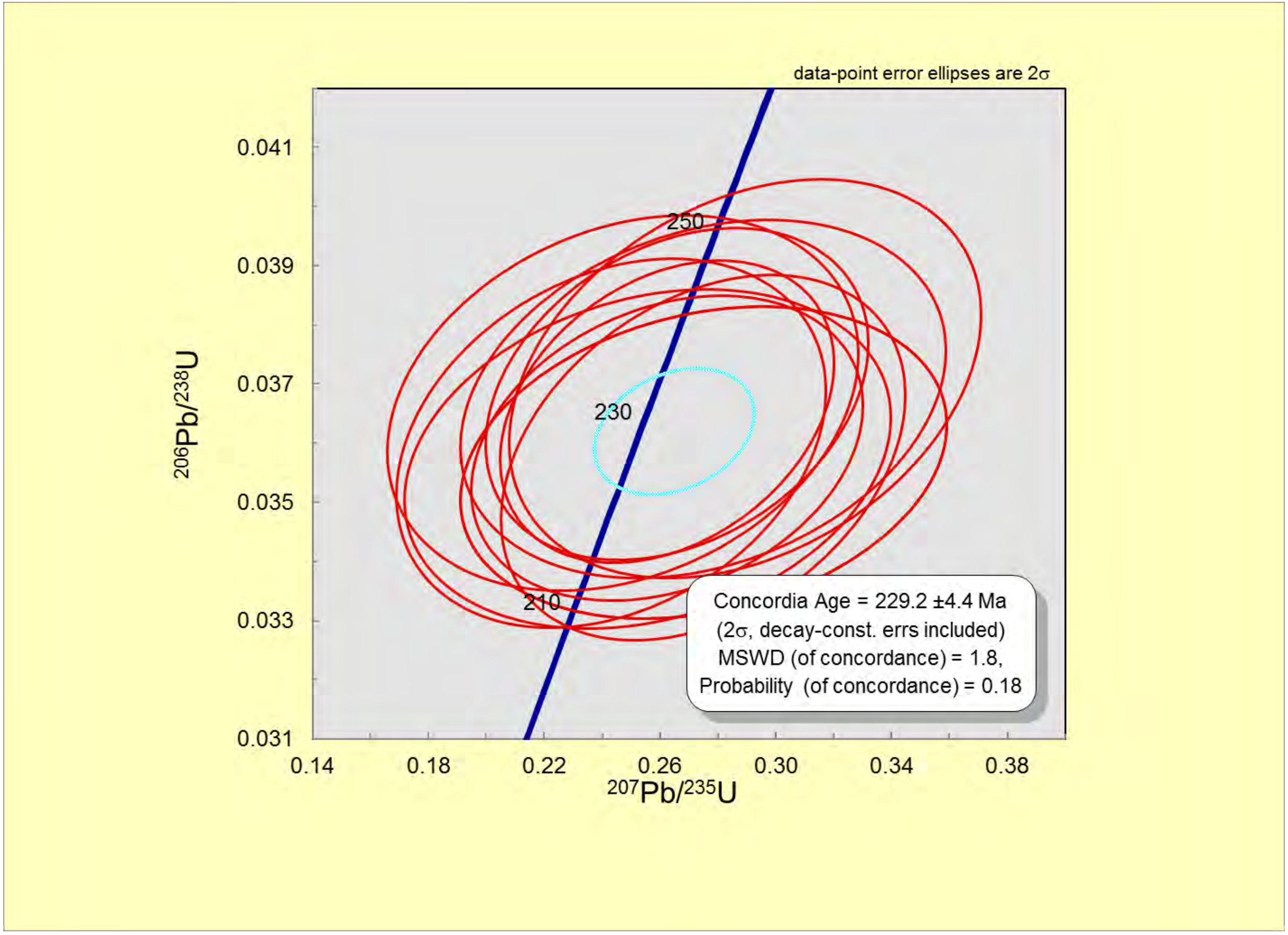

Appendix A2-5. Detailed metadata for LA-ICPMS analysis

Metadata for LA-ICP-MS Trace element analysis. Analysis run on 13/09/2016	
Machine information	
Make, Model and type	Photon Machines Analyte Excite 193 nm excimer laser
Ablation cell and volume	Single volume cell
Laser wavelength (nm)	193
Fluence (J cm^{-2})	4.72
Pulse width (ns)	4
Repetition rate (Hz)	10
Ablation duration (s)	40
Spot diameter (µm)	42
Ablation depth/ablation rate	16 mm pit depth measured using an optical microscope, SEM and interferometry, equivalent to 0.08 µm/pulse
Sampling mode	Static spot ablation
Carrier gas	He and Ar mixture
Cell carrier gas flow (l min^{-1})	0.9 (Ar) and 0.9 (He)
ICP-MS Instrument	
Make, Model and type	Agilent 7700x ICP-MS instrument
Make-up gas flow (l min^{-1})	Sourced from Agilent 7700x ICP-MS instrument
Detection system	Single collector, electron multiplier
RF power (W)	1550
Integration time per peak/ dwell times (ms); quadrupole settlin	^{29}Si 5 ms, ^{31}P 10 ms, ^{42}Ca 10 ms, ^{45}Sc 10 ms, ^{49}Ti49 30 ms, ^{51}V 10 ms, ^{55}Mn 10 ms, ^{56}Fe 10 ms, ^{88}Sr 10 ms, ^{89}Y 10 ms, ^{91}Zr 50 ms, ^{93}Nb 10 ms, ^{98}Mo 10 ms, ^{137}Ba 20 ms, ^{139}La 20 ms, ^{140}Ce 20 ms, ^{141}Pr 20 ms, ^{146}Nd 20 ms, ^{147}Sm 20 ms, ^{151}Eu 20 ms, ^{157}Gd 20 ms, ^{159}Tb 20 ms, ^{163}Dy 20 ms, ^{165}Ho 20 ms, 167Er 20 ms, 169Tm 20 ms, 173Yb 20 ms, 175Lu 20 ms, 177Hf 30 ms, 202Hg 10 ms, 204Pb 10 ms, 206Pb 20 ms, 207Pb 30 ms, 208Pb 20 ms, 232Th 10 ms, 235U 20 ms and 238U 10 ms 141Pr 20 ms, 146Nd 20 ms, 147Sm 20 ms, 151Eu 20 ms, 157Gd 20 ms, 159Tb 20 ms, 163Dy 20 ms, 165Ho 20 ms, 167Er 20 ms, 169Tm 20 ms, 173Yb 20 ms, 175Lu 20 ms, 177Hf 30 ms, 202Hg 10 ms, 204Pb 10 ms, 206Pb 20 ms, 207Pb 30 ms, 208Pb 20 ms, 232Th 10 ms, 235U 20 ms and 238U 10 ms
Data Processing	
Gas blank	30s on-peak zero subtracted
Calibration strategy	29 Trace elements calibrated from SiO_2 (converted to Si using GLITTER!) entered manually for each standard from preferred values NIST612 used and primary internal reference/normalizing material (^{29}Si = 72.01) with GSE1G (^{29}Si = 54.4), BCR2G (^{29}Si = 53.7) as secondary standards and zircon 91500 used as validation Data reduction was accomplished using the GLITTER! software (Griffin et al., 2008)
Reference Materiel information	91500 (Wiedenbeck et al., 1995)
	NIST 612 (Jochum et al., 2011)
	GSE1G (Jochum et al., 2011)
	BCR2G (Jochum et al., 2011)
Data processing package used/ Correction for LIEF	Glitter version 4.4.4 software (Griffin et al., 2008) used to reduce data
Quality control/ Validation	^{31}P, ^{42}Ca, ^{88}Sr and ^{56}Fe were used to screen for possible inclusions, samples with marked increased in these masses were screened and discarded by the GLITTER! software (Griffin et al., 2008)
	91500 zircon used for validation. Analysis runs with larger than a 10% error between preferred 91500 values for trace elements and determined 91500 values were discarded

Metadata for LA-ICP-MS U-Pb dating. Analysis run on 21/12/2017	
Machine information	
Make, Model and type	Photon Machines Analyte Excite 193 nm excimer laser
Ablation cell and volume	Single volume cell
Laser wavelength (nm)	193
Pulse width (ns)	4
Fluence (J cm^{-2})	4.72
Repetition rate (Hz)	10
Ablation duration (s)	40
Ablation depth/ablation rate	16 mm pit depth measured using an optical microscope, SEM and interferometry, equivalent to 0.08 µm/pulse
Spot diameter (µm)	32
Sampling mode	Static spot ablation
Carrier gas	He and Ar mixture
Cell carrier gas flow (l min^{-1})	0.9 (Ar) and 0.9 (He)
ICP-MS Instrument	
Make, Model and type	Agilent 7700x ICP-MS instrument
Make-up gas flow (l min^{-1})	Sourced from Agilent 7700x ICP-MS instrument
Detection system	Single collector, electron multiplier
RF power (W)	1550
Integration time per peak/ dwell times (ms); Quadrupole settli	60ms for Pb isotopes, 30 ms for Th isotopes and 30 Ms for U isotopes
Total integration time per output data point (s)	~36s
Data Processing	
Gas blank	30s on-peak zero subtracted
Calibration strategy	91500 used and primary reference material, Plešovice and NIST612 used as secondary verification/validation
	91500 (Wiedenbeck et al., 1995)
Reference Materiel information	Plešovice (Sláma et al., 2008)
	NIST612 (Jochum et al., 2011)
Data processing package used/ Correction for LIEF	Raw count data for U-Pb were reduced using the UPb.age script in the R software environment (Solari and Tanner, 2011). The script reduces/normalizes data based on accepted values of 91500 zircon (Wiedenbeck et al., 1995). UPb.age eliminates outliers (±2σ), corrects instrument drift using a linear model and corrects for downhole fractionation using a mean method
Mass discrimination	^{206}Pb/^{207}Pb additionally normalized to reference material
	Plešovice – Wtd ave 206Pb/238U age = 33.7±2.3 (2s, MSDW = 0.057, n = 21)
Quality control/ Validation	Systematic uncertainties for propagation are 207Pb/235U = 6.8 % (2s) and 206Pb/238U = 3.4 % (2s).
	^{140}Ce, ^{31}P, ^{42}Ca, ^{56}Fe, and ^{88}Sr were used to screen for possible inclusions, samples with marked increased in this mass were screened and discarded by the GLITTER! software (Griffin et al., 2008) and UPb.age script (Solari and Tanner, 2011).

Appendix A2-6. Amphibole compositions, and accuracy, precision and detection limits of analytical data

Samples	SiO2 wt.%	TiO2 wt.%	Al2O3 wt.%	Cr2O3 wt.%	FeO wt.%	MnO wt.%	MgO wt.%	CaO wt.%	Na2O wt.%	K2O wt.%	Cl wt.%	F wt.%	TOTAL	t (°C)*	ƒO2	ΔFMQ*	P (MPa)*
GBR-32-amph1-1	51.18	0.44	3.65	0.02	12.70	1.55	14.92	11.68	0.69	0.30	0.01	0.09	97.24	768	-12.3	2.6	46.9
GBR-32-amph1-2	52.18	0.38	3.17	0.01	12.36	1.35	15.16	11.77	0.62	0.24	0.01	- 0.06	97.19	755	-12.6	2.6	41.7
GBR-32-amph1-3	51.90	0.48	3.37	0.01	12.33	1.60	15.67	11.50	0.60	0.28	0.01	0.03	97.78	780	-12.5	2.7	43.3
GBR-32-amph1-4	51.74	0.51	3.60	0.01	12.53	1.36	15.21	11.58	0.78	0.30	0.01	0.03	97.65	765	-12.4	2.6	46.1
GBR-32-amph1-5	51.42	0.40	3.63	b.d.l	12.55	1.58	15.08	11.67	0.70	0.27	0.02	- 0.02	97.31	769	-12.3	2.6	46.5
GBR-32-amph1-6	51.64	0.43	3.49	b.d.l	12.28	1.49	15.59	11.57	0.65	0.29	0.01	0.13	97.57	777	-12	2.7	44.8
GBR-32-amph1-7	51.63	0.50	3.68	b.d.l	12.22	1.51	15.38	11.50	0.83	0.27	b.d.l	0.08	97.61	770	-12.2	2.6	46.9
GBR-32-amph2-1	51.19	0.57	3.86	b.d.l	12.86	1.48	15.21	11.29	0.96	0.31	0.01	0.12	97.85	776	-12.1	2.6	48.9
GBR-32-amph2-2	51.80	0.45	3.31	b.d.l	12.57	1.57	15.12	11.64	0.70	0.26	0.01	- 0.02	97.40	761	-12.5	2.6	43.1
GBR-32-amph2-3	52.74	0.02	2.12	0.02	17.02	1.38	11.95	12.25	0.30	0.14	0.01	- 0.01	97.93	698	-15	1.8	32.6
GBR-32-amph2-4	53.14	0.04	1.93	0.02	16.29	1.39	12.28	12.20	0.28	0.10	b.d.l	- 0.11	97.56	695	-15	1.8	31.1
GBR-32-amph2-5	51.81	0.33	3.57	0.02	12.36	1.54	15.32	11.68	0.73	0.23	b.d.l	- 0.08	97.51	767	-12.3	2.7	45.7
GBR-32-amph2-6	52.64	0.27	2.87	0.01	12.28	1.54	15.48	11.79	0.56	0.21	b.d.l	- 0.01	97.63	754	-12.6	2.7	38.5
GBR-32-amph3-1	50.84	0.61	3.94	0.01	12.74	1.41	15.08	11.39	0.85	0.31	0.01	- 0.01	97.19	779	-12	2.6	50.3
GBR-32-amph3-2	51.29	0.55	3.78	0.01	12.51	1.46	15.40	11.46	0.75	0.30	b.d.l	0.09	97.61	781	-11.9	2.7	48.1
GBR-32-amph3-3	52.09	0.43	3.35	b.d.l	13.02	1.48	14.77	11.64	0.67	0.27	0.01	0.09	97.83	757	-12.7	2.5	43.4
GBR-32-amph3-4	51.26	0.50	3.93	0.02	12.46	1.69	15.04	11.63	0.76	0.29	0.02	0.12	97.72	776	-12.1	2.5	50.0
GBR-32-amph3-5	51.42	0.45	4.02	0.01	13.21	1.45	14.73	11.70	0.78	0.33	0.02	0.05	98.17	770	-12.3	2.4	51.0
GBR-32-amph4-1	51.73	0.53	3.63	0.01	12.36	1.54	15.51	11.21	0.91	0.31	0.01	0.15	97.90	774	-12.1	2.7	46.2
GBR-32-amph4-2	52.63	0.34	3.10	0.01	11.99	1.58	15.84	11.69	0.59	0.23	0.03	0.07	98.09	766	-12.2	2.8	40.6
GBR-32-amph4-3	51.60	0.54	3.59	0.01	12.33	1.43	15.38	11.38	0.83	0.31	0.01	0.08	97.49	769	-12.2	2.7	46.0
GBR-32-amph4-4	51.24	0.52	3.97	b.d.l	12.91	1.45	15.25	11.52	0.75	0.28	0.01	- 0.06	97.84	784	-11.9	2.6	50.2
GBR-32-amph5-1	52.04	0.25	3.65	0.01	12.22	1.46	15.19	11.75	0.66	0.22	0.01	0.00	97.47	765	-12.3	2.6	46.6
GBR-32-amph5-2	51.18	0.43	4.06	0.01	13.00	1.44	15.00	11.63	0.73	0.29	0.01	0.04	97.82	779	-12	2.6	51.4
GBR-32-amph5-3	51.18	0.49	3.91	0.01	12.97	1.72	15.01	11.62	0.84	0.30	0.01	0.03	98.08	777	-12.1	2.5	49.6

***For ƒO_2 , P and T calculations see Ridolfi et al., 2010**

b.d.l = below detection limits

Analytical conditions

Element/Line	Detection Limit(99%)	Accuracy (%)	Standard	Precision (%)
K ka	0.012	99.744	Sanidine	96.979
Ca ka	0.016	94.142	Diopside #1	99.368
Na ka	0.016	91.101	Albite	97.760
Al ka	0.009	99.188	Sanidine	99.243
Fe ka	0.037	98.936	Hematite	98.712
Mn ka	0.038	95.384	Tephroite	89.210
Ti ka	0.013	93.868	Rutile	98.457
Si ka	0.009	99.744	Sanidine	99.761
Mg ka	0.010	94.021	Diopside #1	99.537
Cr ka	0.016	N/A	Chromite	N/A
F ka	0.117	N/A	Fluorite	89.193
Cl ka	0.006	54.806	Tugtupite	96.066

Analytical error on F and Cr is too high, these mesurements are not considred for calculations

Appendix 3. Supplementary material for Chapter 5

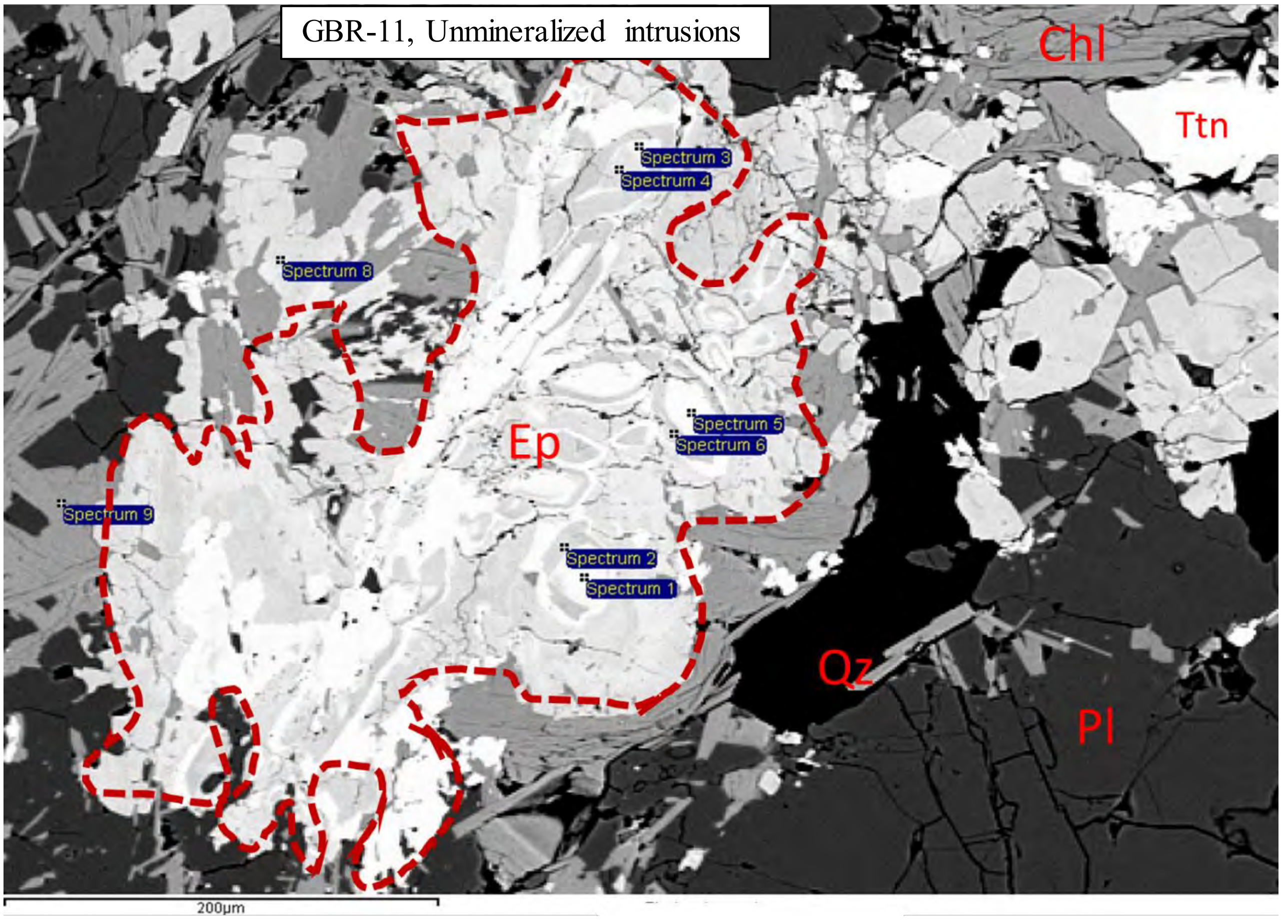

Figure A3-1: Back scatter electron image of an epidote aggregate. Area surrounded in red dashed line shows epidote grains with multiple repeating zoning patterns with variable Fe contents contributing to the changes in grey scale brightness.

Appendix 4. Abstracts of conference presentations

Abstract for poster presentation at the PDAC-SEG 2016 Student Minerals Colloquium, 2016:

Composition and assemblage of minerals associated with the porphyry Cu-Mo Mineralization at the Gibraltar deposit, south central British Columbia

CH Kobylinski[1], K Hattori[1], A Plouffe[2], S Smith[3]

[1]Department of Earth Sciences, University of Ottawa, Ottawa, Ontario;

[2]Geological Survey of Canada, Ottawa, Ontario;

[3]Taseko Gibraltar, Mining Offices, McLeese Lake, British Columbia

Glacial sediments commonly contain resistant heavy minerals, such as zircon, rutile, and epidote. To identify the source of these minerals and to use them as a tool to vector mineralization, it is critical to understand the mineral assemblages and compositional variations of heavy minerals in deposits and to determine if the signatures are distinct from barren rocks. The Gibraltar deposit in southcentral British Columbia, with the geological reserves (past production plus reserves) of 2.5 Mt Cu, is hosted by the late Jurassic Granite Mountain batholith. The batholith is mainly composed of tonalite with minor variation in modal abundance of felsic and mafic minerals. Igneous minerals include plagioclase, quartz, biotite, hornblende, titanite, zircon, apatite and magnetite. The mineralization is accompanied by extensive phyllic alteration in the tonalite, which produced illite, quartz, rutile, titanite, magnetite, apatite, chlorite and epidote. Epidote group minerals are ubiquitous alteration minerals as they replace plagioclase and hornblende, chlorite is common after hornblende and biotite, and a mixture of titanite and rutile replace biotite and hornblende. Alteration, mostly Fe-rich epidote, often appears light green in thin section but because there is a large compositional variation, even within a single sample, from Al-rich (high clinozoisite component) to significant La and Ce (allanite component) and/or Ferich phases, it is suggested that multiple alteration events have occurred. Another abundant igneous alteration mineral is titanite, which shows a wide compositional variation that correlates to varying concentrations of Al, Mg, and Fe. Preliminary observations suggest that in the preexisting potassic alteration zone biotite, occurring as an alteration mineral, has been replaced by chlorite. High FeOt (>25wt.%) chlorite is abundant in the rocks and appears to be related to the occurrence of epidote, whereas low FeOt (<25wt.%) and high Mg chlorite occurs as isolated aggregates. Identifying geochemical signatures of these minerals and their assemblages is a key component to developing a method of using heavy minerals as a vectoring tool.

Abstract for the poster presentation at the GAC-MAC Annual meeting 2016:

Mineral chemistry of greenrock alteration associated with the porphyry Cu-Mo mineralization at the Gibraltar deposit, south central British Columbia, Canada

Christopher H. Kobylinski[1], Keiko Hattori[1], Alain Plouffe[2], Scott Smith[3]

[1]Department of Earth Sciences, University of Ottawa, 25 Templeton Street, Ottawa, Ontario, K1N 6N5
[2]Geological Survey of Canada, 601 Booth Street, Ottawa, Ontario, S7M 1J3
[3]Taseko Gibraltar, Mining Offices, 10251 Gibraltar Road, McLeese Lake, British Columbia, V0L 1P0

The Gibraltar Cu-Mo porphyry deposit with the geological reserves (past production plus reserves) of 2.8 Mt Cu is hosted in the late Triassic Granite Mountain batholith the Quesnel Terrane. The batholith, which has the surface exposure of 15 km x 10 km, is mostly composed of tonalite with minor variation in modal abundances of felsic and mafic minerals. Igneous minerals are plagioclase, quartz, biotite, hornblende, with minor amounts of titanite, zircon, apatite and magnetite. Bulk rocks show a typical subduction-related geochemical signature with negative anomalies of high field strength elements, such as Nb, Ta and Ti, with minor positive and negative Eu anomalies (Eu/Eu*=0.09-1.2). The mineralization is accompanied by extensive alteration in the tonalite, which produced illite, quartz, rutile, titanite, magnetite, apatite, chlorite and epidote. The high-temperature potassic alteration zone was likely present in the centre of the current mining operation, but the alteration has been obscured by the replacement of secondary biotite by chlorite. Among alteration minerals, epidote and chlorite are ubiquitous in the tonalitic rocks in and around the mine, producing green rock alteration. Epidote group minerals primarily replace plagioclase. Chlorite is also common after hornblende and biotite, and a mixture of titanite and rutile replaces biotite and hornblende. Epidote minerals are light grass green in hand specimens and also thin sections. They show a large compositional variation even within one sample from Al-rich (high clinozoisite component) to Fe-rich epidote, suggesting multiple alteration events or reflecting varying fluid composition within a hydrothermal system. Some are yellowish in thin sections and they contain significant allanite component with high La2O3 (up 9.54 wt%) and Ce2O3 (up to 14.7 wt%). These Ce-La-rich epidote grains contain higher concentrations of other REEs, Mn, Y and Th than Fe-rich epidote. These LREE-rich epidotes form isolated grains within chlorite aggregates in epidote-rich tonalities. In contrast, Fe-rich, REE-poor epidote is abundant and preferentially replaces plagioclase.

Igneous titanite (up to 2 mm) is low in Al2O3 (~1.2 wt%) whereas hydrothermal titanite contains high Al2O3 ranging from 2 to 6 wt%. Hydrothermal titanite is more abundant than its igneous counterpart, and shows a wide compositional variation of Mg and Fe. Rocks with greenrock alteration show high abundances of U, Pb and K in bulk rocks compared to epidote-poor samples. The enrichment of U and Pb in bulk rocks is likely due to their incorporation in epidote as minor components.

Abstract for poster presented at PDAC-SEG Student Minerals colloquium 2017:

Epidote and zircon associated with the porphyry Cu mineralization at the Gibraltar Mine in southcentral British Columbia

C Kobylinski[1], K Hattori[1], S Smith[2], A Plouffe[3]

[1]Department of Earth and Environmental Sciences, University of Ottawa, Ottawa, Ontario;
[2]Taseko Gibraltar, McLeese Lake, British Columbia;
[3]Geological Survey of Canada, Ottawa,Ontario

The Gibraltar porphyry-Cu deposit in the Canadian Cordillera is hosted within the late Triassic, tonalitic Granite Mountain batholith. This study aims to link the geochemistry of key robust minerals (epidote, rutile, titanite and zircon) from the granite mountain batholith to surrounding glacial till. Additionally, this study aims to constrain the timing and paragenesis of the deposit using primary and alteration mineral geochemistry and distribution patterns. Understanding this porphyry deposit is key to refining our understanding of the mechanics that lead to formation of other porphyry deposits worldwide. The Granite Mountain batholith is composed of tonalitic rock suites that are primarily composed of quartz, plagioclase, hornblende, biotite, titanite, apatite and zircon, whereas their altered equivalents are dominated by an epidotechlorite-rutile-titanite-iron oxide mineral assemblage. Propylitic alteration (epidote-chlorite–albite) is extensive through the batholith. The epidote group minerals can be directly associatedwith Cu mineralization and the subsequent alteration halos that extend up to 10 km from the deposit. Epidote minerals occur as replacement phases of plagioclase, in disseminated grains and in veins of varying width. Wide epidote veins (>2cm) strike towards the mineralized centers and contain epidote zoned with Fe-rich rims and Al-rich cores. Dissemination of epidote occurs both in the tonalitic batholith rocks and the surrounding Nicola volcanic rocks, however, there is a higher concentration of disseminated epidote closer to the mineralized centers. There is a large compositional variation in the epidote group minerals, including clinozoisite and REE-rich allanite that occurs in the outer alteration halos, 1-2 km from the deposit and can be used as a tool to vector towards other similar deposits if found an outlying till. Minor and trace elements (titanium and rare earth elements) in zircon grains show cooler crystallization temperatures (785°C near mineralized phases compared to >817°C moving away from mineralized phases, as determined through Ti in zircon geothermometry). Relatively oxidized magmatic conditions are

found in the mineralized phases of the deposit using Ce4+/Ce3+ as a proxy for oxidation state and a combination of the lattice strain model for mineral-melt partitioning of elements, Blundy and Wood 1994, and the calculation proposed by Ballard et al. 2004.

Abstract for OCGC Graduate Student Seminars, April 6th, 2017

Tonalitic intrusions hosting the Gibraltar porphyry Cu-Mo mine and associated green rock alteration

Kobylinski, Christopher; Department of Earth and Environmental Sciences, University of Ottawa, 25 Templeton St., Ottawa, Ontario, K1N 6N5

The Gibraltar porphyry Cu-Mo deposit is hosted by the late Triassic, Granite Mountain batholith. It has three phases; Border Phase Quartz Diorite, Granite Mountain Tonalite, and foliated Mine Phase Tonalite. Zircon saturation temperatures and Ti in zircon geothermometry show hot crystallization temperatures, 780 -850 C, in the centre of the Mine Phase Tonalite compared 670-750 C recorded from other rocks. Elevated Ce4+/Ce3+ (32 -138 for quartile values) for zircon reflects moderately oxidized conditions of the parental magmas. The rocks in the batholith show phyllic and propylitic alteration. Propylitic alteration (green rock alteration) forms epidote, chlorite, and albite, and is extensive throughout the batholith. Epidote occurs as dissemination, isolated grains, and forms monomierallic veins and quartz-epidote veins in the batholith. These veins strike towards the mineralized centre. Epidote in contact with chalcopyrite is unzoned and Fe poor, suggesting Fe is preferentially incorporated into sulfides. Veins consist of unzoned, Fe poor epidote in the middle bordered by late-crystallizing Fe rich epidote. Disseminated epidote shows Fe poor cores and Fe rich rims. Epidote zoning suggests sulfur-rich mineralized hydrothermal activity, followed by sulfur-poor barren hydrothermal activity in the batholith. In addition, epidote in the centre of the Mine Phase Tonalite is REE-rich (high allanite component) and elevated concentrations of REEs (> 54 ppm) in bulk rocks. Allanite is not found >4km away from the mineralized centre. We suggest the mineralized hydrothermal activity is responsible for the REE enrichment in the centre of the Mine Phase Tonalite.

Abstract for poster presented at SEG meeting 2018:

Zircon from the Granite Mountain Batholith, a Host of the Gibraltar Porphyry Cu-Mo Deposit, in the Canadian Cordillera

Christopher H. Kobylinski[1], Keiko Hattori[1], Alain Plouffe[2], Scott Smith[3]

[1]University of Ottawa, Ottawa, ON, Canada

[2]Geological Survey of Canada, Ottawa, ON, Canada

[3]Taseko Gibraltar, Mcleese Lake, BC, Canada

The Mesozoic Quesnel terrane in the Canadian Cordillera contains numerous porphyry Cu deposits, including the Gibraltar porphyry Cu deposit (3.687 Mt Cu, 0.123 Mt Mo) in south-central British Columbia. The deposit is hosted by tonalitic rocks of the Granite Mountain batholith (14 x 20 km), which intruded mafic volcanic rocks of the Nicola volcanic rocks. The Mine phase (3 x 13 km), which is primarily composed of foliated tonalite and hosts the mineralization, is extensively altered to form K-feldspar, white mica, epidote, and pyrite. U-Pb dating of zircons from the Mine phase reveals at least four age groups, ranging from 219 to 202 Ma. Zircons from the oldest group (219.6 ± 1.5 Ma) record the highest Ce4+/Ce3+ (680 ± 180, 1 s, n = 14), whereas zircons from the other three groups in the Mine phase are low in Ce4+/Ce3+ (214 ± 64, n = 43). Zircons from the Border and Granite Mountain phases report even lower Ce4+/Ce3+ (128 ± 35, n = 108). The oldest group of intrusions likely contributed the majority of the Cu mineralization, based on the high-Cu contents in the rocks and highly oxidized conditions of its parental magma. Younger groups of intrusions made moderate contributions to the Cu budget, whereas the youngest intrusion in the Mine phase did not contribute any Cu. Ages and Ce4+/Ce3+ values of zircons from the mineralized Mine phase are very similar to the values for zircons in mineralized intrusions in the Highland Valley porphyry Cu deposit, ~ 240 km south of the Gibraltar deposit and also within the Quesnel terrane. Ce4+/Ce3+ values positively correlate with Ce/Nd and Ce/Ce* in zircon at Gibraltar, suggesting that the compositions of zircons in glacial sediments and streams may be useful during exploration for fertile intrusions associated with porphyry Cu mineralization.

Appendix 5. Presented Posters for Conferences

Poster presented at the PDAC-SEG 2016 Student Minerals Colloquium, 2016

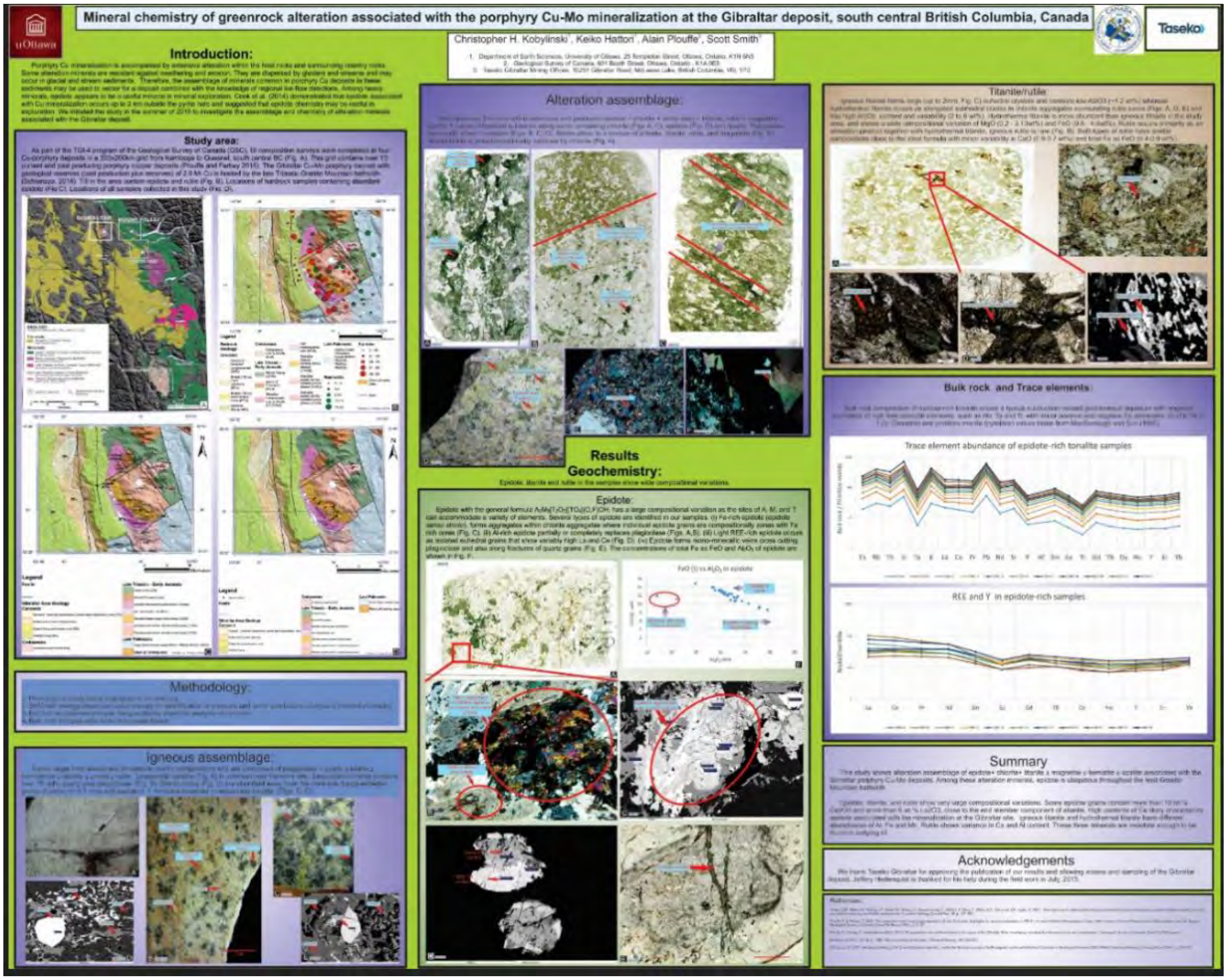

Mineral chemistry of greenrock alteration associated with the porphyry Cu-Mo mineralization at the Gibraltar deposit, south central British Columbia, Canada

Christopher H. Kobylinski, Keiko Hattori, Alain Plouffe, Scott Smith

Introduction:

Study area:

Methodology:

Igneous assemblage:

Alteration assemblage:

Results

Geochemistry:

Epidote:

Titanite/rutile:

Bulk rock and Trace elements:

Summary

Acknowledgements

Poster presented at the GAC-MAC Annual meeting, 2016

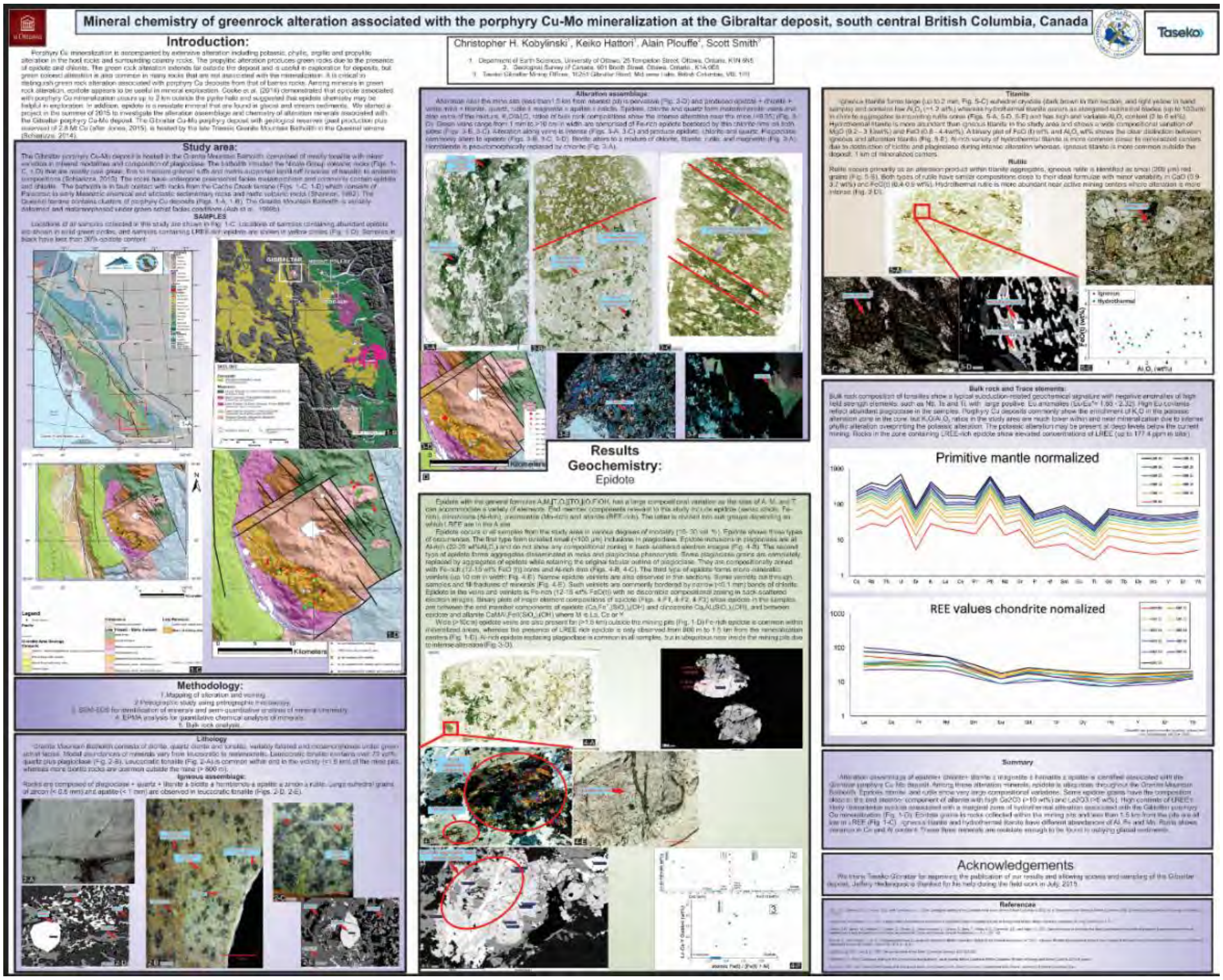

Mineral chemistry of greenrock alteration associated with the porphyry Cu-Mo mineralization at the Gibraltar deposit, south central British Columbia, Canada

Christopher H. Kobylinski[1], Keiko Hattori[1], Alain Plouffe[2], Scott Smith[3]

Introduction:

Study area:

SAMPLES

Methodology:

Lithology

Igneous assemblage:

Alteration assemblage:

Results Geochemistry:

Epidote

Titanite

Rutile

Bulk rock and Trace elements:

Summary

Acknowledgements

References

Poster presented at PDAC-SEG Student Minerals Colloquium 2017

Epidote and zircon associated with the porphyry copper mineralization at the Gibraltar mine in south central British Columbia

Christopher H. Kobylinski[1], Keiko Hattori[1], Alain Plouffe[2], Scott Smith[3]

1. Department of Earth and Environmental Sciences, University of Ottawa, 25 Templeton Street, Ottawa, Ontario, K1N 6N5
2. Geological Survey of Canada, 601 Booth Street, Ottawa, Ontario K1A 0E8
3. Taseko Gibraltar Mining Offices, 10251 Gibraltar Road, McLeese Lake, British Columbia, V0L 1P0

Introduction:

Porphyry Cu mineralization is accompanied by extensive alteration including potassic, phyllic, argillic and propylitic alteration in the host rocks and surrounding country rocks. The propylitic alteration (greenrock alteration) extends far outside the deposit and is useful in exploration for deposits, but green colored alteration is also common in many rocks that are not associated with the mineralization. It is critical to distinguish green rock alteration associated with porphyry Cu deposits from that of barren rocks. Cooke et. al. (2014) demonstrated that epidote associated with porphyry Cu mineralization occurs up to 2 km outside the pyrite halo and suggested that epidote chemistry may be helpful in exploration. In addition, epidote is a resistate minerals that are found in glacial and stream sediments. Epidote associated with Cu-mineralization is defined by its zoning pattern, spatial distribution and Fe content.

Study area:

The Gibraltar Cu-Mo porphyry deposit with geological reserves of 2.8 Mt Cu (Jones, 2015), is hosted by the late Triassic Granite Mountain Batholith in the Quesnel terrane (Schiarizza, 2014). The batholith is comprised of mostly tonalite with minor variation in mineral modalities. The batholith intruded the Nicola Group volcanic rocks (Figs. 1-B, 1-C) that are tuffs and lapilli tuff breccias of basaltic to andesitic compositions (Schiarizza, 2015).

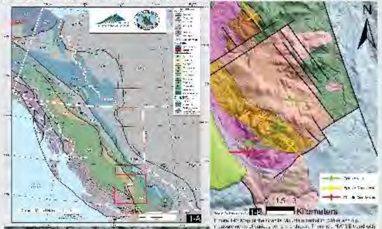

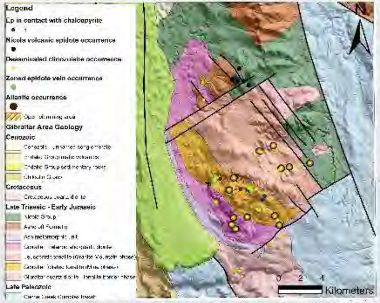

Figure 1-C: Map of the Granite Mountain batholith and phases. Epidote types and occurrences are shown. Allanite (red circles) are found in and proximal (<2km) from the mineralization centre. Epidote in contact with Cu-minerals are shown in blue and are limited to the mineralized centre. Clinozoisite and epidote are found together (zoning), with the exception of inside the Cretaceous quartz diorite (clinozoisite only).

Methodology:

1. Mapping of alteration and veining.
2. Petrographic study.
3. SEM-EDS and EPMA for identification of minerals and analysis of mineral chemistry.
4. LA ICPMS for trace element composition of zircons.
5. Bulk rock analysis.

Lithology

The batholith consists of 4 phases; Gibraltar foliated tonalite (Mine phase), leucocratic tonalite (Granite Mountain phase), Gibraltar quartz diorite (Tonalite border phase), Gibraltar melanocratic quartz diorite. The Granite Mountain phase, mine phase and tonalite border phase are leucocratic 75% quartz-plagioclase vol%. The melanocratic quartz diorite phase has >20% ferromagnesian minerals (Fig. 2-A, B, C).

Igneous assemblage:

Rocks are composed of plagioclase ± quartz ± titanite ± biotite ± hornblende ± apatite ± zircon ± rutile.

Results

Alteration assemblage and bulk rock :

Alteration near the mine site (less than 1.5 km from nearest pit) is strongest and produces epidote + chlorite + white mica + titanite + rutile + magnetite + apatite + calcite. Sericitization of plagioclase is strongest (>50% of plagioclase replacement) and epidotisation overprints sericite alteration and is less intense (<30% plagioclase replacement), igneous plagioclase textures are preserved. Loss on ignition values are higher near the mineralization centre, mostly ranging from 2 to 7%. Phyllic alteration produces sericite + quartz + pyrite, and dominates the mineralization centre. Propylitic alteration replaces plagioclase with epidote and hornblende with chlorite. Propylitic alteration overprints phyllic alteration in the batholith.

Epidote and epidote-quartz veins (Figs. 1-C, D) (1 mm - >10 cm in width) are comprised of zoned epidote (Fig 4-D). Plagioclase commonly alters to zoned epidote (Fig. 4-F). Epidote veins contain a variable amount of magnetite and hematite. LREE's are elevated in bulk rock near mine pits (Figs. 3-A, B, C, D, F) and fluctuate moving outwards. Bulk rock plots show more evolved rocks south east of the foliated mine phase (>4 km away) with lower total REE's and MgO (Figs. 3-A, B, C). A positive correlation between P and LREEs suggests that apatite is the major host of LREE. (Fig. 3-D). REE content does not affect epidote modalities (Fig. 3-E). High REE in allanite suggests introduction of LREE by hydrothermal fluids or allanite occurrence reflects high REE content in original rocks.

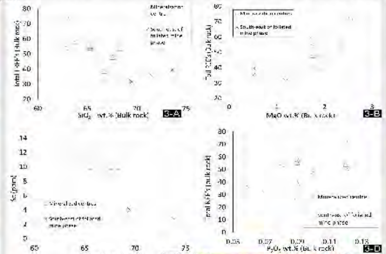

Epidote type	FeO(t) (wt% average)	Al2O3 (wt% average)	Mn (wt% average)	Zoning type	Textures/Inclusions
Ep with Py	11.16	24.77	0	No zoning	Clean subhedral grains, no inclusions
Ep with Cpy	12.23	23.07	0.01	No zoning	Clean subhedral grains, no inclusions
Nicola volcanics large Ep (>100um)	15.24	22.3	0.04	No zoning	Subhedral with Ap and Ttn inclusions
Nicola volcanics small Ep (<100um)	15.82	21.31	0.64	No zoning	Clean subhedral grains, no inclusions
Ep in veins	Variable (zoned)	Variable (zoned)	0.13	Zoned; Fe poor cores, Fe rich rims	Veins contain Fe oxides
Tonalite ep large isolated grains (>100um)	Variable (zoned)	Variable (zoned)	0.03	Variably zoned	Clean subhedral grains, no inclusions
Tonalite disseminated ep (<50um)	Variable (zoned)	Variable (zoned)	0.34	Zoned; Fe poor cores, Fe rich rims	Clean subhedral tabular grains, no inclusions

Table-1

Bulk rock and zircon trace element geochemistry:

Bulk rock composition of tonalites show varying Eu anomalies (Eu/Eu* = 0.55-1.24). Low Eu/Eu* are observed near mineralization and increase outwards (Fig. 5-A). Ti in zircon thermometry (Watson 2007) was applied to zircons assuming aTiO2= 0.7, hotter temperatures are calculated near the mineralized centre (Fig.5-B).

The contents of Sr, K2O, Ba, CaO do not show any correlation with Eu/Eu* (Figs. 5 D, E, F, G). This suggests Eu/Eu* is not controlled by plagioclase crystallization. There is weak positive correlation between Eu/Eu* in bulk rock and Eu/Eu* in zircon Eu/Eu*. This suggests that zircon is recording the low Eu/Eu* of the parental magma, or that there is post crystallization modification of Eu/Eu*.

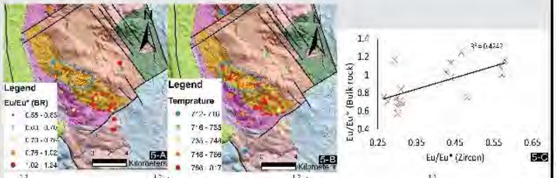

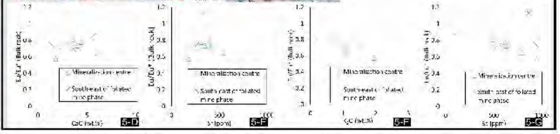

Epidote mineral chemistry

Epidote with the general formula A2M3[T3O11](O,F)OH, has a large compositional variation as the sites of A, M and T can accommodate a variety of elements. End member components include epidote (sensu stricto, Fe-rich), clinozoisite (Al-rich), and allanite (REE-rich). Epidote shows 8 types of occurrences (Table-1). Epidote in contact with chalcopyrite is Fe-poor (Figs. 5-A, G) due to Fe preferentially incorporated by sulphides. Other types of epidote in the batholith show zoning with a Fe-poor (Al-rich) core and Fe-rich rims (Figs. 4-C, D, E, F). The occurrence of Fe-poor cores suggest that they are contemporaneous with the mineralization. Epidote veins striking towards mineralized centres record these hydrothermal events by their zoning pattern (Fig. 4-D). Allanite shows patchy zoning due to variations in Ce content (10-14%) (Figs. 4-B). Allanite is spatially associated with Cu-Mo mineralization at Gibraltar. Allanite is Fe-Rich (17-19 wt.%) and is not associated with Cu-mineralization. No allanite is found in samples >4 km away from the mineralization centre.

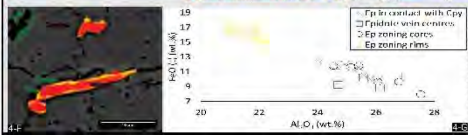

Figure 4-G: Epidote in contact with chalcopyrite has contains low Fe and high Al as do the cores of the zoned epidotes and epidote veins centres found throughout the batholith. The rims of the epidotes are Fe-Rich and Al-poor. The association of zoned epidote cores and epidote in contact with mineralization is shown. Zoned epidote rims are not related.

Summary

Zoning in epidote suggests that there were at least two different hydrothermal events that affected the batholith. The first was sulphur-rich fluid that created sulphide mineralization and alteration defined by Fe-poor epidote. A later hydrothermal event generated sulphur poor magmatic fluid create the Fe-rich rims of epidote. Allanite is Fe-rich and not associated with Cu mineralization at Gibraltar.

Epidote in the Cretaceous quartz diorite and the Nicola volcanics has different compositions as that in the Gibraltar deposit. High Fe contents suggest that the epidote is not associated with Cu-Mo mineralization at Gibraltar (Table 1).

Cu-Mo mineralization at Gibraltar is hosted in the more primitive section of the Gibraltar foliated tonalite (Mine phase) which is enriched in REE's. The south-east section of the mine phase is barren, more evolved and relatively depleted in REE's.

Allanite is spatially associated with Cu-Mo mineralization at Gibraltar.

The more evolved rocks of the mineralized phase have a lower crystallization temperature, the more primitive mineralization centre has a higher crystallisation temperature.

Acknowledgements

We thank Taseko Gibraltar for approving the publication of our results and allowing access and sampling of the Gibraltar deposit.

We thank the LA-ICMPS laboratory at the University of Ottawa

We thank the SEM and EPMA laboratories at the University of Ottawa

References

Ash, C. H., Rydman, M. O., Payne, C. W., and Panteleyev, A. [illegible]

[illegible] British Columbia Ministry of Energy and Mines, British Columbia Geological Survey [illegible]

Cooke, D.R., [illegible] [illegible] Economic Geology [illegible]

Jones, [illegible] of the Gibraltar mine as of December 2014 [illegible]

[illegible] Geological Survey of Canada, Open File [illegible]

[illegible]

Schiarizza, P. (2014) [illegible]

Schiarizza, P. [illegible]

Sharman, K.R., 1992. Cache Creek Group [illegible] near Cache Creek, British Columbia. Unpublished MSc Thesis, University of British Columbia. 72 p.

Ferry, J. M., & Watson, E. B. (2007). [illegible] Contributions to Mineralogy and Petrology [illegible]

Poster presented at SEG meeting 2018

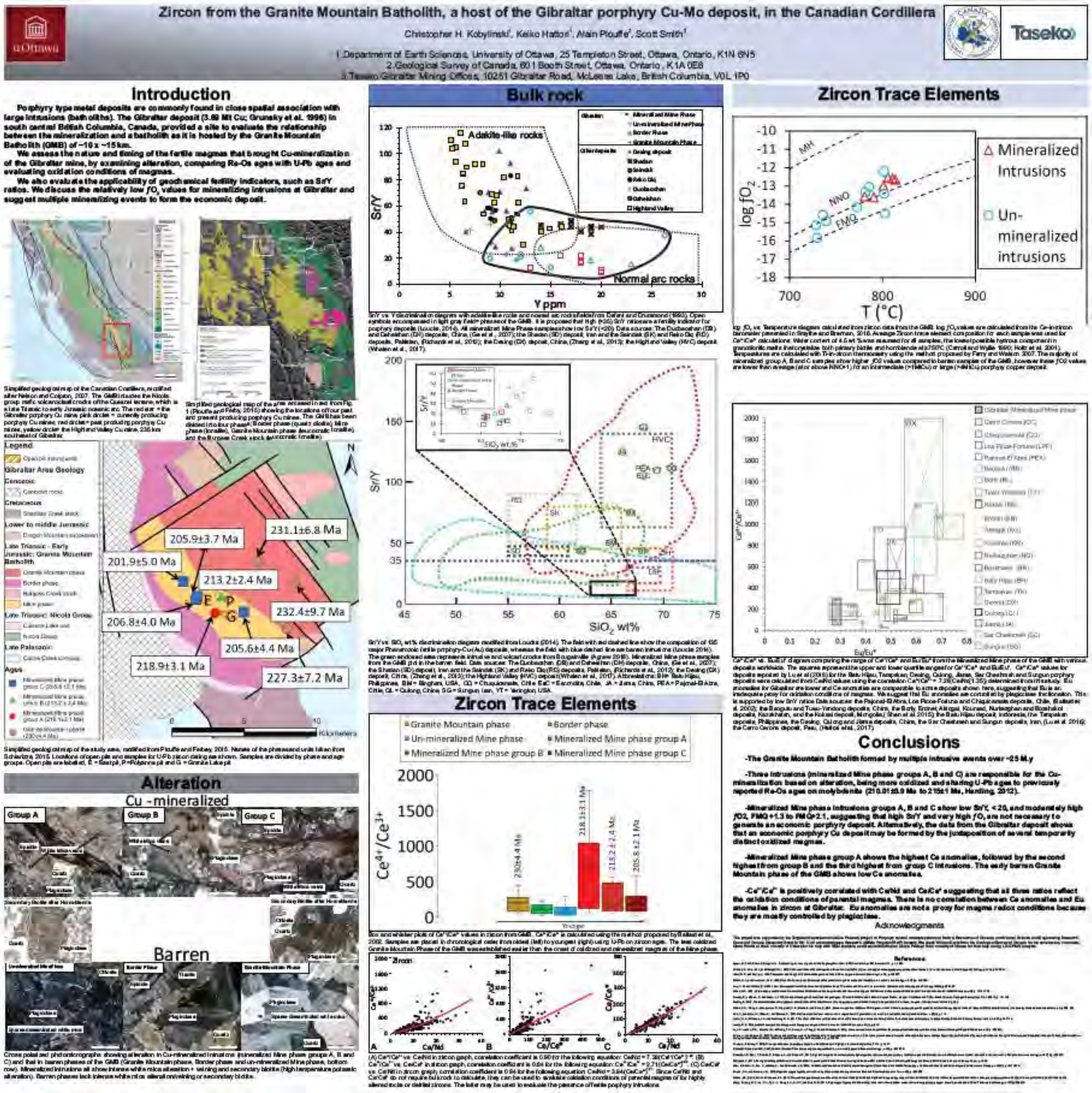

Zircon from the Granite Mountain Batholith, a host of the Gibraltar porphyry Cu-Mo deposit, in the Canadian Cordillera

Christopher H. Kobylinski[1], Keiko Hattori[1], Alain Plouffe[2], Scott Smith[3]

1.Department of Earth Sciences, University of Ottawa, 25 Templeton Street, Ottawa, Ontario, K1N 6N5
2.Geological Survey of Canada, 601 Booth Street, Ottawa, Ontario, K1A 0E8
3.Taseko Gibraltar Mining Offices, 10251 Gibraltar Road, McLeese Lake, British Columbia, V0L 1P0

Introduction

Porphyry type metal deposits are commonly found in close spatial association with large intrusions (batholiths). The Gibraltar deposit (3.69 Mt Cu; Grunsky et al. 1996) in south central British Columbia, Canada, provided a site to evaluate the relationship between the mineralization and a batholith as it is hosted by the Granite Mountain Batholith (GMB) of ~10 x ~15 km.

We assess the nature and timing of the fertile magmas that brought Cu-mineralization of the Gibraltar mine, by examining alteration, comparing Re-Os ages with U-Pb ages and evaluating oxidation conditions of magmas.

We also evaluate the applicability of geochemical fertility indicators, such as Sr/Y ratios. We discuss the relatively low fO_2 values for mineralizing intrusions at Gibraltar and suggest multiple mineralizing events to form the economic deposit.

Alteration

Cu -mineralized

Barren

Bulk rock

Zircon Trace Elements

Conclusions

-The Granite Mountain Batholith formed by multiple intrusive events over ~25 M.y

-Three intrusions (mineralized Mine phase groups A, B and C) are responsible for the Cu-mineralization based on alteration, being more oxidized and sharing U-Pb ages to previously reported Re-Os ages on molybdenite (210.01±0.9 Ma to 215±1 Ma, Harding, 2012).

-Mineralized Mine phase intrusions groups A, B and C show low Sr/Y, < 20, and moderately high fO_2, FMQ+1.3 to FMQ+2.1, suggesting that high Sr/Y and very high fO_2 are not necessary to generate an economic porphyry deposit. Alternatively, the data from the Gibraltar deposit shows that an economic porphyry Cu deposit may be formed by the juxtaposition of several temporarily distinct oxidized magmas.

-Mineralized Mine phase group A shows the highest Ce anomalies, followed by the second highest from group B and the third highest from group C intrusions. The early barren Granite Mountain phase of the GMB shows low Ce anomalies.

-Ce^{4+}/Ce^{3+} is positively correlated with Ce/Nd and Ce/Ce* suggesting that all three ratios reflect the oxidation conditions of parental magmas. There is no correlation between Ce anomalies and Eu anomalies in zircon at Gibraltar. Eu anomalies are not a proxy for magma redox conditions because they are mostly controlled by plagioclase.

Acknowledgments

References

Appendix 6. SEM-CL Images of all zircon

Below are all zircons examined for this study, only grains without sector zoning were used for trace element analysis. Grains with a green X in the bottom right hand corner were used for U-Pb dating and grains with a green circle in the bottom right hand corner were used for trace element analysis. Not all grains were used. Some of the larger grains are used multiple times in different unablated areas of the grain.

GBR-2, 1-12, 80-212µm fraction

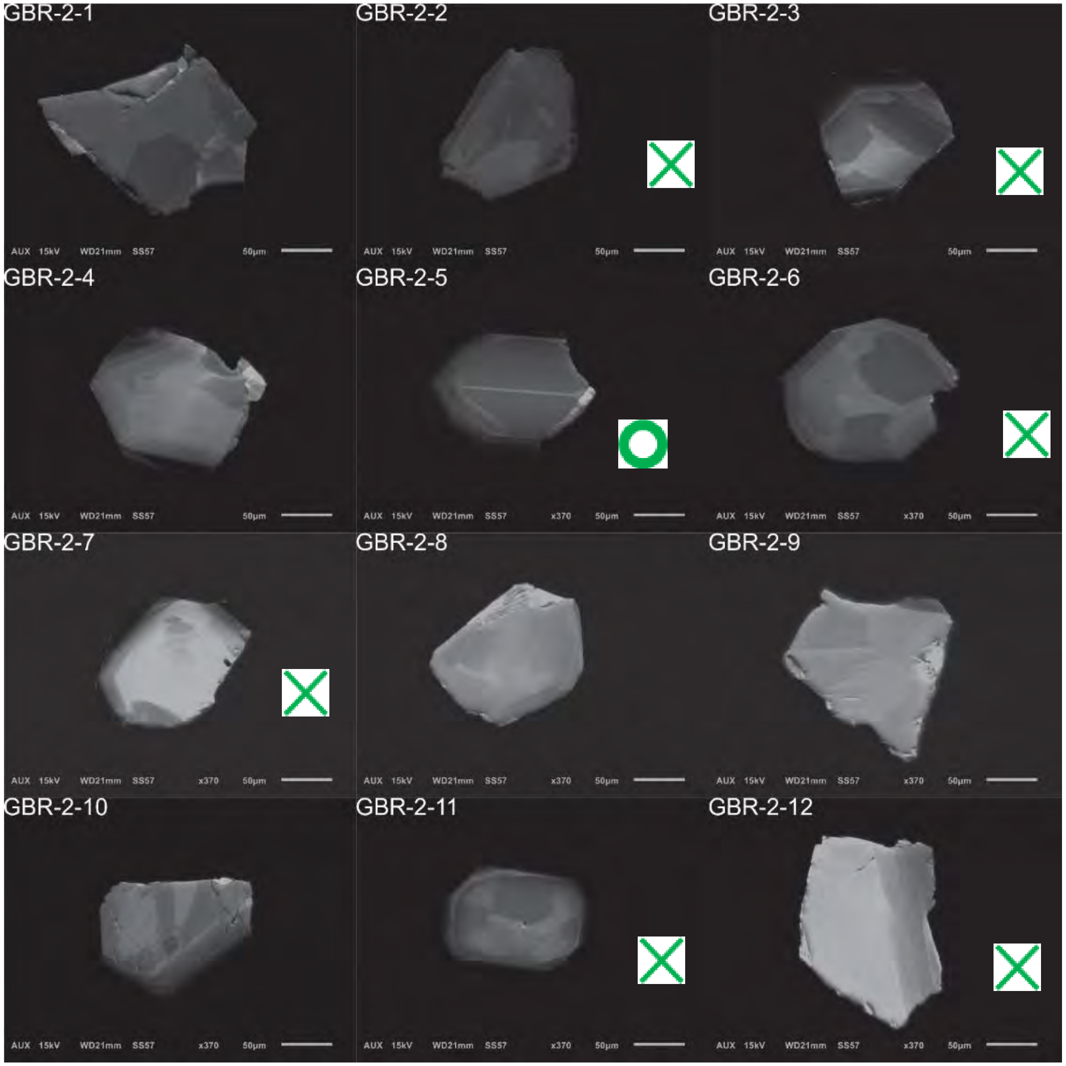

GBR-2, 1-12, 212-350μm fraction

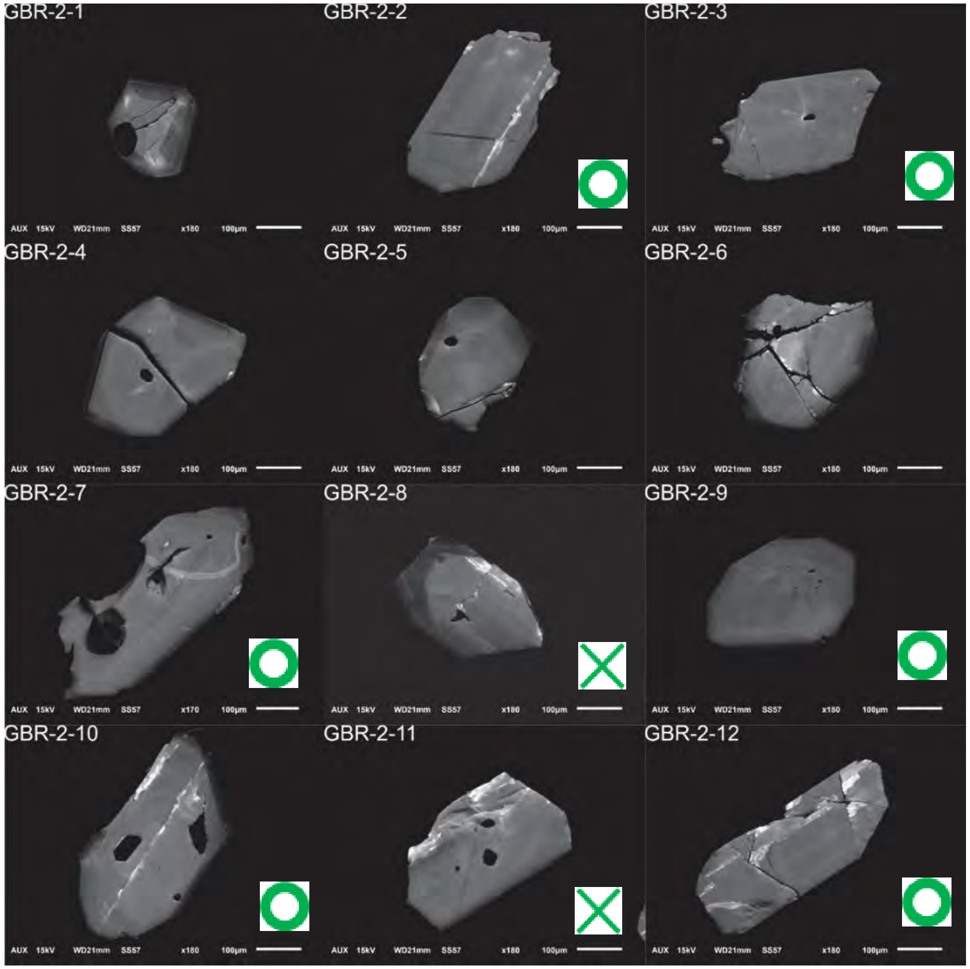

GBR-2, 13-24, 212-350µm fraction

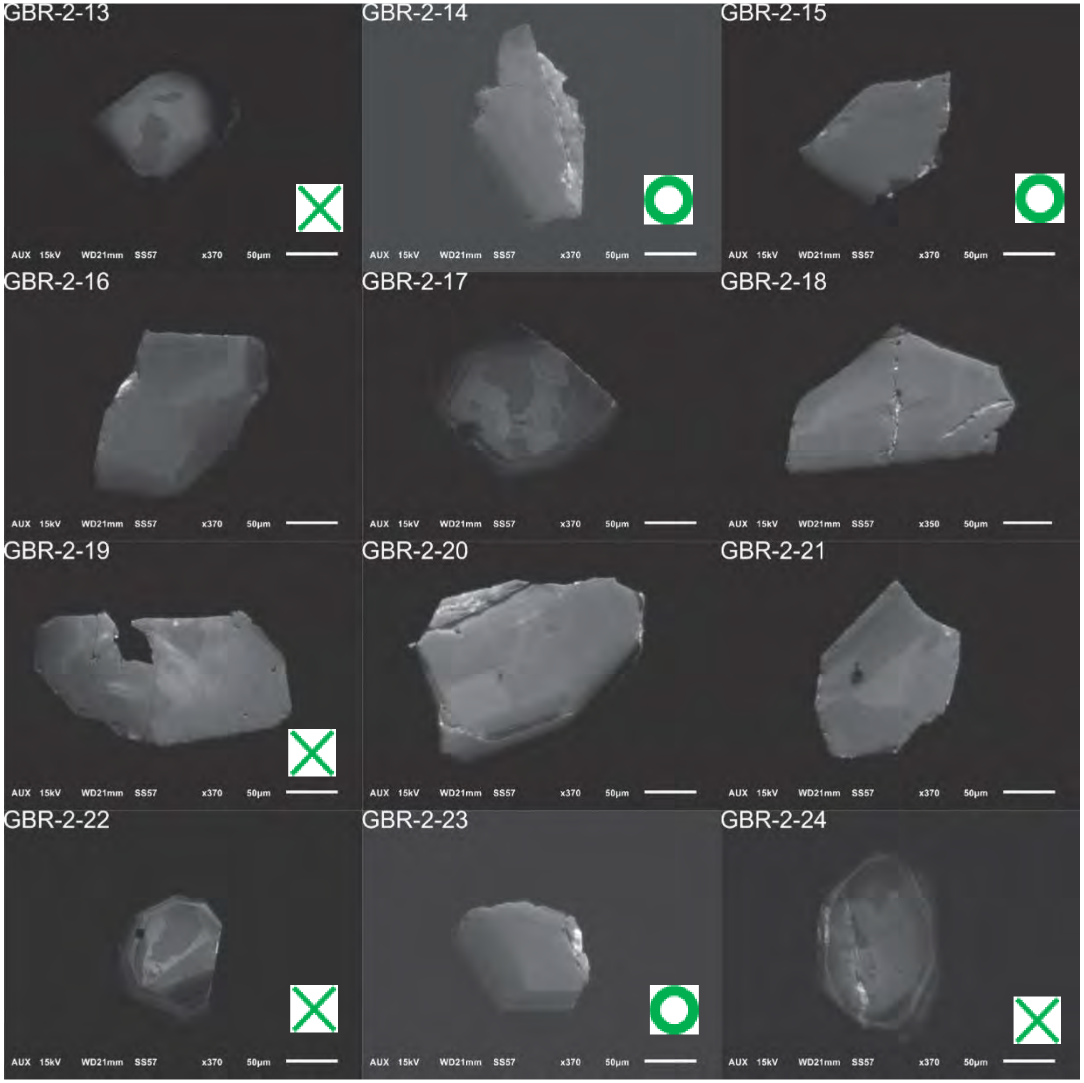

GBR-2, 13-24, 80-212µm fraction

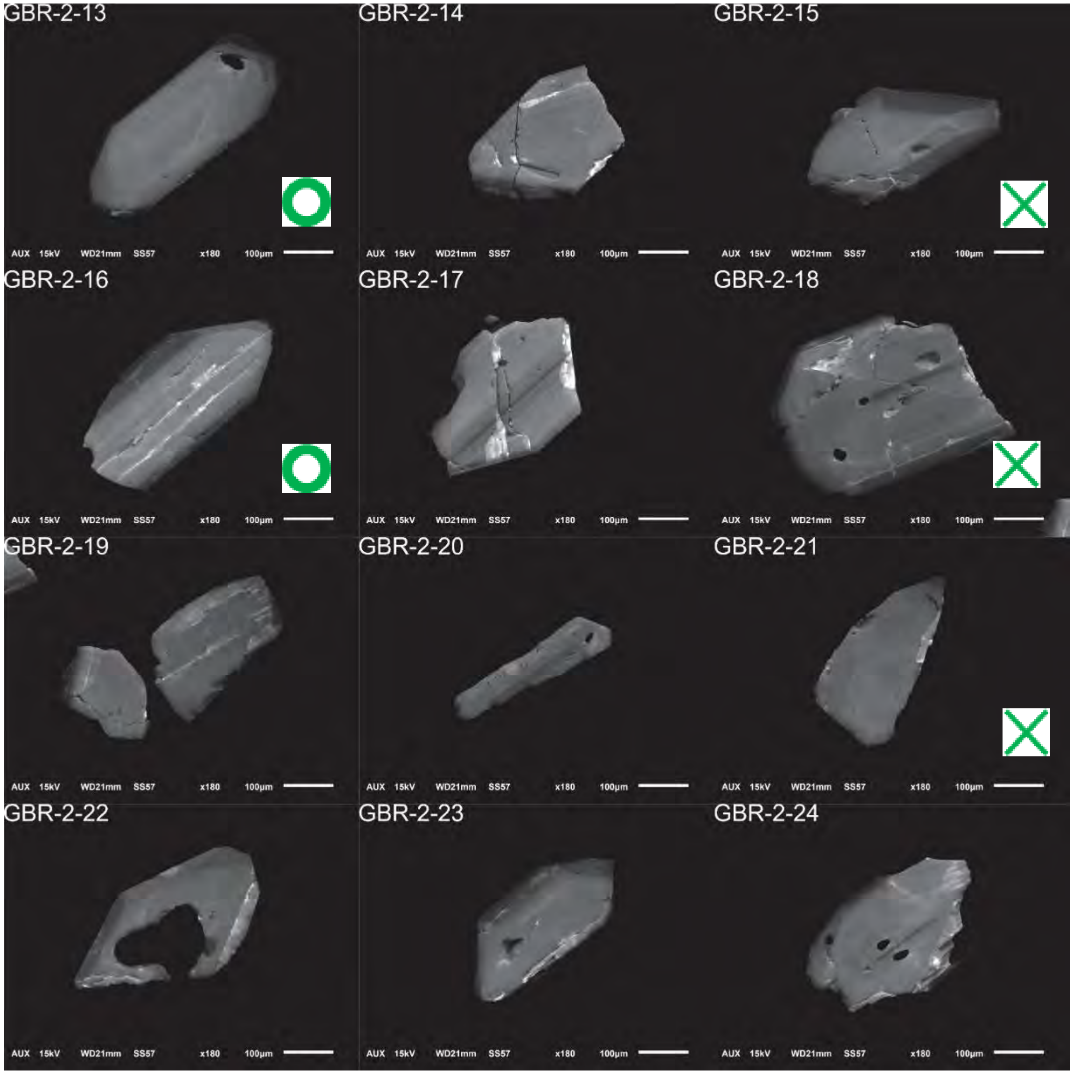

GBR-2, 25-35, 80-212µm fraction


GBR-2-25

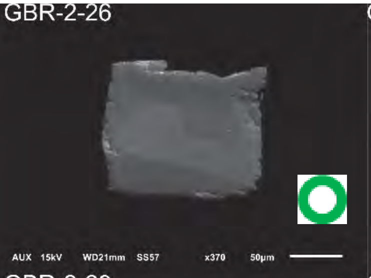
GBR-2-26


GBR-2-27

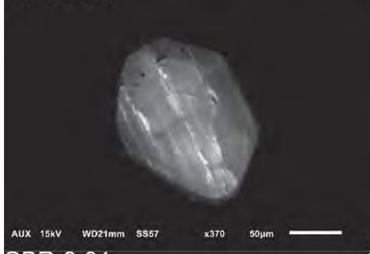
GBR-2-28

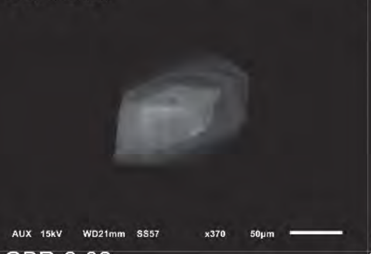
GBR-2-29

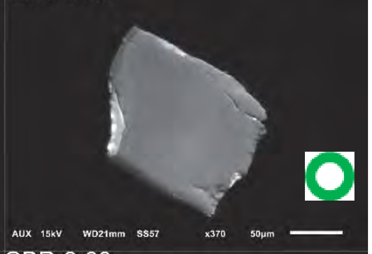
GBR-2-30

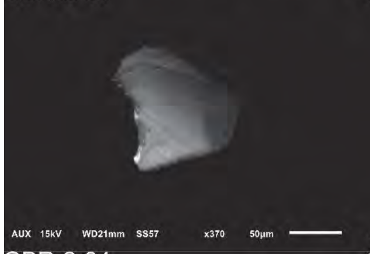
GBR-2-31


GBR-2-32

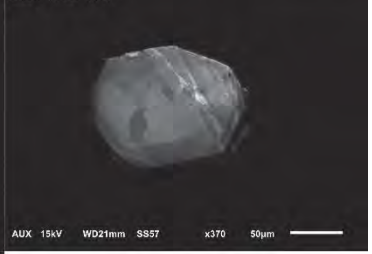
GBR-2-33


GBR-2-34

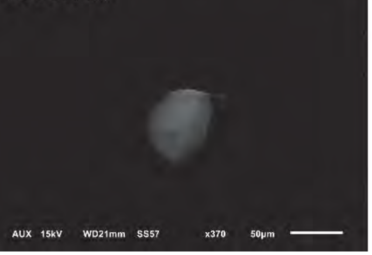
GBR-2-35

GBR-2, 25-36, 212-350µm fraction

GBR-2-25

GBR-2-26

GBR-2-27

GBR-2-28

GBR-2-29

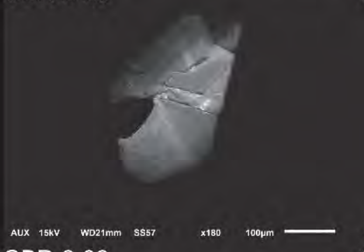

GBR-2-30

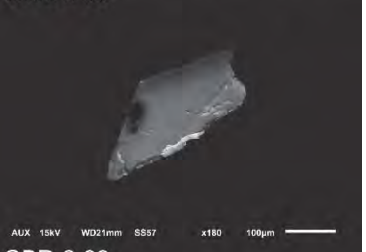

GBR-2-31

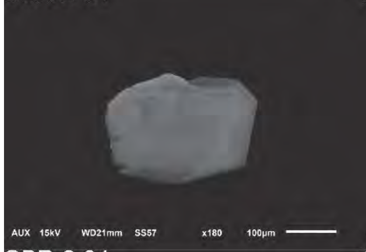

GBR-2-32

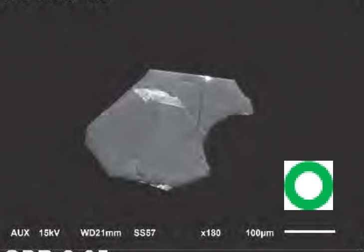

GBR-2-33

GBR-2-34

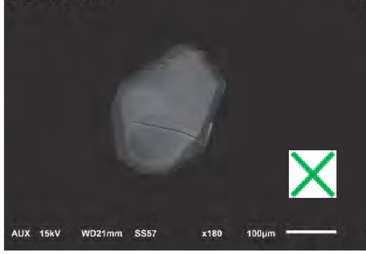

GBR-2-35

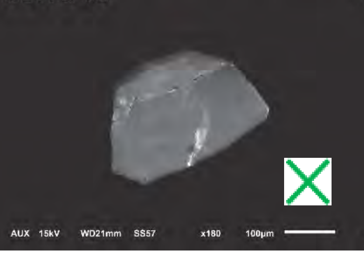

GBR-2-36

GBR-2, 49-53, 212-350µm fraction

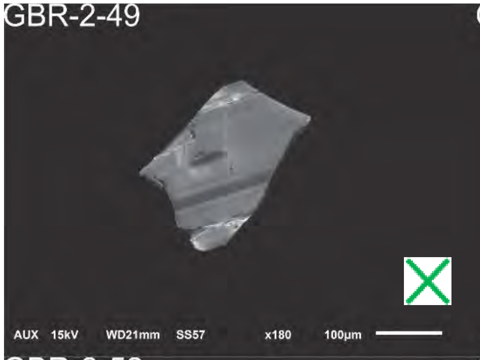
GBR-2-49


GBR-2-50

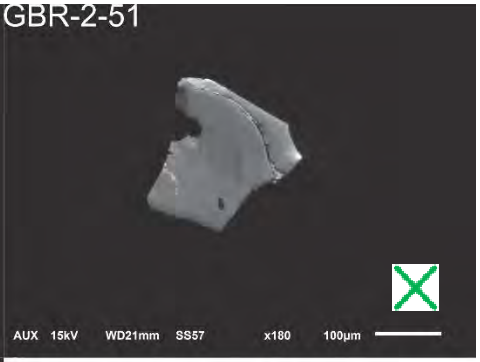
GBR-2-51

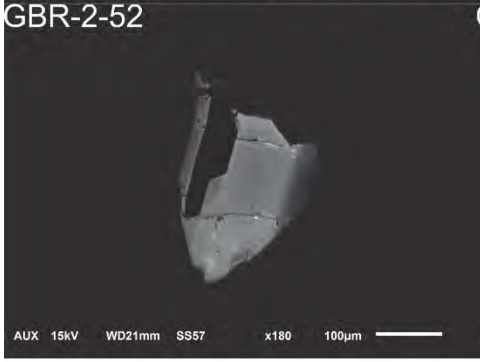
GBR-2-52


GBR-2-53

GBR-2-2, 1-12, 212-350µm fraction

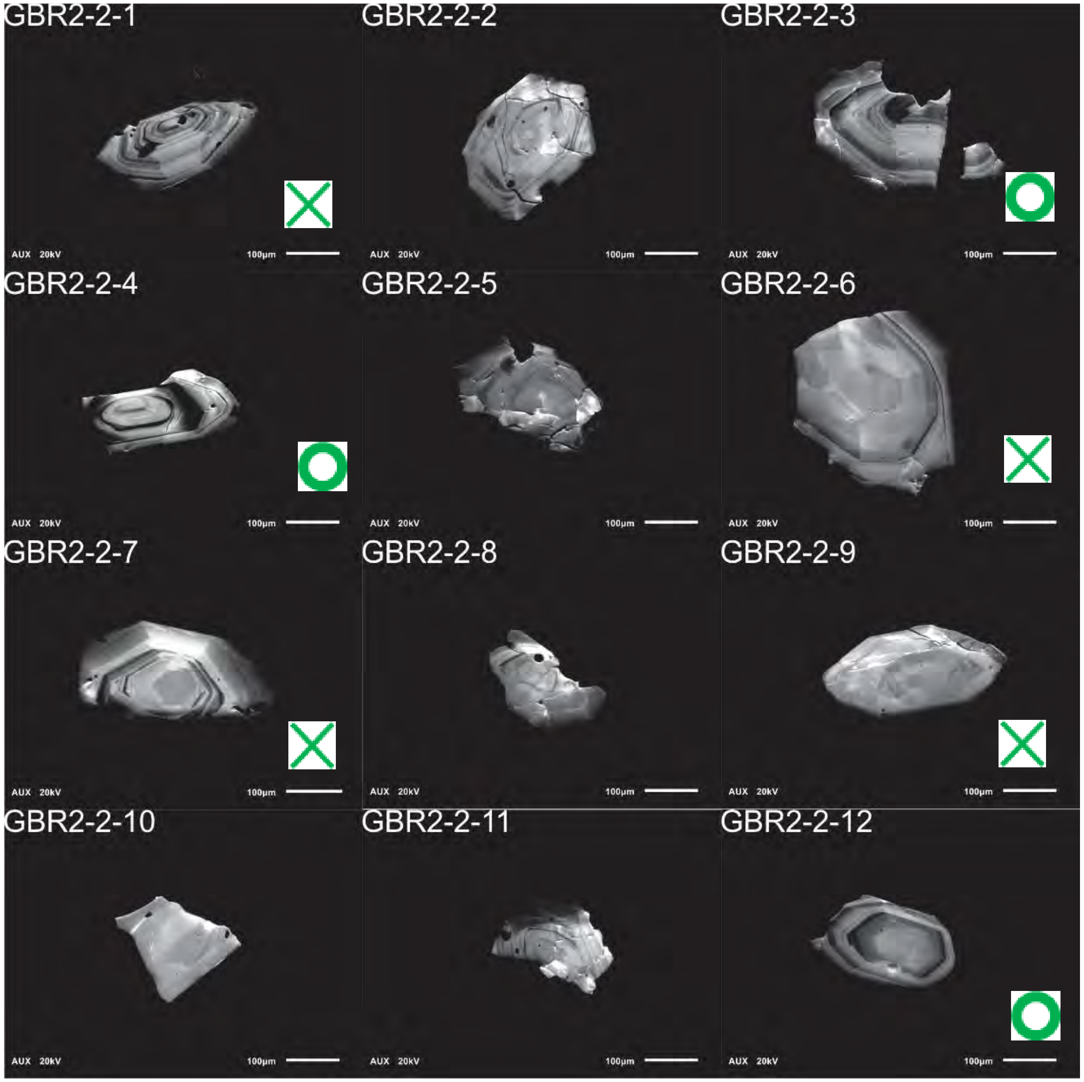

GBR-2-2, 25-27, 212-350µm fraction

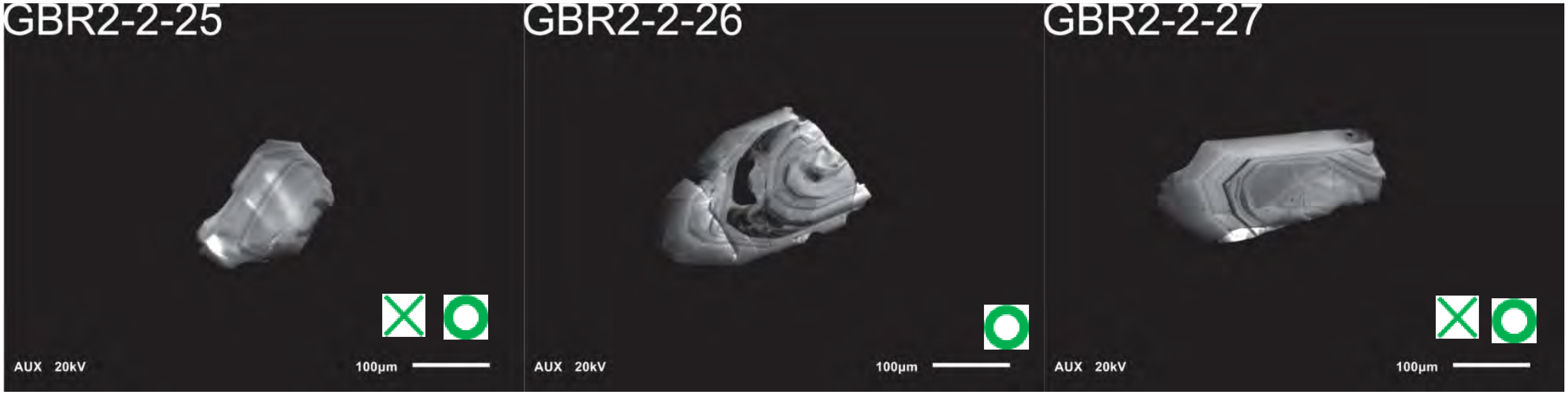

GBR-2-15, 1-12, 212-350µm fraction

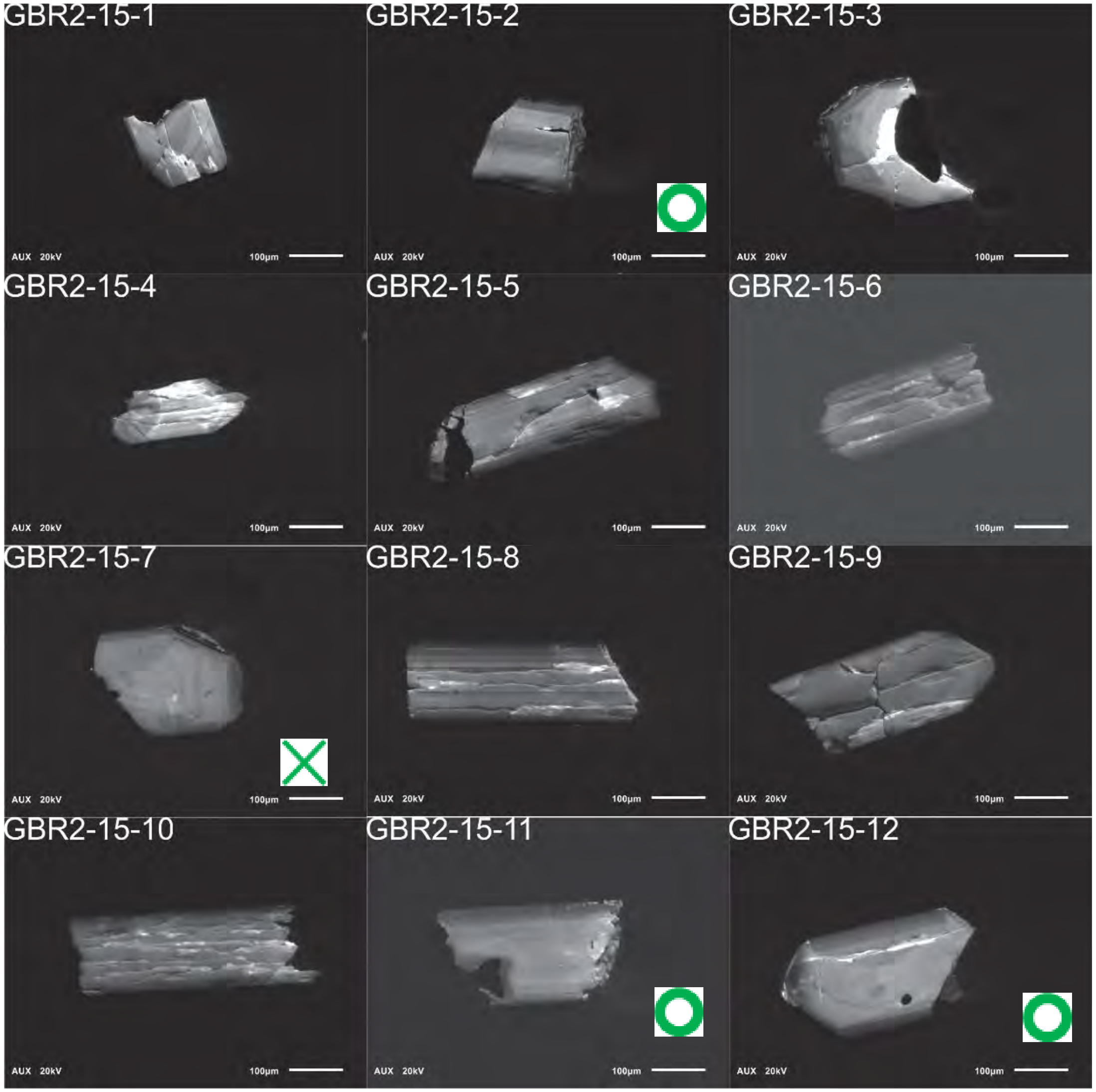

GBR-2-2, 13, 212-350µm fraction

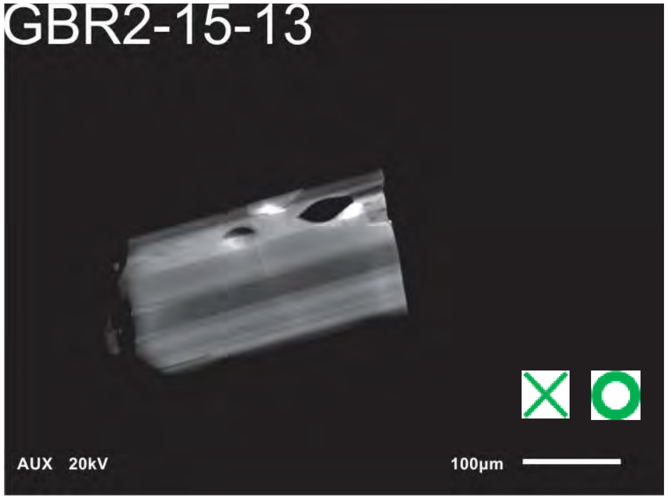

GBR-2-16, 1-12, 212-350μm fraction

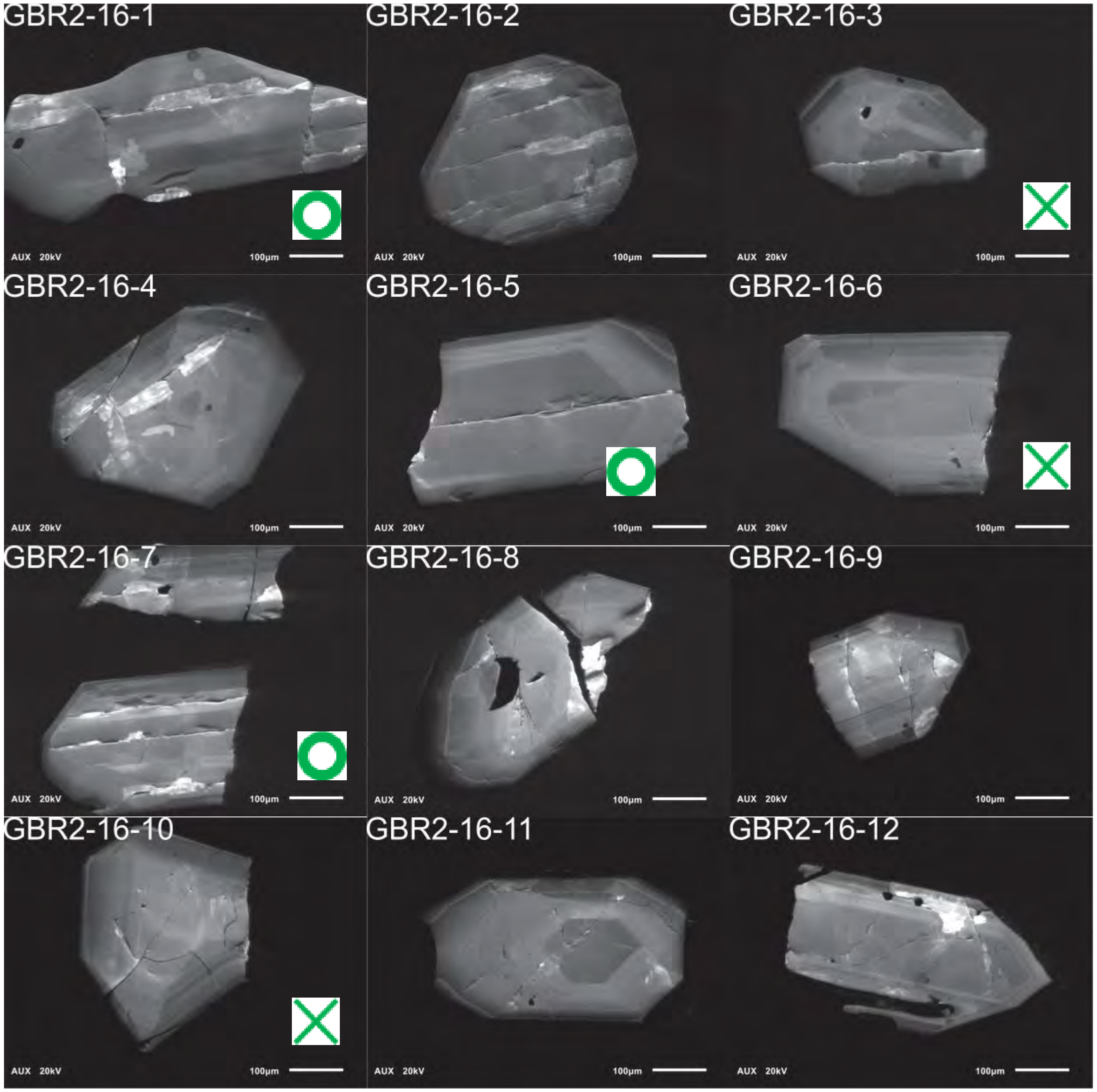

GBR-2-16, 13-24, 212-350µm fraction

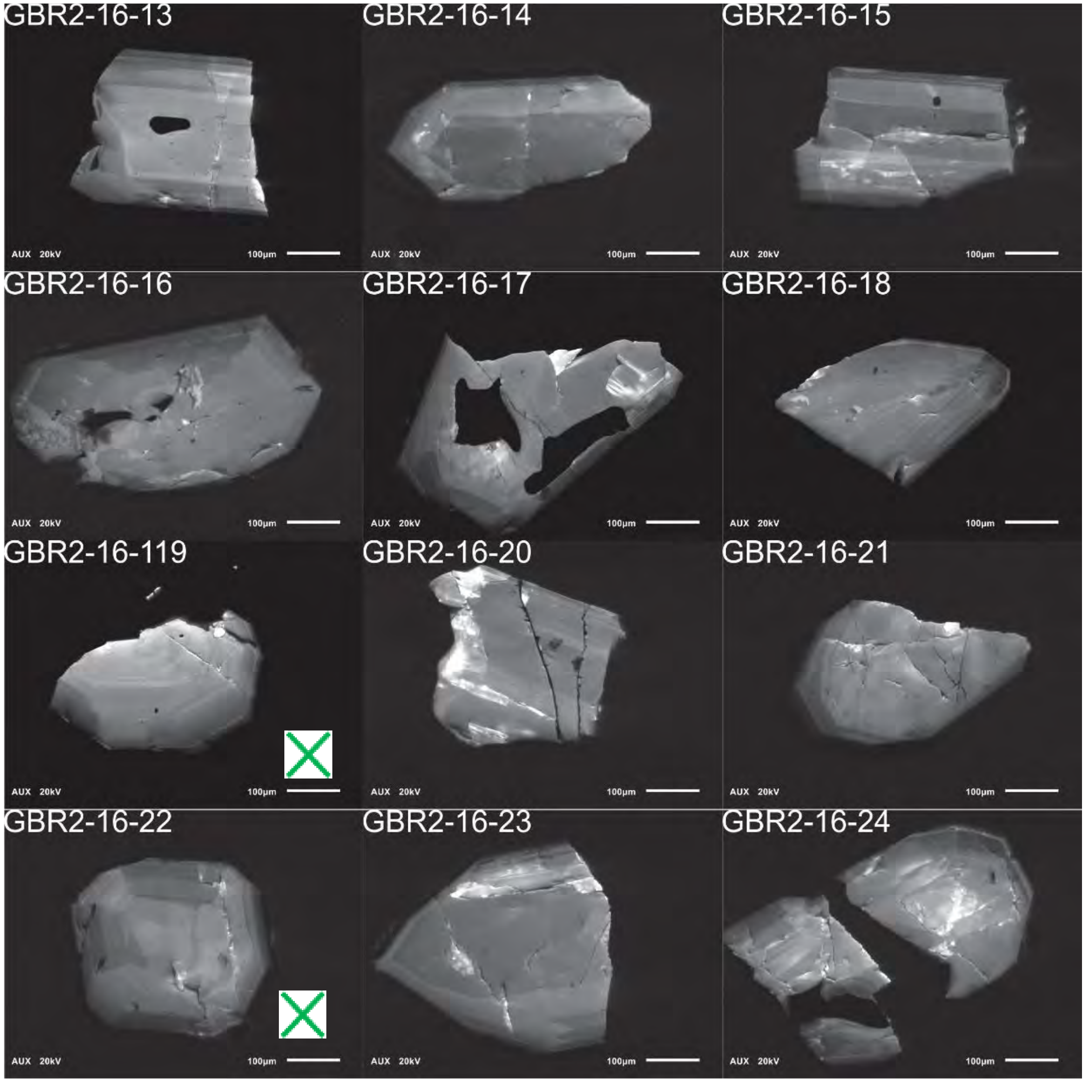

GBR-2-2, 25-33, 212-350µm fraction

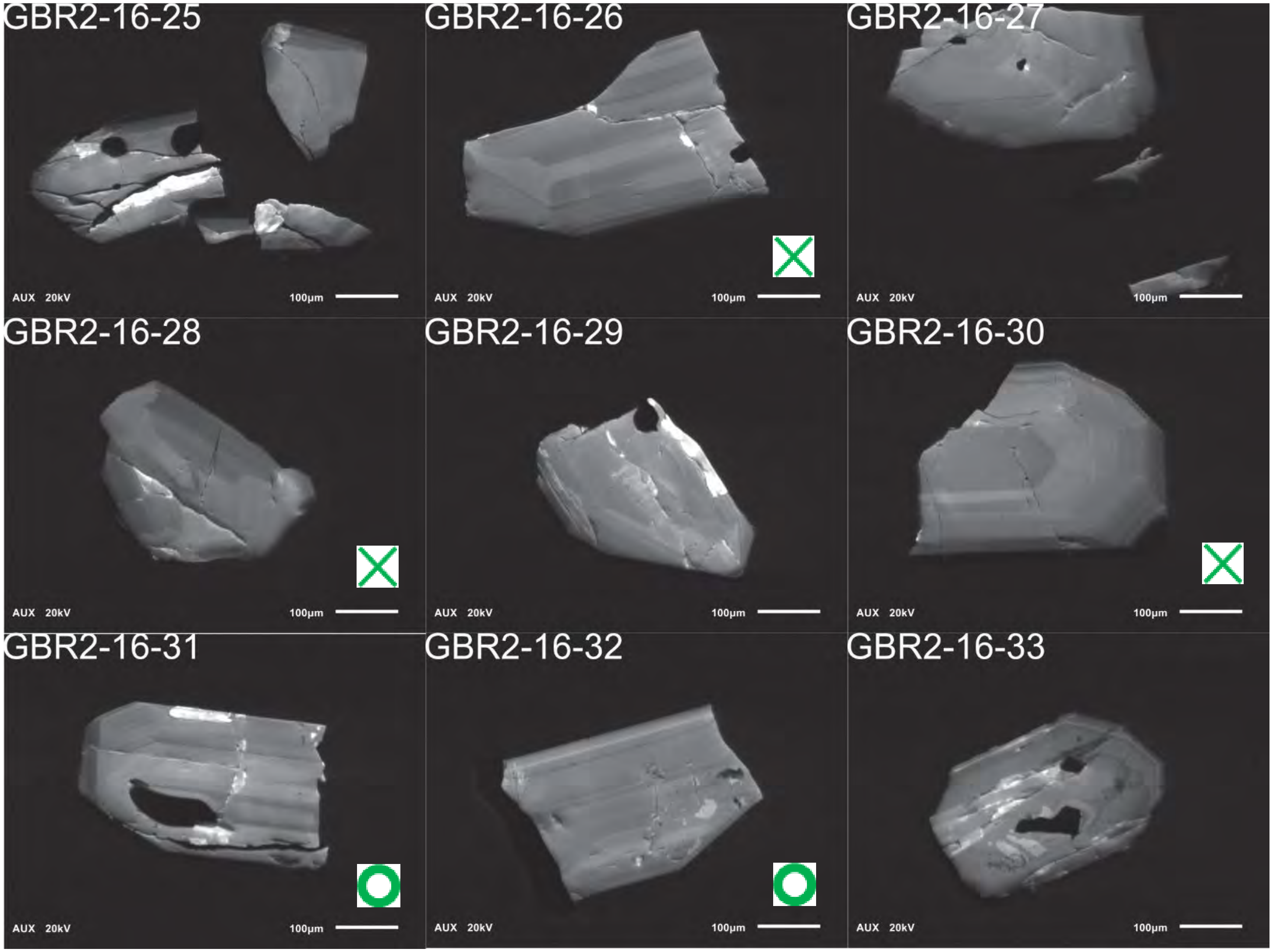

GBR-2-17, 1-12, 212-350µm fraction

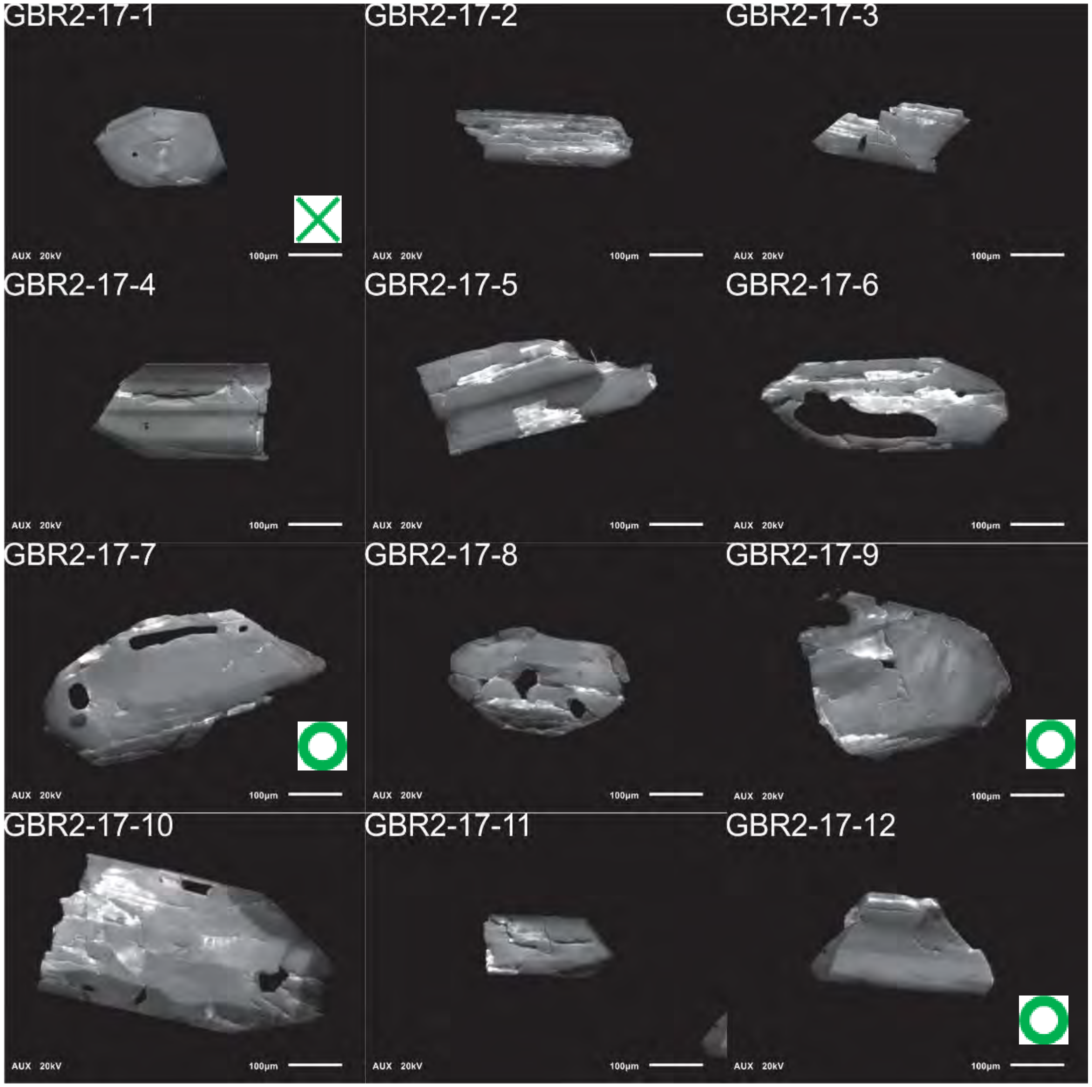

GBR-2-17, 13-44, 212-350µm fraction

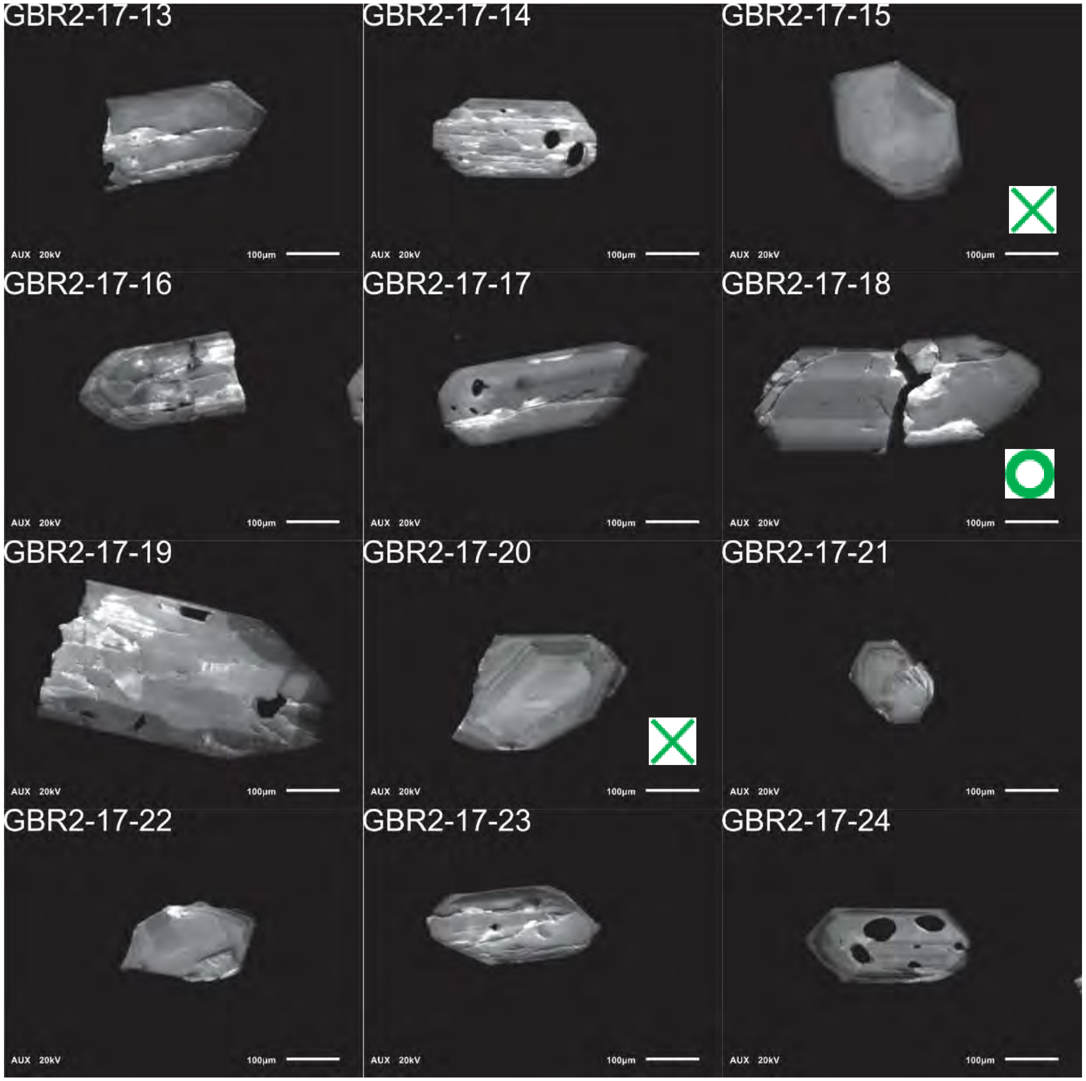

GBR-2-17, 25-32, 212-350µm fraction

GBR2-17-25

GBR2-17-26

GBR2-17-27

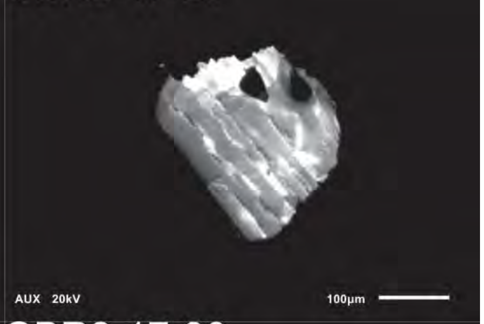

GBR2-17-28

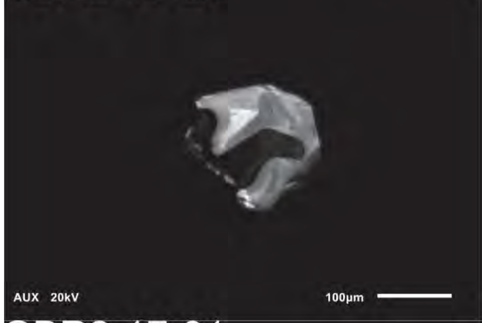

GBR2-17-29

GBR2-17-30

GBR2-17-31

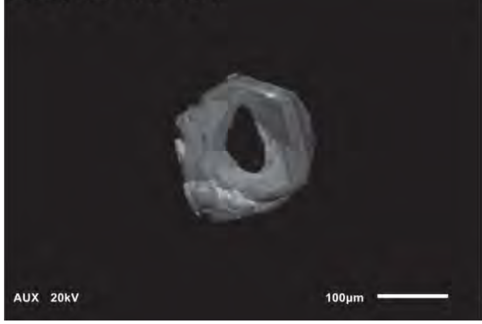

GBR2-17-32

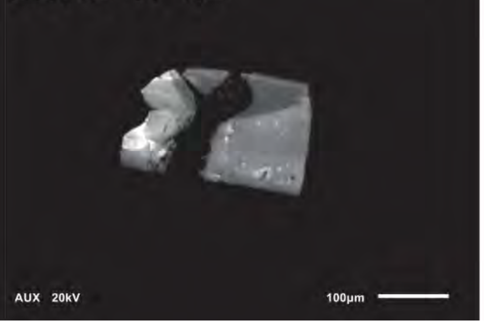

GBR-2-19, 1-12, 212-350µm fraction

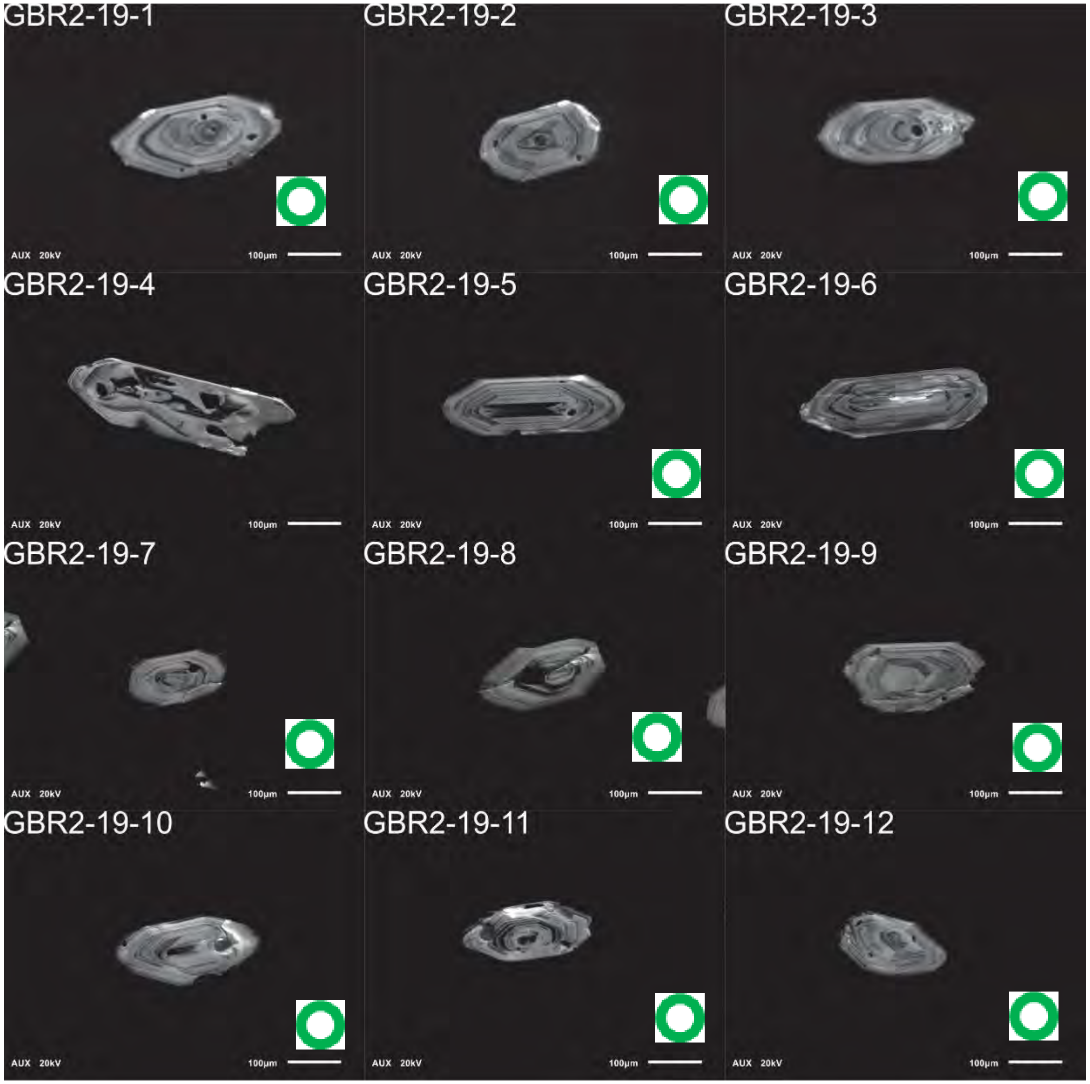

GBR-2-19, 13-24, 212-350μm fraction

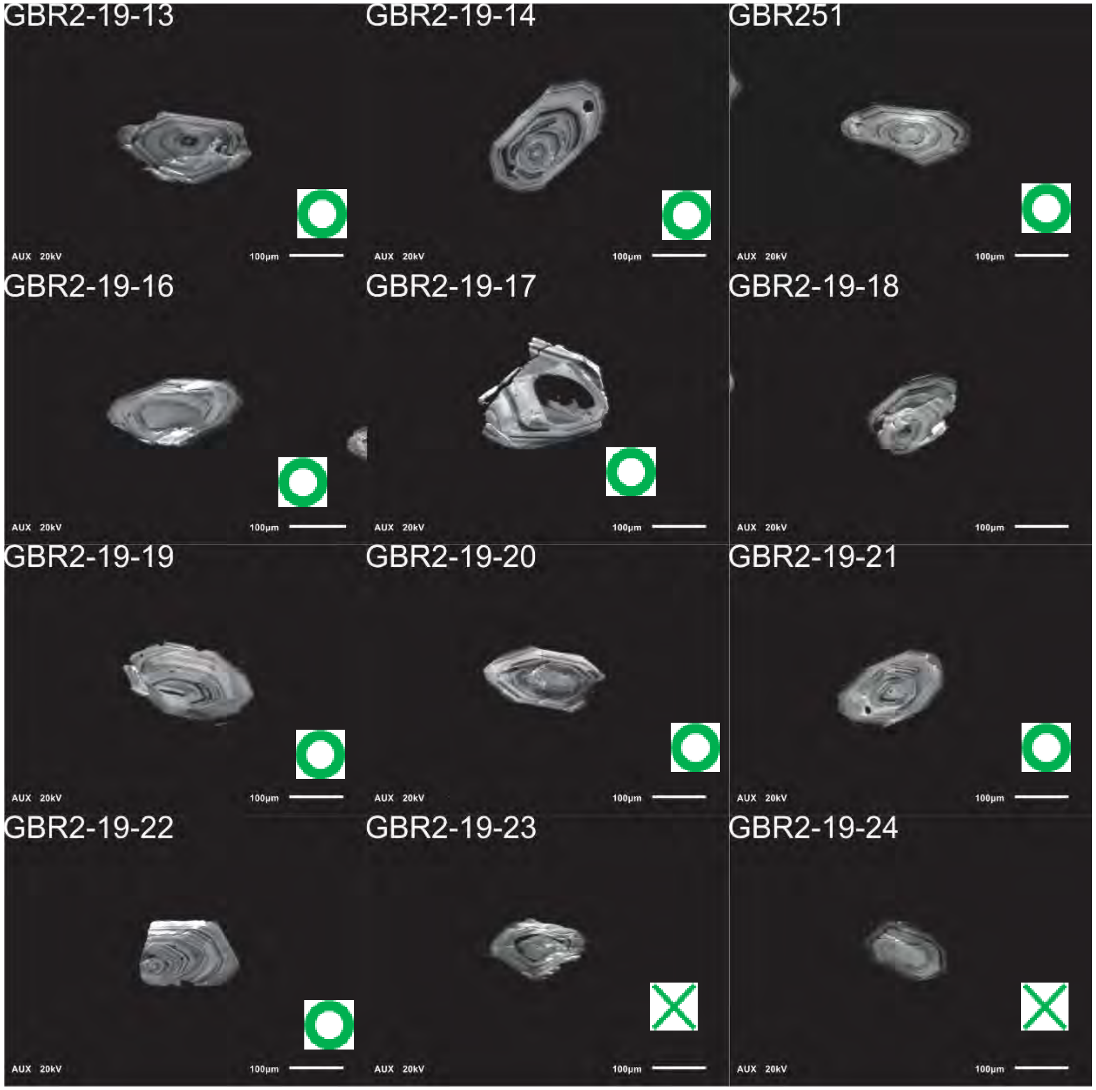

GBR-2-23, 1-12, 212-350µm fraction

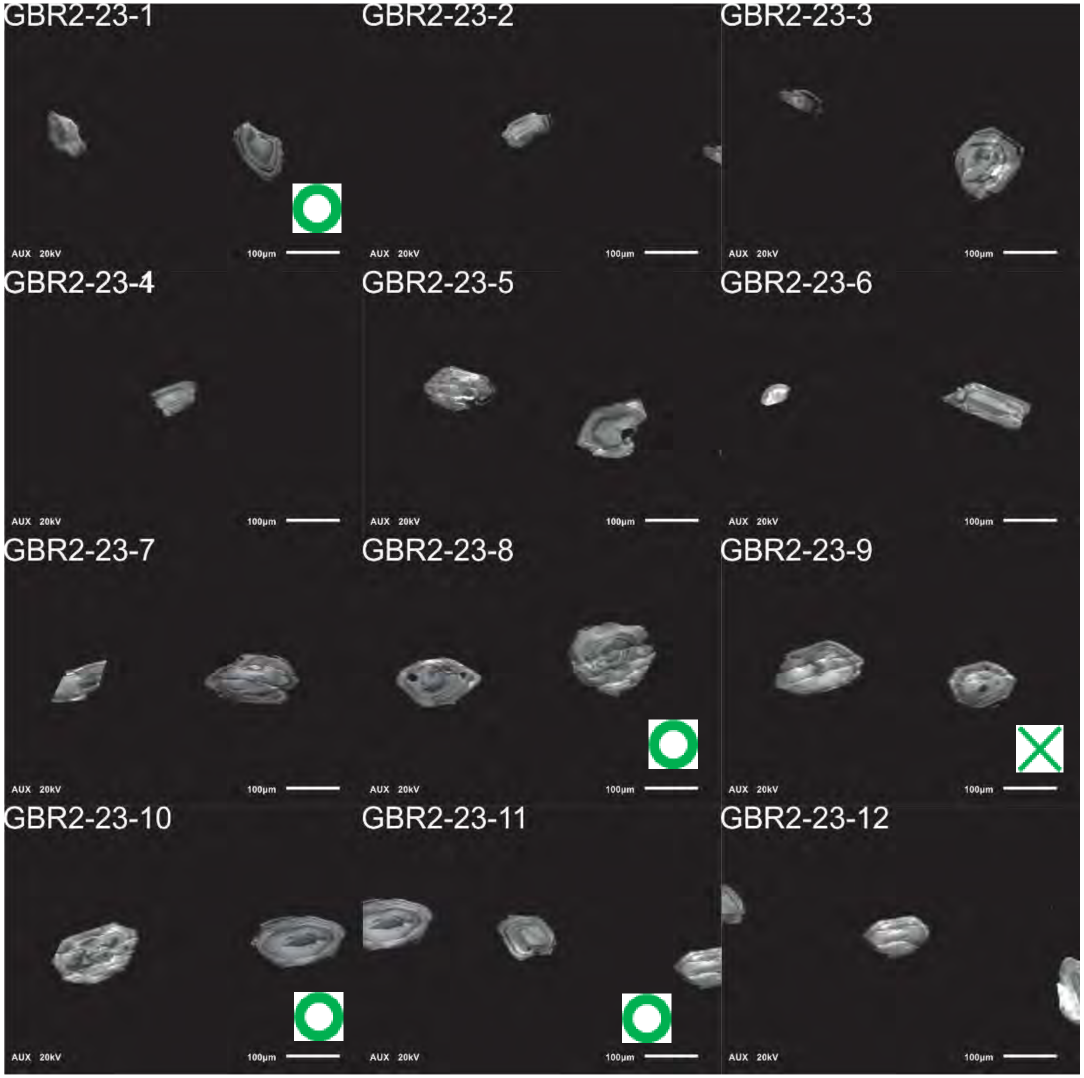

GBR-2-23, 13-17, 212-350µm fraction

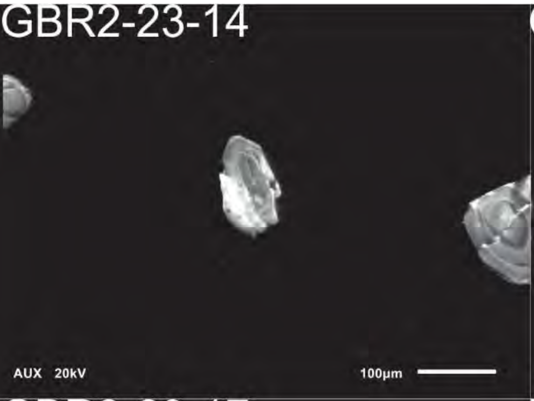

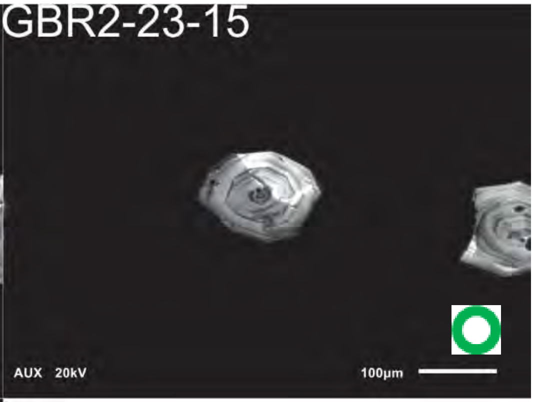

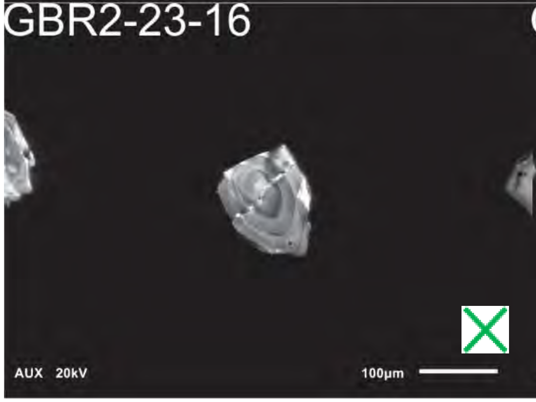

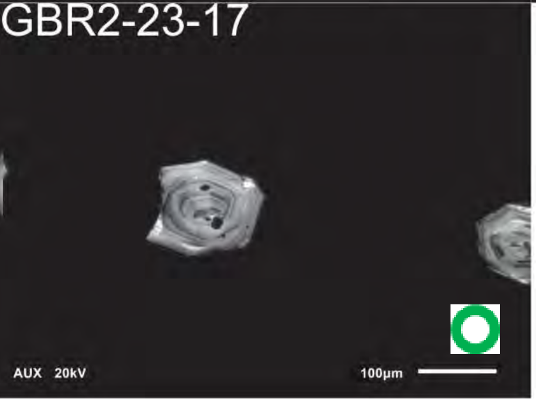

GBR-2-25, 1-12, 212-350µm fraction

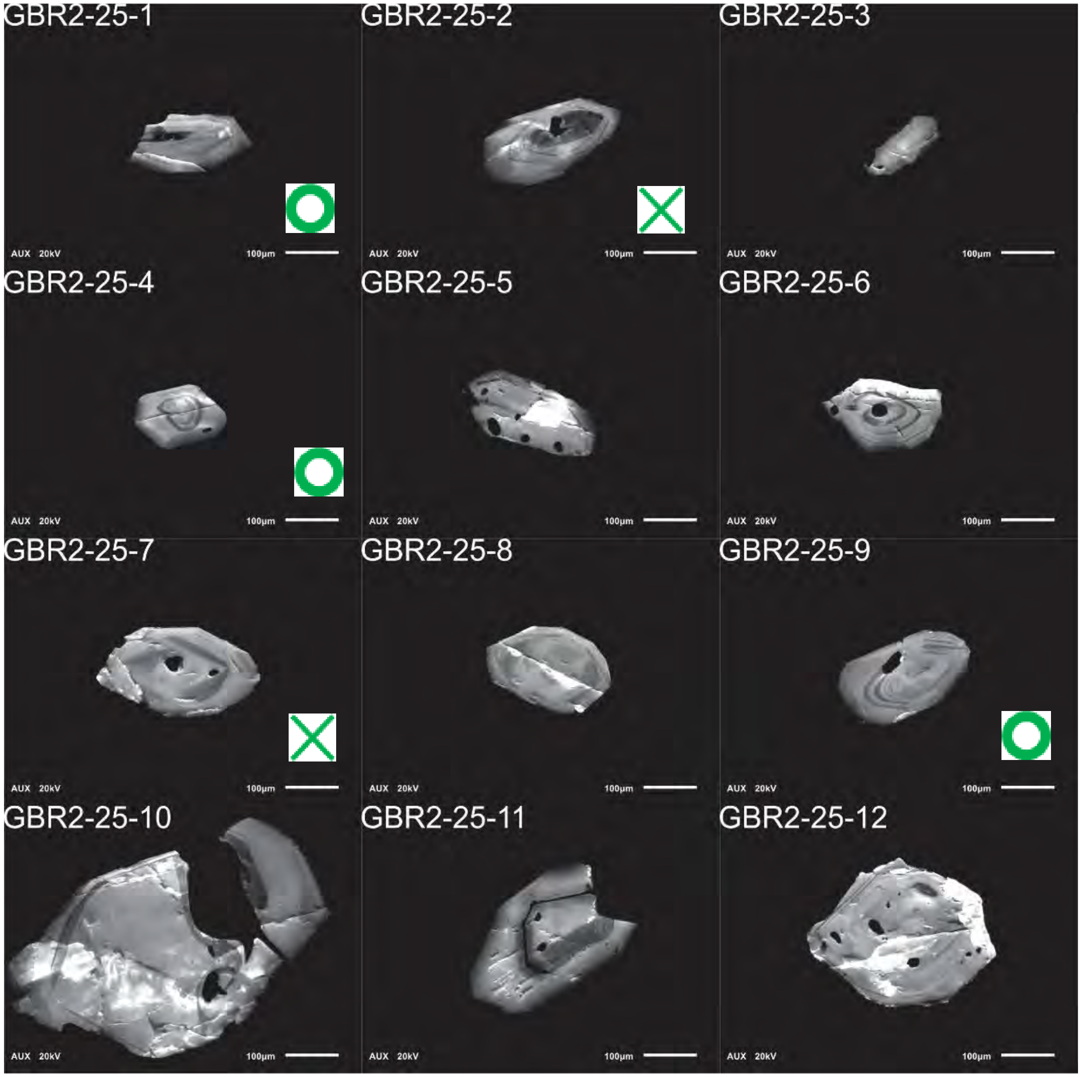

GBR-2-2, 13-24, 212-350µm fraction

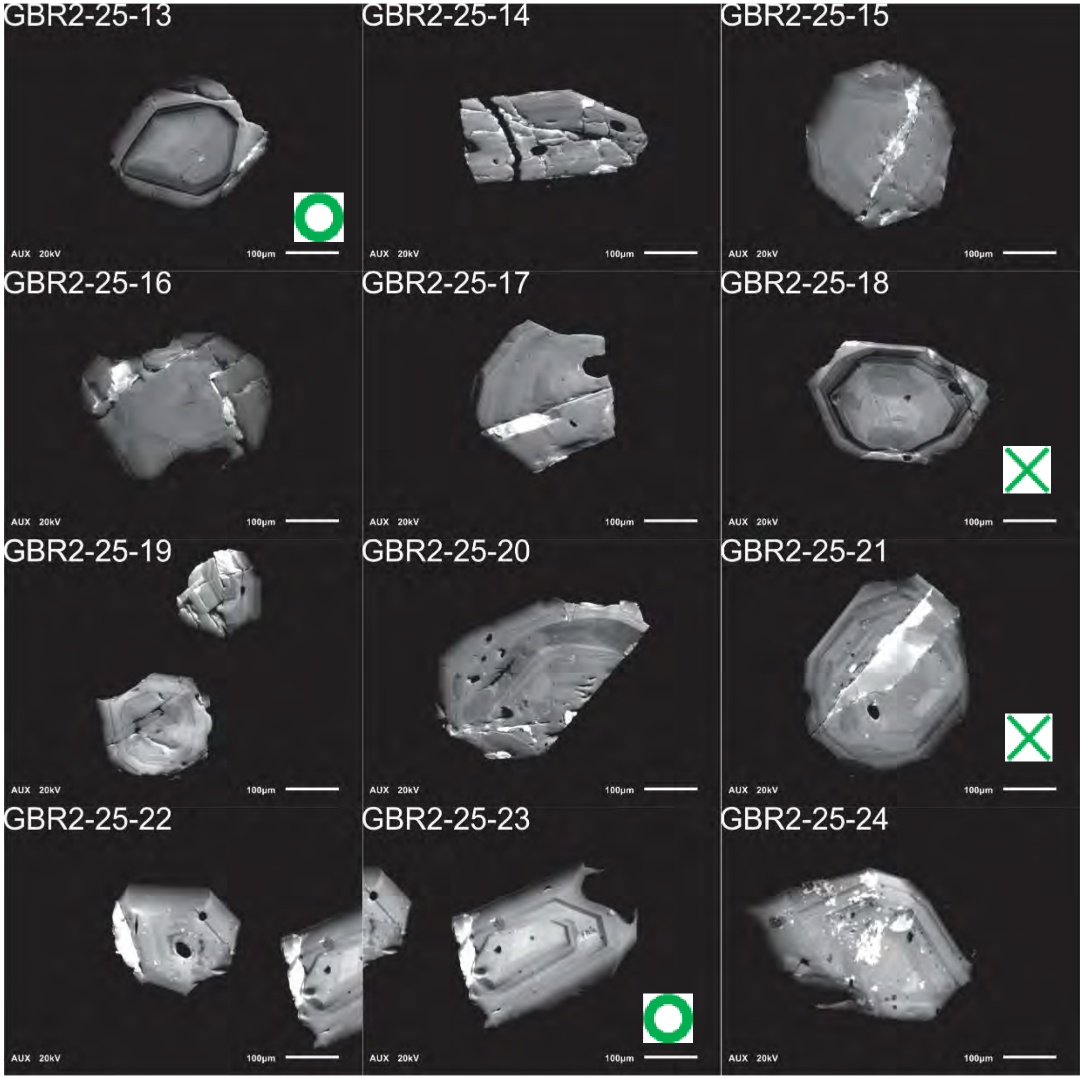

GBR-2-25, 25-36, 212-350µm fraction

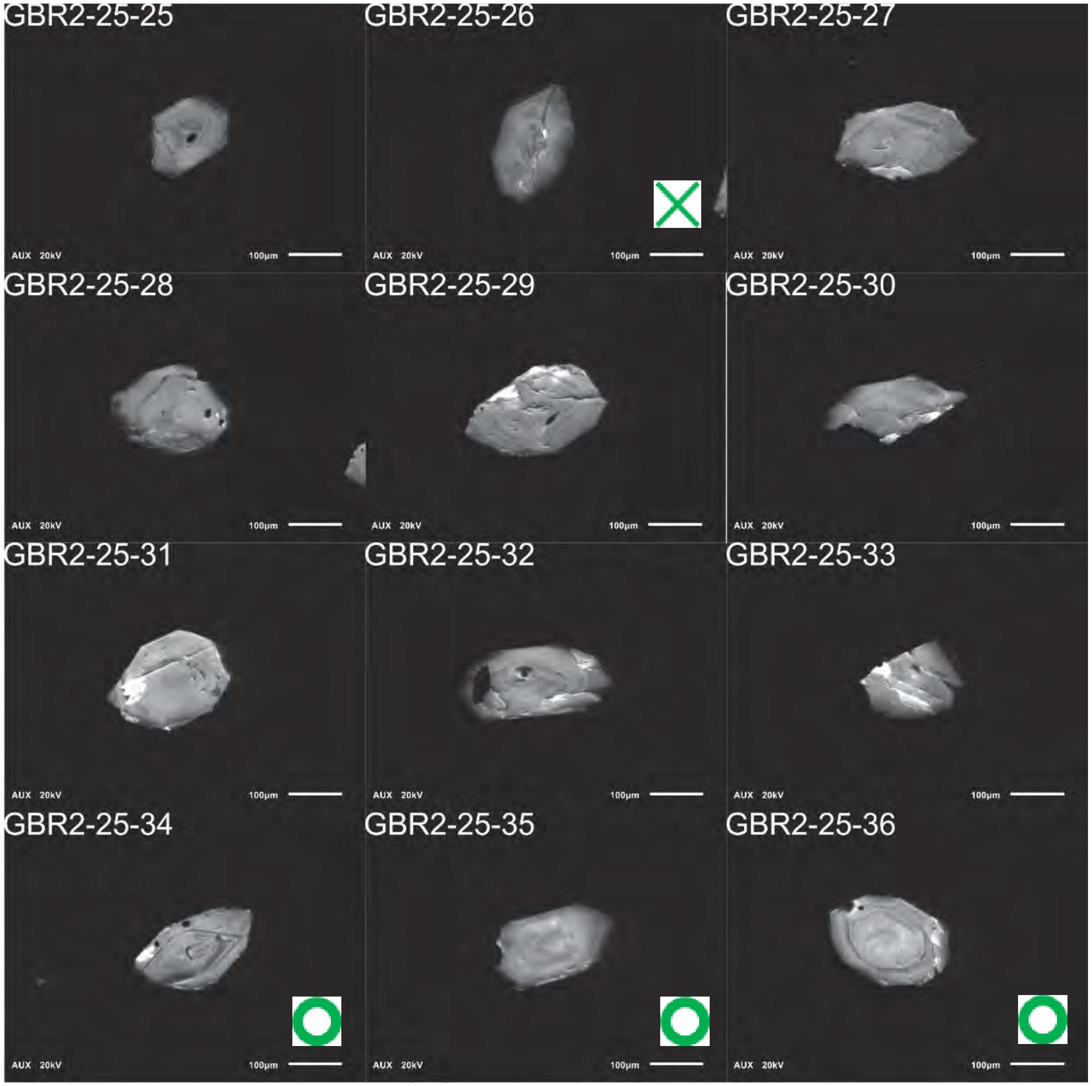

GBR-2-26, 1-5, 212-350µm fraction

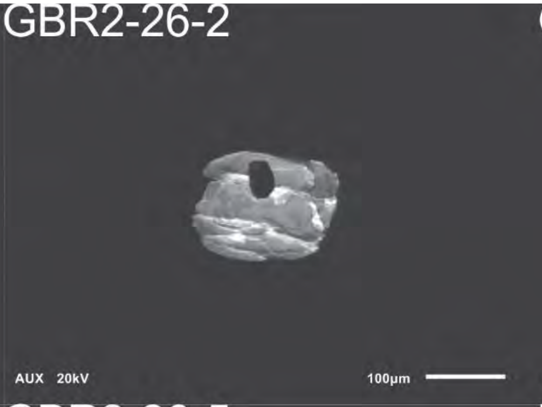

GBR-2-28, 1-12, 212-350µm fraction

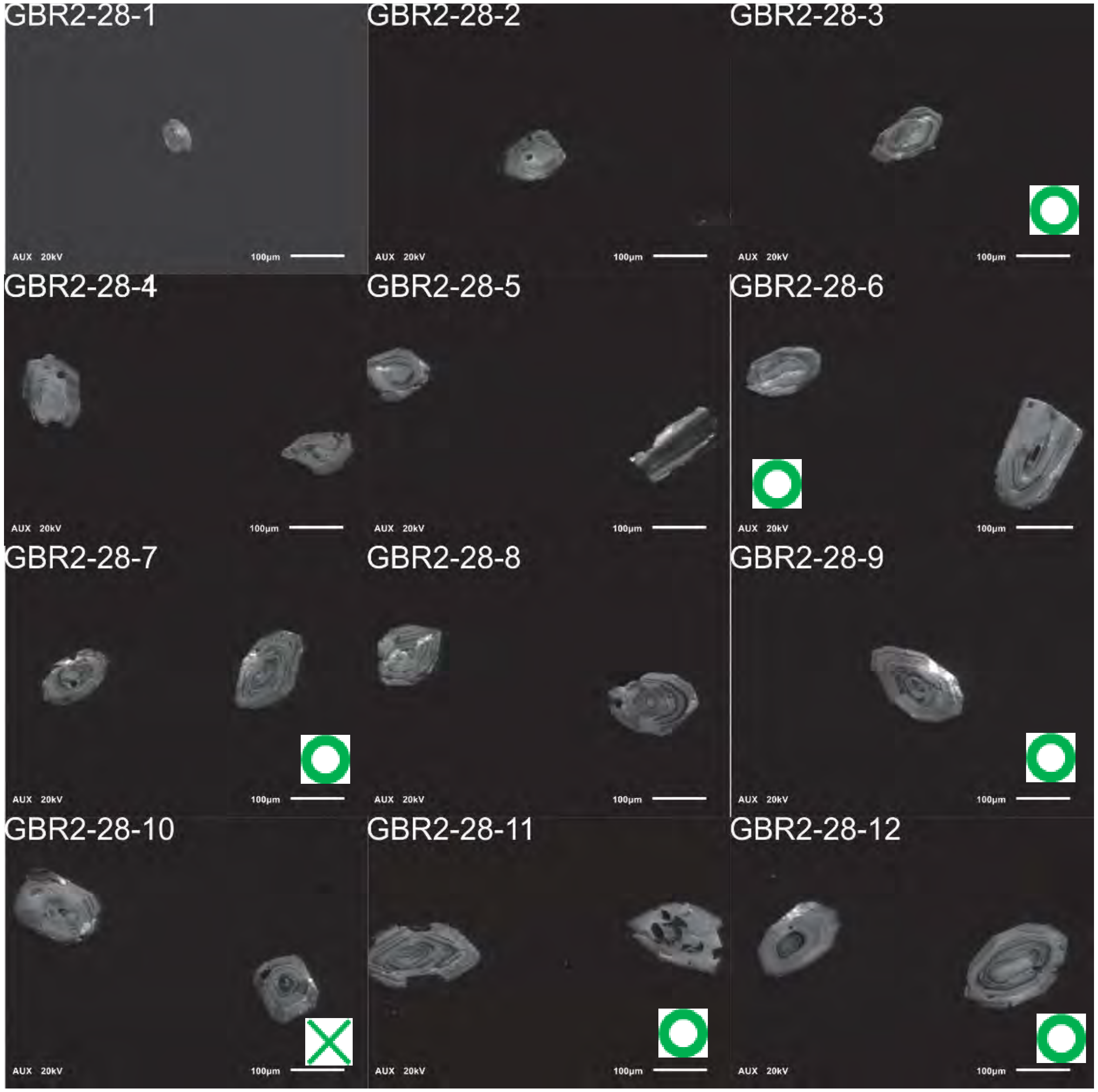

GBR-2-28, 13-14, 212-350μm fraction

GBR-2-30, 1-12, 212-350µm fraction

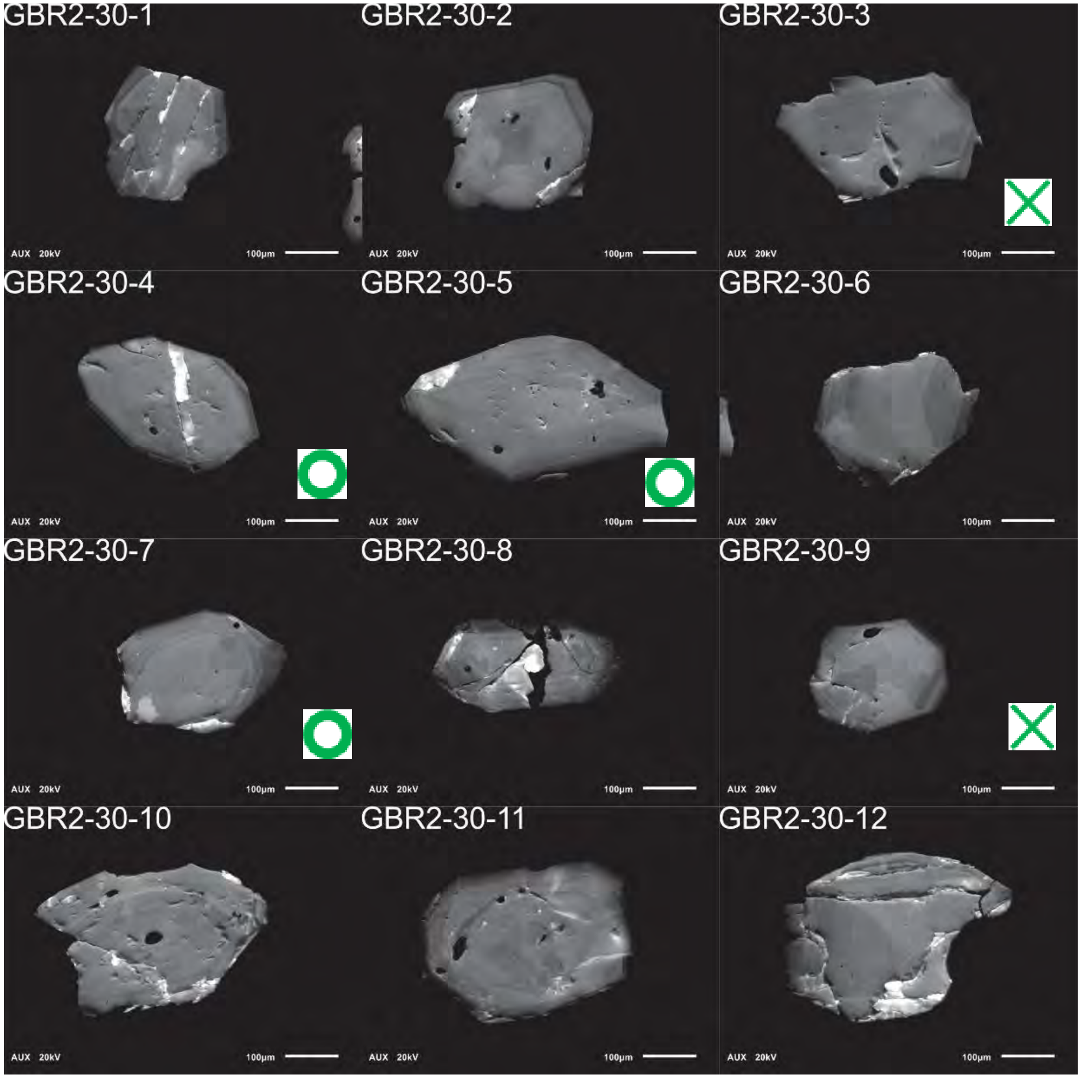

GBR-2-30, 13-22, 212-350µm fraction

GBR2-30-13

GBR2-30-14

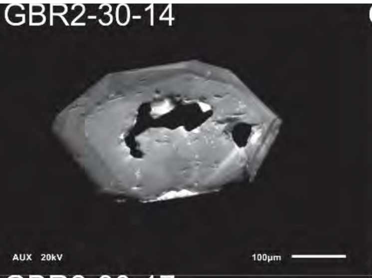

GBR2-30-15

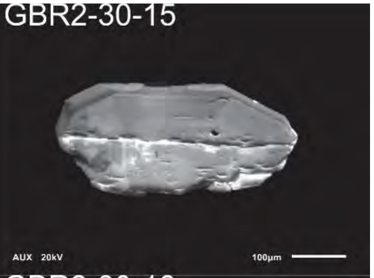

GBR2-30-16

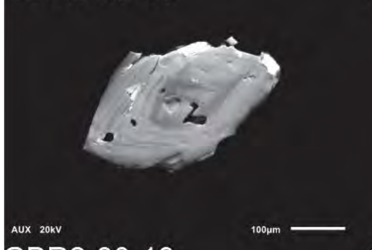

GBR2-30-17

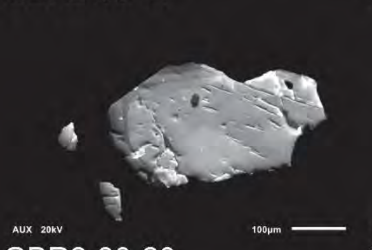

GBR2-30-18

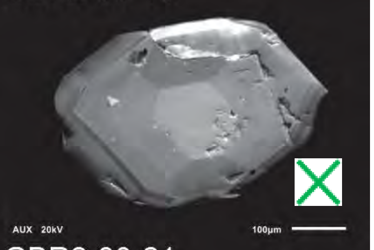

GBR2-30-19

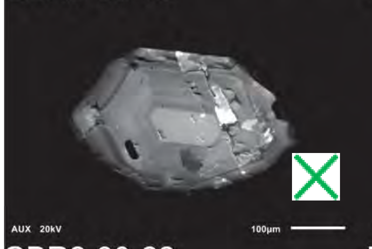

GBR2-30-20

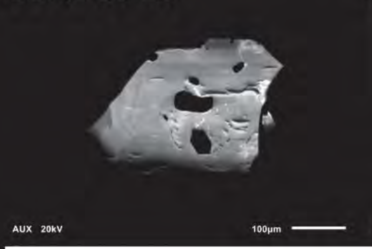

GBR2-30-21

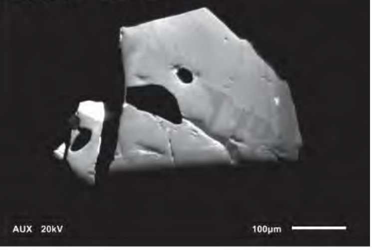

GBR2-30-22

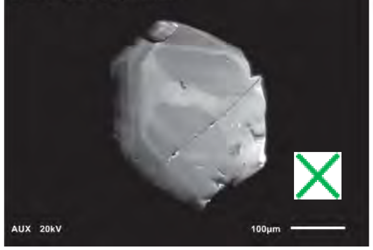

GBR-2-37, 1-12, 212-350µm fraction

GBR-2-37, 13-24, 212-350µm fraction

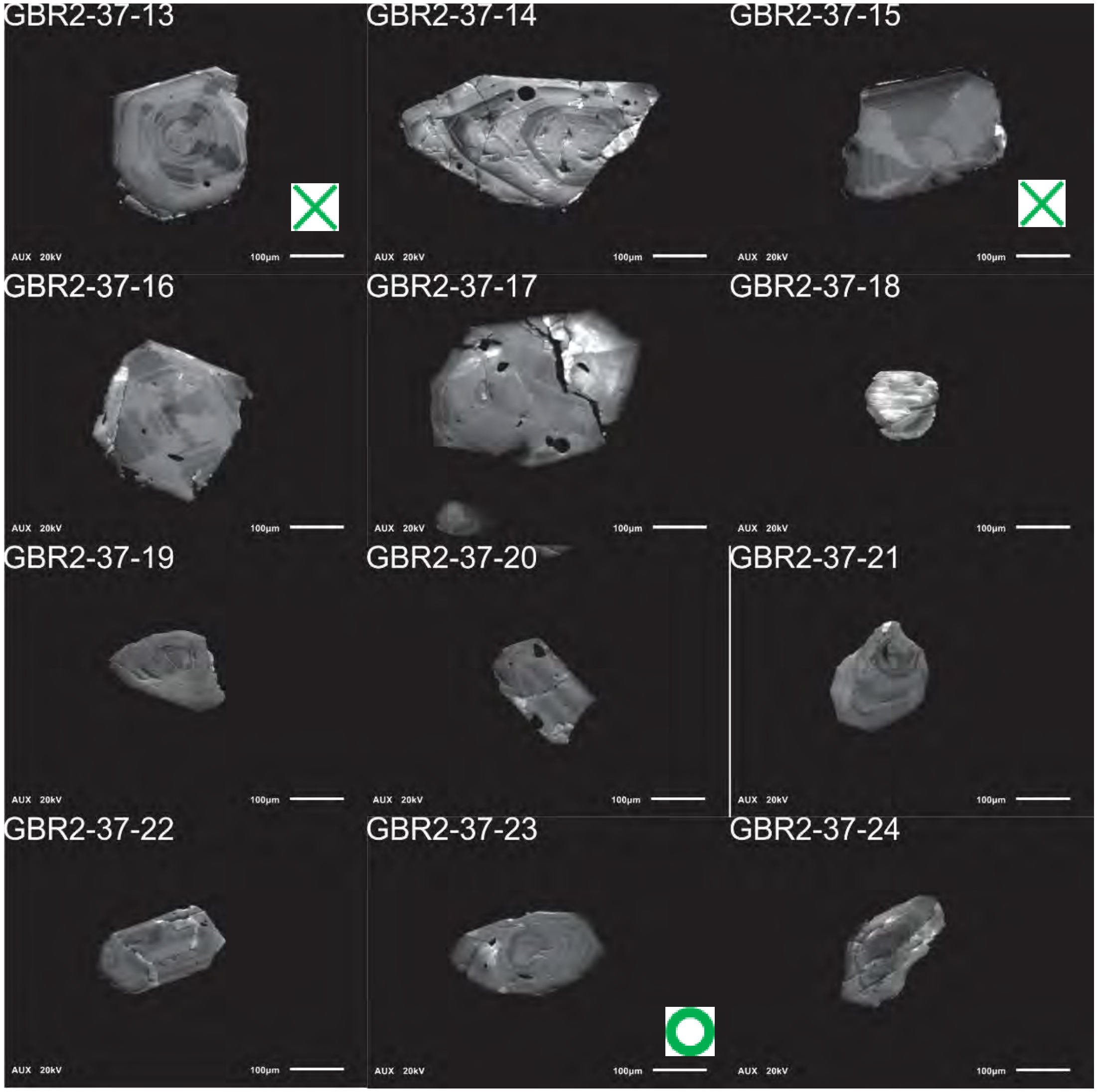

GBR-2-37, 25-36, 212-350µm fraction

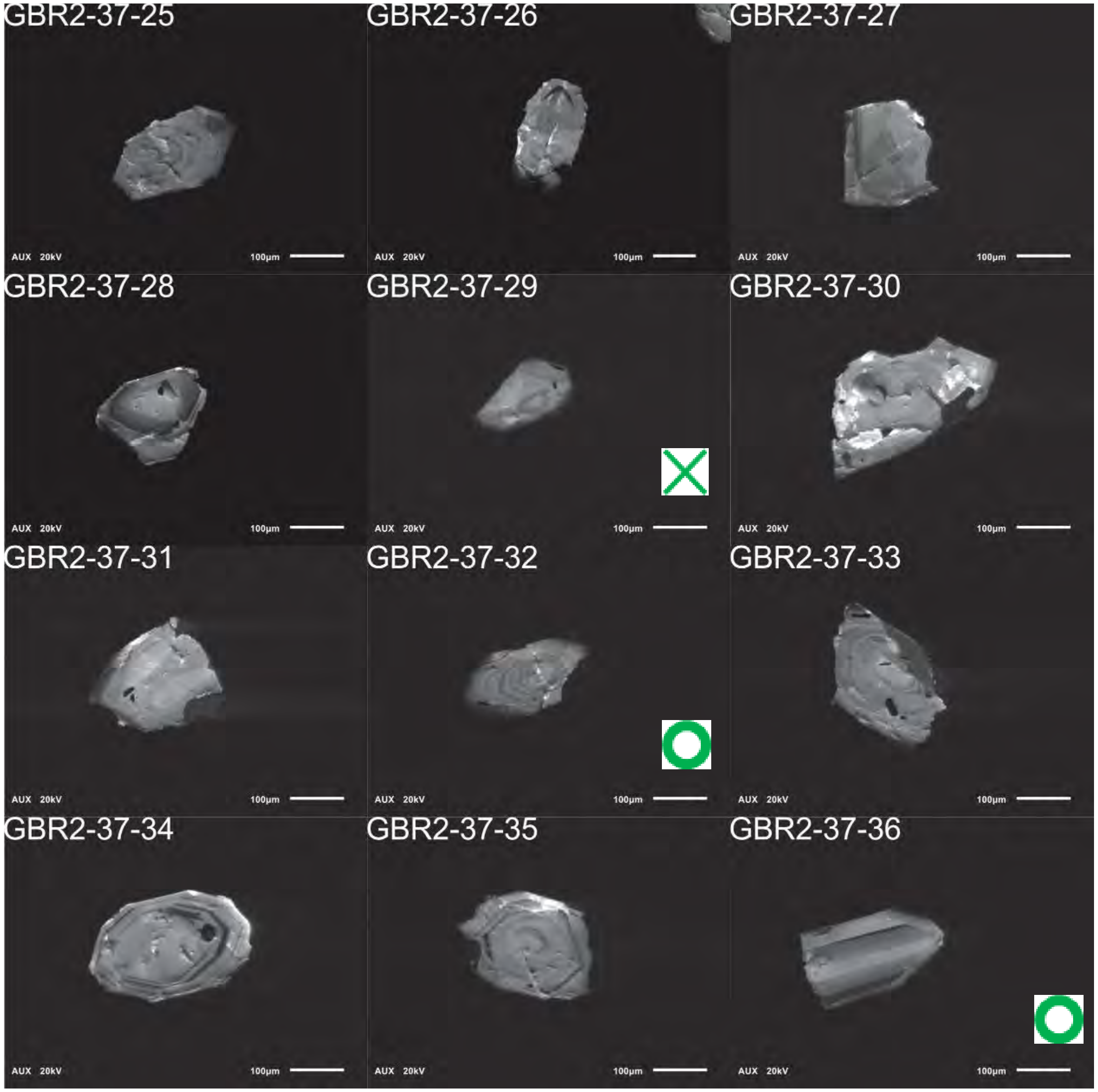

GBR-2-37, 37-38, 212-350µm fraction

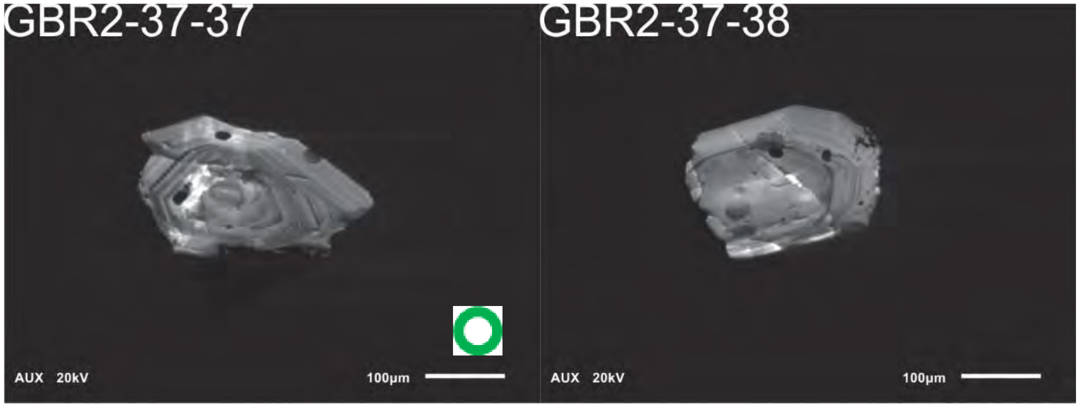

GBR-2-38, 1-12, 212-350μm fraction

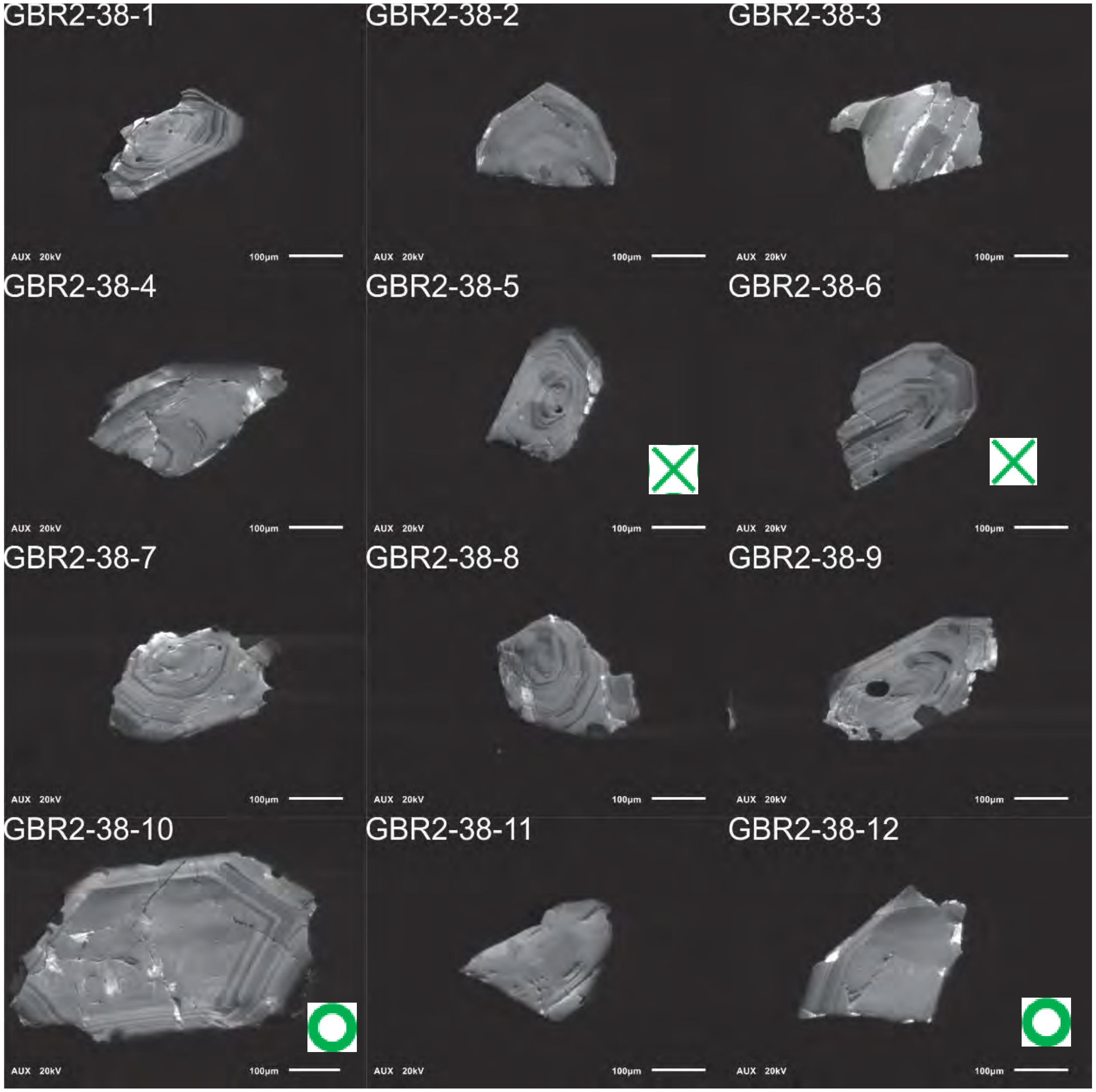

GBR-2-38, 13-24, 212-350µm fraction

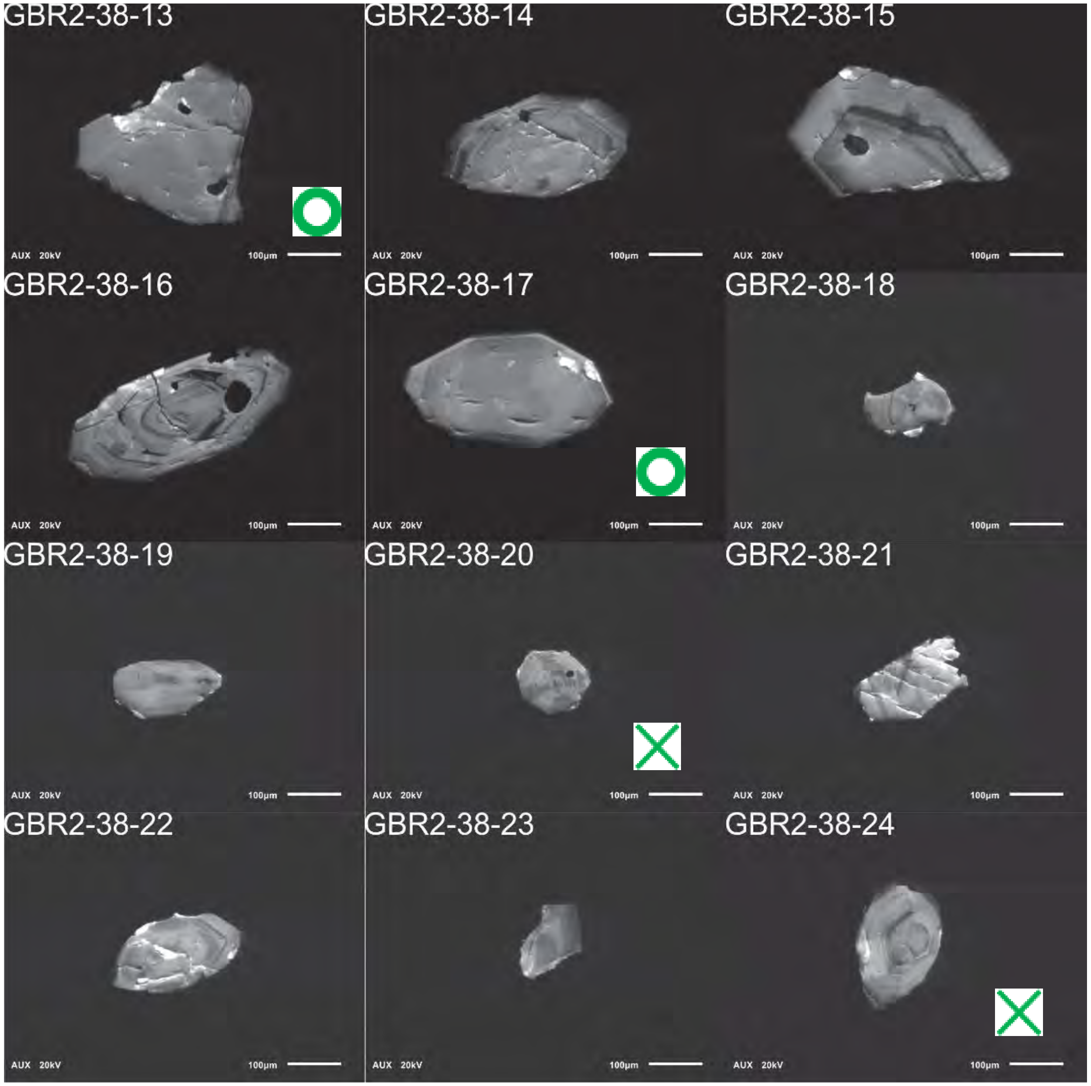

GBR-2-38, 25-30, 212-350µm fraction

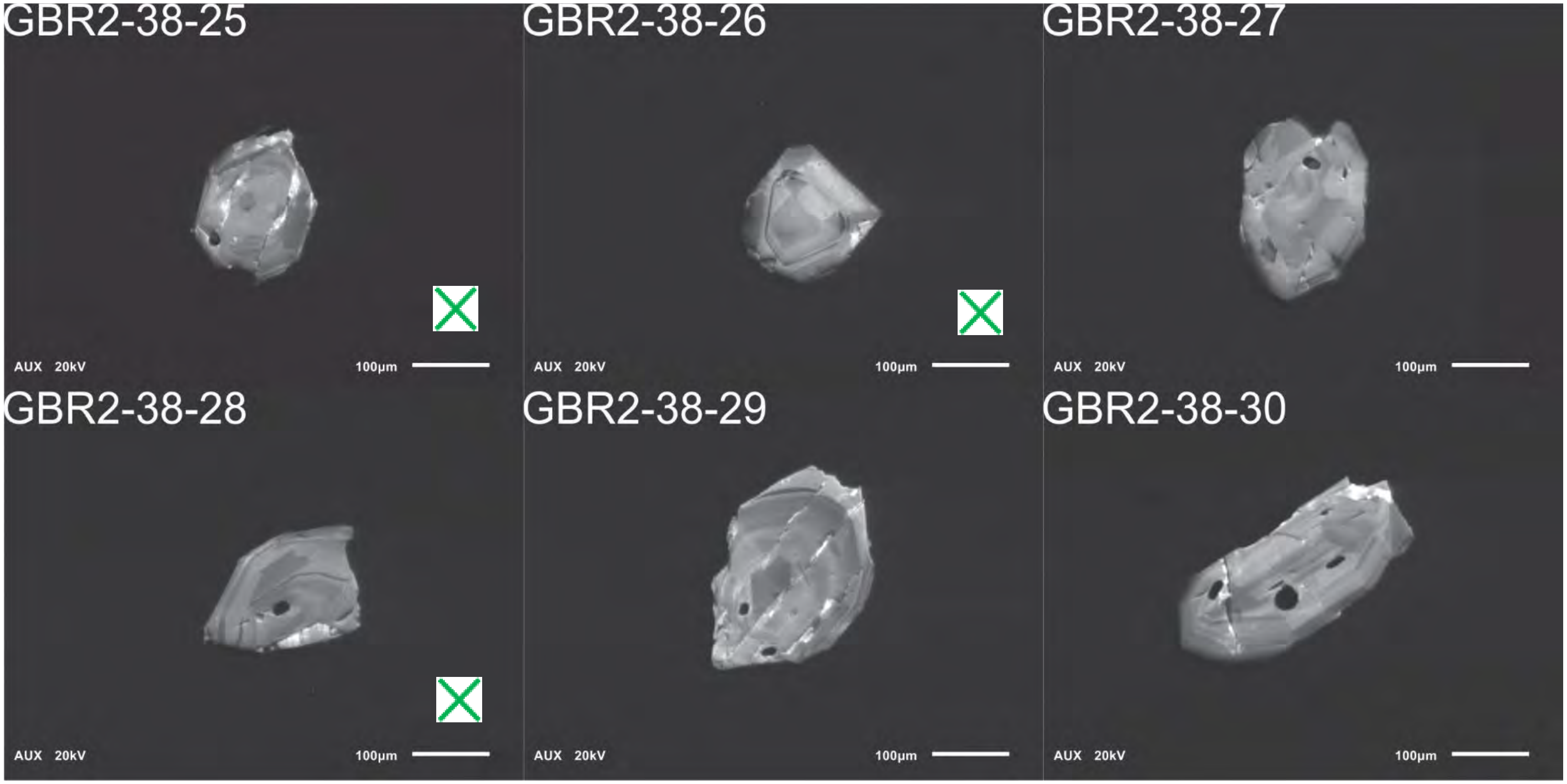

GBR-4, 1-12, 212-350µm fraction

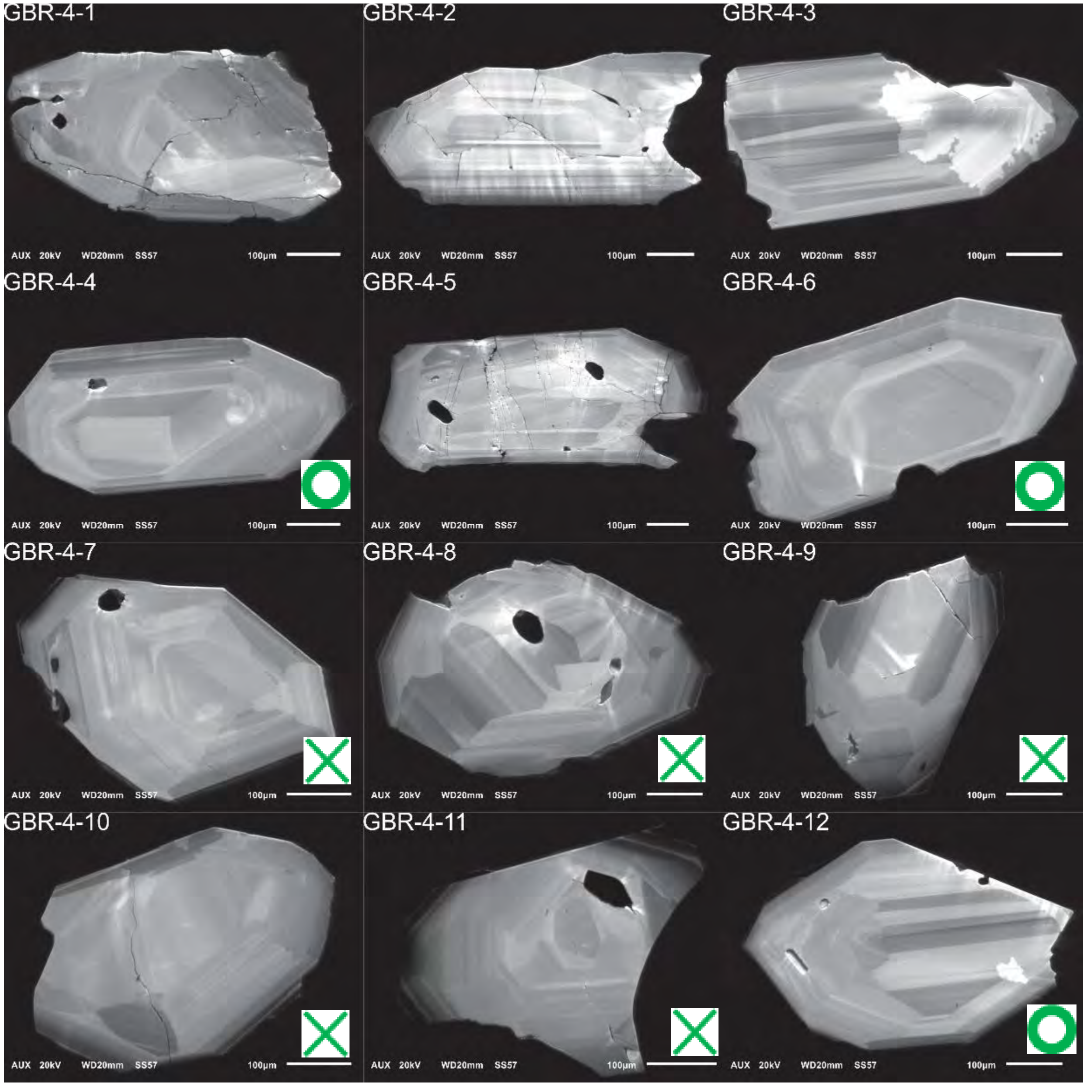

GBR-4, 13-20, 212-350µm fraction

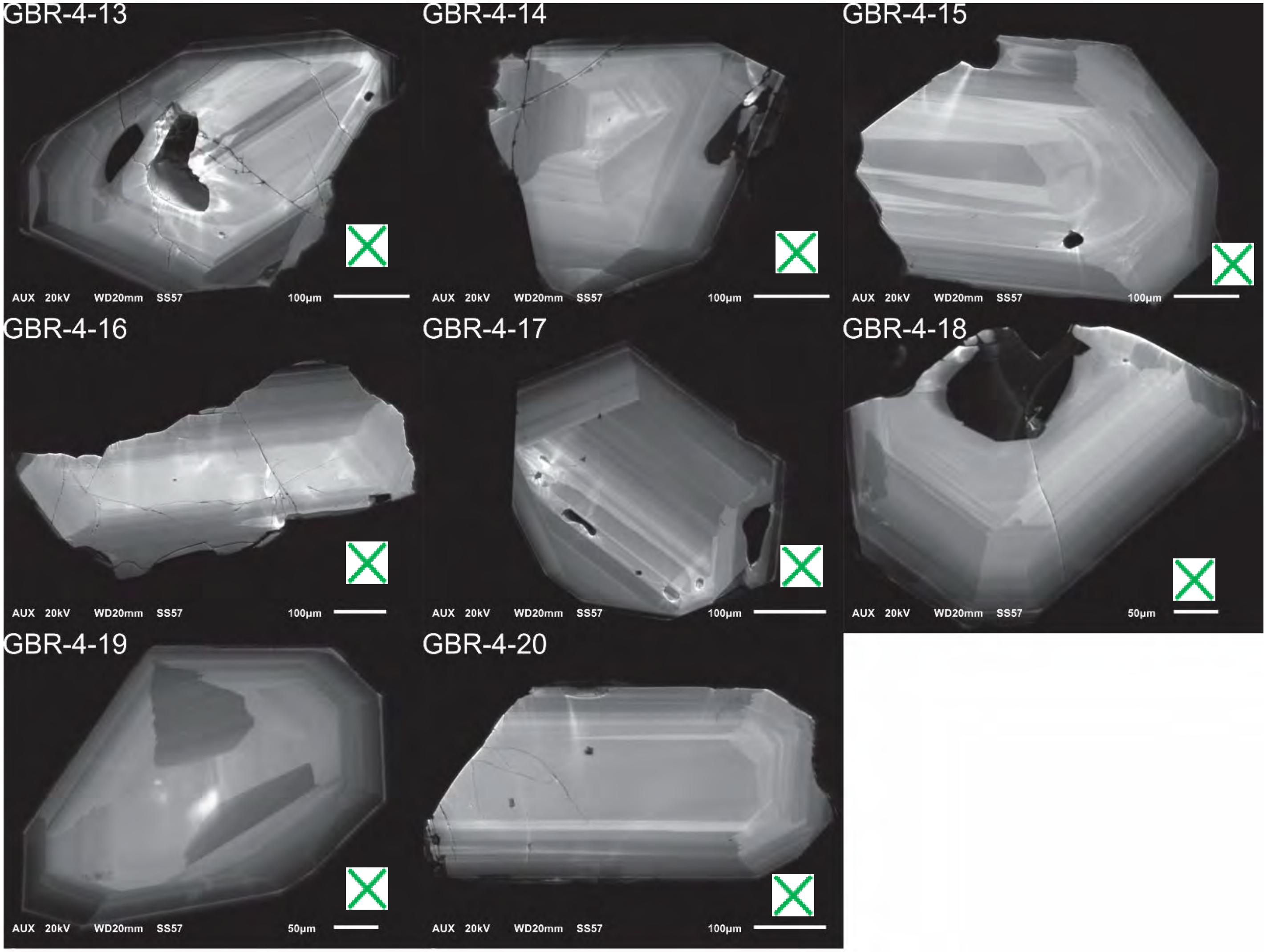

GBR-7, 1-5, 80-212μm fraction

GBR-7-1

GBR-7-2

GBR-7-3

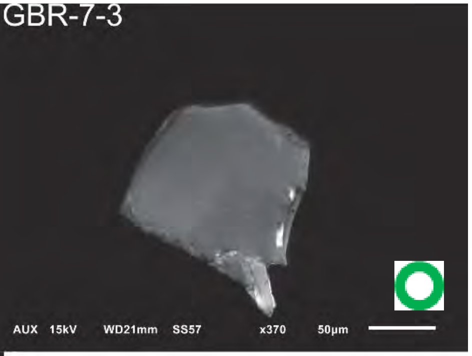

GBR-7-4

GBR-7-5

GBR-7, 1-12, 212-350µm fraction

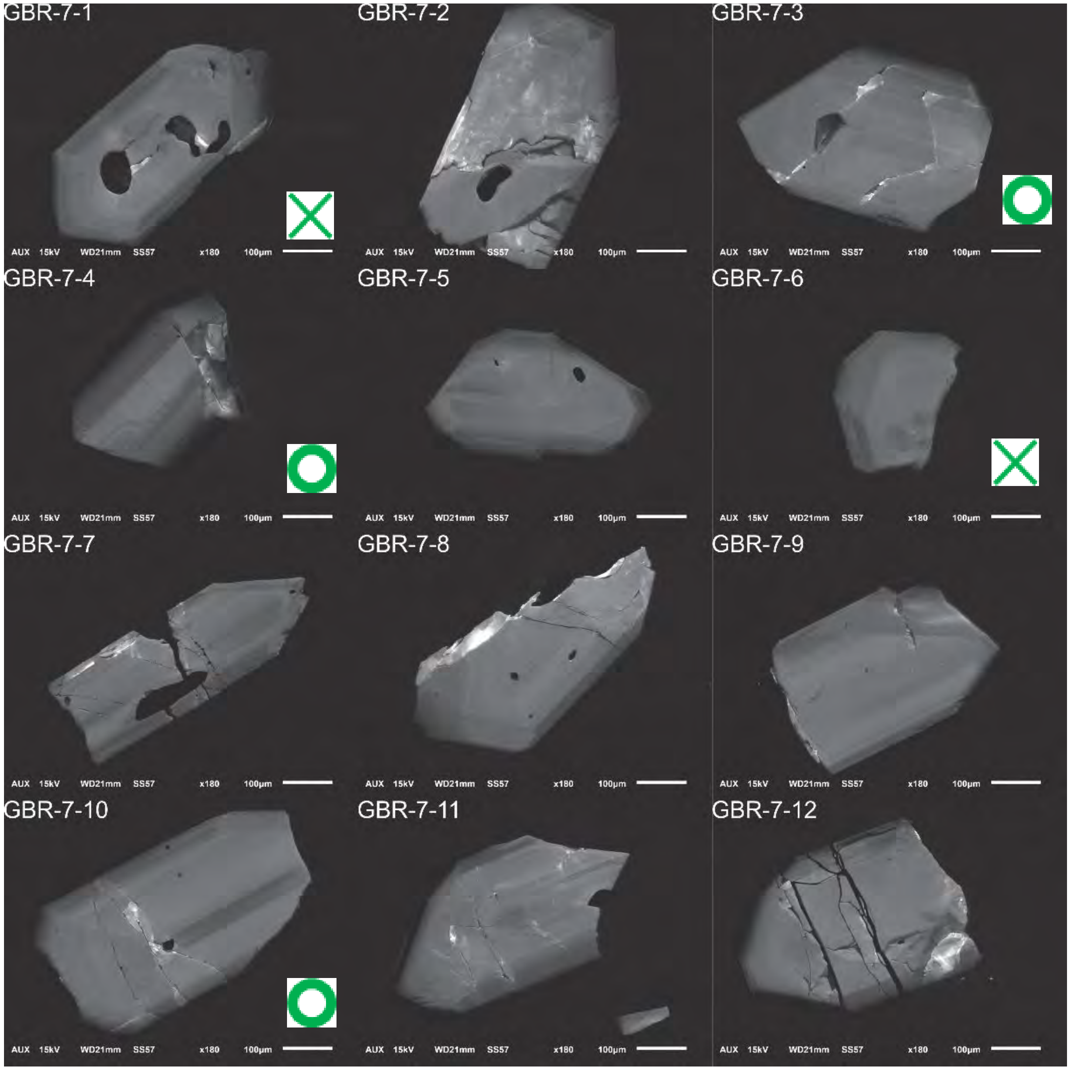

GBR-7, 13-24, 212-350µm fraction

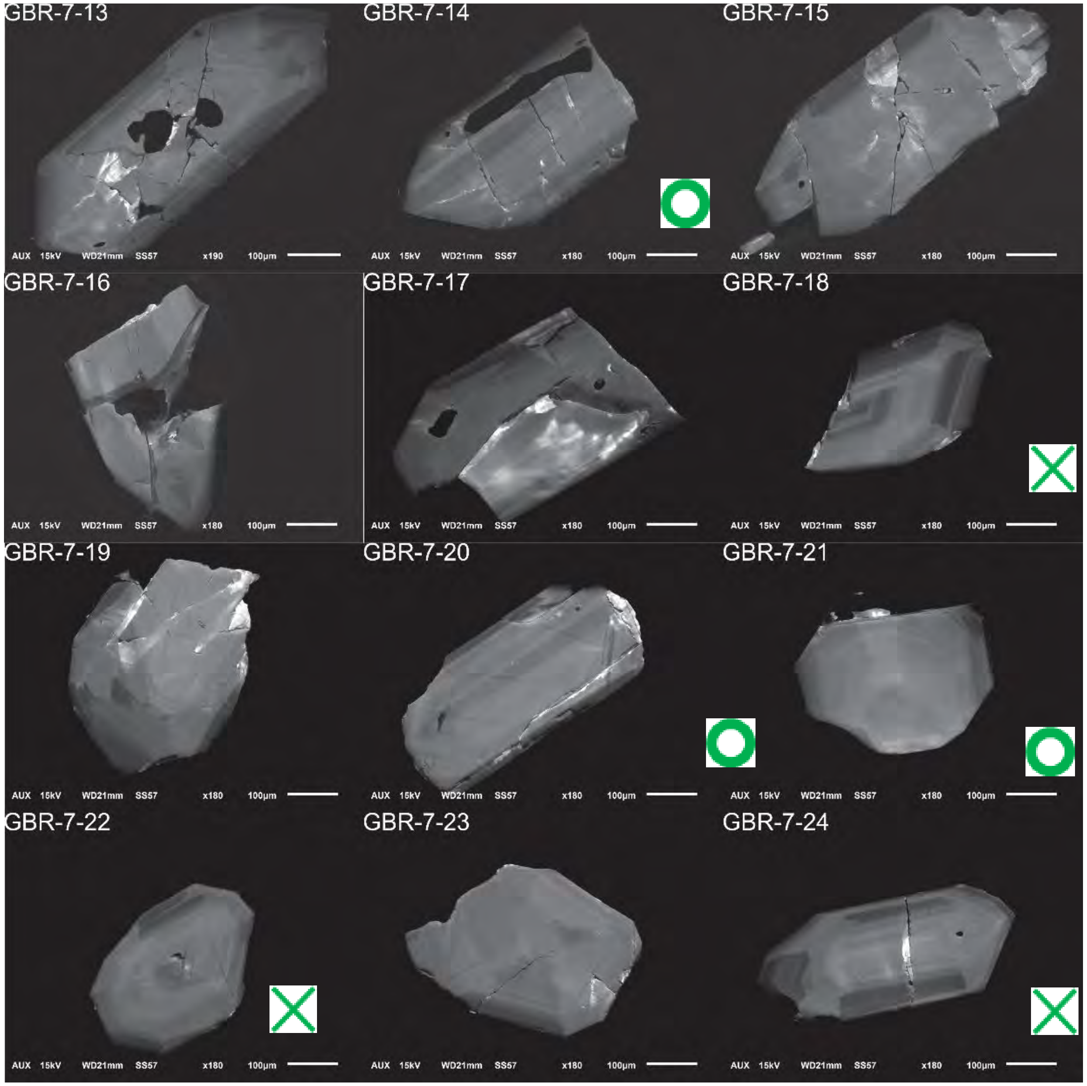

GBR-7, 25-36, 212-350µm fraction

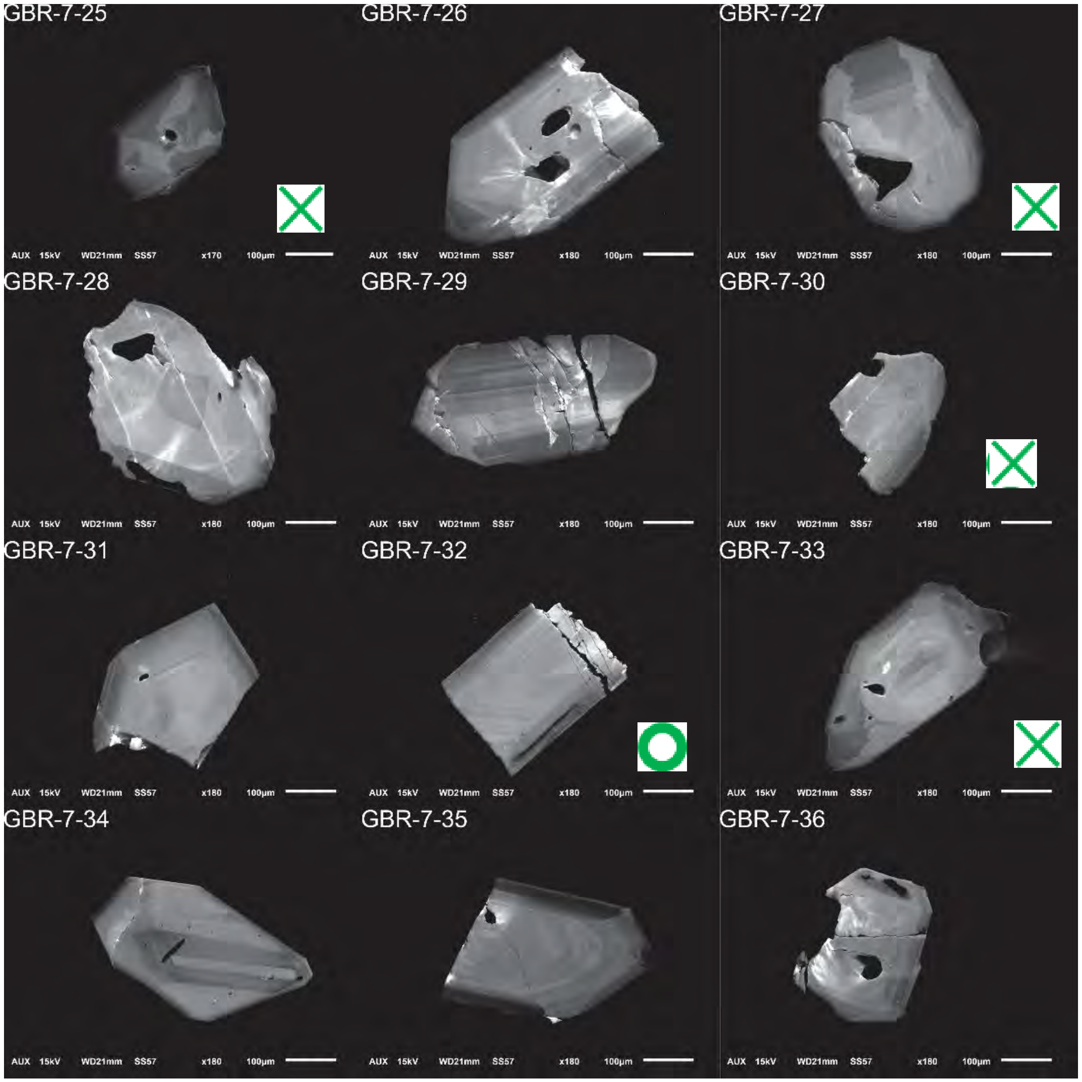

GBR-7, 37-40, 212-350µm fraction

GBR-7-37

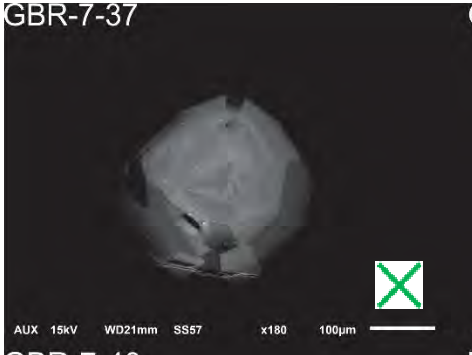

GBR-7-38

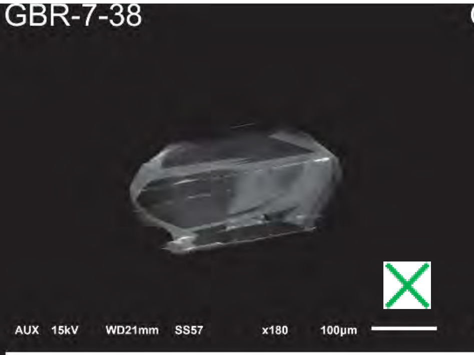

GBR-7-39

GBR-7-40

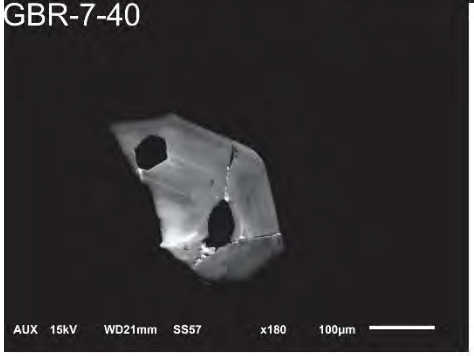

GBR-11, 1-12, 212-350µm fraction

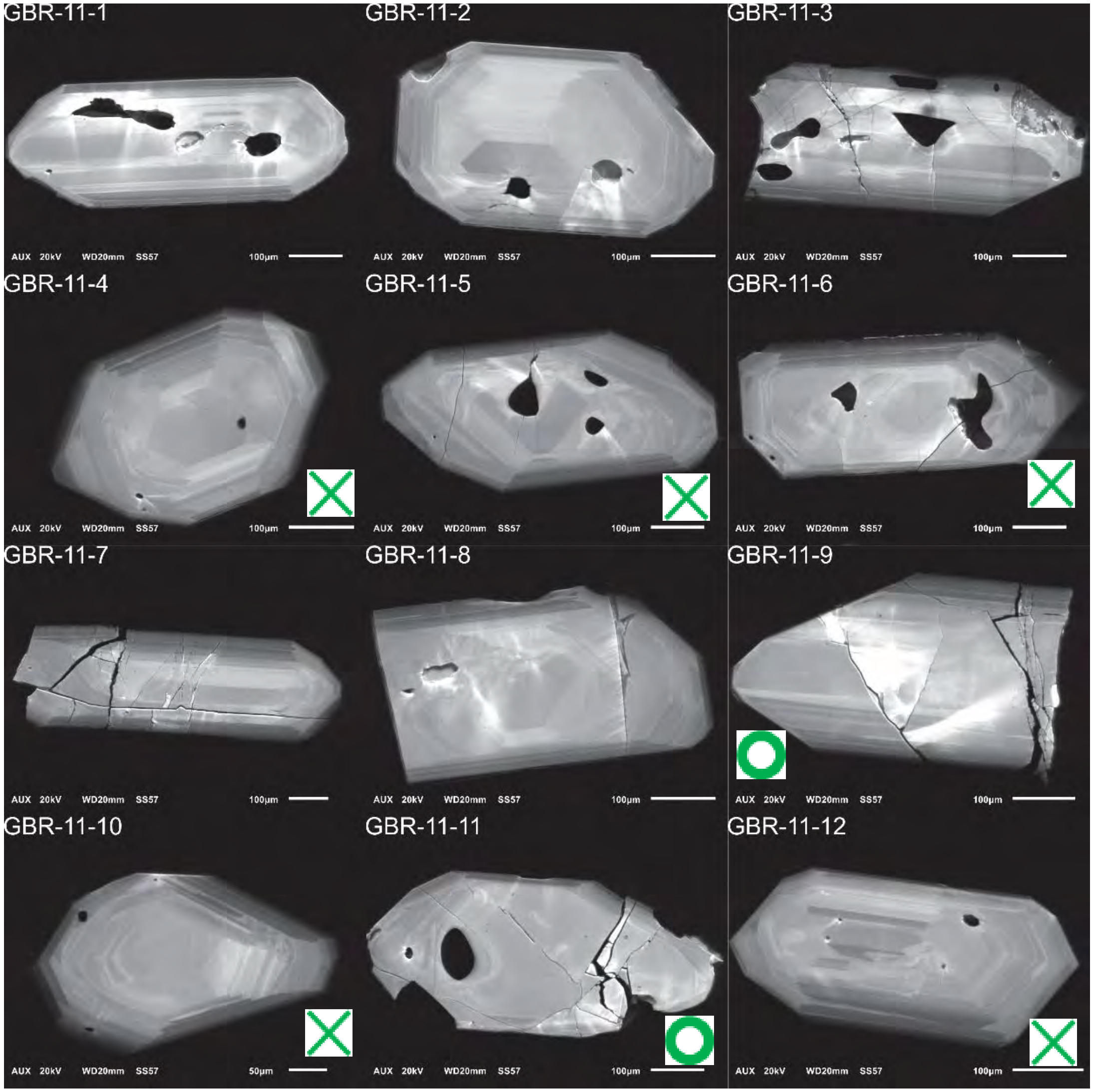

GBR-11, 13-24, 212-350µm fraction

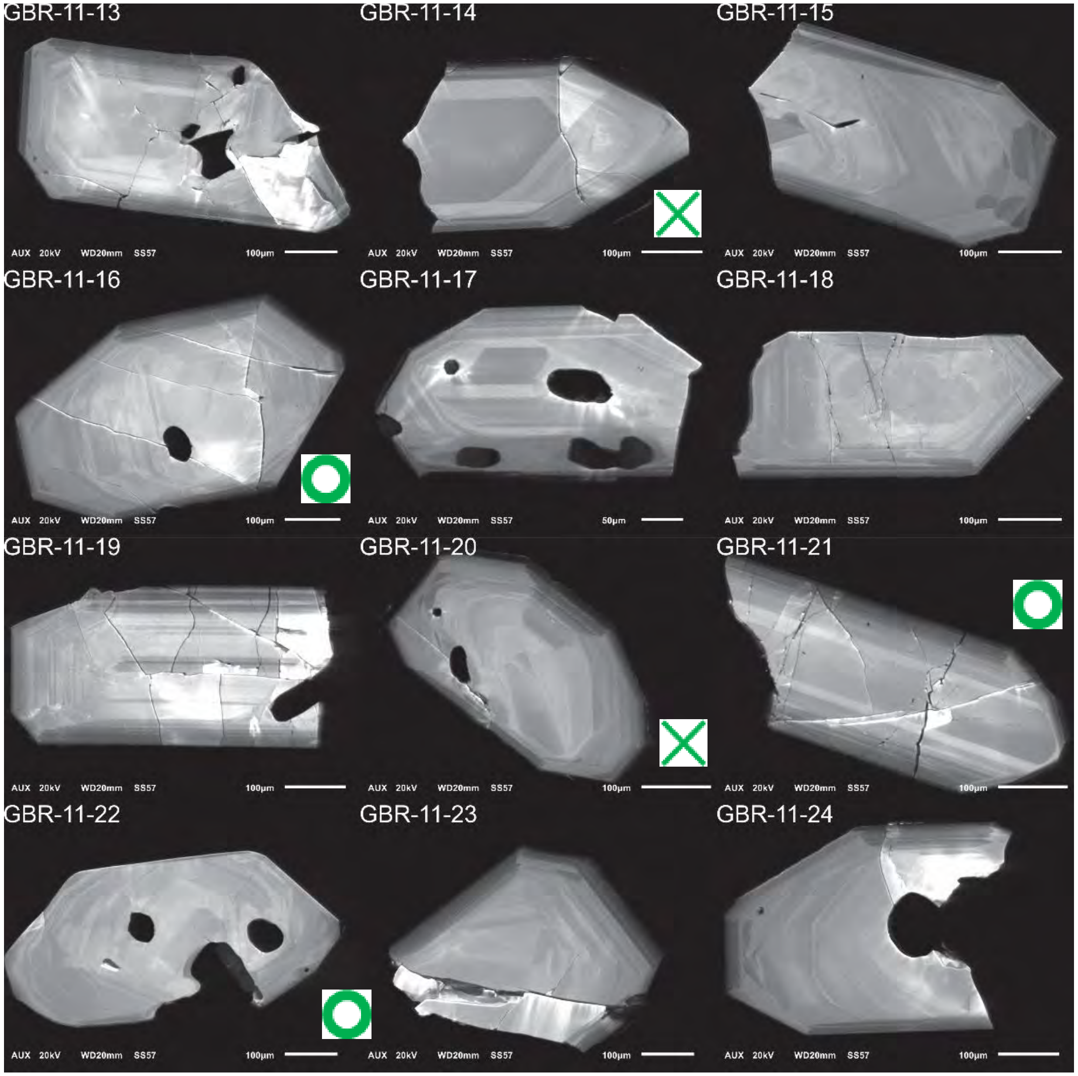

GBR-11, 25-36, 212-350μm fraction

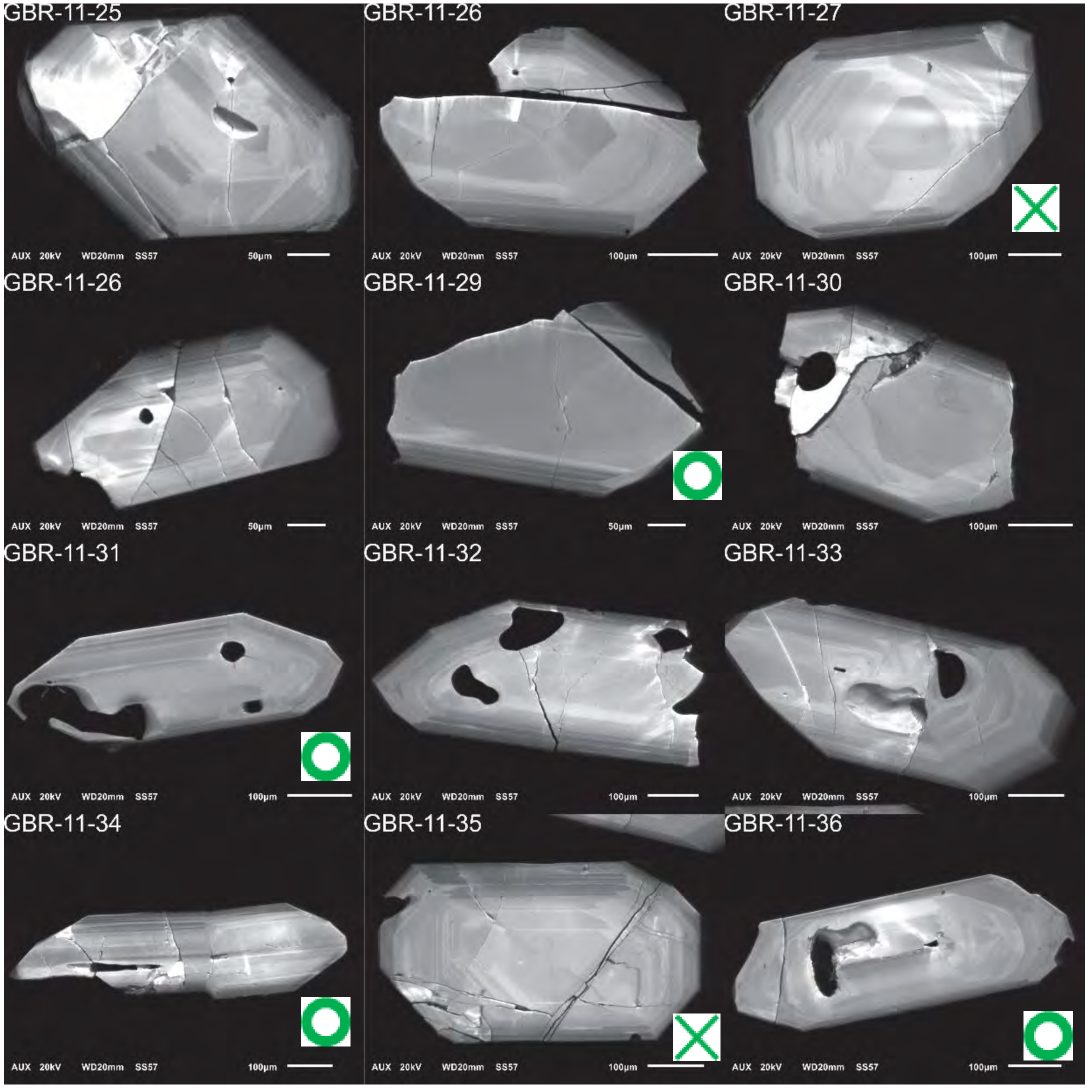

GBR-11, 37-48, 212-350µm fraction

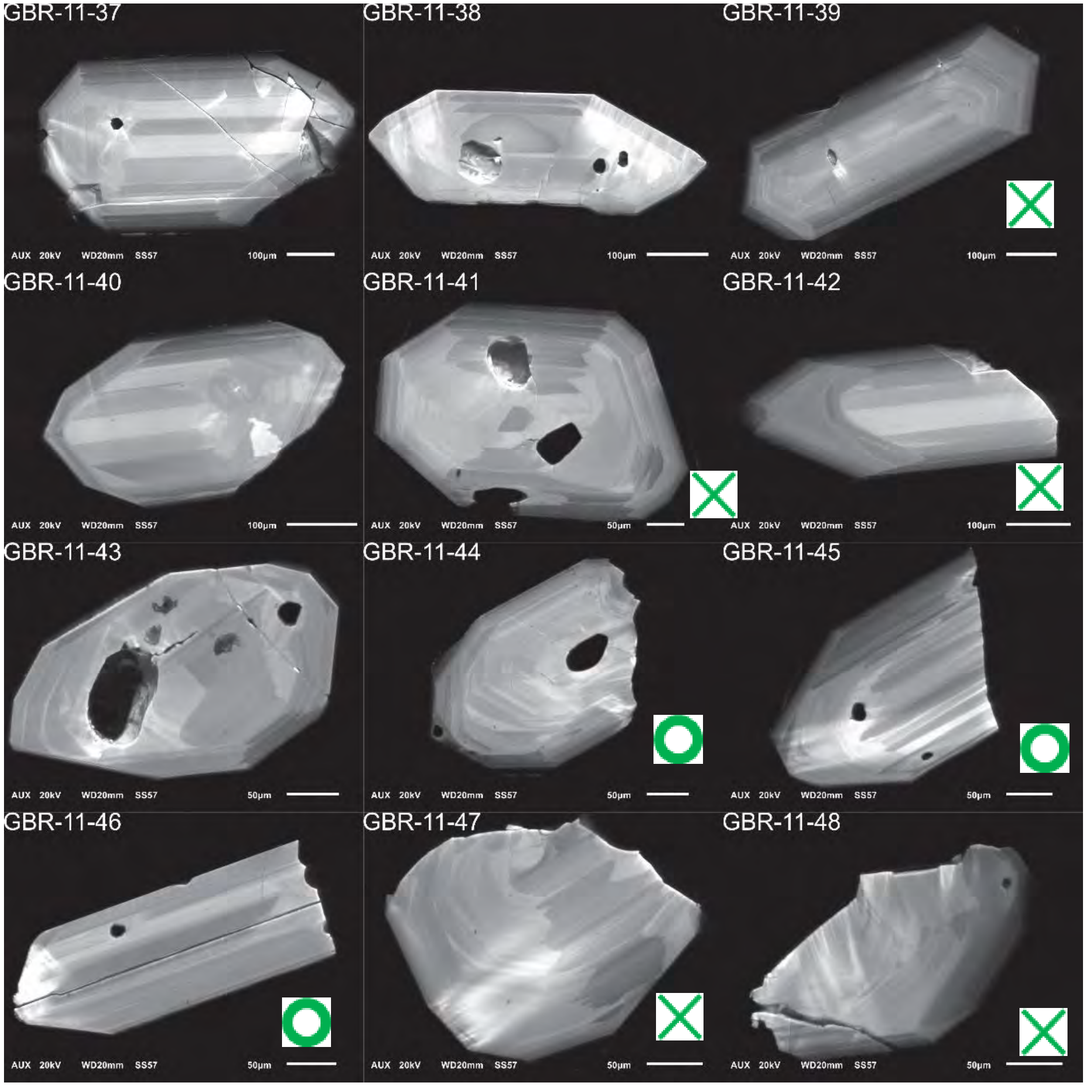

GBR-11, 49-55, 212-350µm fraction

GBR-11-49

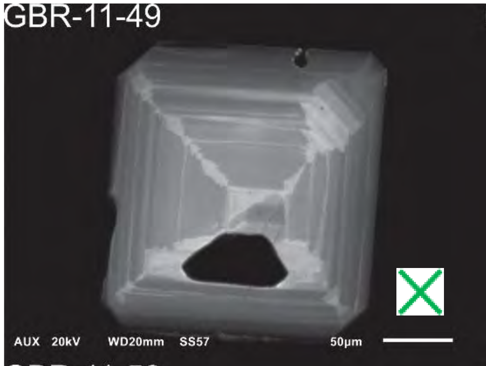

GBR-11-50

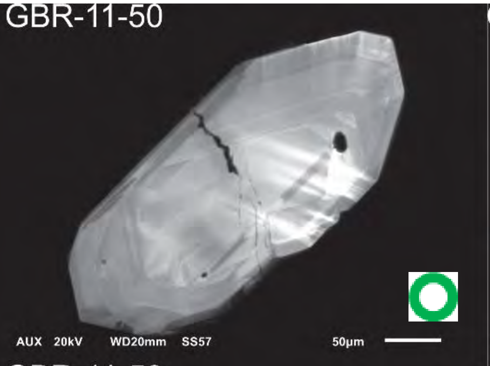

GBR-11-51

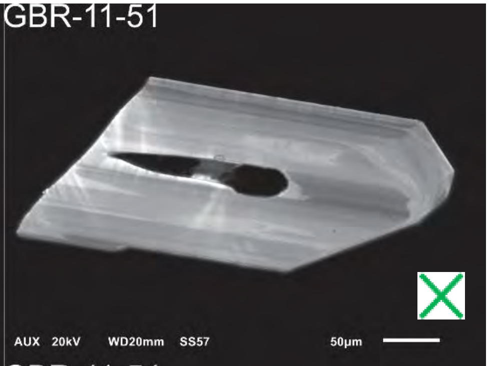

GBR-11-52

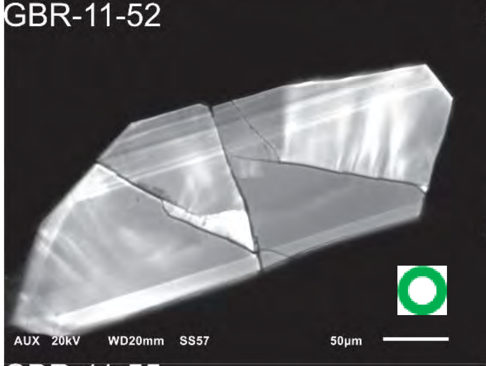

GBR-11-53

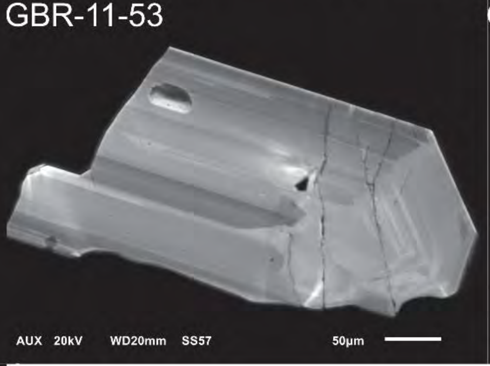

GBR-11-54

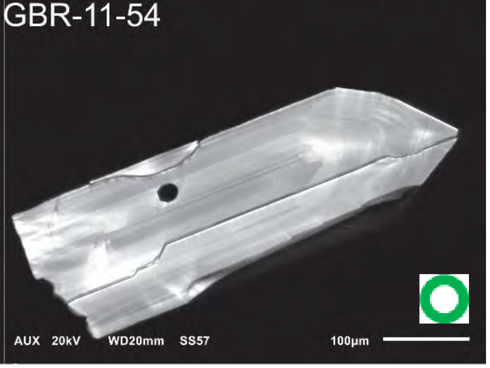

GBR-11-55

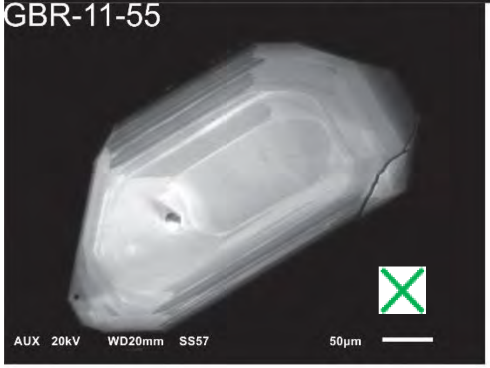

GBR-12, 1-12, 80-212μm fraction

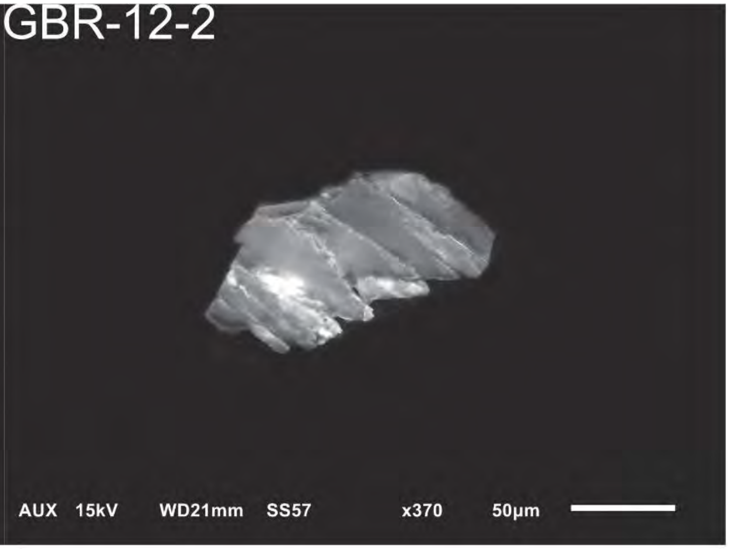

GBR-12, 1-12, 212-350μm fraction

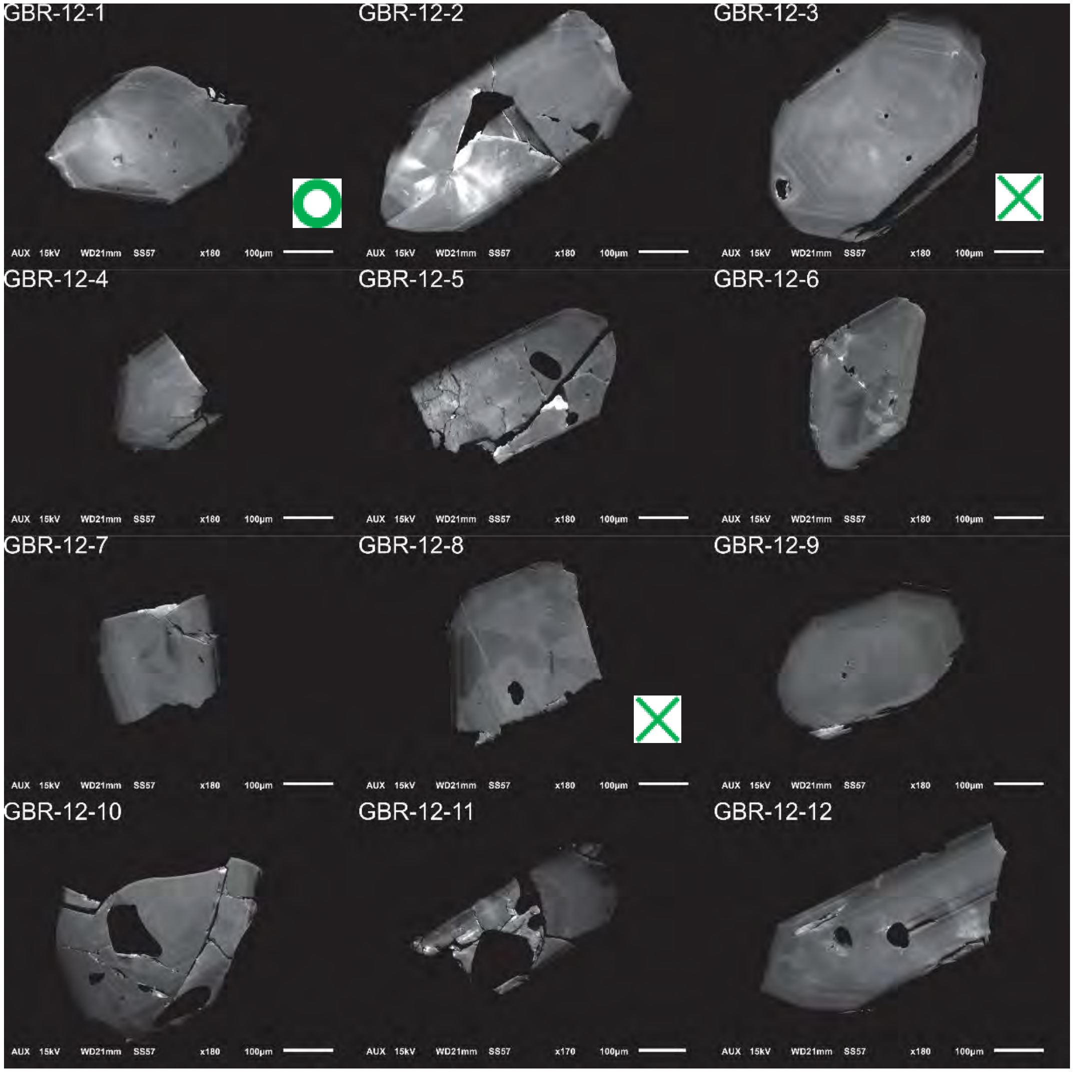

GBR-12, 13-24, 212-350µm fraction

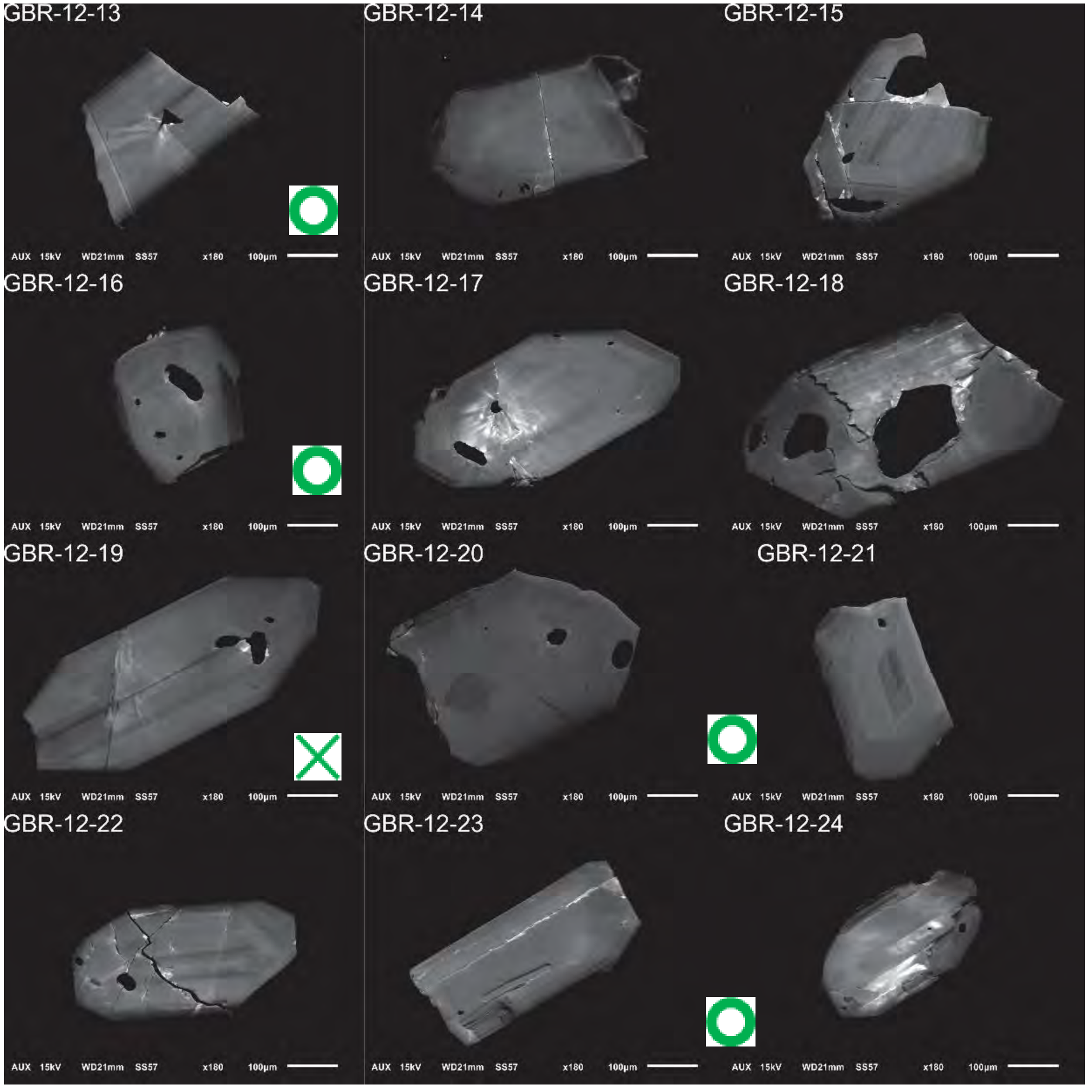

GBR-11, 25-33, 212-350µm fraction

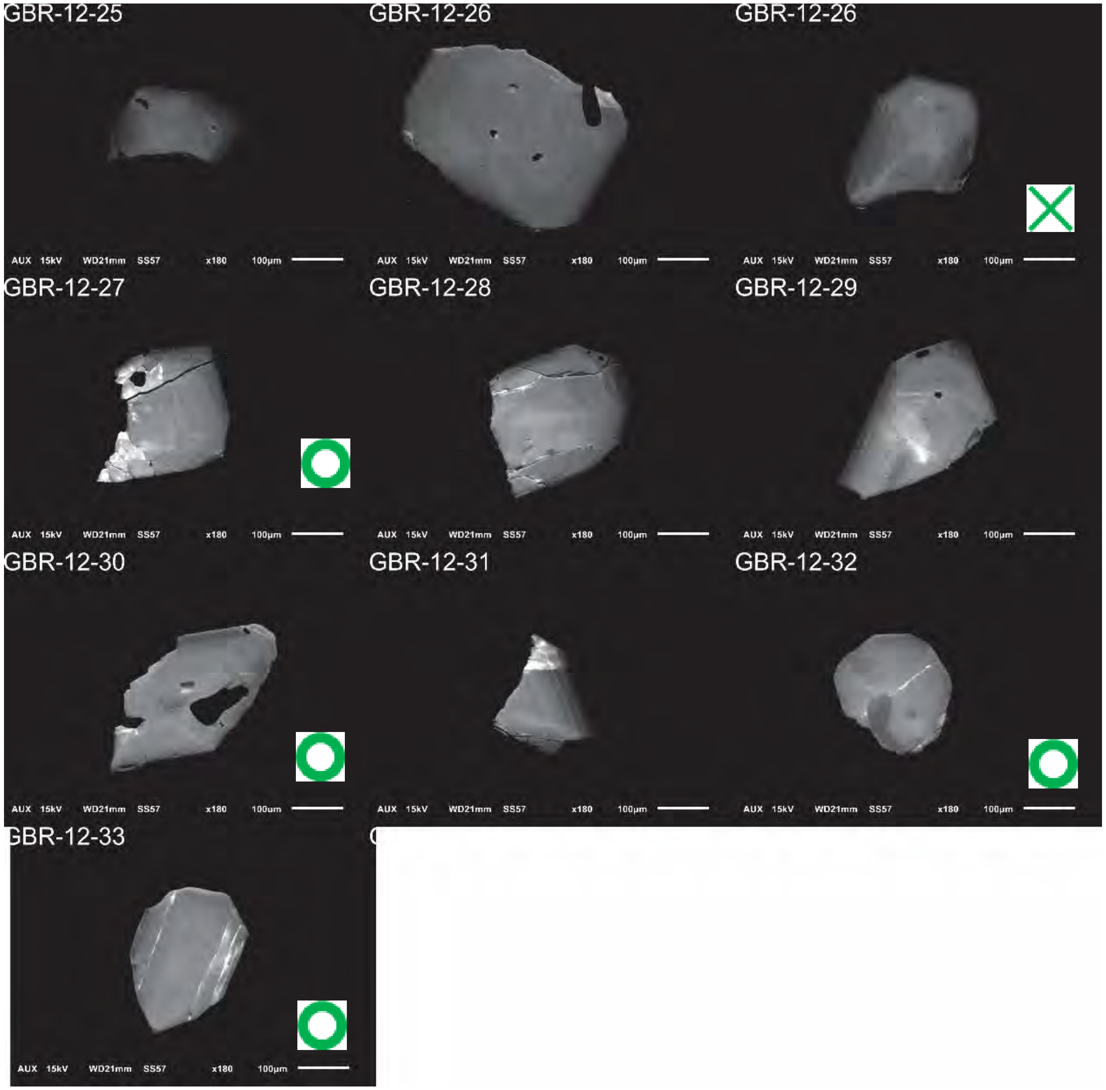

GBR-15, 1-12, 80-212µm fraction

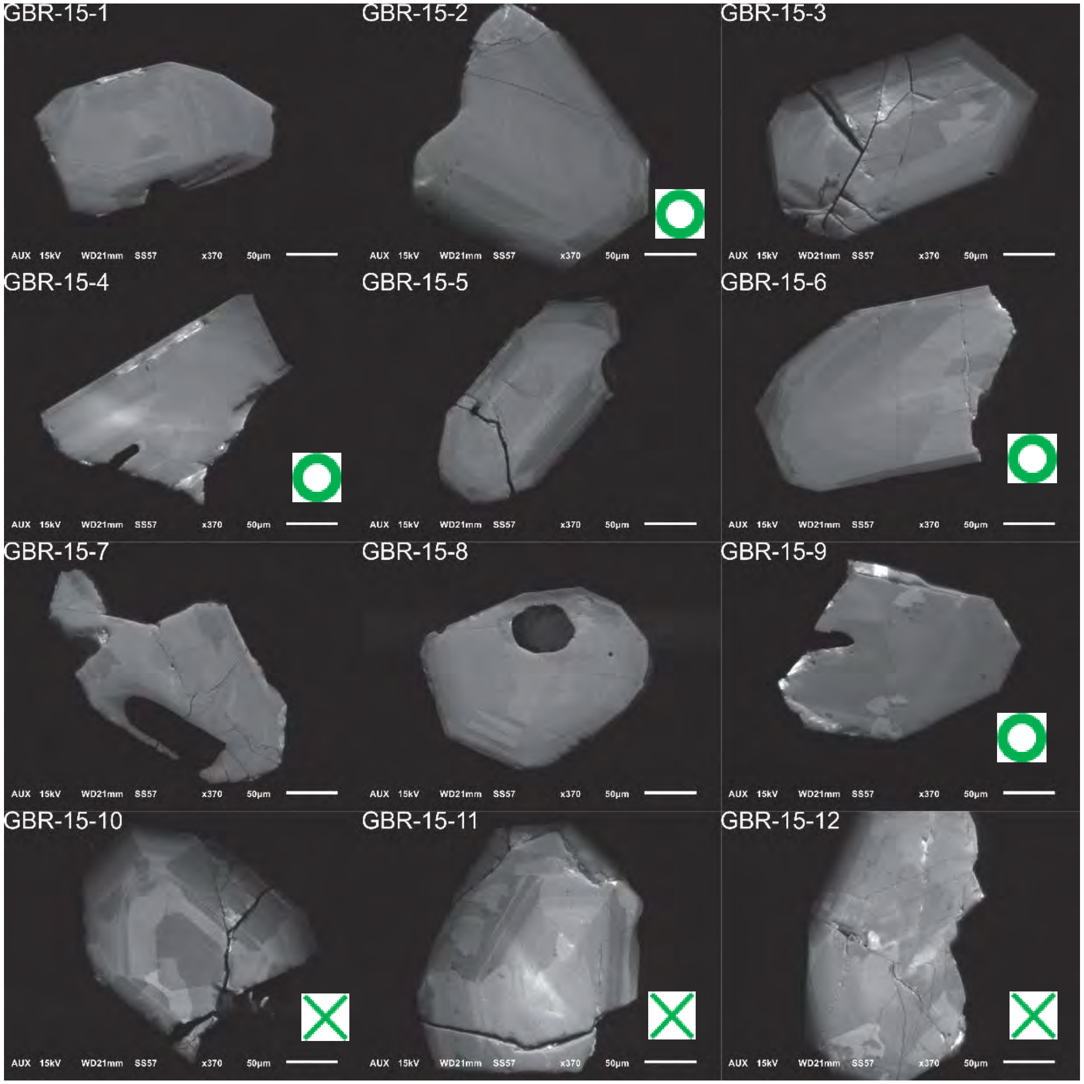

GBR-15, 13-24, 80-212µm fraction

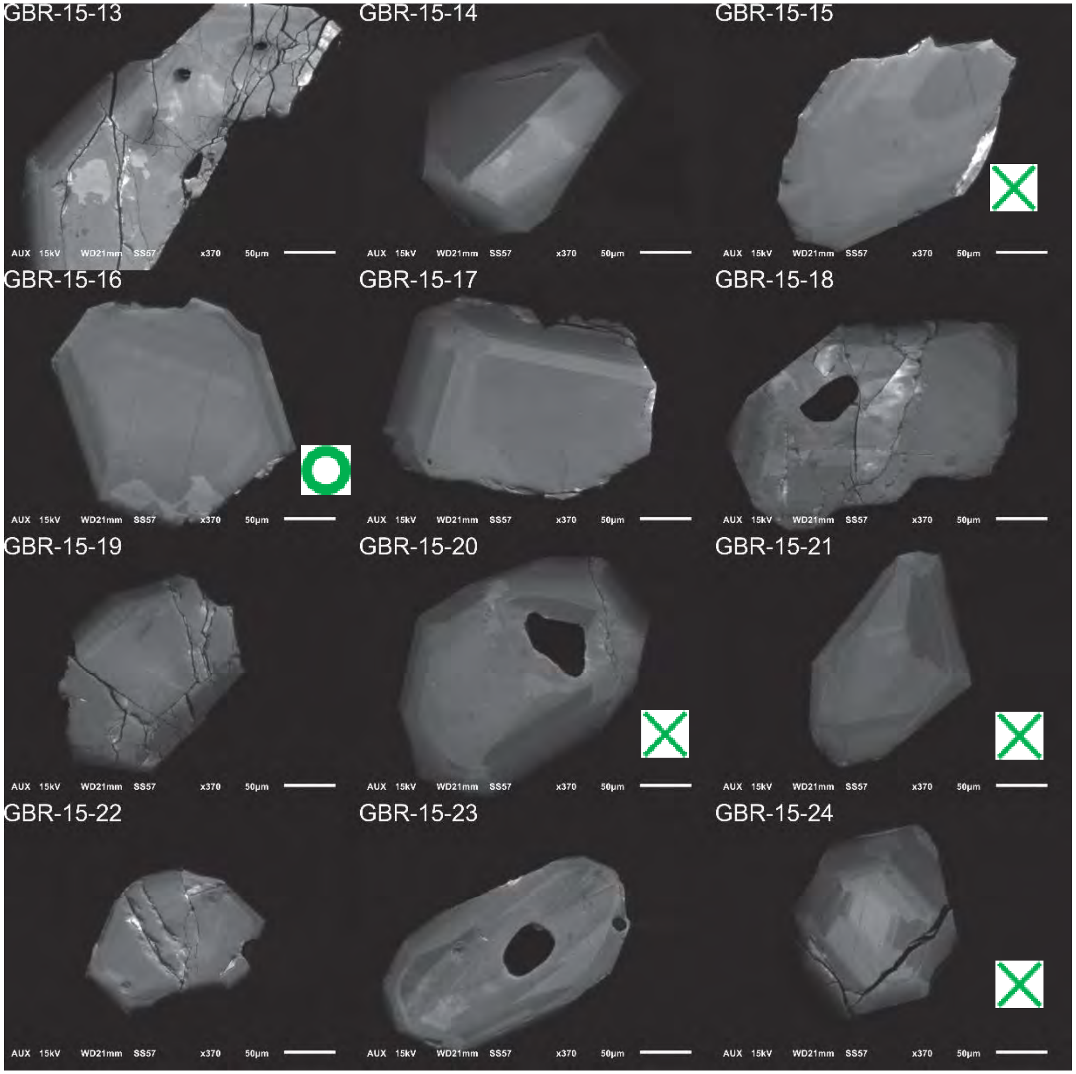

GBR-15, 25-30, 80-212µm fraction

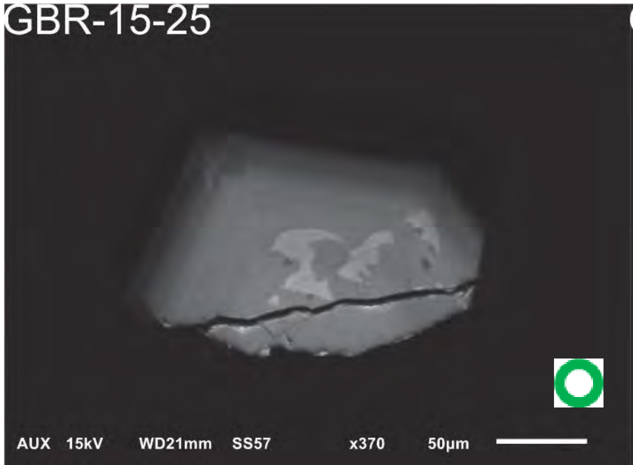

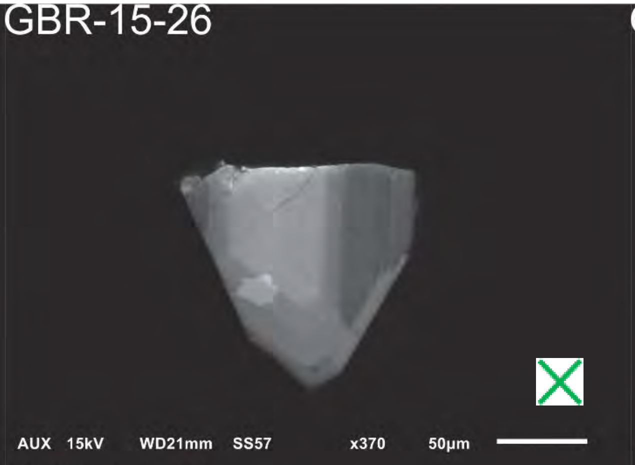

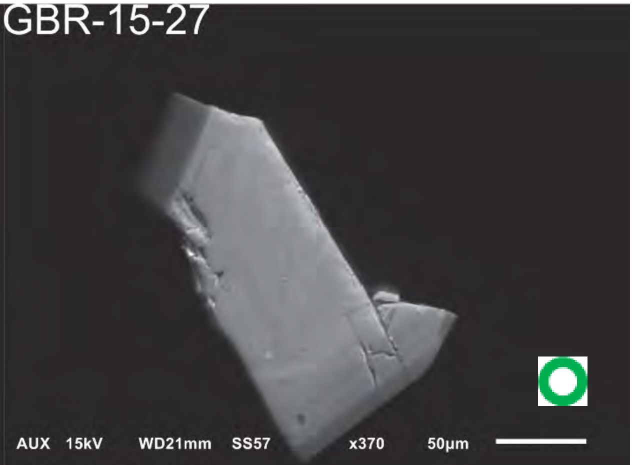

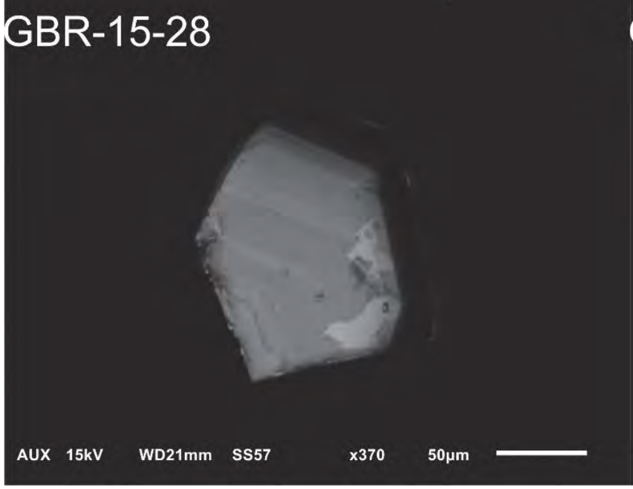

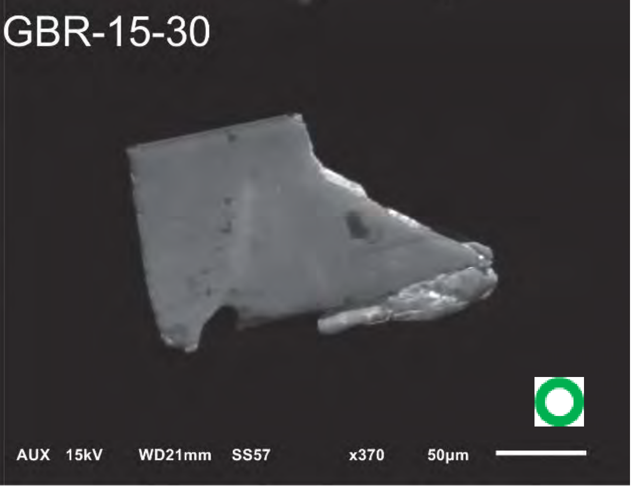

GBR-15, 1-12, 212-350µm fraction

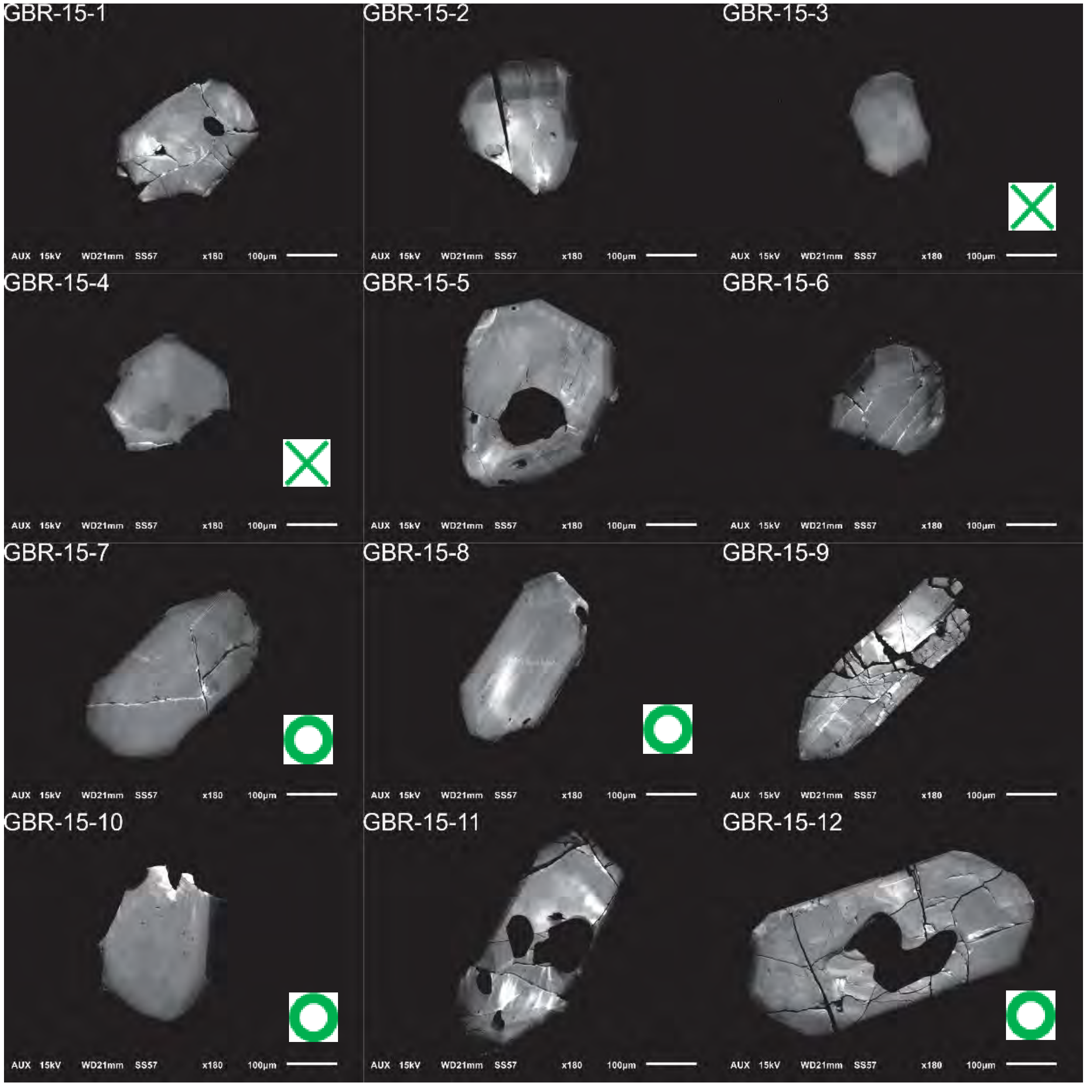

GBR-16, 1-3, 80-212µm fraction

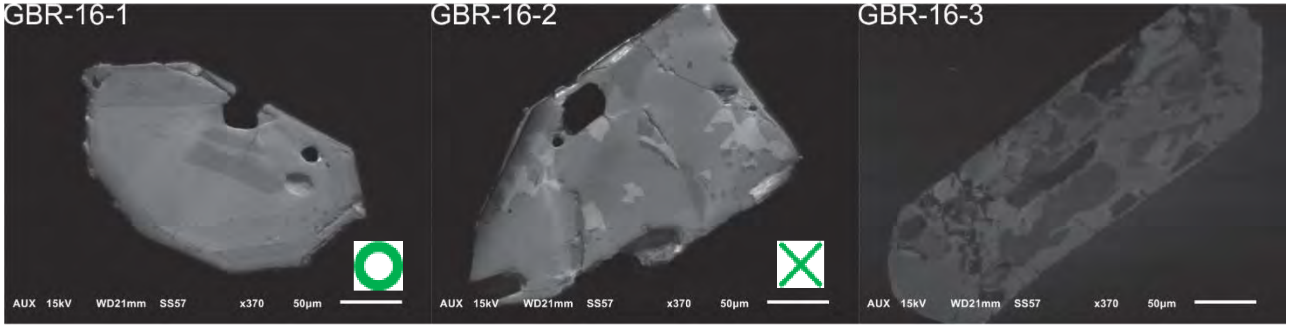

GBR-16, 1-3, 212-350µm fraction

GBR-16, 1-2, 212-350µm fraction, second session

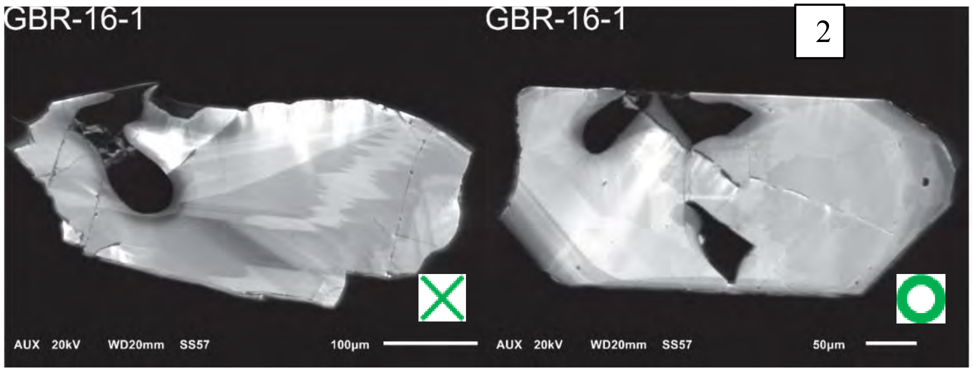

GBR-21, 1-12, 80-212μm fraction

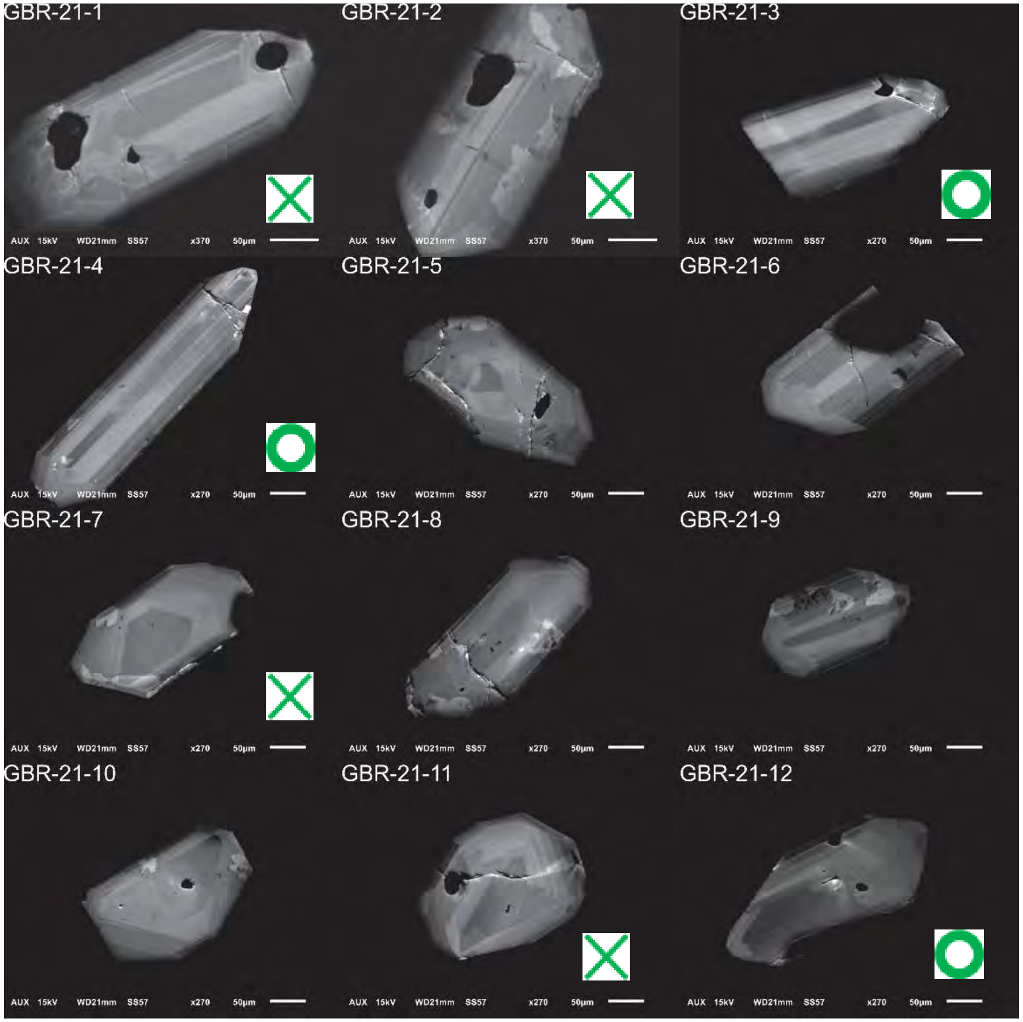

GBR-21, 12-24, 80-212μm fraction

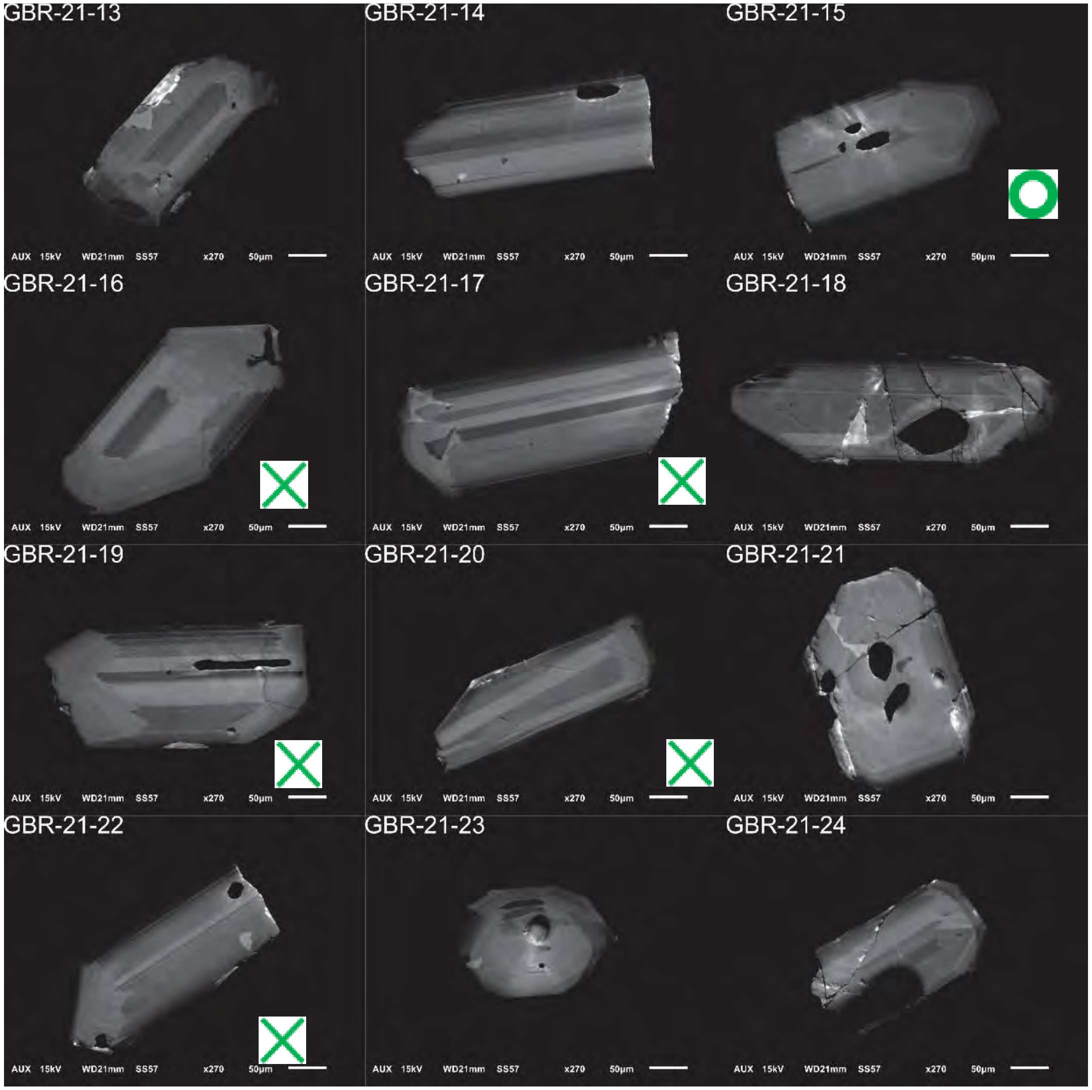

GBR-21, 25-36, 80-212μm fraction

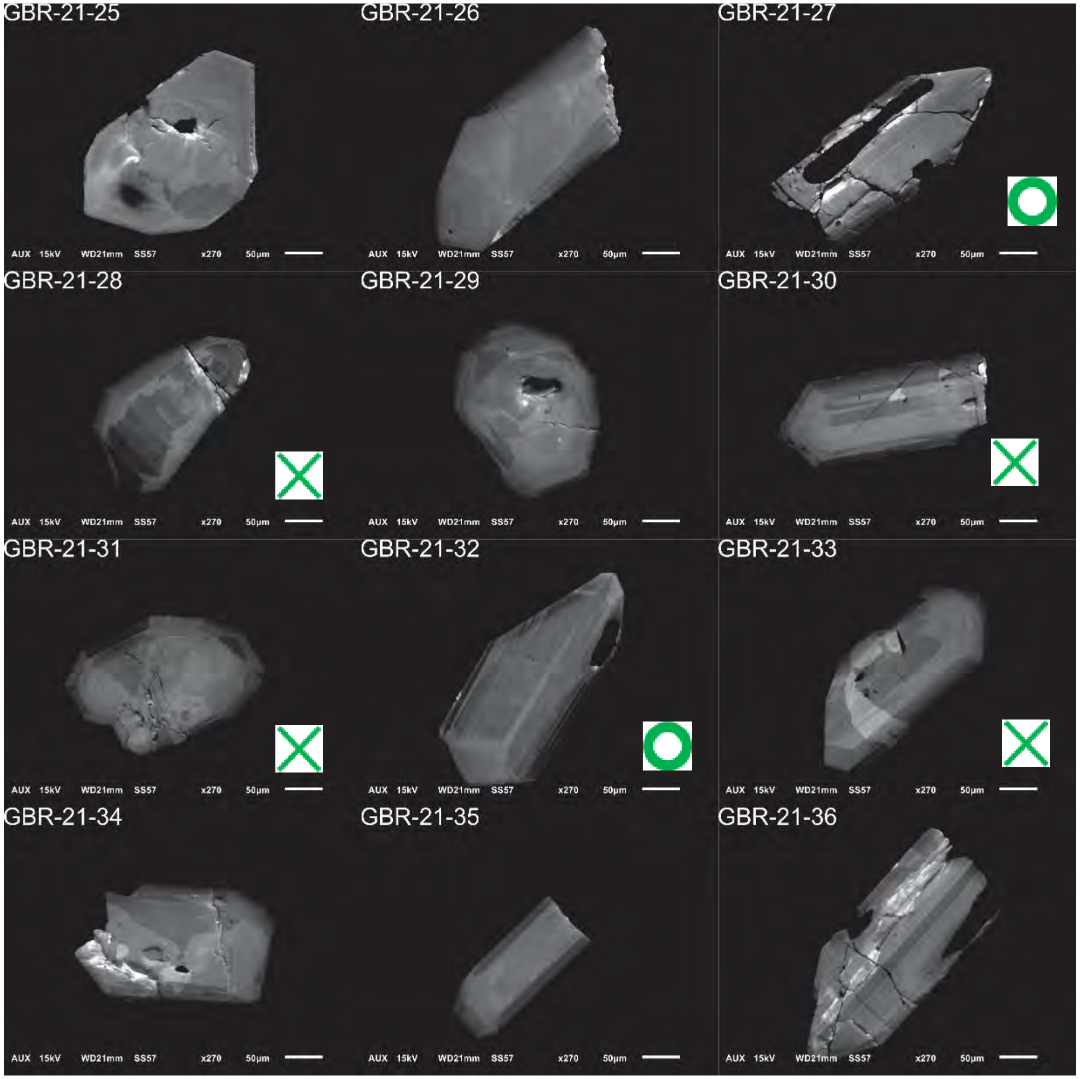

GBR-21, 37-48, 80-212µm fraction

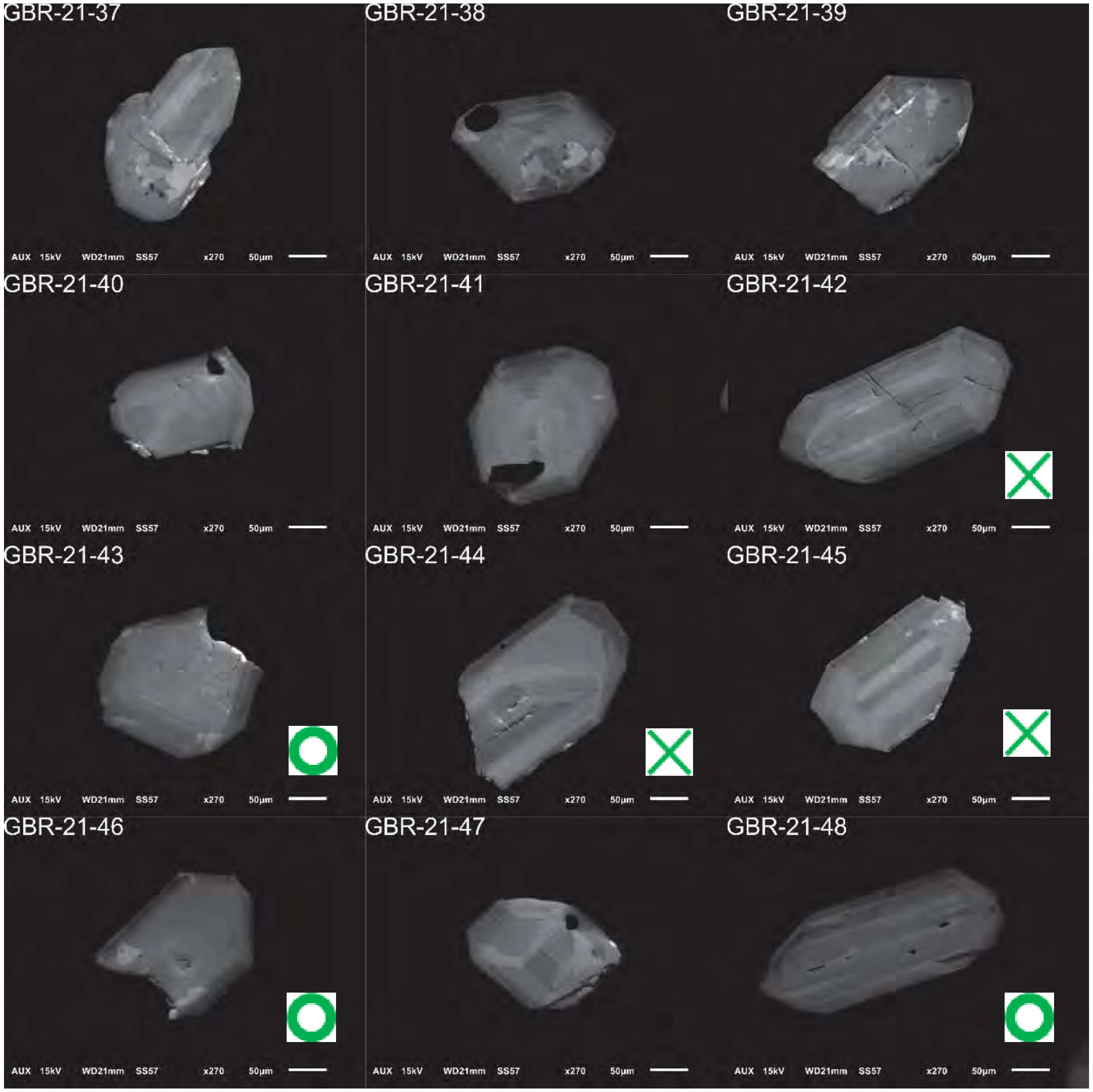

GBR-21, 49-60, 80-212µm fraction

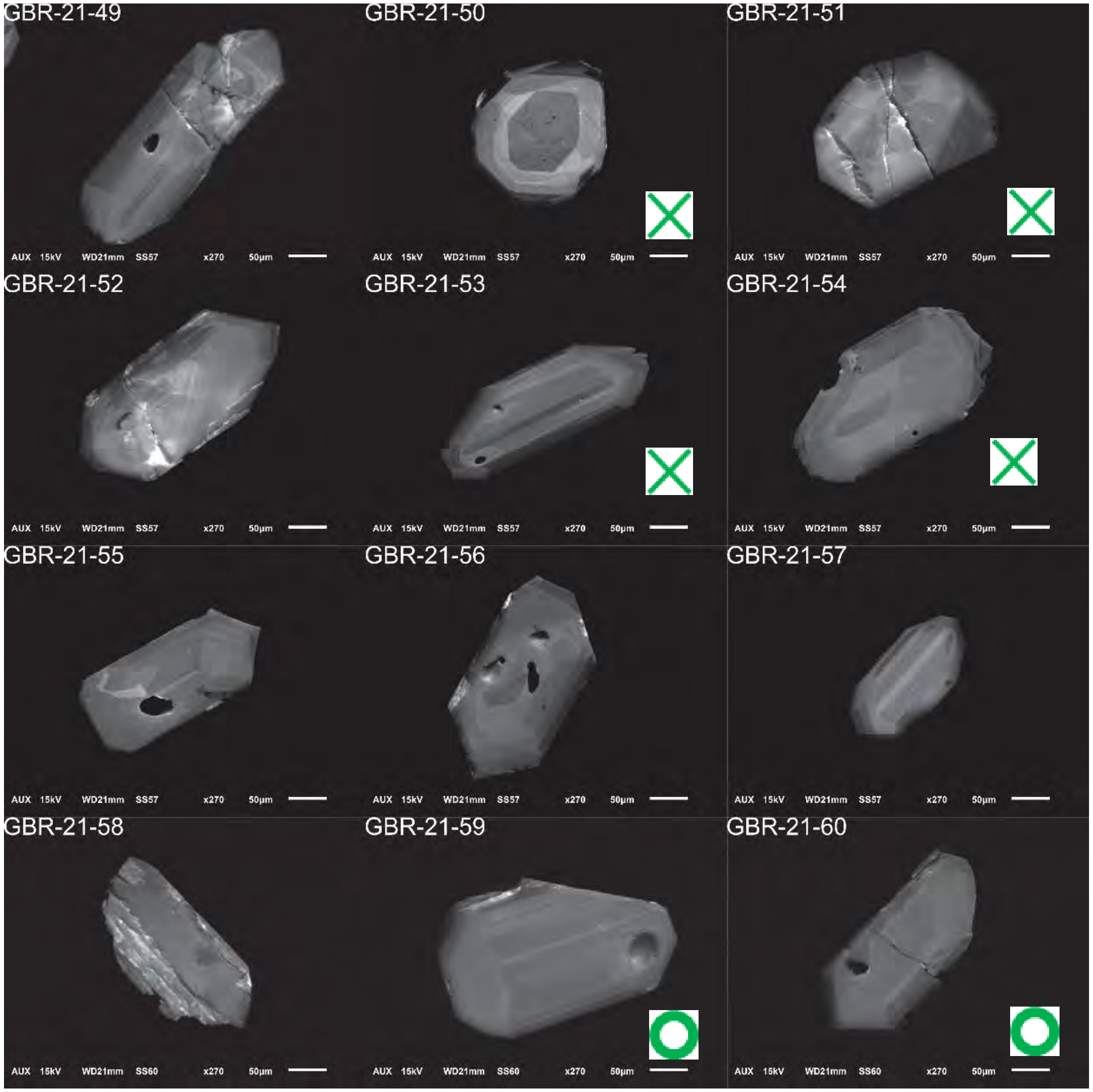

GBR-21, 73-84, 80-212µm fraction

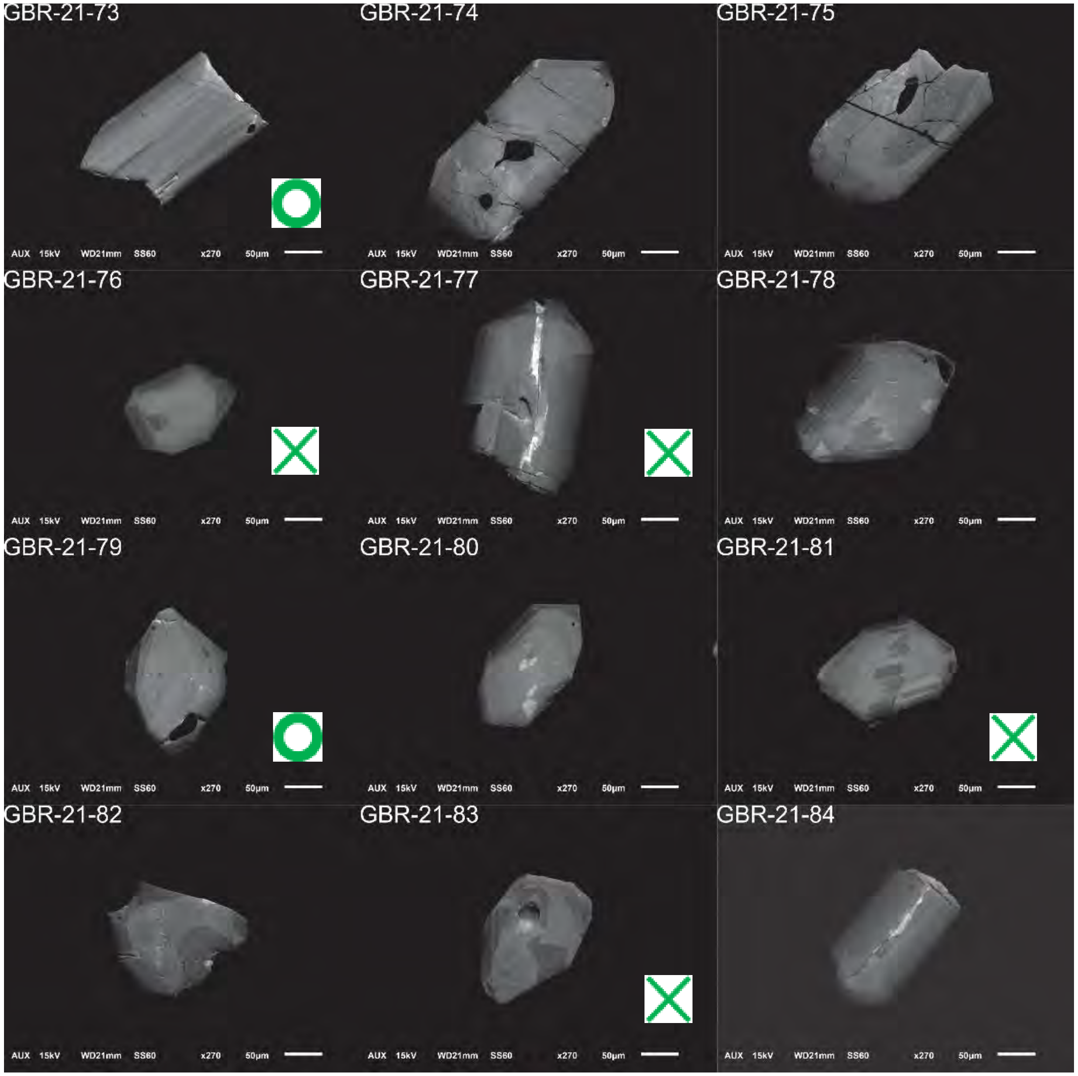

GBR-21, 85-96, 80-212µm fraction

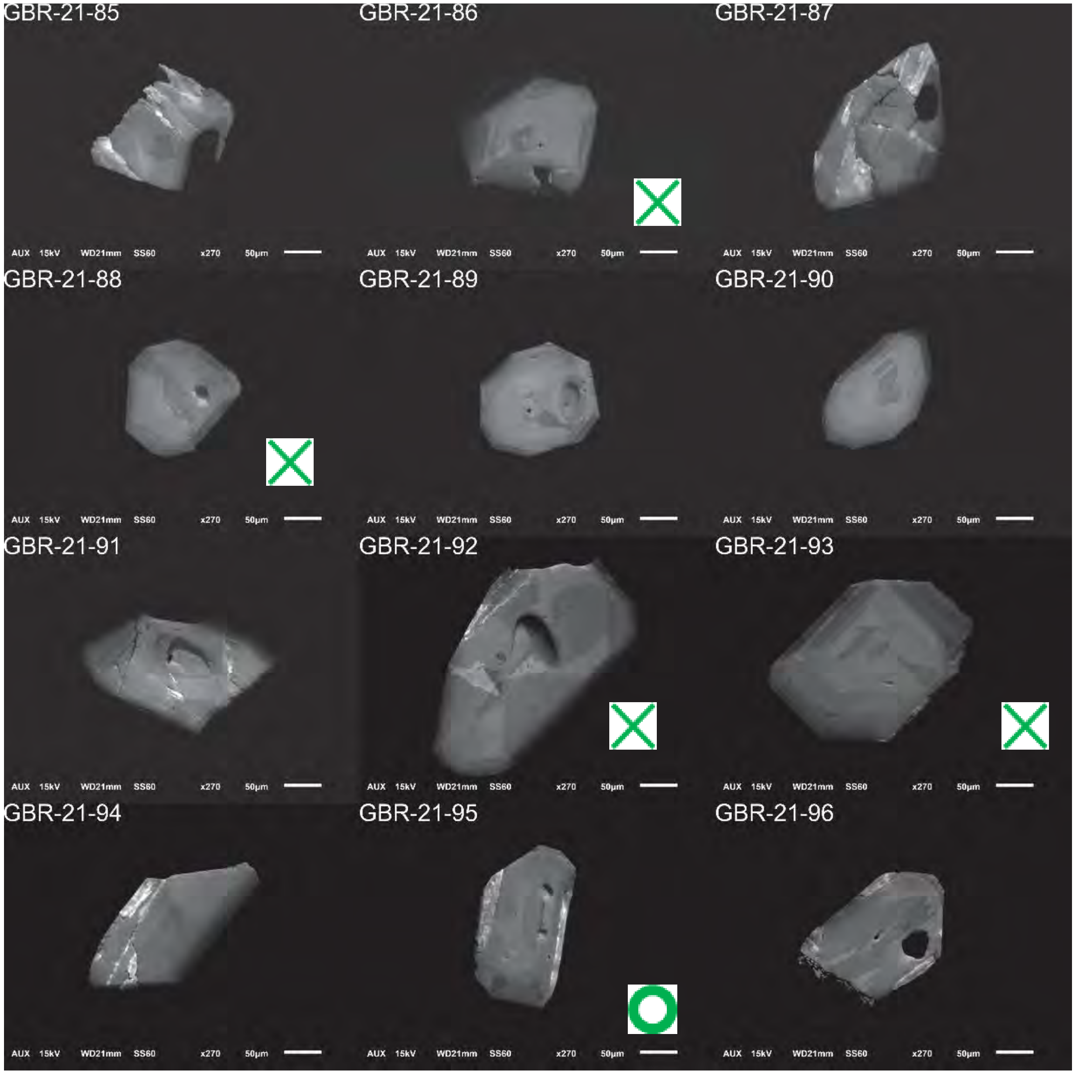

GBR-21, 85-96, 80-212µm fraction

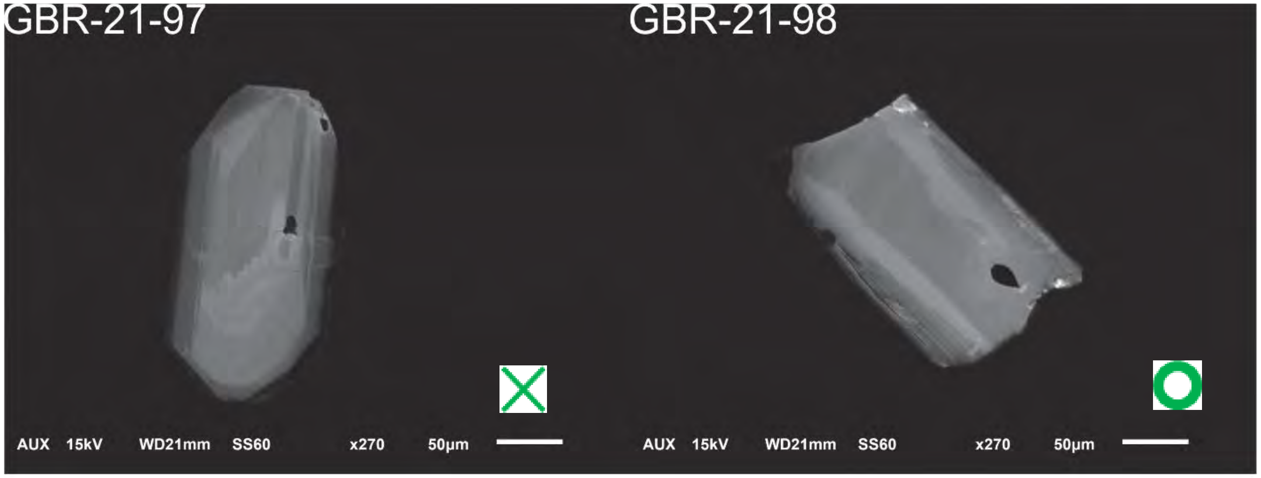

GBR-21, 1-12, 212-350μm fraction

GBR-21-1

GBR-21-2

GBR-21-3

GBR-21-4

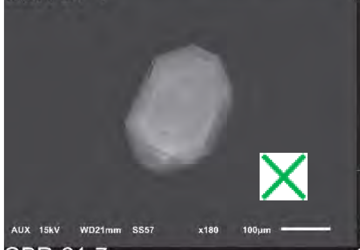

GBR-21-5

GBR-21-6

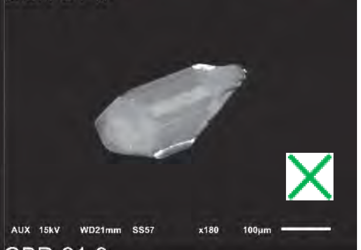

GBR-21-7

GBR-21-8

GBR-21-9

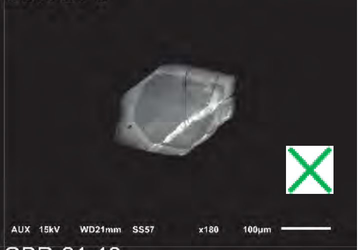

GBR-21-10

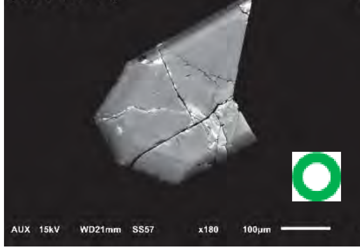

GBR-21-11

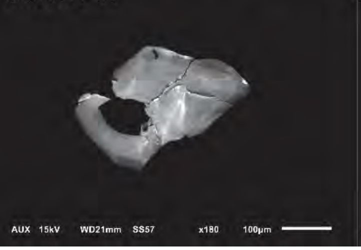

GBR-21-12

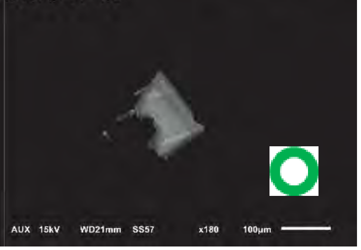

GBR-21, 13-20, 212-350µm fraction

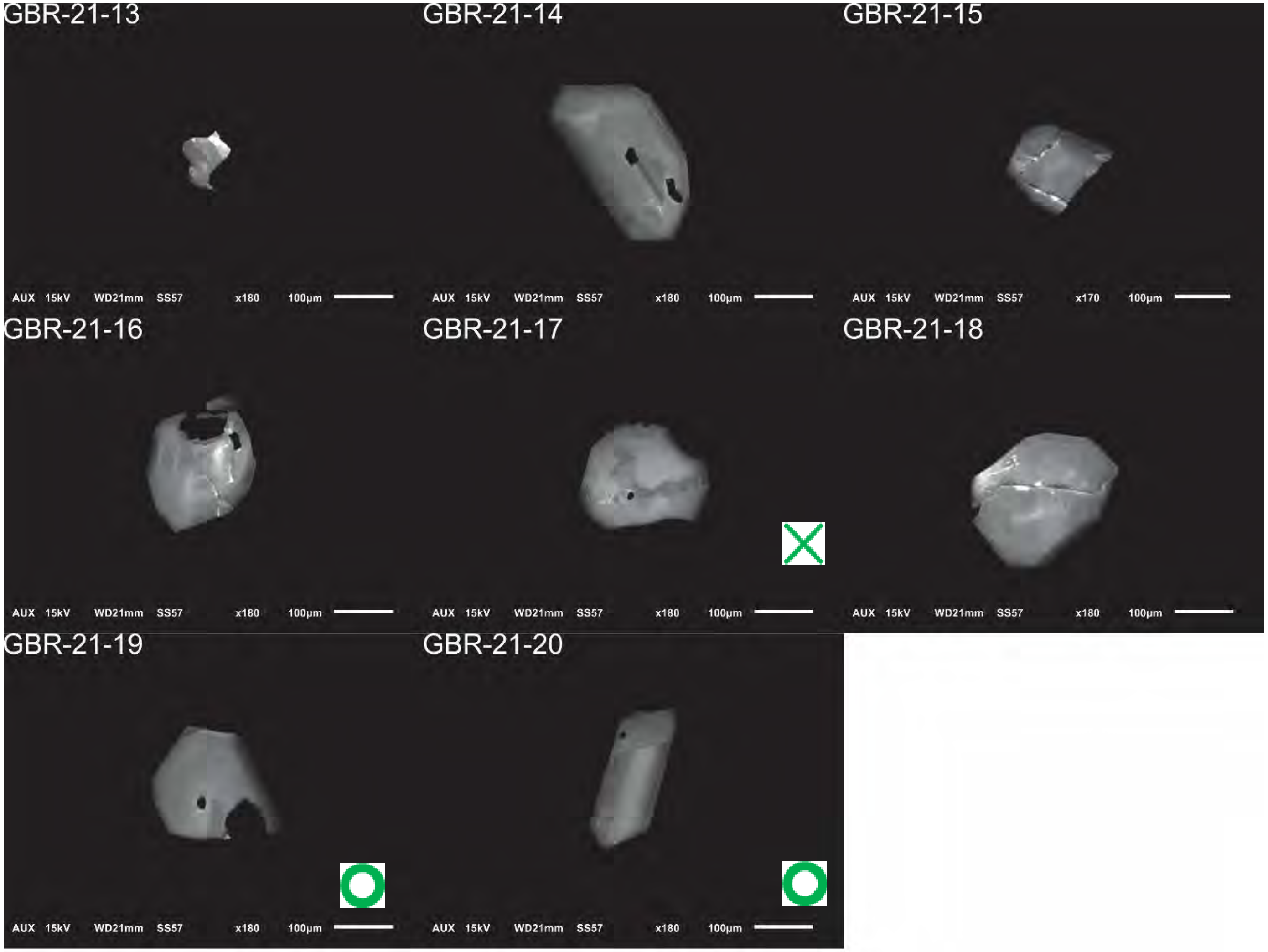

GBR-28, 1-4, 80-212µm fraction

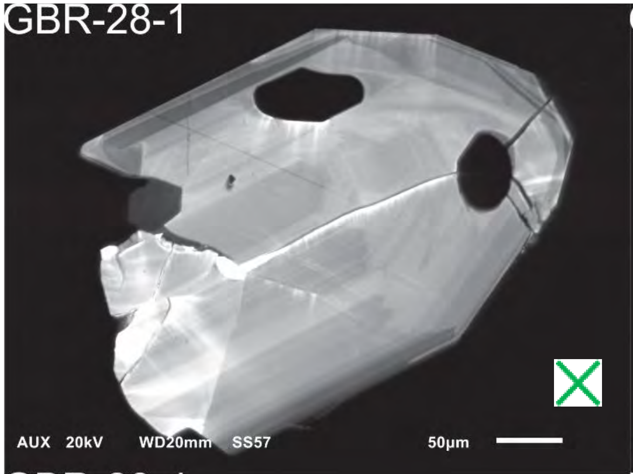

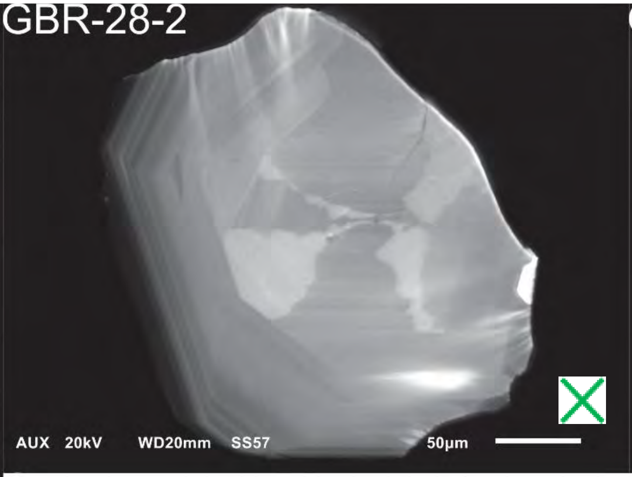

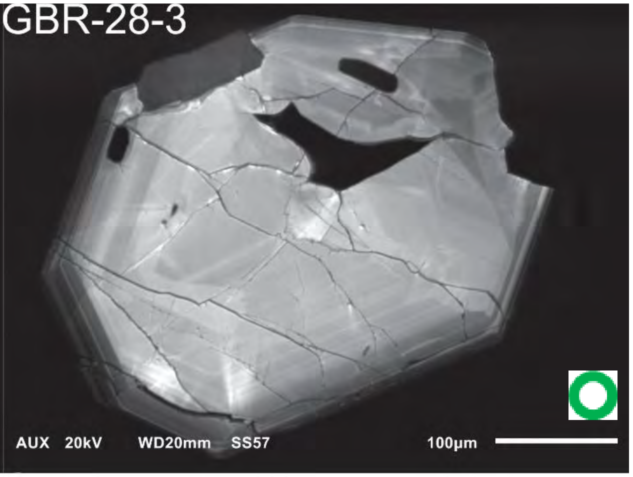

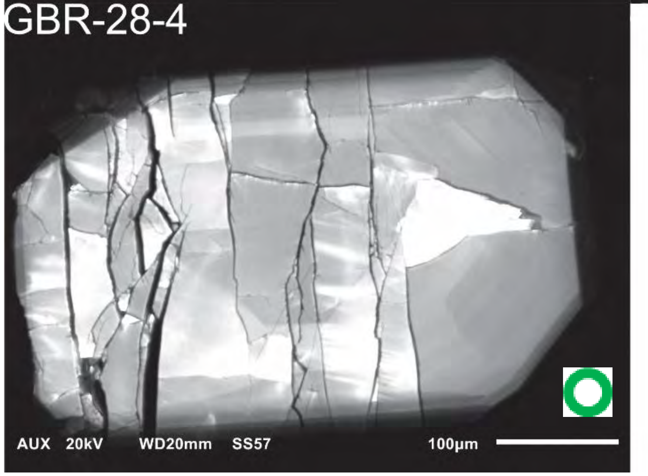

GBR-32, 1-12, 212-350µm fraction

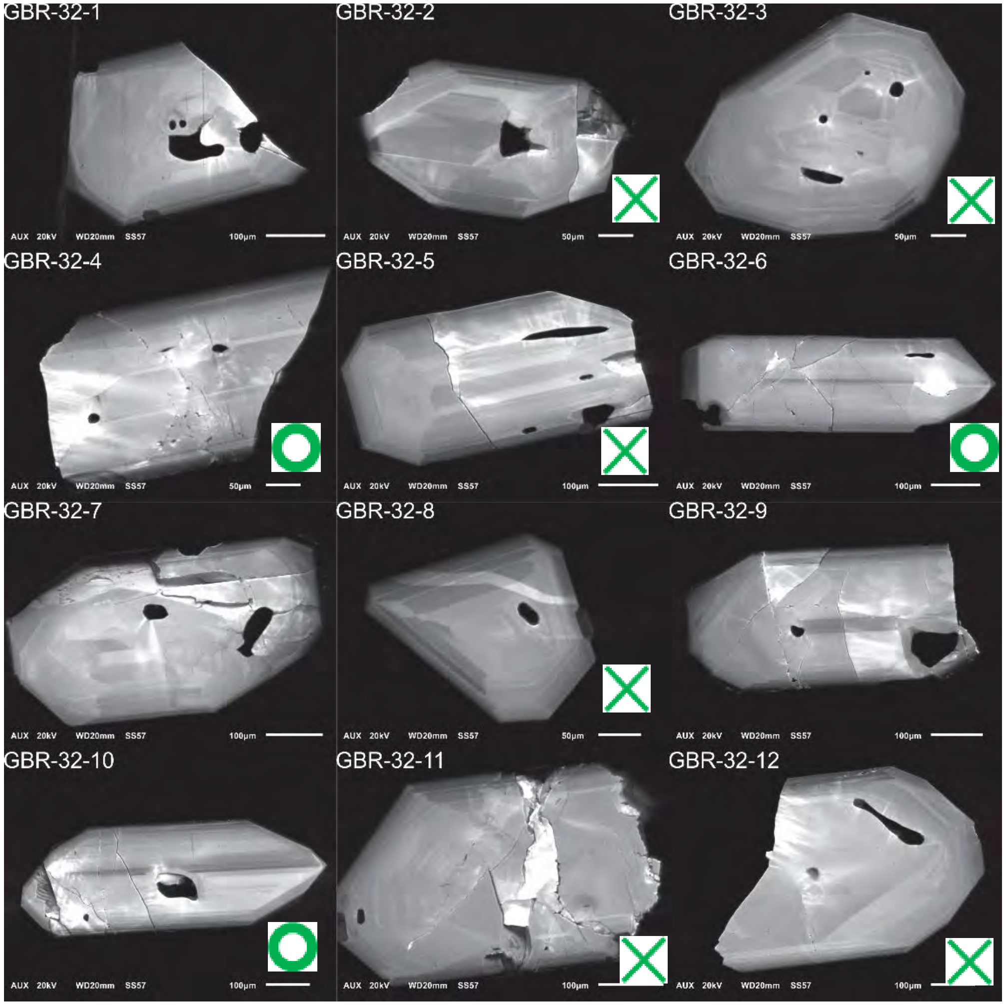

GBR-32, 13-24, 212-350μm fraction

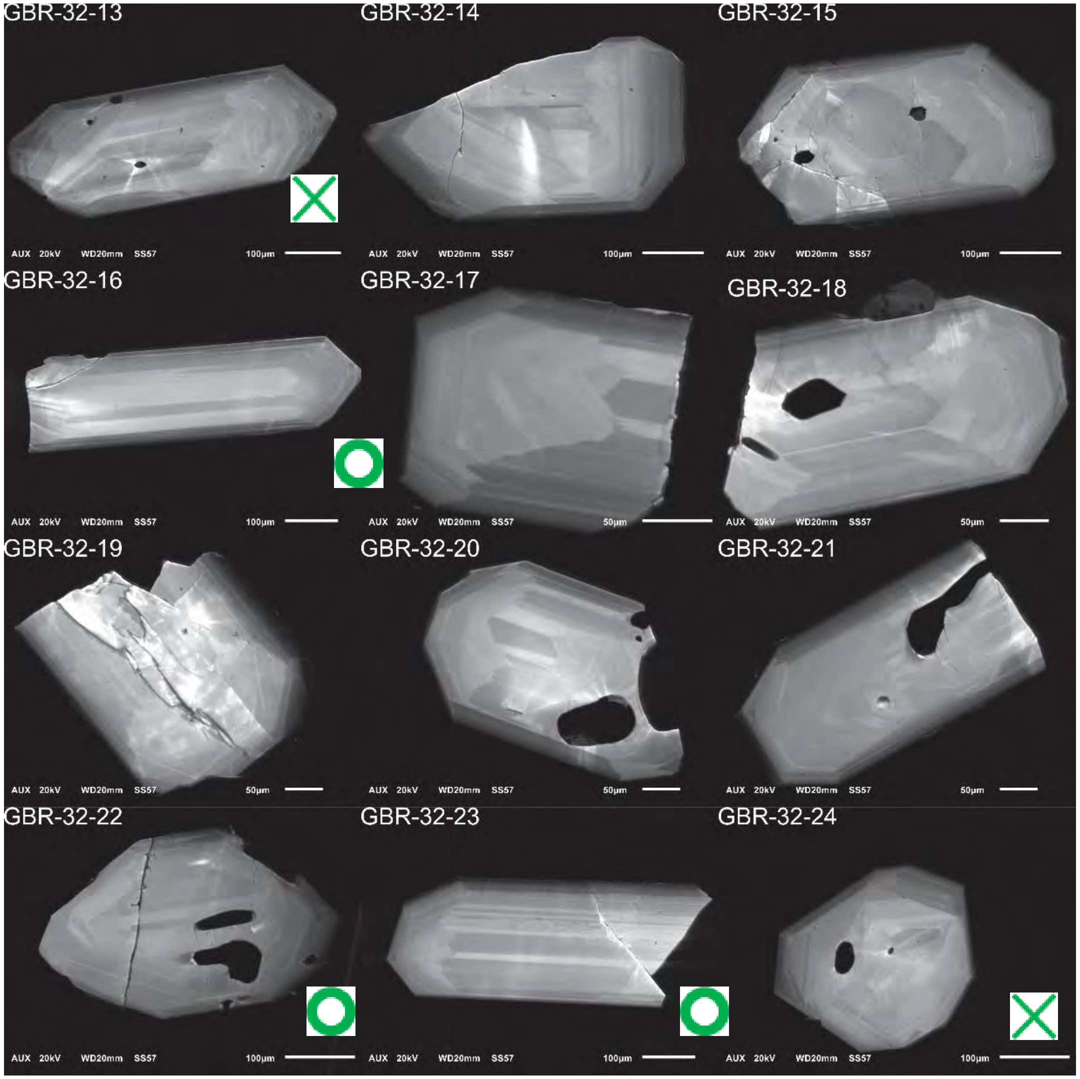

GBR-32, 25-33, 212-350µm fraction

GBR-32-25

GBR-32-26

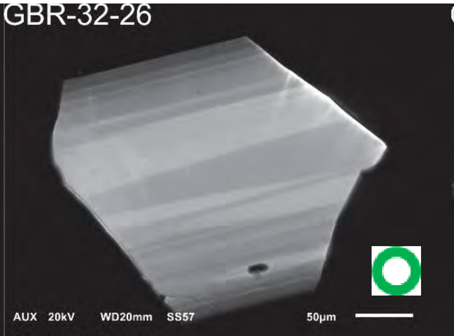

GBR-32-27

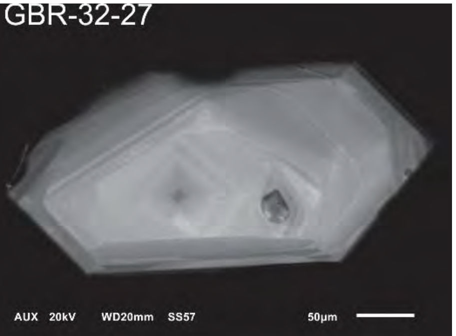

GBR-32-28

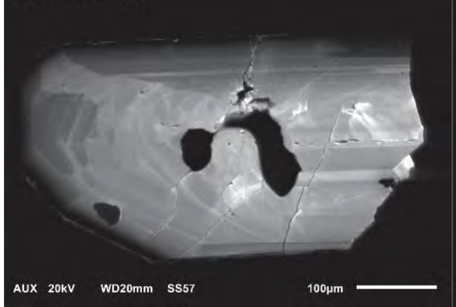

GBR-32-29

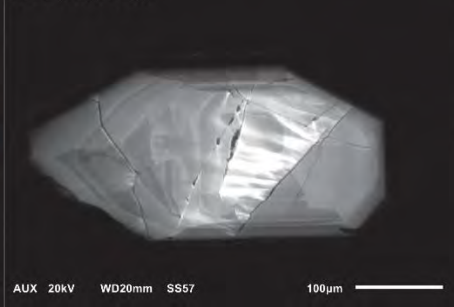

GBR-32-30

GBR-32-31

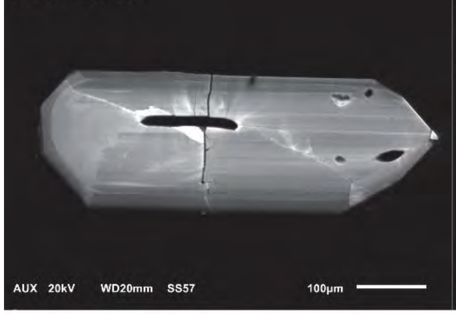

GBR-32-32

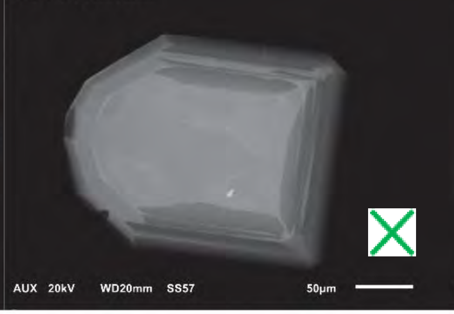

GBR-32-33

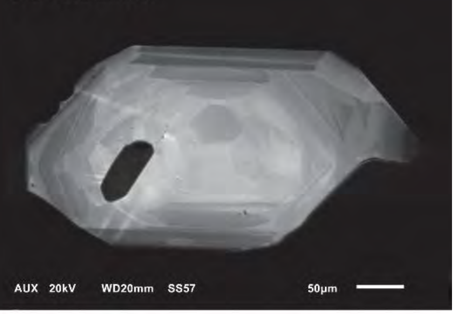

Appendix 7. Sample descriptions

Sample	Lithology	Description	Structure	Alteration	Igneous minerals	Modality	Alteration minerals	Modality	Sulphide/oxides
GBR-1	Coarse grained tonalite	Tonalite with moderate Ep/Chl and Wm alteration, Mineralized	Porphyry texture with coarse grained Qz crystals and Pl, isotropic	Moderate white mica alteration (partial replacement of Pl) with a moderate Ep overprint (partial replacement of Pl). Some Pl is preferentially and completely replaced by Ep within Chl aggregates	**Pl**	30	**Wm**	10	Tr Ccp, Py, Bn and Mag
							Chl	10	
					Qz	40	**Ep**	8	
				Ep veins/veinlets	**Ttn**	Tr	**Ttn + Rt**	2 (in Chl aggregates)	
				Allanite present Relict mafics (Bt, Hbl), fully replaced by Chl±Bt±Ttn±Rt	**Zr**	Tr			
GBR-2	Tonalite	Medium grained mineralized tonalite with intense Wm	Weak foliation	Intense Wm alteration overprinting weak Ep alteration, 5%	**Pl**	25	**Wm**	25	Ccp and Tr Py in Chl aggregates
					Qz	25	**Chl**	20	
					Zr	Tr	**Ep**	5	

		and weak Ep alteration		of Qz is secondary, Wm forms veins Allanite present Relict mafics (Bt, Hbl), fully replaced by Chl±Bt±Ttn±Rt	**Ttn**	Tr	**Ttn+Rt**	Tr (in Chl aggregates)	
GBR-3	Tonalite	Medium grained tonalite with intense Wm alteration and calcite	Isotropic	Intense Wm alteration and weak Ep alteration, Cal forms in aggregates. Ep overprints Wm Allanite present Relict mafics (Bt, Hbl), fully replaced by Chl±Bt±Ttn±Rt	**Qz**	35	**Cal**	15	Tr Py, Mag
					Pl	30	**Wm**	10	
					Ttn	Tr	**Chl**	Tr	
					Zr	Tr	**Ep**	Tr	
GBR-4	Tonalite	Coarse grained tonalite with intense Wm alteration, mineralized	Weak foliation, not equigranular	Most Pl grains are completely altered to Wm and Ep. Relict Hbl and Bt completely biotized and/or chloritized. Ep occurs as veinlets, aggregates and disseminated, weak Cu mineralization,	**Pl**	40	**Wm**	20	Tr Bn, Ccp, Py, Mag, Mal
					Qz	25	**Chl**	10	
					Ttn	Tr	**Ep**	5	

				signs of some supergene alteration, 5 % of Qz is secondary recrystalized Allanite present Relict mafics (Bt, Hbl), fully replaced by Chl±Bt±Ttn±Rt	**Zr**	Tr			
GBR-5	Tonalite	Mineralized medium grained tonalite	Isotropic	Intense Wm and weak Ep alteration. Ep and Wm occurs in aggregates and with Ccp veins Allanite present Relict mafics (Bt, Hbl), fully replaced by Chl±Bt±Ttn±Rt	**Qz**	40	**Wm**	20	Ccp in Qt veins rimmed by Chl and in Ep Chl aggregates
					Pl	35	**Chl**	5	
					Ttn	Tr	**Ep**	Tr	
					Zr	Tr			
GBR-6	Qt vein thin section	Qt – Chl vein	Vein	Chl + Wm veinlet between two quartz veins	**Qz**	90	**Wm**	5	Tr Py, Mag
							Chl	5	
							Ttn-Rt	Tr (in Chl aggregates)	
GBR-7	Tonalite	Mineralized medium	Isotropic and equigranular	Isolated sections of intense Ep alteration, overall	**Qz**	35	**Wm**	20	Py, Mag, Ccp
					Pl	30	**Chl**	10	

		grained tonalite		intense Wm alteration, Ep-Chl-Qz veins, allanite present Allanite present Relict mafics (Bt,Hbl), fully replaced by Chl±Bt±Ttn±Rt	**Ttn**	Tr	**Ep**	5	
					Zr	Tr	**Ttn + Rt**	Tr (in Chl aggregates)	
GBR-8	Leucocratic Tonalite		Isotropic	Intense Wm and moderate Ep alteration Allanite present Relict mafics (Bt, Hbl), fully replaced by Chl±Bt±Ttn±Rt	**Qz**	40	**Wm**	10	Tr Py, Mag
					Pl	35	**Chl**	10	
					Ttn	Tr	**Ep**	5	
					Zr	Tr	**Ttn + Rt**	Tr (in Chl aggregates)	
GBR-9	Tonalite	Quartz rich tonalite, most Pl is altered Un-mineralized	Isotropic, equigranular	Intense Wm and trace Ep alteration Allanite present Relict mafics (Bt, Hbl), fully replaced by Chl±Bt±Ttn±Rt	**Qz**	35	**Wm**	20	Tr Py, Mag
					Pl	10	**Chl**	20	
					Ttn	Tr	**Ep**	10	
					Zr	Tr	**Ttn + Rt**	5 (in Chl aggregates)	
GBR-10	Tonalite	Mineralized rich coarse	Isotropic		**Pl**	40	**Chl**	10	Tr Py, Mag, Cov
					Qz	35	**Ep**	10	

		grained tonalite		Supergene alteration Allanite present 10% of Qz is secondary	**Ttn**	Tr	**Wm**	5	
					Zr	Tr			
GBR-11	Tonalite	Pl rich leucocratic medium grained unmineralized tonalite	Foliated	Tr Qz is secondary Moderate Wm alteration and weak Ep alteration Chl-Ep veinlets present Relict mafics (Bt, Hbl), fully replaced by Chl±Bt±Ttn±Rt	**Pl**	40	**Wm**	10	Tr Py, Mag
					Qz	30	**Chl**	10	
					Ttn	Tr	**Ep**	5	
					Zr	Tr	**Ttn-Rt**	Tr (in Chl aggregates)	
GBR-12	Tonalite	Mineralized medium grained tonalite	Foliated	Chl and Wm veins present Intense Wm alteration Weak Ep alteration Relict mafics (Bt, Hbl), fully replaced by Chl±Bt±Ttn±Rt	**Pl**	25	**Chl**	20	Tr Py, Mag, Ccp
					Qz	30	**Wm**	15	
					Ttn	Tr	**Ep**	Tr	
					Zr	Tr	**Ttn-Rt**	Tr (in Chl aggregates)	
					Pl	40	**Wm**	20	Tr Py, Mag

GBR-13	Melanocratic tonalite	Coarse grained melanocratic medium grained un-mineralized tonalite	Strongly foliated	Chl and Ep occur is foliated aggregates Ep-Chl veinlets common following foliation Intense Wm alteration Weak Ep alteration Relict mafics (Bt, Hbl), fully replaced by Chl±Bt±Ttn±Rt	**Qz**	20	**Chl**	15	
					Ttn	Tr	**Ep**	5	
					Zr	Tr	**Ttn-Rt**	Tr (in Chl aggregates)	
GBR-14	Tonalite	Leucocratic Qz-rich coarse grained tonalite, mineralized	Isotropic, equigranular	Tr Ep alteration and intense Wm alteration Intense Wm alteration limited to veins and area surrounding Wm-Py-Ccp-Qz veins Remaining areas shows weak Wm alteration with relatively fresh Pl Relict mafics (Bt, Hbl), fully replaced by Chl±Bt±Ttn±Rt	**Qz**	50	**Cal**	20	Tr Py, Mag Disseminated Ccp associated with Wm
					Pl	20	**Wm**	10	
					Ttn	Tr	**Ep**	Tr	
					Zr	Tr	**Chl**	Tr	
							Ttn-Rt	Tr (in Chl aggregates)	

GBR-16	Quartz Diorite	Coarse grained mineralized Quartz Diorite	Isotropic, equigranular	Moderate Wm and Ep alteration Some Pl is relatively fresh Ep replaces Pl Allanite present Ep and Chl are disseminated and in aggregates Relict mafics (Bt, Hbl), fully replaced by Chl±Bt±Ttn±Rt	**Pl**	60	**Wm**	10	Tr Py, Mag, Ccp
					Qz	10	**Ep**	10	
					Ttn	Tr	**Chl**	10	
					Zr	Tr	**Ttn-Rt**	Tr (in Chl aggregates)	
GBR-18	Tonalite	Coarse grained Qz-rich medium grained tonalite	Isotropic, equigranular	Intense Ep alteration with moderate Wm alteration Allanite present Relict mafics (Bt, Hbl), fully replaced by Chl±Bt±Ttn±Rt	**Qz**	30	**Ep**	30	Tr Py, Mag
					Pl	20	**Chl**	10	
					Ttn	5	**Wm**	5	
					Zr	Tr	**Ttn-Rt**	Tr (in Chl aggregates)	
GBR-19	Tonalite	Medium grained Pl-rich mineralized tonalite	Foliated	Allanite present Pl is intensely altered by Ep and Wm	**Pl**	30	**Ep**	Tr	Tr Py and Mag, Cpy
					Qz	30	**Chl**	20	
					Zr	Tr	**Wm**	20	

				Weak Ep alteration Ep occurs as small isolated grains with Chl Pl grains are difficult to differentiate due to intense Wm alteration Wm veins present Relict mafics (Bt, Hbl), fully replaced by Chl±Bt±Ttn±Rt	**Ttn**	Tr	**Ttn-Rt**	Tr	
GBR-21	Tonalite	Medium grained Pl-rich mineralized tonalite	Intensely foliated	Allanite present Pl is intensely altered by Ep and Wm	**Pl**	50	**Ep**	Tr	Tr Py and Mag, Ccp
					Qz	20	**Chl**	10	
					Zr	Tr	**Wm**	25	

				Intense Wm and weak Ep alteration Ep occurs as small isolated grains with Chl WM is replacing Pl Pl grains are difficult to differentiate due to intense Wm alteration Wm veins present Relict mafics (Bt, Hbl), fully replaced by Chl±Bt±Ttn±Rt	**Ttn**	Tr	**Ttn-Rt**	Tr	
GBR-22	Tonalite	Corse grained un-mineralized tonalite	Isotropic		**Pl**	35	**Ep**	15	Tr Py and Mag
					Qz	30	**Chl**	15	
					Zr	Tr	**Wm**	5	

				Chl aggregates are very large (large relict Bt) Pl grains are recognisable with moderate replacement by Ep, twinning still discernible 5% of Qz is secondary Qz in Ep-Chl-Qz veins Cross cutting Ep and Chl veinlets through Pl Moderate Ep alteration and weak Wm alteration Relict mafics (Bt, Hbl), fully replaced by Chl±Bt±Ttn±Rt	**Ttn**	Tr	**Ttn-Rt**	Tr	
GBR-23	Tonalite	Medium grained un-mineralized tonalite	Isotropic	Moderate Wm alteration Weak Ep alteration, ep	**Pl**	35	**Ep**	5	Tr Py and Mag in Chl aggregates
					Qz	45	**Chl**	10	
					Zr	Tr	**Wm**	15	

				occurs as small isolated grains and dissemination No veins Relict mafics (Bt, Hbl), fully replaced by Chl±Bt±Ttn±Rt	**Ttn**	Tr	**Ttn-Rt**	Tr	
GBR-24	Tonalite	Ep-poor Chl-rich medium grained un-mineralized tonalite	Isotropic	Allanite present Disseminated Chl and Ep Ep alteration is weak, Chl and Wm are dominant alteration minerals Relict mafics (Bt, Hbl), fully replaced by Chl±Bt±Ttn±Rt	**Pl**	30	**Ep**	5	Tr Py and Mag
					Qz	30	**Chl**	20	
					Zr	Tr	**Wm**	10	
					Ttn	5	**Ttn-Rt**	Tr (in Chl aggregates)	
GBR-27	Tonalite	Pl-rich un-mineralized medium grained tonalite	Isotropic	Moderate Wm alteration Weak Ep alteration	**Pl**	40	**Ep**	Tr	Tr Py and Mag
					Qz	25	**Chl**	10	
					Zr	Tr	**Wm**	15	

				No veins Allanite present Relict mafics (Bt, Hbl), fully replaced by Chl±Bt±Ttn±Rt	**Ttn**	Tr	**Ttn-Rt**	Tr	
GBR-28	Tonalite	Pl-rich un-mineralized medium grained tonalite	Isotropic and equigranular	Most Pl Phenocrysts are partially altered to Wm and Ep Sample is moderately altered with some Pl relicts discernable and twining is still observed Allanite present Relict mafics (Bt, Hbl), fully replaced by Chl±Bt±Ttn±Rt	**Pl**	40	**Ep**	5	Tr Py and Mag
					Qz	20	**Chl**	10	
					Zr	Tr	**Wm**	10	
					Ttn	Tr	**Ttn-Rt**	Tr (in Chl aggregates)	
GBR-30	Tonalite	Coarse grained Qt-rich un-mineralized tonaltie	Isotropic	Ep present in 2 distinct forms: Cross cutting veins and subhedral crystals within	**Pl**	35	**Ep**	10	Tr Py and Mag
					Qz	55	**Chl**	5	
					Zr	Tr	**Wm**	5	

			Qz is coarser grained than Pl grains	plagioclase phenocrysts and within chlorite aggregates Wm contours Pl grains and weakly replaces some Pl grains Weakly altered Ep-Chl-Qz veins present Relict mafics (Bt, Hbl), fully replaced by Chl±Bt±Ttn±Rt	**Ttn**	Tr	**Ttn-Rt**	Tr (in Chl aggregates)	
GBR-32	Tonalite	Pl-rich coarse grained un-mineralized tonalite	Isotropic Qz is coarser grained than Pl grains	Moderate Ep alteration and weak Wm alteration of Pl Absence of veins Relict mafics (Bt, Hbl), fully replaced by Chl±Bt±Ttn±Rt	**Pl**	55	**Ep**	10	Tr Py and Mag
					Qz	20	**Chl**	5	
					Zr	Tr	**Wm**	5	
					Ttn	Tr	**Ttn-Rt**	Tr (in Chl aggregates)	
GBR-35	Tonalite	Pl-rich relatively fresh un-	Isotropic and equigranular		**Pl**	30	**Wm**	20	Tr Py and Mag in Chl aggregates
					Qz	20	**Chl**	10	

		mineralized medium grained tonalite		Primary mafic minerals pseudomorphs detected partially replaced by Chl-Ttn+Rt	**Hbl**	15	**Ep**	5	
					Zr	Tr	**Ttn-Rt**	Tr (in Chl aggregates)	
					Ttn	Tr			
GBR-37	Tonalite	Qz-rich relatively fresh un-mineralized medium grained tonalite	Isotropic and equigranular	Weakly altered tonalite Most Pl is unaltered, some is partially replaced by Ep and Wm Many cross-cutting mono mineralic Ep veins, and Ep-Chl veins. Primary mafic minerals pseudomorphs detected partially replaced by Chl-Ttn+Rt Allanite present	**Pl**	30	**Ep**	10	Tr Py and Mag in Chl aggregates
					Qz	45	**Chl**	10	
					Zr	Tr	**Wm**	5	
					Ttn	Tr	**Ttn-Rt**	Tr (in Chl aggregates)	

GBR-39	Tonalite	Pl-rich leucocratic un-mineralized medium grained tonalite	Isotropic and equigranular	Wp and Wm alteration is weak Pl grains are replaced by Ep and Wm 5% of quartz is secondary Qz in the Ep-Qz vein Relict mafics (Bt, Hbl), fully replaced by Chl±Bt±Ttn±Rt Cross cut by large cm scale Ep-Qz vein	**Pl**	60	**Ep**	10	Ep vein contains Tr Ccp
					Qz	20	**Chl**	5	
					Zr	Tr	**Wm**	5	
					Ttn	Tr	**Ttn-Rt**	Tr (in Chl aggregates)	
GBR-40	Tonalite	Un-mineralized medium grained tonalite	Isotropic and equigranular	Weakly altered tonalite Primary mafic minerals pseudomorphs detected partially replaced by Chl-Ttn+Rt Most Pl is unaltered, some is partially replaced by Ep and Wm	**Pl**	35	**Ep**	5	Tr Py, Mag
					Qz	35	**Chl**	5	
					Hbl	5	**Wm**	5	
					Bt	5	**Ttn-Rt**	5 (in Chl aggregates)	
					Zr	Tr			
					Ttn	Tr			
GBR-44	Meta Basalt	Fine grained basalt	Isotropic and equigranular		**Pl**	20	**Ep**	30	N/A
					Px	10	**Chl**	30	

				Chl and Ep aggregates are common Pl grains are replaced by weak Wm and intense Ep and Chl			**Wm**	10	
GBR-45	Serpentinite	Serpentinite	Relict Ol grains evident	Serpentinization is complete	**Ol**	Tr	**Srp**	100%	N/A
GBR-49	Mafic volcanoclastic	Fine grained Nicola mafic volcano-clastic rock	No lithic fragments only fine grained volcaniclastics Coarser Pl phenocrysts in a fine-grained volcanoclastic matrix of Ep and Chl and Qt and Hbl	Presence of cross cutting Ep veinlets Intense Ep and Chl alteration	**Hbl**	30	**Ep**	20	N/A
					Pl	20	**Chl**	20	
					Qt	10	**Ttn-Rt**	Tr (in Chl aggregates)	
GBR-50	Mafic volcanoclastic	Fine grained Nicola mafic	Fine grained matrix supported	Alteration is pervasive and intense with intense	**Pl**	30	**Ep**	25	N/A
					Hbl	15	**Chl**	10	

		volcanoclastic rock	volcanoclastic rock with larger lithic fragments imbedded	Ep and Chl alteration Ep forms veinlets Ep forms coarse grained aggregates in the lithic fragments Qz is fine grained and may be secondary	**Qz**	20	**Ttn-Rt**	Tr (in Chl aggregates)	
GBR 2-7	Tonalite	Medium grained un-mineralized tonalite	Isotropic equigranular	Wm alteration varies from moderate to intense and forms veins in some areas	**Pl**	30	**Wm**	15	Tr Py, Mag
					Qz	30	**Ep**	10	
					Ttn	Tr	**Chl**	10	
				Wm alteration is weak and forms around grain boundaries within Pl and Chl aggregates after mafics	**Zr**	Tr	**Ttn-Rt**	5 (in Chl aggregates)	
				Relict mafics (Bt, Hbl), partially replaced by Chl±Bt±Ttn±Rt, some sections remain unaltered (centres)	**Hbl**	Tr			

GBR 2-11	Tonalite	Medium grained un-mineralized tonalite	Isotropic equigranular	Moderate Wm alteration Weak Ep alteration Relict mafics (Bt, Hbl), fully replaced by Chl±Bt±Ttn±Rt	**Pl**	30	**Ep**	10	Tr Py, Mag
					Qz	20	**Wm**	15	
					Ttn	Tr	**Chl**	10	
					Zr	Tr	**Ttn-Rt**	Tr (in Chl aggregates)	
GBR 2-14	Tonalite	Medium grained un-mineralized tonalite	Isotropic equigranular	Intense Wm alteration and weak Ep alteration Wm veins present Ep occurs as aggregates and isolated grains Relict mafics (Bt, Hbl), fully replaced by Chl±Bt±Ttn±Rt	**Pl**	30	**Ep**	10	Tr Py, Mag
					Qz	20	**Wm**	30	
					Ttn	Tr	**Chl**	10	
					Zr	Tr	**Ttn-Rt**	Tr (in Chl aggregates)	
GBR 2-32	Tonalite	Coarse grained un-mineralized tonalite	Isotropic equigranular	Weak Wm alteration and weak propylitic alteration Mafics are intact and unaltered (Hbl, Bt)	**Pl**	25	**Ep**	10	Tr Py, Mag
					Qz	30			
					Bt	10	**Wm**	10	
					Hbl	10			
					Ttn	Tr			
					Zr	Tr			

GBR 2-34	Tonalite	Coarse grained un-mineralized tonalite	Isotropic equigranular	Weak Wm alteration and weak propylitic alteration Mafics are intact and unaltered (Hbl, Bt)	**Pl**	30	**Ep**	10	Tr Py, Mag
					Qz	30			
					Hbl	10			
					Bt	10	**Wm**	10	
					Ttn	Tr			
					Zr	Tr			
GBR 2-42	Quartz Diorite	Coarse grained diorite with a large cross cutting Ep-Cal-Chl veins that has trace Ccp and border	Isotropic	Strong propylitic alteration, replacement of Pl is partial to complete	**Pl**	30	**Ep**	40	Tr Py, Mag, Ccp
					Qz	10	**Wm**	10	
					Ttn	Tr	**Chl**	10	
					Zr	Tr	**Ttn-Rt**	Tr (in Chl aggregates)	

Abbreviations: Bn = bornite, Cal = calcite, Ccp= chalcopyrite, Chl = chlorite, Cov = Covellite, Ep= epidote, Hbl = hornblende, Mag = magnetite, Mal = malachite, Ol = olivine, Pl = plagioclase, Px = pyroxene, Py = pyrite, Qz = Quartz, Rt= rutile, Srp = serpentine, Tr = trace, < 2 vol%, Ttn = titanite, Wm= white mica, Zr = Zircon

Weak alteration= <10% replacement of Pl by Ep or W`m

Moderate alteration = 10-30% replacement of Pl by Ep or Wm

Intense alteration = >30% replacement of Pl by Ep or Wm

Fine grained= major grains (Pl, Qt) are between <1mm

Medium grained= major grains (Pl, Qt) are between 1-2 mm

Coarse grained= major grains (Pl, Qt) are >2mm

Appendix 8

Report on the composition and assemblage of minerals associated with the porphyry Cu Mo mineralization at the Gibraltar deposit, south central British Columbia, Canada

C.H. Kobylinski, K. Hattori, S. Smith and A. Plouffe

Published as GEOLOGICAL SURVEY OF CANADA OPEN FILE 8025, in 2016

Abstract

Glacial sediments commonly contain resistate heavy minerals, such as zircon, rutile and epidote. To identify the sources of these minerals and use them as a vectoring tool for mineral deposits, it is critical to understand the compositional variations and assemblages of these minerals in mineral deposits and whether they are distinct from those in barren rocks. This paper reports the occurrence and assemblages of igneous and alteration minerals in the Gibraltar porphyry Cu deposit, south central British Columbia.

The Gibraltar deposit is the largest of three porphyry-Cu deposits in the region, the others being the Mount Polley mine and the Woodjam prospect. The Gibraltar deposit is hosted by the Granite Mountain batholith and has reserves of over 749 million tons at 0.249% Cu and 0.008% Mo. The batholith is mostly tonalite, with minor variation in modal abundances of felsic and mafic minerals. Igneous minerals are plagioclase, quartz, biotite, hornblende, titanite, zircon and apatite. The mineralization is accompanied by extensive phyllic alteration in the tonalite, which produced illite, quartz, rutile, titanite, magnetite, apatite, chlorite and epidote. Hydrothermal titanite is distinctly different from igneous titanite in crystal habits, optical properties and chemical compositions. Epidote shows a large compositional variation even within one sample from Al-rich (high clinozoisite component) to Fe-rich epidote. Some epidote grains contain significant La and Ce (allanite component), which could be diagnostic of the porphyry mineralization. Preliminary observations suggest the presence of a potassic alteration zone forming hydrothermal biotite but is now replaced by chlorite.

Introduction

Porphyry Cu mineralization is accompanied by extensive alteration within the host rocks and surrounding country rocks. Some of these minerals are resistant to weathering and erosion. They can be dispersed by glaciers and streams and may occur in glacial and stream sediments. Therefore, the assemblage of minerals common in porphyry Cu deposits in these sediments may vector to a deposit when combined with knowledge of regional ice-flow directions. Among heavy minerals, epidote (the Fe-rich end member of epidote group minerals) has the potential to be useful in mineral exploration. Cooke et al. (2014) reported that spatial variation of epidote chemistry in bedrock can be used to predict the occurrence and size of Cu mineralization. Their study around porphyry Cu-Mo deposits (3 Mt Cu in total) found that epidote in the immediately surrounding area (up to 1.5 km from the deposit centres) contains low concentrations of light rare earth elements (LREE; < 8 ppm La in most grains) and high abundances of Pb (up to 186 ppm), As (up to 180 ppm), Sb (up to 64ppm), Zr (up to 347 ppm) and Nb (up to 1230 ppm). Epidote enriched in LREE (up to 730 ppm La) occurs farther outside of the deposits, outside the pyrite halo (2-3km from mineralization). The data demonstrate that epidote chemistry records a larger footprint of the mineralization than the traditional alteration mineral zoning. Cooke et al. (2014) suggest an exploration method based on the intensity of epidote veining and the modal distribution of this mineral. The use of epidote has also been suggested in exploration for Au deposits by Roache et al. (2011), who demonstrated a positive relationship between the abundance of Fe-rich epidote and the size of Au deposits in Archean greenstone belts in Western Australia. They also show that the composition of epidote group minerals is correlated with that of co-existing chlorite. Chlorite is a common mineral in a variety of rocks and the composition of chlorite associated with porphyry-type mineralization appears to be distinct (Wilkinson et al. 2015). The chemistry of chlorite may be useful in exploration for porphyry type deposits.

Glacial sediments in the study area contain abundant epidote, apatite, jarosite, magnetite, titanite, rutile, and zircon and their distribution has been documented by the Geological Survey of Canada researchers in collaboration with the British Columbia Geological Survey (Fig. 1; Plouffe et al., 2014; Plouffe and Ferbey, 2015). These minerals are common in mineralized rocks, as well as in barren igneous and metamorphic rocks that are not related to porphyry Cu deposits. The objective of this project is to characterize the composition of resistate minerals associated with porphyry Cu mineralization at Gibraltar and to compare them with those in barren rocks and tills. Ultimately, characterizing the composition of key minerals in till and stream sediments could be used as a fertility indicator vectoring to porphyry Cu mineralization concealed by glacial sediments. This paper reports the occurrence and major element composition of alteration minerals in samples collected in July, 2015 in the Gibraltar mine and the areas immediately surrounding the mine.

Access

The study area is located approximately 60 km north of the town of Williams Lake, and 20 km N-NE of the northeastern shore of McLeese Lake, British Columbia. The study area is accessed by highway 97 and a paved road to the mine. The eastern part of the study area has abundant logging roads, which allow the access to the eastern and northern parts of the Granite Mountain batholith, and country rocks of the batholith. The Beaver Lake Road runs east to connect to the Philemon Lake Road (an old logging road), which leads to the northern part of the Granite Mountain batholith. The Gibraltar quartz diorite and Nicola Group volcanic rocks are exposed along this road. Farther north on the Philemon Lake Road, a foliated tonalite phase of the Granite Mountain batholith is exposed.

Regional geology

The Gibraltar porphyry Cu-Mo deposit is hosted in the Granite Mountain batholith (Fig. 2). The batholith yields U-Pb zircon ages of 217 ± 12 Ma (Bysouth et al., 1995), 215 ± 0.8 Ma (Ash et al., 1999a and b; Ash and Riveros, 2001), and 209.6 ± 6.3 Ma (Oliver et al., 2009). Drummond et al. (1976) reported K-Ar ages of 203 ± 6 and 204 ± 6 Ma on hornblende in leucocratic tonalite. Although the U- Pb zircon ages are overlapping, the age range suggest that this batholith may have formed through multiple intrusions of magmas with similar tonalitic compositions.

The batholith is variably deformed and metamorphosed under greenschist facies conditions (Ash et al., 1999b). To the south, it is in fault contact with the Cache Creek Terrane (Figs. 1, 2) that mainly consists of Paleozoic to early Mesozoic chemical and siliclastic sedimentary rocks and mafic volcanic rocks (Shannon, 1982).

There is a debate whether the Granite Mountain batholith belongs to the Paleozoic Cache Creek Terrane or Mesozoic Quesnel Terrane. The close proximity of the batholith to rocks from both terranes and the relatively poor bedrock exposure in the region have contributed to the debate. Since the batholith is in contact with late Paleozoic rocks of the Cache Creek Terrane to the south and east, Drummond et al. (1973, 1976) and Bysouth et al. (1995) suggested that the batholith belongs to the Cache Creek Terrane, with the local limestones, skarns and schists that occur along the southwest margin of the batholith interpreted to be metamorphosed Cache Creek rocks (Drummond et al., 1976; Panteleyev, 1978; Bysouth et al., 1995). On the other hand, Ash et al. (1999a, b) suggested that the Granite Mountain batholith is part of the Mesozoic Quesnel Terrane and that the batholith was faulted against Cache Creek rocks in post-Triassic time. Ductile shear zones and the associated post- mineralization deformation within the Gibraltar deposit would have formed during this tectonic event. Recent mapping by Schiarizza (2014; 2015) demonstrated that the batholith intruded Nicola Group rocks of Quesnel Terrane, confirming that the batholith does not belong to old Cache Creek Terrane.

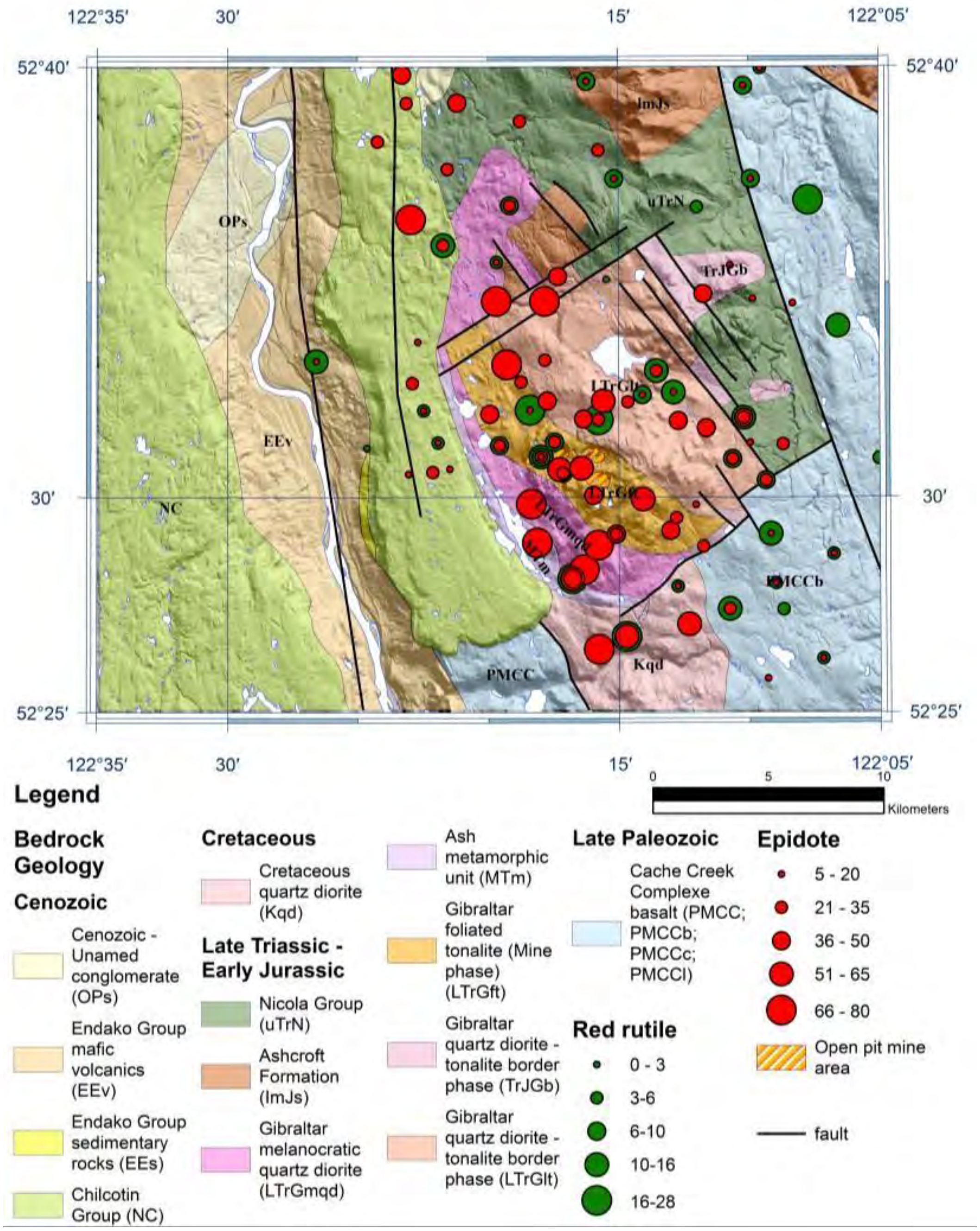

Figure 1. Bedrock geological map and the abundance of epidote and red rutile in tills in the study area. Epidote values are reported as percent of grains of heavy minerals (>3.2 g/cm3) in size fractions ranging from 0.25 to 0.5 mm. Rutile is reported as the number of grains recovered from 10 kg till samples. Abbreviations, PM: Cache Creek basalt complex, EEs: Endako Group sedimentary rocks. EEv: Endako Group mafic volcanic rocks, Kqd: Cretaceous quartz diorite, LTrGlt: Gibraltar leucocratic tonalite (Granite Mtn phase), LTrGmqd: Gibraltar quartz diorite - tonalite border phase; MTm: Ash metamorphic unit, NC: Chilcotin Group, OPs: Cenozoic sedimentary rocks, TrJGb:

Gibraltar tonalite border phase, lmJs: Ashcroft Formation, UtrN: Nichola Group volcanics. (modified after Plouffe et al., 2014).

The volcanic rocks of the Nicola Group are mostly pale green, fine to medium grained tuff and matrix-supported lapilli tuff breccias of basaltic to andesitic compositions (Schiarizza, 2015). The Nicola Group also contains intercalated siliclastic sedimentary rocks that are dominated by laminated mudstone-siltstone and lesser medium grained volcanic sandstone. These rocks in the proximity to the Granite Mountain batholith show evidence of ductile deformation and similar greenschist metamorphic conditions observed in the batholith.

Conglomerate, sandstone, siltstone and slate present in the north central part of the batholith were originally considered to be the Ashcroft Formation (Logan et al., 2010). More recently, these rocks have been correlated to the Dragon Mountain succession which rests unconformably on the Nicola Group (Schiarizza, 2014).

Geology of the Gibraltar deposit

The Gibraltar mine is a Cu-Mo deposit and is the second largest open pit mine in Canada. The mine initially opened in 1972 and processed ore at 36,000 tons/day with 0.3% Cu. In 1996, total geological tonnage (past production plus reserves) of the mine was estimated to be 1,229 Mt ore with 0.3 % Cu (3.69 Mt Cu; Grunsky et al., 1996). It closed in 1999 and reopened in 2004 after realizing the unexploited resource of this deposit. As of 2015, ore extracted from the Gibraltar deposit is estimated to be in excess of 749 Mt at 0.256 wt. % Cu (total 1.92 Mt Cu) and 0.008 wt. % Mo (Taseko website 2015 http://www.tasekomines.com/gibraltar).

Reserves and Resources of the Gibraltar deposit, December 31, 2014

	Size (Mt)	Grade (wt%)		Tonnage of Cu (Mt)
		Cu	Mo	
Proven and probable reserves	679.481	0.256	0.008	1.74
Measured & Indicated Resources	990.646	0.254	0.008	2.51

Based on the cut-off of 0.15 wt% Cu (after Jones, 2015).

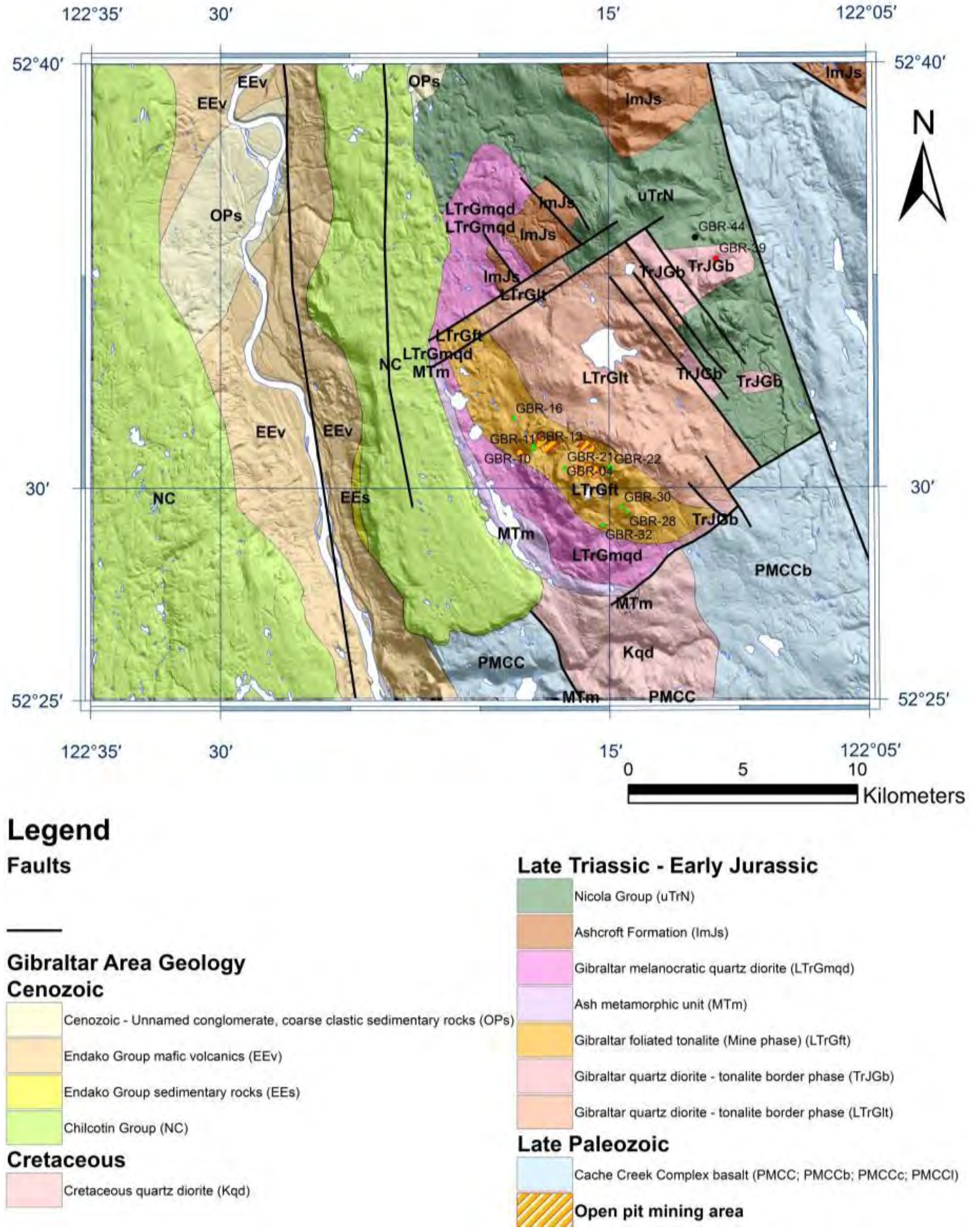

Figure 2. Location map of the Gibraltar Cu-Mo mine and the bedrock geology of the area. Small green circles show the locations of the samples. Bedrock geological map simplified from Ash et al. (1999a), Massey et al. (2005) and Schiarizza (2014).

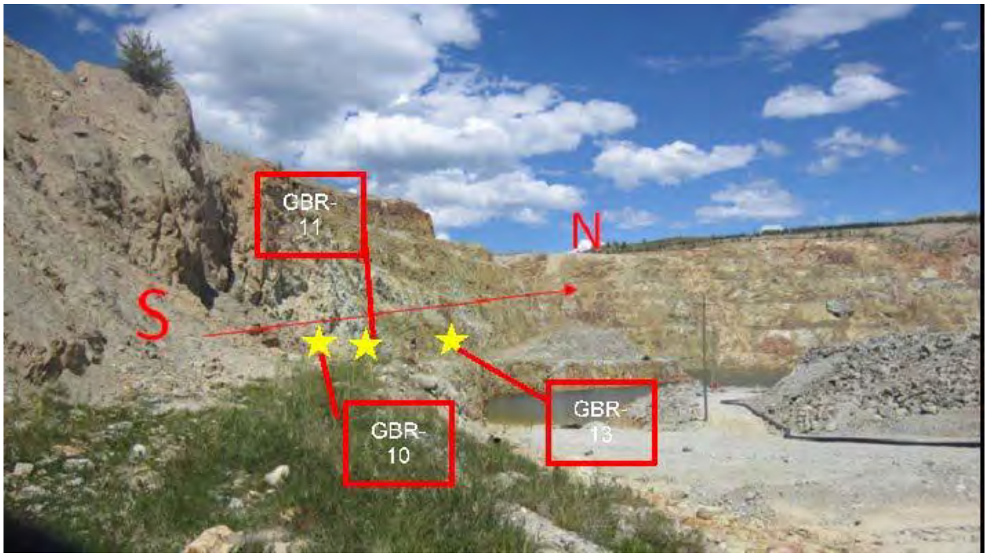

Figure 3. Photograph of the west wall of the East pit at Gibraltar mine, both diorite (GBR-13) and leucocratic tonalite (GBR-11) samples were taken along this traverse including one epidote- and rutile rich sample (GBR-10). The area is moderately mineralized with visible Cu sulphide minerals and oxidation of sulphides due to weathering from the surface. Epidote appears stable during the weathering and is omnipresent along the traverse. Distances between GBR-10 and -11 and between GBR-11 and GBR-13 are 28 m and 118 m, respectively.

Figure 4. Epidote veining (pointed with a pencil) and dissemination of chlorite-rich aggregates in the leucocratic tonalite phase of Granite Mountain batholith. Sample GBR-30 was collected at this location. Location: Easting 0551505 Northing 5816016 (NAD 83).

Figure 5. Outcrop at sample site GBR-39. Note the wide irregular epidote veining in leucocratic tonalite of the Granite Mountain batholith. Location: Easting 0555489 Northing 5826958 (NAD 83).

Methodology

Petrographic studies using plane polarized and cross polarized transmitted and reflected light microscopy was carried out on 13 representative thin sections for this study. Chemical compositions of minerals were determined on 6 carbon-coated polished thin sections using a JEOL 6610LV scanning electron microscope equipped with energy dispersive spectroscopy (SEM-EDS) at the University of Ottawa. Total Fe content is expressed as FeO(t).

Granite Mountain batholith

Lithology and igneous mineralogy

The rocks of the batholith in the area are mostly tonalite (Figs. 3, 4 and 5) with minor variation in abundance of quartz, plagioclase and hornblende. Some parts of the batholith are quartz diorite (Fig. 2). Cobaltinitrite staining of saw-cut hand specimens of all samples confirms the absence of K-feldspar phenocrysts in all samples. Holocrystalline rocks contain plagioclase phenocrysts (> 5 mm) and quartz. Pegmatitic rocks are composed of coarse- crystalline quartz (< 20 mm) and plagioclase (< 20 mm). The igneous mineral assemblage is plagioclase + quartz ± biotite ± hornblende ± apatite ± zircon (Figs. 6 B, C). Epidote appears to be an alteration product, but some coarse-grained crystals and inclusions in plagioclase are possibly magmatic, as magmatic epidote has been reported in tonalitic rocks in many areas (*e.g.*, Schmidt and Poli, 2004; Masumoto et al., 2014). Some samples do not contain hornblende or biotite phenocrysts, but there is the evidence for pseudomorphic replacement of hornblende and biotite by chlorite. Pseudomorphs retain cleavages and crystal habits of the original igneous minerals. Some contain grains of columnar apatite (< 0.5 mm) and euhedral zircon (< 0.5 mm).

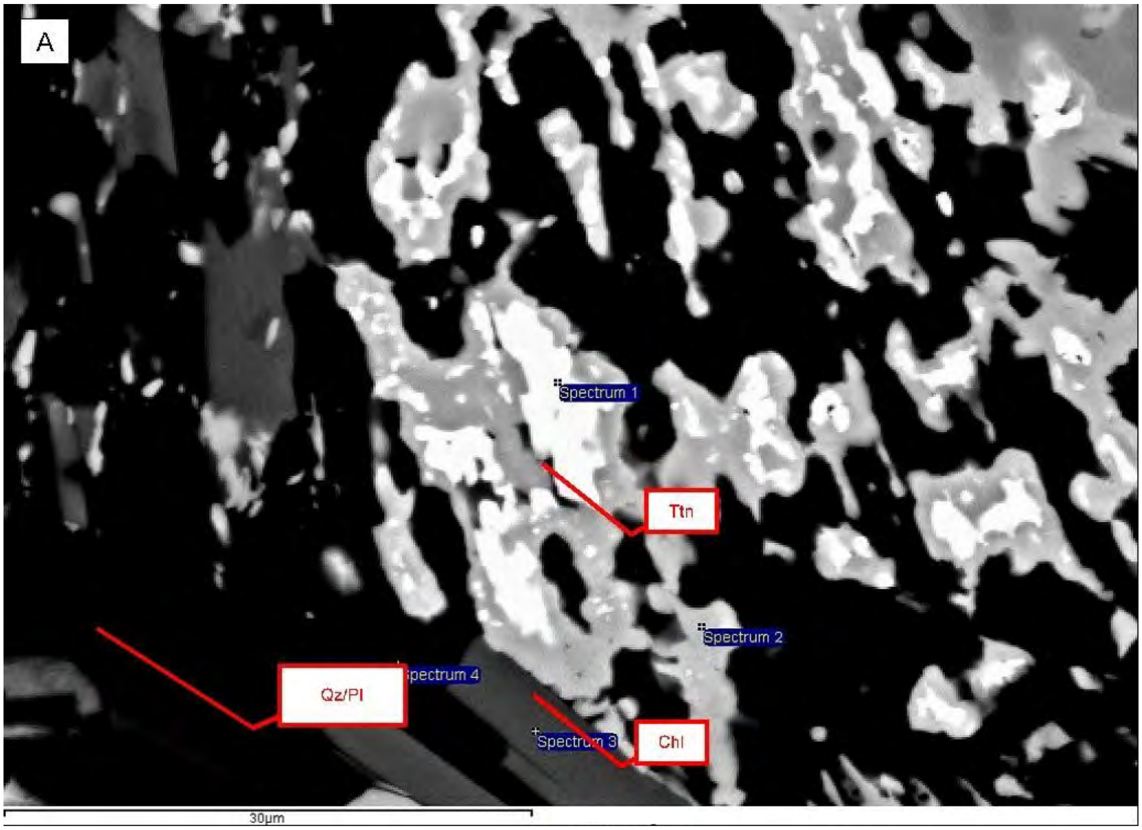

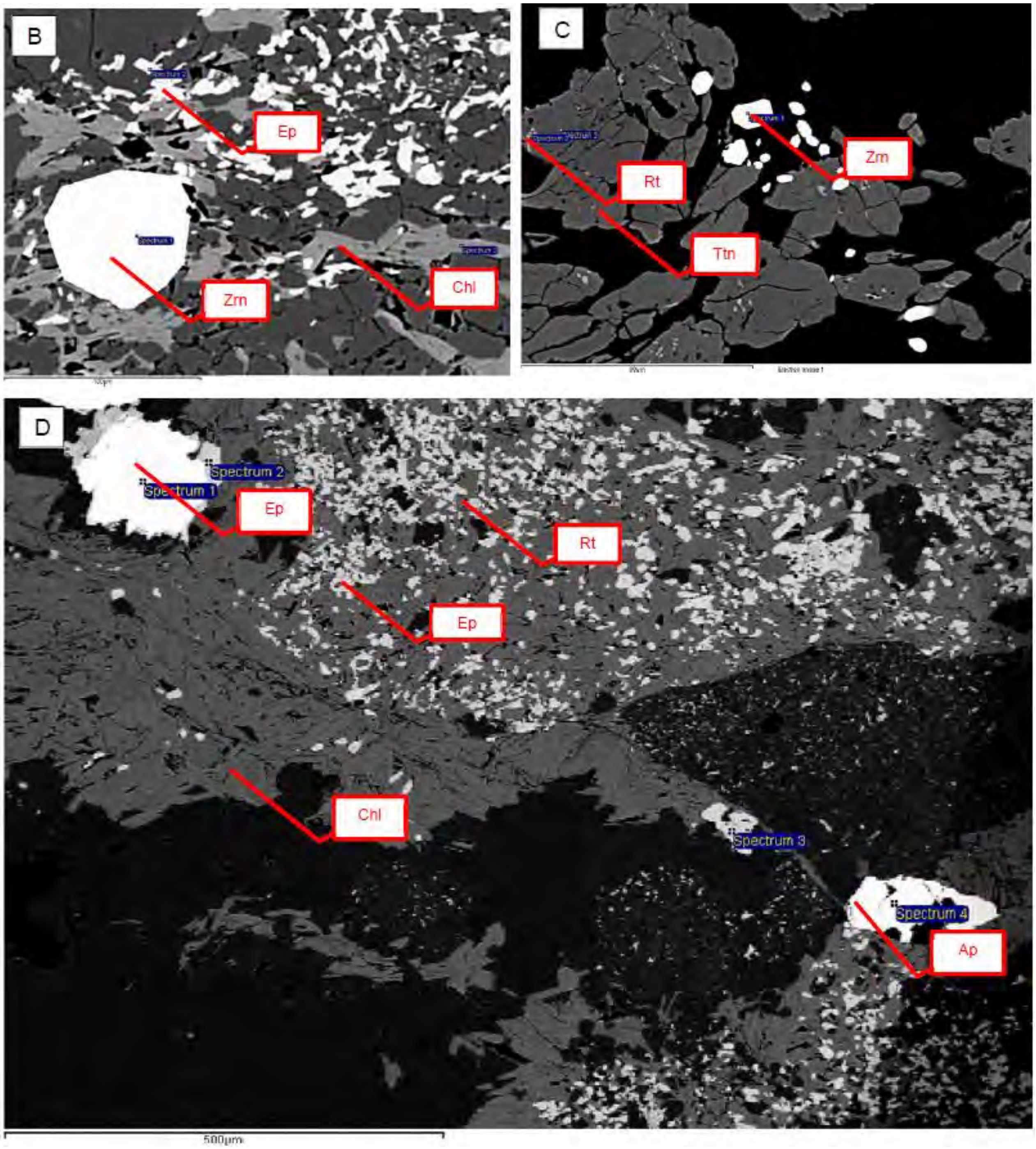
B
Ep
Zrn
Chl
C
Rt
Ttn
Zrn
D
Spectrum 2
Spectrum 1
Ep
Rt
Ep
Chl
Spectrum 3
Spectrum 4
Ap
500µm

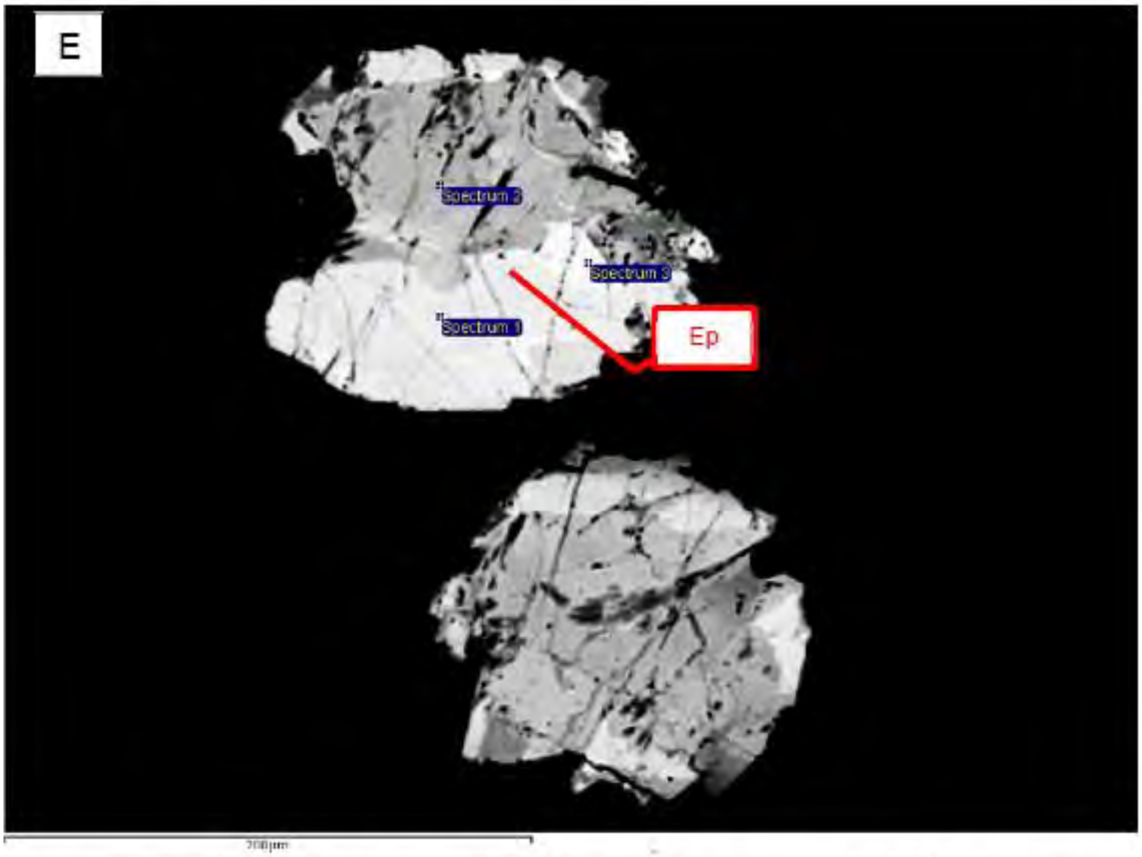
E
Spectrum 2
Spectrum 3
Spectrum 1
Ep
200µm

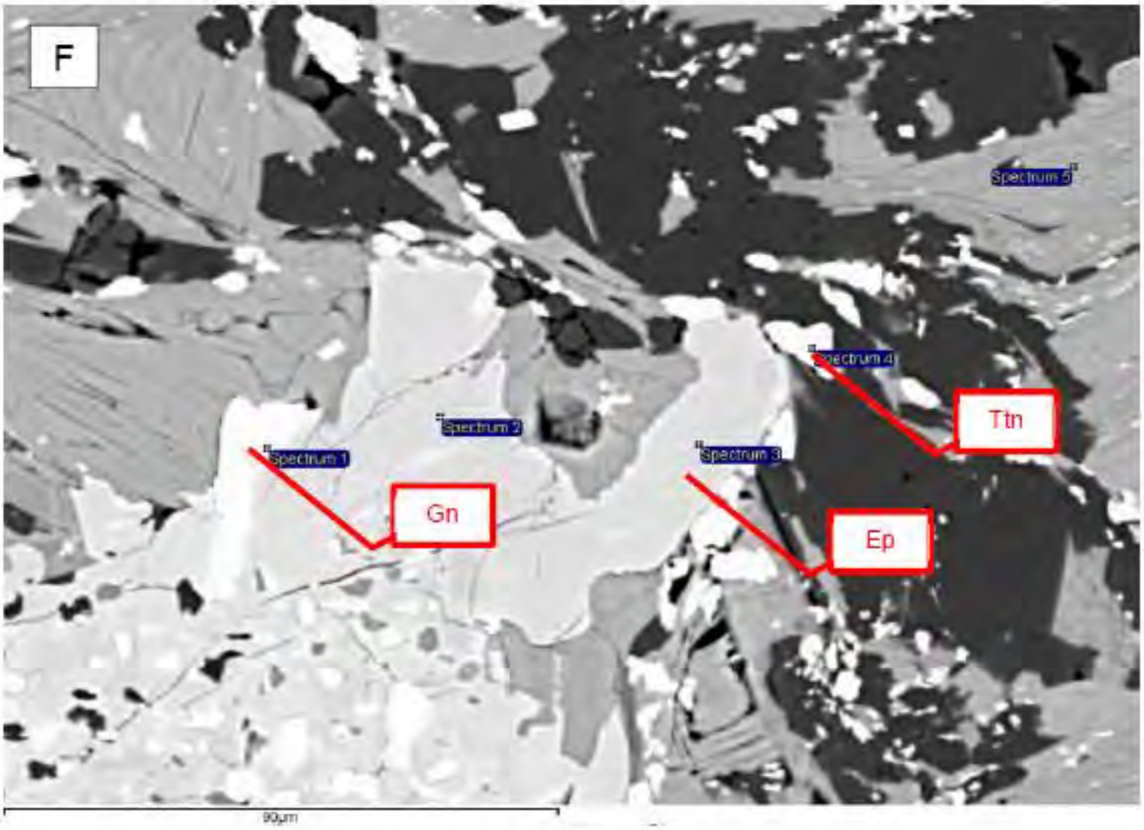
F
Spectrum 5
Spectrum 4
Ttn
Spectrum 2
Spectrum 1
Spectrum 3
Gn
Ep
90µm

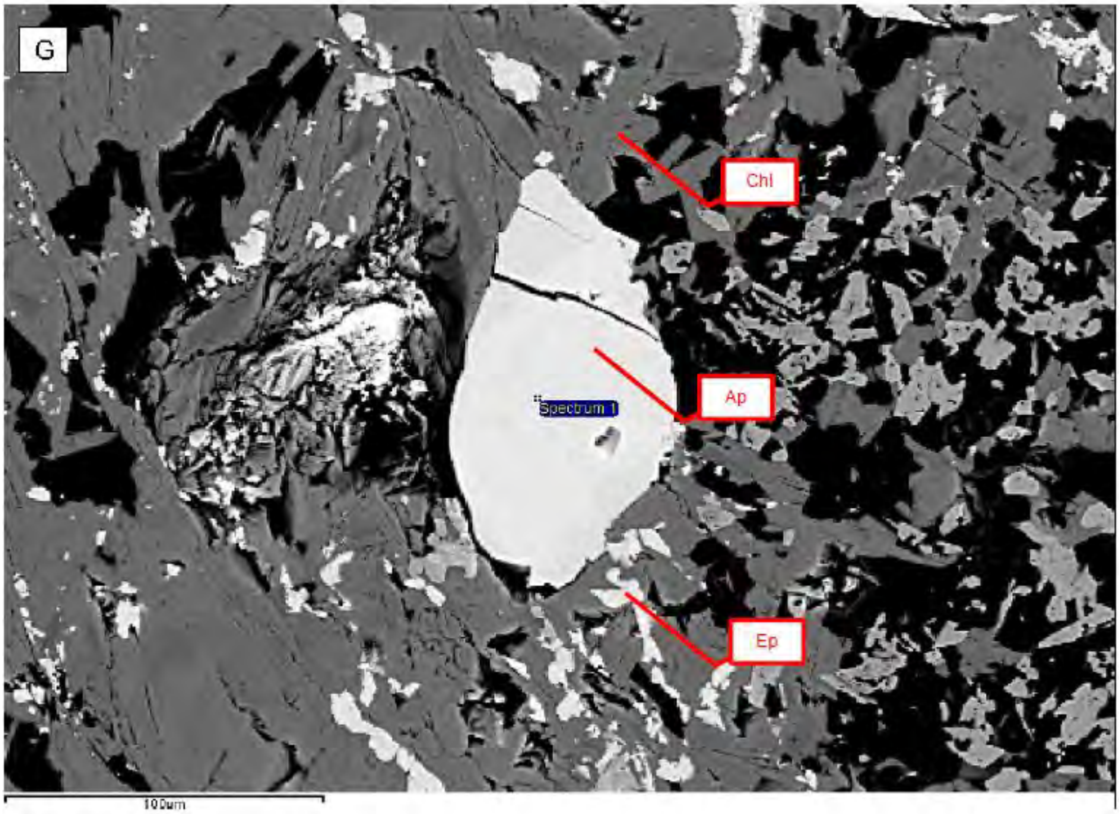

Figure 6. Backscattered electron images showing the common occurrences of titanite, rutile, and epidote. (A) Common occurrence of titanite (Ttn) around rutile (Rt) within aggregates of chlorite Chl). The aggregates are in the groundmass of quartz (Qz) and plagioclase (Pl), sample GBR-04. (B) epidote (Ep) and zircon (Zrn) in sample GBR-28, (C) titanite (Ttn), rutile (Rt) and zircon (Zrn) in sample GBR-16. (D) La- and Ce-rich epidote (Ep) within an aggregate of chlorite (Chl) in the top left and apatite (Ap) bottom right, the epidote contains 6.2 wt %La_2O_3 and 10.6 wt.%Ce_2O_3 (Analysis point 6 of Table 1), sample GBR-28. (E) Compositional zoning of REE-rich epidote (Ep). Greater abundance of La and Ce in brighter parts and the composition is close to the end member component of allanite with 5.04 wt.% La_2O_3 and 14.7 wt.% Ce_2O_3. (Analysis point 9 in Table 1). Dark part still contains significant light REE; 5.41 wt.% La_2O_3 and 11.1 wt.% Ce_2O_3 (Analysis point 7 of Table 1), sampleGBR-28. (F) galena (Gn) within an aggregate of chlorite (Chl), epidote (Ep), and titanite (Ttn), sample GBR-04. (G) a subhedral apatite (Ap) within an aggregate of chlorite (Chl) and epidote (Ep) in sample GBR-04.

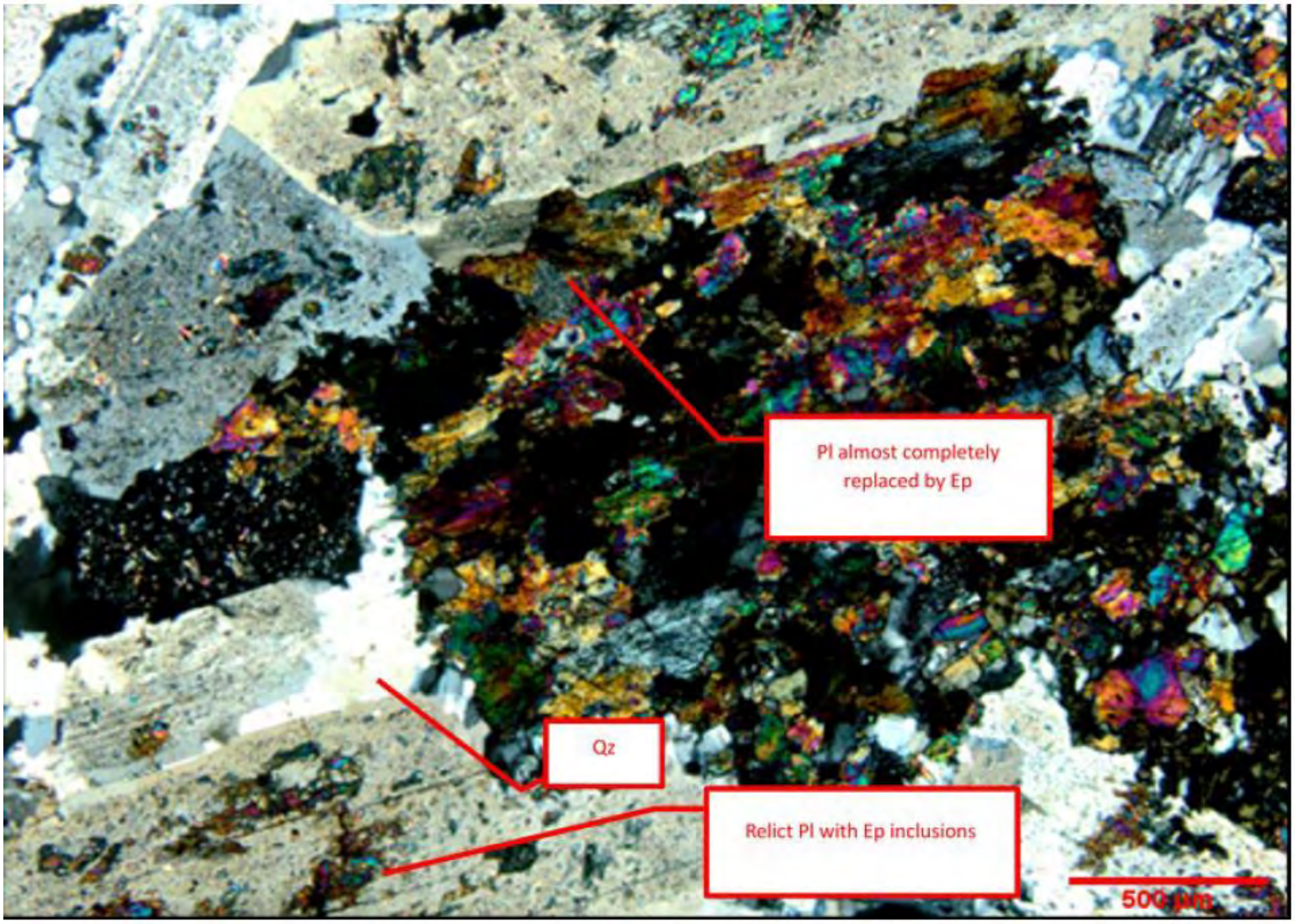

Figure 7. A photomicrograph of the area of plagioclase-rich tonalite (sample GBR-16) in the thin section shown in Fig. 8 C under cross polarized light. The sample GBR-16 was collected along the Gibraltar Mine Road at Easting of 0546717 and Northing of 5819933.

Thin Section Photographs

GBR-10
Easting 0547585, northing 5818572
West wall, East Pit, Gibraltar mine

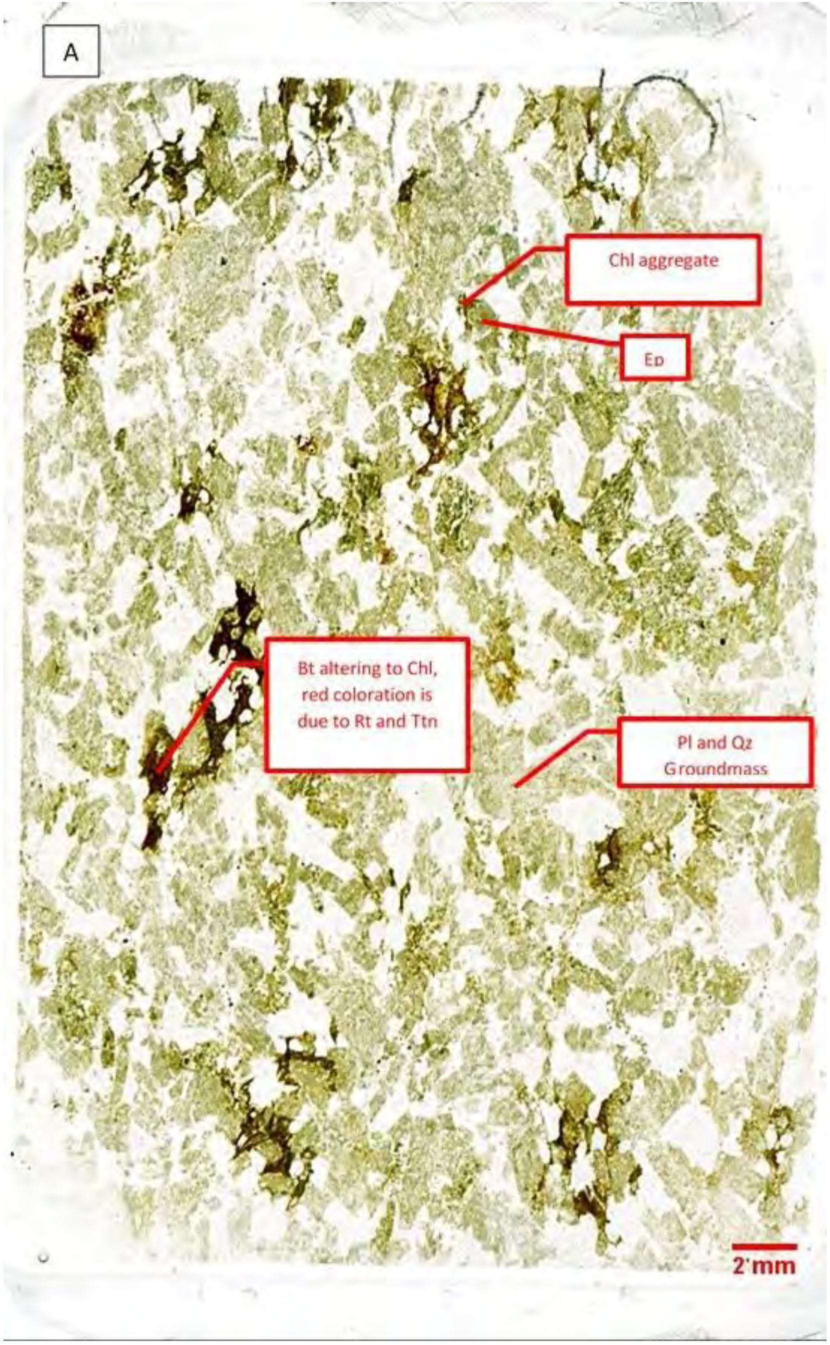

Epidote-rich tonalite

Igneous minerals: Plagioclase (Pl)-quartz (Qz) –biotite (Bt; partially replaced by chlorite (Chl), rutile (Rt) and titanite (Ttn).

Hornblende is not observed

Alteration minerals: Chlorite dissemination and replacing biotite.

Epidote (Ep) within plagioclase crystals.

Apatite or zircon are not observed

GBR-04
Collected at
Easting 0548947, Northing 5817768
West wall, East Pit Gibraltar mine

Melanocratic tonalite

Igneous minerals:
Plagioclase (Pl)-quartz (Qz)-biotite (altered to chlorite)- Hornblende (Hbl; partially altered to chlorite)

Alteration Minerals:
Chlorite (Chl) –epidote (Ep) –titanite (Ttn)

Biotite (Bt) pseudomorphically replaced by chlorite aggregates.

Hornblende (Hbl) pseudomorphically replaced by chlorite aggregates.

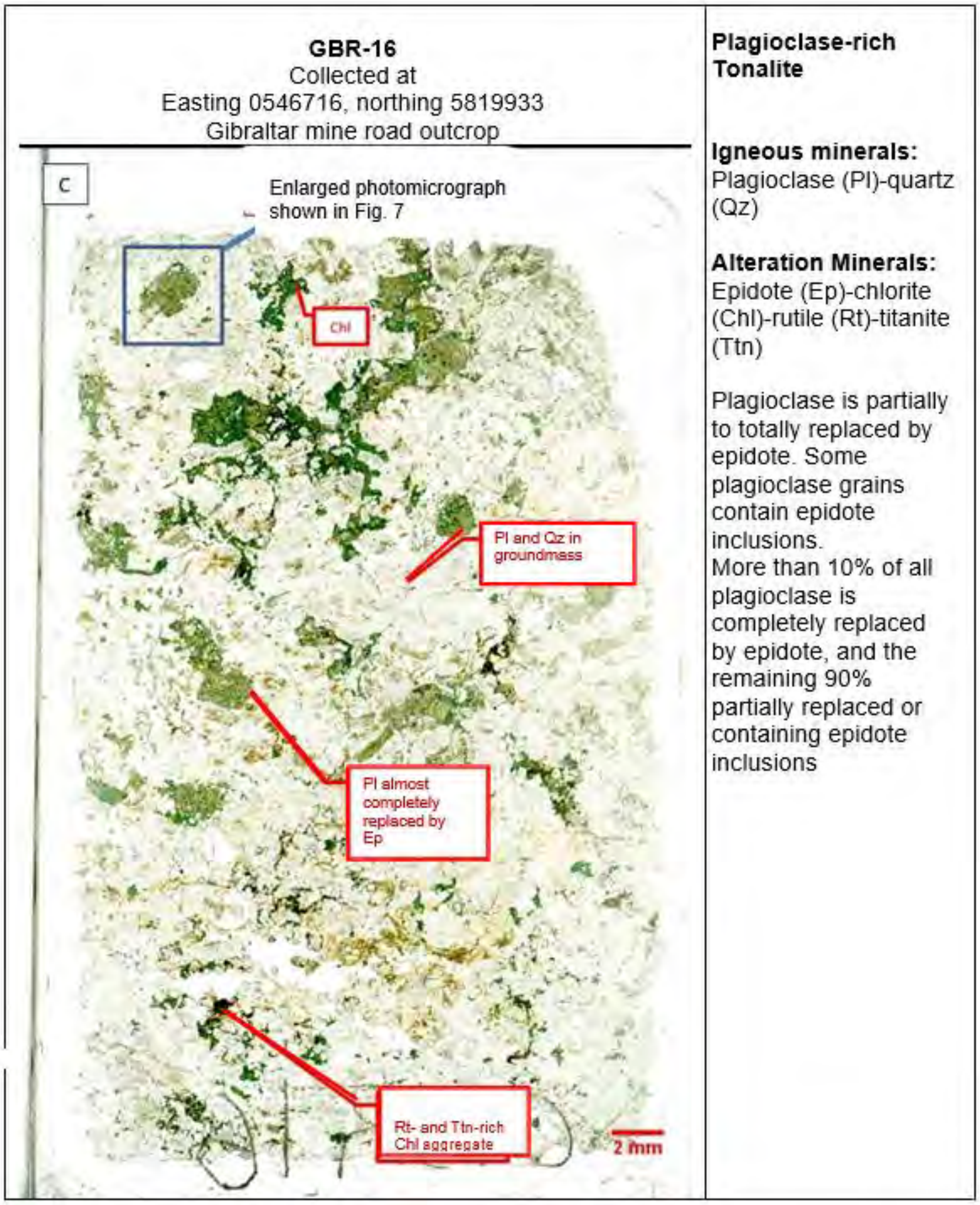

GBR-16
Collected at
Easting 0546716, northing 5819933
Gibraltar mine road outcrop

Plagioclase-rich Tonalite

Igneous minerals:
Plagioclase (Pl)-quartz (Qz)

Alteration Minerals:
Epidote (Ep)-chlorite (Chl)-rutile (Rt)-titanite (Ttn)

Plagioclase is partially to totally replaced by epidote. Some plagioclase grains contain epidote inclusions.
More than 10% of all plagioclase is completely replaced by epidote, and the remaining 90% partially replaced or containing epidote inclusions

Figure 8. Photographs of thin sections of samples shown in Fig. 6. They illustrate the igneous assemblage of a plagioclase- rich tonalite in the Granite Mountain batholith. Igneous minerals, such as plagioclase, biotite and hornblende are commonly altered, and the relict morphologies give an indication of the primary mineralogy. (A) epidote-rich tonalite, sample GBR-10. (B) melanocratic tonalite, sample GBR-04. (C) leucocratic tonalite, sample GBR-16.

Hand sample photographs	**Lithology and mineralogy**
Easting 0547585, Northing 5818572 West wall, East Pit of the Gibraltar mine 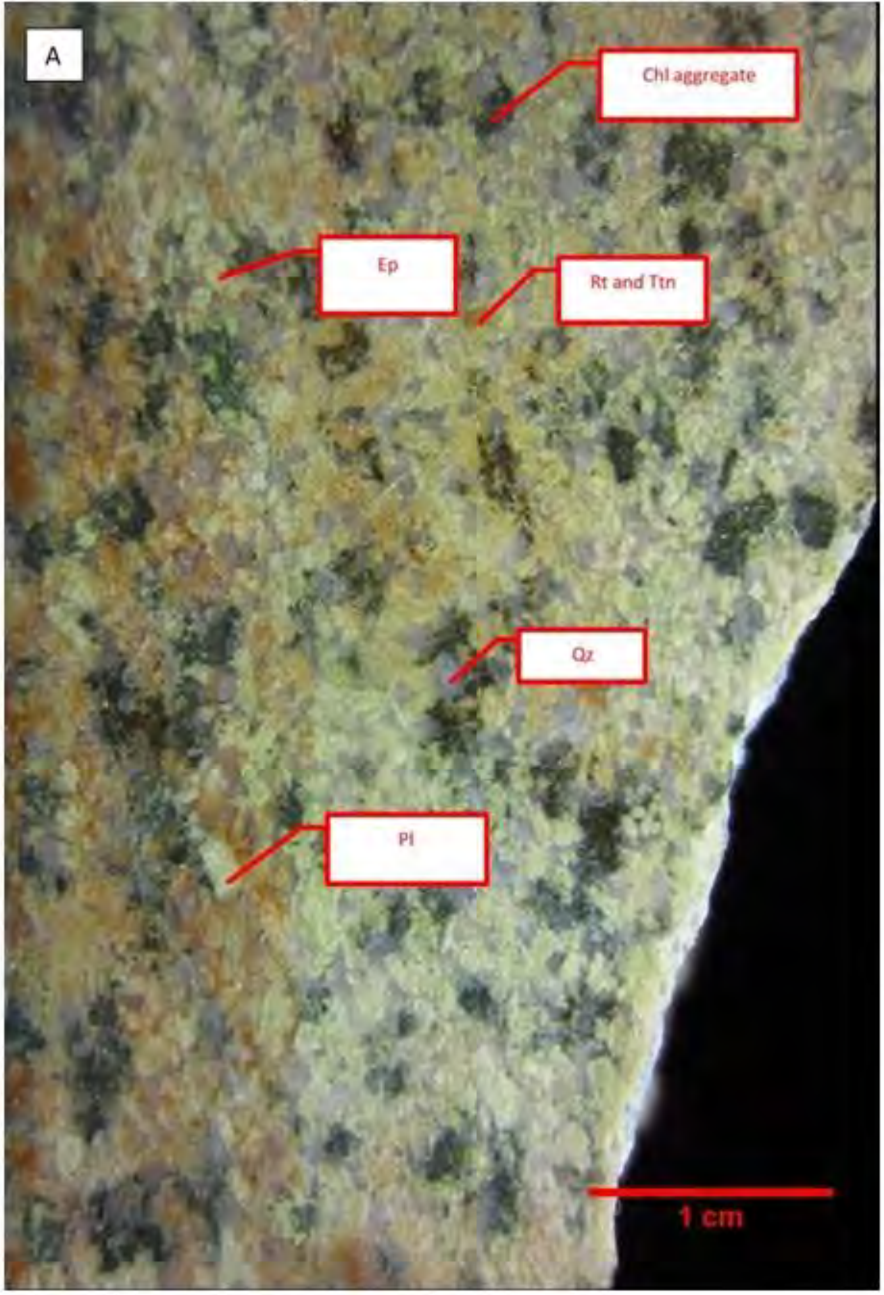	**Epidote-rich tonalite** **Igneous minerals:** Plagioclase (Pl)-quartz (Qz)- biotite (Bt). Biotite is pseudomorphically replaced by chlorite aggregates. No apatite and zircon grains are observed. **Alteration minerals:** Rutile (Rt) –titanite (Ttn) from biotite. White mica and disseminated epidote (Ep) after plagioclase

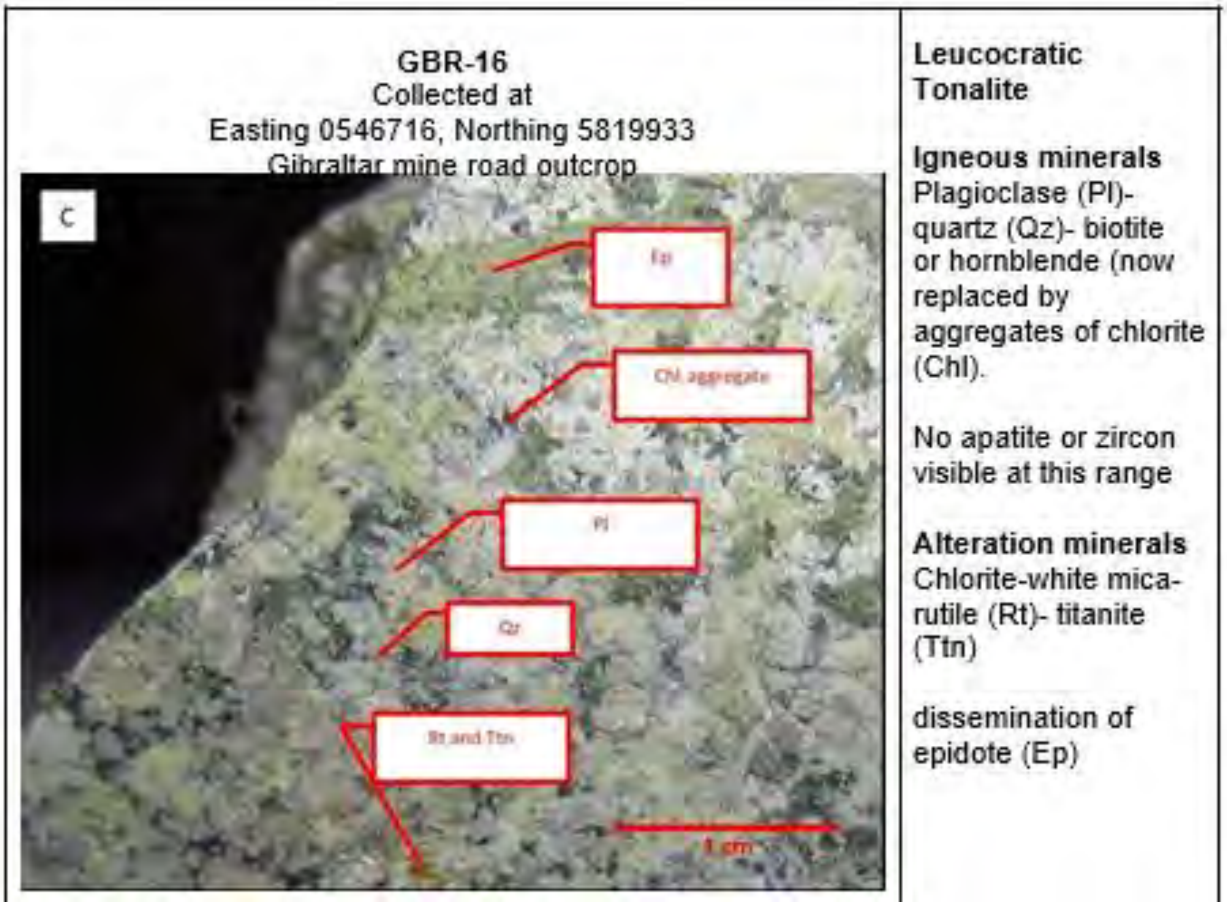

GBR-16
Collected at
Easting 0546716, Northing 5819933
Gibraltar mine road outcrop

Leucocratic Tonalite

Igneous minerals
Plagioclase (Pl)- quartz (Qz)- biotite or hornblende (now replaced by aggregates of chlorite (Chl).

No apatite or zircon visible at this range

Alteration minerals
Chlorite-white mica- rutile (Rt)- titanite (Ttn)

dissemination of epidote (Ep)

Figure 9. Representative hand sample photographs showing the primary igneous phases and alteration minerals in the tonalitic rock of the Granite Mountain batholith. (A) epidote-rich tonalite, sample GBR-10. (B) melanocratic tonalite, sample GBR-04. (C) Leucocratic tonalite, sample GBR-16.

Hydrothermal alteration and alteration minerals

The effect of hydrothermal alteration affects the minerals formed during the igneous processes. Some samples (Samples GBR-4, -10, -11, -13, and -22) are intensely altered and most igneous minerals are completely lost (Fig. 7).

Alteration assemblages

Three types of alteration assemblages are recognized. Type 1 contains epidote, chlorite, apatite, magnetite and hematite (samples GBR-21, -28, -39), Type 2 shows an assemblage of epidote, chlorite, illite, magnetite, titanite and calcite (sample GBR-30). Type 3 contains an assemblage of epidote, chlorite, illite, titanite, rutile and apatite (samples GBR-04, -11, -13, -16, and -22).

Alteration is intense along veins containing chlorite, epidote and quartz (Figs. 8 B, 9 B, 9 C). There are mono-minerallic veins of epidote, but most veins are composed of a mixture of epidote, chlorite ± quartz.

Epidote

Epidote with the general formula $A_2M_3[T_2O_7][TO_4](O,F)(OH,O)$, has a large compositional variation as the sites of A, M, and T can accommodate a variety of elements. The A site can accommodate Ca, Mn^{2+}, Na, Fe^{2+}, REEs, Sr, Ba, K, Pb and Th. The M site can accommodate Al, V, Cr, Ti, Fe^{3+}, Fe^{2+} Mn^{2+}, Mn^{3+}, Mg and Zn. Within epidote supergroup, there are several subgroups and wide solid solution relationships among subgroups. Subgroups include allanite subgroup with high concentrations of Y and LREE, and piemontite subgroup for Mn-rich members (Armbruster et al., 2006). In hand specimens and thin sections under transmitted light, all grains in our samples are greenish colour and proper identification of epidote minerals requires quantitative analysis of their compositions. For the purpose of this open file report, all green coloured-minerals with optical properties of epidote in hand specimens and thin sections are named epidote including allanite (Figs. 9 D, E).

Epidote occurs in all samples from the study area in various degrees of modality (10- 30 vol. %). Epidote shows three types of occurrences. The first type occurs as isolated small (<100 μm) inclusions in plagioclase. The second type of epidote forms aggregates that are disseminated in rocks and plagioclase phenocrysts. Some plagioclase grains are completely replaced by aggregates of epidote while retaining the original tabular shape of plagioclase (Figs. 7, 8 C, 9 A, 9 B). Colours vary from pistachio green to pale greenish yellow even within individual grains in thin section under transmitted light. They are compositionally zoned with Fe-poor (12-15 wt%FeO (t)) cores and Fe-rich rims. The third type of epidote forms mono-mineralic veinlets (up 10 cm in width; Figs. 4, 5). Narrow epidote veinlets are also observed in thin sections. Some veinlets cut through samples and fill fractures of minerals (Fig. 6 F). Such veinlets are commonly bordered by narrow (<0.1 mm) bands of chlorite or white mica (Fig. 6 F). Epidote in the veinlets is Fe-rich (12-15 wt% FeO(t)).

The compositions of twenty-four epidote grains were determined with SEM-EDS. Some approach the clinozoisite classification, however none of them qualify due to elevated $FeO_{(t)}$ >10 wt.% (Figs. 10 A, B). Several grains contain LREE, up to 9.54 wt.% La_2O_3 and 14.7 wt.% Ce_2O_3, which qualifies them as allanite (Figs. 10 A, B). These grains have a brown-yellow hue in thin sections. Epidote in the Gibraltar mine pits is all low in LREE (<6 wt% total REE+Y oxides). The LREE-rich epidote occurs >2 km south from the Gibraltar mine pits in samples GBR-16, -21 and -28 (Figs. 6 D, E). The spatial relationship between the occurrences of LREE-bearing epidote and the mineralization in the study area are consistent with the findings by Cooke et al. (2014) in the Baguio district of the Philippines, although the absolute concentrations of REE in our samples are much higher than those of their epidote samples. Cooke et al. (2014) reported low concentrations of LREE in epidote close to the mineralized areas and elevated concentrations of LREE (up to 1487 ppm La) in epidote farther outside the area surrounding the mineralization.

Table 1. Major element abundances of epidote expressed in wt. % determined with SEM-EDS.

Sample	**Grain #**	**SiO_2**	**TiO_2**	**$Al2O_3$**	**$FeO_{(t)}$***	**MnO**	**MgO**	**CaO**	**Na_2O**	**SrO**	**Ce_2O_3**	**La2O3**	**Total**
GBR-11	1	39.7	0.4	25.3	10.5	0.7	<0.1	23.5	<0.1	0	<0.1	<0.1	100.1
GBR-11	2	38.4	0.3	22.5	11.2	0.4	<0.1	21.6	<0.1	2.2	<0.1	<0.1	96.6
GBR-11	3	39.2	<0.1	24.9	11.4	0.6	<0.1	23.6	<0.1	0.3	<0.1	<0.1	100
GBR-32	4	39.9	<0.1	24.5	11.4	0.5	<0.1	23.6	<0.1	0	<0.1	<0.1	99.9
GBR-11	5	39.6	<0.1	23.9	11.6	1	<0.1	22.3	<0.1	0.8	<0.1	<0.1	99.2
GBR-11	6	39	0.5	22.6	11.6	0.3	<0.1	23.6	<0.1	2.5	<0.1	<0.1	100.1
GBR-11	7	38.4	0.4	22.4	11.8	0.5	<0.1	22	<0.1	2	<0.1	<0.1	97.5
GBR-32	8	40.1	<0.1	24.4	12.4	<0.1	<0.1	23	<0.1	0	<0.1	<0.1	99.9
GBR-32	9	42.5	<0.1	22.5	12.5	<0.1	<0.1	20.8	1.7	<0.1	<0.1	<0.1	100
GBR-04	10	39.6	0.2	23.9	12.9	<0.1	<0.1	23.4	<0.1	<0.1	<0.1	<0.1	100
GBR-21	11	38.3	<0.1	22.1	12.9	<0.1	<0.1	17.1	<0.1	<0.1	5.6	<0.1	96
GBR-04	12	39.3	<0.1	23.7	13.1	<0.1	<0.1	23.9	<0.1	<0.1	<0.1	<0.1	100
GBR-28	13	39.5	<0.1	23.6	13.1	0.4	<0.1	23.3	<0.1	<0.1	<0.1	<0.1	99.9

GBR-28	14	39.2	<0.1	23.7	13.3	0.5	<0.1	23.2	<0.1	<0.1	<0.1	<0.1	99.9
GBR-04	15	39.4	<0.1	22.9	13.7	<0.1	<0.1	23.6	<0.1	<0.1	<0.1	<0.1	99.6
GBR-11	16	39.5	0.6	22.7	13.7	<0.1	<0.1	23.4	<0.1	<0.1	<0.1	<0.1	99.9
GBR-21	17	38.9	0	22.9	14.4	<0.1	<0.1	23.9	<0.1	<0.1	<0.1	<0.1	100.1
GBR-32	18	38.9	0.3	22.2	14.7	<0.1	<0.1	23.9	<0.1	<0.1	<0.1	<0.1	100
GBR-21	19	39.9	<0.1	22.2	15	<0.1	<0.1	23	<0.1	<0.1	<0.1	<0.1	100.1
GBR-11	20	39.3	<0.1	22.1	15.5	<0.1	<0.1	23.1	<0.1	<0.1	<0.1	<0.1	100
GBR-11	21	38.8	<0.1	21.7	15.6	0.2	<0.1	23.6	<0.1	<0.1	<0.1	<0.1	99.9
GBR-28	22	34.4	<0.1	15.9	17.5	0.9	<0.1	14.2	0.9	<0.1	10.1	6.2	100.1
GBR-28	23	34.7	<0.1	15.4	17.5	0.9	1	13.9	<0.1	<0.1	11.1	5.4	99.9
GBR-28	24	33.7	<0.1	13.1	18.5	1	1.3	11.8	<0.1	<0.1	11.1	9.5	100
GBR-28	25	34.3	<0.1	12.5	19.4	1	1.6	11.5	<0.1	<0.1	14.7	5	100

*Total Fe expressed as FeO(t)

The concentration values are based on the sum of anhydrous components to be 100 %.

Description of analyzed areas:

1= Outer darker rim of zoned grain (back scatter image), surrounded by other unzoned epidote grains within a chlorite and epidote rich quartz vein, 2= zoned epidote grain (inner brighter core (back scatter image), surrounded by other epidote grains (unzoned), within a chlorite and epidote rich quartz rich vein, 3= zoned epidote grain (outer darker rim, back scatter image), surrounded by other epidote grains (unzoned), within a chlorite and epidote rich quartz vein, 4= zoned epidote grain (inner brighter core, back scatter image), surrounded by other epidote grains (unzoned), within a chlorite and epidote rich quartz rich vein, 5= zoned epidote grain (inner brighter core, back scatter image), surrounded by other epidote grains (unzoned), within a chlorite and epidote rich quartz rich vein, 6= Unzoned epidote grain, in contact with darker epidote grains (back scatter image) with no detectable REEs and chlorite and quartz, 7= Zoned epidote grained (darker part, back scatter image) in contact with quartz grains, 8= Zoned epidote grained (brighter part, back scatter image) in contact with quartz grains, 9= Zoned epidote grained (brightest part, back scatter image) in contact with quartz grains, 10=Unzoned epidote grain in contact with titanite grain within chlorite aggregate, 11= Zoned epidote grain (inner brighter core, back scatter image), surrounded by other epidote grains (unzoned), within a chlorite and epidote rich quartz rich vein, 12= Unzoned tabular epidote grain in contact with plagioclase grains and chlorite grains, 13= Elongate epidote grain within a relict plagioclase grain, 14= Unzoned epidote grain in contact with plagioclase and chlorite within a chlorite aggregate, 15= Small epidote grain (<0.5um long) surrounded by chlorite in a quartz/chlorite vein, 16= Unzoned epidote grain in contact with chlorite within a chlorite aggregate, 17= Unzoned isolated epidote grain surrounded by chlorite in a large chlorite aggregate (1mm across), 18= Unzoned epidote on the fringe of a larger Ce/La rich epidote grain in contact with chlorite in a chlorite aggregate, 19= Unzoned epidote grain in contact with quartz and plagioclase grains, 20= Unzoned epidote grain in contact with plagioclase and chlorite grains within a chlorite aggregate, 21= Unzoned epidote grain in contact with plagioclase and other epidote grains in an epidote aggregate, 22= Unzoned elongate epidote grain within a relict plagioclase grain, 23= Unzoned elongate epidote grain within a relict plagioclase grain, 24= Unzoned epidote grain surrounded by chlorite, in a chlorite rich aggregate that contains titanite, 25= Unzoned epidote grain surrounded by chlorite in a chlorite/epidote aggregate, this aggregate contains zoned epidote grains in its center.

Titanite

Titanite has two populations; a discrete phenocryst of igneous origin and an alteration product of biotite. Two types of titanite show distinctly different crystal habits, optical properties and compositions. Igneous titanite contains lower Al2O3 (1.20- 1.21 wt. %) whereas hydrothermal titanite contain high Al_2O_3 ranging from 2 to 6 wt. % (Fig. 10 C). Igneous titanite forms euhedral tabular crystals (>1 mm long and >0.3 mm wide), shows brown hue with high relief. Igneous titanite is observed in samples GBR-13, -16, and -22. Hydrothermal titanite is observed in most samples within the aggregates of chlorite and epidote, and in chlorite-quartz veins. It forms needles (<50μm in length, <10μm in width; Figs. 8, 9 A). Hydrothermal titanite is almost opaque in thin sections under transmitted light.

Table 2. Major element concentrations of titanite in wt.%.

Sample	**Grain#**	**SiO_2**	**TiO_2**	**Al_2O_3**	**$FeO_{(t)*}$**	**MnO**	**MgO**	**CaO**	**Na_2O**	**V_2O_3**	**Total**
Alteration Titanite											
GBR-	1	36.7	31.2	5.72	1.9	<0.1	<0.1	23.4	1.18	<0.1	100.1
GBR-	2	32	32.7	4.99	1.8	<0.1	<0.1	28.6	<0.1	<0.1	100.09
GBR-	3	31.6	32.7	4.95	2.9	<0.1	0.96	25.9	<0.1	1.05	100.06
GBR-	4	31.5	33.2	5.4	1.9	<0.1	0.56	27.5	<0.1	<0.1	100.06
GBR-	5	30.3	33.6	5.1	4.4	<0.1	3.13	23.5	<0.1	<0.1	100.03
GBR-	6	31.6	34.2	4.92	0.9	<0.1	<0.1	28.3	<0.1	<0.1	99.92
GBR-	7	39.5	34.4	1.14	1.5	<0.1	<0.1	23.4	<0.1	<0.1	99.94
GBR-	8	29.9	34.9	5.76	1.6	<0.1	0.57	27.2	<0.1	<0.1	99.93
GBR-	9	31.3	35.7	4.08	0.5	<0.1	<0.1	28.4	<0.1	<0.1	99.98
GBR-	10	31.7	36	3.04	1.8	0.22	1.14	26.1	<0.1	<0.1	100
GBR-	11	31.8	36.6	1.92	1.9	<0.1	0.6	27.2	<0.1	<0.1	100.02
GBR-	12	31.2	37	2.6	0.9	<0.1	<0.1	28.2	<0.1	<0.1	99.9

GBR-	13	30.9	37.7	3.09	1.7	<0.1	<0.1	26.6	<0.1	<0.1	99.99
GBR-	14	30.6	37.7	3.23	2.1	<0.1	<0.1	26.4	<0.1	<0.1	100.03
GBR-	15	30.9	38.1	2.24	1	<0.1	<0.1	27.7	<0.1	<0.1	99.94
GBR-	16	31	38.2	2.03	1.1	<0.1	<0.1	27.6	<0.1	<0.1	99.93
GBR-	17	30.8	38.3	1.78	0.8	<0.1	<0.1	28.3	<0.1	<0.1	99.98
GBR-	18	32.2	38.3	1.4	1.5	<0.1	<0.1	26.6	<0.1	<0.1	100
GBR-	19	31	38.5	3	1.6	<0.1	0.41	25.6	<0.1	<0.1	100.11
Igneous Titanite											
GBR-	20	30.9	38.7	1.3	1.9	<0.1	<0.1	27.1	<0.1	<0.1	99.9
GBR-	21	30.1	38.7	1.2	2.4	<0.1	<0.1	27.7	<0.1	<0.1	100.1
GBR-	22	30.3	38.8	1.3	1.8	<0.1	<0.1	27	<0.1	<0.1	99.2
GBR-	23	31	38.8	1.6	0.5	<0.1	<0.1	28.1	<0.1	<0.1	100
GBR-	24	31.9	38.9	1.5	1.1	<0.1	<0.1	26.5	<0.1	<0.1	99.9
GBR-	25	30.6	39.1	1.2	1.5	<0.1	<0.1	27.6	<0.1	<0.1	100
GBR-	26	30.7	39.5	1.2	1.4	<0.1	<0.1	27.2	<0.1	<0.1	100

**Total Fe expressed as FeO (t)*

<u>Description of analyzed areas:</u>

1= elongate grain in contact with quartz and chlorite grains, 2= isolated grain in contact with chlorite grains within a chlorite- epidote-rich quartz vein, 3= elongate grain within a titanite aggregate in contact with chlorite grains, 4= tabular grain within a titanite aggregate in contact with other grains and rutile gains, 5= isolated grain surrounded by chlorite grains within a quartz vein, 6= isolate grain in contact with quartz and epidote within a chlorite-epidote rich quartz vein, 7= grain fracture filling fractures in a quartz grain, 8= Titanite grain within the centre of a chlorite aggregate within a quartz vein, in contact with rutile in the centre of the grain, 9= subhedral grain within a chlorite aggregate in a quartz veins, 10= isolated grain surrounded by chlorite grains within a quartz vein, 11= isolated grain surrounded by chlorite grains within a quartz vein, 12=isolated grain surrounded by chlorite grains within a quartz vein, 13= subhedral grain in the centre of a chlorite aggregate in a quartz vein, 14= subhedral grain in the centre of a chlorite aggregate in a quartz vein, 15= subhedral grain in the centre of a chlorite aggregate in a quartz vein, 16= subhedral grain in the centre of a chlorite aggregate in a quartz vein, 17= subhedral grain in contact with epidote and chlorite, 18= isolated grain surrounded by chlorite grains within a quartz vein,19= grain in contact with quartz containing rutile in its centre, 20= large euhedral titanite (<100 µm) in contact with quartz, 21= large euhedral titanite (<400 µm) in contact with quartz, 22= large euhedral titanite (<400 µm) in contact with quartz, 23= Small euhedral grain in contact with quartz and titanite, 24= subhedral grain with chalcopyrite and pyrite inclusions in contact with quartz and chlorite, 25= large euhedral grain (600 µm) surrounded by plagioclase and quartz, 26= large euhedral grain (600 µm) surrounded by plagioclase and quartz

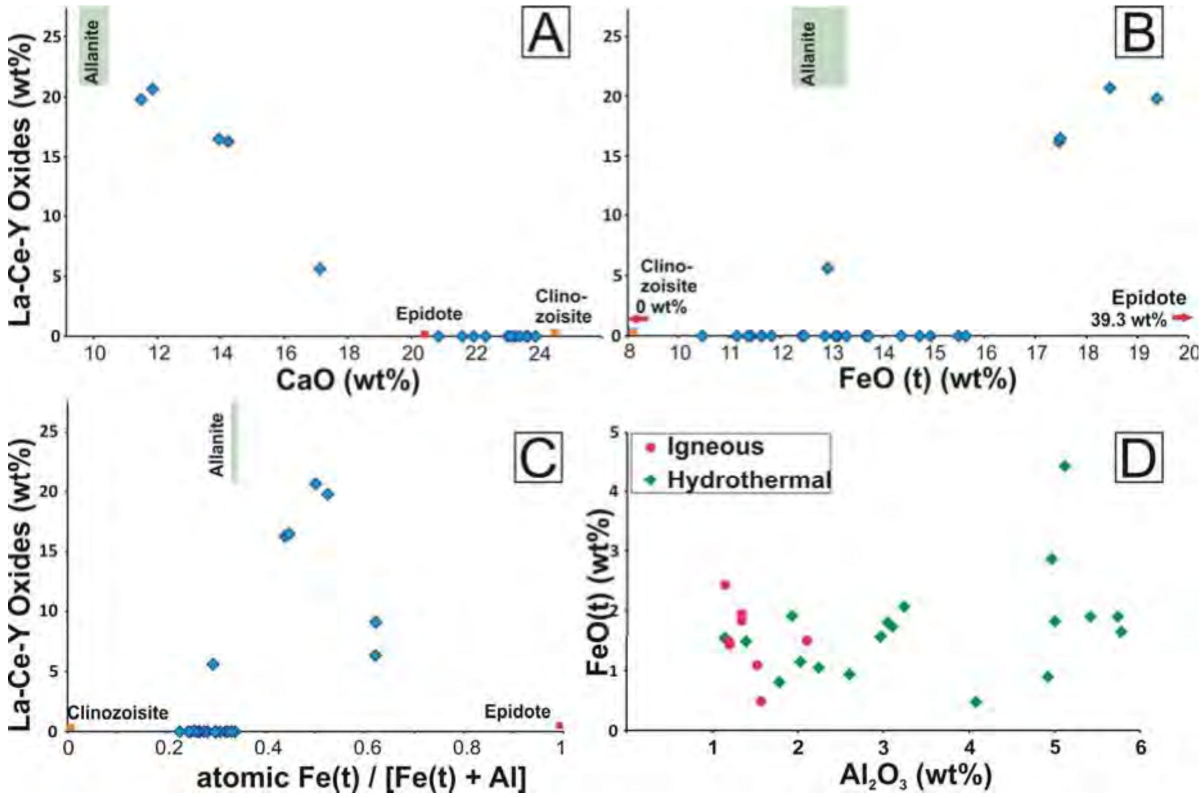

Figure 10. Binary plots of major element compositions of epidote (A, B, C) and titanite (D) in the samples. They show the end member components of epidote $Ca_2Al_2Fe^{III}(SiO_4)_3(OH)$, clinozoisite $Ca_2Al_3(SiO_4)_3(OH)$, and allanite $CaMAl_2Fe^{II}(SiO_4)_3(OH)$ where M is La, Ce or Y.

Rutile

Rutile in the samples is an alteration product of biotite. Rutile occurs with titanite in the aggregates of chlorite and epidote, and in chlorite-epidote veins as small elongated crystals (<20 m in length) within titanite aggregates in most cases. Rutile grains are opaque in thin sections under transmitted light and are disseminated within dark brown to opaque aggregates of titanite (Fig. 6 A). This makes it difficult to observe red coloration of rutile in thin sections. Large (approx. 0.2 mm long and <0.1mm wide), subhedral and red-colored rutile crystals have been observed in chlorite and epidote aggregates in 3 samples (GBR-10, -16, and -28). Rutile contains minor Al_2O_3 (up to 0.3 wt.%) and CaO (up to 3.7 wt.%) suggesting it may be derived from titanite since rutile is rimmed by titanite within altered chlorite (Fig 6 A).

Table 3. Major element concentrations of rutile expressed in wt. %

Sample	Grain #	SiO_2	TiO_2	Al_2O_3	CaO	$FeO_{(t)}$*	Total

GBR-04	1	1.4	96.5	0.3	1.2	0.5	99.9
GBR-	2	0.3	97.7	0.3	0.9	0.9	100.1
GBR-	3	1.8	95.8	0.2	1.6	0.6	100
GBR-	4	3.6	92.4	<0.1	3.7	0.4	100.1

**Total Fe expressed as FeO (t).*

Description of analyzed areas:

1= Grain in the centre of a titanite grain within a quartz vein, 2= Grain in the centre of a titanite grain within a chlorite aggregate in a quartz vein, 3= Grain in the centre of a titanite grain within a chlorite aggregate in a quartz vein, 4= Grain in the centre of a titanite grain within a quartz vein

Apatite

Apatite occurs in most samples (GBR-04, -10,-11,-13,-16,-21,-22,-30, and -32) and shows the typical bluish grey color in thin sections under crossed polarizers. It occurs within epidote-rich aggregates, relict plagioclase and the groundmass with plagioclase and quartz. Crystals are up to 100µm in length and are typically subhedral to anhedral (Fig. 6 G). Apatite grains in GBR-04, -13, -16, -28 and -30, are most likely primary igneous, as they occur as isolated euhedral crystal of approximately 100µm in length and 50µm in width, away from veins and intensely altered areas of samples. All grains have compositions close to the ideal formula of apatite. Several grains in Sample GBR-21 contain up to 0.4 wt. % MnO, which results in Mn/Ca molar ratios up to 0.006. Apatite composition in till and bedrock near porphyry deposits of British Columbia was studied by Rukhlov et al. (2016) and Bouzari et al. (2011). They found using EPMA technics on pristine apatite grains from till near Gibraltar that average Mn content yielded logfO_2-14.1 ±0.7 and apatite showed weak positive Ce anomalies (1.00 and 1.24) and strong negative Eu anomalies (0.11 and 0.47). They suggest that higher Mn content coupled with low Mg and Sr content and strong negative Eu anomalies points to a more fractionated magma.

Table 4. Apatite compositions expressed in wt %

Sample	Grain #	SiO_2	$FeO_{(t)*}$	MnO	CaO	P_2O_5	Total
GBR-	1	<0.1	0	<0.1	55.8	44.2	100
GBR-	2	<0.1	0.2	<0.1	55.1	43.9	99.2
GBR-	3	0.9	0.3	0.4	54.1	44.3	100
GBR-	4	1	<0.1	0.4	54.4	44.2	100

**Total Fe expressed as FeO (t)*

Description of analyzed areas:

1= large subhedral grain (100 m in length) in a chlorite aggregate within a epidote quartz vein, 2= large subhedral grain (100 m in length) in a chlorite-epidote aggregate, 3= small grain (<50 m) surrounded by chlorite, 4= small isolate grain (<30 m) surrounded by quartz, 5= large euhedral grain (250 m in length) in contact with chlorite and epidote altered plagioclase.

Summary

This study shows an alteration assemblage of epidote, chlorite, rutile, titanite ± magnetite, ± hematite associated with the Gibraltar porphyry Cu-Mo deposits. Among these alteration minerals, epidote is ubiquitous throughout the Granite Mountain batholith.

Preliminary analyses of the compositions of epidote, titanite, and rutile show very large variations. Some epidote grains contain more than 10 wt.% Ce_2O_3 and more than 5 wt.% La_2O_3, approaching allanite. Based on a comparison with the reported epidote composition near porphyry mineralization, the Ce and La enrichment in epidote at Gibraltar could be a diagnostic feature of epidote associated with mineralization.

Acknowledgements

Jeffrey Hedenquist is thanked for his help during the field work in July 2015. The project was supported by Discovery Grant from Natural Science and Engineering Council of Canada to KH. This project is part of the M.Sc. thesis of C.K. Neil Rogers completed the internal GSC review. ESS Contribution number 20150489.

References

Armbruster, T., Bonazzi, P., Akasaka, M., Bermanec, V., Chpin, C., Giere, R., Heuss-Assbichler, S., Liebscher, A., Menchetti, S., Pan, Y., and Pasero, M., 2006. Recommended nomenclature of epidote-group minerals; European Journal of Mineralogy, v. 18, p. 551-567.

Ash, C.H., Panteleyev, A., MacLellan, K.L., Payne, C.W., and Rydman, M.O., 1999a. Geology of the Gibraltar Mine area (93B/6&9); British Columbia Ministry of Energy and Mines; Open File 1999-7, scale 1:50 000.

Ash, C.H., Rydman, M.O., Payne, C.W., and Panteleyev, A., 1999b. Geological setting of the Gibraltar mine south central British Columbia (93B/8, 9); *in* Exploration and Mining in British Columbia 1998, British Columbia Ministry of Energy and Mines, p. A1-A15.

Ash, C.H., and Riveros, C.P., 2001. Geology of the Gibraltar copper-molybdenite deposit, east-central British Columbia (93B/9); *in* Geological Fieldwork 2000, British Columbia Ministry of Energy and Mines, Paper 2001-1, p. 119-134.

Bouzari, F., Hart, C.J.R., Barker, S., and Bissig, T., 2011. Porphyry indicator minerals (PIMS): a new exploration tool for concealed deposits in south-central British Columbia; Geoscience BC Report 2011-17, 31 p.

Bysouth, G.D., Campbell, K.V., Barker, G.E., and Gagnier, G.K., 1995. Tonalite-trondhjemite fractionation of a peraluminous magma and the formation of syntectonic porphyry Cu mineralization, Gibraltar mine, central British Columbia; *in* Porphyry Deposits of the Northwestern Cordillera of North America, (ed.) T.G. Schroeter; Canadian Institute of Mining, Metallurgy and Petroleum, Special Volume 46, p. 201–213.

Cooke, D.R., Baker, M., Hollings, P., Sweet, G., Chang, Z., Danyushevsky, L., Gilbert, S. Zhou, T., White, N.C., Gemmell, J.B., and Inglis, S., 2014. New advances in detecting the distal geochemical foot prints of porphyry systems-epidote mineral chemistry as a tool for vectoring and fertility assessments; Economic Geology Special Publication, v.18, p. 127-152.

Drummond, A.D., Tennant, S.J., and Young, R.J., 1973. The interrelationship of regional metamorphism, hydrothermal alteration and mineralization at the Gibraltar mines copper deposit in B.C.; Canadian Mining and Metallurgical Bulletin, v. 66, p. 48-55.

Drummond, A.D., Sutherland Brown, A., Young, R.J., and Tennant, S.J., 1976. Gibraltar - Regional metamorphism, mineralization, hydrothermal alteration and structural development; *in* Porphyry deposits of the Canadian Cordillera, (ed.) A. Sutherland Brown; Canadian Institute of Mining and Metallurgy, Special Volume 15, p. 195-205.

Grunsky, E., Lefebure, D., and Jones, L., 1996. Grade and tonnage data for selected deposit types; *in* Selected British Columbia Mineral Deposit Profiles, (eds.) D.V. Lefebure and T. Höy; British Columbia Geological Survey Open File 1996-13, p. 121–146.

Jones, S., 2015. 43-101 of the Gibraltar mine as of December 2014 http://sedar.com/FindCompanyDocuments.do and http://www.tasekomines.com/gibraltar/ID540174

Logan, J.M., Schiarizza, P., Struik, L.C., Barnett, C., Nelson, J.L., Kowalczyk, P., Ferri, F., Mihalynuk, M.G., Thomas, M.D., Gammon, P., Lett, R., Jackaman, W., and Ferbey, T. (compilers), 2010. Bedrock geology of the Quest map area, central British Columbia; Geoscience BC Report 2010-5, British Columbia Geological Survey, Geoscience Map 2010-1 and Geological Survey of Canada Open File 6476, scale 1:500 000.

Massey, N.W.D., MacIntyre, D.G., Desjardins, P.J., and Cooney, R.T., 2005. Digital Geology Map ofBritish Columbia - Whole Province, British Columbia Ministry of Energy and Mines, GeoFile 2005-1.

Masumoto, Y., Enami, M., Tsuboi, M., and Hong, M., 2014. Magmatic zoisite and epidote in tonalite of the Ryoke belt, central Japan; European Journal of Mineralogy, v. 26, p.279-291.

Oliver, J., Crozier, J., Kamionko, M., and Fleming, J., 2009. The Gibraltar Mine, British Columbia. A billion tonne deep copper-molybdenum porphyry system: structural style, patterns of mineralization and rock alteration; Association for Mineral Exploration British Columbia, 2009 Mineral Exploration Roundup, Vancouver, British Columbia, Abstracts, p. 35-36.

Panteleyev, A., 1978. Granite Mountain project (93B/8); *in* Geological Fieldwork 1977, British Columbia Ministry of Energy and Mines, British Columbia Geological Survey, Paper 1978-1, p. 39-42.

Plouffe, A., and Ferbey, T., 2015. Till composition near Cu-porphyry deposits in British Columbia: Highlights for mineral exploration; *in* TGI 4 - Intrusion Related Mineralisation Project: New Vectors to Buried Porphyry-Style Mineralisation, (ed.) N. Rogers; Geological Survey of Canada, Open File 7843, p. 15-37.

Plouffe, A., Ferbey, T., and Anderson, R.G., 2014. Till composition and ice-flow history in the region of the Gibraltar Mine: developing indicators for the search of buried mineralization; Geological Survey of Canada, Open File 7592, poster.

Roache, T.J., Walshe, J.L., Huntington, J.F. Quigley, M.A., Yang, K., Bil, B.W., Blake, K.L., and Hyvarinen, T., 2011. Epidote-clinozoisite as a hyperspectral tool in exploration for Archean gold. Australian Journal of Earth Sciences, v. 58, p. 813-822.

Rukhlov, A.S., Plouffe, A., Ferbey, T., Mao, M., and Spence, J., 2016. Application of trace-element compositions of detrital apatite to explore for porphyry deposits in central British Columbia *in* Geological Fieldwork 2015, British Columbia Ministry of Energy and Mines, British Columbia Geological Survey, Paper 2016-1, p. 145-179.

Schiarizza, P., 2014. Geological setting of the Granite Mountain batholith, host to the Gibraltar porphyry Cu-Mo deposit, south-central British Columbia; *in* Geological Fieldwork 2013, British Columbia Ministry of Energy and Mines, British Columbia Geological Survey, Paper 2014-1, p. 95-110.

Schiarizza, P., 2015. Geological setting of the Granite Mountain batholith, south-central British Columbia; British Columbia Ministry of Energy and Mines, GeoFile 2015-5, poster.

Schmidt, M.W., and Poli, S., 2004. Magmatic epidote; *in* Epidote (eds.) Axel Libscher and Gerhard Franz; Reviews in Mineralogy and Geochemisty, v.56, p. 399-430.

Shannon, K.R., 1982. Cache Creek Group and contiguous rocks, near Cache Creek, British Columbia, Unpublished MSc thesis, University of British Columbia, 72 p.

Wilkinson, J.J., Chang, Z., Cooke, D.R., Baker, M.J., Wilkinson, C.C., Inglis, S., Chen, H., and Gemmell, B.J., 2015. The chlorite proximitor: A new tool for detecting porphyry ore deposits; Journal of Geochemical Exploration, v. 152, p. 10-26.

Addendum: Origin of apatite clarification

Appendix 8 briefly discusses the origins of apatite. Apatite is wrongly placed within the alteration assemblage type 3 in the hydrothermal alteration and alteration minerals section above. If apatite was a hydrothermal product there would need to be a mineral with the chemical elements necessary to form it (eg. P and Ca). Many studies of porphyry-Cu deposit use apatite as an indicator of various magmatic processes (degree of assimilation/fractionation, characteristics of mantle fluids and magmatic oxidation states; Bouzari et al., 2015 and references therein). Apatite is most likely magmatic in the GMB. However, apatite composition can be subsequently affected by hydrothermal fluids. A recent study of apatite from several porphyry-Cu deposits in British Columbia, Canada, found that magmatic apatite from unaltered and least altered rocks associated with these deposits was different (changes in luminescence, Mn, S, REE, Fe, Na, Cl content and Mn/Fe ratios) then apatite associated with potassic and sericite altered rocks (Bouzari et al., 2015).

References in addendum

Bouzari, F., Hart, C. J., Bissig, T., and Barker, S. 2016, Hydrothermal alteration revealed by apatite luminescence and chemistry: a potential indicator mineral for exploring covered porphyry copper deposits. Economic Geology, v. 111(6), p. 1397-1410.